EROSION: Prevention and Useful Applications

W. F. Adler, *editor*

ASTM STP 664

AMERICAN SOCIETY FOR TESTING AND MATERIALS

EROSION: PREVENTION AND USEFUL APPLICATIONS

A symposium
sponsored by ASTM
Committee G-2 on
Erosion and Wear
AMERICAN SOCIETY FOR
TESTING AND MATERIALS
Vail, Colo., 24-26 Oct. 1977

ASTM SPECIAL TECHNICAL PUBLICATION 664
W. F. Adler, Effects Technology Inc.
editor

List Price $55.00
04-664000-29

AMERICAN SOCIETY FOR TESTING AND MATERIALS
1916 Race Street, Philadelphia, Pa. 19103

Library of Congress Catalog Card Number: 78-068438

NOTE

The Society is not responsible, as a body,
for the statements and opinions
advanced in this publication.

Printed in Baltimore, Md.
February 1979

Foreword

The papers contained in this Special Technical Publication are an outgrowth of the papers presented at the American Society for Testing and Materials Symposium on Erosion: Prevention and Useful Applications sponsored by Committee G-2 on Erosion and Wear. The symposium was held in Vail, Colo., 24-26 Oct. 1977. Dr. W. F. Adler, Effects Technology, Inc., Santa Barbara, Calif., Dr. D. A. Summers, University of Missouri, Rolla, Mo., and Dr. Fun-Den Wang, Colorado School of Mines, Golden, Colo., were members of the organizing committee. This was the fifth symposium on erosion to be sponsored by ASTM. Previous symposia were held in 1961, 1966, 1969, and 1973.

Related ASTM Publications

Erosion, Wear, and Interfaces with Corrosion, STP 567 (1974), $35.00, 04-567000-29

Unified Numbering System for Metals and Alloys, DS 56A (1977), $49.00, 05-056001-01

A Note of Appreciation to Reviewers

This publication is made possible by the authors and, also, the unheralded efforts of the reviewers. This body of technical experts whose dedication, sacrifice of time and effort, and collective wisdom in reviewing the papers must be acknowledged. The quality level of ASTM publications is a direct function of their respected opinions. On behalf of ASTM we acknowledge with appreciation their contribution.

ASTM Committee on Publications

Editorial Staff

Contents

Introduction

Erosion of materials is becoming more generally recognized as a restraint on engineering designs which can no longer be ignored. Performance restrictions on the useful life of blading in gas and steam turbines due to particle impacts, all-weather requirements for supersonic aircraft, helicopters operating in sandy terrains, high-performance marine vehicles, and the extended operation of coal conversion plants are illustrations of the significance of erosion in engineering practice.

On the other hand, the destructive aspects of the erosion process are being effectively utilized and enhanced in the development of liquid jets for a variety of applications in drilling, tunneling, rock cutting, and mining. Useful applications of waterjets for cutting and cleaning are also becoming more evident. High-speed precision cutting of fabric, jigsaw puzzles, and high-volume mining of coal exemplify the range of materials in which cutting jets are used, while jet cleaning uncovers airport runways, buildings, and chemical plant components, as well as having submarine applications.

The investigations presented in this publication form the basis for technical information concerning a broader range of erosion-related topics than is normally assembled in one source. The information provided is intended to expose an audience composed of diverse backgrounds to current advances in the field of erosion as well as to some of the major problem areas requiring attention. Unfortunately not all areas in which erosion is important are represented; however, an attempt has been made to provide an interchange of ideas between those who view erosion as a blessing and those who view it as a problem.

The papers in this volume on solid particle erosion provide a balanced perspective of the current work on understanding microscopic erosion mechanisms, correlation of erosion data with material properties, testing and evalution procedures, and application of the test data to operating systems. There is now a need for studying erosive effects at elevated temperatures and in conjunction with chemically active environments. Some initial efforts in these directions are reported in several of the papers.

Current work on liquid drop impingement from both a numerical analysis and materials approach is presented. The use of high-velocity jets to simulate rain erosion effects is also included along with representative work on the response of carbon-carbon materials exposed to hypervelocity particle impacts.

The observations pertaining to liquid impact and cavitation erosion damage may provide important insights into the effectiveness of liquid jet cutting and cleaning. This association has not been adequately exploited; however, the work reported on waterjets should be useful in establishing potential relationships. The papers on waterjets emphasize the many areas of application where they can be effectively utilized, the range of concepts pertaining to the most efficient and practical means for cutting or cleaning, and a much needed initial assessment of how one system can be compared with another.

W. F. Adler
Effects Technology, Inc., Santa Barbara, Calif. 93111; editor.

Solid Particle Impingement

L. K. Ives[1] *and A. W. Ruff*[1]

Electron Microscopy Study of Erosion Damage in Copper

REFERENCE: Ives, L. K. and Ruff, A. W., "**Electron Microscopy Study of Erosion Damage in Copper**," *Erosion: Prevention and Useful Applications, ASTM STP 664*, W. F. Adler, Ed., American Society for Testing and Materials, 1979, pp. 5–35.

ABSTRACT: Solid-particle erosion data have been reported for many materials. The mechanics of the impact process has also been examined. However, relatively little effort has been expended in studying the microstructural aspects of material response to erosion. Effects such as deformation hardening, plastic flow, and particle embedding are recognized as being important but have not been subjected to careful study. Understanding the erosion mechanism at large attack angles and accounting for differences in erosion behavior of different metals and alloys are areas where knowledge of materials response factors will be most important. In the present work surface and subsurface erosion damage in copper is investigated by transmission and scanning electron microscopy techniques.

KEY WORDS: erosion, impingement erosion, copper, wear, electron microscopy, metal erosion

The erosion of metals by solid particles is often compared mechanistically to a metal cutting or grinding operation, on a small scale. In this treatment, different properties of metals are usually distinguished by a single parameter related to strength, such as hardness [*1*].[2] Perhaps the most significant success of this approach—and certainly one of the most important milestones in understanding erosion—was Finnie's [*2*] model relating solid-particle impingement erosion of ductile metals to a micro-machining process. Using this model, Finnie was able to account correctly for the maximum in erosion rate that occurs near 20 deg, Fig. 1. The model did not, however, predict the substantial erosion that occurs at large attack angles. Bitter [*3*], noting that brittle materials exhibit a maximum in erosion rate at normal incidence (Fig. 1) and, furthermore, recognizing that ductile materials work-harden and eventually fail by microfracture processes, proposed that the angular de-

[1]Physicist and acting division chief, respectively, Metallurgy Division, National Bureau of Standards, Washington, D.C. 20234.

[2]The italic numbers in brackets refer to the list of references appended to this paper.

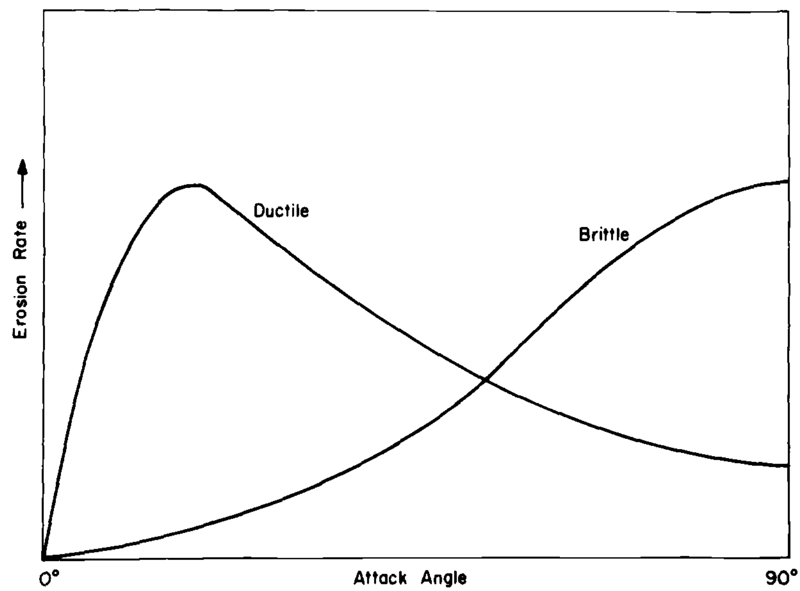

FIG. 1—*Dependence of erosion rate on attack angle is shown schematically for ductile and brittle materials.*

pendence of erosion could be regarded as the superposition of ideally ductile (cutting mode) and brittle (deformation mode) behaviors. Several modifications and improvements to these models have been made [*4–8*] and additional mechanisms have been proposed recently [*9,10*]. While a much better picture of the mechanics of material removal has been gained, principally through the single-particle studies of Hutchings et al [*11*], little effort has been reported on material response at the microstructural level.

Reference is often made in erosion studies to such effects as plastic flow, work-hardening, recovery, fracture, and particle embedding, but little relevant information detailing these phenomena has been published. Understanding the erosion mechanism at large attack angles, predicting the erosion behavior of different metals and alloys, and accounting for the effects of elevated temperatures and chemically active environments are areas where knowledge of materials response factors will be most needed.

In the present investigation techniques of scanning electron microscopy (SEM) and transmission electron microscopy (TEM) are used to study microstructural features associated with multiple particle erosion damage to a ductile metal, namely, copper.

Experimental Procedure

Erosion test specimens were prepared from OFHC copper, ASTM B170

Grade 1. Specimens 1 cm square were cut from 2-mm-thick cold-rolled sheet and annealed under vacuum for 24 h at 1000°C, producing a grain size of approximately 1 mm. Immediately prior to erosion exposure, each specimen was electropolished in a solution composed of equal parts of phosphoric acid (H_3PO_4) and water (H_2O.)

Tests were conducted in air at approximately 23°C and a relative humidity of 50 percent. Two particle velocities, 20 and 60 m/s, were employed, providing approximately one order of magnitude difference in erosion rate. Particle velocities were measured by the rotating-disk method [*12*]. Attack angles of 20 and 90 deg were studied at each velocity with the intention of comparing material response under so-called cutting and deformation modes of erosion. For convenience, we shall use the notation (velocity-attack angle) when identifying specimens.

A schematic drawing of the erosion test device is shown in Fig. 2. This device, fitted for high-temperature operation, has been described previously [*13*]. An important feature with respect to the present study concerns the fact

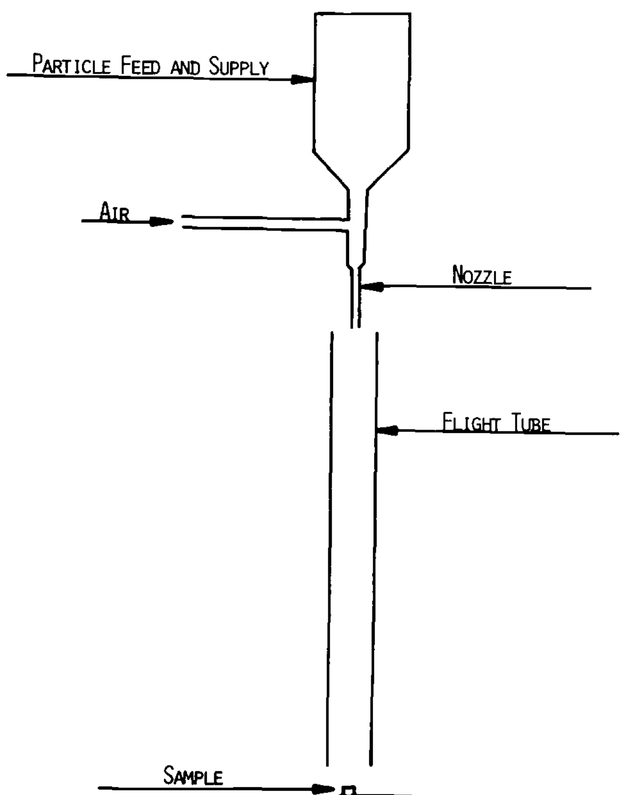

FIG. 2—*Schematic drawing of erosion test device.*

that the entire 1-cm-square face of the test specimen could be immersed in the beam of particles. Thus, a relatively large uniformly eroded surface area was provided for subsequent specimen preparation and study.

The erosive particle material was a high-purity grade of Al_2O_3 (99.28 percent according to the supplier). The nominal particle diameter was specified as 50 μm, and the size distribution given was such that approximately 80 percent by weight of the particles were in the range 35 to 65 μm. A collection of particles is shown in Fig. *3a*. On close examination it was found that each of the primary particles was covered with a fine Al_2O_3 particulate dust as shown in Fig. *3b*.

In most cases, specimens for microscopic examination were prepared in duplicate. One set of specimens was used for direct study of the eroded surface in the SEM while the other set was cross sectioned and used in both SEM and TEM studies. Prior to sectioning the specimens, a layer of copper approximately 1.5 mm thick was electrodeposited on the eroded surface. This electrodeposition step was carried out immediately after erosion was terminated without any additional treatment to the surface. The plating bath was an aqueous solution of 250 g/litre $CuSO_4 \cdot 5H_2O$ and 75 g/litre H_2SO_4. Plating was carried out at a current density of 40 to 60 mA/cm^2 and a temperature of 23°C. As illustrated in Fig. 4, the specimens were sectioned along a plane that was perpendicular to the eroded surface and parallel to the direction of the eroding particle stream. Sectioning was carried out with a spark erosion cutting machine.

Slices 1 mm thick (Fig. 4) were taken for SEM and TEM specimens. These slices were thinned to 0.1 to 0.2 mm either by etching in a 1:1 (by volume) solution of concentrated mitric acid (HNO_3) and H_2O or chemically polishing at 45°C in a solution consisting of equal parts of HNO_3, acetic acid (CH_3COOH), and H_3PO_4. After electropolishing in the 50 percent H_3PO_4 solution, these slices were suitable for SEM study, both for the purpose of examining the interface structure and obtaining selected area electron channeling patterns. Further electropolishing produced electron transparent regions ($<$0.5 μm thick) suitable for TEM study at 200 kV. In some cases, additional thinning was carried out by ion beam bombardment with 3 to 4 kV argon ions at 15 deg. This method was particularly useful in thinning the outermost eroded surface layer, which in most cases contained a significant concentration of embedded AL_2O_3 particles.

Results and Discussion

Erosion Rate Results

Values for the erosion rate of copper obtained in this investigation are plotted in Fig. 5 together with data on copper collected from the literature. The usual log-log representation is employed and straight lines were fitted to the

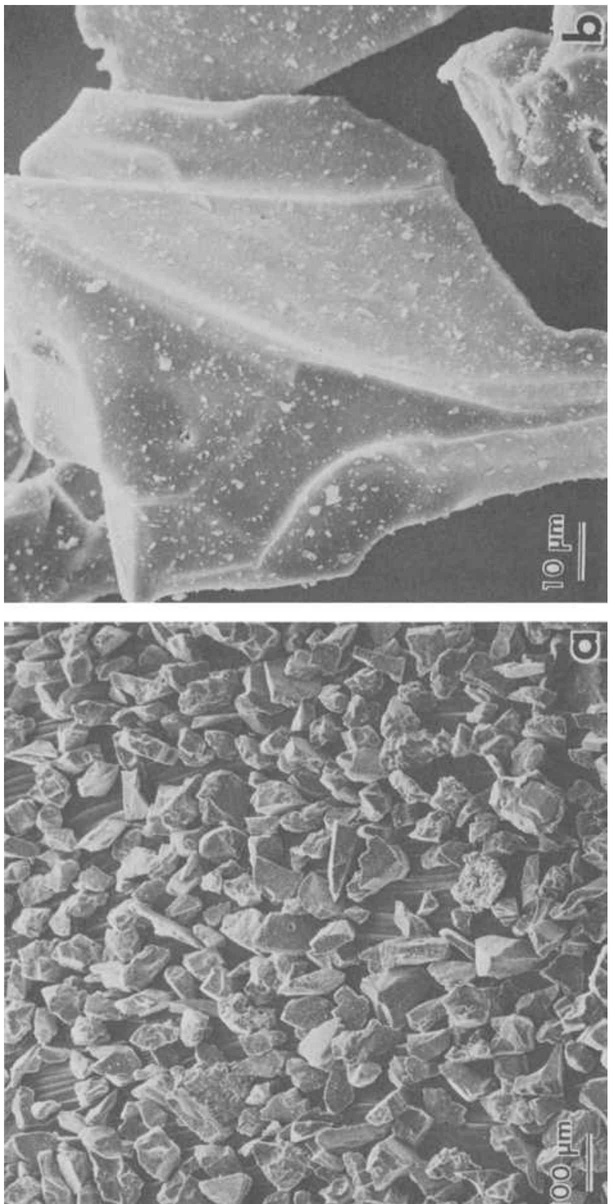

FIG. 3—(a) 50-μm Al_2O_3 erosion particles. (b) Fine Al_2O_3 dust attached to particles.

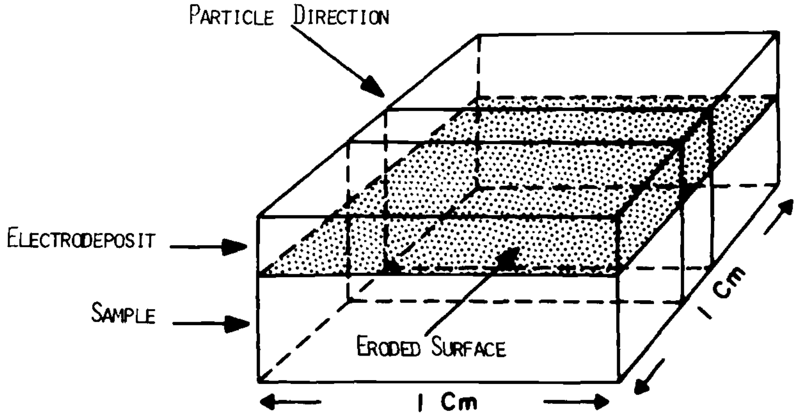

FIG. 4—*Schematic drawing of erosion test specimen after copper has been electrodeposited on eroded surface. Specimen was sectioned perpendicular to eroded surface for subsurface examination.*

data by a least-squares analysis to reflect the expected power law relationship between velocity and erosion rate. The consistency among these data is surprisingly good when one realizes that the various points refer to tests that were conducted with a wide variety of different particle types, sizes, and fluxes, and different test apparatus. The only criteria used in selecting data were that the material be "pure" copper and the attack angle be either 20 or 90 deg. The slope of 2.4 at 20 deg is in good agreement with a value of 2.3 which is found for most metals [*6*]. The slope of 2.8 at 90 deg appears somewhat high; however, in view of the small amount of data at this angle, this departure may not be significant. The erosion rates obtained in this study at 60 m/s appear somewhat low relative to the other data. It is not known at this time whether this results from test materials and conditions or is due to experimental scatter.

The relationship between erosion rate and accumulated mass of particle exposure is shown in Fig. 6. At 90 deg for both 20 and 60 m/s there is a brief induction period in which specimen mass first increases and then decreases. This is followed by the attainment of a steady-state condition of linear mass loss. The slope of the specimen mass change versus exposure curve is the erosion rate. The initial increase in mass is, of course, the result of embedment or deposition of erosion particles. This effect has been discussed previously by Nielson and Gilchrist [*4*] and is characteristic of many ductile materials. Nielson and Gilchrist found that the length of the induction period decreased with increasing velocity, as is the case here. At low angles, deposition is substantially less. No increase in weight was detected at 20 deg. The induction period shown in Fig. 6 consisted of a slight increase in erosion rate leading to the steady-state condition.

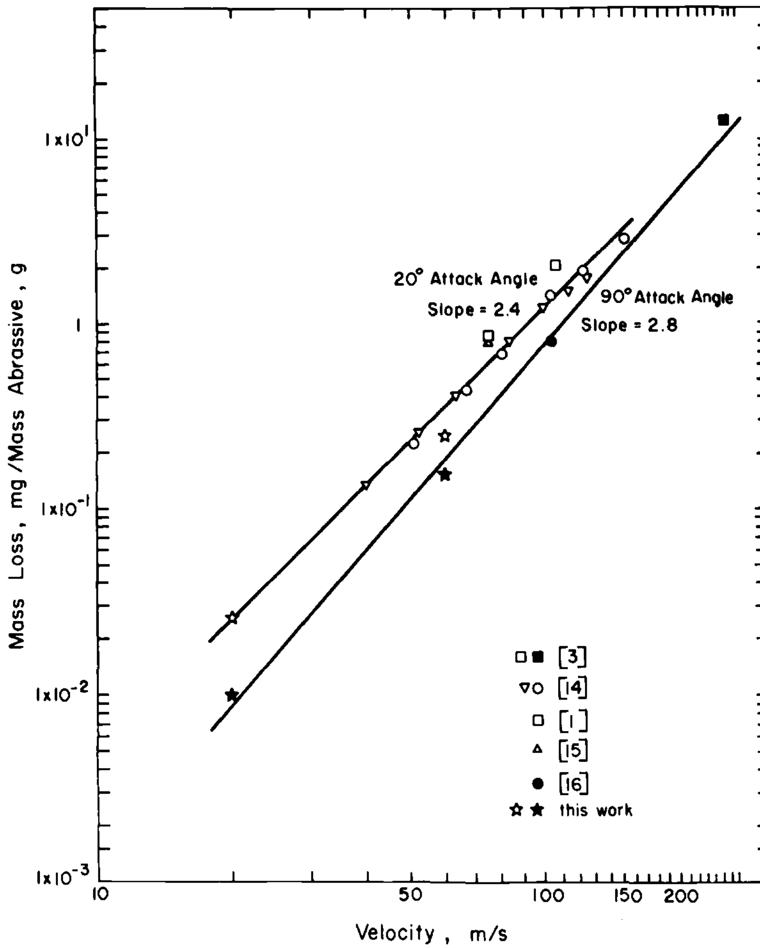

FIG. 5—*Collected erosion results (see references) for copper at attack angles of 20 and 90 deg. Straight lines represent a least-squares fit to the data.*

Specimens for microstructural examination were taken at three points on the weight-change versus exposure curves: (1) after a brief exposure producing isolated impacts on the surface, (2) during the initial stage of the induction period (at 90 deg while the specimen mass was still increasing), and (3) after a steady-state erosion condition had been attained. Points at which induction period and steady-state condition specimens were taken are indicated by arrows in Fig. 6. TEM studies were confined to the steady-state specimens.

Surface Topographic Features

In the following discussion, the results of a systematic SEM examination of

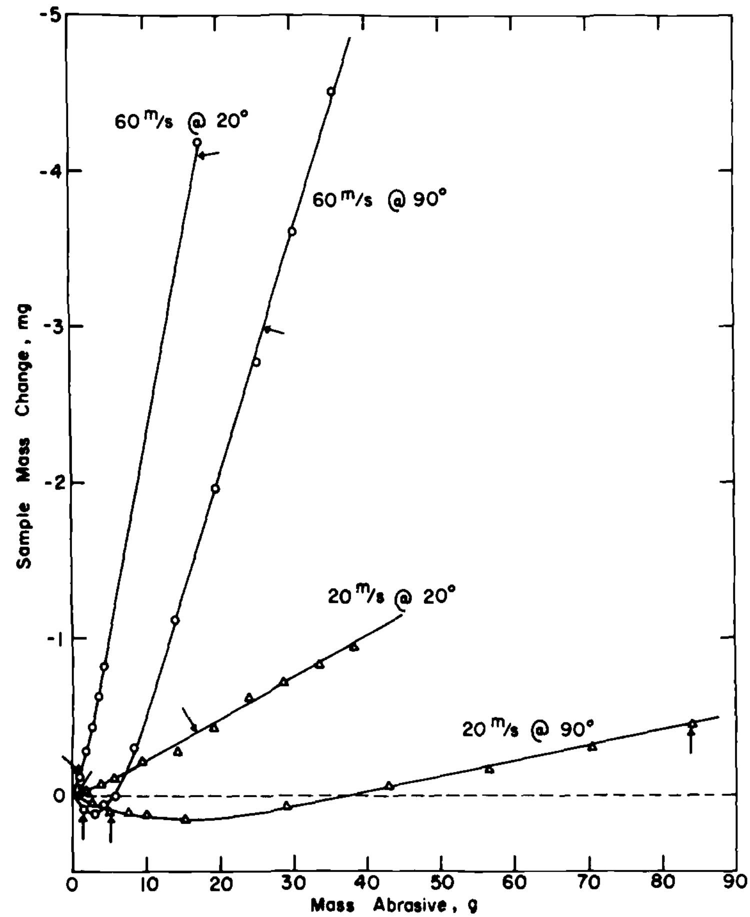

FIG. 6—*Dependence of specimen mass change on accumulated erosion exposure. Arrows indicate points at which specimens were prepared for microscopic study.*

surface topographic characteristics will be illustrated by a few representative examples. Figure 7 shows surfaces after brief exposure at 60 m/s at attack angles of 20 and 90 deg. The indentation size is somewhat larger at 90 deg; however, the indentation shapes are qualitatively similar without any apparent significant elongation in the direction of particle motion at 20 deg. The most important observation concerns the presence of a lip of material at the exit end of many 20 deg craters. Thus, material has been plowed or displaced from the crater and is now much more susceptible to complete removal by subsequent particle impacts. Hutchings et al [*11*] have made a detailed study of this crater-forming process using well-characterized large single particles. The observations made here appear to be in good agreement with their results. In most cases, material did not appear to be

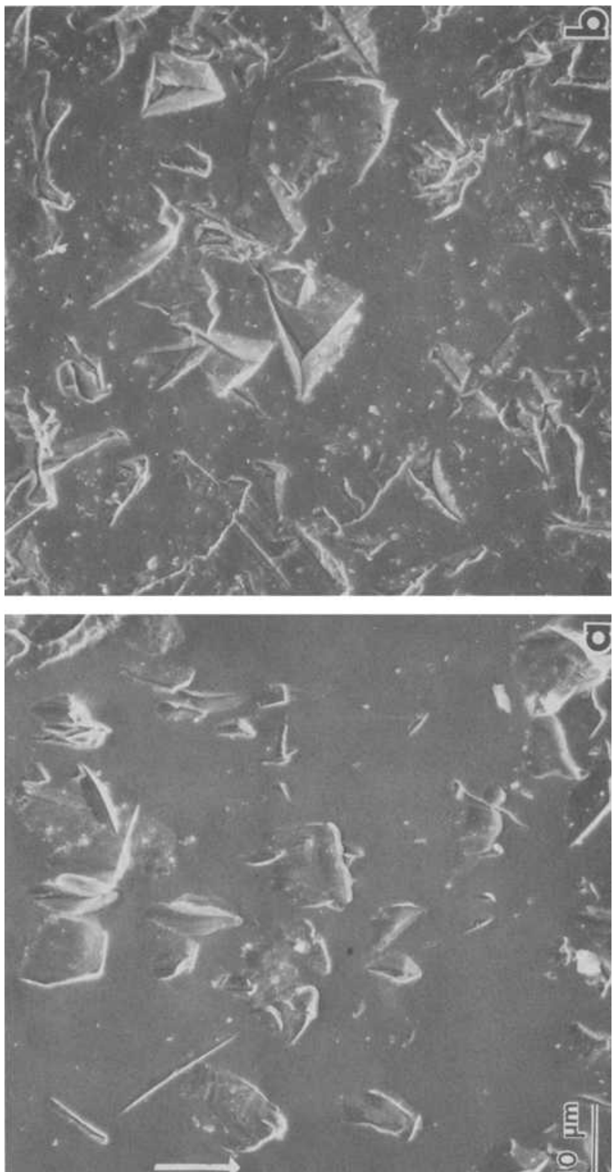

FIG. 7—SEM micrographs of annealed and electropolished copper surfaces after a few particle impacts at (a) *60 m/s, 20 deg and* (b) *60 m/s, 90 deg. Arrow in* (a) *indicates projected direction of particle motion.*

removed by the initial impact. Whether or not material is removed from a smooth surface on initial impact is a function of particle density, velocity, and attack angle [*11*].

A higher magnification view of the 60-m/s, 90-deg surface is shown in Fig. 8. An Al_2O_3 erosion particle 10 μm in diameter is seen embedded in the surface. The particle conforms to the bottom portion of a crater and has apparently fractured from a much larger particle. Since there are on the order of 2×10^6 particles per gram of 50-μm material, if even a small fraction of the incident particles leave embedded fragments, the concentration of embedded material will increase rapidly. This is demonstrated in the mass change versus exposure curves, Fig. 6. In addition to the large fragment, a quantity of fine "dust" particles has accumulated on the surface shown in Fig. 8. These particles appear to be loosely attached to the surface but in some cases have been pressed into the surface by larger impacting particles. These fine particles undoubtedly make a significant contribution to the net concentration of embedded material.

Surfaces eroded at a particle velocity of 60 m/s in the steady-state stage are shown in Fig. 9, where Fig. 9*a* and *b* were obtained at an attack angle of 20 deg and Fig. 9*c* and *d* at an attack angle of 90 deg. At 20 deg, features characteristic of isolated impact sites are still retained. In particular, the

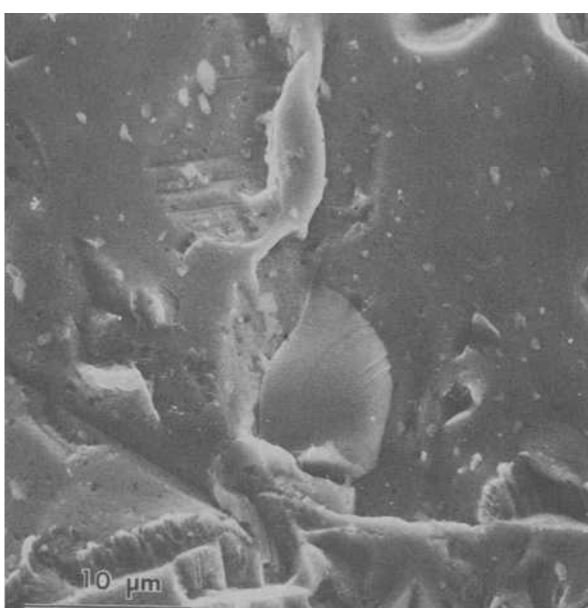

FIG. 8—*Large embedded Al_2O_3 fragment and fine dust particles after brief exposure at 60 m/s, 90 deg.*

ductile material response is still evidenced by the apparent plowing of material; lips are formed at the exit ends of craters. This response is clearly demonstrated in Fig. 9*b*.

Indentations formed at 90 deg, Fig. 9 *c*, also seem to result from plastic flow. However, examination at higher magnification, Fig. 9*d*, reveals a surface that appears to consist almost entirely of fragments derived both from the copper surface and the erosion particles. Development and eventual loss of this fragmented surface structure are apparently responsible for the attrition of surface material.

The examples shown in Fig. 7 to 9 and the accompanying discussion referred to specimens eroded at 60 m/s. Similar observations were made at 20 m/s, where the topography appeared to differ only with respect to the much smaller indentation size.

The topography developed under steady-state and induction-period conditions did not differ significantly at an attack angle of 90 deg. However, at 20 deg, where the induction period consisted of a slight increase in erosion rate, the induction-period specimen surfaces were incompletely covered with particle impacts. At a nominal crater diameter of 5 to 10 μm, a uniform distribution of 1×10^6 to 4×10^6 impacts would be required to completely cover the surface. This would correspond to 0.5 to 2 g of the 50-μm Al_2O_3 particles. Since the impacts are actually randomly distributed, this would represent a minimum quantity for complete coverage. This rough estimate agrees with the observed induction-period length of about 5 g at 20 m/s and 2 g at 60 m/s. Thus at 20 deg, steady-state erosion determined from mass loss measurements appears to commence once the surface is fully covered with particle impacts.

SEM Study of Cross Sections

Sections through steady-state surfaces exposed at 20 and 90 deg are shown in Fig. 10. The large-scale roughness of the surface reflects the size and depth of individual particle impacts. This can be seen by comparing Fig. 10*a* and *c* with Fig. 9*a* and *c*, respectively. Embedded Al_2O_3 erosion particles are present at both 20 and 90 deg but are more concentrated and extend to a greater depth at 90 deg. The embedded particles undoubtedly originate both through fracturing of large 50-μm-size particles and through accumulation of the fine dust that coats the larger particles. Most of the particle debris in the 20 deg surface is less than a micrometre in size, while a number of larger particles are embedded in the case of 90 deg impingement. The thickness of the embedded layer varies considerably at both attack angles. Locations can be found in Fig. 10*a* and *c* where there are no embedded particles. At 90 deg, there appear to be "pockets" of embedded particles. Plastic flow of the metal surface layer seems to play an important role in the embedding process. In Fig. 10*b* particles appear to have become trapped beneath layers of deformed

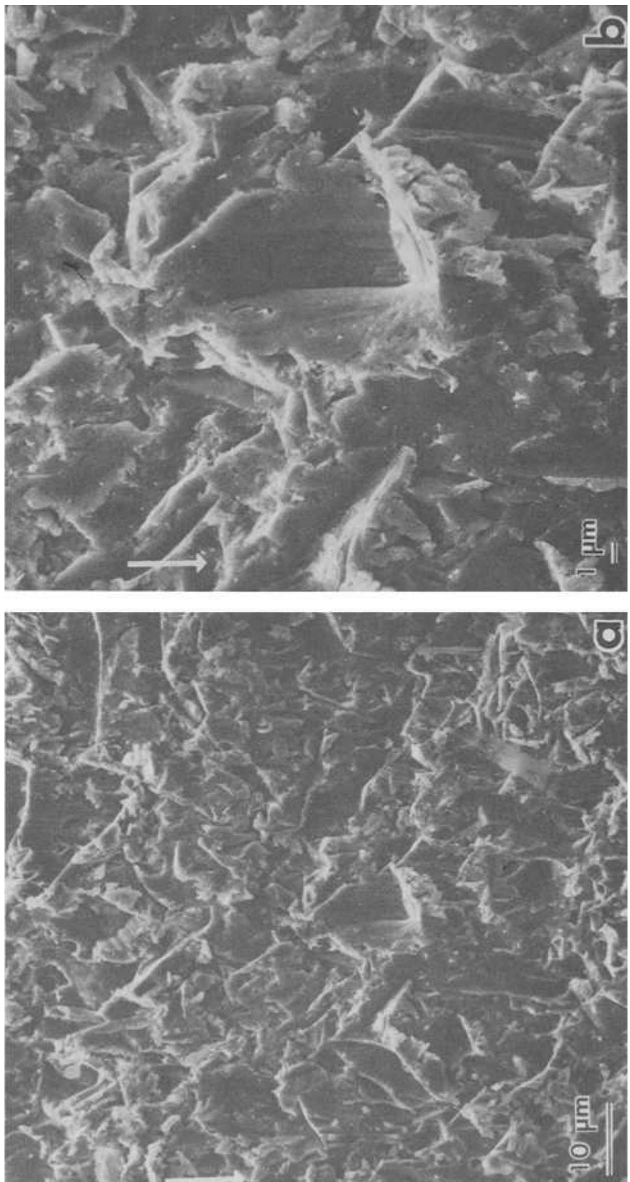
b
1 μm
a
10 μm

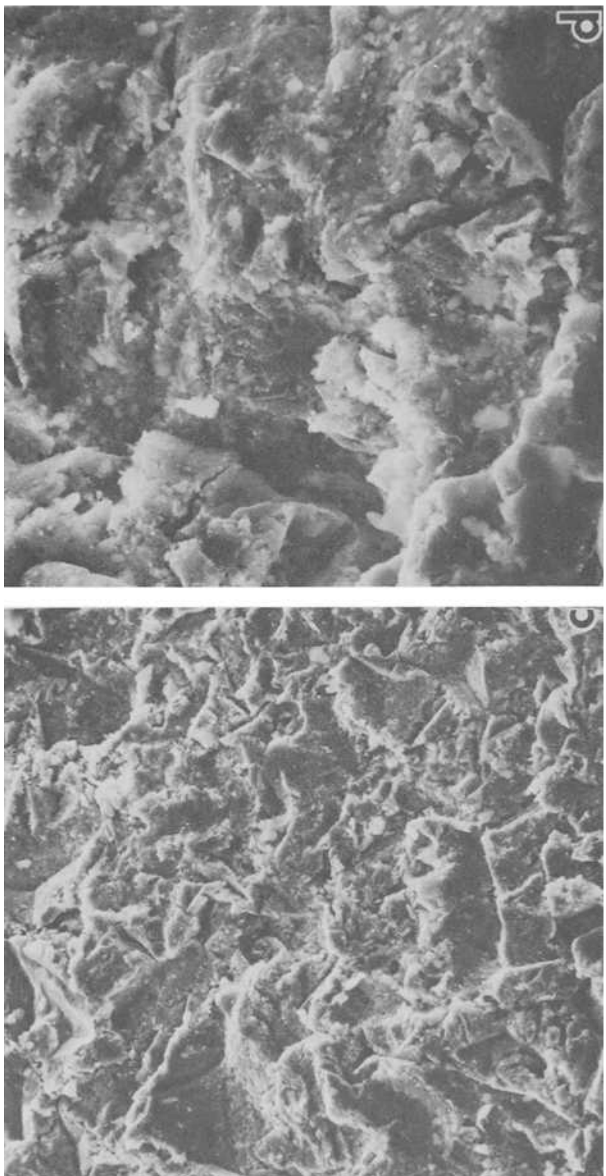

FIG. 9—SEM micrographs of surfaces exposed in steady-state regime. (a) and (b) at 60 m/s, 20 deg, (c) and (d) at 60 m/s, 90 deg. Arrows indicate projected direction of particle motion. Magnifications of (a) and (c) are the same; similarly, (b) and (d) are the same.

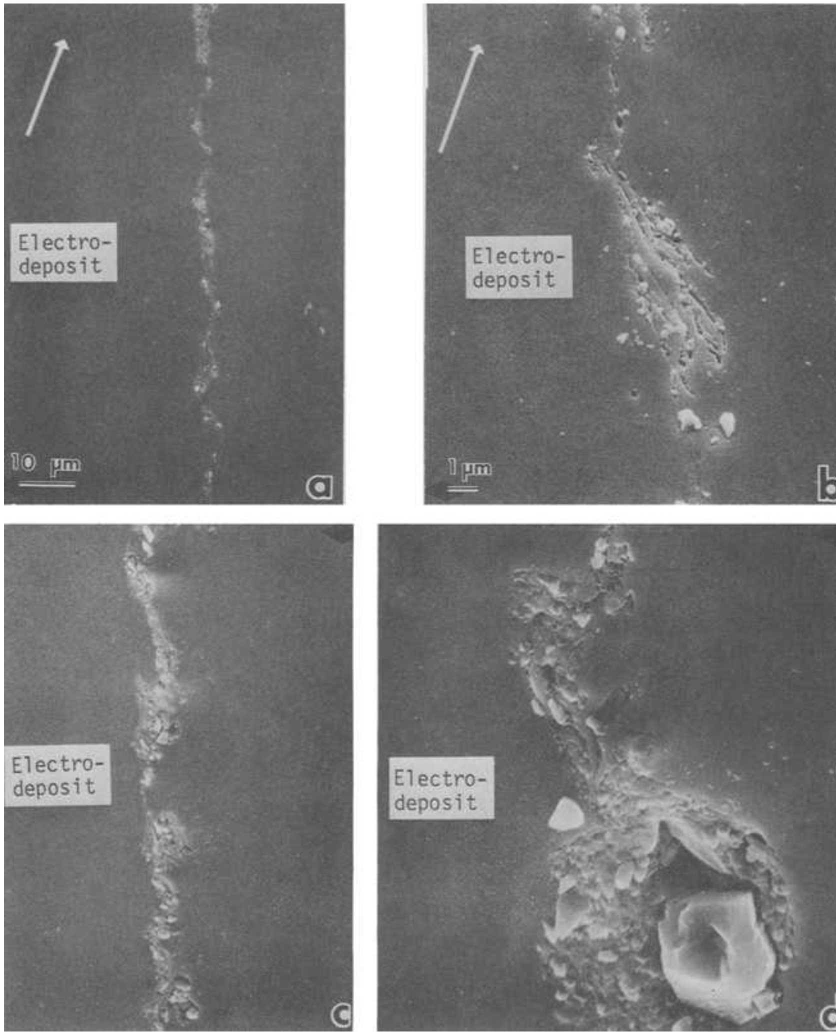

FIG. 10—*Cross sections through steady-state eroded surfaces:* (a) *and* (b) *at 60 m/s, 20 deg;* (c) *and* (d) *at 60 m/s, 90 deg. Arrows indicate approach direction of particles. Magnification of* (a) *and* (c) *are the same; similarly,* (b) *and* (d) *are the same.*

metal. Thus, in Fig. 10*b*, we attribute the fissures in the surface to the flow of metal along the surface rather than arising from surface cracks. The flow pattern in Fig. 10*b* is consistent with the particle impingement direction. Flattening or folding over of peaks produced by prior impacts would also result in embedment. The latter effect almost certainly plays a major part in the embedding process at 90 deg. Evidence of this can be seen in Fig. 10*d*.

It was noted earlier that the surface topography of the induction-period specimens and steady-state specimens was quite similar. Cross sections of these specimens are shown in Fig. 11. The thickness of the embedded layer on the induction period specimen, Fig. 11*a*, is much less than that on the steady-state specimen, Fig. 11*b*. This agrees with the fact that the induction period specimen was in a regime of weight increase at the time exposure was terminated.

Influence of Particle Embedding on Erosion

It is reasonable to assume that particle embedding has a significant influence on the erosion process, particularly at 90 deg, where the concentration of embedded particles is greatest. A model illustrating the embedding process and suggesting a mechanism by which attrition of surface material may occur is shown in Fig. 12. A cross section through the surface is depicted and normal particle impingement is assumed. In Fig. 12*a* numerous small particles and a much larger fragment are embedded in the surface. At a later time, in Fig. 12*b*, the large fragment has been fractured into small pieces and driven farther into the surface on being struck by one or more incident particles. Smaller scattered particles became buried when metal projections were deformed over them. Consistent with experimental observations, the concentration of embedded particles is shown to vary along the surface. The locations containing a high concentration of embedded particles would be expected to exhibit different mechanical properties than surrounding metal. In

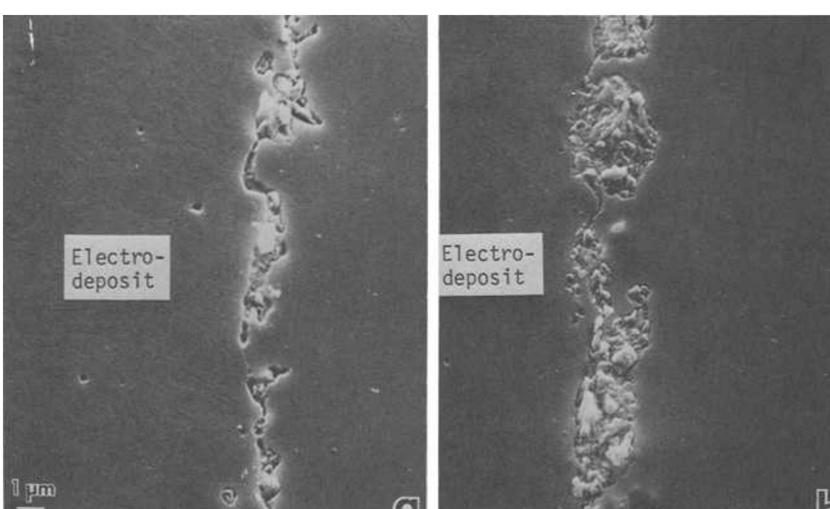

FIG. 11—*Cross section through surfaces eroded at 20 m/s, 90 deg:* (a) *erosion terminated in induction period while mass is increasing;* (b) *steady state exposure.*

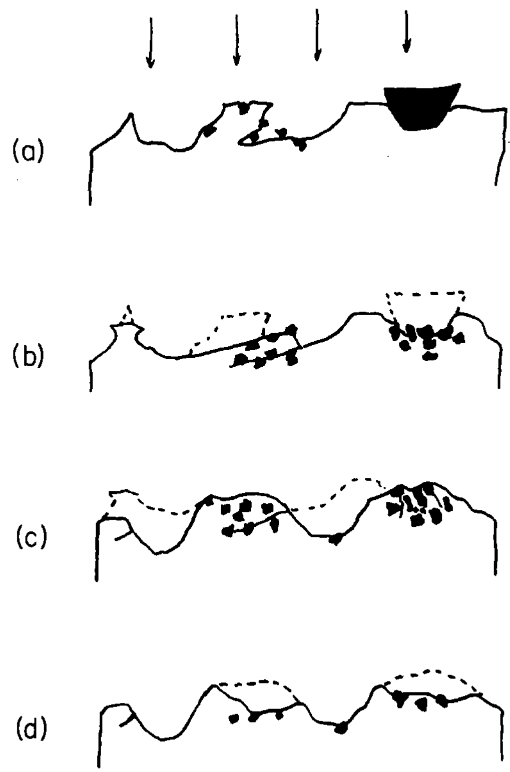

FIG. 12—*Model illustrating possible mechanism for particle embedding and surface attrition processes.*

particular, they are likely to be harder under compressive impact loading, with the result that they may tend to become gradually higher than the average surface, Fig. 12*c*. On the other hand, the composite mixture of loosely adherent erosion particles and metal fragments is probably much weaker in shear and less ductile than the surrounding metal. Thus the raised composite structure should be more susceptible to fracture and removal from the surface once it is exposed.

Since previous investigations have not involved a careful study of eroded surfaces in cross section, the extent to which embedding occurs in various metal erosion experiments is not well known. Nielson and Gilchrist [*4*] related embedding to an increase in weight during the induction stage. The method is certainly capable of detecting the most prominent cases of embedding, that is, ductile materials at large attack angles. However, as was shown here at an attack angle of 20 deg, significant embedding can also occur without a detectable increase in weight. Further studies are strongly indicated both with respect to delineating the influence of material properties and impact parameters on embedding and to determining under what condition embedding enhances or decreases erosion rate. As a limiting case, one might cite the situation where sintering to the surface occurs at elevated temperatures and erosion is effectively eliminated.

Plastic Strain Measurements Below the Eroded Surface

Measurements were made of the plastic strain developed below the eroded surface using a selected-area electron channeling (SACP) method [*17,18*]. The method involves the determination of loss of contrast in certain electron channeling bands [*19*] that results from the development of a deformation structure in the metal, analogous to the broadening of X-ray diffraction lines from deformed metals. The SACP variation with plastic strain was determined using a copper calibration specimen that had been deformed in compression. Strains as large as 35 percent could be measured. The SACP patterns were obtained from circular regions about 10 μm in diameter and about 500 Å in depth. The measured value refers to the average strain in that volume.

SACP measurements were made on cross sections of specimens eroded in the steady state regime at 20 m/s, 90-deg and 60 m/s, 90 deg. Figure 13 shows two SACP's obtained at distances 10 and 80 μm below the erosion surface on the 20-m/s, 90-deg specimen. The 111 channeling band used in these measurements is vertically oriented in the patterns. The loss of contrast and sharpness seen in the SACP at 10 μm is a result of the large plastic strain that is present. The results of measurements of strain at various distances below the eroded surface are shown in Fig. 14. At a given depth it is seen that strains are about three times larger at the higher velocity. In both cases studied, the strains decrease rapidly below the eroded surface,

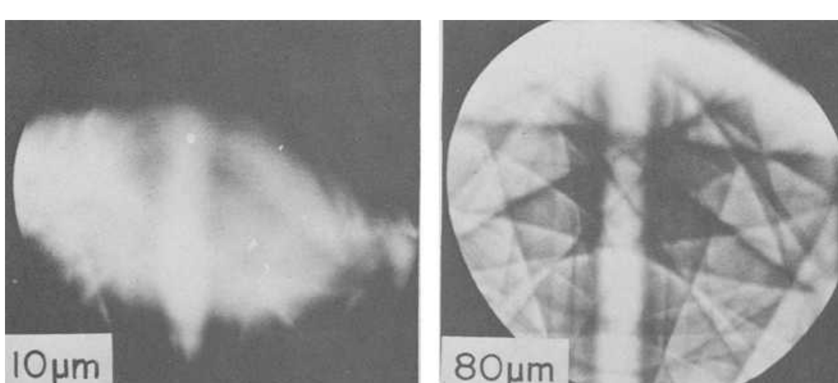

FIG. 13—*Selected area electron channeling patterns obtained at 10- and 80-μm depth for 20-m/s, 90-deg specimen cross section. Strain measurements were made on the vertical 111 band.*

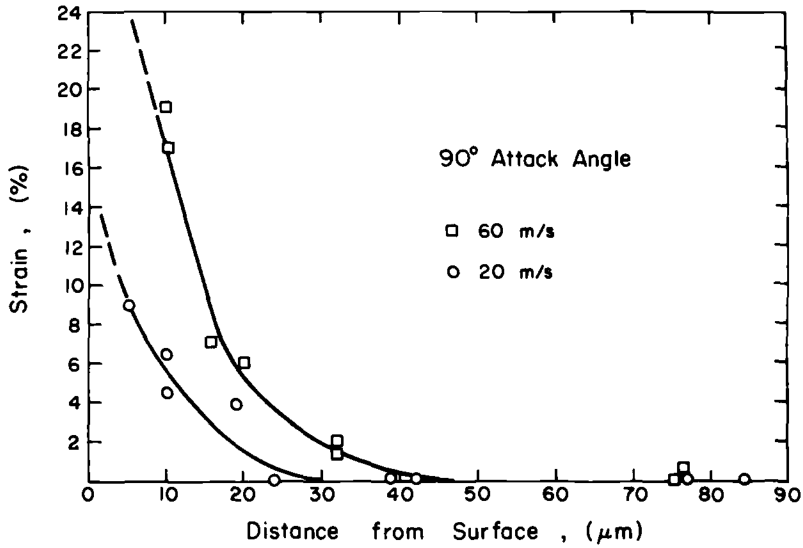

FIG 14—*Variation in strain determined from SACP measurements with distance below eroded surface.*

vanishing at distances of about 30 and 45 μm for particle velocities of 20 and 60 m/s, respectively. A previous study [*18*] of erosion damage at isolated impact craters in copper (50-μm particles, 59 m/s) found that strains in excess of 30 percent were reached at the surface, and decreased to about 5 percent at depths of about 25 μm. Those results are consistent with the findings here for 60-m/s velocity exposure.

TEM Observations

In the same study cited in the foregoing [*18*], TEM micrographs were obtained illustrating the damage at isolated impact sites in annealed 310 stainless steel. A high concentration of dislocations was found to extend for a distance of a few micrometres from the indentation. The dislocation density was quite low outside of this high damage zone. Deformation twins were also identified at some impact sites. In the present investigation, specimens subjected to steady-state erosion sustained considerably greater damage. This was evident at an attack angle of 90 deg without making any measurements. Specimens were visibly bent after exposure. The eroded surface was convex in shape, indicating that significant compressive stresses were developed within that surface. The effect was much less at an attack angle of 20 deg.

TEM micrographs from regions 6 and 14 μm below the eroded surface of a specimen exposed at 20 m/s, 20 deg are shown in Fig. 15. The dislocation

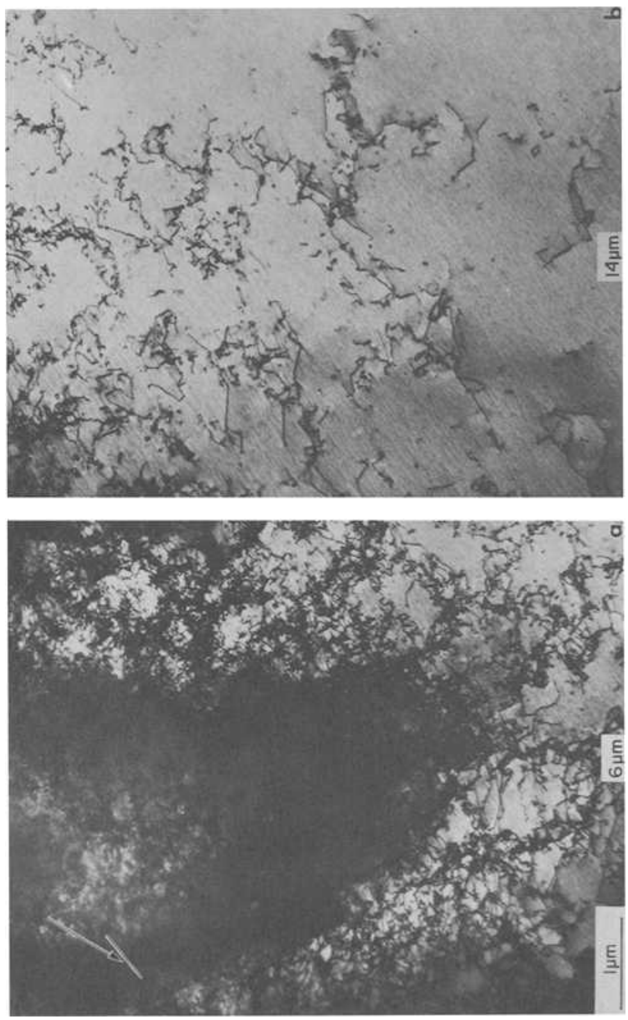

FIG. 15—TEM micrographs of dislocations in steady-state specimen exposed at 20 m/s, 20-deg: (a) center of micrograph is about 6 μm from eroded surface and (b) center about 14 μm from surface. Arrow in (a) indicates direction of particle approach. The eroded surface is nearly perpendicular to the plane of the micrographs.

density decreases rapidly with increasing distance below the surface. At 40 μm beneath the surface, very few dislocations could be found in an area equivalent to that shown in Fig. 15. In contrast, at 60 m/s, 90 deg, the most severe condition studied, a high dislocation density was observed at distances greater than 200 μm below the surface. TEM micrographs at 10, 52, and 160 μm from the eroded surface are shown in Fig. 16. The dislocations are arranged in a distinct cell structure; that is, regions relatively free of dislocations are surrounded by walls of high dislocation density. Cells are also evident in Fig. 15.

The formation of a cell structure is characteristic of many materials at a sufficiently high dislocation density under conditions of multiple slip. Cell formation is retarded by a low stacking fault energy and the concomitant tendency toward coplanar slip. The presence of obstacles to dislocation motion such as fine precipitates may preclude cell formation entirely. Neither of the foregoing factors is operative in the relatively pure copper used here.

In general, cell size decreases with increasing strain. Thus, in Figs. 15 and 16 a much smaller cell size is found near the surface, where the strain is greatest. A number of studies have attempted to relate cell size to flow stress. Although a generally accepted relationship has not been firmly established, recent work suggests a reciprocal dependence [*20*]. In Fig. 17, the reciprocal of cell diameter, d^{-1}, is plotted against distance below the eroded surface. Since to a good approximation flow stress is proportional to hardness [*21*], the curves in Fig. 17 also indicate the variation in hardness as a function of distance from the surface. The electron channeling results previously discussed (Fig. 14) are qualitatively similar to the results obtained here at 90 deg. However, the actual strains may be somewhat greater than those derived using the channeling analysis. Preliminary dislocation density measurements have been made for some of the erosion specimens. For the 20-m/s, 90-deg specimen, the dislocation density is about $2 \times 10^{10}\,\text{cm}^{-2}$ at 40-μm depth and is higher for the 60-m/s, 90-deg specimen. According to measurements of Bailey [*22*] on tension specimens, this dislocation density is equivalent to a tensile strain in excess of 10 percent. The channeling method determined a strain of about 1 percent compressive at this same depth. However, factors other than dislocation density, such as dislocation type and distribution, are also involved and probably are responsible for this discrepency.

It should be noted that although these specimens had reached a steady-state condition with respect to erosion rate, this does not necessarily apply to the state of deformation below the surface. Damage at some distance below the surface could still continue to accumulate without strongly influencing erosion rate. No attempt was made in this investigation to determine whether the accumulation of subsurface deformation had reached a steady-state condition.

Now consider the nature of the microstructure at the eroded surface, which in these specimens is the interface between the copper specimen and the electrodeposited copper layer. As might be anticipated from our earlier topographic observations, there was considerable variation in the microstructure along the surface. One would not expect to find the same structure in displaced crater lip material as would exist at the bottom of an indentation, nor would the same features prevalent at 20 deg also be equally prevalent at 90 deg. The presence of embedded Al_2O_3 particles introduces further complexities, not the least of which concerns the preparation of uniformly thin specimen areas. An example of the microstructure at the surface of a 20-m/s, 20-deg specimen is shown in Fig. 18. At distances greater than about ~ 1 μm below the surface, the damage is manifested by a high dislocation density, as we have seen in Fig. 15. Closer to the surface, a significant change in microstructure occurs. Columnar grains can be seen in Fig. 18 curved in the direction of particle impact. A more striking example of apparently similar grains is shown in Fig. 19 obtained at 60 m/s, 20 deg. Here the grains were identified as deformation twins. The zone of high deformation apparently corresponded to a condition where plastic flow at the imposed strain rate could no longer be accommodated by dislocation generation and motion. In some cases, a dark band (corresponding to a surface in three dimensions) could be seen at the boundary of the high deformation zone. Such bands are visible in both Figs. 18 and 19 and may be similar to observations by Hutchings et al [*11*]. In single-particle impact studies on polycrystalline steel, Hutchings et al found that metal removal occurred along a band of intense subsurface shear. Further study is required to provide a better understanding of the bands observed here.

In some cases the outermost layer was distinctly polycrystalline in appearance. Electron diffraction patterns consisted of arcs and spots that were not consistent with a single crystalline orientation. Although grains could be distinguished, they were not sharply defined and bounded as in annealed polycrystalline material. A similar highly distorted layer, referred to as a "fragmented layer," is observed at abraded metal surfaces [*23*]. Other similarities seem to exist between these eroded surfaces and abraded surfaces. In a TEM study of 70-30 brass, Turley and Samuels [*24*] found that below the fragmented layer a zone of deformation twins was present, followed by dislocations alone at greater depths.

Although it was difficult by electrochemical means to obtain suitably thin areas for TEM study at the surface of 90-deg specimens because of embedded Al_2O_3 particles, a highly deformed polycrystalline structure was found. An example of the microstructure from a 20-m/s, 90-deg specimen is shown in Fig. 20. Highly deformed grains of irregular shape are visible. The contrast and delineation of the various grains are mainly a function of TEM imaging conditions. Several previous investigations have suggested that melting may occur at eroded surfaces [*10,25*]. Although features such as droplets of

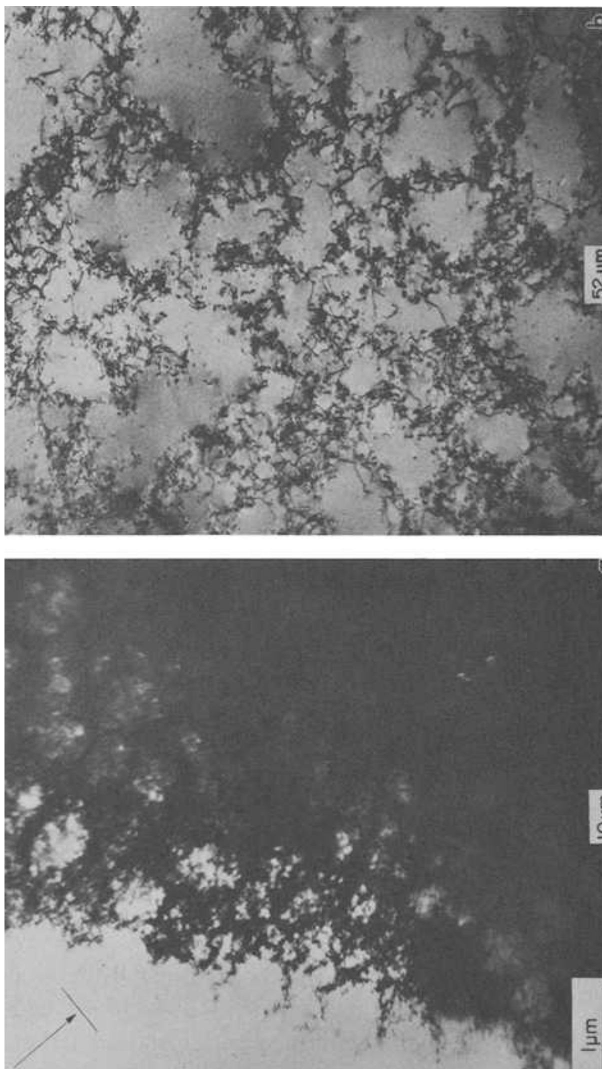
b
52 µm
a
10 µm
1µm

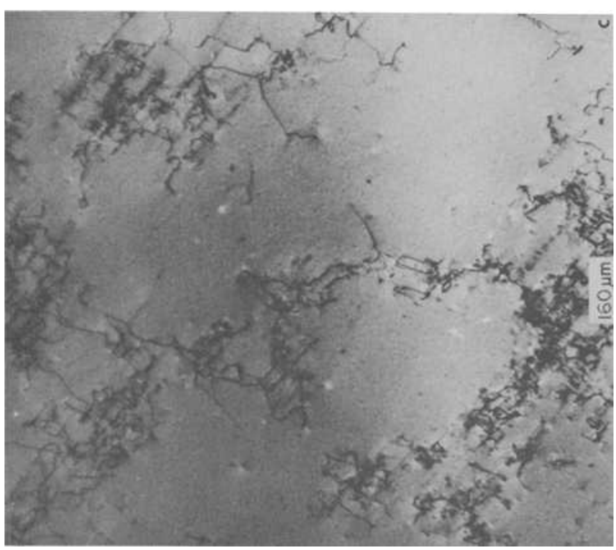

FIG. 16—*TEM micrographs of dislocations in steady-state specimen eroded at 60 m/s, 90-deg. Approximate distances of center of each micrograph from eroded surface are indicated. Arrow in* (a) *refers to direction of particle approach. The eroded surface is approximately perpendicular to the plane of the micrographs.*

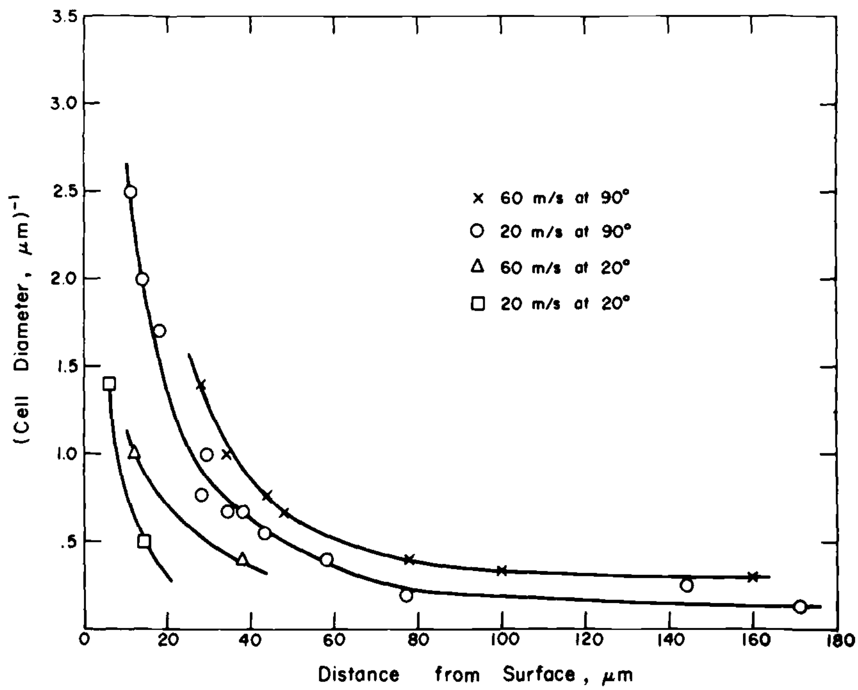

FIG. 17—*Dependence of dislocation cell size on distance below eroded surface for steady-state specimens.*

metal that might be associated with melting were not observed here, thermally induced recovery effects cannot be ignored. Thermal recovery may indeed play some part in developing the polycrystalline-like grain structure at the surface of specimens exposed at 20 deg and within the embedded layer of those exposed at 90-deg particle incidence.

As a final observation of subsurface microstructure, Fig. 21 shows an area within the embedded layer of a specimen exposed at 60 m/s, 90 deg. The specimen was thinned by ion beam bombardment. With this method both the embedded Al_2O_3 particle and surrounding copper are thinned simultaneously (not necessarily at the same rate). Relief effects are minimized by employing a low bombardment angle of about 15 deg and rotating the specimen during thinning. The central feature in Fig. 21 is a relatively large Al_2O_3 particle. The surrounding copper has conformed almost completely with the particle without visible separation or voids over most of its boundary. There are, however, separations or voids within the metal. The metal in this region is highly deformed. Single-crystal diffraction patterns which could be obtained at greater distances below the surface, in Fig. 16, for example, are completely obliterated.

FIG. 18—*TEM micrograph showing microstructure near eroded surface. Specimen exposed under steady-state conditions at 20 m/s, 20 deg. Dashed line indicates approximate position of eroded surface plane. Arrow indicates particle direction approach.*

Summary and Conclusions

Surface topographic features and subsurface microstructure in copper erosion specimens were studied by scanning and transmission electron microscopy. Emphasis was placed on examining the material response at attack angles of 20 and 90 deg. At 20 deg, topographic features observed here resemble those generally believed to result from a cutting process.

Subsurface damage at 20 deg could often be separated into three loosely defined zones. The first zone consisted of a layer of highly deformed grains. The second zone was characterized by the presence of deformation twins and was often separated from the third zone by a definite boundary possibly associated with an intense shear deformation. The third zone consisted of dislocations at a concentration that decreased with increasing distance below the surface. The first two zones occurred within a few micrometres of the surface and were not always identified at all locations due to variations inherent

FIG. 19—*TEM micrograph of steady-state eroded specimen exposed at 60 m/s, 20 deg. Dark acicular features are deformation twins. Dashed line indicates position of surface plane. Arrow refers to particle direction of approach.*

in the impact process and experimental difficulties in observing the immediate surface layer.

At 90-deg particle incidence, the deformation damage was more severe than at 20 deg. A high density of dislocations, extended to greater depths and metal near the surface, invariably gave the appearance of a highly deformed polycrystalline structure. However, the most marked difference between the two attack angles concerned the amount of particle embedding. While some particle embedding was observed at 20 deg and undoubtedly had an influence on the erosion process, embedding was extensive at 90 deg. Under the conditions of this investigation, the embedded layer was nominally a few micrometres thick; however, the thickness varied considerably along the surface, even in steady-state conditions.

Although embedding in ductile metals has been noted by several investigators, its influence on the erosion process has not been considered in any detail. Our observations indicate that this embedded layer can, in effect, be regarded as a composite material having entirely different properties from the base metal. An erosion model is suggested in which regions containing a

FIG. 20—*TEM micrograph illustrating highly deformed polycrystalline structure within embedded layer of steady-state eroded specimen exposed at 20 m/s, 90 deg.*

FIG. 21—*Al_2O_3 particle embedded in surface of specimen exposed to 60 m/s, 90 deg. Specimen thinned by ion bombardment. Arrow indicates direction of particle approach.*

locally high concentration of particles tend to be raised above the surface due to their greater indentation hardness. Once exposed, however, these regions are likely to be fractured away by impact-imposed tensile and shear stresses.

References

[1] Sheldon, G. L., *Journal of Engineering Materials and Technology*, Vol. 99H, 1977, pp. 133-137.
[2] Finnie, I. in *Proceedings*, 3rd National Congress of Applied Mechanics, American Society of Mechanical Engineers, 1958, pp. 527-532.
[3] Bitter, J. G. A. *Wear*, Vol. 6, 1963, pp. 5-21 and pp. 169-190.
[4] Neilson, J. H. and Gilchrist, A., *Wear*, Vol. 11, 1968, pp. 111-122.
[5] Sheldon, G. L. and Finnie, I., *Journal of Engineering for Industry*, Vol. 88B, 1966, pp. 393-400.
[6] Sheldon, G. L. and Kanhere, A., *Wear*, Vol. 21, 1972, pp. 195-209.
[7] Finnie, I. and Levy, A., this publication, pp. 36-58.
[8] Hutchings, I. M., this publication, pp. 59-76.

[9] Smeltzer, C. E., Gulden, M. E., and Compton, W. A., *Journal of Basic Engineering*, Vol, 92D, 1970, pp. 639-654.
[10] Tilly, G. P., *Wear*, Vol. 23, 1973, pp. 87-96.
[11] Hutchings, I. M., Winters, R. E., and Field, J. E. in *Proceedings of the Royal Society*, Vol. 348, 1976, pp. 379-392.
[12] Ruff, A. W. and Ives, L. K., *Wear*, Vol. 35, 1975, pp. 195-199.
[13] Wiederhorn, S. M. and Roberts, D. E., *Bulletin of the American Ceramic Society*, Vol. 55, 1976, pp. 185-189.
[14] Sheldon, G. L., *Journal of Basic Engineering*, Vol. 92D, 1970, pp. 619-626.
[15] Finnie, I., Wolak, J., and Kabil, Y., *Journal of Materials*, Vol. 2, 1967, pp. 682-700.
[16] Wood, C. D. and Espenschade, P. W., *Transactions*, Society of Automotive Engineers, Vol. 73, 1973, pp. 515-523.
[17] Ruff, A. W., *Wear*, Vol. 40, 1976, pp. 59-74; see also Vol. 46, 1978, pp. 251-261.
[18] Ives, L. K. and Ruff, A. W., *Wear*, Vol. 46, 1978, pp. 149-162.
[19] Stickler, R., Hughes, C. W., and Booker, G. R. in *Proceedings*, Fourth Annual Scanning Electron Microscopy Symposium, IIT Research Institute, Illinois Institute of Technology, 1971, pp. 473-480.
[20] Thompson, A. A. W., *Acta Metallurgica*, Vol. 23, 1975, pp. 1337-1342.
[21] Bowden, F. P. and Tabor, D., *Friction and Lubrication*, Vol. 2, Clarendon Press, Oxford, U. K., 1964, Chapter 16.
[22] Bailey, J. E., *Philosophical Magazine*, Vol. 8, 1963, pp. 223-236.
[23] Scott, V. D. and Wilman, H. in *Proceedings of the Royal Society*, Vol. A247, 1958, pp. 353-368.
[24] Turley, D. M. and Samuels, L. E., *Journal of the Australian Institute of Metals*, Vol. 17, 1972, pp. 114-119.
[25] Jennings, W. H., Head, W. J., and Manning, C. R., Jr., *Wear*, Vol. 40, 1976, pp. 93-112.

DISCUSSION

A. Levy[1] *(written discussion)*—Were any deformation patterns, such as ripples, seen on the surface? Was there any evidence of void formation and cracks in the surface layer that had embedded particles?

L. K. Ives and A. W. Ruff (author's closure)—No patterns were observed. There were pores and fissures in the surface; however, the origin of these features was not established. This was particularly the case for TEM specimens where images were complex and preparation of thin foils could introduce artifacts. Undoubtedly, smearing of metal and flattening of asperities played an important role in generating crack-like features and porosity. This was especially clear from examination of SEM micrographs of cross sections through the eroded surface.

D. M. Mattox[2] *(written discussion)*—Under equilibrium conditions, what is the surface coverage by abrasive particles at the various attack angles? What particle flux was utilized in this study?

[1]University of California, Berkeley, Calif.
[2]Sandia Laboratories, Surface Metallurgy Division, Kirtland AFB, Albuquerque, N. Mex. 87115.

L. K. Ives and A. W. Ruff (author's closure)—We have not yet measured the amount of embedded abrasive material under the various test conditions. This could be done by dissolving away the copper and weighing the Al_2O_3 residue. Examination of cross sections in the SEM did indicate that the amount of embedded material was significantly greater at an attack angle of 90 deg than at 20 deg.

The particle flux was approximately 1 g/cm^2 min at normal incidence and about one third of that on the specimen surface at an attack angle of 20 deg.

M. E. Gulden[3] *(written discussion)*—Does amount of embedded material remain constant with increasing number of impacts?

L. K. Ives and A. W. Ruff (written discussion)—We have shown that embedding increases during the induction period, particularly at normal incidence. However, no measurements were made to determine whether some change might still be occurring during the steady-state erosion condition.

G. A. Savanik[4] *(written discussion)*—Can you make any statement regarding the mechanism of adhesion between the particle and the metal? Do you consider this to be true adhesion?

L. K. Ives and A. W. Ruff (author's closure)—We do not have any direct measurements regarding the extent to which the impacting particles might adhere to the metal surface. However, under the conditions of erosion, the impacting particle surface may come into intimate—that is atomic—contact with the metal surface. The high stresses involved and flow of metal could effectively eliminate an intervening layer of air or other absorbed species and also allow the particle to break through an oxide layer that would otherwise interfere with adhesion. Adhesion could, of course, occur between the particle and an oxide on the metal surface.

We would regard this as true adhesion in the sense that there is actual atomic bonding between the particle and metal surfaces.

A. C. Buckingham[5] *(written discussion)*—The particle impact-impregnation for normal (perpendicular) impact leads to apparent new roughness (new hills and valleys) on the surface. What is the height or depth of these new hills and valleys?

If impact had been severe enough to produce new hills and valleys of the order of 100 μm, a very great change in the surface environment must be considered if the eroding surface is in a gas flow. The analogy is drawn to gas-borne particulate erosion on turbine blades in coal combustion electrical energy conversion cycles. What happens is that for changes to surface roughness heights of the order of 100 μm in a gas flow of from several hundred to 1000 cm/s, the critical Reynolds number for transition from laminar to turbulent boundary layer flow drops. The boundary layer becomes

[3]Solar Turbines International, Operating Group of International Harvester, San Diego, Calif. 92138.
[4]U. S. Bureau of Mines, Twin Cities Mining Research Center, Twin Cities, Minn. 55111.
[5]Lawrence Livermore Laboratory, Livermore, Calif. 94550.

turbulent at the site of the impact-induced roughness. The surface shear stress and proportional heat transfer will increase locally one to a few orders of magnitude. The resulting higher surface temperatures and gas-surface shear will probably significantly affect the surface erosion rate. Even if the gas flow boundary layer is already turbulent at the site of impact-induced roughness, a considerable change in the surface heat transfer and mechanical shear will occur for roughness height changes of the order of 100 μm. This is because the shear or resistance varies exponentially with surface roughness height (as does the proportional heat transfer) for these roughness amplitudes at gas flow velocities of a few hundred cm/s or greater.

L. K. Ives and A. W. Ruff (author's closure)—The roughness observed is on the order of 1μm, depending on particle velocity—about the same as the topographic roughness.

G. Mayer[6] *(written discussion)*—Do fractured particles cause more or less damage than unfractured particles? In this regard, is there a distinction between initially acicular and initially rounded particles?

How were standards made for estimating the strain induced by erosion for electron channeling? Since there is probably a temperature change at the surface of the copper during erosion, the strain that you subsequently assessed by electron channeling may be lower because of relief through recovery processes, and, thus, the compression standard may not be realistic.

L. K. Ives and A. W. Ruff (author's closure)—We did not conduct any experiments to determine the effects of particle fracturing on erosion rate. Tilly [*10*] has done extensive work in this area. However, particle fracture did appear to play an important part in the embedding process. Fragments from large 50-μm particles rather than the entire particle were embedded. None of our observations were able to detect an effect that particle shape might have on a tendency to fracture.

Recovery effects due to a temperature rise at the surface were not accounted for in the compression standard.

[6]Army Research Center, Research Triangle Park, N. C. 27709.

I. Finnie,[1] *A. Levy,*[1] *and D. H. McFadden*[1]

Fundamental Mechanisms of the Erosive Wear of Ductile Metals by Solid Particles

REFERENCE: Finnie, I., Levy, A., and McFadden, D. H., "**Fundamental Mechanisms of the Erosive Wear of Ductile Metals by Solid Particles,**" *Erosion: Prevention and Useful Applications, ASTM STP 664,* W. F. Adler, Ed., American Society for Testing and Materials, 1979, pp. 36–58

ABSTRACT: A brief survey is presented of the mechanisms which have been proposed for the erosion of ductile metals by solid particles. After reviewing these and examining scanning electron microscope photographs, it is concluded that a ductile cutting mode applies when the velocity vector of the eroding particle makes an angle of less than about 45 deg with the surface. Above this angle the removal process appears to involve quite different mechanisms. An earlier analysis of the cutting mechanism is reexamined and shown to predict many features of the erosion process. In particular, the roles of particle velocity, elevated temperatures, and material properties are discussed. Some preliminary results are presented for erosion at higher angles, and possible mechanisms for material removal are discussed. Finally, some suggestions are made for future directions in erosion research in view of the current interest in coal-hydrogenation processes.

KEY WORDS: abrasion, coal-hydrogenation, cutting, ductile metals, erosion, erosive wear, flow stress, grinding, hardness, heat treatment, machining, metals, scratching, size effect, wear, work-hardening

Erosion by solid particles in a fluid stream has been a problem in many industrial processes. Currently, there is a great deal of interest in coal-hydrogenation. From pilot plant results and experience with similar operations, erosion appears to be an important factor in the development of novel hydrogenation processes. The need for a better understanding of erosion in this connection is the motivation for the present work.

This type of wear has been studied for many years, and the classic monograph of Wahl and Hartstein [*1*],[2] *Strahlverschleiss*, published in 1946 contains some 233 references. It was known, by this time, that erosion depends

[1] Professor of mechanical engineering, staff senior scientist, Lawrence Berkeley Laboratory, and graduate student, respectively, University of California, Berkeley, Calif.

[2] The italic numbers in brackets refer to the list of references appended to this paper.

markedly on the angle of impingement, with the dependence being quite different for ductile metals and brittle solids. This early work compared the erosion resistance of different materials, and many ingenious solutions to practical problems were devised. However, an interest in the fundamental mechanisms by which solid particles remove material during erosion has developed only within the past 20 years. Work in this direction is stimulating because of the many different viewpoints which have been proposed. It is also somewhat frustrating because of the difficulty in relating the conditions occuring during erosion to those in conventional materials tests. Since the literature on the mechanisms of erosive wear has been reviewed in detail in recent publications [*2,3*], we will present here only a brief summary.

In 1958, one of the co-authors [*4*] considered the trajectory of the tip of a rigid abrasive grain which cuts the surface of an ideally ductile metal. Making a number of assumptions which were spelled out in this and later work [*5,6*], the volume V removed from a surface by a mass M of eroding particles was predicted to be

$$V \sim MU^2 f(\alpha) \div p \tag{1}$$

where

U = particle velocity,
$f(\alpha)$ = function of α, angle measured from plane of this surface to particle velocity vector, and
p = horizontal component of flow pressure between particle and surface.

As we will discuss later, this approach predicts, successfully, many features of the erosion of ductile metals when the angle α is less than say 45 deg but is incapable of predicting the erosion observed for higher values of α. By contrast with ductile metals, in which material can be removed by the cutting action of a particle, as well as by other mechanisms, in ideally brittle solids removal must occur by the propagation and intersection of cracks. Analyses of this type of erosion presented in 1966 [*7*] and later [*8*] showed encouraging agreement with experiment. We will not pursue the topic of the erosion of brittle solids in the present paper since we are treating ductile metals. However, it is important to realize that the mechanisms of material removal for ductile and brittle behavior are completely different.

With this in mind, one has to be skeptical about the analysis of Bitter [*9*] which attempted to cover both brittle and ductile solids with the same equations. Following earlier workers, he considered erosion to consist of two simultaneous processes, "cutting wear" and "deformation wear." For ductile metals at low angles, cutting wear predominates, while at high angles deformation wear predominates. The analysis is elaborate, being based on elastic contact stress calculations and energy balances. Later it was simplified by Neilson and Gilchrist [*10*], who presented equations which gave a good fit to experimental data. Our viewpoint may be partisan, but it is difficult to view this approach as other than "curve fitting," and it sheds little light on the fundamental processes involved in erosion.

An extensive series of erosion studies was carried out by Tilly and his colleagues [*11-17*] in connection with sand erosion of gas turbine compressors. A great deal of useful information was obtained, for the first time, on the effect of the properties of the eroding particles on erosion. By contrast with earlier workers who assumed the eroding particles to be rigid, Tilly proposed a two-stage process in which particles produce some erosion and then fragment to produce additional damage. On the basis of this model, the erosion which occurs at $\alpha = 90$ deg was attributed to the radial motion of the fragmented particle. However, this explanation has been questioned by Kleis and his colleagues [*18*]. The two-stage process was used also to explain the effect of particle size in erosion since large particles should fragment more easily and produce more damage than small ones. However, such a size-effect is observed also in slow-speed abrasion tests. Finally, the additional fragmentation which should occur at higher velocities was offered as an explanation for the observed dependence of volume removal on velocity $V \sim U^n$ where $n > 2$. By contrast with Eq 1, which predicts $n = 2$, virtually all erosion tests on ductile metals show higher values of the exponent n. In Tilly's tests the value reported was $n = 2.3$. While fragmentation may play a role in some cases, the wide variety of situations in which values of the exponent n greater than 2 have been reported leads us to seek a more general explanation for this result.

Continuing with these different viewpoints, the next approach is that of Smeltzer, Gulden, and Compton [*19*]. They suggest that local melting during impact and attachment of surface material to the impacting particles produce erosion. Again the generality of this hypothesis may be questioned, because materials of widely differing thermal properties show a similar response to eroding particles.

Another model for erosion was suggested by Sheldon and Kanhere [*20*]. Their derivation, which applies for $\alpha = 90$ deg, consists of an energy balance between the kinetic energy of the particle and the work expended during indentation. The result is

$$V \sim D^3 U^3 (\rho/Hv)^{3/2}$$

where

ρ = particle density,
D = particle diameter, and
H_v = Vicker's hardness of surface.

Sheldon [21] contends that the appropriate value to use for the Vicker's hardness is that of the material in the "fully work-hardened" condition, which may be as much as five times greater than that of the annealed metal. Again, this analysis is lacking in generality since the velocity exponent is usually between 2 and 3 and the derivation based on an energy balance appears to be oversimplified.

An important contribution to our fundamental studies of erosion mechanism in recent years has been the work of Hutchings and Winter [22-25]. Using single particles, they have shown that cutting or plowing may occur, depending on the rake angle. The plowing or extruding of material above the surface can lead also to erosion if this raised and more vulnerable material is removed by subsequent particles. These authors have observed bands of localized deformation in the material raised by particle impact. These bands are attributed to thermal softening, and the mechanism by which fracture propagates in these bands to remove material has been discussed [25].

From this brief review it is seen that a variety of opinions exists on the mechanism or mechanisms of material removal in erosion. For this reason, it appears worthwhile to reexamine the original cutting analysis [4] to assess its range of validity and to suggest directions in which it may be improved.

The Cutting Analysis

For completeness we will summarize the assumptions and the final results. Details of the derivation have been given elsewhere [4,6,26].

A rigid polyhedral grain as shown in Fig. 1 strikes the surface and does not fracture. Although the analysis can be extended to the three-dimen-

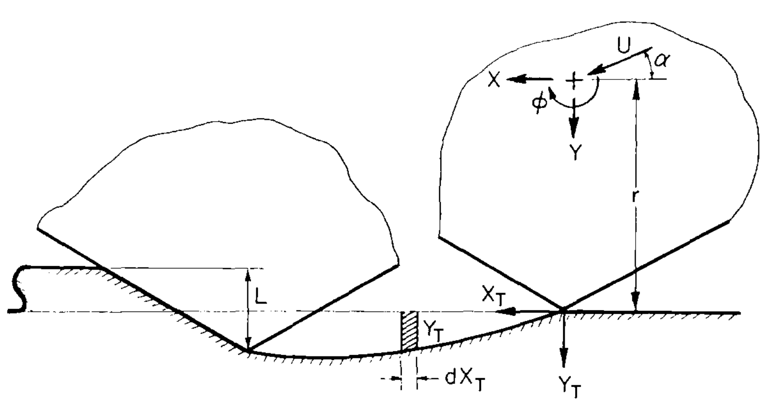

FIG. 1—*Idealized two-dimensional model of a rigid grain cutting into a ductile metal.*

sional case [5], for simplicity we consider the two-dimensional case in which the grain of Fig. 1 has a uniform width, b. Little rotation of the particle occurs during cutting, so for polyhedral particles the coordinates of the particle center of gravity X, Y and its tip X_T, Y_T are related by $X_T \simeq X + r\phi$ and $Y_T \simeq Y$. If particle rotation is limited, the cutting configuration should be approximately geometrically similar while the particle cuts into the surface. Also, with sharp particles, large strains should occur from the beginning of the cutting process. These conditions lead us to assume that the ratio K of vertical to horizontal force on the particle is a constant during cutting and that a constant plastic flow pressure exists during cutting with its horizontal component being denoted by p. Before writing the equations of motion, an assumption has to be made for the ratio ψ of the vertical distance L over which the particle contacts the surface relative to the depth of cut Y_T. In previous work [1], based on metal cutting experience this value was estimated as 2. For the present, however, we leave it as an unknown but fixed ratio. Finally, the volume removed was taken as the product of the area swept out by the tip of the particle and the width b of the cutting edge. That is

$$V = b \int Y_T \, dX_T = b \int_o^{t_c} Y_T \left(\frac{dX_T}{dt} \right)$$

where t is time from the start of cutting and t_c the time at which the particle ceases to cut.

Having made these assumptions, the equations of motion for the particle in the X, Y, and ϕ-directions may be solved and expressions determined for V. In presenting the results it is convenient to make use of the quantity

$$P = \frac{K}{\left(1 + \frac{mr^2}{I}\right)}$$

where m is the mass of an individual particle and I the mass moment of inertia about its center of gravity. Also, recognizing that not all particles will cut in the idealized manner, we denote the fraction which cut in the manner assumed by c. The resulting expressions for the volume removed by a total mass M of abrasive grains are

$$V = \frac{cMU^2}{2\psi p} \left[\frac{2}{K} \left(\sin 2\alpha - \frac{2}{P} \sin^2\alpha \right) \right] \qquad \alpha \le \tan^{-1} \frac{P}{2} \qquad (2)$$

$$V = \frac{cMU^2}{2\psi p}\left[\frac{\cos^2\alpha}{\left(1 + \frac{mr^2}{I}\right)}\right] \qquad \alpha \geq \tan^{-1}\frac{P}{2} \tag{3}$$

Equation 1 applies when the particle leaves the surface while still cutting, Eq 2 when the particle comes to rest while cutting (that is, t_c corresponds to $Y_T = 0$ and $dX_T/dt = 0$, respectively). The two expressions for volume removal coincide for $\tan\alpha = P/2$, while maximum removal is predicted to occur at the slightly lower angle given by $\tan 2\alpha = P$. Taking a value of $K = 2$ based on grinding data and tests with single abrasive grains, and choosing $I = ⅓\, mr^2$ for a polyhedral grain, $P = 0.5$ and maximum erosion is predicted to occur at $\alpha = 13$ deg. The angle for maximum erosion is fortunately not very sensitive to the choice of P. For example, for $P = 1.0$, $\alpha_{max} = 22.5$ deg. In previous work we have shown that the predicted variation of volume removal with angle agrees very well with experiment for angles less than say $\alpha = 45$ deg. This is illustrated by Fig. 2, which compares the predicted result with recent experiments on 1100-0 aluminum. Also, a modification of the analysis to treat curved surfaces provides

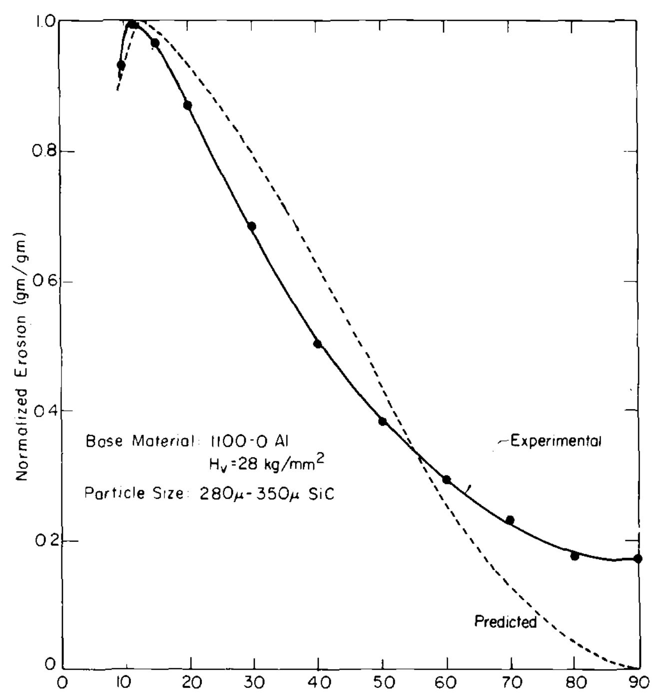

FIG. 2—*Predicted and experimental curves for erosion as a function of angle, normalized to give the same maximum erosion in both cases. Velocity, 78 m/s.*

a qualitative explanation [27] for the ripple patterns which form when ductile metals are eroded at low angles of impingement.

To study, in a more fundamental way, the variation of erosion damage with angle, a series of single particle impacts was examined using stereo scanning electron microscopy (SEM). In addition, profiles were traced through the approximate center of the "crater" produced by the impacting particle. There is considerable variability in the craters produced at a given angle because of the irregularity in the shape of the abrasive grains. However, after examining five or six craters for each angle, we get the "typical" results shown in Figs. 3-6 for α = 10, 30, 60, and 90 deg. At α = 10 deg, the particles, in general, leave the surface while still cutting; at α = 30 deg the particles cut but are trapped by the surface. These mechanisms correspond to those involved in the cutting analysis. However, much of the material which has been cut is displaced rather than removed, as described by Hutchings and Winter. We will return to this aspect later. At α = 60 and 90 deg, no cutting is involved and the original surface markings can be seen in the region stuck by the particles. When very many particles strike the metal to produce a rough surface, the situation becomes more complicated. However, it appears inappropriate to apply a cutting type of analysis for higher angles (say $\alpha > 45$ deg).

Returning to Eqs 2 and 3, we note two simple predictions which are confirmed by experiment. The volume removed is observed to be proportional to the total mass of the eroding particles except for an incubation period, which is most pronounced for the higher angles. The particle size does not influence the volume removal provided it is greater than about 50 to 100 μm. The reduction in volume removal ("size effect") which occurs with smaller particles has been discussed by one of the authors [6] and there is little we can add to this topic at the present time.

As pointed out earlier, a puzzling feature of erosion has been its dependence on velocity. Rather than the value $V \sim U^2$ predicted by Eqs 2 and 3, the observed values of the exponent are more typically 2.3 to 2.4 and can range from 2 to 3. This was explained recently [26] by a slight modification of the original cutting analysis. In the original derivation, based on Fig. 1, the vertical and horizontal forces were assumed to act at the tip of the particle. By moving these forces to the center of the contact region between the particle and the surface, only the equation of motion in the ϕ-direction is changed. This change depends on the ratio ψ and the depth of cut, which in turn depends on the velocity. As a result, velocity exponents are predicted which agree with the range of values observed experimentally. The modified analysis predicts a velocity exponent which increases with angle in the range for which cutting occurs and a slight increase in the angle for maximum erosion. The crater shape predicted by the original and modified analysis for α = 10 and α = 30 deg

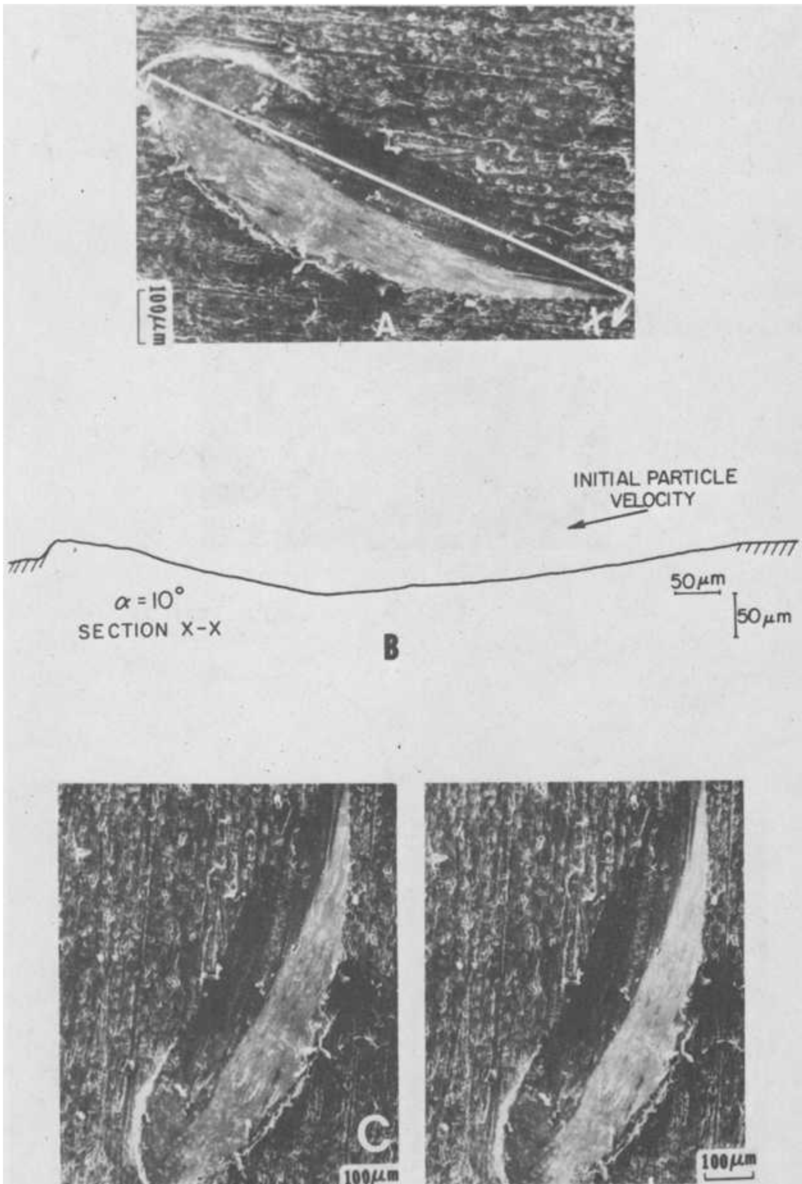

FIG. 3—(A) *Damage caused by a single 1100-μm-diameter silicon carbide particle at 10-deg angle of impingement with initial velocity of 67 m/s on 1100-0 aluminum.* (B) *Crater profile along Section XX.* (C) *Stereo photographs of impact (use stereo viewer provided in* Metals Handbook, *Vol. 9).*

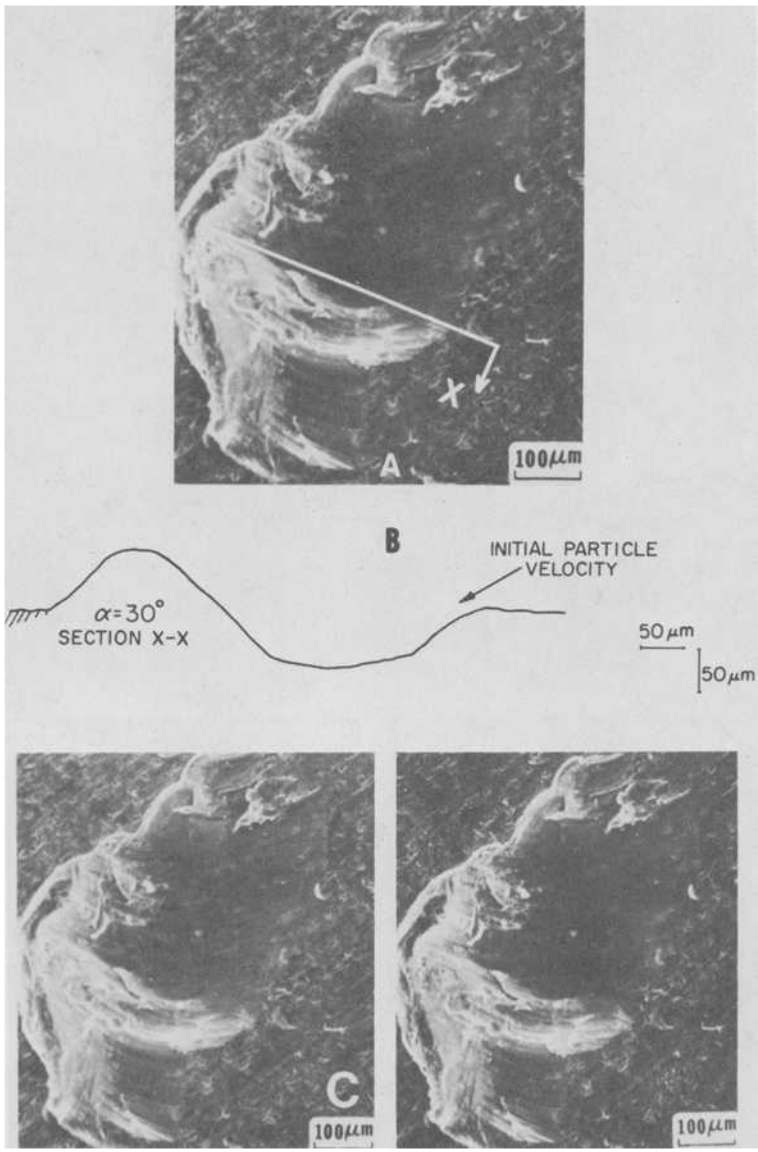

FIG. 4—*Same conditions as Fig. 3 except α is now 30 deg.*

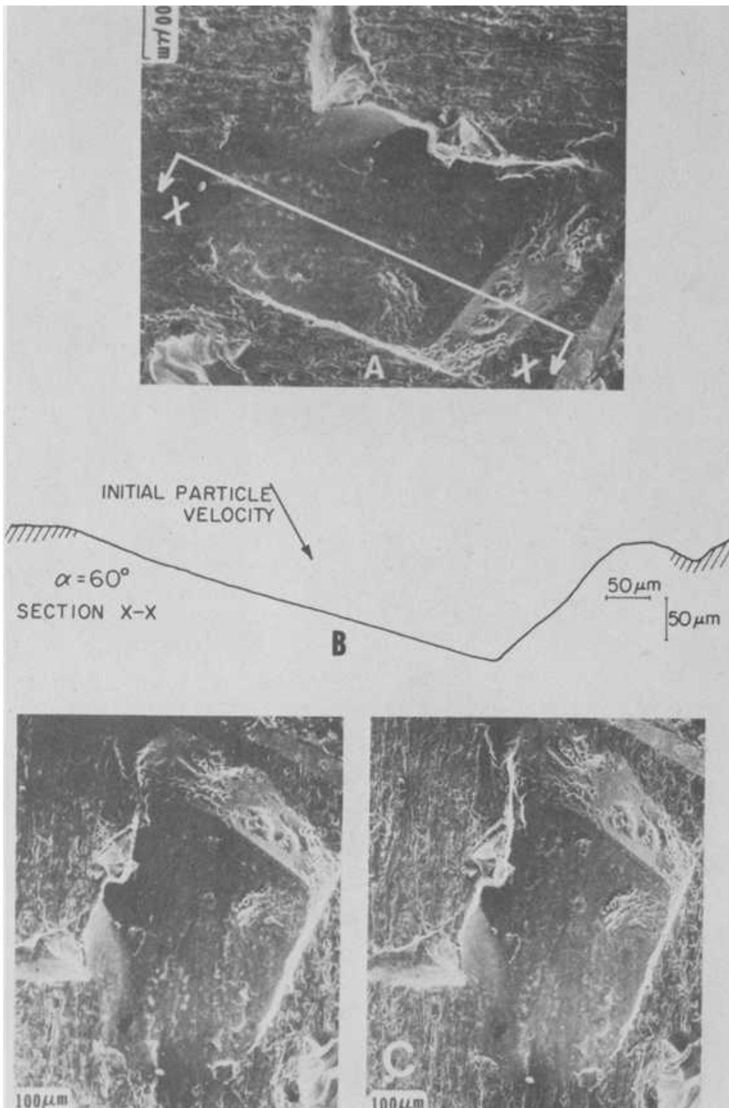

FIG. 5—*Same conditions as Fig. 3 except α is now 60 deg.*

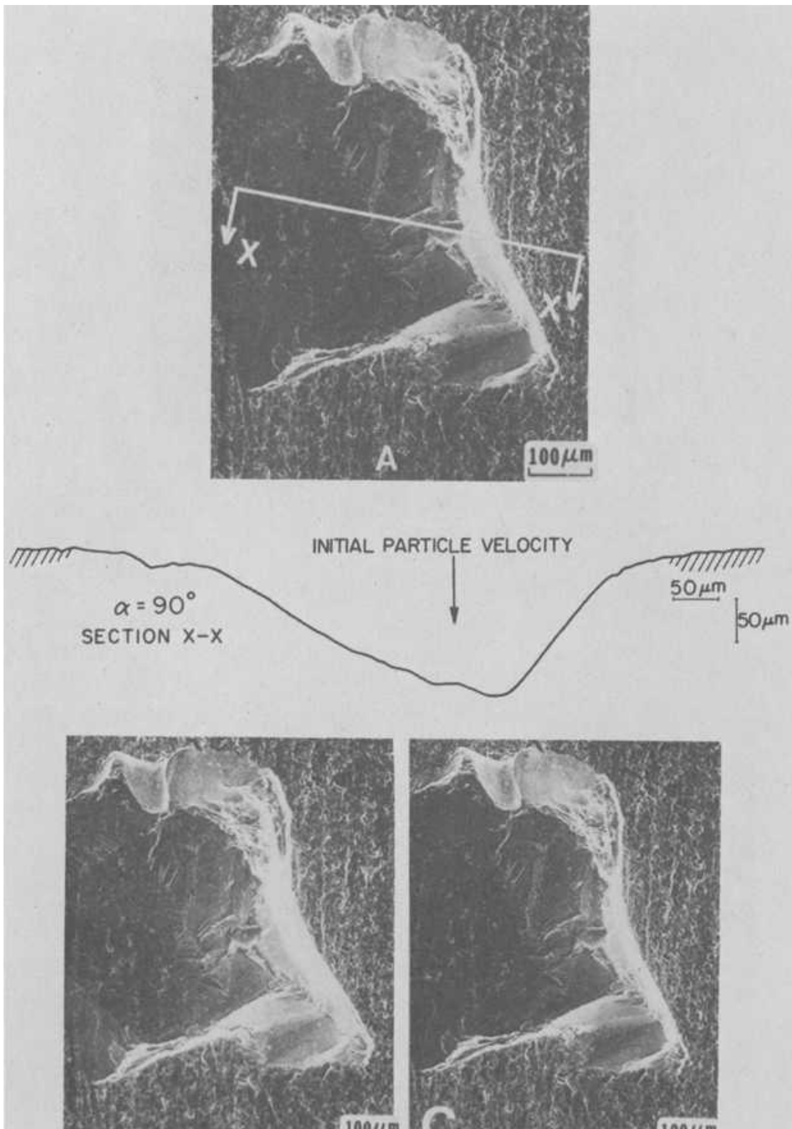

FIG. 6—*Same conditions as Fig. 3 except α is now 90 deg.*

is compared in Fig. 7 with experimentally observed values. The experimental curve was taken as the median one for all craters examined for each angle (that is, some were longer, some shorter). The maximum depth was scaled to be the same in each case. For α = 10 deg, the crater profile is predicted quite well. For α = 30 deg, it must be remembered that the particle comes to rest while cutting and only the coordinates of its tip are being predicted. The additional area removed may correspond to the region occupied by the particle. Perhaps fortuitously, this is approximately equal to the area piled up above the surface ahead of the arrested particle. However, stereo-viewing of the lower photographs in Figs. 3 and 4 also shows material piled up at the sides of the craters.

Influence of Material Properties on Cutting Erosion

So far, we have examined the effect of angle and velocity in a relative sense to avoid discussing the uncertain quantities c, p and to a lesser extent ψ. In previous work [*28*] it was found that the volume removed at $\alpha = 20$ deg and $U = 76$ m/s for several high-purity annealed face-centered cubic (fcc) metals was inversely proportional to their Vickers hardness, H_v. Since this result has been quoted on a number of occasions, and extended

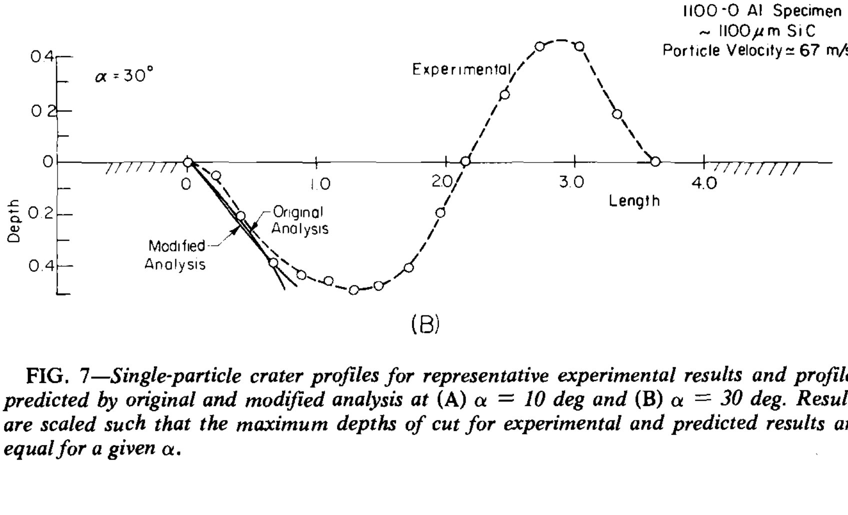

FIG. 7—*Single-particle crater profiles for representative experimental results and profiles predicted by original and modified analysis at* (A) α = *10 deg and* (B) α = *30 deg. Results are scaled such that the maximum depths of cut for experimental and predicted results are equal for a given* α.

beyond the range of validity claimed in the original work, it may be worth discussing in some detail. First of all, from volume removal measurements and Eq 3 with $\psi = 2$, an approximate value quoted [6] from these tests was $c/p = 0.1/H_v$. A more precise value would be $c/p = 0.15/H_v$, or in the more general case with ψ left as an unknown, $c/\psi p = 0.075/H_v$. Anyway, returning to the original expression $c/p \simeq 0.1/H_v$, this was used along with observations made in abrasion experiments that $c \simeq 0.1$ to deduce $p \simeq H_v$. However, SEM observations on single impacts in the cutting range show that almost all particles cut a crater with some of the material being displaced above the surface rather than being removed. To estimate p, the horizontal component of the flow pressure, the crater shapes shown in Fig. 7 were compared with those predicted analytically. For annealed commercially pure aluminum (1100-0), the average value obtained in the cutting range is $p \simeq 2H_v$ where H_v applies to the annealed material. On this basis we would deduce $c = 0.3$ for $\psi = 2$ or $c = 0.45$ for $\psi = 3$. Values of this magnitude for the fraction of particles cutting in an idealized manner appear reasonable. The raised material observed in single-particle experiments has to be removed by subsequent particles when multiple particle impact is involved. At this stage it appears difficult to be more quantitative about the values of the variables c, p, and ψ, but their combined value $c/p\psi$ may be deduced from experiments on a given material.

We return now to the relationship of p, the horizontal component of the flow pressure to the hardness or other material properties, since p is the only means of comparing the relative erosion resistance of different materials in the cutting analysis. In comparing different materials, we recall that erosion involves large strains, large strain-rates, and elevated temperatures in the region being deformed. By contrast, the Vickers hardness test is a measure of the flow stress at low strains and ambient temperature. A common approximation is to equate the Vickers hardness to three times the tensile stress at 8 percent strain. To a large extent, one would expect the effects of high strain rate and high temperature in erosion to offset one another. Thus, in comparing annealed high-purity fcc metals, which should have approximately similar stress-strain curves, it is not unreasonable to assume that the Vickers hardness is proportional to the flow pressure reached in erosion. However, if the annealed material is cold-worked before erosion, its Vickers hardness will be increased, but little change would be expected in the flow stress at very large strains where the stress-strain curve tends to become flatter. Thus, it is not surprising to find that prior cold work has essentially no effect on the erosion resistance of ductile metals [28]. In steels, large increases may be produced in the yield strength by alloying and heat treatment, but the strain-hardening following yield is much less pronounced than in, say, annealed fcc metals. Thus, we would expect the hardness of steels to overestimate their erosion resistance when using the result $V \sim (1/p) \sim (1/H_v)$ obtained from annealed fcc metals. Another illustration that the Vickers hardness cannot be relied upon to predict relative erosion resistance is the work of Brass [*29*] on AISI 1075 in pearlitic and spherodized forms. Comparing a fine pearlite with $H_v = 250$ kg/mm^2 and a spherodized structure with $H_v = 162$ kg/mm^2, the "softer" material is seen to erode about 15 percent less at $\alpha = 15$ deg, with both materials showing the same weight loss at $\alpha = 90$ deg. After correcting Brass's observations for the difference in velocity between his tests and those in Ref *28*, we found that his results for spherodized steel fell quite close to the relation obtained for annealed fcc metals. The most striking feature of these tests is, perhaps, that a dramatic difference in microstructure leads to relatively little change in erosion resistance. Tests [*29*] on an Al-4.75Cu alloy heat treated to give fine Guinier-Preston (GP) zone precipitates with a lower yield and a higher work-hardening rate than the larger precipitate θ' microstructure led to the unexpected result that GP-zone material eroded about 20 to 30 percent more at $\alpha = 15$ deg than θ' material, with relatively little difference being observed at $\alpha = 90$ deg. Again, after correction for the different velocities in these tests and Ref *28*, the erosion rate at $\alpha = 20$ deg is less than a factor of two greater than would be expected from the tests on annealed fcc metals.

The picture that emerges is a discouraging one from the point of view of material selection, if we consider ductile metals tested in air with hard abrasive particles. The result obtained with annealed high-purity fcc metals, $c/p \simeq 0.15/H_v$ at $\alpha = 20$ deg, appears to provide a lower bound for the volume removal when erosion occurs by a cutting mechanism. For practical purposes an upper bound would be more desirable. From previous work [*28*] and the tests of Brass [*29*] it is seen that prior cold-work or microstructural changes have little influence on erosion. While these conclusions are based primarily on tests at low values of α, where cutting is involved, they appear to apply also for erosion at higher angles. However, changing tests conditions such as softer and more friable particles or a corrosive environment could well alter these conclusions.

Erosion by Perpendicular Impingement

Our analytical treatment of erosion has been based on the cutting mechanism which has been shown to be limited to angles less than $\alpha \simeq 45$ deg. Various mechanisms have been postulated for removal when the particles impinge normally onto the surface, but these are all intuitive without any convincing proof. Among the mechanisms suggested for removal are: work-hardening and embrittlement [*9*], fracture of the particles with radial flow of fragments [*17*], an extrusion or pushing up of the surface [*20*], delamination of subsurface material [*29,30*], melting [*19*], and low-cycle fatigue [*6*]. The difficulty in deciding between these mechanisms is clear if we compare the volume removed by a typical particle at $\alpha = 90$ deg with the volume of the crater formed when a single particle indents the surface. If the hardness of the surface can be described by the Vickers hardness of the annealed material, this ratio is about 1:200. On the other hand, if we accept Sheldon's explanation [*21*] that the surface may be about five times harder than the annealed material, the ratio is about 1:40. In any event, the conclusion is that about 1 percent of the indentation volume, within a factor of two, is actually removed from the surface. With such a small fraction of the deformed volume removed, many removal mechanisms are plausible. However, several may be discounted by SEM. An examination of the same region as erosion progresses [*31*] eliminates both the embrittlement and melting mechanisms, and fracture of the particles does not appear to be a general explanation. The process is best described as a continuous "battering" of the surface, leading to removal when extrusion of vulnerable material leads to a ductile fracture. The removed material is "flake-like" which is consistent with either an "extrusion" type of mechanism or the concepts of "delamination wear" advanced by Suh [*30*]. This is illustrated by Fig. 8, which shows an aluminum surface eroded at $\alpha = 90$ deg [*31*]. Both photographs are of the same surface and have the same magnification. One was taken at 63 deg to the normal and the other is a cross section of the surface. For the present we favor, as the mechanism of removal, an extrusion process ending in ductile fracture, but we cannot exclude "low-cycle fatigue" or "delamination wear" as potential mechanisms. In fact, we believe that with further study these three potential mechanisms may prove to be interrelated rather than distinct.

Influence of Temperature and Environment

Although many erosion problems occur at elevated temperature and in a corrosive environment, there have been few basic studies which involved these variables. Unless elevated temperature tests are run in a vacuum or inert atmosphere, the effects of oxidation or other surface reactions may influence the results. Further complications would be expected if changes in particle strength, size, velocity, or flow rate alter the extent to which the surface scale is removed relative to the removal rate of the base metal.

Considering first the role of temperature, it is found in static tests that most metals cease to be of structural value when their homologous temperature (HT = temperature ÷ melting temperature in degrees absolute) is about one-half. However, because of the extremely high strain rate in erosion, one might expect to find strength levels maintained to higher temperatures than in static tests. The most extensive collection of experimental results reported to date is that of Tilly [*13*], who tested materials

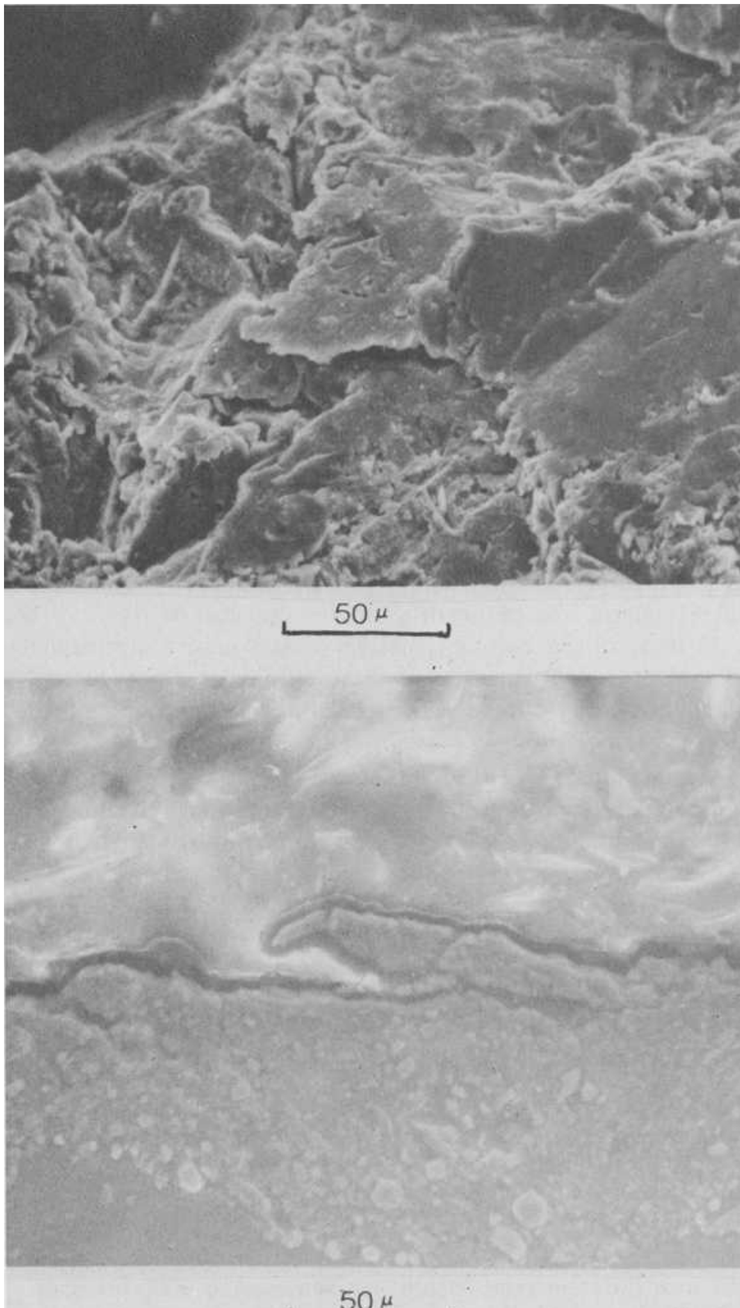

FIG. 8—*SEM photographs of 1100-0 aluminum eroded at* $\alpha = 90$ *deg and a velocity of 61 m/s by 600-µm silicon carbide particles. Top view is taken at 63 deg to the normal; lower view is a cross section of the surface.*

using a resistance-heated specimen in an airstream. From room temperature to about 500°C, a nickel alloy and a titanium alloy at $\alpha = 40$ deg and $\alpha = 90$ deg as well as an 11 percent chromium steel at $\alpha = 90$ deg showed little effect of temperature on erosion. On the other hand, the erosion *resistance* of a beryllium copper, an aluminum alloy, and a mild steel increased as the temperature was increased. For both the aluminum alloy and the steel the erosion at 400°C was only about a third of that at room temperature. The tests of Smeltzer et al [*19*] on four materials (2024 aluminum, 17-7 PH steel, 410 stainless, and Ti-6Al-4V) also showed little effect on erosion of gas temperatures ranging from ambient to 370°C. Recently, Young and Ruff [*32*] reported that at 500°C the oxide coating on certain alloys could decrease the erosion due to small particles (5 μm) relative to that due to larger particles. However, little difference was noted in the erosion at 25 and 500°C when larger particles (50 μm) were used at the same velocity and angle (52 m/s, 45 deg). These results point out the importance of the particle depth of cut relative to the thickness of the oxide coating. At the same time, Ives [*33*], using an ingenious test fixture which permits simultaneous testing of multiple specimens, examined the effect of temperature and environment on Type 310 stainless, a prime candidate material for coal-hydrogenation systems. At $\alpha = 90$ deg and 15 to 70 m/s, silicon carbide particles of 100 mesh (approximately 124 to 150 μm) produced considerably more erosion at 975°C than at 25°C. At the lowest velocity where the particles did not penetrate the oxide scale, the effect of temperature was more pronounced.

In another study [*34*], several metallic alloys and silicon nitride were exposed to oxidizing combustion gases at 870°C and velocities up to 270 m/s with and without 130 ppm of 20-μm aluminum oxide (Al_2O_3) particles. While the silicon nitride was relatively unaffected in either case, the metallic alloys showed two to three orders of magnitude more weight loss under erosion-corrosion conditions than with corrosion alone. In this case, each region of the eroded surface is being struck on the order of once per second. The oxide scale forming in this period is so thin that metal erosion governs removal rather than scale erosion. Additional evidence of the predominance of erosion under these types of turbine operating conditions relates to the differences in alloy behavior found with and without erosion. Iron- and nickel-base alloys that showed different behavior in corrosion tests behaved similarly in combined erosion-corrosion tests. The surface features which developed in these tests after exposure were typical of those observed in eroding ductile metals at both shallow and steep angles of impingement. As might be expected, smaller size (2 μm) Al_2O_3 particles resulted in a different relationship between erosion and corrosion. References *32–34* are notable for combining elevated temperature erosion measurements with microscopic observations of the surface and illustrate the complexity of the high-temperature erosion-corrosion problems.

For further experimental work we have designed a high-temperature erosion test facility which permits temperatures up to 1000°C with gas compositions typical of coal-hydrogenation processes. Details of the apparatus will be reported later. For the present we give only preliminary results on 1100-0 aluminum and 310 stainless steel with 250 μm particles, using nitrogen as the carrier gas. Particle velocities were measured using the rotating-disk technique of Ruff and Ives [*35*]. Figures 9 and 10 show the results of tests at 30.5 and 61 m/s on 1100-0 aluminum with HT = 0.32 (room temperature), 0.4 (99°C), 0.6 (285°C), and 0.8 (471°C). At the lower velocity the curves for the lower three temperatures are quite similar. Even the curve for HT = 0.8 shows a peak at about the same angle as the other tests. This indicates that a cutting mechanism is still involved at low angles even at the elevated temperatures. The decrease in erosion at low angles as temperature is increased, as in some of Tilly's tests, is unlikely to be due to an oxide scale. While his tests were run in air, ours were in nitrogen, and one would expect a shift in the angle for maximum erosion if a brittle material were being eroded. For α = 90 deg, the picture is reversed, with no change in erosion occurring up to HT = 0.6 and then a sudden increase for HT = 0.8. At the higher velocity, Fig. 10, the effect of angle on erosion is decreased. The curves still show a maximum at about α = 15 deg, but for HT = 0.8 the difference between the maximum erosion and that at 90 deg is only about 15 percent. At the higher velocity, the erosion rate increases with increasing temperature,

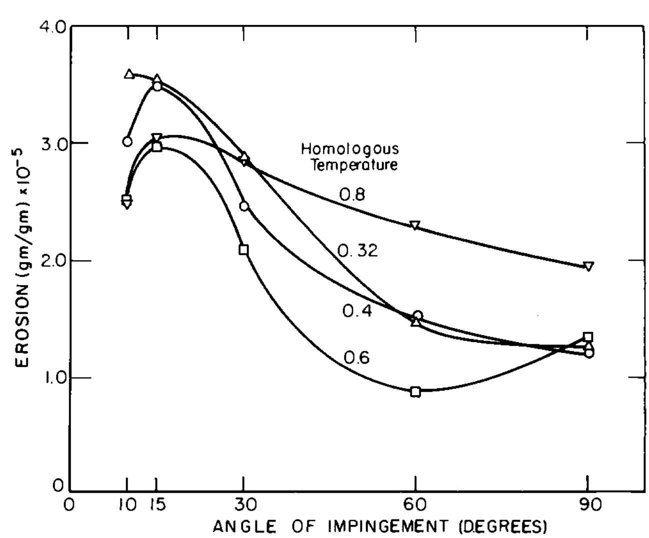

FIG. 9—*Erosion of 1100-0 aluminum at a velocity of 30.5 m/s as a function of angle for several temperatures.*

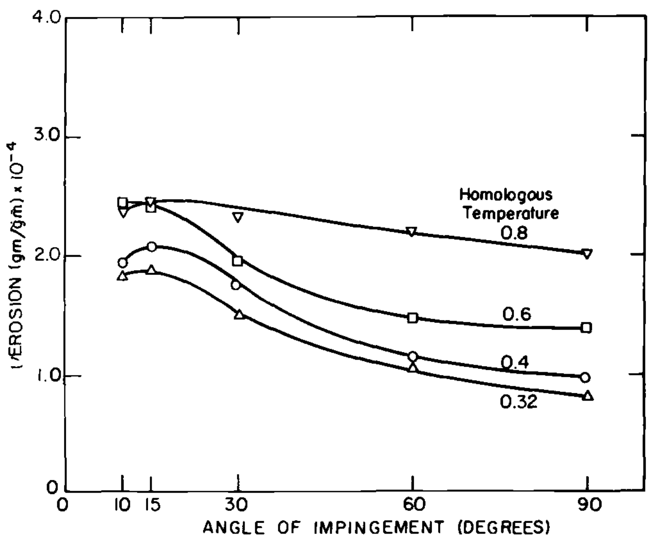

FIG. 10—*Erosion of 1100-0 aluminum at a velocity of 61 m/s as a function of angle for several temperatures.*

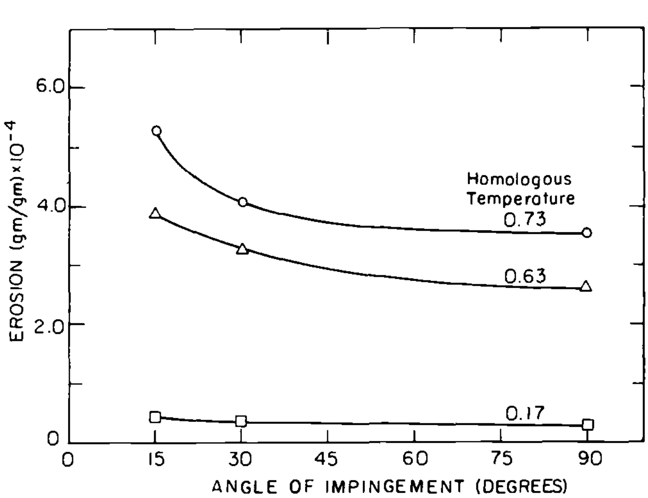

FIG. 11—*Erosion of Type 310 stainless at a velocity of 30.5 m/s as a function of angle for several temperatures. HT 0.73 = 982°C; HT 0.63 = 820°C; HT 0.17 = 20°C.*

which is a result that might be expected from a decrease in flow pressure with temperature. However, the increase in erosion is much smaller than would be expected from the effect of temperature on, say, the tension test. The preliminary tests on 310 stainless are shown in Fig. 11. By contrast with the tests on aluminum, increasing temperature has a profound effect on erosion, but the maximum erosion again occurs at low angles. At $\alpha = 25$ deg, $U = 30$ m/s and 975°C, Ives [*33*] found an increase in erosion by a factor of about five compared with tests at 25°C when testing with excess oxygen or excess propane. Our results at 982°C and 20°C in nitrogen show an increase due to temperature by a factor of about 11. This further illustrates the need to test with the corrosive environment expected in service.

From the references we have cited and Figs. 9-11, it is clear that additional work needs to be done to clarify the effect of temperature on the flow stress and other variables. Generally, the factors such as velocity and angle that influence the ambient temperature behavior of ductile and brittle materials appear to play a similar role in elevated-temperature testing. However, the particle size and concentration in the fluid stream are much more important at elevated temperature. Along with the velocity and angle, these variables will determine whether the particles remove a ductile metal or a brittle corrosion product. At the same time, the corrosive environment and temperature will control the growth rate of protective oxide scales and in some cases destructive sulfur compounds.

Conclusions

Many aspects of the erosion of ductile metals by rigid particles in the inert environment are quite well understood. The challenging and important problem, now, is to extend this work to elevated temperatures, corrosive environments, and particles which are typical of those found in service. An improved understanding of this complex problem will call for careful and extensive mechanical testing and metallurgical studies using specialized apparatus.

Acknowledgment

The tests at ambient temperature were carried out on test apparatus originally designed by Professor G. L. Sheldon. It was refurbished and fitted with new velocity calibration equipment by Mr. W. Toutolmin. Professor Sheldon also participated in the design of the high-temperature apparatus, which was constructed under the supervision of Mr. Toutolmin. Mr. P. Doyle helped construct the high-temperature apparatus and carried out the tests on aluminum.

The work was carried out at the Lawrence Berkeley Laboratory in a project funded by the Division of Physical Research of the U.S. Energy Research and Development Administration.

References

[1] Wahl, H. and Hartstein, F., *Strahlverschleiss*, Franckh'sche Verlagshandlung, Stuttgart, West Germany, 1946.
[2] Engel, P. A., *Impact Wear of Materials*, Elsevier, Amsterdam, The Netherlands, 1976.
[3] Preece, C. M. and Macmillan, N. H. in *Annual Reviews of Materials Science*, Vol. 7, 1977, pp. 95-121.
[4] Finnie, I. in *Proceedings*, 3rd U.S. National Congress of Applied Mechanics, 1958, pp. 527-532.
[5] Finnie, I. in *Symposium on Erosion and Cavitation, ASTM STP 307*, American Society for Testing and Materials, 1962, pp. 70-82.
[6] Finnie, I., *Wear*, Vol. 19, 1972, pp. 81-90.
[7] Sheldon, G. L. and Finnie, I., *Transactions*, American Society of Mechanical Engineers, Vol. 88B, 1966, pp. 393-400.
[8] Oh, H. L. et al in *Proceedings*, Symposium on the Science of Ceramic Machining and Surface Finishing, U.S. National Bureau of Standards Special Publication 348, U.S. Government Printing Office, 1972, pp. 119-132.
[9] Bitter, J. G. A., *Wear*, Vol. 6, 1963, pp. 5-21 and pp. 169-190.
[10] Neilson, J. H. and Gilchrist, A., *Wear*, Vol. 11, 1968, pp. 111-122 and pp. 123-143.
[11] Goodwin, J., Sage, W., and Tilly, G. P. in *Proceedings*, Institute of Mechanical Engineers, Vol. 184, Part 1, 1969-70, pp. 279-292.
[12] Sage, W. and Tilly, G. P., *Aeronautical Journal*, Royal Aeronautical Society, Vol. 73, 1969, pp. 427-428.
[13] Tilly, G. P., *Wear*, Vol. 14, 1969, pp. 63-79.
[14] Tilly, G. P., *Wear*, Vol. 14, 1969, pp. 241-248.
[15] Tilly, G. P. and Sage, W., *Wear*, Vol. 16, 1970, pp. 447-465.
[16] Tilly, G. P., *Wear*, Vol. 23, 1973, pp. 87-96.
[17] Tilly, G. P. and Sage, W., ASME Preprint 69-WA/Met-6, American Society of Mechanical Engineers, 1969.
[18] Kleis, I. et al., *Wear*, Vol. 31, 1975, pp. 403-408.
[19] Smeltzer, C. E., Gulden, M. E., and Compton, W. A., *Transactions*, American Society of Mechanical Engineers, Vol. 92, 1970, pp. 639-654.
[20] Sheldon, G. L. and Kanhere, A., *Wear*, Vol. 21, 1972, pp. 195-209.
[21] Sheldon, G. L., *Transactions*, American Society of Mechanical Engineers, Vol. 99H, 1977, pp. 133-137.
[22] Winter, R. E. and Hutchings, I. M., *Wear*, Vol. 29, 1974, pp. 181-194.
[23] Hutchings, I. M. and Winter, R. E., *Journal of Physics. D: Applied Physics*, Vol. 8, 1975, pp. 8-14.
[24] Hutchings, I. M. and Winter, R. E., *Wear*, Vol. 27, 1974, pp. 121-128.
[25] Winter, R. E. and Hutchings, I. M., *Wear*, Vol. 34, 1975, pp. 141-148.
[26] Finnie, I. and McFadden, D. H., *Wear*, Vol. 48, 1978, pp. 181-190.
[27] Finnie, I. and Kabil, Y. H., *Wear*, Vol. 8, 1965, pp. 60-69.
[28] Finnie, I., Wolak, J., and Kabil, Y. H., *Journal of Materials*, Vol. 12, 1967, pp. 682-700.
[29] Brass, L. L., "The Effects of Microstructure of Ductile Alloys on Solid Particle Erosions," MS Thesis in Materials Science and Engineering, University of California, Berkeley, Calif., June 1977.
[30] Suh, N., *Wear*, Vol. 25, 1973, pp. 111-124.
[31] Mayville, R., private communication.
[32] Young, S. P. and Ruff, A. W., *Transactions*, American Society of Mechanical Engineers, Vol. 99H, 1977, pp. 121-125.
[33] Ives, L. K., *Transactions*, American Society of Mechanical Engineers, Vol. 99H, 1977, pp. 126-132.

[34] Barkalow, R. H. and Pettit, F. S., Quarterly Progress Report (10/15/76-1/15/77) on EPRI Project RP 543-1, prepared by Pratt and Whitney Aircraft, Reference No. 75-200-7107-5, Electric Power Research Institute, Palo Alto, Calif., 1977.
[35] Ruff, A. W. and Ives, L. K., *Wear*, Vol. 35, 1975, pp. 195-199.

DISCUSSION

S. M. Wolf[1] (*written discussion*)—Your erosion model results from cutting by isolated particles. The substructure developed in the impacted region will be different from that after multiple impacts (in terms of dislocation network, subsurface crack formation). Therefore doesn't your model implicitly assume little or no effect of the aforementioned structural changes?

You showed erosion of steel by silicon carbide particles becoming more dependent on angle as the temperature increased. This is contrary to recent experimental results (at Lawrence Berkeley Laboratory and Battelle-Columbus). Please comment.

I. Finnie, A. Levy, and D. H. McFadden (*author's closure*)—Although the analysis is based on the action of an individual particle, the predictions are compared with test results using many particles in an attempt to deduce the flow pressure *p*. The approach of glossing over structural changes and characterizing a material only by a flow pressure that it experiences during erosion appears to be a good first approximation for ductile metals eroded at low angles.

Figure 11 for Type 310 stainless steel shows an increase in overall erosion with increasing temperature. At the same time the ratio of the erosion at 90 deg to that at 15 deg is increasing slightly less with increasing temperature, as is true also for our tests on aluminum. For the present we can offer only experimental results for the effect of temperature on erosion. It is perhaps premature to attempt to explain why the angular dependence changes with temperature until we understand better the mechanisms causing removal at large angles of impingement.

N. H. Macmillan[2] (*written discussion*)—You have used a two-dimensional (plane strain) analysis to relate erosive weight loss to particle impact angle and velocity, even though particle impacts do not result in plane-strain deformation. I would therefore like to ask if you have been able to make any progress with the (admittedly far more difficult) three-dimensional

[1] Department of Energy, Basic Energy Sciences Division, Washington, D.C. 20545.
[2] Pennsylvania State University, Materials Research Laboratory, University Park, Pa. 16802.

problem; and, if so, whether this latter approach predicts a similar dependence of erosion on impact angle and velocity.

I. Finnie, A. Levy, and D. H. McFadden (*authors' closure*)—In earlier work [5] it was shown that an irregular particle gives rise to the same dependence of erosion on angle and velocity as a two-dimensional particle. However, this analysis was based on the assumption that the resultant force during cutting acts on the tip of the particle. For the more realistic model that we have now discussed, in which the location of the resultant force moves as the particle makes a deeper cut, we have studied only the two-dimensional case. For typical values of the parameters used in erosion studies, this analysis predicts trends in the velocity exponent and explains why exponents greater than two are observed. It seems likely that similar results would be obtained with a three-dimensional analysis.

I. M. Hutchings[1]

Mechanisms of the Erosion of Metals by Solid Particles

REFERENCE: Hutchings, I. M., "**Mechanisms of the Erosion of Metals by Solid Particles,**" *Erosion: Prevention and Useful Applications, ASTM STP 664,* W. F. Adler, Ed., American Society for Testing and Materials, 1979, pp. 59-76.

ABSTRACT: The behavior of spherical and angular particles on oblique impact with a metal surface is illustrated by experiments using macroscopic projectiles. Three classes of behavior are identified: plowing and two types of cutting. Results of energy loss and crater volume determinations are given which agree with theoretical predictions. The strain rates occurring in erosion are estimated and shown to be extremely high (10^5-10^7 s^{-1}). This may explain the failure of quasi-static strength measurements to predict erosion resistance. The possibility of erosion being caused by melting is discussed and it is concluded that the process is primarily mechanical, with thermal effects playing only a subsidiary part.

KEY WORDS: erosion, impact, impingement, metals

Despite widespread interest in the problem of erosion by solid particles, and a growing understanding of the complex processes involved, there is still radical disagreement among workers in this field on the mechanisms by which hard particles remove material from a metal surface on impact.

This paper presents results from a study of the damage caused by single impacts of rigid projectiles of well-defined shape on to ductile metals. The impact behavior observed in these model experiments is compared with that predicted by a simple theory and with impact damage caused by hard irregular abrasive grains. The possible mechanisms by which erosion might occur are then discussed in the light of these results.

Since maximum erosion in ductile metals is always found to occur at low angles of impact, the experiments were carried out with impact angles between 20 and 40 deg to the metal surface.

[1] University demonstrator and Fellow of St. John's College, University of Cambridge, Department of Metallurgy and Materials Science, Pembroke Street, Cambridge, England; formerly with Cavendish Laboratory, Madingley Road, Cambridge, England.

The single-impact studies were carried out using very hard steel projectiles and work-hardened low-carbon steel targets (BS 970/En 1A, 0.15 percent carbon, Vickers Pyramidal Hardness = 235 kg/mm^{-2} ≃ 2.35 GPa). Two shapes of projectile were used: spheres of 9.5 mm diameter, weighing 3.5 g, and square plates 8 by 8 by 1.5 mm. Details of how the projectiles were accelerated and the impacts photographed using a high-speed camera are available elsewhere [*1-3*].[2] The square plates struck the target edge-on; the problem could therefore be treated theoretically as one in plane strain. This considerably simplified the theory and also meant that the experimental results should be applicable to square plates of any thickness, or to cubes, impacting edge-on.

The aims of the experiments were twofold: first, to identify the mechanisms by which metal may be removed from a surface in a single impact, and second, for comparison with theory, to make measurements of the motion of the projectile during and after impact.

In order to compare the results of the single-impact experiments with damage caused by irregular abrasive grains of submillimetre dimensions, targets were also impacted with sieved fractions of quartz sand, silicon carbide grit, and spherical glass beads at controlled velocities and impact angles using a gas gun [*1*]. The targets were then examined by scanning electron microscopy.

Single-Impact "Model" Experiments

Results

The single-impact experiments using spherical and square plate projectiles were carried out in order to simulate the various classes of impact which occur with irregular grains. Earlier experimental studies of single-particle impact [*4-6*] had identified two classes of surface deformation at oblique impact angles: plowing deformation, usually caused by spherical projectiles, and a type of deformation caused by angular particles and termed "cutting deformation" by Winter and Hutchings [*6*]. A third type of deformation, also caused by angular particles, has since been distinguished [*8*]. The classification of these three modes of deformation is best illustrated by reference to the series of high-speed photographs (Fig. 1) and to the outlines of crater sections (Fig. 2).

Figure 1*a* depicts a typical impact of a spherical projectile at an impact angle of 30 deg. In Frame 2 the sphere strikes the surface, leaving it again in Frame 4 and removing a fragment of material which is clearly visible in subsequent frames. The source of this material is evident in Fig. 2*a*, which shows a sectional view through a similar crater from which no material has

[2] The italic numbers in brackets refer to the list of references appended to this paper.

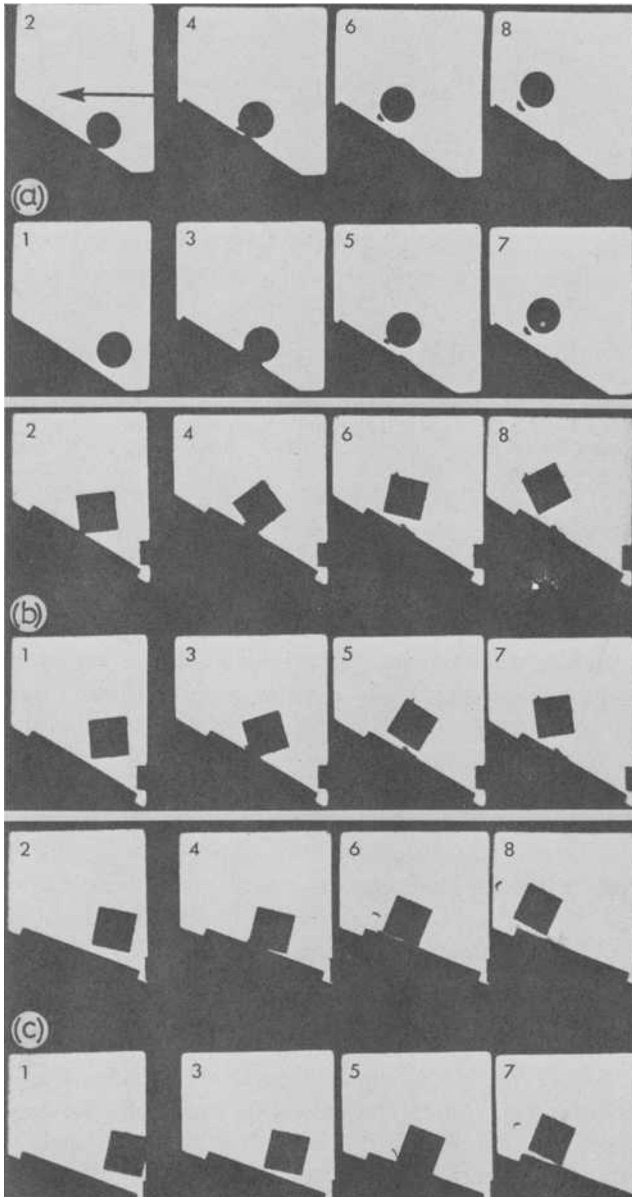

FIG. 1—*High-speed photographs (19-μs interframe time). Frames are numbered sequentially.* (a) *9.5-mm hard steel ball striking mild steel at 212 m s^{-1} and 30 deg impact angle. The initial direction of motion of the ball is indicated by the arrow. Plowing deformation.* (b) *8-mm square plate impacting mild steel at 153 m s^{-1}. Impact angle 30 deg, rake angle −35 deg. Type I cutting deformation.* (c) *8-mm square plate at 152 m s^{-1}. Impact angle 20 deg, rake angle −7 deg. Type II cutting deformation.*

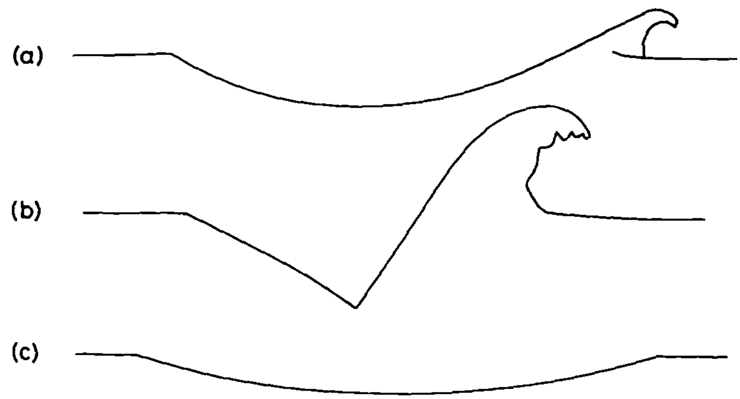

FIG. 2—*Sections through impact craters showing typical shapes. Impact direction left to right.* (a) *Plowing deformation by a sphere.* (b) *Type I cutting.* (c) *Type II cutting.*

been removed. The lip of material at the exit end of the crater has been pushed up in front of the ball and folded over onto the undisturbed surface of the metal; at a higher impact velocity or lower impact angle the lip shown in the diagram would have been removed in exactly the same way as the lip seen in the high-speed photographs. By no means all the metal displaced from the crater in Fig. 2*a* has been extruded into the lip; the lip represents typically only 10 to 25 percent of the total crater volume at an impact angle of 30 deg [*7*]. The other material displaced forms less highly strained ridges around the sides of the crater. We may describe this form of deformation, by a spherical particle or by a rounded surface of an irregular particle, as "plowing."

The study of square-plate impacts revealed two quite different types of behavior. A further impact variable now becomes important: the orientation of the plate at impact. This may be described by the "rake angle" as defined later in Fig. 5*a*. It is convenient to adhere to the convention adopted in metal-cutting studies whereby the rake angle shown in the figure is *negative*. In these experiments the rake angle of the plate could be adjusted independently of the impact angle (see Ref *2*). The predominant type of deformation, observed over a wide range of rake angles, was the "cutting" deformation described previously [*6*] and seen in Fig. 1*b* and 2*b*.

The plate seen in Fig. 1*b* strikes the surface with an impact angle of 30 deg and a rake angle of −35 deg. It rebounds from the surface with appreciable rotational velocity in the forward direction. The indentation formed by this type of impact has the characteristic triangular shape shown in Fig. 2*b*. Under these plane-strain conditions, all the metal displaced from the indentation is pushed forward into the large lip at the exit end, which is clearly vulnerable to removal by subsequent impacts. This type of behavior was observed for plates impacting at rake angles between −17 and −90 deg at a 30-deg impact angle.

For rake angles between 0 and −17 deg at this impact angle, however, the plate was found to execute a backward rotation as shown in Fig. 1*c*, and the impact resulted in a crater of the shape shown in Fig. 2*c*, from which *all* the metal was removed. Backward rotation of the plate results in a perfect machining action, cutting out the chip of metal which is clearly visible moving away from the target in Fig 1*c*, Frames 5 to 8.

Since the behavior of the plate in cases of both forward and backward rotation may be broadly termed "cutting," although only the backward rotation leads to the removal of a machined chip, it is proposed to distinguish between the two senses of rotation by referring to the more common, forward rotation, as "Type I cutting" and the backward rotation as "Type II cutting." Type II cutting, since it occurs over a narrower range of rake angles than Type I cutting, would be observed in only about one sixth of the impacts of randomly oriented plates at 30-deg impact angle.

The volumes of the indentations below the original surface of the target were measured for plowing and Type I cutting impacts. Volumes were measured for only a few Type II cutting impacts and were found in all cases to be less than those resulting from Type I cutting impacts at the same velocity. The crater volumes measured for plowing and Type I cutting impacts are plotted against impact velocity in Fig. 3. To aid comparison, the volumes measured for the plate impacts have been multiplied by a scaling factor so that the volumes plotted are those which would have been caused by plates 8 mm square and of the same mass as the spheres. The same scaling factor was applied to the results of energy loss plotted in Fig. 4; the results represent the initial kinetic energy of the projectile minus its final kinetic energy of translation and rotation, and therefore correspond to the amount of energy available for deformation of the targets. The total kinetic energy of a 3.5-g projectile traveling at the impact velocity is shown for comparison.

Theoretical treatment

The solid lines plotted in Figs. 3 and 4 represent the predictions of a theoretical treatment developed in the course of this work. The details of its application to the impact of spherical and square-plate projectiles are available elsewhere [*7,8*] but the assumptions of the theory will be briefly summarized here.

In the quasi-static formation of a plastic impression by the indenter in a conventional hardness test, the force on the indenter may be represented fairly accurately by a constant pressure acting on the area of the indenter in contact with the metal. This pressure is a measure of the hardness of the

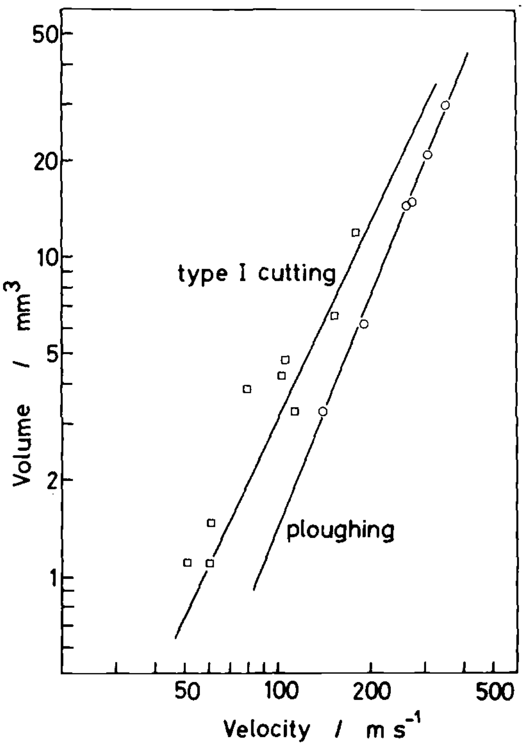

FIG. 3—*Indentation volume measured after impact for 30-deg impact angle, plotted against impact velocity. Square symbols denote Type I cutting results, circles are plowing results. The solid lines are the theoretical predictions for Type I cutting (−30 deg rake angle) and plowing.*

metal [*9*]. By extending the idea of a constant indentation pressure to the case of oblique impact, the equations of motion of a projectile can be written at any stage during its impact. In general, these equations cannot be solved analytically, but numerical treatment using a computer enables the motion of the projectile during impact and its final velocity and rate of rotation to be predicted.

The theory therefore assumes a constant pressure to act over that part of the projectile which is in contact with the target at any instant. In the case of a spherical projectile which will be sliding over the surface during oblique impact, an additional tangential frictional force is assumed to act, related to the normal force by a conventional coefficient of friction. Measurements with the steel balls used in this work revealed [*7*] that at the high sliding speeds involved the coefficient of friction had the very low value of about 0.04. Friction, therefore, has a correspondingly small effect on the predictions of the theory. The plastic indentation pressure and the frictional force are assumed to be the only forces acting on the projectile, which is assumed

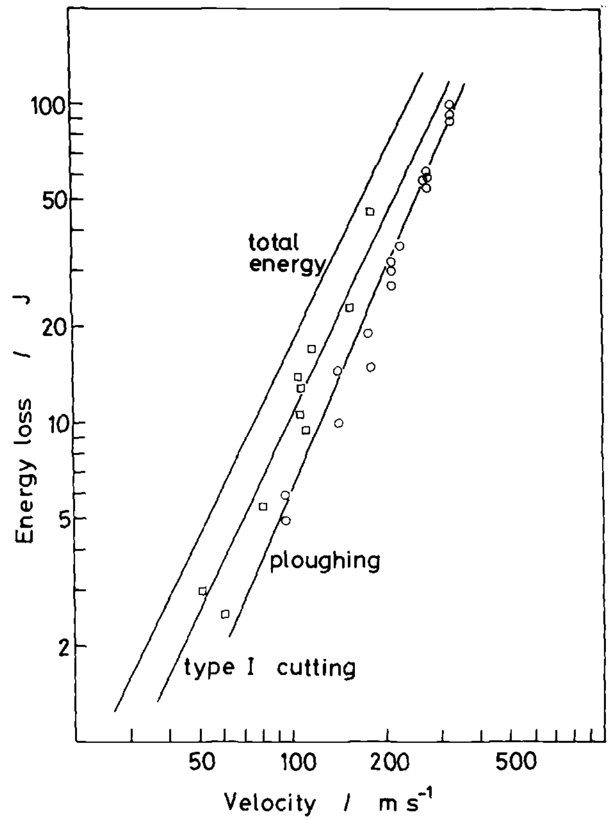

FIG. 4—*Kinetic energy lost by the projectile for 30-deg impact angle, plotted against impact velocity. Square symbols denote Type I cutting results, circles are plowing results. The solid lines are theoretical predictions for Type I cutting (−30-deg rake angle) and plowing. The total kinetic energy of the projectile at the impact velocity is also shown.*

to behave rigidly. Elastic stresses and strains are neglected since the plastic strains are much larger. The properties of the target material are therefore represented by only one undetermined variable: the plastic indentation pressure. Since the crater volumes predicted by the theory are sensitive to variations in the plastic indentation pressure, its value was determined empirically to ensure the best correlation with the experimental data.

Figures 3 and 4 show the predictions of the theory (solid lines), taking the indentation pressure to be 4 GPa. An indentation pressure somewhat higher than the quasi-static hardness of the target material (~ 2.35 GPa) is not unreasonable in view of the high strain rates and inertial effects associated with impact. The correspondence between theory and experiment is good. Particularly noteworthy are the velocity exponents of 2.0 predicted and observed for crater volumes and energy losses in square-plate impact, and the values of 2.3 to 2.4 predicted and observed for sphere impacts. In the case of square-plate impact, the model also predicts the possibility of both senses of rotation, leading to the two types of cutting. The computer-generated diagrams in Fig. 5 show the predicted behavior of the plate as the rake angle is changed at a constant impact angle. In Fig. 5*b* the rake angle is −10 deg and the plate rotates backwards during impact, executing a Type II cutting action. As the rake angle is changed to −30 deg in Fig. 5*c*, the direction of rotation changes; the crater form now has the characteristic triangular section of Type I cutting. Figure 5*d* shows that as the rake angle changes further, to −45 deg, the rate of spin of the plate can be such that a secondary impact occurs as the plate "cartwheels" over the surface. Such behavior has been observed experimentally [*8*]. The rake angle at which the sense of rotation changes is predicted theoretically to be

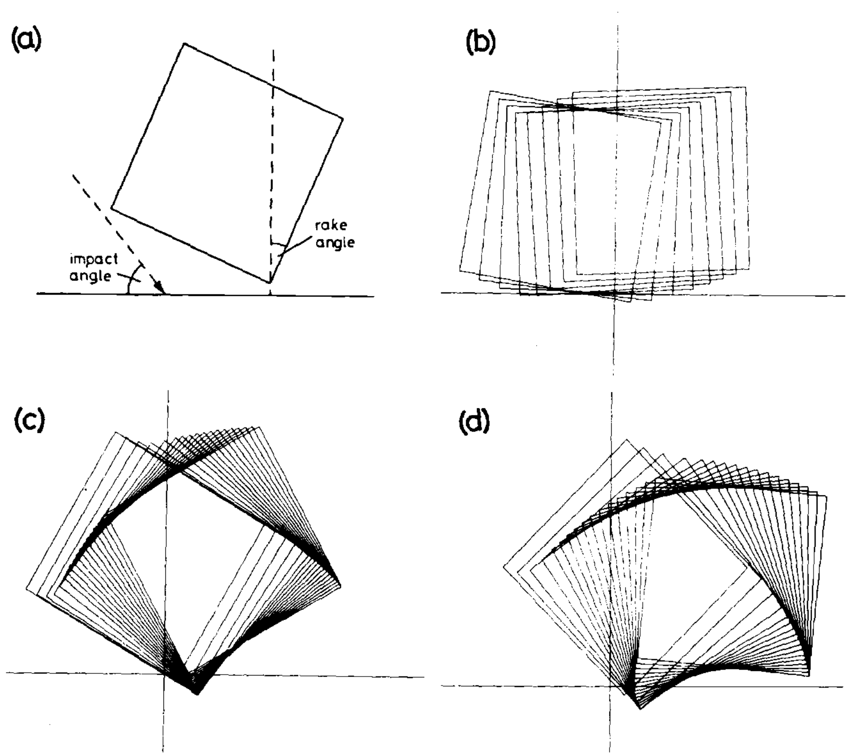

FIG. 5—*Computer-generated diagrams of the position of a square steel plate at 2-μs intervals during impact, predicted theoretically. The impact angle and rake angle are defined as shown in* (a). (b) *Impact angle 30 deg, rake angle −10 deg, velocity 200 m s*$^{-1}$. (c) *Impact angle 30 deg, rake angle −30 deg, velocity 150 m s*$^{-1}$. (d) *Impact angle 30 deg, rake angle −45 deg, velocity 200 m s*$^{-1}$. *The origin of the axes marks the point of initial contact between the plate and the target.*

-15 deg for impacts at 30-deg impact angle, and to be largely independent of impact velocity. Other values of critical rake angle predicted by the theory are -11 deg for impacts at 20 deg and -16 deg for impacts at 40 deg.

Discussion

The three types of deformation revealed in this experimental study point to three possible mechanisms of metal removal by hard irregular particles. In all cases of Type II cutting observed, the machined chip was completely removed from the surface; this mechanism will, therefore, lead to a loss of material in a single impact. Plowing impacts lead to weight loss in a single impact only within a certain regime of velocity and impact angle, but clearly in a realistic erosive environment, where the surface is being continually bombarded by particles, not only the vulnerable lip at the crater end but also the metal extruded into the side ridges will be removed by subsequent impacts. Similarly in the case of Type I cutting the metal raised in front of the indentation is liable to be removed by another impact of an angular particle, whatever its rake angle.

Figures 3 and 4 show that the crater volumes are predicted theoretically and found experimentally to be proportional to the energy lost by the projectile during impact, for both plowing and Type I cutting cases. It is of interest to note that in the case of cutting impacts, where geometric similarity of the indentation applies, the velocity exponent is 2.0, but that for plowing impact caused by spheres, the velocity exponent is close to 2.4. The origin of this higher exponent, which is predicted from the simple theoretical assumptions presented in the foregoing, may be explained in the following way. As the impact velocity of a sphere increases, so the geometry of the indentation changes; in particular, the angle of the exit "ramp" of the crater becomes steeper and the sphere loses more of its energy in the later stages of the impact. For the same reason that the energy loss shows this high velocity exponent, so does the crater volume, and the proportionality between volume and energy loss is preserved. But if a larger proportion of the initial kinetic energy of the sphere is being dissipated as the impact velocity increases, as is implied by a velocity exponent greater than 2, then there must come a point when all the energy is dissipated in the impact and the exponent therefore must fall to 2.0. The velocity exponent of 2.4 can therefore only apply over a finite velocity range.

Irregular-Particle Impacts

Impact experiments using hard irregular particles of about 400-μm dimensions were carried out so that the results of the model experiments could be compared more closely with the impacts of real erosive particles. The same low-carbon steel target material was used, and the particles studied were silicon carbide grits (350 to 420 μm), quartz sand (420 to 500 μm), and glass beads (420 to 500 μm). The glass beads were very nearly spherical. The silicon carbide grits were angular, with some acute-angled corners; typical profiles are depicted in Fig. 6*a*. The quartz grains tended to be more rounded but still irregular with occasional sharp-cornered particles. Figure 6*b* shows some shapes of the quartz sand grains.

Scanning electron microscopy of polished steel surfaces impacted with these grits revealed that most of the impact craters could be classified in terms of the three impact modes discussed earlier. The glass beads caused uniform craters exactly similar to those observed with spherical projectiles in the model experiments. Figure 7*a* shows a plowing impact caused by a glass bead. Many of the impact craters caused by quartz sand grains were of the plowing form, as seen in Fig. 7*b*, although some impacts were of a cutting type and presumably resulted from more angular grains. Figure 7*c* shows Type I cutting deformation (foreground) with a plowed crater behind. In Fig. 7*d* another Type I cutting impact has formed a characteristic triangular-sectioned crater with raised material at its end. Only occasionally was impact damage found which could definitely be attributed to Type II cutting (true machining action). Figure 7*e* shows one such case; the very long crater with a complete absence of raised material at the exit end points to this type of behavior. Some craters could not be unequivocally classified, Fig. 7*f* being an example. The length/breadth ratio of the crater is suggestive of a Type II cutting impact, yet the crater has clearly been formed by a particle with a rounded edge in contact with the surface. The many

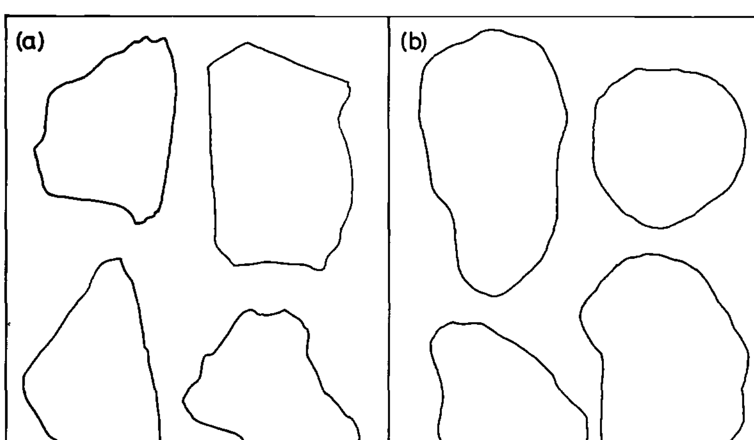

FIG. 6—*Typical particle shapes of abrasive grains.* (a) *Silicon carbide grit.* (b) *Quartz sand.*

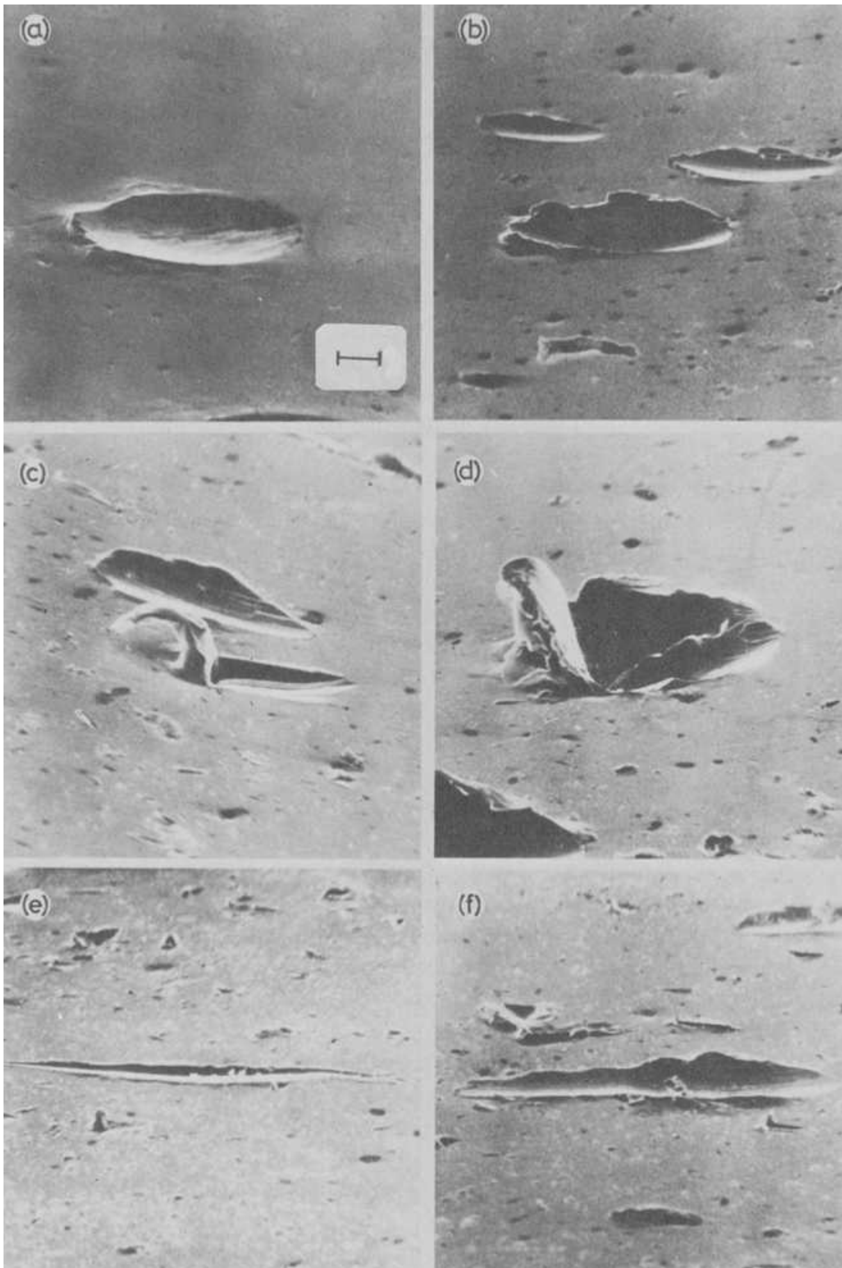

FIG. 7—*Scanning electron micrographs of impact sites in mild steel caused by abrasive grains. Impact angle 25 deg. Impact direction right to left.* (a) *Glass bead, 500 to 420 μm, 142 m s^{-1}. Scale bar represents 50 μm.* (b) *to* (f) *Quartz sand grains, 500 to 420 μm, 130 m s^{-1}. (See text for detailed descriptions.)*

much smaller impact sites visible in the micrographs resulted from fragments of quartz grains which broke up on impact.

Surfaces impacted with silicon carbide grit showed the same types of impact damage, but with rather fewer craters attributable to plowing and more to Types I and II cutting. However, Type II cutting was still only rarely observed.

Discussion of Erosion Mechanisms

The theories of erosion proposed by previous writers may be broadly classified into those which are mechanical, in which impact stresses lead to deformation or fracture of the metal and its consequent removal, and the thermal mechanisms in which melting of the material is postulated, metal being removed in the form of molten droplets.

Foremost among the mechanical theories is that of Finnie [*10-12*], who pictured a sharp-cornered particle striking a plane surface and assumed that it would rotate only slightly while in contact with the surface. Solving simplified equations of motion by analytical methods, Finnie predicted the trajectory of the tip of the particle through the metal and hence the volume of metal removed by this "machining" action from the surface. This theoretical treatment was found to overestimate erosion rates, and a factor was introduced to allow for the considerable proportion (perhaps 90 percent) of particles which do not cut in an idealized manner. These particles, impinging with an unfavorable orientation, were assumed to remove no material. Finnie's model differs in only one important respect from that employed in the present work. Whereas we have assumed a constant yield pressure acting over that area of the particle which is plastically deforming the substrate, and therefore a force vector continually changing in direction during impact, Finnie assumes a constant ratio of normal to tangential force, and hence a force vector of constant direction. The ratio of normal to tangential force assumed by Finnie, namely, 2.0, is close to the values which may be deduced from the critical rake angles predicted by the current theory. These ratios are 1.48 for impacts at 20 deg, 1.73 at 30 deg, and 1.80 at 40 deg. Finnie's assumption of a constant force ratio effectively represents an averaging over all the possible orientations or rake angles of the particle. His model does not, therefore, predict the variations in behavior with rake angle predicted by the model used here and observed experimentally: the phenomena of forward and backward rotation. As shown in the foregoing, a true machining action in which a chip of metal is removed by Type II cutting is rare; this explains the lack of experimental evidence for a machining mechanism in erosion. Many more particles displace and remove metal by the plowing and Type I cutting processes.

The relative importance of the types of deformation discussed in the previous sections depends not only on their frequency of occurrence, but also on the efficiency of metal removal in the three cases. Although metal removal was not observed in single Type I cutting impacts with mild steel, it has been shown to occur if the metal is particularly susceptible to failure by an adiabatic shear mechanism [*13*]. However, any subsequent suitably placed impact would remove a raised lip of material which was not removed in the first impact. In such a case the volume of the lip, which in plane-strain deformation is the same as the indentation volume, determines how much metal is removed by the second impact. Similar arguments would apply in the case of plowing impacts. All three types of deformation can therefore lead to metal removal, and it is suggested that these are responsible for the weight loss in ductile erosion at low impact angles.

Proponents of thermal mechanisms of erosion tend to emphasize the correlations observed between erosion rates and thermal properties of the target materials. Ascarelli [*15*] has found excellent correlation between the erosion rates of pure metals and a "thermal pressure" defined as the product of the linear thermal expansion coefficient, the temperature rise required for melting, and the bulk modulus of the metal. Some correspondence exists between erosion rate and melting point [*16,17*], and a correlation as good as that found by Ascarelli is found with the product of density, specific heat, and temperature rise required for melting [*18*]. More recently, correlation has been found for several alloys with the cube root of the mean molecular weight divided by the thermal conductivity, the melting temperature, the enthalpy of melting, and the cube root of the density of the metal [*19*]. Other correlations have, however, been found between erosion rates and the hardness of the annealed metal [*20*], Young's modulus [*21*], and interatomic bond energy [*22*], suggesting that consideration of thermal properties is not essential to obtaining a correlation.

It is clear that some temperature rise in the target material adjacent to an impacting particle must be expected, since the kinetic energy lost by the projectile in an inelastic impact will be largely (>90 percent) degraded into heat. An estimate can be made of this energy loss, based on the experimental evidence presented earlier; for a Type I cutting impact at 30-deg impact angle, between 40 and 80 percent of the energy of the incoming square plate is dissipated in the target metal. However, in order to arrive at a figure for the temperature rise, an estimate must be made of the volume of metal in which this energy is dissipated. Metallographic examination of the oblique impact sites of spheres and angular particles suggests that the deformed volume is about twice the volume of the indentation. Making this assumption, if 80 percent of the kinetic energy of a 3.5-g projectile at 100 m s^{-1} is dissipated in a volume of twice 3.2 mm^3 (from Fig. 3), the temperature rise in mild steel would be about 500 K. If only 40 percent of the energy were lost, then the rise would be 250 K. These temperatures are high, but not high enough to cause melting. At other impact velocities, since the crater volume has been found experimentally to be proportional to the energy loss, the predicted rises would be the same. Ascarelli [*15*] and

Smeltzer et al [*16*] have both suggested that, in the impacts of sharp particles, "snagging" of the corner of the particle will lead to the highest temperatures and to melting. But "snagging" of the corner of a particle is essentially the same as the Type I cutting discussed earlier, and we have seen that in an extreme-case calculation the temperature rise is insufficient for melting. In proposing a melting mechanism for erosion, it is not enough to show, as has been done [*16*], that there is ample energy available to melt the *mass of metal removed*; a plausible mechanism must be suggested by which the energy can be concentrated in a volume very much less than that of the indentation.

Mention must be made here of the possible role of localized shear deformation in erosion. Metallographic studies of the deformed metal around plowing and Type I cutting impact sites formed in the model experiments reveal that the plastic deformation is not always homogeneous. Figure 8 shows examples of localized shear observed in mild steel. At the base of the lip of the plowed crater (Fig. 8*a*) a band of intense deformation is visible; at higher impact velocities the lip detaches along the line of this band. Bands of shear are also seen in Type I cutting impacts in mild steel (Fig. 8*b*) although failure of the metal along these bands was not observed. It has been suggested that the formation of these bands is aided by the local temperature rise resulting from adiabatic high-strain deformation [*6,7*]; certainly titanium, which is highly susceptible to failure by adiabatic shear, forms very pronounced bands in Type I cutting impacts [*13*]. These shear bands are formed, however, within the deformed metal and, although high temperatures are associated with them, any melting of the metal is very localized and simply aids the detachment of a lip of material formed by a plowing or cutting process. The fundamental mechanism operating is therefore mechanical, melting playing only a subsidiary role in aiding the removal of deformed metal.

If the erosion of ductile metals is predominantly mechanical in origin, with thermal phenomena being of only secondary importance, it remains to be explained why conventional strength measurements and hardness tests on a metal give such poor indication of its erosion resistance, as several authors have noted [*20,24*]. One possible explanation lies in the rate at which metal around the impact site is deformed. By applying simple elastic and plastic indentation theories to the normal impact of a sphere on a plane, the impact duration and mean strain rate around the indentation may be estimated. Details of the calculation are given elsewhere [*25*]. It is found that the elastic and plastic theories give very similar results; for the normal impact of a 200-μm-diameter quartz sphere onto mild steel at 100 m s^{-1} an impact time of about 100 ns is predicted, with a mean strain rate of around 5×10^5 s^{-1}. Both impact time and strain rate vary with particle size; for a 2-μm sphere the values are 1 ns and 5×10^7 s^{-1}. Erosion therefore involves very high strain rates, a point which has only briefly been

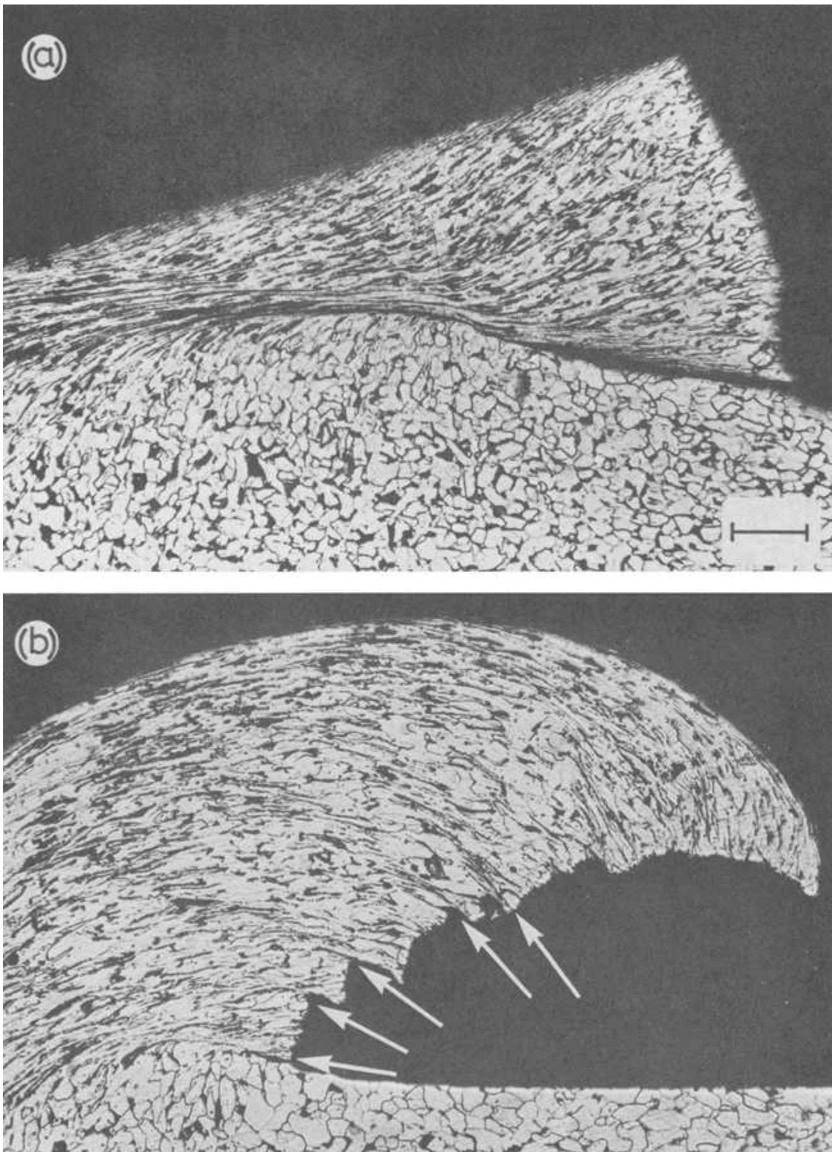

FIG. 8—*Sections through crater lips formed in mild steel, etched in 2 percent nital, showing bands of localized shear. Impact direction left to right.* (a) *Plowing deformation. Scale bar = 100 μm.* (b) *Type I cutting. Arrows indicate shear zones.*

made in the literature [20]. Very little is known of the behavior of metals at such high rates of strain, since conventional dynamic testing techniques can be applied only up to rates of about 10^5 s^{-1} (see for example Ref 26]. Possibly the combinations of physical properties used as predictors of erosion resistance and discussed earlier do in fact provide estimates of the strengths of metals at very high plastic strain rates. It is clear, however, why quasi-static measurements cannot be used to predict the behavior of metals under erosion conditions, and the variation of strain rate with particle size provides a plausible explanation for the size effect in erosion reported by several authors [16,27,28].

Conclusions

Three types of deformation have been identified which occur in the oblique impact of hard irregular grains onto ductile metals. All three can lead to weight losses from the surface in multiple-impact erosion; although thermal effects may be of secondary importance, the predominant mechanism of erosion appears to be mechanical. Very high strain rates are associated with the impact of small hard particles. This may explain the particle size effects observed in erosion and the lack of correlation between erosion rates and quasi-static strength measurements.

Acknowledgments

D. R. Andrews carried out the impact experiments with the small abrasive grits. I thank St. John's College, Cambridge for a Research Fellowship and the Science Research Council for a grant to the laboratory.

References

[1] Hutchings, I. M. and Winter, R. E., *Journal of Physics E: Scientific Instruments*, Vol. 8, 1975, pp. 84-86.
[2] Hutchings, I. M., Rochester, M. C., and Camus, J.-J., *Journal of Physics E: Scientific Instruments*, Vol. 10, 1977, pp. 455-457.
[3] Hutchings, I. M., "The Erosion of Metals by Solid Particles—A Study Using High-Speed Photography," *Proceedings*, 12th International Congress on High Speed Photography, Toronto, Canada, Aug. 1976, pp. 358-361.
[4] Sheldon, G. L. and Kanhere, A., *Wear*, Vol. 21, 1972, pp. 195-209.
[5] Hutchings, I. M. and Winter, R. E., *Wear*, Vol. 27, 1974, pp. 121-128.
[6] Winter, R. E. and Hutchings, I. M., *Wear*, Vol. 29, 1974, pp. 181-194.
[7] Hutchings, I. M., Winter, R. E., and Field, J. E., *Proceedings of the Royal Society*, London, Vol. A348, 1976, pp. 379-392.
[8] Hutchings, I. M., *International Journal of Mechanical Sciences*, Vol. 19, 1977, pp. 45-52.
[9] Tabor, D., *The Hardness of Metals*, Clarendon Press, Oxford, 1951.
[10] Finnie, I. in *Proceedings* 3rd U.S. National Congress of Applied Mechanics, American Society of Mechanical Engineers, 1958, pp. 527-532.
[11] Finnie, I., *Wear*, Vol. 3, 1960, pp. 87-103.
[12] Finnie, I., *Wear*, Vol. 19, 1972, pp. 81-90.

[13] Winter, R. E. and Hutchings, I. M., *Wear*, Vol. 34, 1975, pp. 141-148.
[14] Bitter, J. G. A., *Wear*, Vol. 6, 1963, pp. 5-21 and 169-190.
[15] Ascarelli, P., "Relations Between the Erosion by Solid Particles and the Physical Properties of Metals," Report AMMRC TR 71-47, Army Materials and Mechanics Research Center, Watertown, Mass., 1971.
[16] Smeltzer, C. E., Gulden, M. E., McElmury, S. S., and Compton, W. A., "Mechanics of Sand and Dust Erosion in Gas Turbine Engines," USAAVLABS Technical Report 70-36, U.S. Army Aviation Material Laboratories, Fort Eustis, Va., 1970.
[17] Smeltzer, C. E., Gulden, M. E., and Compton, W. A., *Journal of Basic Engineering*, Sept. 1970, pp. 639-654.
[18] Hutchings, I. M., *Wear*, Vol. 35, 1975, pp. 371-374.
[19] Jennings, W. H., Head, W. J., and Manning, C. R., *Wear*, Vol. 40, 1976, pp. 93-112.
[20] Finnie, I., Wolak, J., and Kabil, Y., *Journal of Materials*, Vol. 2, pp. 682-700.
[21] Brauer, H. and Kriegel, E., *Chemie-Ingenieur-Technik*, Vol. 37, 1965, pp. 265-276.
[22] Vijh, A. K., *Wear*, Vol. 39, 1976, pp. 173-175.
[23] Uetz, H. and Gommel, G., *Wear*, Vol. 9, 1966, pp. 282-296.
[24] Tilly, G. P., *Wear*, Vol. 14, 1969, pp. 241-248.
[25] Hutchings, I. M., "Strain Rate Effects in Microparticle Impact," *Journal of Physics D: Applied Physics*, Vol. 10, 1977, pp. L179-L184.
[26] Lindholm, U. S. in *Mechanical Properties at High Rates of Strain*, Conference Series No. 21, Institute of Physics, London, 1974, pp. 3-21.
[27] Goodwin, J. E., Sage, W., and Tilly, G. P. in *Proceedings*, Institution of Mechanical Engineers, Vol. 184, 1969, pp. 279-291.
[28] Tilly, G. P., *Wear*, Vol. 23, 1973, pp. 87-96.

DISCUSSION

G. Mayer[1] (*written discussion*)—Has anyone attempted to do a slip-line field analysis of an asymmetric plowing (or indentation) by either a cylindrical or a sharp-edged particle?

I. M. Hutchings (*author's closure*)—The problem of oblique indentation by a tilted wedge has been studied by several workers, the earliest being R. Hill and E. H. Lee ("The Theory of Wedge Penetration at Oblique Incidence and Its Application to the Calculation of Forces on a Yawed Shot Impacting on Armour Plate at Any Angle," Selected Government Research Reports, Vol. 6 *Strength and Testing of Materials*, Part 1: *Theoretical Papers on Strength and Deformation*, H. M. Stationery Office, London, U.K., 1952, p. 36). Subsequently K. L. Johnson (University Engineering Laboratory, Trumpington Street, Cambridge, England, private communication) and S. A. Meguid and I. F. Collins (*International Journal of Mechanical Sciences*, Vol. 19, 1977, pp. 361-371) have investigated the problem theoretically and experimentally. Plane-strain indentation by a cylinder is very much more complex, and to my knowledge no satisfactory

[1] Army Research Center, Research Triangle Park, N.C. 27709.

slip-line field has been published; physically impossible velocity diagrams or negative plastic work are predicted by the few which have been proposed. However, if friction is incorporated in the analysis, one can imagine a wedge of "dead metal" in front of the cylinder, and the problem becomes similar to that of the rigid wedge.

It would not be easy to treat the impact of an abrasive particle using such slip-line fields, though, because the orientation and direction of motion of the particle are changing throughout the impact; so is the shape of the crater. One would be forced to compute the slip-line field and the forces at every time increment during the calculation. I doubt whether this extra complication would be justified, since we know that the pattern of deformation around an indentation formed by impact is very different from that around the same shape and size of indentation formed by slow loading (I. M. Hutchings, Ph.D. Dissertation, Cambridge University, 1975). If a slip-line field is accurate for the slow loading case, it cannot be so for the impact situation.

G. A. Sargent,[1] *P. K. Mehrotra,*[1] *and H. Conrad*[1]

Multiparticle Erosion of Pyrex Glass

REFERENCE: Sargent, G. A., Mehrotra, P. K., and Conrad, H., **Multiparticle Erosion of Pyrex Glass,"** *Erosion: Prevention and Useful Applications, ASTM STP 664,* W. F. Adler, Ed., American Society for Testing and Materials, 1979, pp. 77-100.

ABSTRACT: Multiparticle erosion tests were performed on Corning 7740 Pyrex glass using alumina powder of two grit sizes. Erosion was measured as a dimensionless parameter in terms of the loss in weight of the target per unit weight of particles impinged. The erosion characteristics of the Pyrex glass were investigated over a range of particle velocities, angles of impingement, and times of erosion.

It was found that maximum erosion occurred at a normal angle of impact for the 240-grit powder (mean particle size $\simeq$ 30 μm); however, with the 400-grit powder (mean particle size $\simeq$ 10 μm), the maximum was found to occur at a slightly lower angle of about 80 deg. At all angles of impingement it was found that amount of erosion decreased as the erosion time increased.

Erosion (E) was found to be dependent on the average particle velocity (V) by a power relationship of the form

$$E \alpha V^n$$

where n is a material constant. The values of the velocity exponent, n, in the present experiments were found to be between 2.2 and 2.7 and were independent of time of erosion.

The time (t) dependence of erosion was also found to obey a power law relationship of the form

$$E \alpha t^c$$

where c is a material constant. The time exponent c was found to be -0.1 under all conditions of velocity, particle size, and angle of impingement. The decrease in erosion with increase in time has been interpreted in terms of a change in the surface roughness. Scanning electron microscopy (SEM) has been used to establish that the effective average angle of impingement decreased as time of erosion increased until a constant surface roughness was achieved, at which time it was found that the average angle of impingement was about 55 deg instead of 90 deg.

The experimental data obtained in the present work are discussed in terms of existing theories for the erosion of brittle materials.

KEY WORDS: erosion, multiparticle, Pyrex glass

[1]University of Kentucky, Department of Metallurgical Engineering and Materials Science, Lexington, Ky. 40506.

Erosion usually refers to the deterioration of a target material as a result of continued impingements by solid particles or liquid droplets which are carried in a fluid stream. Perhaps the most significant result from previous studies [*1-3*][2] was the finding that two different modes of erosion may be distinguished empirically for two classes of target material. The ductile mode, which is characteristic of most metal targets, is characterized by maximum erosion occurring at an angle of impingement of about 20 to 30 deg. The brittle erosion mode, typical of glasses and ceramics, is characterized by the erosion being a maximum at a normal (90 deg) angle of impingement. Since the fracture behavior of brittle materials is better understood than that of ductile materials, it was decided in the present work to investigate the erosion behavior in an elastically isotropic but inherently brittle material. Corning 7740 Pyrex glass, which was used as the target material for the present work, satisfies these requirements well.

The independent variables which have been found to be of significance in investigating the mechanism of erosion of brittle materials in previous studies [*1,5,6*] are as follows: particle size, shape, velocity and flux, angle of impact, and physical properties of the impinging particles; the physical properties of the target material; and the time duration of the erosion.

In almost all of the data reported to date [*1,4,6,10*], variation of erosion as a function of particle velocity has been expressed in the following form

$$E \alpha V^n \tag{1}$$

where E is erosion in terms of material removed per unit weight of particles impinged and V is the particle velocity. The exponent n is a constant for a given target and particle material.

Erosion, E, also varies with the size of the impinging particles according to the following power relationship [*4*]

$$E \alpha D^m \tag{2}$$

where D is the diameter of the particle and m is a constant for a given target and particle material.

A systematic study of the effect of time of erosion has received rather limited attention. The data available in the literature show three types of behavior: a constant erosion rate [*1,7*], an increasing erosion rate with time [*1,5*], and a decreasing erosion rate with time [*8*]. Previous work on the erosion of glass [*8,9*] indicates an erosion rate which decreases with time.

[2]The italic numbers in brackets refer to the list of references appended to this paper.

In this paper, the effect of angle of impingement and particle velocity on the erosion of Pyrex glass by alumina particles of two different grit sizes has been determined. In addition, special attention has been given to investigating the effect of time of duration of erosion by examination of the eroded surface by both direct observation using scanning electron microscopy (SEM) and by indirect methods utilizing the Hertzian fracture test. The Hertzian fracture test offers a means for assessing target surface characteristics prior to, and following, multi-particle erosion. An attempt has been made to identify the laws which govern erosion as functions of particle velocity and time of erosion.

Experimental Procedure

Multiparticle erosion tests were carried out on Corning 7740 Pyrex glass. Specimens 2.5 by 2.5 by 0.95 cm were cleaned ultrasonically in acetone, dried, and then weighed. The specimens were eroded at room temperature, in an apparatus similar to that described by Ruff and Ives [*23*], by 240- and 400-grit alumina (Al_2O_3) particles (Buehler AB) carried by air. The effects of various particle velocities, angles of impingement, and times of erosion were studied. After erosion the specimens were again cleaned in acetone and weighed. The loss in weight of the specimen was normalized against the weight of impinged particles to obtain a dimensionless erosion parameter.

The particle size distributions of the 240- and 400-grit powders were measured by optical microscopy and are shown in Fig. 1. A mean particle size, as measured by the linear intercept method, of 30 μm for the 240-grit powder and 10 μm for the 400-grit powder was found. It can be seen from the photomicrographs shown in Fig. 2 that both powders consist of sharp angular particles.

The average particle velocity in the airstream at the specimen position was measured by means of the rotating-disk method [*11*].

Erosion of the specimens was measured as a function of angle of impingement, particle velocity, and time. Deterioration and changes in surface characteristics as a result of the erosion were studied both by direct SEM observation and by indirect observation by means of the Hertzian test.

The Hertzian test was carried out by pressing a hardened steel ball of 3.175 mm diameter against the glass surface, at a constant cross-head speed, in a bench model Instron machine. The load was increased until the characteristic ring crack appeared. At this time, the load and ring crack size were recorded. Since the fracture strength of glass depends upon the flaw size distribution at the surface, it was necessary to analyze the results statistically [*12*].

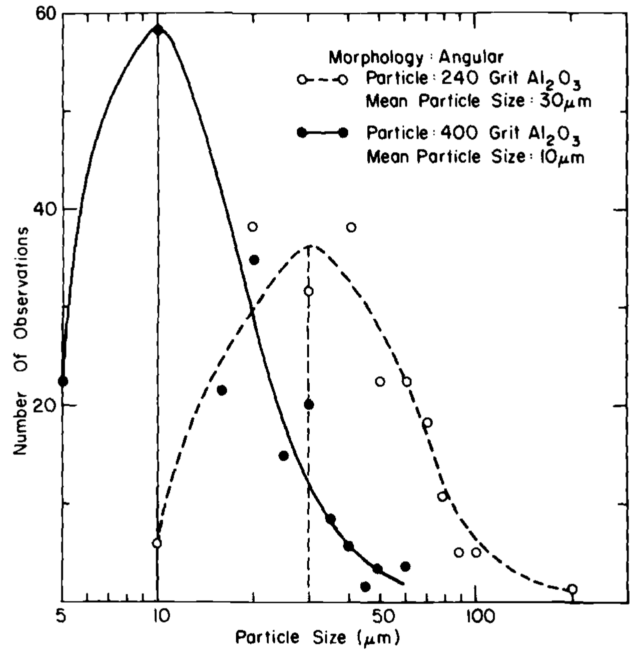

FIG. 1—*Particle size distribution of 240- and 400-grit Al_2O_3 powders.*

Results and Discussion

The effects of angle of impingement and time of erosion on the weight loss of the specimen (in grams/gram of particles) for the 240- and 400-grit Al_2O_3 powders are shown in Fig. 3*a* and 3*b*, respectively. Maximum erosion occurs at an angle of impingement of 90 deg for all erosion times from 5 to 150 s for the glass eroded with the 240-grit alumina. There is a slight shift of the maximum erosion to a lower angle of impingement of about 80 deg for those specimens eroded with the 400-grit powder. It is also of significance to notice that although the particle velocity was slightly higher for the 400-grit powder, the maximum erosion achieved with the 240-grit powder is more than twice that obtained using the 400-grit powder.

Table 1 presents a summary of other studies on the effect of angle of impingement on the erosion of glass. It can be seen that in general for a wide variety of particle materials and velocities the maximum erosion occurs at a normal (90 deg) angle of impingement. With very small particles, however, maximum erosion occurs at lower angles, which is more typical of the behavior observed for ductile materials. The transition from brittle to ductile behavior with small particles has been discussed by Sheldon and Finnie [*13*] and is attributed to the particles being sufficiently small that they impinge between surface flaws and hence propagation of

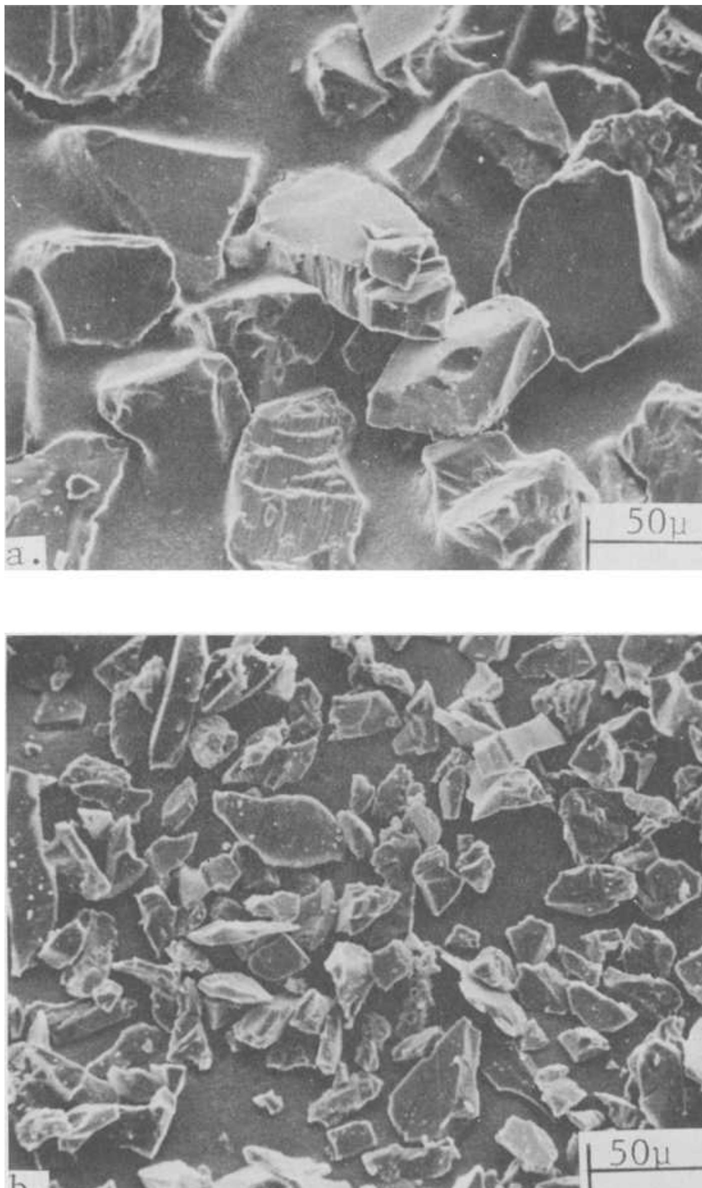

FIG. 2—*SEM micrographs of* (a) *240-grit and* (b) *400-grit* Al_2O_3 *powders.*

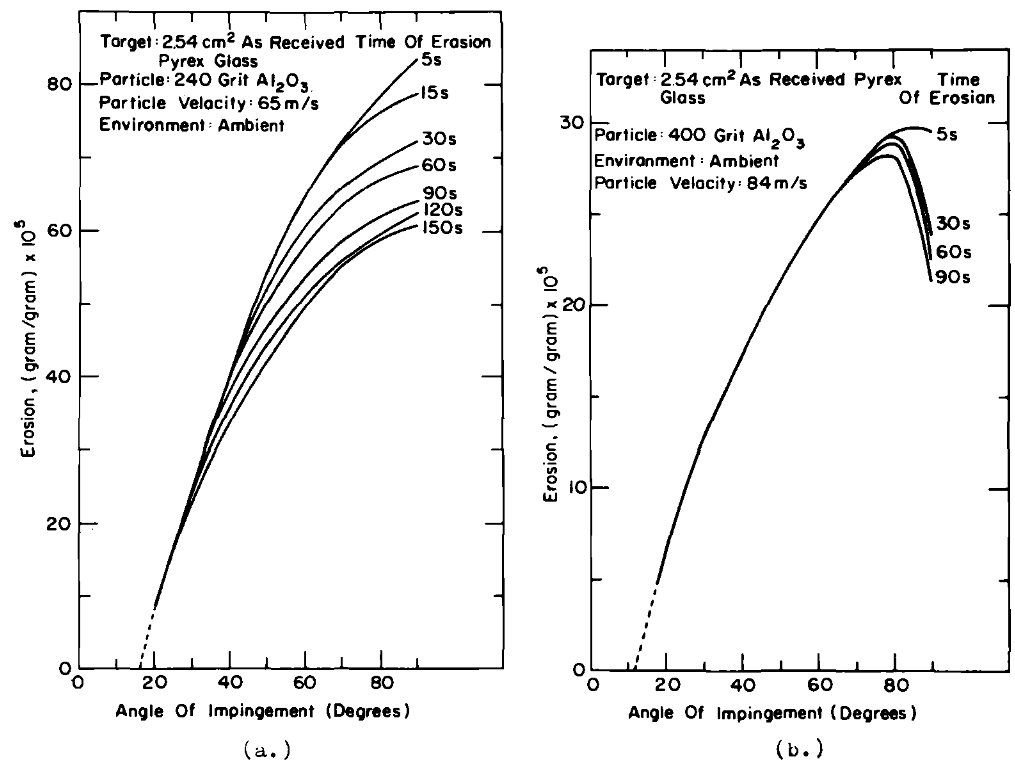

FIG. 3—*Effect of angle of impingement and time on the erosion (grams/gram) using* (a) *240-grit and* (b) *400-grit Al_2O_3 powders.*

TABLE 1—*Angle of impingement for maximum erosion as a function of particle size, velocity, and material.*

Particle Material	Particle Size, μm	Particle Velocity, m/s	Angle for Maximum Erosion, deg	Reference No.
SiC	9	152	25	[*13*]
SiC	21	152	85	[*13*]
SiC	127	152	80	[*13*]
SiC	212	44	72	[*20*]
Al_2O_3	210	107	90	[*21*]
Al_2O_3	297	96	90	[*21*]
Al_2O_3	30	65	90	present work
Al_2O_3	10	84	80	present work
Glass beads	475	80	90	[*21*]
Steel shot	580	45	90	[*1*]
Steel shot	580	30	90	[*1*]
Quartz	—	—	90	[*22*]
Cast iron	300	10	90	[*2*]

cracks is not possible and erosion by other mechanisms occurs. Maximum erosion at an angle of impingement of 90 deg is to be expected for brittle materials, since the maximum normal load is available at this angle of impact for the propagation of surface or subsurface flaws.

In Fig. 4*a* and 4*b* erosion (in grams/gram) is plotted on a log-log scale as a function of particle velocity for exposure times of 5 and 120 s for the 240- and 400-grit powders, respectively. From these results it can be seen that the erosion, E, is related to particle velocity, V, by a simple power law relationship which may be expressed as:

$$E \alpha V^n \tag{3}$$

The velocity exponent, n, from these studies and from other work on glass is presented in Table 2.

From simple energy balance considerations, a velocity exponent of 2 is to be expected. The data presented in Table 2 show, however, that the velocity exponent is dependent on both particle size and material. Finnie and Oh [*14*] and Sheldon and Finnie [*4*] have proposed analytical models for predicting the volume of material removed on each impact V_p, taking into consideration that the mode of failure is by brittle fracture. They suggest that

$$V_p = Kr^c v^b \tag{4}$$

where

K = a constant involving the elastic properties of both the target mate-

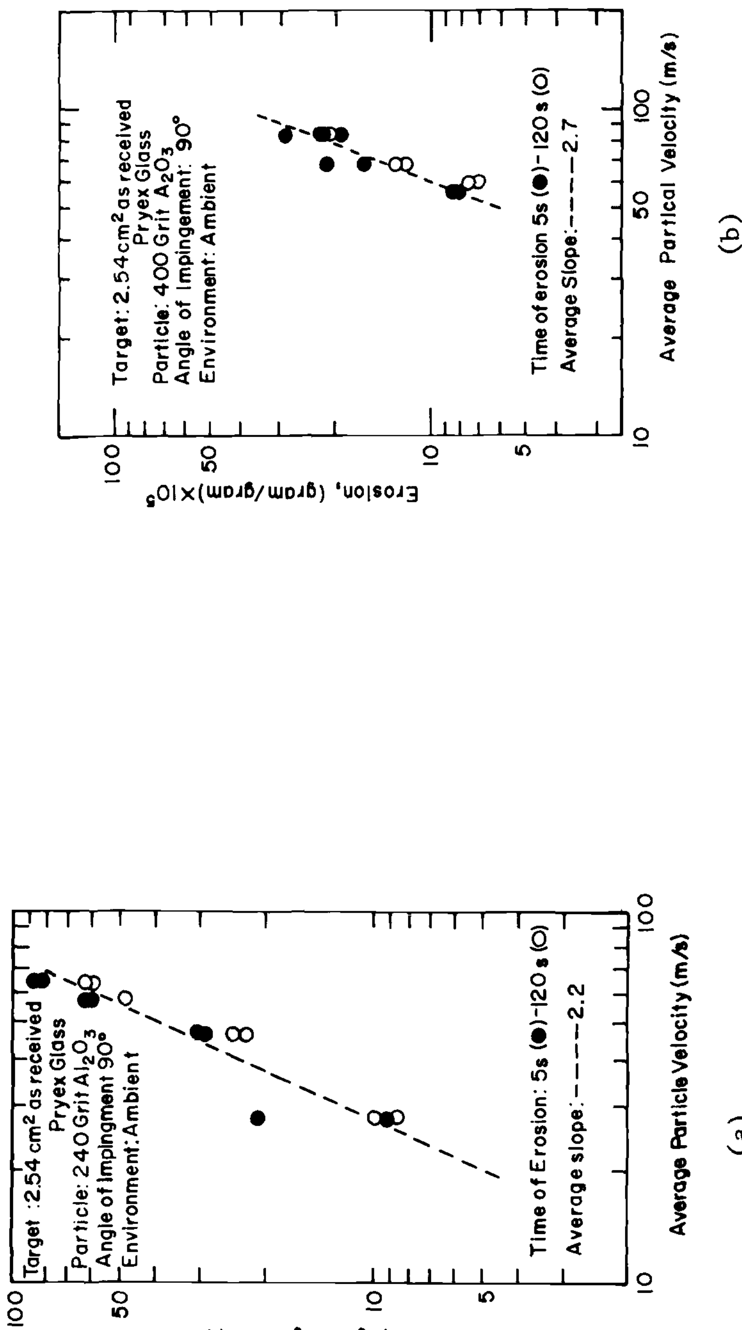

FIG. 4—*Erosion (grams/gram) as a function of particle velocity using* (a) *240-grit Al_2O_3 powder for erosion times of 5 and 120 s and* (b) *400-grit Al_2O_3 powder for erosion times of 5 and 120 s.*

Table 2—*Velocity exponent as a function of particle size and material.*

Particle Material	Particle Size, μm	Velocity Exponent	Velocity Range, m/s	Reference No.
SiC	~200	3.0	60 to 180	[4]
SiC	~100	3.0	60 to 180	[4]
Al_2O_3	30	2.2	28 to 65	present work
Al_2O_3	10	2.7	58 to 84	present work
Quartz	125 to 150	2.3	45 to 244	[6]
Steel shot	280	4.4	42 to 122	[4]
Steel shot	~420	4.4	42 to 122	[4]
Steel balls	~584	6.5	21 to 49	[1]

rial and impinging particle, Weibull [15] distribution parameters of the target material, and other parameters characteristic of the target,

v = particle velocity, and
r = particle radius.

The exponents of the radius and velocity, c and b, respectively, are shown to be functions of the Weibull flaw parameter, m, of the target material surface. Finnie and Oh [14] express the particle radius exponent c as $3m/(m - 2)$ for spherical particles and $6/5\ (3m - 2)/(m - 2)$ for angular particles. Sheldon and Finnie give corresponding values of c to be $3m/(m - 2)$ and $3.6m/(m - 2)$. The value of velocity exponent, b, is given by $4/5\ (3m - 2)/(m - 2)$ by Finnie and Oh and $2.4m/m - 2$ by Sheldon and Finnie. The slight difference between the values of these exponents expressed by the different authors apparently emanates from slightly different approaches to the development of the theory.

The Weibull parameters were measured for the target material (Corning 7740 Pyrex glass) by four-point bend experiments [16] and a value of 2 was obtained for the flaw parameter m. This is considerably less than the value of eight used by Finnie and Oh in their calculation of the velocity exponent b, but it does agree well with other values reported in the literature from three-point bend experiments [17]. By using a value of $m = 2$, the velocity exponents predicted by both the Finnie and Oh equation and by the Sheldon and Finnie equations are indeterminate. Thus comparisons of these values with those measured in the present experimental work are not possible.

One of the basic assumptions of the foregoing analytical studies has been that the brittle target material responds completely elastically to the impacting particle. If this is indeed the case, then one would expect material removal to occur by the intersection of Hertzian cone cracks. However, with relatively small angular particles at high velocities the brittle target may be expected to respond quite differently. Evans et al have considered the case of quasi-static indentations [18] and impacts on brittle surfaces by either sharp indenters or sufficiently small spherical balls [19] and have shown that the material responds in an elastic-plastic regime which requires a completely different mechanism for surface erosion. They suggest [18], for single-particle impacts in the elastic-plastic regime, that the material removed by each impacting particle, E, may be expressed as

$$E \propto \{r^4 \mu^{4/5} v_i^{12/5} \rho^{6/5}\} K_D^{3/2} H_D^{1/2} \tag{5}$$

where

r = radius of impacting particle,
v_i = velocity of impacting particle,
ρ = density of impacting particle,
μ = shear modulus of target material,
K_D = dynamic fracture toughness of target material, and
H_D = dynamic hardness of target material.

The critical load, P_c, in the Hertzian fracture test is related to the radius of the indenter, R, by the following equation

$$P_c = B_1 R^n \tag{6}$$

where, in case of Auerbach's law, $n = 1$ and B_1 is Auerbach's constant. In an indentation test, elastic-plastic deformation in shear occurs, as shown by Evans and Wilshaw [18], if the following relation is satisfied

$$P_I = B_2 \left(\frac{k}{E}\right)^2 H^3 R^2 \tag{7}$$

where

P_I = load,
B_2 = 16.33,
k = elastic constant,
E = Young's modulus for target material, and
H = hardness of target surface.

A schematic plot of log P as a function of log R is shown in Fig. 5, where a critical particle radius R^* can be identified. Since the particles used in the present experiments were angular in shape, the average particle size was measured by a linear intercept method. The mean value of such a measurement would yield the diameter of a spherical particle of equivalent volume to that of the angular particle. Since the angular particles may

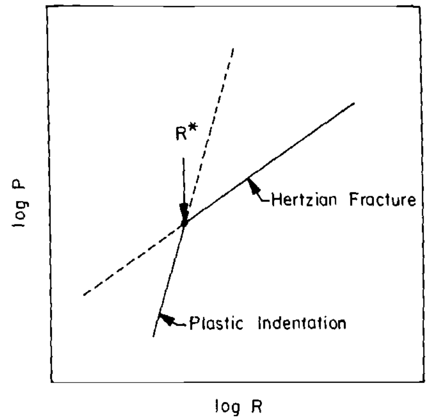

FIG. 5—*Effect of particle radius on the indentation load for Hertzian fracture, and for plastic indentation (schematic).*

have small radii of curvature at pointed ends and relatively large radii of curvature at other positions, it was assumed that the average radii of curvature of the point of contact with the glass surface was that of the equivalent sphere as measured by the mean linear intercept method. The initial fracture caused by a particle of size larger than R^* is completely elastic while that by a particle of size smaller than R^* is elastic-plastic in nature. The value of R^* is given by the following equation

$$R^* = \frac{B_1}{B_2}\left(\frac{E}{k}\right)^2 \frac{1}{H^3} \tag{8}$$

Table 3 gives the values of R^* for glass impacted by various particle materials listed in Table 2 along with the corresponding particle radii, R. Further, it has been shown [*16*] that Pyrex glass employed as the target material in this work follows Auerbach's law, which yields critical loads, P_c, for Hertzian fracture; see Table 3. Finally, an approximate value of total load, P_T, calculated from the following equation, is also shown [*8*]

$$P_T = \left(\frac{4}{3}\pi\rho\right)\left(\frac{k}{E}\right)^{-2/5} V^{6/5} R^2 \tag{9}$$

Although Eq 9 is strictly applicable only to round particles, it has been assumed in the present analysis that the approximate value of the total load can be computed by using the value of R calculated for the sphere of volume equivalent to that of the irregular-shaped particle. A comparison

TABLE 3—*Values of particle radius, critical particles radius, critical load for Hertzian fracture, total load, and velocity exponent as a function of particle material.*

Target Material: Glass							
Particle Material	Particle Radius, R, mm	Critical Particle Radius, R*, mm	Critical Load, $P_c(N)$	Total Load, $P_T(N)$	$\frac{P_T}{P_c}$	Velocity Exponent	Reference
SiC	0.1	0.782	10	27.40	2.74	3	[4]
SiC	0.05	0.782	5	6.90	1.38	3	[4]
Al_2O_3	0.015	0.726	1.5	0.24	0.16	2.2	present work
Al_2O_3	0.005	0.726	0.5	0.04	0.08	2.7	present work
SiO_2	0.062 to 0.075	0.249	6.2 to 7.5	11.00	1.47 to 1.78	2.3	[6]
Steel	0.14	0.6	14	55.00	3.93	4.4	[4]
Steel	0.21	0.6	21	124.00	5.91	4.4	[4]
Steel	0.292	0.6	29.2	86.00	2.95	5.5	[1]

reveals that, for the present work, impacts occur in the completely nonelastic range assumed in the derivation of Eq 5. That the impacts are indeed nonelastic in nature is evidenced in the SEM's of Figs. 6 and 7, which clearly show material removal resulting from the formation and interaction of lateral cracks. In such a case, one predicts from Eq 5 a velocity exponent of 2.4, with which the results of this work are in good agreement.

It should be further noted in Table 3 that in all cases $R < R^*$ and, except for the steel shot, the observed values of velocity exponents (2.2 to 3) are in reasonably good accord with the theoretical value predicted in Eq 5. The much higher values of velocity exponents for steel shot can probably be attributed to the relatively large value of total load, P_T (about five times that for Hertzian fracture), so that material removal occurs by formation and interaction not only of lateral cracks but also of Hertzian cone cracks. Operation of more than one mechanism of material removal is probably also responsible for the slightly higher value of velocity exponent for silicon carbide particles.

In the present work, special attention was given to studying the effect of time of exposure on the erosion. It can be seen from Fig. 8*a* and 8*b* for 240- and 400-grit powders, respectively, that erosion expressed simply as weight of material removed at a normal angle (90 deg) of impact increases with both time of exposure and particle velocity. A log-log plot of erosion (in grams/gram) as a function of exposure time is given in Fig. 9. From these data we may express erosion, E, as a simple power function of exposure time t as follows

$$E \alpha t^c \tag{10}$$

where the exponent c was found to be approximately -0.1 and was independent of particle velocity, angle of impingement, and particle size. The SEM's of the eroded surface as a function of time for erosion with the 240- and 400-grit powders given in Figs. 6 and 7, respectively, do show that initially at short erosion times a high percentage of the target surface is flat and that material removal is by the formation of erosion pits which are created, in this case, by the intersection of lateral cracks. It is possible, however, that a decrease in the rate of material removal with increased time could be due either to an increase in, or change in, surface microstructure due to plastic deformation of the surface. Figure 10 shows cross sections of the surface after erosion for various times by the 240-grit powder. It can be seen that after a few seconds of erosion the surface is considerably roughened and that particle impingement is no longer occurring at a normal (90 deg) angle of impingement. It can be seen from Fig. 3 that, at an exposure time of about 120 s, the effective angle of impingement is about 55 deg. After this exposure time the surface roughness did not change appreciably and the rate of erosion became constant.

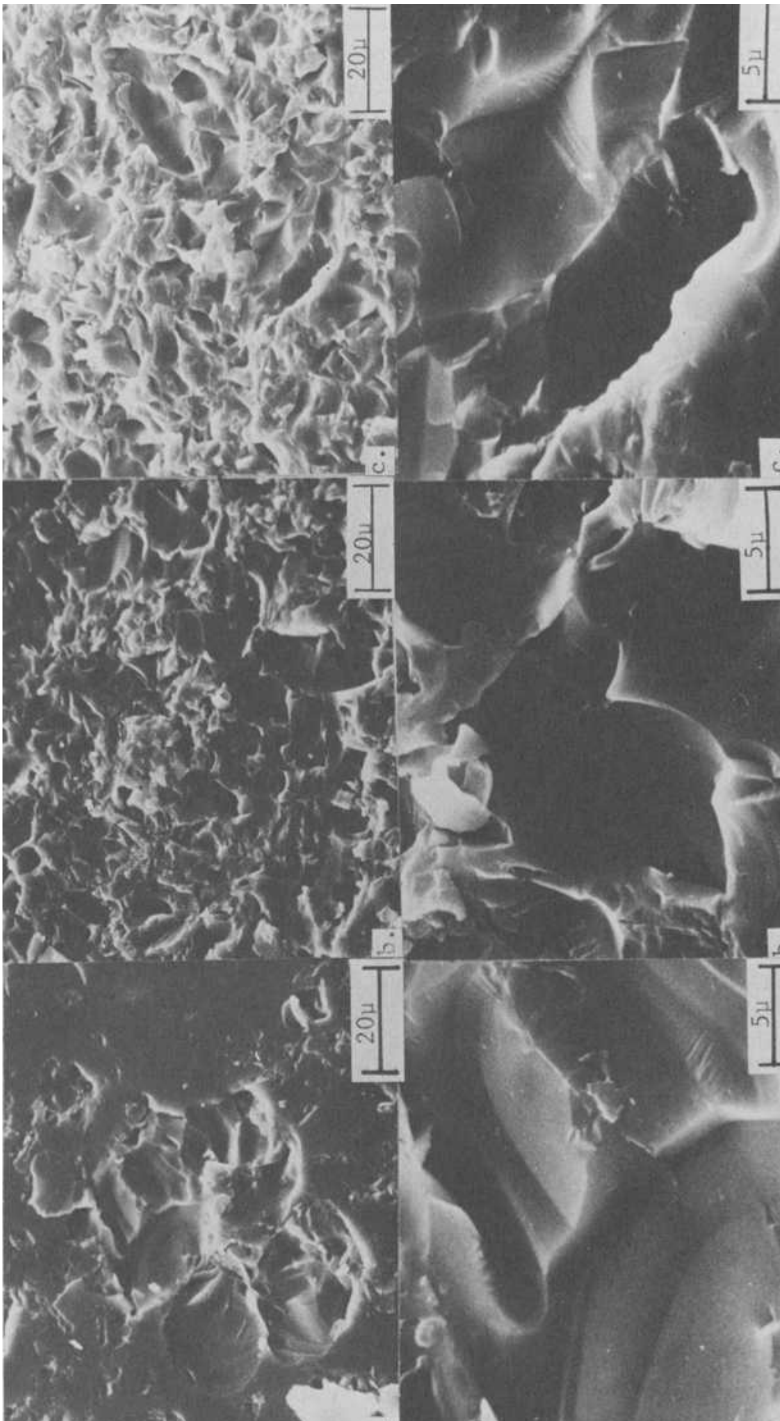

FIG. 6—*SEM micrographs of Pyrex glass surface after erosion with 240-grit Al_2O_3 powder at 90 deg and an average particle velocity of 65 m/s for times of* (a) *5 s,* (b) *10 s, and* (c) *60 s.*

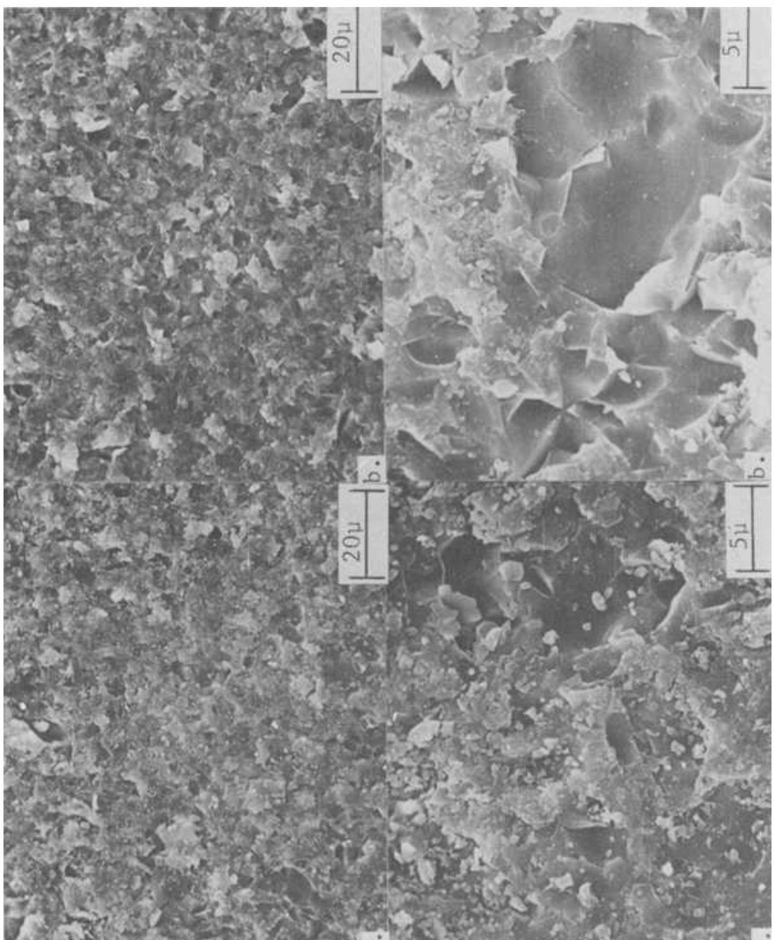

FIG. 7—*SEM micrographs of Pyrex glass surface after erosion with 400-grit Al_2O_3 powder at 90 deg and an average particle velocity of 68 m/s for times of* (a) 2 *s and* (b) 5 *s.*

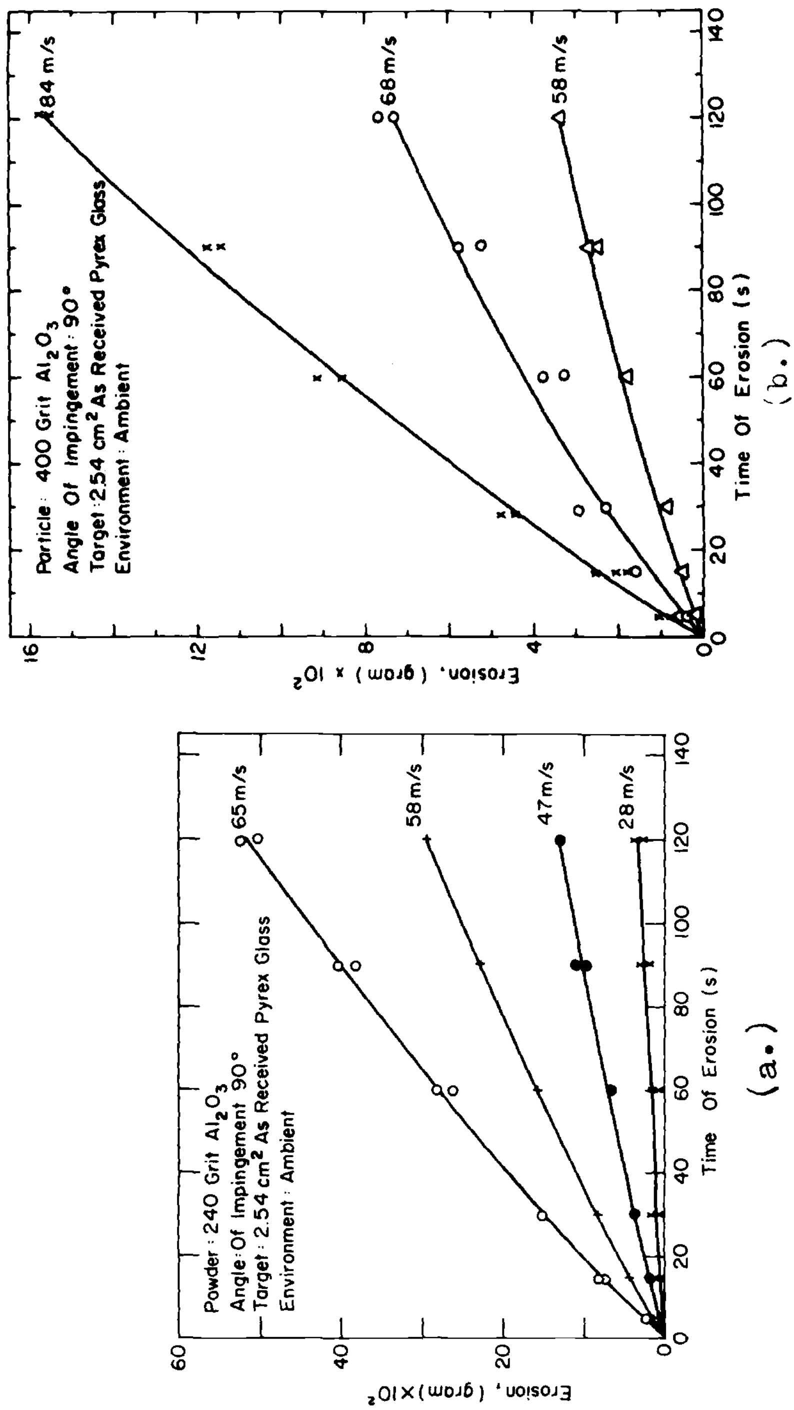

FIG. 8—*Erosion (g) as a function of erosion time using (a) 240-grit and (b) 400-grit Al_2O_3 powders at normal impacting angle.*

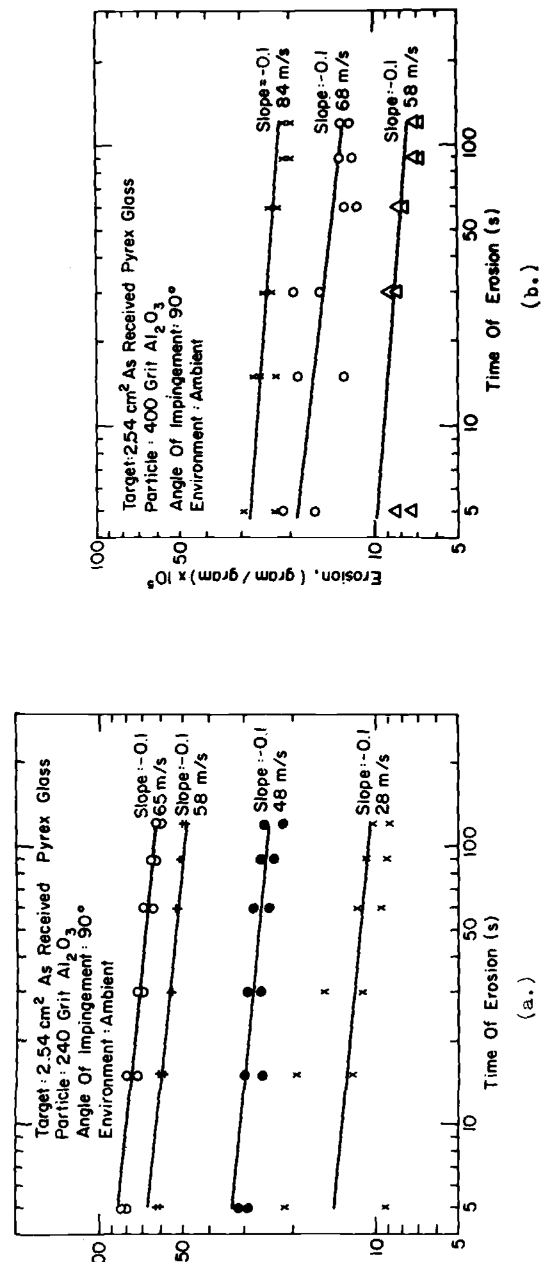

FIG. 9—*Log-log plot of erosion grams/gram as a function of erosion time using (a) 240-grit and (b) 400-grit Al_2O_3 powders.*

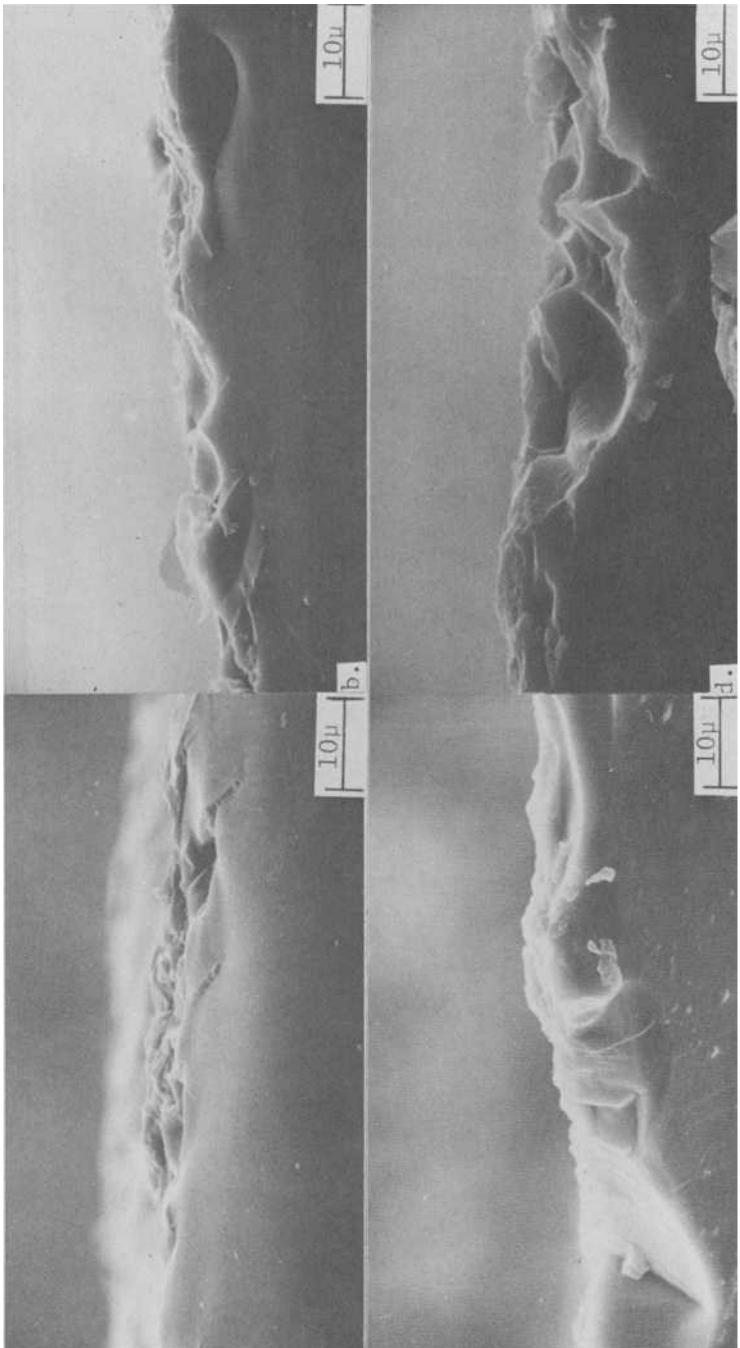

FIG. 10—*SEM micrographs of a transverse section of Pyrex glass surface after erosion with 240-grit Al_2O_3 powder at 90 deg with an average particle velocity of 65 m/s for times of* (a) *2 s,* (b) *5 s,* (c) *10 s, and* (d) *20 s.*

Hertzian fracture tests were performed on the Pyrex glass surfaces which had been eroded at 90 deg by the 240-grit alumina powder at different average particle velocities for various lengths of time. Because of the statistical nature of the fracture of glass, the values of the critical load, P_c, at which the ring crack is first observed in a series of Hertzian fracture tests on a given surface are best expressed in terms of the probability to produce a ring crack as a function of the critical load. Figure 11 shows the typical form of such a probability distribution curve for a surface eroded at an average particle velocity of 65 m/s. To study the influence of test variables on the Hertzian fracture, the value of the critical load at 50 percent probability to produce a ring crack was taken as a representative parameter to describe the fracture behavior of corresponding surfaces. The values of this critical load, $P_{c(0.5)}$, as a function of the erosion time and average particle velocity for erosion of a given surface are listed in Table 4.

Hertzian fracture tests have revealed that the Pyrex glass used as the target material in this work obeys Auerbach's law [*16*], given by the following equation

$$P_c = AR \tag{11}$$

where

P_c = critical load for fracture,
R = particle radius, and
A = the Auerbach constant.

The values of Auerbach constant, using $P_{c(0.5)}$, are listed in Table 4 as a function of time and particle velocity for erosion of the surface. Figure 12 illustrates the variation of Auerbach constant of eroded glass surface with time and particle velocity. It is seen here that A increases with time in the early stages of erosion but tends to become independent of time at about 200 s for the higher velocities (58 and 65 m/s), but any such fluctuation is not discernible at the lower two velocities (28 and 47 m/s). Though the reasons for this behavior are not very clear, it may be suggested for the surfaces eroded by particles at the higher two velocities that an increase in Auerbach constant indicates strengthening of the target surface, for a given particle radius, which tends to become a constant at erosion times of about 200 s. This will result in a drop in erosion which later will become a constant at about 200 s time of erosion. Langitan and Lawn [*23*] have suggested that, as surface damage increases, the critical load to cause the ring fracture also increases. However, because of the limited range of surface damage in their experiments, they could not draw any definite conclusions. The multiparticle erosion of glass as a function of time of erosion and particle velocity presents one way in which a wide range of surface damage can be produced. Thus the results of the Hertzian

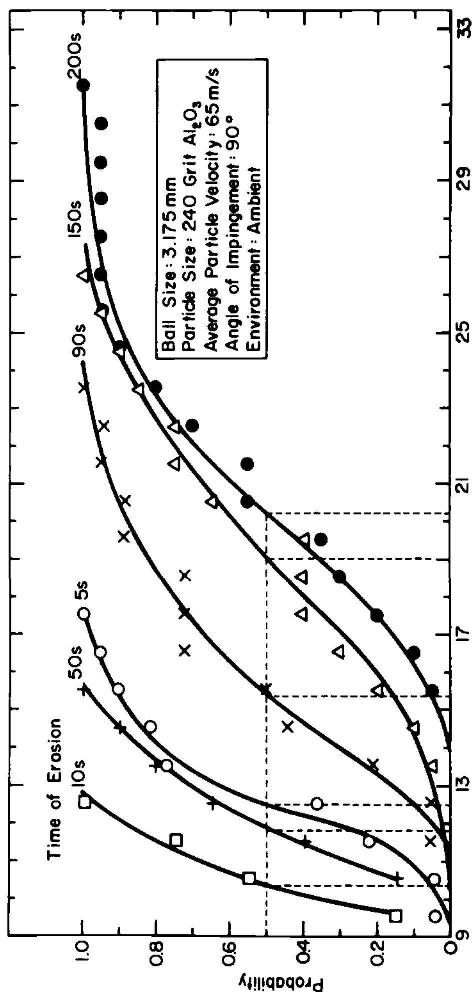

FIG. 11—*Cumulative frequency versus* P_c *for glass eroded by 240-grit* Al_2O_3 *powder at an average particle velocity of 65 m/s.*

TABLE 4—$P_{c(0.5)}$ *and* A *on eroded Pyrex glass.*

Particle	: 240-grit Al_2O_3
Angle of impingement	: 90 deg
Environment	: ambient at room temperature
Crosshead speed	: 5.08 mm/s
Indenter diameter ($2R$)	: 3.175 mm
50% probability critical load	: N
Auerbach constant ($P_{c(0.5)}/R$) = A	: N/mm

Time of Erosion, s	Average Particle Velocity, m/s							
	28.0		47.0		58.0		65.0	
	$P_{c(0.5)}$	A	$P_{c(0.5)}$	A	$P_{c(0.5)}$	A	$P_{c(0.5)}$	A
5	87.28	54.96	98.56	62.07	89.73	56.51	122.58	77.19
10	...	...	...	...	95.62	60.21	101.50	63.92
20	88.26	55.58	91.69	57.74	...	...	...	...
40	80.91	50.95	...	...	...	...	...	...
50	...	...	...	...	99.54	62.68	115.72	72.87
60	...	...	80.42	50.64	...	...	...	...
90	...	...	...	...	...	...	150.53	94.65
100	...	...	...	...	106.40	67.0	...	...
150	80.91	50.95	94.64	59.60	176.52	111.16	186.33	117.34
200	...	...	...	...	...	...	198.10	124.75

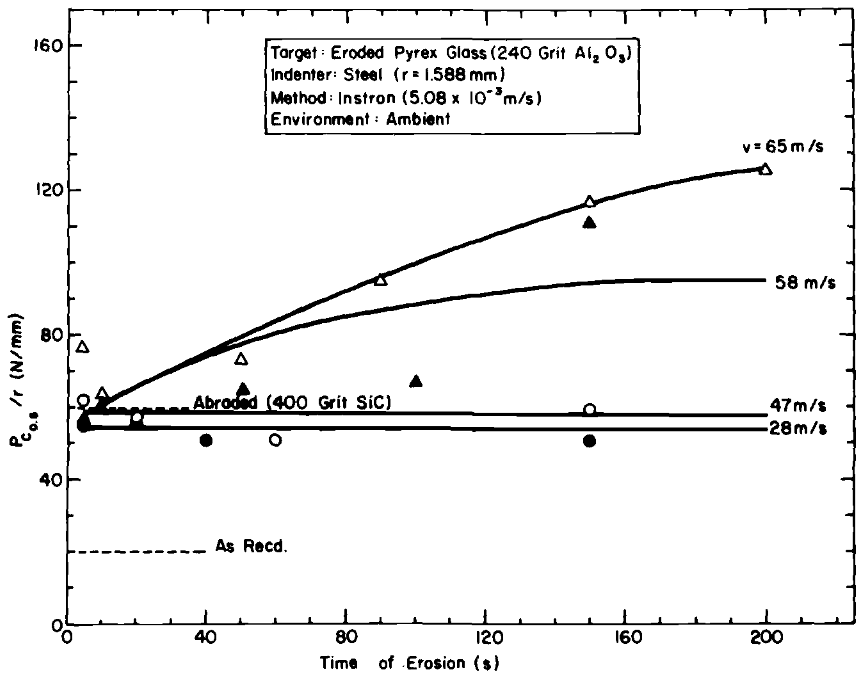

FIG. 12—*Effect of time of erosion on the Auerbach constant* $A(=P_{c(0.5)}/r)$ *for eroded surfaces of Pyrex glass.*

tests presented in this paper not only confirm the suggestion of Langitan and Lawn but also offer a tentative explanation for the effect of time on the erosion of Pyrex glass.

Conclusion

1. Erosion of Pyrex glass by alumina powder increases with angle of impingement with a maxima occurring at 90 deg for 240-grit alumina powder and at about 80 deg for 400-grit alumina powder. At all angles of impingement, erosion decreases as time of erosion increases.

2. Erosion, E, can be related to the average particle velocity, V, by a power relationship of the following form

$$E \alpha V^n$$

where n is a system constant. The value of velocity exponent, n, in the present work was determined to be between 2.2 and 2.7 and was independent of time. This value of velocity exponent is in good accord with that predicted by the analytical model of Evans and Wilshaw [18] which considers elastic-plastic response of the target material. The relatively large values of velocity exponents, even when particle size is smaller than critical particle radius, are probably due to the fact that two mechanisms for material removal are operative, namely, formation and interaction of lateral cracks and Hertzian cone cracks.

3. Erosion, E, can be related to time of erosion, t, by a power relationship of the following form

$$E \alpha t^c$$

where c is a system constant. The value of time exponent, c, in the present work was determined to be -0.1 and was independent of particle velocity and size.

5. Time dependence of erosion may be partly due to increasing roughness of the surface, which later becomes constant, and partly due to increasing Auerbach constant, which also becomes independent of time at large values of time.

Acknowledgments

This project was jointly funded by the National Science Foundation (Grant 751-34) and by the Institute for Mining and Minerals Research as part of a Kentucky Energy Resources Utilization Program.

References

[1] Finnie, I., *Wear*, Vol. 3, 1960, pp. 87-103.
[2] Bitter, J. G. A., *Wear*, Vol. 6, 1963, pp. 5-21.
[3] Sheldon, G. L., *Trans.* ASME, *Journal of Basic Engineering*, Sept. 1970, pp. 619-626.
[4] Sheldon, G. L. and Finnie, I., *Journal of Engineering for Industry*, Nov. 1966, pp. 393-400.
[5] Tilly, G. P. and Sage, W. *Wear*, Vol. 16, 1970, pp. 447-465.
[6] Goodwin, J. E., Sage, W., and Tilly, G. P. in *Proceedings*, Institution of Mechanical Engineers, Vol. 184, No. 15, 1969-70.
[7] Williams, J. H. and Lan, E. K., *Wear*, Vol. 29, 1974, pp. 219-230.
[8] Adler, W. F., "Analysis of Multiple Particle Impacts on Brittle Materials," AFML Technical Report TR-74-210, Air Force Materials Laboratory, Wright-Patterson Air Force Base, Dayton, Ohio, Sept. 1974.
[9] Sargent, G. A., Mehrotra, P. K., and Conrad, H., *Ceramic Microstructures '76*, Westview Press, Boulder, Colo., 1977.
[10] Roberts, A. G., ASTM Bulletin No. 244, American Society for Testing and Materials, 1960, pp. 48-51.
[11] Ruff, A. W. and Ives, L. K., *Wear*, Vol. 35, 1975, p. 195.
[12] Wilshaw, T. R., *Journal of Physics, D. Applied Physics*, Vol. 4, 1971, pp. 1567-1581.
[13] Sheldon, G. and Finnie, I., *Trans.* ASME, Vol. 88B, *Journal of Engineering for Industry*, Nov. 1966, pp. 387-393.
[14] Finnie, I., and Oh, H. in *Proceedings*, 1st Congress of the International Society of Rock Mechanics, Vol. 2, 1966, p. 99.
[15] Weibull, W., *Journal of Applied Mechanics*, Vol. 18, 1951, p. 293.

[16] Conrad, H. and Sargent, G. A., "A Study of the Mechanism of Erosion of Nominally Brittle Materials," Report to the National Science Foundation, NSF Grant DMR 75-10347, April 1977.
[17] Oh, H. L. and Finnie, I., *Journal of the Mechanics and Physics of Solids*, Vol. 15, 1967, p. 401.
[18] Evans, A. G. and Wilshaw, T. R., *Acta Metallurgica*, Vol. 24, 1976, p. 939.
[19] Evans, A. G., Gulden, M. E., Eggum, G. E., and Rosenblatt, M., "Impact Damage in Brittle Materials in the Plastic Response Regime," Technical Report, Office of Naval Research, 1976.
[20] Finnie, I. in *Symposium on Erosion and Cavitation, ASTM STP 307*, American Society for Testing and Materials, 1962.
[21] Neilson, J. H. and Gilchrist, A., *Wear*, Vol. 11, 1968, pp. 111-122.
[22] Tilly, G. P., *Wear*, Vol. 14, 1969, pp. 63-79.
[23] Langitan, F. B. and Lawn, B. R., *Journal of Applied Physics*, Vol. 40, 1969, pp. 4009-4017.

M. E. Gulden[1]

Solid-Particle Erosion of High-Technology Ceramics (Si_3N_4, Glass-Bonded Al_2O_3, and MgF_2)

REFERENCE: Gulden, M. E., "**Solid-Particle Erosion of High-Technology Ceramics (Si_3N_4, Glass-Bonded Al_2O_3, and MgF_2)**," *Erosion: Prevention and Useful Applications, ASTM STP 664,* W. F. Adler, Ed., American Society for Testing and Materials, 1979, pp. 101-122.

ABSTRACT: Four "engineering" ceramics were subjected to impact (single particle) and erosion (multiple impacts) under conditions which simulate a natural dust environment in the subsonic velocity regime. The target materials are hot-pressed silicon nitride (Si_3N_4), reaction-bonded Si_3N_4, a glass-bonded aluminum oxide (Al_2O_3), and hot-pressed magnesium fluoride (MgF_2). Tests were performed with six narrow size ranges of natural quartz between 10 and 385 μm average, and five velocities for each particle size. Hot-pressed Si_3N_4 was also impacted with silicon carbide (SiC) under the same particle size-velocity conditions.

The results are discussed in terms of current erosion and impact models by considering particle size-velocity dependencies, appearance of the impact damage, and the basic properties and structure of the targets.

Under these erosion conditions, the four target materials exhibited widely different behavior not only in absolute amount of material removed, but also in mechanism of removal. The systems hot-pressed Si_3N_4-SiC particles and MgF_2-quartz particles were characterized by a highly deformed, permanent surface crater with associated lateral and radial crack formation, and erosion loss was proportional to particle mass and velocity, both to the fourth power. Erosion of hot-pressed Si_3N_4 impacted with quartz particles was proportional to the third power of particle size and the first power of velocity, and loss occurred by minor chipping with no secondary crack formation. Erosion of glass-bonded Al_2O_3 and reaction-bonded Si_3N_4 did not show a consistent particle size-velocity dependence. The variation is related to the two-phase structure of these materials. It was found that strength is not necessarily reduced for erosion conditions which produce appreciable material removal.

[1] Senior research engineer, Solar Turbines International, an Operating Group of International Harvester, P.O. Box 80966, San Diego, Calif. 92138.

KEY WORDS: impact, erosion, ceramics, bend strength, silicon nitride, aluminum oxide, magnesium fluoride, mechanical properties, microscopy, quartz sand, silicon carbide particles

In recent years, considerable interest has been shown in the use of ceramics for high-technology engineering components in such applications as gas turbine engines, bearings, heat exchangers, radomes, and infrared transparent windows. All of these applications may involve impingement by solid particles. A knowledge of impact and erosion behavior is necessary before ceramics can be used with confidence in these systems. The materials discussed here, namely NC-132 hot-pressed silicon nitride (Si_3N_4), NC-350 reaction-bonded Si_3N_4, Alsimag 614 glass-bonded aluminum oxide (Al_2O_3), and Irtran 1 magnesium fluoride (MgF_2), are either in current use or considered for potential use in one or more of the aforementioned applications.

To date, essentially two types of models have been proposed for impact or erosion of brittle materials [*1*, *2*].[2] The earlier models were based on elastic interaction and predicted that material removal occurs by the intersection of Hertzian ring cracks on the substrate surface. This process has been observed on several materials under static and low-velocity impact conditions with relatively large spherical particles (for example, see Ref *3*). More recent analysis has treated static and dynamic plastic indentation, which is characterized by plastic deformation of the contact area between the particle and the target, with radial cracks propagating outward from the contact zone, and with subsurface lateral cracks propagating outward on planes nearly parallel to the surface. The former are considered a source of strength degradation and the latter a potential source of material removal. These models are based on single impacts and were developed for isotropic materials under idealized conditions. One objective of this investigation was to assess the validity of these models to predict erosion of engineering ceramics by natural dust environments.

The experimental approach for this investigation has been to perform single-impact and erosion (multiple-particle impacts) tests in a controlled manner to simulate a service environment in the subsonic velocity regime. This approach advances the understanding of erosion mechanisms of engineering materials as well as providing data of direct value in application of these materials to engineering structures.

Experimental Procedure

Materials

The target materials exhibit a wide range of properties and structure.

[2] The italic numbers in brackets refer to the list of references appended to this paper.

The properties considered pertinent to erosion response are listed in Table 1. Properties of the particles are also given.

High-purity, natural quartz particles were used for most of the erosion testing. Quartz was chosen because in previous work on metallic erosion it had been found to be the principal erosive component in natural dusts; that is, the amount of erosion was directly proportional to the percentage of quartz in the natural dusts [*4*]. Six particle size ranges were used as follows: less than 30, 44 to 53, 62 to 74, 105 to 125, 250 to 297, and 350 to 420 μm. These size ranges were chosen to be representative of airborne dust and to provide significant particle mass differences of at least one half order of magnitude. The particles are irregularly shaped with rounded corners and edges.

Angular silicon carbide (SiC) particles of the following size ranges—less than 24, 25 to 85, 50 to 165, 203 to 495, 356 to 813, and 660 to 1346 μm—were supplied by Bendix Abrasives Division. The primary reason for selecting SiC as the second particulate was because of its much higher elastic modulus and hardness compared with quartz. However, the results of the SiC particle tests have direct practical value because SiC is used as an additive in aircraft carrier antiskid decking.

Erosion Testing

Erosion tests were performed with a stationary target impacted by particles accelerated in an airstream. Particles are injected into the stream 3 m from the target to provide sufficient distance for acceleration. High-pressure, filtered, and chemically dried air is used for the particle carrier gas. The carrier air velocity is measured using standard Pitot tube techniques. The air velocity variation across the 0.95-cm-diameter nozzle is less than 5 percent and velocity is varied between 15 and 343 ms^{-1} to achieve the desired particle velocity.

Particle velocity is measured using the rotating double disk technique described in Ref *5*. Comparison with calculated velocities based on two-phase flow theory is good [*6*]. Five velocities for each particle size range were used to establish erosion rates.

All erosion tests were performed at 90-deg impingement angle at ambient temperature. Perpendicular impingement is at or near that for maximum erosion of brittle materials. The number of particles used per test was varied from a few particles (to examine single-particle impacts) to as many as 10^8 (to insure initiation of uniform erosion and to avoid incubation effects) over a 0.71-cm^2 target area. The particles are fed into the gas stream using a precision feeder at a sufficiently low concentration ($\sim 10^{-6}$ gm/cm^3) that particle interactions in the carrier gas stream or on the target surface are negligible. For the long-time, large number of particle tests, the specimens were weighed at specific time intervals to assess any changes in

TABLE 1—*Physical properties of target materials and particles.*

	Elastic Modulus, GPa	Fracture Toughness, MPa $m^{1/2}$	Hardness,[a] GPa	Acoustic Impedance, $kgm^{-2}s^{-1} \times 10^7$	Structure
Hot-pressed Si_3N_4 (NC-132)	320	5	16	3.2	pseudo single-phase—2-μm grain size
Glass-bonded Al_2O_3 (Alsimag 614)	324	3.2	12	4	2-phase—4% glass, 96% Al_2O_3, 10-μm grain size
Reaction-bonded Si_3N_4 (NC-350)	170	2.2	8	2	Multiphase—Si_3N_4 + porosity + Si + SiO_2 (surface)
Hot-pressed MgF_2 (Irtran I)	117	1	6	3.2	single phase— ~2-μm grain size
Natural quartz	95	~0.7	~6	1.6	...
SiC	420	~3	~23	...	...

[a] The hardnesses are the quasi-static Vickers hardness in the macro indentation load independent regime.

erosion with number of impacts. A detailed description of the erosion test apparatus is given in Ref *6*.

Strength Measurements

Strength was determined in three-point bending for both forms of Si_3N_4 and the Al_2O_3. Baseline values were obtained on as-received material. To determine a strength loss threshold, strength of eroded specimens was measured over a wide range of test conditions from preweight loss to deeply eroded specimens. Each specimen was visually examined to insure that failure originated in the area subjected to particle bombardment. The eroded areas, which are circular of 1 cm diameter, were located in the center of the 2.5- or 1.25-cm specimens to insure no extraneous edge effects on strength measurements.

Examination of Eroded Surfaces

The eroded surfaces were examined both optically and by replica transmission and scanning electron microscopy. The progression of impact or erosion events was monitored by examining the specimens after various numbers of impacts for several particle size-velocity combinations ranging from single-particle impacts to deeply eroded surfaces. The surfaces were also examined in cross section to assess the nature of subsurface damage.

Experimental Results and Discussion

This section is separated into four parts. Initially, the erosion dependence on particle size and velocity will be presented for the 5 target-particle combinations, followed by discussion and examples of the type of impact damage that occurs. The effect of erosion on strength will then be presented, and in the final section a comparison between erosion behavior in terms of impact models and material properties and structure will be made.

Erosion Dependence on Particle Size and Velocity

The customary method of reporting engineering erosion data is by plotting erosion weight loss versus some function of the erosive environment (that is, particle size, velocity, weight of dust ingested, etc.). Under the same erosion conditions this approach provides a relative ranking of erosion response of the various target materials. Additionally, the phenomenological models proposed for erosion response include dependent functions for particle size and velocity, so that a knowledge of the particle size and velocity dependency of erosion behavior is an important first step to understanding the actual erosion mechanism.

Erosion weight loss as a function of particle mass and velocity was determined for conditions involving millions of particle impacts. This large number of impacts was necessary to insure that uniform erosion is occurring, and that effects from starting surface condition were minimized. In the case of reaction-bonded Si_3N_4 (RB Si_3N_4) the as-fired surface layer was removed prior to erosion testing because it was found to erode at a much more rapid rate than the parent material. Weight loss per particle was plotted versus particle radius (log-log plot) and the slopes at constant velocity were measured to determine the particle size exponent. A similar plot of weight loss per particle versus particle velocity yielded the particle velocity exponent at constant particle size.

Two distinct relationships were observed. For the systems MgF_2 impacted with quartz particles and hot-pressed Si_3N_4 (HP Si_3N_4) impacted with SiC particles, erosion is proportional to the fourth power of both particle size and velocity. The results are shown in Fig. 1 for the three systems. The data are shown as volume loss to give a more meaningful comparison for

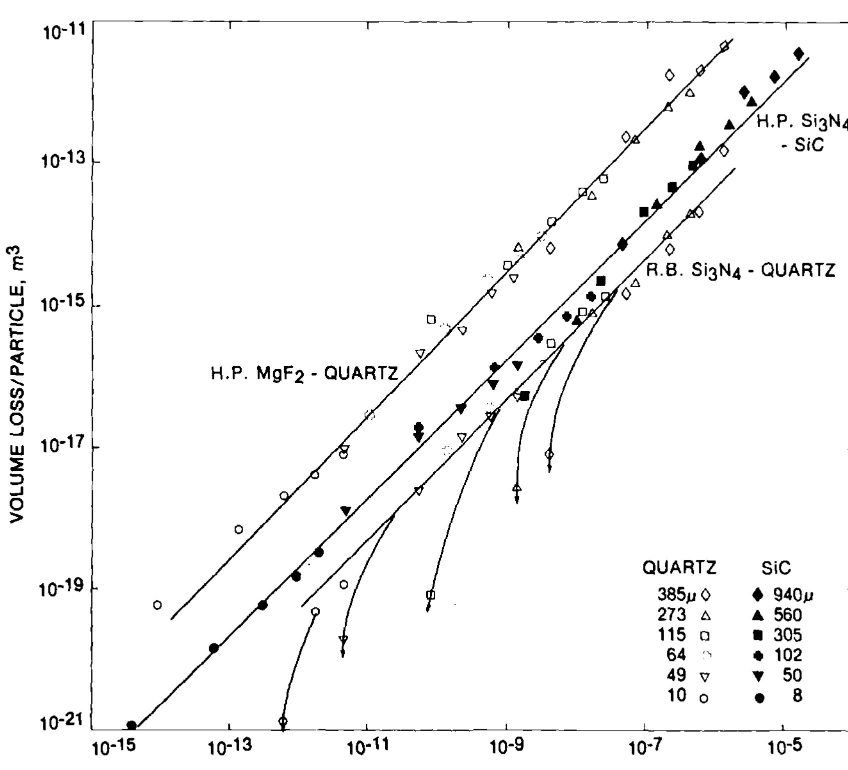

FIG. 1—*Erosion versus particle size and velocity to the fourth power (velocity varied between 40 and 285 m/s).*

the different density targets. The relationship between R^4V^4 and erosion is valid over eight orders of magnitude, which corresponds to six particle size ranges and five velocities between 24 and 285 ms^{-1} for each particle size. The relationship also applies for RB Si_3N_4-quartz for all particle sizes at higher velocities. These results suggest that a single mechanism is controlling erosion under these test conditions. The data points associated with arrows correspond to weight increases that occurred after low-velocity erosion tests on RB Si_3N_4. Since RB Si_3N_4 is an inherently porous (~ 25 percent porosity) material, it is probable that the weight increases correspond to embedding of the quartz particles in the target. This will be discussed later in more detail.

For a given erosion condition with quartz particles, the volume of MgF_2 lost per impact is approximately 1½ orders of magnitude greater than for RB Si_3N_4. HP Si_3N_4 impacted with SiC particles is intermediate between the two.

The system HP Si_3N_4 impacted with quartz particles showed a significantly different erosion dependency on particle size and velocity than the systems previously discussed. Erosion is proportional to particle size to the third power and velocity to the first power, which is a measure of particle momentum (particle mass times velocity). The results for this system are shown in Fig. 2 plotted as volume loss per particle versus a measure of particle momentum. The results are valid over the entire range of particle size-velocity combinations investigated. Deviations from the straight-line relationship occur as the volume or weight loss threshold is approached for 115 and 273-μm particles. The results for this system indicate that a single mechanism or erosion process is operative within this range of test conditions and that the mechanism of erosion of HP Si_3N_4 by quartz particles is significantly different than the other three target-particle systems, which showed an R^4V^4 erosion dependence. For equivalent particle size-velocity tests on HP Si_3N_4, the volume of material lost with SiC impacts was two orders of magnitude greater than for quartz impacts (highest velocity tests).

Glass-bonded Al_2O_3 (GB Al_2O_3) impacted with quartz particles did not exhibit a consistent particle size-velocity dependence. Erosion was proportional to particle radius cubed over the entire range of particle sizes, but the velocity exponent varied between three for the smaller particles and one for the larger particles at higher velocities. The test data for erosion with the larger particles are also shown in Fig. 2. Apparently, the rate-controlling erosion mechanism or process is changing for these test conditions. This change is believed to be related to the two-phase structure of the target and will be discussed further in the following section.

Examination of Eroded Surfaces

Surfaces were examined for a range of erosion conditions varying between

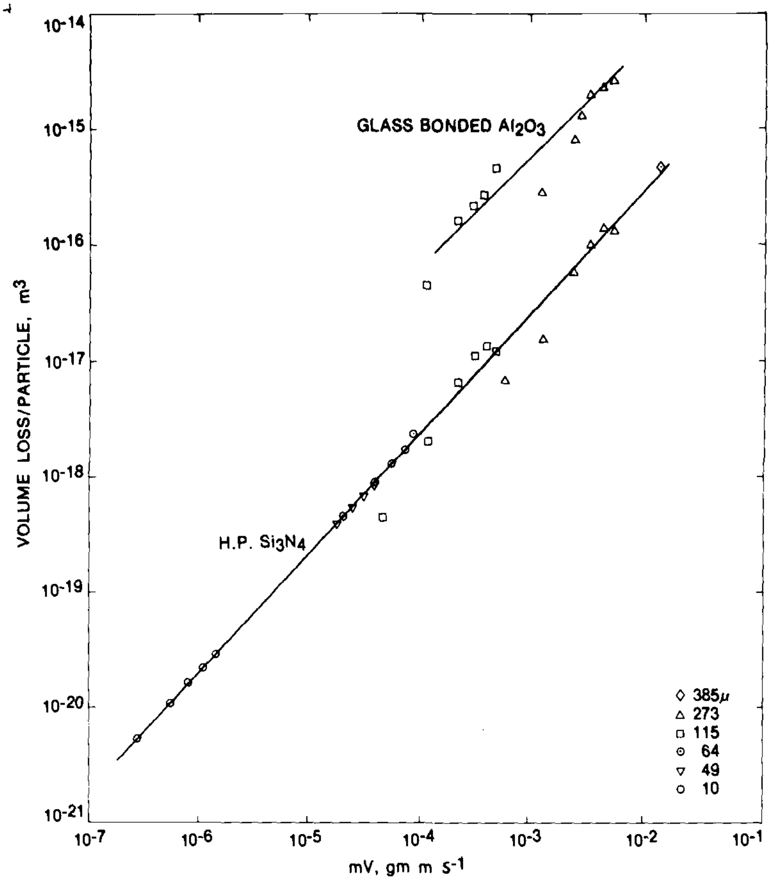

FIG. 2—*Erosion by quartz versus a measure of particle momentum (velocity varied between 40 and 285 m/s).*

single-particle impacts and erosion to a depth of several grain diameters for the various particle size-velocity test conditions. Generally, the heavily eroded surfaces were sufficiently damaged that little information was provided concerning erosion mechanisms or processes. However, single-particle impacts have provided insight into the process of erosion for these target materials. Figure 3 shows examples of single-particle impacts, under similar test conditions, for those target-particle combinations which exhibited a consistent particle size-velocity dependence. The types of impact are typical for each system although average magnitude varied with particle size and velocity. Since the particles can impact on a corner, edge, or face, variation in the shape of single-particle damage is also observed for a given particle size-velocity combination. The contact radii calculated for purely elastic impact by a spherical particle [*1,3*] are given in Fig. 3. Although these calculations do not account for particle irregularity, they do provide a measure of the average elastic impact contact area for a given particle size-velocity combination and serve to illustrate variations in observed damage magnitude between the different target-particle systems. The calculated area is in reasonable agreement with measured contact area for those systems where measurements were possible, that is, Fig. 3*a*, *b*, and *c*.

HP Si_3N_4 impacted with SiC particles and MgF_2 impacted with quartz particles (Fig. 3*a* and *b*) both exhibited a highly deformed, permanent surface indentation accompanied by radial and lateral crack formation. The radial cracks extend outward from the particle contact zone and are generally perpendicular to the surface. Lateral cracks also extend from the contact zone but are subsurface and approximately parallel to the surface. Material removal occurs by loss of a portion or all of the laterally cracked regions. The dark semicircular regions in Fig. 3*a* and *b* correspond to laterally cracked material which has been removed during impact. Also shown in Fig. 3*a* by polarized light reflecting conditions are the lateral cracks which have not resulted in material loss. Since HP Si_3N_4 is opaque, subsurface cracks are not observable by the polarized-light technique. For these two systems, the extent of damage or material loss is much larger than the observed particle contact area (severely deformed surface crater). This type of impact damage has recently been observed in similar single-phase, fully dense systems, and has been associated with plastic deformation of the target [*2,7,8*]. Both static impact with sharp indentors and dynamic impacts with angular particles exhibit dislocation formation associated with the permanent surface pit or crater. The extent of plastic deformation varies appreciably with target material. For a relatively easily deformable ceramic such as magnesium oxide (MgO), plastic flow by slip extends well beyond the initial crater and often encompasses the associated fracture pattern, while, for a relatively rigid material such as silicon or germanium, plastic deformation extends only slightly beyond the region of actual contact. Materials such as Al_2O_3 and SiC exhibit intermediate behavior. Although not specifically determined, it is reasonable to assume that plastic deformation is also associated with quartz particle impacts on MgF_2 and SiC particle impacts on HP Si_3N_4.

Figure 3*c* shows a quartz particle impact on RB Si_3N_4. The impacts in this system are characterized by relatively deep pits with no apparent evidence of secondary cracks intersecting the surface. The approximate calculated contact radius (~ 35 μm) is of the same order as the pit. The appearance of the pit is one of plastic impact. However, since this material is inherently porous (~ 25 percent), the phenomenon could be one of crushing rather than plastic deformation. This porosity might also be expected to arrest crack propagation which would occur in a fully dense material. The type of impact damage shown in Fig. 3*c* is characteristic of the RB Si_3N_4 quartz particle system at higher velocities (see Fig. 1).

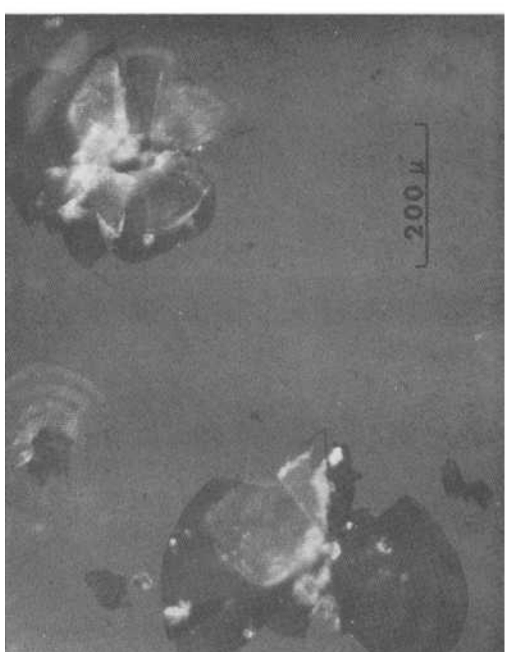

(*a*) Hot-pressed MgF_2 impacted with 273-μm quartz: velocity 188 m/s; contact radius ~27 μm; $E \propto R^4V^4$ (3 impacts).

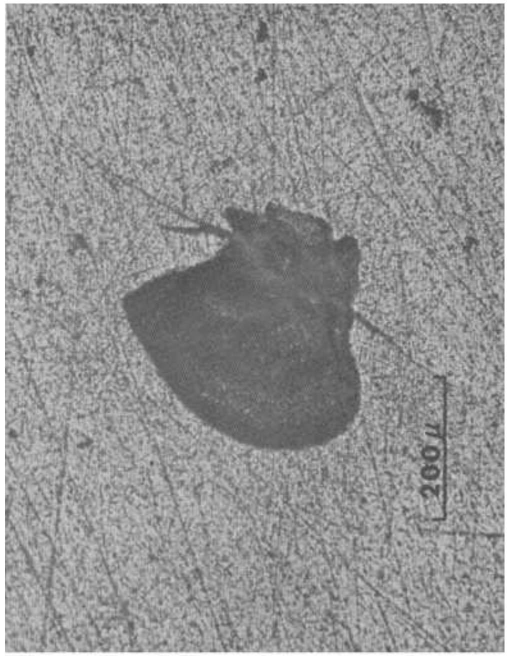

(*b*) Hot-pressed Si_3N_4 impacted with 305-μm SiC: velocity 176 m/s; contact radius ~22 μm; $E \propto R^4V^4$.

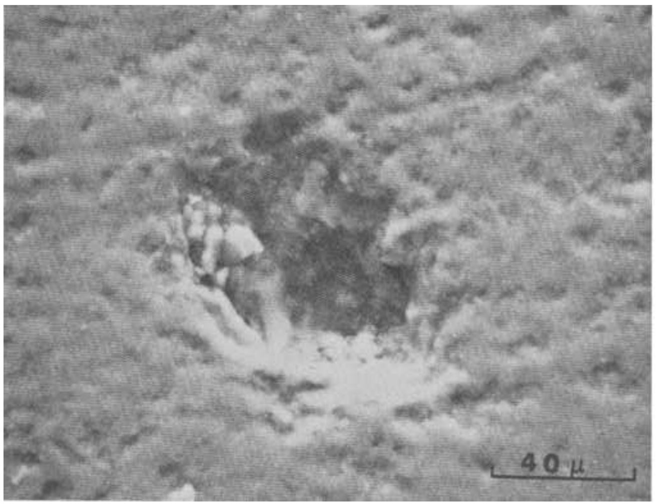

(*c*) Reaction-bonded Si_3N_4 impacted with 385-μm quartz: velocity 174 m/s; contact radius ~35 μm; $E \propto R^4V^4$ (higher velocities).

(*d*) Hot-pressed Si_3N_4 impacted with 273-μm quartz: velocity 188 m/s; contact radius ~25 μm; $E \propto R^3V$.

FIG. 3—*Single-particle impacts for systems which exhibit consistent particle size-velocity functions with erosion.*

Examination in cross section revealed radial cracking beneath the contact area that propagated through the pores.

The type and magnitude of damage produced by quartz particles on HP Si_3N_4 are entirely different from those of the three systems previously discussed. An example is shown in Fig. 3*d*. The chip which has been removed ($\sim$4 μm diameter) is quite small compared with the approximate calculated contact diameter, and no secondary cracking is observed. Examination in cross section revealed no subsurface cracking.

An estimate of the volume of material removed per impact can be made from the weight loss data on heavily eroded surfaces (data from Figs. 1 and 2). For all of the systems shown in Fig. 3, the volume removed per impact for heavily eroded surfaces is within a factor of 2 of that measured from single-particle impacts. Considering the statistical nature of the calculations and the test procedure, this shows quite good agreement between single-particle impacts and bulk erosion and suggests that secondary cracking and residual erosion damage may not play a significant role in the erosion process under these test conditions.

The discussion to this point in this section has concerned the target-particle systems which exhibited a uniform particle size-velocity relationship over the entire range of test conditions (except low-velocity impacts on RB Si_3N_4). The system GB Al_2O_3-quartz particles did not show a consistent relationship. The structure of this material is characterized by Al_2O_3

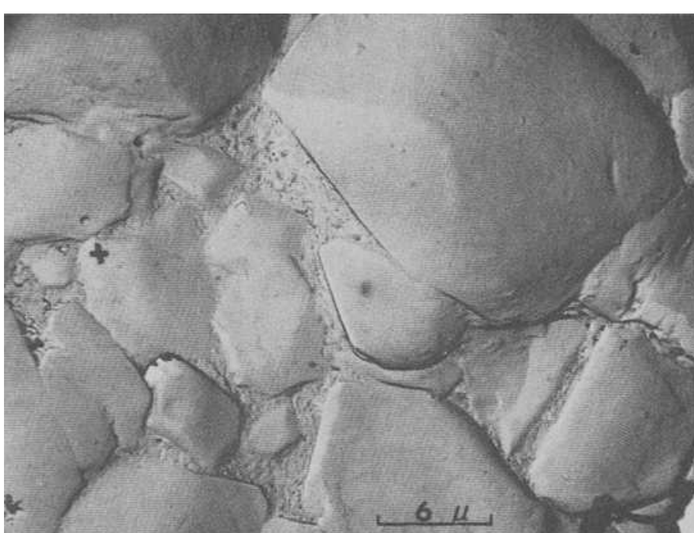

Velocity 285 m/s; contact radius $\sim$2 μm; depth of erosion $\sim$50 μm; 6000 particle impacts per single-particle contact area; $E \propto R^3V^{1 \text{ to } 3}$

FIG. 4—*Glass-bonded* Al_2O_3 *impacted with 10-μm quartz.*

grains (~10 μm diameter) surrounded by a glassy intergranular phase. The glass can be as thick as 4 μm in the vicinity of grain boundary triple points. It was found that single-impact damage for 10-μm impacts produced plastic flow in the grain boundary phase and minimal damage to the Al_2O_3 grains. The erosion process occurred by flow and removal of the glass to the extent that entire grains were lost. An example of a surface heavily eroded by 10-μm quartz is shown in Fig. 4. The depth of erosion corresponds to ~4 grain diameters. As can be seen, little damage has been sustained by the Al_2O_3 grains. As the particle size was increased, chipping of the Al_2O_3 grains occurred in addition to flow of the glass. This chipping is similar in appearance to that which occurs in the HP Si_3N_4-quartz system.

Hertzian-type cone or ring cracking was not observed for any of these systems under these test conditions.

Examination of the impacted and eroded surfaces has shown that more than one type of impact occurs for this group of target materials under these test conditions. A discussion of the reasons for this variation based on properties and microstructure of the targets and particles will be given in the "General Discussion" section.

Strength of Impacted and Eroded Specimens

Strength after heavy erosion was determined for HP Si_3N_4, RB Si_3N_4, and GB Al_2O_3, all impacted with quartz particles (same test conditions used to develop Figs. 1 and 2 plus specimens eroded at particle size-velocity conditions below the weight loss thresholds). It was originally expected from Hertzian-type considerations that a strength decrease would occur for impact conditions below those needed for actual weight loss; that is, cracking would occur, but would be insufficient to produce material loss. Above the weight loss threshold, strengths were expected to decrease.

The strength results are given in Table 2. The baseline strengths plus one standard deviation are given for each target material. An estimate of the critical flaw size is also given. This was calculated from fracture toughness values given in Table 1 using the relationship for three-point bend specimens [*9*]. The strengths after erosion are shown as a function of the baseline strengths by giving the percentages which have strengths greater than $+1$, within ± 1, and less than -1 standard deviation of the noneroded material strength.

HP Si_3N_4 and the GB Al_2O_3 did not exhibit a strength decrease under these test conditions for erosion depths up to 31 μm. For HP Si_3N_4 this depth corresponds to 3×10^8 particle impacts or 600 g of dust on a 0.71-cm^2 area. There was a trend toward strength increase (fracture stress for 50 percent of the specimens was greater than one standard deviation above the baseline strength), which indicates that a "polishing" phenome-

TABLE 2—*Strength distribution of eroded specimens relative to standard strength.*

	Pre-Erosion Baseline		Post-Erosion Strength Distribution, %				
	$\bar{\sigma}_F \pm 1$ Standard Deviation, MPa	≈ Critical Flaw Size, μm	No. of Tests	Max Erosion Depth, μ	Above +1	Within ±1	Below −1
HP Si_3N_4	798 ± 128	11	25	31	50	50	0
GB Al_2O_3	252 ± 21	43	51	35	41	43	16
RB Si_3N_4	278 ± 10	17	17	360	6	12	82[a]

[a] Minimum strength = 81 MPa corresponding to critical flaw size of ~200 μm.

non may be occurring. No specimens failed at a stress lower than the one standard deviation band. The erosion depth is approximately three times the estimated critical flaw size, which indicates that under these test conditions the effective flaw size produced by erosion is no larger than preexisting flaws characteristic of the "standard" machined surface. (Because large numbers of flaws are introduced by erosion or machining, the effective stress concentration will depend on both size and spacing of flaws. In contrast, critical flaw sizes were calculated for isolated flaws.) In confirmation, examination of the eroded surfaces in cross section did not reveal apparent subsurface damage; that is, the structure under the eroded area was indistinguishable from that below the as-machined surface and subsurface cracking was not apparent.

The trend toward a strength increase is not as conclusive with GB Al_2O_3 as with HP Si_3N_4 since 16 percent of the specimens failed at stresses below the one standard deviation range. Furthermore, although the maximum depth of erosion ($\sim$35 μm) is approximately four grain diameters, this also corresponds to the estimated critical flaw size of the baseline material. However, the results indicate that erosion under these test conditions does not produce flaws greater than those inherent to the as-sintered surface.

RB Si_3N_4 did exhibit a marked strength decrease under these erosion test conditions. Strength decreased rapidly for the first 100-μm erosion depth and remained essentially constant at 100 MPa up to the maximum depth tested (350 μm). The tests were performed in the as-fired surface condition where the surface oxide layer is $\sim$100 μm deep. The lowest strength (81 MPa) corresponds to an increase in estimated critical flaw size over the baseline material of one order of magnitude (17 μm compared with 200 μm). The depth of subsurface cracks perpendicular to the surface is also $\sim$200 μm for this erosion condition.

According to the model for plastic impact response, the strength of the target (σ_F) should be dominated by radial crack formation by the following relation [2]

$$\sigma_F \propto \frac{K_c^{\,1.4}}{V^{0.5}R^{0.8}}$$

where

K_c = target fracture toughness,
V = particle velocity, and
R = particle radius.

A log-log plot of strength versus $(V^{0.5}R^{0.8})^{-1}$ for reaction-bonded Si_3N_4 is shown in Fig. 5. The data fall roughly into two groups, both of which have slopes close to one on a log-log basis. The major difference between these two groups is particle size and depth of erosion. The depth of erosion

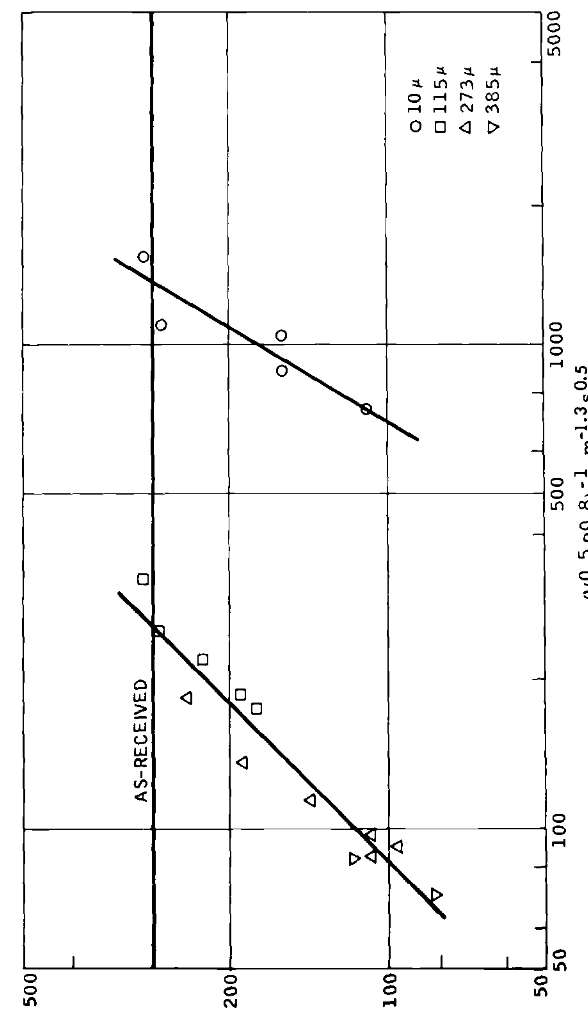

FIG. 5—*Strength versus function of predicted radial crack formation for reaction-sintered Si_3N_4 eroded by quartz.*

for those particular specimens subjected to 10-μm particle bombardment was still within the surface layer, which has different material properties and composition than the bulk material. Furthermore, the type of damage, and hence flaw type, apparently differs from that produced with the larger particles. Subsurface cracking is minor compared with that produced with larger particles, and embedding of the 10-μm particles was observed.

Since quartz is the most erosive constituent of natural dusts and the particle size-velocity conditions are typical of airborne dust, these results have direct practical significance and indicate that a strength decrease does not necessarily occur for erosion conditions which produce appreciable material removal (HP Si_3N_4 and Alsimag 614 glass-bonded Al_2O_3). This would be expected to apply as long as the load-bearing volume is not reduced significantly.

General Discussion

In this section a comparison will be made between the erosion behavior of the various target materials, and the results will be discussed in terms of impact models and material properties and structure.

Four "engineering" ceramics have been subjected to erosion conditions considered characteristic of a natural dust environment. Under these conditions, the erosion response differs markedly (Figs. 1 and 2), and for a given condition there is approximately one order of magnitude difference in volume loss between each of the targets. There is also considerable variation in material properties and structure between the targets. Table 1 lists the mechanical properties considered relevant to erosion response. Of the properties listed, fracture toughness and hardness are the properties which varied consistently with erosion. The other properties (elastic modulus and acoustic impedance) would predict either less separation in erosion loss or a different ranking of erosion resistance. Furthermore, the particle properties can also have a strong effect on erosion as evidenced by the fact that erosion of HP Si_3N_4 by SiC particles is approximately two orders of magnitude greater than with quartz particles for equivalent particle size-velocity test conditions, and the type of impact damage is entirely different.

To date, essentially two types of models have been proposed for solid-particle impact or erosion at subsonic velocities. The earlier model was based on Hertzian-type purely elastic interaction where material removal occurs by the intersection of ring cracks on the substrate surface. This model was expanded to include Weibull statistics whereby erosion was a function of the distribution and size of flaws under the particle contact area [1]. This relationship predicted that

$$E \propto R^4 V^{2.7}$$

(where E is volume removed per particle) for a Weibull modulus greater than 12 and impact with angular particles [1]. This velocity dependence was not observed for these test conditions, nor was ring cracking.

The second model has treated static, and more recently dynamic, plastic indentation, which is characterized by plastic deformation of the contact area between particle and target, radial cracks propagating outward from the contact zone, and lateral cracks that initiate beneath the contact zone and propagate between the radial cracks on planes nearly parallel to the surface. It has been observed for a variety of single-phase targets impacted with relatively incompressible projectiles (impact conditions above plastic impact threshold) that the length of radial cracks, and the depth of lateral cracks, for single impacts, followed the relationships predicted by the model [2].

If it is assumed that maximum erosion loss per impact is proportional to the volume encompassed by the lateral cracks, then the plastic impact model predicts

$$E \simeq V^{2.5} R^4 \left(\frac{\rho_p}{H K_c^6} \right)^{0.25} f(M)$$

where

ρ_p = particle density,
H = target hardness, and
$f(M)$ = fraction of volume encompassed by the lateral cracks that is actually removed and is considered a material-dependent variable.

Since the experimental erosion data for this type of impact (HP Si_3N_4 impacted with SiC, and MgF_2 impacted with quartz) revealed both a radius and velocity dependence to the fourth power, the term $f(M)$ would have to include a velocity dependence, to obtain conformance with experimental data. This would require that the formation of lateral cracks as well as the volume of laterally cracked material actually removed be velocity dependent.

A log-log plot of $E/V^{2.5}R^4$ versus $\rho_p/H\ K_c^6$ for the four target materials shows a slope of 0.25 between the two target-particle conditions which exhibited typical plastic impact response (Fig. 6). The erosion data in Fig. 6 are an average of all of the particle size-velocity test conditions plus or minus one standard deviation. However, a plot of E/R^4V^4 versus $\rho_p/H\ K_c^{\ 6}$ using all of the erosion data (much smaller data band than for $E/R^4V^{2.5}$) also exhibited a slope of 0.25 between HP Si_3N_4-SiC and MgF_2-quartz.

Erosion for the other target-particle combinations falls below that expected from the plastic impact model, although the relative rank is consistent with the model. In the case of HP Si_3N_4 impacted with quartz particles, this is expected since the impact conditions are apparently below

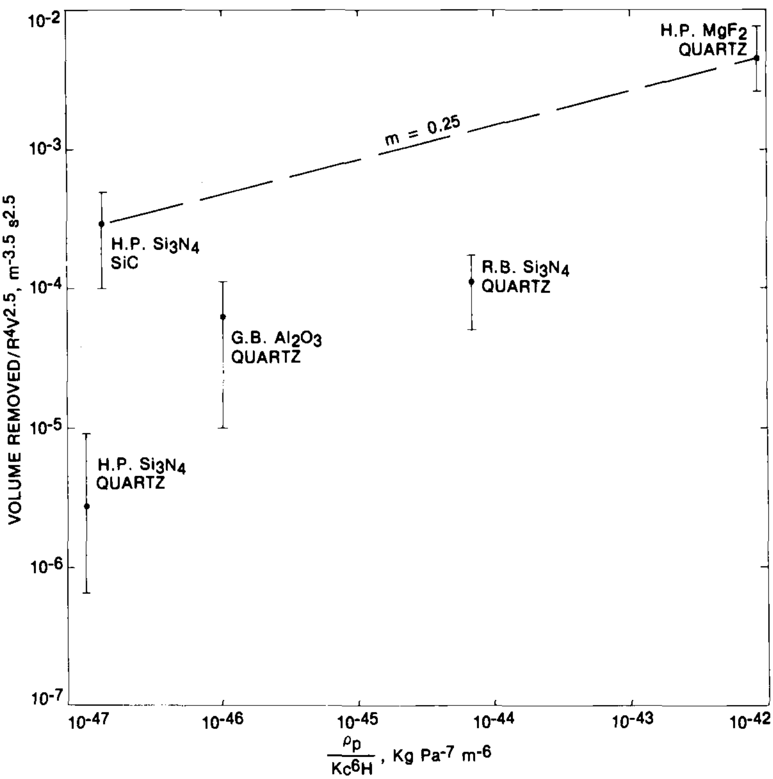

FIG. 6—*Relationship between erosion data and plastic impact model.*

the plastic impact fracture threshold (material removal occurs by minor chipping with no apparent secondary crack formation). However, GB Al_2O_3 did exhibit plastic deformation of the glass phase, and RB Si_3N_4 exhibited permanent craters similar in appearance to plastic impacts.

The model assumes an isotropic material. For the purposes of this investigation, both MgF_2 and HP Si_3N_4 can be assumed to be single-phase materials. (HP Si_3N_4 contains a minor grain boundary phase, but the 2-μm grain size would average this effect over the particle contact area.) However, GB Al_2O_3 and RB Si_3N_4 are not single-phase materials. RB Si_3N_4 contains ~25 percent porosity, and although the impact craters had the appearance of plastic impact, it is possible that crushing is occurring under the contact area. Support for this hypothesis is given by the fact that particles embedded in the surface at low velocities for all particle sizes. Also, the lack of secondary cracking outside of the contact area may be related to the crack-blunting ability of the pores. Erosion of GB Al_2O_3 is a two-step process which is directly attributable to the two-phase nature of the structure.

The particle composition and properties obviously affect the type of erosion response. From this investigation, however, only general comments can be made concerning the influence of particle type on erosion of a given target. It appears that, for plastic impact response, the particle mechanical properties must closely approach or exceed those of the target. For impact and erosion conditions where the particle properties are appreciably lower than the target, the erosion process is less efficient.

Conclusions

Four ceramic materials with widely different properties and structure were eroded under conditions which simulate a service dust environment, that is, 10- to 385-μm natural quartz particles at subsonic velocities. Additionally, one of the targets (HP Si_3N_4) was impacted with SiC particles over the same particle size-velocity conditions. The following particle size-velocity relationships for erosion were observed

$E \propto R^4V^4$	MgF_2-quartz, RB Si_3N_4-quartz (higher velocities)
	HP Si_3N_4-SiC
$E \propto R^3V$	HP Si_3N_4-quartz
$E \propto R^3V^{1\ \mathrm{to}\ 3}$	GB Al_2O_3 - quartz

Single-particle damage for the systems HP Si_3N_4 impacted with SiC and MgF_2 impacted with quartz was characterized by a highly deformed surface crater and radial and lateral cracks propagating from the contact area (plastic impact). The diameter of material removed could be as much as three times the measured contact diameter (corresponds to a portion of lateral crack formation). The diameter of material removed for RB Si_3N_4 was essentially the same as the estimated contact diameter. Erosion of HP Si_3N_4 impacted with quartz occurs by minor chipping which is an order of magnitude less than the estimated contact radius. In the latter two cases, secondary cracking was not observed on the surface. However, RB Si_3N_4 exhibited extensive subsurface radial cracks under the contact area. Erosion on glass-bonded Al_2O_3 is a two-step process involving plastic deformation of the glass plus chipping of Al_2O_3 grains.

Based on these results, erosion is a function of particle radius and velocity, both to the fourth power for a plastic impact response. For a single-phase material (HP Si_3N_4, MgF_2) erosion appears to follow the function of fracture toughness and hardness predicted by the model for plastic impact. However, for multiphase materials, structure also influenced erosion response. Below the plastic impact threshold, erosion is a much lesser function of velocity, and elastic ring cracking was not observed. The plastic impact threshold was more a function of relative target-particle properties than of particle size and velocity.

Strength measurements after erosion with quartz revealed that strength is not necessarily reduced after pre-eroding under conditions which produce significant material removal. (HP Si_3N_4 and GB Al_2O_3 did not show a strength decrease, while RB Si_3N_4 exhibited a major strength decrease.)

It is concluded that more than one mechanism of erosion exists under "natural" dust environments, and that the mechanisms are dependent not only on target physical properties, but also to a large extent on structure.

Acknowledgments

This work was performed under Contract N00014-73-C-0401, sponsored by the Office of Naval Research, Department of the Navy. The author appreciates the technical discussions with Dr. A. G. Metcalfe and the experimental assistance of R. B. Domes.

References

[*1*] Oh, H. L., Oh, K. D. L., Vaidyanathan, S., and Finnie, I., *On the Shaping of Brittle Solids by Erosion and Ultrasonic Cutting,* NBS Special Publication 348, National Bureau of Standards, Washington, D.C., 1972, p. 119.

[*2*] Evans, A. G., Gulden, M. E., Eggum, G. E., and Rosenblatt, M., "Impact Damage in Brittle Materials in the Plastic Response Regime," Contract N00014-75-C-0069, Report No. SC5023.9TR, Rockwell International Science Center, Thousand Oaks, Calif., 1976.

[*3*] Adler, W. F., "Analysis of Multiple Particle Impacts on Brittle Materials, AFML Technical Report 74-210, Air Force Materials Laboratory, Wright-Patterson Air Force Base, Ohio, 1974.

[*4*] Smeltzer, C. E., Gulden, M. E., McElmury, S. S., and Compton, W. A., "Mechanisms of Sand and Dust Erosion in Gas Turbine Engines," USAAVLABS Technical Report 70-36, United States Army Aviation Material Laboratories, Fort Eustis, Va., 1970.

[*5*] Ruff, A. W. and Ives, L. K., *Wear,* Vol. 35, 1975, p. 195.

[*6*] Gulden, M. E. and Metcalfe, A. G., "Study of Erosion Mechanisms of Engineering Ceramics," Solar Report RDR 1778-4, Solar Turbines International, San Diego, Calif. Contract N00014-73-C-0401, 1976.

[*7*] Hockey, B. J., Widerhorn, S. M., and Johnson, H., "Erosion of Brittle Materials by Solid Particle Impact" in *Fracture Mechanics of Ceramics,* R. C. Bradt, D. P. H. Hasselman, and F. F. Lange, Eds., Plenum Press, New York, 1978.

[*8*] Hockey, B. J. and Lawn, B. R., *Journal of Materials Science,* Vol. 10, 1975, p. 1275.

[*9*] Evans, A. G. in *Fracture Mechanics of Ceramics 1,* R. C. Bradt, D. P. H. Hasselman, and F. F. Lange, Eds., Plenum Press, New York, 1974, p. 17.

DISCUSSION

G. Mayer[1] (*written discussion*)—In connection with your last conclusion, that frequently erosion damage has less effect than the natural flaws in a

[1] Army Research Center, Research Triangle Park, N.C. 27709.

number of brittle materials, we should recognize that erosion may become much more important when better processing techniques for ceramics reduce the severity of the "natural" flaws.

M. E. Gulden (author's closure)—I agree with Dr. Mayer's comment. However, the conclusion that, under conditions of relatively severe dust erosion, the strength of a component is not necessarily reduced, is still valid. For those systems where processing improvements do produce increased strength, further testing will be necessary.

A. Levy[2] *(written discussion)*—How applicable would the study be to behavior of the ceramics at the elevated temperatures that will be experienced in service?

M. E. Gulden (author's closure)—The applicability will depend on the high-temperature properties of the target and particulates in the service environment. Of the target materials investigated, only the silicon nitrides are being considered for high-temperature use. For these applications, such as heat exchangers and gas turbine engines, fouling by the particulates in the gas stream can be a much more severe problem than erosion. For high-temperature impacts where erosion is expected (particle integrity maintained), the type of damage which occurs at room temperature would also be expected at elevated temperatures although the magnitude is expected to vary. For example, a degree of plastic deformation can occur during impact at room temperature and ease of plastic deformation increases with temperature.

J. Zahavi[3] *(written discussion)*—In your well-presented and important work you found and pointed out the importance of structure and properties of two-phase brittle materials in regard to solid-particle erosion processes. The results of eroded surfaces of two-phase ceramic materials obtained by scanning electron microscope revealed that local material removal processes were characterized by undermining around hard microconstitutes and by cratering. These observations confirm our results obtained on ductile materials and actually provide additional evidence that local erosion processes of a substrate containing microconstitutes in the range of 10 μm are affected by these phases and occur by undermining around them.

M. E. Gulden (author's closure)—Dr. Zahavi's results further illustrate the complexity of erosion processes and the need to consider microstructure and microproperties in order to more fully understand erosion response and mechanisms.

[2] University of California, Berkeley, Calif. 94720.

[3] University of Illinois at Urbana, Champaign, Urbana, Ill.

W. Tabakoff[1] *and T. Wakeman*[1]

Test Facility for Material Erosion at High Temperature

REFERENCE: Tabakoff, W. and Wakeman, T., "**Test Facility for Material Erosion at High Temperature,**" *Erosion: Prevention and Useful Applications, ASTM STP 664,* W. F. Adler, Ed., American Society for Testing and Materials, 1979, pp. 123-135.

ABSTRACT: One of the next steps in experimental material erosion investigation is the testing at high temperatures comparable to those found inside a jet engine. Described in this paper is the design of the high-temperature erosion facility at the University of Cincinnati. This facility has the capability of providing between ambient and a 1093°C (2000°F) environment temperature for erosion testing of various materials. In addition, this facility has the capability for varying material, specimen size, angle to the flow, particle concentration, particle size, and velocity. This facility is expected to provide basic material erosion data which will be used in predicting erosion in jet engines and other devices.

KEY WORDS: erosion test facility, high temperatures, high-speed particles, particle feeder assembly, wind tunnel, gas turbines, erosion

In many industrial and military applications the erosive action of high-speed particles results in serious problems. Erosion has been pointed out as as problem in as diverse areas as aero gas turbines [*1,2*],[2] rocket nozzles [*3*], coal-fired boiler systems [*4*], and others. Recent interest in this old problem coincides with increased usage of gas turbines in dusty terrains. The cost of maintaining such engines in dusty environments is great. Air filtration has alleviated the problem somewhat, but filtration reduces both payload and engine performance. If erosion can be incorporated as an engine design parameter, perhaps an erosion-tolerant engine can be produced.

A description of a sand-blasting erosion test facility, in which a small jet of particle-laden air was impacted on a stationary specimen, was provided by Finnie [*5*]. Extensive erosion research has been conducted using this facility or modifications of it. Other testing methods used an apparatus

[1] Professor and graduate research assistant, respectively, Department of Aerospace Engineering and Applied Mechanics, University of Cincinnati, Cincinnati, Ohio 45221.

[2] The italic numbers in brackets refer to the list of references appended to this paper.

where particles dropped through a vacuum impact a stationary specimen, or a specimen attached to the end of a rotating arm [*6, 7*]. A common characteristic among all these test facilities is that the fluid profile over the specimen is completely or partially eradicated.

Experimental Equipment

From the literature reviewed, it was concluded that the design of the test facility can affect the resulting erosion rate. Further, the test facilities designed thus far do not investigate the influence of a flow field on erosion. This factor is especially important in rotating machinery, where the fluid is abruptly turned by the rotating or stationary blades. The test facilities reported herein have been designed to investigate these problems.

Stationary Specimen Test Facility

Previously, a wind tunnel was constructed at the University of Cincinnati to obtain the basic erosion data and to photograph the particle impacts on the specimen. Controlling the primary variables of fluid velocity, particle velocity, particle flow rate, and particle sizes in a representative aerodynamic environment were main considerations in designing this tunnel. A detailed description of this test facility can be found in Ref *8*. A significant amount of research has been carried out using this facility, which provided basic erosion data and particle rebound characteristics for various test materials [*9*]. These data have been used in analytical models to predict turbomachinery erosion. This was accomplished by following a sufficiently large number of particles through the turbomachine and determining these individual contributions to arrive at a general erosion pattern for the machine.

In many applications, however, erosion takes place at elevated temperatures near the strength-limiting temperatures of the materials used. As an example, titanium used in early stages of jet engine compressors and INCO 718 used in aft stages are operated at metal temperatures in excess of 316 and 593°C (600 and 1100°F), respectively. In both cases, these temperatures are near the maximum operating temperatures used for these materials. Such elevated temperatures can have a significant effect on erosion characteristics as evidenced in data presented by Tabakoff and Hamed [*10*]. These data were obtained in the same facility as the Ref *8* data, except that the specimen was heated to a maximum of 204°C (400°F). Although this temperature falls far short of those experienced in jet engines, the data indicate the significance of the effect of temperature on erosion and probably on the rebound characteristics.

The erosion test facility described herein is designed to provide erosion and rebound data in the range of operating temperatures experienced in jet engine compressors and low-temperature turbines. For that purpose, the facility has been designed to operate at a test section temperature in the range of ambient to 1093°C (2000°F). The facility properly stimulates, in addition to high temperatures, all erosion parameters found to be important from previous testing at ambient temperatures. These parameters include velocity, angle of impact, particle size, particle concentration, and specimen size.

In designing the high-temperature erosion facility, close attention was given to aerodynamic effects to insure that important parameters such as angle of attack are not masked or altered. To insure the correlation of data from the high-temperature facility with those of Ref *8*, the facility flowpath and acceleration tunnel length are almost identical with those of the facility described in that reference. The flowpath cross section was increased, however, from 76.2 by 25.4 mm to 88.9 by 25.4 mm (3 by 1 in. to 3½ by 1 in.). This change was instituted to decrease tunnel blockage by the test specimen.

The particle rebound characteristic velocities will be obtained photographically and with the laser velocimeter. Presently, we do not have any data at the maximum temperature of 1093°C, but we do not anticipate any difficulties. The velocities of the particles in the range of 20 μm and smaller are measured strictly with the laser velocimeter.

General Description of High-Temperature Erosion Rig

A schematic of the test apparatus is shown in Fig. 1; it consists of the following components: particle feeder (A), main air supply pipe (B), combustor (C), particle preheater (D), particle injector (E), acceleration tunnel (F), test section (G), and exhaust tank (H).

The equipment functions as follows. A measured amount of abrasive grit of a given constituency is placed into the particle feeder (A). The particles are fed into a secondary air source and blown up to the particle preheater (D), and then to the injector (E), where they mix with the main air supply (B), which is heated by the combustor (C). The particles are then accelerated by the high-velocity air in a constant-area steam-cooled duct (F) and impact the specimen in the test section (G). The particulate flow is then mixed with the coolant and dumped in the exhaust tank. This facility is capable of supplying erosion data at temperatures in the range of ambient to 1093°C (2000°F). The expected range of testing parameters is given in Table 1, but is not necessarily restricted to the tabulated values.

The individual components which make up the high-temperature erosion facility are described in the following. Each component was designed with cost, maintainability, availability, and functionality as prime considerations.

Particle Feeder Assembly (*A*)—The particles from the feeder (Fig. 2) are blown up to the particle injector area. The feeder is designed as a pressure

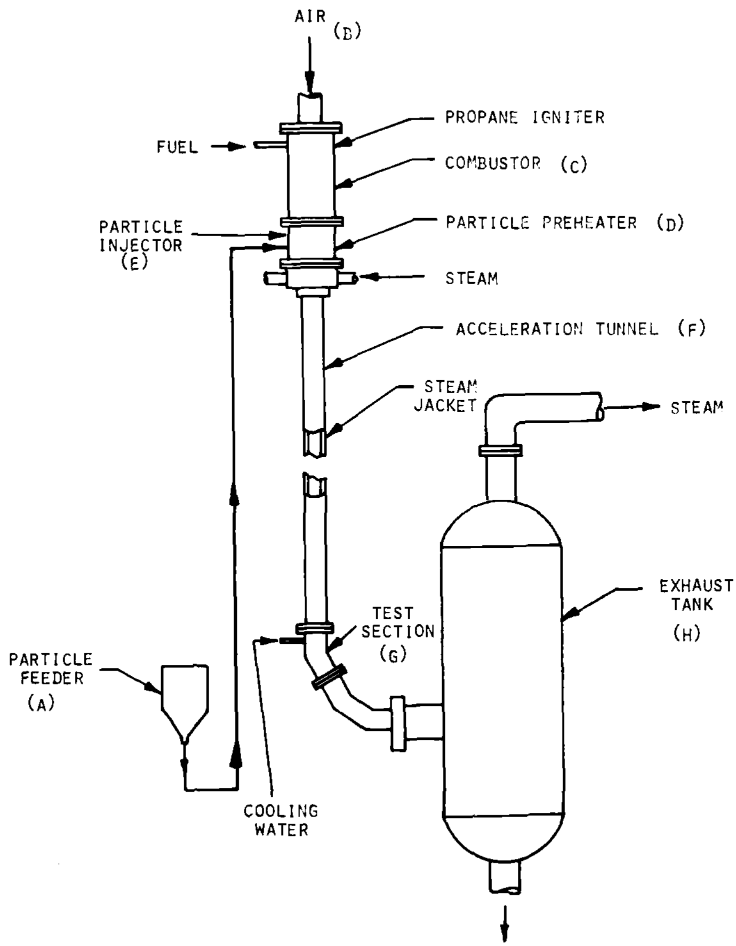

FIG. 1—*Schematic of erosion test facility.*

TABLE 1—*Erosion parameters.*

Parameters	
Temperature	10 to 1093°C (50 to 2000°F)
Particle angle of attack	0 to 90 deg
Particle velocity	60 to 450 m/s (200 to 1500 ft/s)
Particle concentration	0 to 5 percent
Particle size	1 to 2000 μm
Particle type and material	silica sand, alumina, ash
Specimen size	6.35 to 25.4 mm (¼ to 1 in.)
Specimen material	various jet engine materials

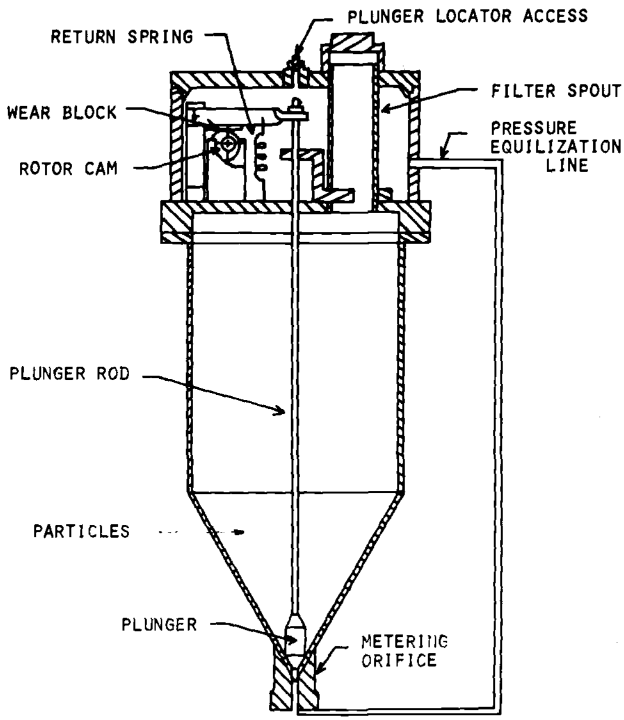

FIG. 2—*Particle feeder assembly.*

vessel to operate at high air pressures. However, this pressure is equalized above and below the plunger by a bypass line. This allows the system to be calibrated under gravity feed conditions. Further, an electric eye records the plunger rpm such that the operating conditions are maintained. The metering orifice is designed to be replaceable. In this manner, a larger (or smaller) orifice may be used, along with corresponding rod diameter, to allow versatility of the feeder.

Main Air Supply (*B*)—This air is drawn from air tank storages, which allow continuous testing.

Combustor (*C*)—High-temperature combustion products are supplied by a modified General Electric J93 can combustor as shown in Fig. 3. The J93 can is encased in a 228.6-mm (9 in.) inside-diameter stainless steel pipe with provisions for the fuel nozzle and igniter. Due to heat loss in the acceleration tunnel, achieving the maximum test section temperature of 1093°C (2000°F) requires a combustor exit temperature of 1204.4°C (2200° F). To obtain this temperature from a J93 can combustor, certain modifications were required, including use of a large fuel nozzle and blanking off most of the downstream dilution air ports. In order to obtain low com-

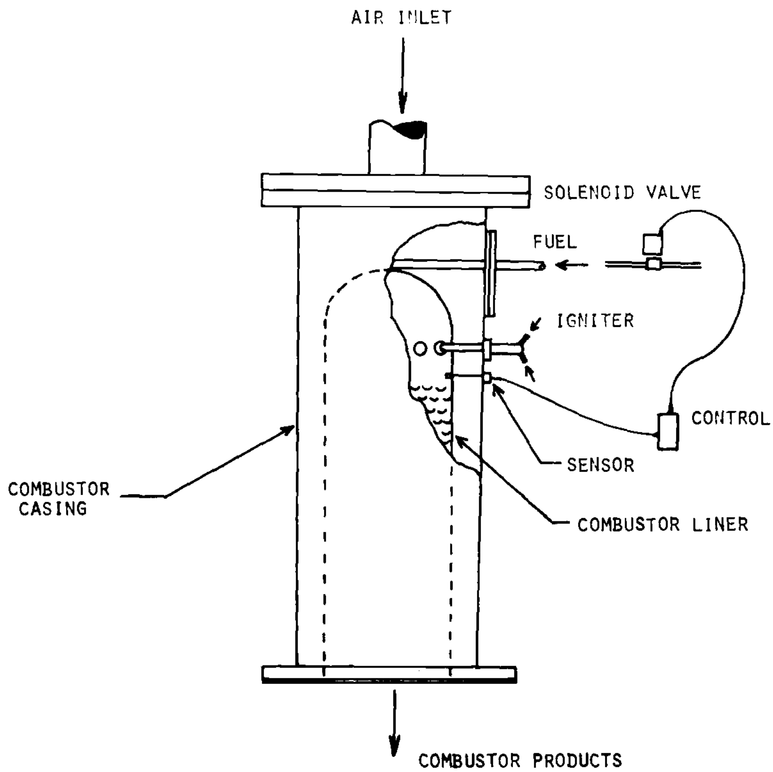

FIG. 3—*Combustion chamber schematic.*

bustion temperatures in the range of 93 through 260°C (200 through 500°F), a smaller fuel nozzle is used. The fuel is ignited by a system consisting primarily of a propane-fired torch containing a spark plug.

Particle Preheater (D) and Injector (E)—The preheater consists of a coil contained in a 203.2-mm (8 in.) inside-diameter pipe section with a distributor/injector to provide a well-distributed preheated particle supply (Fig. 1). The particles are blown up to the accelerating section of the tunnel by secondary air which flows from the particle feeder and passes through the preheater coils. As the particulate air mixture passes through the coils, it is heated by the combustion products to a temperature of 538°C (1000°F) before being injected into the tunnel. The spread-out of the particles in the main airstream is accomplished by impinging them on a specially contoured ball, and then accelerating them through an elliptical nozzle to the acceleration duct section.

Acceleration Section (F)—Figure 4 shows the acceleration section, which is 3.66 m (12 ft) long with a rectangular cross section [89 by 25.4 mm (3½ by 1 in.)]. The acceleration tunnel is steam cooled to minimize heat loss.

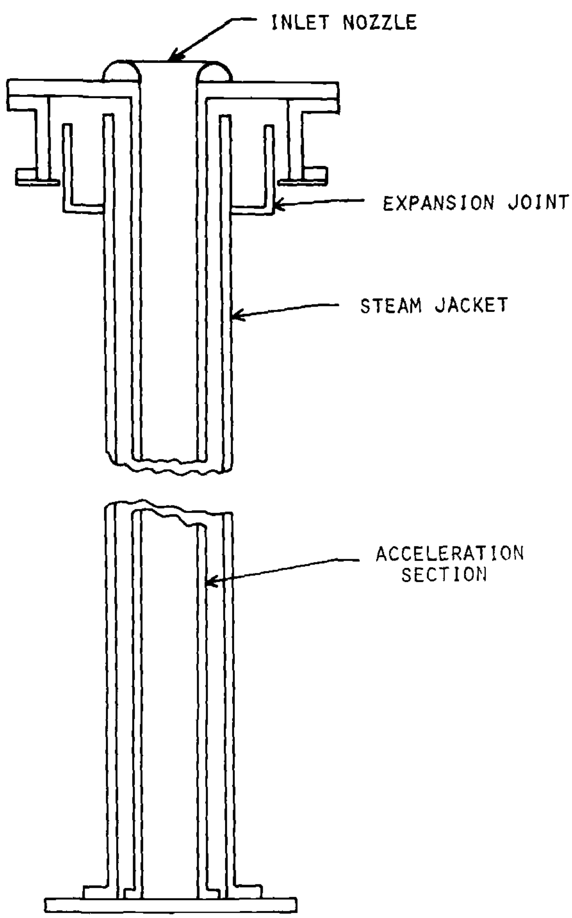

FIG. 4—*Schematic of acceleration tunnel.*

The use of steam coolant allows the 316 stainless steel liner to operate at a maximum of 760°C (1400°F). This maximum operating temperature results in a temperature drop in the gas stream of about 93°C (200°F), which is quite acceptable. The use of water as a coolant would have resulted in at least three times the heat loss.

The particle velocities attained in this acceleration section are predicted analytically and verified by experimental methods. Since the particles are accelerated by aerodynamic drag forces imparted by the high-velocity air, it is necessary to know the air velocity at all locations in the tunnel. For this reason, the tunnel pressure is measured at the inlet, midsection, and exhaust. Using these data, the tunnel friction is accounted for when calculating the fluid velocity. The dynamics of relatively large and small particles (200 and 20 μm) for ambient and 1093°C (2000°F) temperatures for low-speed fluid velocity [122 m/s (400 ft/s)] are shown in Fig. 5. From this figure it can be seen that the particle velocity is an exponential function of tunnel length. The law of diminishing returns would indicate that a tunnel length of 0.61 to 0.92 m (2 to 3 ft) would be sufficient; however, a tunnel length of 3.66 m (12 ft) was chosen, for several theoretical and practical reasons. An additional plot of the ratio between particle and fluid velocity at the end of the acceleration section (starting test section) for various particle sizes is given in Fig. 6. This figure illustrates the obvious fact that a longer tunnel will result in higher particle velocities, but that the rate of change of particle velocity with particle size is smaller for a longer tunnel.

Test Section (*G*)—The test section (Fig. 1) is designed such that the particle-laden air is channeled over the specimen and the aerodynamics of the fluid surrounding the test specimen are preserved. This section contains several interchangeable inserts such that the fluid profile can be determined using conventional instrumentation, and the particle trajectories can be recorded using high-speed photographic methods.

The test specimen can be oriented at different angles to the gas stream by rotating the specimen holder. The test section flow path turns 30 deg at the plane of the test section to help turn the flow when the test specimen is oriented at an angle. The test section is water-cooled. This does not significantly cool the primary gas stream due to the section's small size. The

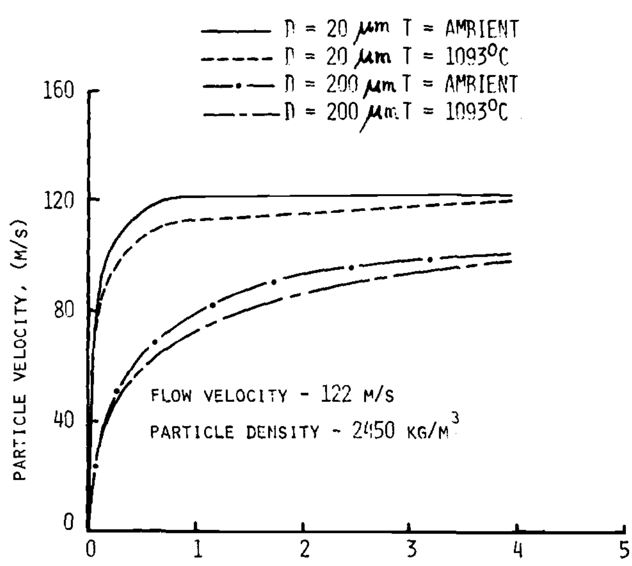

FIG. 5—*Particle dynamics in a constant-area acceleration tube.*

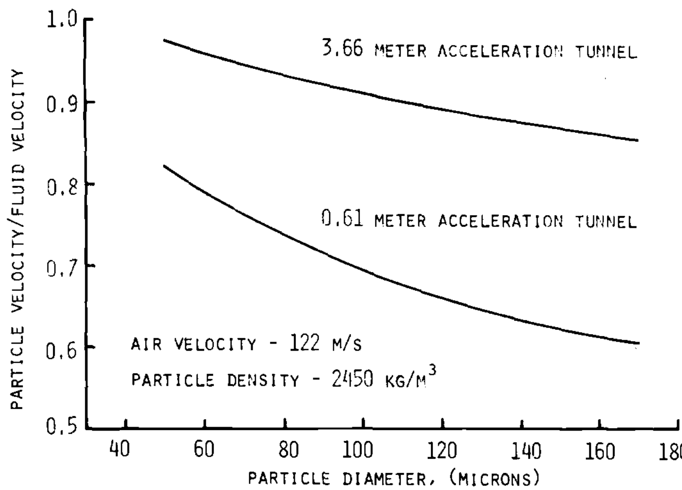

FIG. 6—*Effect of acceleration tunnel length on particle dynamics.*

coolant water is discharged into the particulate gas stream at the downstream end of the test section.

Testing of particle rebound characteristics is also planned, using photographic means to measure the speed and angle of the impinging and rebounding particles. For this purpose, a special test section with a glass window has been constructed.

Exhaust System (*H*)—The erosion rig exhaust system consists primarily of a settling tank (Fig. 1). The exhaust from the erosion test section is loaded with cooling water. In the settling tank, the water is removed from the air, taking with it most of the erosion particles. The particle-laden water is drained from the bottom of the tank through a 101.6-mm (4 in.) line. The air leaves the top of the tank through a 152.4-mm (6 in.) line which discharges the air outside the building. The steam used in cooling the 3.66-m (12 ft) acceleration tunnel is also discharged through the same exit line.

Analysis of Photographic Data

In the previous tunnel [*8*], two techniques of analyses were used in reducing the photographic data. The same techniques may be used in the high-temperature erosion tunnel. These techniques are complimentary in that one was used to check the other. Both of these methods relied on a reference distance which was marked on the test section background. The particle velocities were obtained by comparing the distance traveled by the particle in two successive frames to this reference distance.

The first method of analysis is essentially one of streak photography. The velocity is determined by dividing the distance traveled by the particle during the exposure for one frame.

The velocity is calculated using

$$V = \left(L \frac{r}{R}\right) \Big/ t_e \tag{1}$$

where

V = particle velocity, m/s,
L = length of particle streak on screen, m,
r = actual length of reference line, m,
R = reference line projected on screen, m, and
t_e = exposure time of frame observed, s.

The second method of analysis was based on the distance a particle travels in successive frames. The basic concept is the same as the first method; however, it was found to give more accurate results. The particle velocity is determined using

$$V = n \frac{r}{R} S \tag{2}$$

where

n = length traveled by particle between two successive frames, m,
S = film speed (local quantity), m/s, and
r, R = same as in Eq 1.

In practice, a combination of the two methods was used and checked against each other.

Test Results

To date, erosion data have been accumulated for three target materials (2024 aluminum, Ti-6Al-4V and INCO 718) varying particle velocity, impingement angle, and target temperature. Figure 7 shows preliminary results for Ti-6Al-4V. These data indicate that for Ti-6Al-4V target material with impingement angle of 25 deg, the erosion rate increases with increasing target temperature. Additionally, the slope of the data appears to be decreasing with increasing temperature; however, more data are required to substantiate this trend.

The accuracy of the erosion rates presented depends on the errors accrued in measuring the amount of erosion and in the independent parameters influencing the erosion. At present the most significant error results from

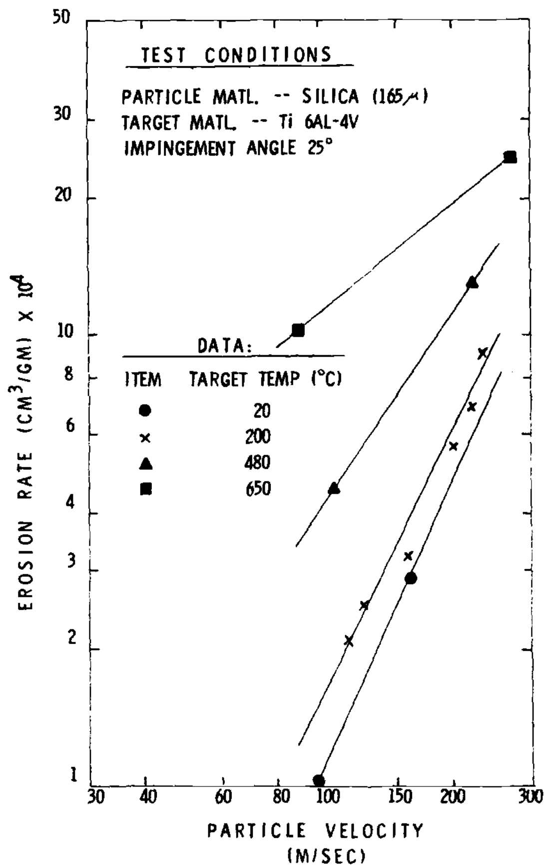

FIG. 7—*Effect of erosion versus particle velocity.*

the calculation of the particle velocity from air pressure, temperature, and flow plus the flow path metal temperature. An estimated maximum error of ±5 percent in particle velocity results in a ±8 percent error in erosion rate due to the strong dependence of erosion on particle velocity. Smaller errors of the order of ±1 percent result from the measurement of impact angle, specimen weight, specimen temperature, and particle weight. The mean square error of all these errors is ±8.2 percent maximum. This maximum error will be substantially reduced by calibrating the calculated particle velocity with measured values. The measured velocities will be obtained using both photographic techniques and a laser velocimeter.

Acknowledgment

This work was sponsored under Grant No. DAAG-29-76-G-0229, U.S. Army Research Office, Research Triangle Park, N.C.

References

[1] Montgomery, J. E. and Clark, J. M., Jr., "Dust Erosion Parameters for a Gas Turbine," SAE Summer Meeting Preprint No. 538A, Society of Automotive Engineers, New York, 1962.
[2] Hibbert, W. A., *Journal of the Royal Aeronautical Society*, Vol. 69, Nov. 1965, pp. 769-776.
[3] Neilson, J. H. and Gilchrist, A., *Wear*, Vol. 11, 1968, pp. 301-315.
[4] Raask, E., *Wear*, Vol. 13, 1969, pp. 301-315.
[5] Finnie, I. in *Proceedings*, Society for Experimental Stress Analysis, Vol. 17, No. 2, 1960, pp. 65-70.
[6] Kleis, I., *Wear*, Vol. 13, 1969, pp. 199-215.
[7] Tilly, G. P. and Sage, W., *Wear*, Vol. 16, 1970, pp. 447-465.
[8] Grant, G. and Tabakoff, W., *Journal of Aircraft*, Vol. 12, No. 5, May 1975, pp. 471-478.
[9] Ball, R. and Tabakoff, W., "An Experimental Investigation of the Particle Dynamics of Quartz Sand Impacting 6Al-4V Titanium in an Erosive Environment," Technical Report No. 74-43, University of Cincinnati, Cincinnati, Ohio, Oct. 1974.
[10] Tabakoff, W. and Hamed, A., "Aerodynamic Effects on Erosion in Turbomachinery," JSME and ASME Paper No. 70, Japan Society of Marine Engineers and American Society of Mechanical Engineers Joint Gas Turbine Congress, Tokyo, Japan, May 22-27, 1977.

DISCUSSION

G. Mayer[1] *(written discussion)*—In the schematic of your apparatus a fairly sharp angle was shown in the flow system as it enters the test section. Was the flow in the test section laminar?

W. Tabakoff and T. Wakeman (authors' closure)—The flow in the wind tunnel test section is turbulent. The size of the particles which we used in this investigation are large—this means over 50 μm. Despite the high turbulence in the flow, these particles follow very much established particle streamwise paths which to the outside observer look like laminar paths (this depends strongly on the particle sizes). This observation was made by high-speed film camera, approximately 40 000 frames per second. The turbulence of the main flow core is measured with optical devices.

A. Levy[2] *(written discussion)*—What was the particle velocity profile across the containment pipe into test section and what was the size of the specimen? Was there a velocity variation across the specimen?

W. Tabakoff and T. Wakeman (authors' closure)—The particle velocity profile across the test section was uniform. The specimen sizes were 6.35, 12.70, 19.05, 25.4, and 31.75 mm (0.25, 0.50, 0.75, 1.0, and 1.25 in.). The approach velocity to the specimen was uniform.

I. Finnie[3] *(written discussion)*—Do the velocity fluctuations in turbulent

[1] Army Research Center, Research Triangle Park, N.C. 27709.
[2] University of California, Berkeley, Calif.
[3] University of California, Berkeley, Calif.

boundary layers formed around turbine blades have a strong effect on the particle trajectories and on the resulting erosion damage?

M. Menguturk[4] *(written discussion)*—Since the main flow turbulence level is quite high in gas turbines, the boundary layers developing around the blades are predominantly turbulent. The turbulent velocity fluctuations inside the boundary layer are small in magnitude compared with the local root-mean-square velocity of the fluid, and they occur very rapidly. Particles which possess considerable inertia to impact blade surface with sufficient velocity to effectively remove blade material will not even feel the presence of these fluctuations. Only extremely fine particles can adjust to the turbulent velocity fluctuations owing to their negligible inertia. However, these particles will cause virtually no erosion. By the time they reach the surface, they will nearly assume the surface gas velocity, which is zero. The result is deposition. Deposition rates of such small particles can be calculated by considering their diffusion due to Brownian motions, turbulent fluctuations, and temperature gradients in the case of cooled blades. Professor Tabakoff is justified in neglecting the flow turbulence in his erosion measurements.

W. Tabakoff and T. Wakeman (authors' closure)—Professor Finnie's question is well answered by the comment of Dr. Menguturk.

[4]Westinghouse Electric Corp., Research and Development Center, Pittsburgh, Pa. 15235.

J. Maji[1] *and G. L. Sheldon*[1]

Mechanisms of Erosion of a Ductile Material by Solid Particles

REFERENCE: Maji, J. and Sheldon, G. L., "**Mechanisms of Erosion of a Ductile Material by Solid Particles**," *Erosion: Prevention and Useful Applications, ASTM STP 664*, W. F. Adler, Ed., American Society for Testing and Materials, 1979, pp. 136–147.

ABSTRACT: Erosion of flat plates and tubular test specimens by spherical 270-μm steel shot showed appreciable differences in the amount of material removed, depending on the condition of the steel shot used. Ductile shot removed considerably less material than brittle or more frangible shot. In addition, lower-velocity exponents were obtained for the tougher, more ductile abrasive.

The evidence presented here supports the view of Tilly that erosion by frangible particles may be viewed as a two-stage process. According to this view, the first stage is due to surface indentation by the particle, forming vulnerable lips around the crater, and the second is due to removal of these lips by radially projecting particle fragments.

KEY WORDS: erosion, impact, wear, fracture, mechanical properties

When studying the erosion of materials by solid-particle impact, the removal mechanism is often studied by classifying the eroded surface as either ideally ductile or ideally brittle. By so classifying materials, models of the particle-surface interaction can be postulated and theoretical predictions of erosion resistance made. The influence of basic material properties on erosion resistance is often evident from these predictions and gives one a rational basis of material selection [*1,2*].[2]

The characteristic shape of the impacting particle is also a factor in the erosion process. As would be expected, angular particles (grit) will often remove an order of magnitude more surface material than spherical particles (shot) of the same material. Hence, in studying erosion processes, it is important to know whether the impacting particles have sharp cutting edges or a more rounded surface. Interestingly enough, many of the erosion effects, except for the actual magnitude of material eroded, are quite similar for angular and spherical particles [*3*].

[1]Graduate student and professor, respectively, Department of Mechanical Engineering, Washington State University, Pullman, Wash. 99164.

[2]The italic numbers in brackets refer to the list of references appended to this paper.

A third, less-studied area affecting erosion is concerned with the frangibility of the eroding particles. If the particles fracture upon impact, additional mechanisms for surface material removal will exist than if the particle remains in one piece. Tilly showed that some aspects of erosion of ductile materials are due to particle fracture [4], using high-speed photography, electron microscopy, and actual particle size measurements to study this effect. According to him, erosion by fragmenting particles can be thought of as due to two effects or stages. In the first stage, called primary erosion, particles indent the surface, removing chips and forming vulnerable hillocks. The other stage, called secondary erosion, is due to particles breaking upon impact so that the fragments are projected radially to produce secondary damage to the craters. The primary stage predominates for glancing impacts and the secondary stage for normal impacts, as shown in Fig. 1 (taken from Tilly's work).

Measurements by Tilly showed the extent of fragmentation to be dependent on initial particle size and velocity, as well as on impact angle. Particles too small to break up cause primary erosion alone, while increasing particle size causes an increase in secondary erosion. Similarly, increased velocity causes an increase in secondary damage.

From his two-stage erosion equations, Tilly concluded that for the extreme conditions of small particles which do not fracture (no secondary erosion) and for large particles and high velocity (maximum fragmentation), the total

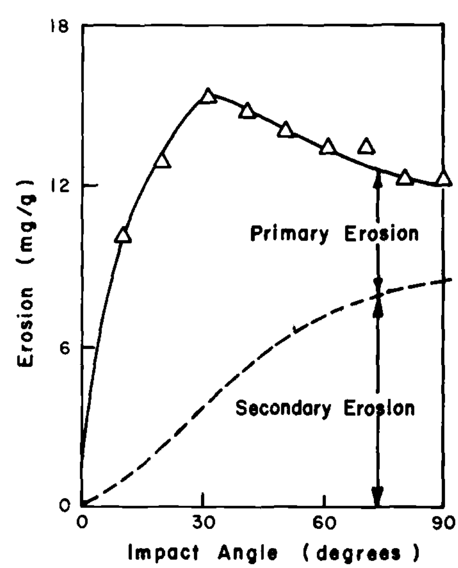

FIG. 1—*Influence of impact angle for 135 μm quartz against H46 steel at 366 m/s (1200 ft/s) (from Ref 4).*

erosion will tend to a velocity-squared dependence. In-between conditions of particle velocity and size result in particle velocity exponents greater than two; these predictions have been confirmed by Tilly and others for silicon carbide grit impacting against several metals [5].

Using the concept of particle threshold size and velocity below which no erosion would occur, Tilly was also able to show the influence of particle size on erosion. This is the well-known effect, in which the amount of erosion for a fixed quantity of abrasive (gram/gram) is found to decrease as particle size is decreased below the 100-μm size.

Further Effects of Particle Frangibility

The effects of frangibility of large spherical steel particles on aluminum are shown in this section. Generally these results are in agreement with those of Tilly and show the importance of secondary-impact effects on material removal. In addition, it is shown that particle fragmentation, the cause of second-stage erosion, is important not only at near-normal impact angles (as shown in Fig. 1), but also at glancing impact angles, that is, impingement below 5 deg.

Tube Erosion

A transfer line or a cylindrical duct is often used to convey particles of an erosive nature. A numerical model of the particle path down the tube shows impact angles in the range of 0 to 5 deg, with a majority of impact angles in the 2 to 3 deg range [*6*]. Wellinger and Uetz have also estimated that the particle impingement angle for pipe flow to be on the order of 5 deg [*7*]. Hence, study of the erosion wear of a tube can provide insight into erosion effects at small impact angles [*8*].

The transfer tube used in the study was 6061-T6 aluminum, 4.95 mm in diameter by 30.5 cm long. It was carefully sectioned into individual short tube lengths 2.54 cm long. Each individual tube length was carefully weighed, and the tube lengths then reassembled to form a tube of original length, using clamping fixtures to align the tube in a straight configuration. Considerable care was taken to assure that the tube reassembled from short tube lengths was straight. The tube was mounted in the same air-blast erosion tester used for previously described investigations, and 2500 g of 270-μm (average diameter) hardened steel shot (HRC 65) was blasted through the tube at an average rate of 1.26 g/s. The gas pressure at the inlet of the tube was 172 kPa (25 psig). After eroding the bore, the assembly was then carefully disassembled and each 2.54-cm tube length carefully weighed. The erosive wear in grams of aluminum per gram of abrasive used was determined and plotted. The middle curve in Fig. 2 shows the results. It is noted that the wear is zero at the inlet end of the tube, where the velocity is very

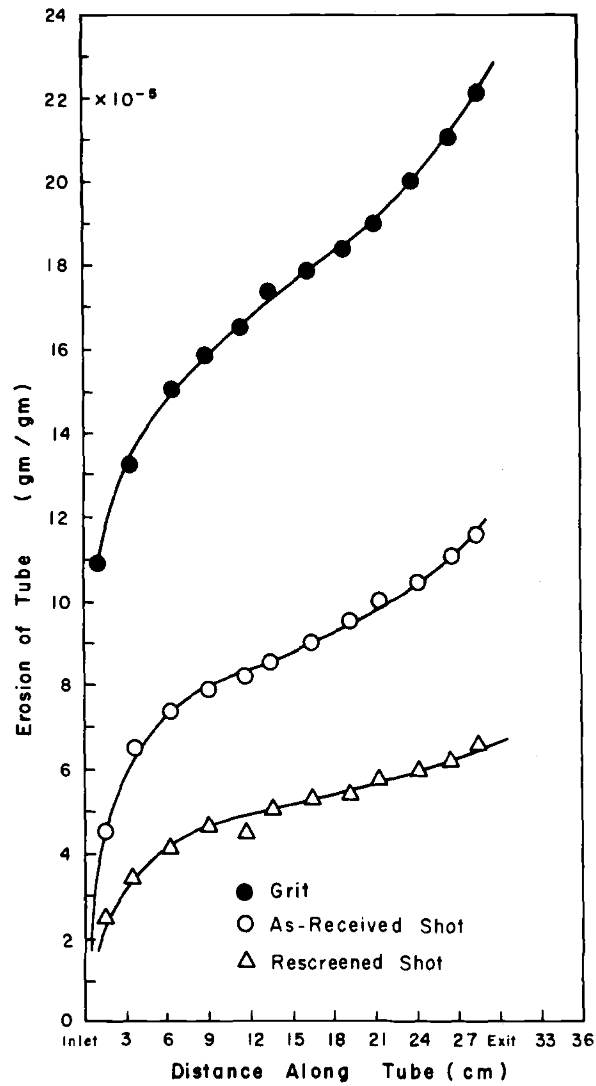

FIG. 2—*Erosion of 4.95-mm-inside-diameter aluminum (6061-T6) tube using 270-µm hardened steel particles (brittle). Inlet gas pressure was 172 kPa.*

low, and rises in nonlinear manner to a maximum value at the exit end of the tube, where the velocity is highest. The lower curve in Fig. 2 is for shot collected after erosion and rescreened to eliminate fragmented pieces. It is noted that the magnitude of erosion for the rescreened shot is about one-half that of the as-received "new" shot.

An examination of the particle debris of both new and reused shot showed a great deal of fragmentation of new shot and very little fragmentation of reused shot. So much fragmentation of new shot occurred that a very large amount of screening was required to collect sufficient whole shot for the second erosion test.

Evidently a large amount of tube erosion by the new, as-received shot is by secondary erosion. Upon screening, only tougher particles which survived the initial impact are used; these particles are also quite likely to survive the second impact when they are reused in a repeat test. It follows that the lowest erosion curve is for erosion by primary impact alone with very little secondary impact of fragments. As stated earlier, this reduction in secondary impacts reduces the amount of erosion by approximately one-half along the tube length. This shows that secondary impacts caused by particle fragmentation are important in the material removal mechanism not only at near normal impact, but also for low-angle or glancing impact. Also shown in Fig. 2 are the erosion characteristics of the aluminum tube using angular steel grit of the same screened size as the shot.

Flat-Plate Erosion

To further study the effects of particle frangibility when eroding softer metal surfaces, a series of flat-plate erosion tests was conducted using 6061-T6 specimens. These tests used a conventional blast tube device in which the particles were accelerated down a 4.95-mm-inside-diameter by 30-cm-long tube by a high-velocity gas stream. The tube interior was lined with a tough, replaceable plastic liner. This liner effectively prevented the particles from fracturing by impacting the tube wall. Actual particle velocities were measured very near the impact position using the multiple-flash photographic technique, the double rotating disk method, and the laser-Doppler technique.

To study the effect of particle fragmentation, 270-μm steel shot was procured in both a ductile and a brittle condition. The ductile shot was a softer, tough material of hardness HRC 45. The brittle shot was much harder, quenched to a hardness HRC 65. Erosion weight-loss tests as a function of particle velocity were performed for a glancing 20-deg impact condition and for a near normal 70-deg impact condition using both the ductile and brittle shot.

The test results for the 20-deg impact condition are shown in Figs. 3 and 4. Figure 3, for ductile shot, shows identical results for both the as-received and rescreened abrasive. Since this material is predominantly ductile, very little fragmentation occurred upon impact and no change is noted between the two conditions. A velocity exponent of 2.2 is estimated from the data points. Examining Fig. 4, for the brittle shot, it is to be noted that the new, as-received shot gives a higher velocity exponent, due to the additional effects of particle fragmentation. When this shot has been collected and rescreened, the veloc-

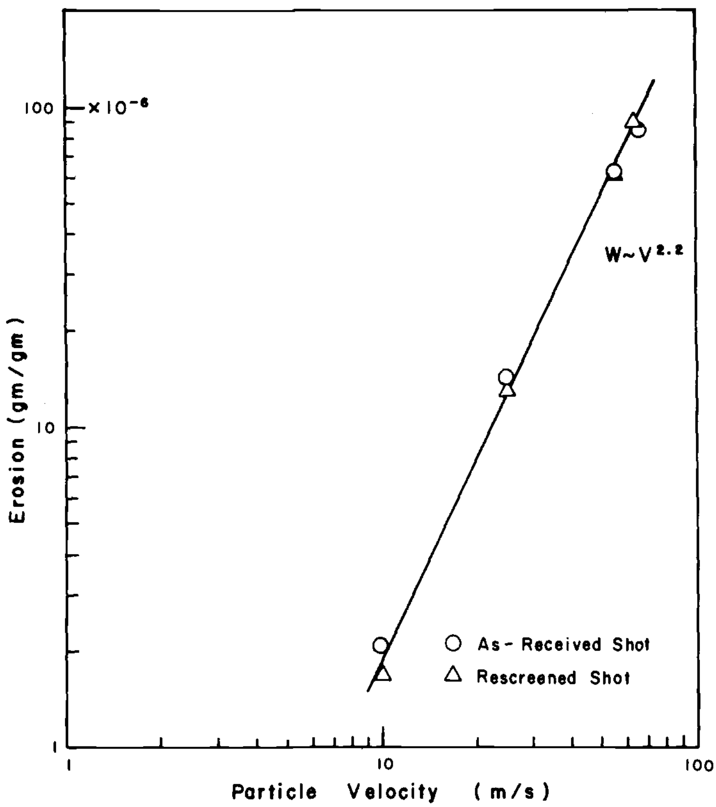

FIG. 3—*Influence of particle type and velocity on erosion. Particles were 270-μm annealed steel shot (ductile) impacting at a glancing angle (20 deg) on aluminum (6061-T6) surface.*

ity exponent drops from 2.4 to 2.2, the same as for ductile shot. This clearly shows the effect of particle fragmentation at a 20-deg impact angle. For comparison, results for hardened steel grit of the same size are included; a velocity exponent of 2.7 is obtained. Whether this increase is due to the angular shape of the grit or due to a large amount of fragmentation is not known. Probably both changes have an effect.

Similar results were obtained for the case of particles impacting at the more normal angle of 70 deg. Figure 5, for ductile shot, shows identical results for both the as-received and rescreened abrasive; the velocity exponent was found to be 2.1. Again, no particle fragmentation occurs with this abrasive, and a low exponent value (close to 2) is found. Figure 6 shows the results for the brittle shot using 70-deg impact. The new, as-received material exhibits considerable fragmentation causing secondary erosion, while the collected and rescreened material exhibits primarily primary erosion. Rescreened brittle shot and all-ductile shot show identical erosion

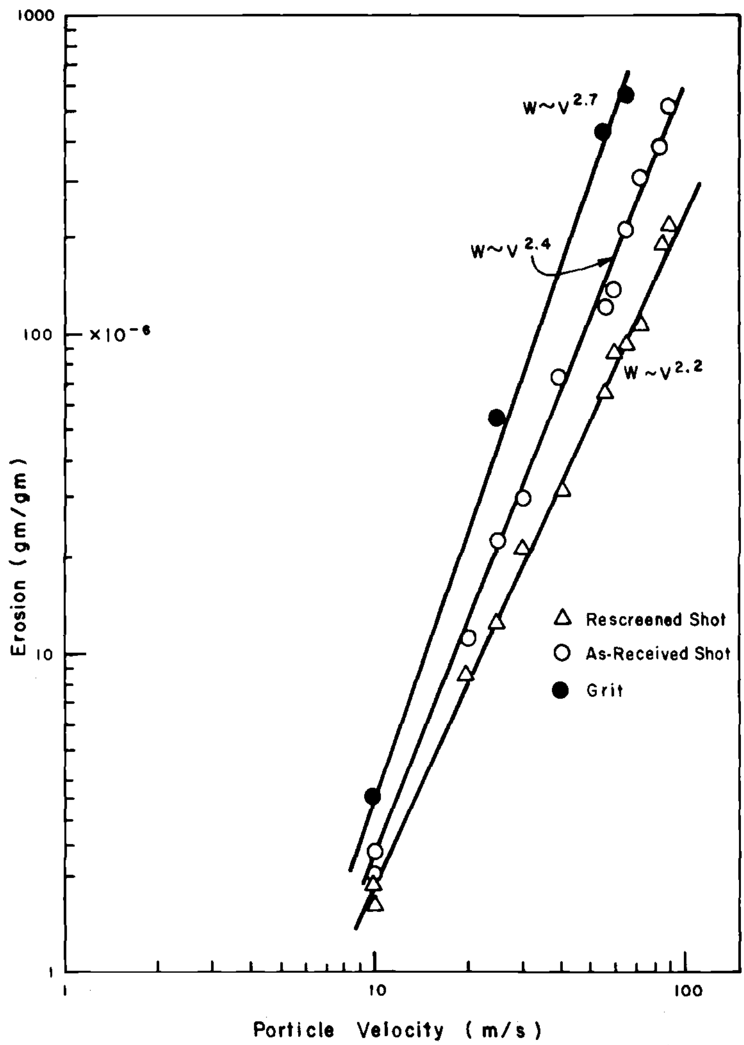

FIG. 4—*Influence of particle type and velocity on erosion. Particles were 270-μm hardened steel shot and grit (brittle) impacting at a glancing angle (20 deg) on aluminum (6061-T6) surface.*

characteristics. The velocity exponents correspondingly drop from 2.5 to 2.1. Again, for comparison, hardened steel grit gives a high value, 2.5.

Shown in Fig. 7 are the results of a sieve analysis for both the ductile and brittle shot as originally received (Curve 4), after leaving the plastic-lined blast tube (Curve 4), and after striking the flat test surface (Curves 3, 2). This analysis shows that the cushioned tube effectively prevents particle fragmentation. Confirming the earlier discussion on impact effects, the ductile shot is

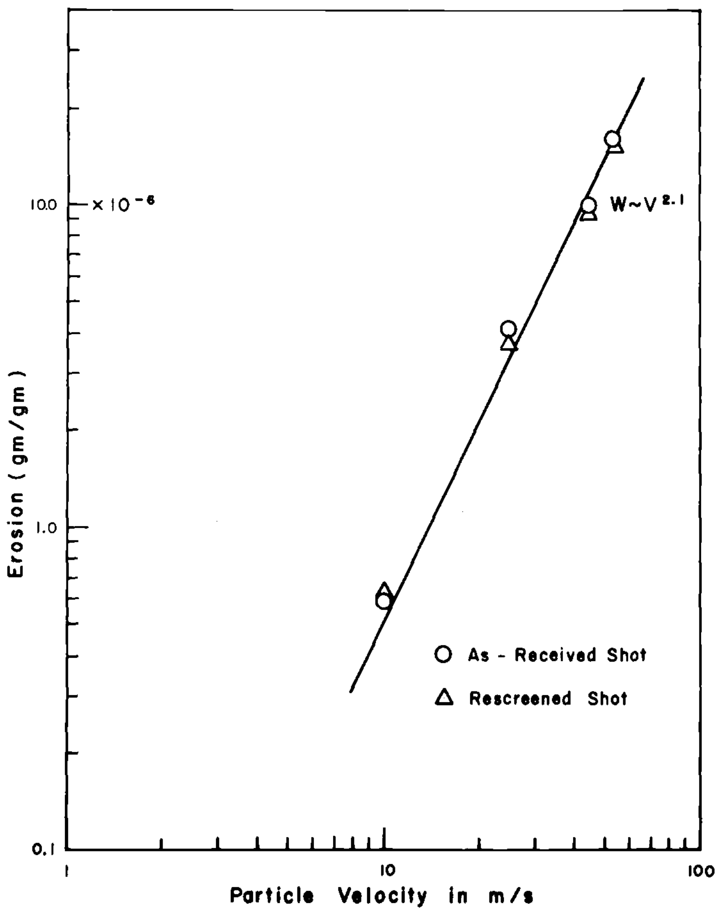

FIG. 5—*Influence of particle type and velocity on erosion. Particles were 270-μm annealed steel shot (ductile) impacting at a near normal angle (70 deg) on aluminum (6061-T6) surface.*

virtually unaffected by impact with the test specimen, while the brittle shot is heavily fragmented. The effect of using a hardened steel blast tube without the cushioning liner is also shown in this figure.

Eroded Surface Appearance

Examination of the impact sites for both the ductile and brittle shot, using the scanning electron microscope, revealed no clues as to the different mechanism of material removed by the two types of particle. The aluminum surface is indented and pushed out by the particle moving through it, perhaps visualized as similar to a Brinell hardness test. A vulnerable lip or

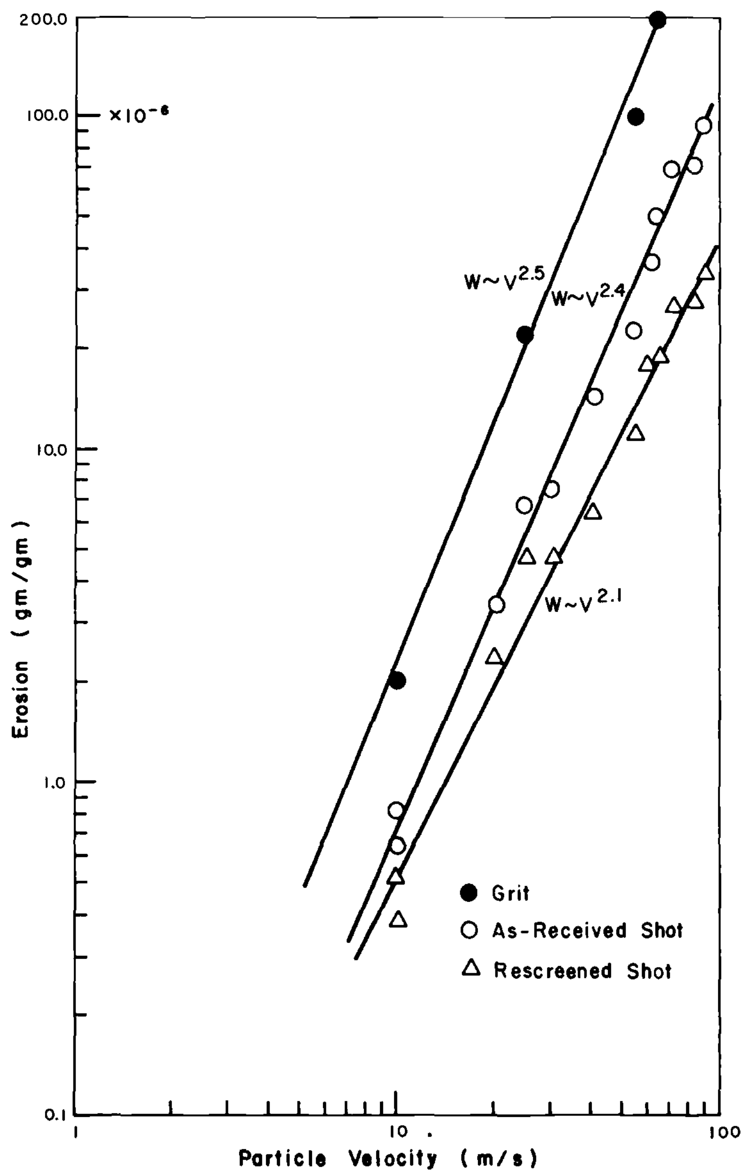

FIG. 6—*Influence of particle type and velocity on erosion. Particles were 270-μm hardened steel shot (brittle) and grit impacting at near normal conditions (70 deg) on aluminum (6061-T6) surface.*

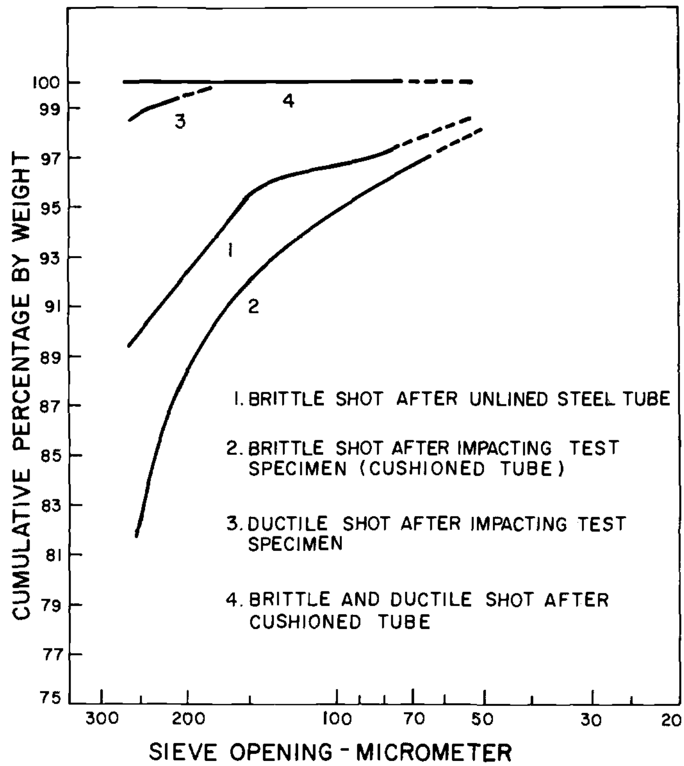

FIG. 7—*Cumulative size distribution (sieve analysis) of steel shot.*

hillock is formed around the front of the impact scar. Shown in Fig. 8 is a typical crater formation using either shot type. Though not evident from the photographs, the second-stage erosion due to particles breaking up on impact is probably due to more efficient removal of the vulnerable lips around the impact scar by radially projected fragments.

Conclusions

The concept of a two-stage model of the erosion process as proposed by Tilly has been examined. The effects of secondary-stage erosion caused by particle fragmentation upon impact were shown using one size of an annealed ductile steel shot and a heat-treated brittle steel shot. Erosion tests were made at both glancing and normal impact angles on a tubular aluminum specimen and on flat aluminum specimens. The effects of secondary erosion were quite evident. Additional material is removed when a parti-

FIG. 8—*Craters formed by the impact of ductile 270-μm steel shot on aluminum. Impact angle was 20 deg; impact velocity was 65 m/s (213 ft/s) on aluminum (6061-T6) surface* (× 222).

cle fractures on impact, resulting in more material loss and a higher velocity exponent.

While this study was undertaken to investigate the effects of particle fracture and subsequent material removal at the general conditions of near-normal and glancing impact, the effects of particles fragmenting in an erosion tester of the type which accelerates particles down a hard surface tube are also revealed in this study. Applied to erosion testing, the results presented here show that particles can fragment in the blast tube and therefore may be more erosive than the original specimen. To illustrate this effect, the particle size distribution at the exit of the tube of brittle particles blasted through an unlined hardened steel blast tube is shown by Curve 1 of Fig. 7.

Note the large amount of fragmentation shown. At the tube inlet, the particles were all of uniform size, shown by the top curve of Fig. 7, that is, screened to 270-μm. Of course, fragmenting effects will vary with particle velocity and length of blast tube, introducing undesirable variables into test results.

References

[1] Finnie, I. in *Symposium on Erosion and Cavitation, ASTM STP 307*, American Society for Testing and Materials, 1961, pp. 87-103.

[2] Sheldon, G. L. and Finnie, I., *Journal of Engineering for Industry, Trans.* American Society of Mechanical Engineers, Series B, No. 4, 1966, pp. 393-399.

[3] Sheldon, G. L. and Kanhere, Ashok, *Wear*, Vol. 21, 1972, pp. 195-209.

[4] Tilly, G. P., *Wear*, Vol. 23, 1973, pp. 87-96.

[5] Sheldon, G. L., *Journal of Basic Engineering, Trans.* American Society of Mechanical Engineers, Series D, No. 3, 1970, pp. 619-626.

[6] Means, P., Crowe, C. T., and Sheldon, G. L. in *Proceedings*, American Institute of Chemical Engineers, 17th National Heat Transfer Conference, Salt Lake City, Utah, Aug. 1977, pp. 125-126.

[7] Wellinger, K. and Uetz, H., *Zeitschrift Des Vereins Der Deutschen Ingenieure*, Vol. 96, 1954, pp. 43.

[8] Sheldon, G. L., Maji, J., and Crowe, C. T., *Journal of Engineering Materials and Technology, Trans.* American Society of Mechanical Engineers, April 1977, pp. 138-142.

DISCUSSION

A. P. L. Turner[1] *(written discussion)*—You showed an increase in erosion rate and velocity exponent due to fragmentation of spherical particles. Would you expect a similar result if the particles were angular before fragmentation?

J. Maji and G. L. Sheldon (authors' closure)—Yes, similar secondary erosion of frangible particles would occur.

G. Mayer[2] *(written discussion)*—Since you indicated a substantial secondary erosion effect from fragmenting particles, was there an effort made initially to shake out and screen flawed (precracked) particles prior to test?

J. Maji and G. L. Sheldon (authors' closure)—We were not able to identify flawed particles from perfect ones. The particles impacted with the test surface fractured flawed particles and the fragments were screened out to obtain flawless ones for retesting.

[1]Materials Science Division, Argonne National Laboratory, Argonne, Ill. 60439.
[2]Army Research Center, Research Triangle Park, N.C. 27707.

J. S. Hansen[1]

Relative Erosion Resistance of Several Materials

REFERENCE: Hansen, J. S., "**Relative Erosion Resistance of Several Materials,**" *Erosion: Prevention and Useful Applications, ASTM STP 664,* W. F. Adler, Ed., American Society for Testing and Materials, 1979, pp. 148–162.

ABSTRACT: Over 200 materials were screened by a high-velocity sandblast-type erosion test to determine their suitability for application in coal gasifier valves. Most metals had relatively similar and low erosion resistances. Ceramics and cermets such as boron carbide (B_4C), tungsten carbide (WC), silicon carbide (SiC), silicon nitride (Si_3N_4), and titanium diboride (TiB_2), if manufactured to minimize porosity, had more than four times the erosion resistance of metals. Several coatings such as boronized molybdenum and tungsten carbide, chemical vapor-deposited titanium carbon nitride (TiCN), and electrodeposited TiB_2 also proved highly erosion resistant when applied in sufficient thicknesses. Additional findings confirmed that cermet binder content and ceramic porosity are related to erosion resistance.

KEY WORDS: solid particle erosion, erosion, erosion resistance, damage, temperature, metal, ceramic, cermet, coal gasification

The Bureau of Mines, U.S. Department of the Interior, has established a long and productive tradition of research and development in coal gasification technology. Recently, in 1972, the Bureau began operation of a stirred-bed, low-Btu producer gas pilot plant at Morgantown, W. Va. Shortly thereafter, the Bureau built a high-Btu synthetic natural gas facility at Bruceton, Pa., for the purpose of demonstrating the Bureau's Synthane process. In 1975, the Energy Research and Development Administration (ERDA) assumed responsibility for both facilities.

One of the general problems that emerged from the operation of these and other coal gasification pilot plants was the short life, due to erosion, of various valves used for the transfer of solids as dry bulk, slurries, or gas-born particulates. Figure 1, for example, shows erosion damage to a Stellite[2] hardfaced ball valve seat. The valve was used to seal an ash re-

[1]Metallurgist, Materials Physics, Albany Metallurgy Research Center, Federal Bureau of Mines, Albany, Oregon 97321.

[2]Specific brand names are used for identification and description only and do not imply endorsement by the Bureau of Mines. Some brand names are registered company trademarks.

moval lock hopper at 2.07 $\times$ 10^6 N/m^2 (300 psig) against atmospheric pressure. A small leak developed, possibly from an abrasive wear scar, and was enlarged by escaping high-velocity ash-laden gases. This type of erosion failure is common and is known as the "wire drawing effect."

Unlike other erosion problems, coal gasifier valve erosion is complicated by a large number and variety of environments. The valves seldom face the same pressures, temperatures, particle velocities, particle sizes and hardnesses, chemical species, or impingement angles. The literature [*1-7*][3] has defined the effects of several variables upon erosion and has suggested plausible erosion mechanisms. With the use of this information, engineers can attack erosion through design modifications. Unfortunately, the literature has not provided any universal relationships which can be used to propose materials of construction. All equations linking variables to measurable material factors are of limited practical significance—only narrow classes of materials are covered, the use of difficult-to-measure properties are involved, no account is made for all variables, or special tests are required for the determination of constants. Furthermore, there is a lack of published data that might be helpful to engineers, and there are no standard erosion tests.

This study has taken an engineering approach to the problem. A large and diverse sampling of materials has been screened for resistance to erosion under a few standardized conditions which are representative of the gasifier environments. The information can serve as a guide for more detailed work or, with the careful application of known variable effects, for the production of trial parts for *in situ* testing.

Equipment

A sandblast-type tester was built to accomplish the screening. An S. S. White Model H Airbrasive Unit was used as a regulated supply of gasborn particles in both room temperature and elevated temperature test systems. The tests were conducted with 27-μm alumina particles; the particle velocity, as measured on a two-disk device after Ruff and Ives [*8*] was 170 m/s (558 ft/s); the particle mass flow was about 5 g/min; the test duration was 3 min; and the atmosphere was usually high-purity dry nitrogen.

In addition to the Airbrasive Unit, the room temperature test equipment included an adjustable-angle stage to hold the specimens and an adjustable nozzle made up of a molybdenum shank with a 0.58-mm (0.023 in.)-inside-diameter sapphire tip glued into one end. The elevated temperature test equipment (see Fig. 2) consisted of the Airbrasive Unit, a furnace and, within the furnace, a multi-faceted turret to secure 12 specimens, a shutter

[3] The italic numbers in brackets refer to the list of references appended to this paper.

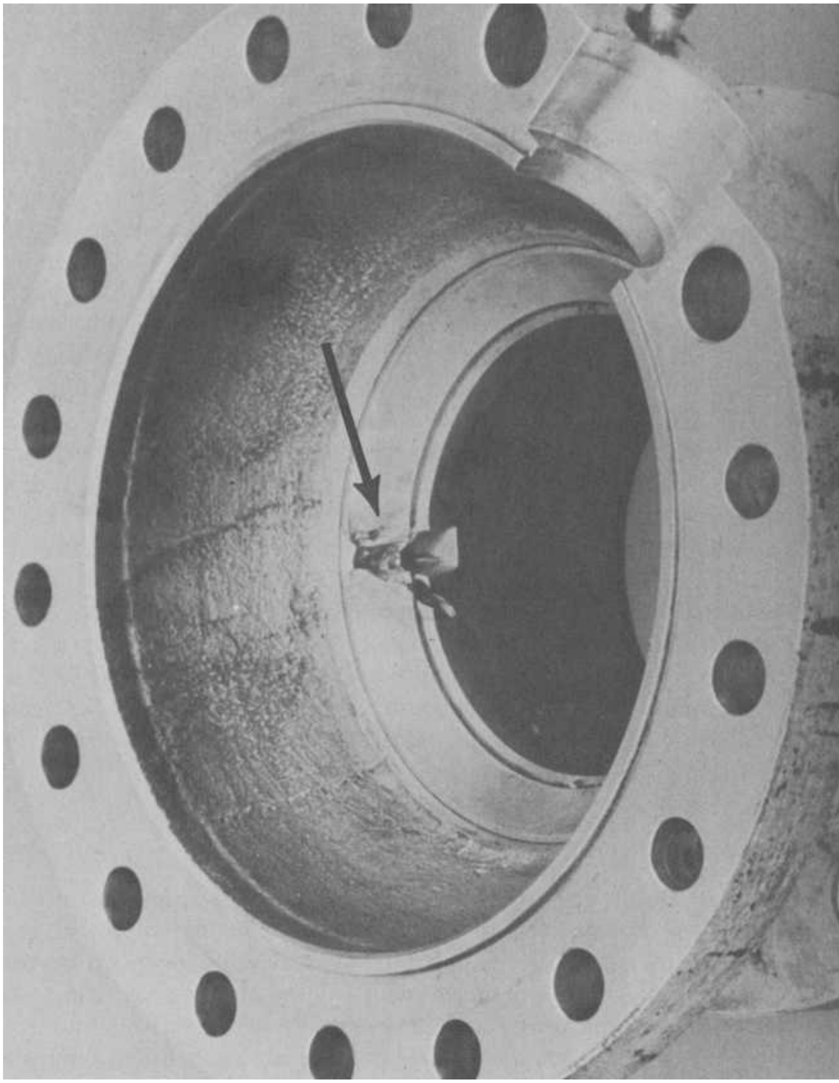

FIG. 1—*Erosion damage to a lock hopper ball valve seat (courtesy of Morgantown Energy Research Center).*

to control the particle blast duration, and the same nozzle that was used in room temperature tests. A tube to evacuate the furnace or to deliver an atmosphere was positioned near the specimen, and an infrared pyrometer was used to monitor the temperature of the specimen impingement area.

The multispecimen system was an improvement over a similar earlier system which contained dummy specimens that experienced all test con-

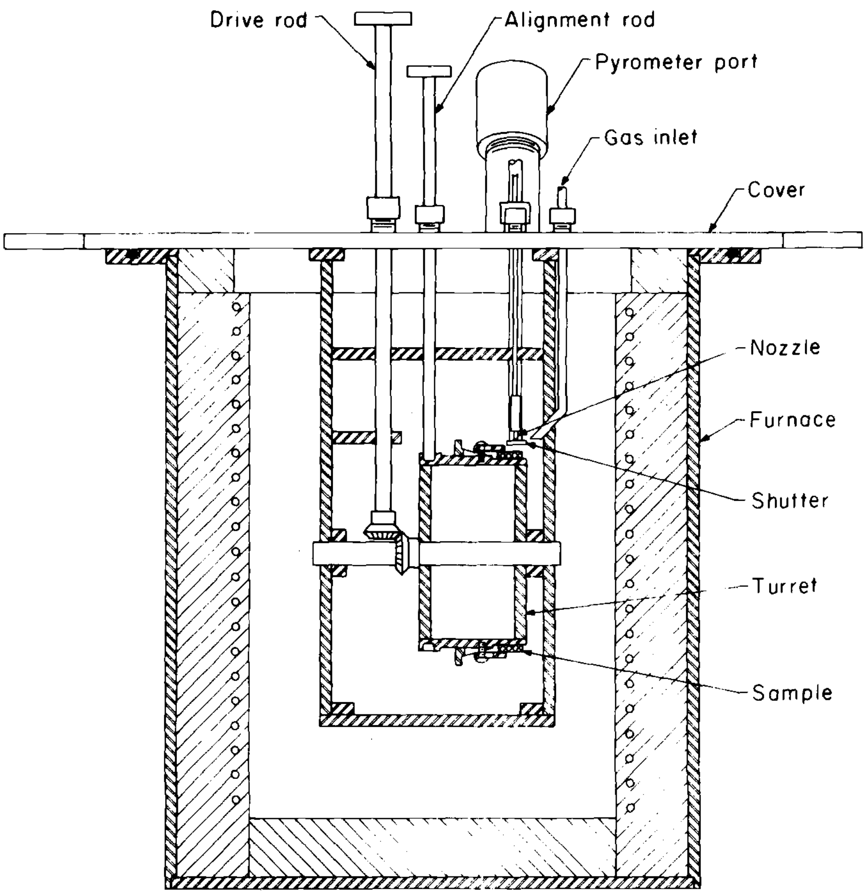

FIG. 2—*Cross section of the internals of the multispecimen high-temperature erosion test system.*

ditions except the particle blast. Since the dummy specimens in the first tester showed negligible weight gains or losses, no provision was made for them in the second tester.

Procedure

The specimens were used as-received and subjected only to an ultrasonic cleaning in acetone prior to testing. After weighing to the nearest 0.1 mg, they were set upon the adjustable-angle stage or turret, and the nozzle was positioned 9.5 mm (0.375 in.) above the surface. In room temperature testing, the particle blast was allowed to impinge against a hand-operated shutter between the nozzle and the specimen until the flow was steady. The test was begun following the removal of the shutter, and, at the test termination, the specimens were recleaned and reweighed. Few alumina particles were evident on the tested surfaces when viewed under a ×30 microscope.

The same parameters were used and the same basic test procedures were performed in elevated temperature determinations except that the 12 specimens on the turret were heated in a vacuum or in nitrogen before testing. At the test temperature, a quantity of nitrogen was directed to the specimen surface at a rate equal to that flowing through the particle nozzle during a test. When the specimen temperature returned to a steady state, the shutter was positioned between the nozzle and the specimen, the particle blast was begun, and the shutter was removed. Although the transfer of heat from the massive turret reduced thermal shock, the impingement area temperature dropped an average of 63°C from tests started at 700°C and remained at this temperature for the 3-min test duration. The other specimens on the turret were tested in like manner.

A control and computation procedure was necessary to minimize a small source of inconsistency which resulted from particle flow variations caused by the Airbrasive Unit feeder system. In the procedure, three Haynes Stellite 6B (Stellite 6 is a common valve material) wrought standards from a single source were run at equal intervals with each set of nine test specimens. If the standards' weight losses were within 10 percent of a value established from preliminary tests, the equipment was assumed to be operating satisfactorily. The weight losses of the 6B standards and the specimens were converted to volume losses, and a relative erosion factor (REF) for each material was computed by dividing the mean specimen volume loss by the mean volume loss of the three 6B standards from the same test set. A series of tests showed that the ratio remained constant over a range of particle flows to a degree that one standard deviation of a group of five tests on a material was generally within 10 percent of the mean specimen weight loss. The REF was adopted as the means by which all materials were evaluated.

Results and Discussion

Over 200 materials were tested and ranked. Some of the results, the approximate chemical compositions of the materials, and the manufacturing methods are tabulated in the Appendix. Examples of the REF's of metals, cermets, and ceramics are illustrated graphically in Figs. 3, 4, and 5.

From Fig. 3 it is clear that nearly all metals and metallic alloys except tungsten and molybdenum have relatively the same room temperature erosion resistances for 90-deg impingement. At best, there is only a 30 percent improvement over Stellite 6B. Moreover, all of the metals and metallic alloys tested at a 20-deg impingement (but not shown) except

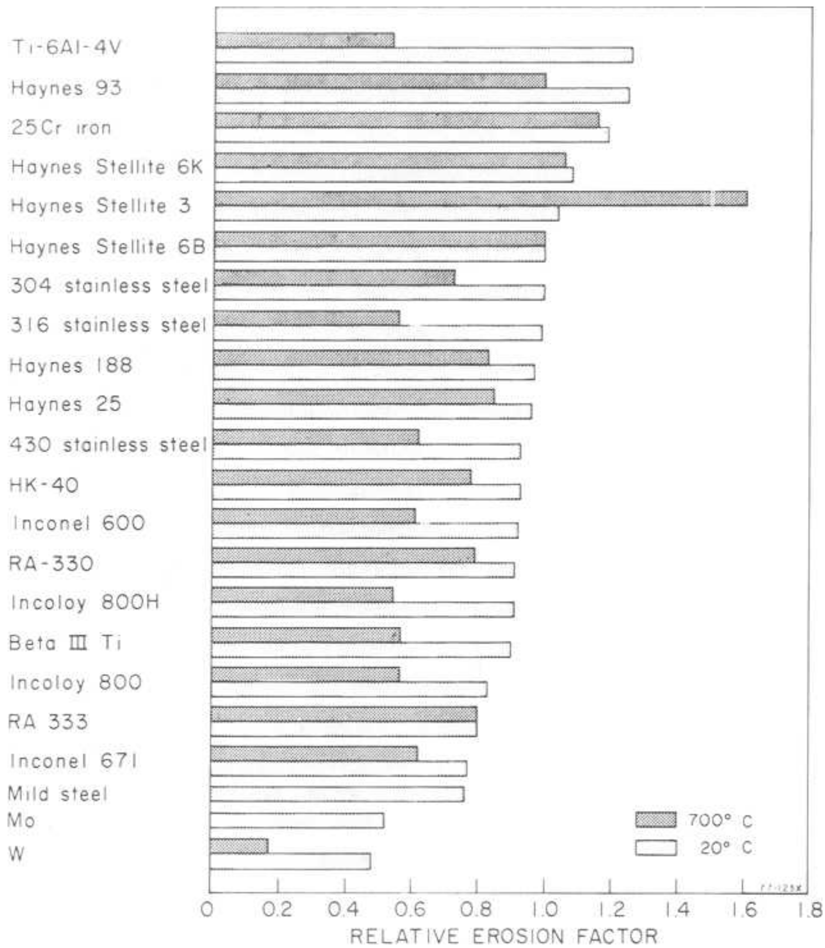

FIG. 3—*Commercially available metals (90-deg impingement).*

tungsten and molybdenum again have similar erosion resistances and increased erosion volumes. At 700°C, many alloys eroded more than at room temperature, but a few eroded less. However, this is not reflected in the REF's since the Stellite 6B upon which the REF is based also eroded 20 percent more at 700°C. No apparent explanation for the high-temperature behavior was found.

By comparison, numerous cermets and ceramics, Figs. 4 and 5, have erosion resistances that are greater than twice that of Stellite 6B. Notable among these are a series of mixed ceramics that were prepared by pressing and sintering at the Oregon Graduate Center; several commercially available hot-pressed ceramics such as boron carbide (B_4C), silicon carbide

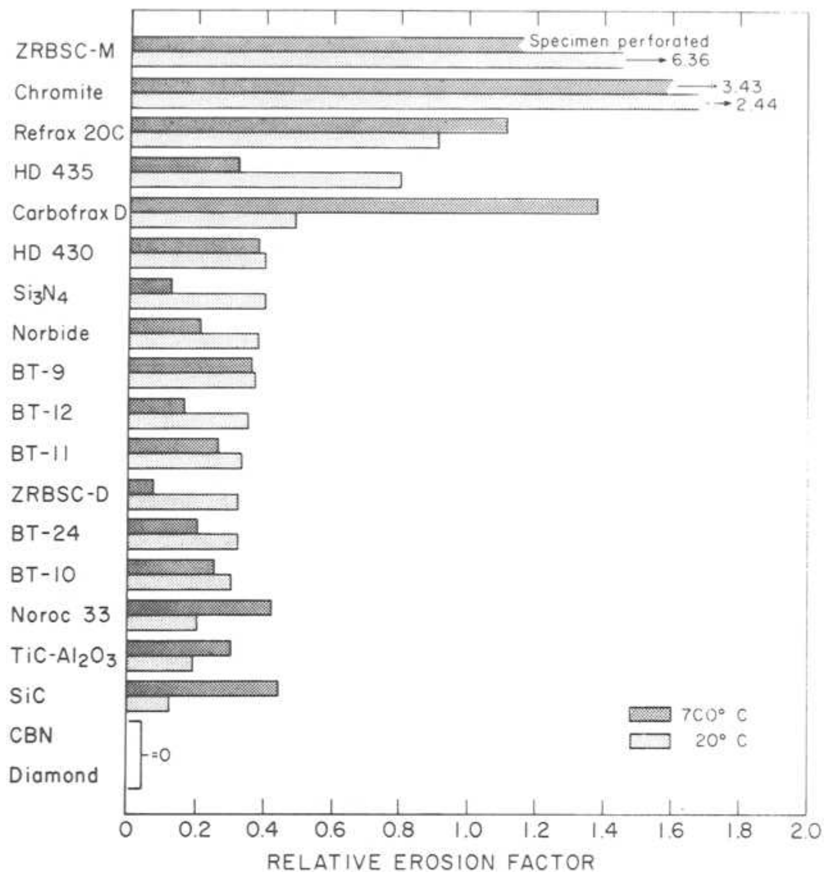

FIG. 4—*Ceramics (90-deg impingement).*

(SIC), silicon nitride (Si_3N_4), cubic boron nitride (CBN), and diamond; and several tungsten carbides (WC).

That some ceramics of equal chemistry and purity have unequal erosion factors can be explained through differences in the proportions of porosity. For example, a near 100 percent dense alumina such as Lucalox is greater than 1.5 times more erosion resistant than 95 to 98 percent dense aluminas. At the extreme, Lucalox has more than ten times the erosion resistance of 99P, a porous alumina that is less than 70 percent dense. Similarly, hot-pressed Si_3N_4 has more than ten times the erosion resistance of reaction-bonded (and less dense) Si_3N_4.

On the other hand, the behavior of the tungsten carbide cermets is indicative of a relationship between erosion and binder content. Figure 6 shows this relationship—namely, that with an increase in binder, irrespective of the binder element, a corresponding decrease in erosion resistance

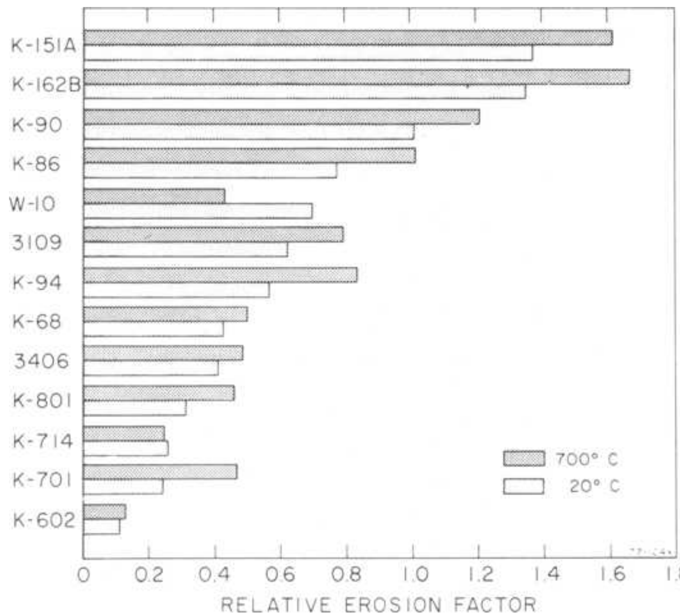

FIG. 5—*Kennametal cemented carbides (90-deg impingement).*

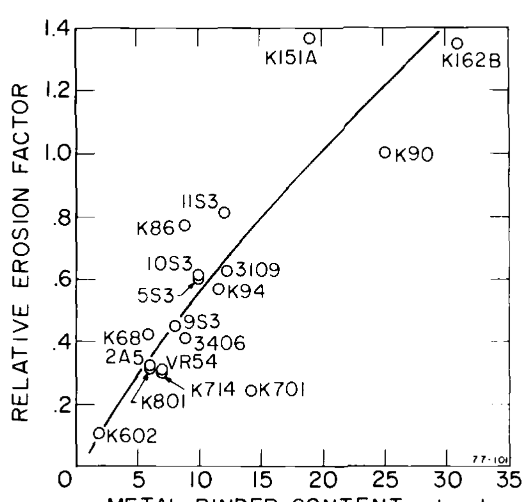

FIG. 6—*Relative erosion resistance of cemented carbides as a function of metal binder content (room temperature, 90-deg impingement).*

results. Uuemyis and Kleis [9] have verified a mechanism in which the metallic binder is eroded from around the carbide grains.

Although ceramics and cermets can be made into valve parts with present technology, size and toughness limitations preclude their use in many instances. Ideally, large valves might be made from easily fabricable and economical materials and protected with erosion-resistant coatings. Some promising coatings were tested, and the results are listed in Tables 3 and 4 of the Appendix.

Chemical vapor deposition (CVD) silicon carbide that was applied over carbon converted to silicon carbide remained completely intact at both test temperatures; a slight surface buffing was the only evidence that it had been tested. Electrodeposited titanium diboride (TiB_2) is another coating that possessed outstanding erosion resistance and remained intact at room temperature even after the test duration was extended to 10 min. The TiB_2 also had excellent erosion resistance at 700°C, but that which was applied over 310 stainless steel spalled upon cooling. When retested at room temperature, the spalled TiB_2 eroded, conceivably because several cracks were large enough for particles to undermine the substrate and loosen the coating. However, the TiB_2 applied over electrolytic nickel did not exhibit the spalling tendency. The two TiB_2 examples amplify the importance of matching the thermal expansion rates of coatings and substrates.

The diffusion coatings listed in the Appendix tables not only eliminated all difficulties of thermal mismatch and inadequate bond strength but proved to be highly erosion resistant as well. Boriding, for instance, improved the erosion resistance of tungsten carbide and molybdenum at room temperature and a 90-deg impingement by more than 80 percent, while at a 20-deg impingement the improvement was more than fivefold.

As a rule, to provide adequate protection, most coatings had to be 50 to 80 μm (0.002 to 0.003 in.) in thickness. Thin-sputtered titanium carbon nitride (TiCN) over Inconel 671 provided no substrate protection, yet when applied by CVD in thicknesses of 50 μm (0.002 in.) it retarded penetration at a 90-deg impingement and halted penetration at a 20-deg impingement in most tests. Other coatings showed related characteristics.

Conclusion

With the exception of tungsten and molybdenum, metallic-base materials have relatively low erosion resistances for severe erosion situations. Therefore, if a metallic component has failed prematurely by erosion, no better performance can be expected from a metallic substitution, regardless of hardness. Fortunately, several ceramics, cermets, and ceramic coatings have greatly improved erosion resistances. These include tungsten carbide, silicon carbide, Si_3N_4, B_4C, cubic boron nitride, ZrB_2, electrodeposited TiB_2, and boronized tungsten carbide, molybdenum, and tungsten. Ceramics are most resistant when manufactured by a method that will insure optimum density. With cermets, a minimum amount of metallic binder is desirable, and with coatings a sufficient coating-substrate compatibility and coating thickness are essential.

The likelihood exists that solutions to valve erosion problems that are based entirely on material choices will be expensive and, in some cases, impossible. The best solutions will involve both the wise selection of materials and the use of innovative design techniques based upon the knowledge gained through the diligent efforts of previous erosion researchers.

Acknowledgments

The author is grateful to the many manufacturers who provided materials.

APPENDIX

Erosion Test Data

TABLE 1—*Room temperature erosion test results: 90-deg impingement, 27-μm Al_2O_3 particles, 5-g/min particle flow. 170-m/s particle velocity, 3-min test duration, N_2 atmosphere.*

Material	Manufacturing Method	Composition	REF[a]
99P	ps[b]	$99Al_2O_3$ (Krohn)[b]	12.49
ZRBSC-M	hp	ZrB_2-SiC-graphite(N)	6.36
chromite	ps	(UCAR)	2.44
K151A	ps	19Ni binder (K)	1.37
K162B	ps	25Ni+6Mo binder (K)	1.35
98D	ps	$98Al_2O_3$ (Krohn)	1.29
Ti-6Al-4V	w	...	1.26
Haynes 93	c	17Cr-16Mo-6.3Co-3C-bal Fe (Stellite)	1.25
Graph-Air	w	1.4C-1.9Mn-1.2Si-1.9Ni-1.5Mo-bal Fe (TRB)	1.19
25Cr iron	c	25Cr-2Ni-2Mn-0.5Si-3.5C-bal Fe (OGC)	1.19
Stellite 6K	w	30Cr-4.5W-1.5Mo-1.7C-bal Co (Stellite)	1.08
Stellite 3	c	31Cr-12.5W-2.4C-bal Co	1.04
K90	ps	25 binder (K)	1.01
Stellite 6B	w	30Cr-4.5W-1.5Mo-1.2C-bal Co (Stellite)	1.00
304 SS	w	17Cr-9Ni-2Mn-1Si-bal Fe	1.00
316 SS	w	17Cr-12Ni-2Mn-1Si-2.5Mo-bal Fe	0.99
Haynes 188	w	22Cr-14.5W-22Ni-0.15C-bal Co (Stellite)	0.97
Haynes 25	w	20Cr-15W-10Ni-1.5Mn-0.15C-bal Co (Stellite)	0.96
430 SS	w	17Cr-1Mn-1Si-0.1C-bal Fe	0.93
HK-40	c	26Cr-20Ni-0.4C-bal Fe	0.93
Inconel 600	w	76Ni-15.5Cr-8Fe (HA)	0.92
RA 330	w	19Cr-35Ni-1.5Mn-1.3Si-bal Fe (RA)	0.91
Refrax 20C	ps	SiC-Si_3N_4 bond (Carbor)	0.91

TABLE 1—*Continued*

Material	Manu-facturing Method	Composition	REF[a]
Incoloy 800H	w	32.5Ni-21Cr-0.07C-46Fe (HA)	0.91
Beta III Ti	w	11.5Mo-6Zr-4.5Sn-bal Ti	0.90
Incoloy 800	w	32.5Ni-46Fe-21Cr (HA)	0.83
HD 435	...	recrystallized SiC (N)	0.80
RA 333	w	25Cr-1.5Mn-1.3Si-3Co-3Mo-3W-18Fe-bal Ni (RA)	0.80
K86	ps	8.8Co binder (K)	0.78
Inconel 671	w	50Ni-48Cr-0.4Ti (HA)	0.77
Lucalox	...	densified Al_2O_3 (GE)	0.76
mild steel	w	0.15C-bal Fe	0.76
W10	ps	90W-10(Ni,Cu,Fe) (K)	0.70
3109	ps	12.2 binder (K)	0.62
K94	ps	11.5 binder (K)	0.57
Mo	w	...	0.52
Carbofrax D	ps	SiC-ceramic bond (Carbor)	0.49
W	w	(GE)	0.48
K68	ps	5.8 binder (K)	0.43
3406	ps	7.8 binder (K)	0.42
HD 430	...	recrystallized SiC (N)	0.40
Si_3N_4	hp	(N)	0.40
Norbide	hp	B_4C (N)	0.38
BT-9	ps	2MgO-25TiB_2-3.5WC-bal Al_2O_3(OGC)	0.37
BT-12	ps	1.5MgO-49TiB_2-3.5WC-bal Al_2O_3(OGC)	0.35
BT-11	ps	1.7MgO-38TiB_2-3.5WC-bal Al_2O_3(OGC)	0.33
ZRBSC-D	hp	ZrB_2-SiC (N)	0.32
VR-54	ps	WC-7Co binder (F)	0.32
BT-24	ps	2MgO-30TiB_2-3.5WC-bal Al_2O_3(OGC)	0.32
K801	ps	6Ni binder (K)	0.32
BT-10	ps	2MgO-30TiB_2-3.5WC-bal Al_2O_3(OGC)	0.30
K714	ps	6Co+1Cr binder (K)	0.26
K701	ps	10.2Co+4Cr binder (K)	0.25
CA 306	ps	WC-6Co binder (Carmet)	0.23
Noroc 33	hp	Si_3N_4-SiC (N)	0.20
TiC-Al_2O_3	ps	(B and W)	0.19
895	ps	WC-6Co binder (Carb)	0.19
SiC	hp	(N)	0.12
K602	ps	<1.5 binder (K)	0.11
SiC	...	(GE)	0.05
CBN	...	(GE)	0
GE diamond	...	(GE)	0

[a] REF (relative erosion factor) = $\dfrac{\text{Volume loss material}}{\text{Volume loss Stellite 6B}}$.

[b] Abbreviations are listed in Table 5.

TABLE 2—*700°C erosion test results: 90-deg impingement, 27-μm Al_2O_3 particles, 5-g/min particle flow, 170-m/s particle velocity, 3-min test duration, N_2 atmosphere.*

Material	Manu-facturing Method	Composition	REF[a]
ZRBSC-M	hp[b]	ZrB_2-SiC-graphite (N)[b]	>5.00
99P	ps	$99Al_2O_3$ (Krohn)	>4.00
chromite	ps	(UCAR)	3.43
K162B	ps	25Ni+6Mo binder (K)	1.67
K151A	ps	19Ni binder (K)	1.62
Stellite 3	c	31Cr-12.5W-2.4C-bal Co (Stellite)	1.61
Carbofrax D	ps	SiC-ceramic bond (Carbor)	1.38
895	ps	WC-6Co binder (Carb)	1.32
K90	ps	25 binder (K)	1.21
25Cr iron	c	25Cr-2Ni-2Mn-0.5Si-3.5C-bal Fe (OGC)	1.16
Refrax 20C	ps	SiC-Si_3N_4 bond (Carbor)	1.15
98D	ps	$98Al_2O_3$ (Krohn)	1.12
Stellite 6K	w	30Cr-4.5W-1.5Mo-1.7C-bal Co (Stellite)	1.06
K86	ps	8.8Co binder (K)	1.03
Stellite 6B	w	30Cr-4.5W-1.5Mo-1.2C-bal Co (Stellite)	1.00
Haynes 93	c	17Cr-16Mo-6.3Co-3C-bal Fe (Stellite)	1.00
Haynes 25	w	20Cr-15W-10Ni-1.5Mn-0.15C-bal Co (Stellite)	0.85
K94	ps	11.5 binder (K)	0.84
Haynes 188	w	22Cr-14.5W-22Ni-0.15C-bal Co (Stellite)	0.83
RA 333	w	25Cr-1.5Mn-1.3Si-3Co-3Mo-3W-18Fe-bal Ni (RA)	0.80
3109	ps	12.2 binder (K)	0.80
RA 330	w	19Cr-35Ni-1.5Mn-1.3Si-bal Fe (RA)	0.79
HK-40	c	26Cr-20Ni-0.4C-bal Fe	0.78
304 SS	w	17Cr-9Ni-2Mn-1Si-bal Fe	0.73
Inconel 671	w	50Ni-48Cr-0.4Ti (HA)	0.62
430 SS	w	17Cr-1Mn-1Si-0.1C-bal Fe	0.62
Inconel 600	w	76Ni-15.5Cr-8Fe (HA)	0.61
Lucalox	...	densified Al_2O_3 (GE)	0.57
Beta III Ti	w	11.5Mo-6Zr-4.5Sn-bal Ti	0.57
Incoloy 800	w	32.5Ni-21Cr-46Fe (HA)	0.57
316 SS	w	17Cr-12Ni-2Mn-1Si-2.5Mo-bal Fe	0.56
Ti-6Al-4V	w	...	0.54
Incoloy 800H	w	32.5Ni-21Cr-0.07C-46Fe (HA)	0.54
K68	ps	5.8 binder (K)	0.50
VR-54	ps	WC-7Co binder (F)	0.50
3406	ps	7.8 binder (K)	0.49
K701	ps	10.2Co+4Cr binder (K)	0.47
K801	ps	6Ni binder (K)	0.46
SiC	hp	(N)	0.44
W-10	ps	90W-10(Ni,Cu,Fe) (K)	0.44
Noroc 33	hp	Si_3N_4-SiC (N)	0.42
HD 430	...	recrystallized SiC (N)	0.38
CA 306	ps	WC-6Co binder (Carmet)	0.36
BT-9	ps	2MgO-25TiB_2-3.5WC-bal Al_2O_3 (OGC)	0.36
HD 435	...	recrystallized SiC (N)	0.32
TiC-Al_2O_3	ps	(B and W)	0.30
BT-11	ps	1.7MgO-38TiB_2-3.5WC-bal Al_2O_3 (OGC)	0.26
K714	ps	6Co + 1Cr binder (K)	0.25
BT-10	ps	2MgO-30TiB_2-3.5WC-bal Al_2O_3 (OGC)	0.25
Norbide	hp	B_4C (N)	0.21
BT-24	ps	2MgO-30TiB_2-3.5WC-bal Al_2O_3 (OGC)	0.20

TABLE 2—*Continued*

Material	Manu-facturing Method	Composition	REF[a]
W	w	(GE)	0.17
BT-12	ps	1.5MgO-49TiB_2-3.5WC-bal Al_2O_3 (OGC)	0.16
K602	ps	<1.5 binder (K)	0.13
Si_3N_4	hp	(N)	0.12
ZRBSC-D	hp	ZrB_2-SiC (N)	0.07
SiC	...	(GE)	0.02
diamond	...	(GE)	0
CBN	...	(GE)	0

[a] REF (relative erosion factor) = $\frac{\text{Volume loss material}}{\text{Volume loss Stellite 6B}}$

[b] Abbreviations are listed in Table 5.

TABLE 3—*Room temperature erosion test results on coated materials: 90-deg impingement, 27-μm Al_2O_3 particles, 5-g/min particle flow. 170-m/s particle velocity, 3-min test duration, N_2 atmosphere.*

Material	Composition and Coating Method	REF[a]
Borofuse Stellite 31	25Cr-10.5Co-2Fe-7.5W-O.5C-bal Co w/diffused B (MDC)[b]	1.40
Ni-Cr-B	plasma 0.5C-4Si-16Cr-4B-4Fe-2.4Cu-2.4Mo-2.4W-bal Ni (CWS)	1.32
Borofuse Stellite 6	29Cr-4.5W-1C-bal Co w/diffused B (MDC)	1.29
Cr_2O_3	plasma Cr_2O_3-5SiO_2-3TiO_2 (CWS)	1.23
WC	plasma 35(WC+8Ni)-11Cr-2.5B-2.5Fe-2.5Si-0.5C-bal Ni (CWS)	1.11
Borofuse Stellite 3	31Cr-12.5W-2.4C-bal Co w/diffused B (MDC)	0.92
W	pure CVD coating (RMRC)	0.53
Borofuse MT-104	0.5Ti-0.08Zr-0.03C-bal Mo w/diffused B (MDC)	0.30
Borofuse PM moly	Mo w/diffused B (MDC)	0.25
SiC	CVD SiC on C converted to SiC	0.06
SiC	pure CVD coating	0.05
Borofuse WC	WC w/diffused B (MDC)	0.02
TiB_2	electrodeposited over Ni (CPMRC)	0
18B-11	TiB_2 electrodeposited over 310 SS (UT)	0
19A-13	TiB_2 electrodeposited over 310 SS (UT)	0

[a] REF (relative erosion factor) = $\frac{\text{Volume loss material}}{\text{Volume loss Stellite 6B}}$.

[b] Abbreviations are listed in Table 5.

TABLE 4—*700°C erosion test results on coated materials: 90-deg impingement, 27-μm Al_2O_3 particles, 5-g/min particle flow, 170-m/s particle velocity, 3-min test duration, N_2 atmosphere.*

Material	Composition and Coating Method	REF[a]
Ni-Cr-B	plasma 0.5C-4Si-16Cr-4B-4Fe-2.4Cu-2.4Mo-2.4W-bal Ni (CWS)[b]	2.79
WC	plasma 35(WC+8Ni)-11Cr-2.5B-2.5Fe-2.5Si-0.5C-balNi (CWS)	2.06
Borofuse Stellite 6	29Cr-4.5W-1C-bal Co w/diffused B (MDC)	1.40
Borofuse Stellite 31	25Cr-10.5Co-2Fe-7.5W-0.5C-bal Co w/diffused B (MDC)	1.37
Borofuse Stellite 3	31Cr-12.5W-2.4C-bal Co w/diffused B (MDC)	0.83
Borofuse WC	WC w/diffused B (MDC)	0.72
Borofuse PM moly	Mo w/diffused B (MDC)	0.28
W	pure CVD coating (RMRC)	0.25
Borofuse MT-104	0.5Ti-0.08Zr-0.03Cr-bal Mo w/diffused B (MDC)	0.19
SiC	pure CVD coating	0
SiC	CVD SiC on C converted to SiC	0
TiB_2	electrodeposited on Ni (CPMRC)	0
18B-11	TiB_2 electrodeposited on 310 SS (UT)	0
19A-13	TiB_2 electrodeposited on 310 SS (UT)	0

[a] REF (relative erosion factor) $= \dfrac{\text{Volume loss material}}{\text{Volume loss Stellite 6B}}$.

[b] Abbreviations are listed in Table 5.

TABLE 5—*Abbreviations used in Tables 1-4.*

B and W	Babcock and Wilcox
Carb	Carboloy Systems Dept., General Electric Corp.
Carbor	Carborundum Co.
Carmet	Carmet Co., Allegheny Ludlum Steel Corp.
c	cast
CPMRC	College Park Metallurgy Research Center
CWS	CWS Corp.
F	Fansteel, Inc.
GE	General Electric Co.
hp	hot pressed
HA	Huntington Alloy Products Div., International Nickel Co.
K	Kennametal, Inc.
Krohn	Krohn Ceramics Corp.
MDC	Materials Development Corp.
N	Norton Co.
OGC	Oregon Graduate Center
ps	pressed and sintered
RMRC	Rolla Metallurgy Research Center
RA	Rolled Alloys Corp.
Stellite	Stellite Div., Cabot Corp.
TRB	Timken Roller Bearing Co.
UT	United Technologies Corp.
UCAR	Union Carbide Corp.
w	wrought

References

[*1*] Finnie, I., Kabil, Y., and Wolak, J., *Journal of Materials*, Vol. 2, No. 3, Sept. 1967, pp. 682-700.

[*2*] Smeltzer, C. E., Gulden, M. E., and Compton, W. A., *Journal of Basic Engineering*, Vol. 92, 1970, pp. 639-654.

[*3*] Head, W. J. and Harr, M. E., *Wear*, Vol. 15, 1970, pp. 1-46.

[*4*] Sheldon, G. L., "Erosion of Brittle Materials," Ph.D. Thesis, University of California, 1965.

[*5*] Young, J. P. and Ruff, A. W., *Journal of Engineering Materials and Technology*, Vol. 99, No. 2, April 77, pp. 121-125.

[*6*] Bitter, J. G. A., *Wear*, Vol. 6, 1963, pp. 5-169.

[*7*] Neilson, J. H. and Gilchrist, A., *Wear*, Vol. 11, No. 2, 1968, pp. 111-122.

[*8*] Ruff, A. W. and Ives, L. K., *Wear*, Vol. 35, 1975, pp. 195-199.

[*9*] Uuemyis, K., Kleis, I., Tumanov, V., and Tiideman, T., Translated from *Poroshkovaya Metallurgiya*, No. 3 (135), July 1972. Appeared in *Soviet Powder Metallurgy and Metal Ceramics*, March 1974, pp. 248-250.

R. H. Barkalow,[1] J. A. Goebel,[1] and F. S. Pettit[1]

Erosion-Corrosion of Coatings and Superalloys in High-Velocity Hot Gases

REFERENCE: Barkalow, R. H., Goebel, J. A., and Pettit, F. S., "**Erosion-Corrosion of Coatings and Superalloys in High-Velocity Hot Gases,**" *Erosion: Prevention and Useful Applications, ASTM STP 664*, W. F. Adler, Ed., American Society for Testing and Materials, 1979, pp. 163–192.

ABSTRACT: Degradation of nickel- and cobalt-base superalloys in corrosive, particle-laden gas streams is being investigated by injecting salt and abrasive particles into a high-velocity combustor. The test conditions being used are intended to simulate the mechanism of materials degradation expected in coal-fired gas turbines where components will be subjected to hot corrosion from impurities in the coal and high-velocity impingement of fly ash particles. Oxidation-erosion experiments (with abrasive particles but no salt), considered a prerequisite for understanding the more complex case of erosion-hot corrosion, defined regimes of particle size and flux where the following situations were observed: (1) material loss predominantly by mechanical erosion, (2) material loss by an oxidation-erosion interaction, and (3) deposition of the solid particles on the leading edge of the cylindrical test specimens. A preliminary erosion-hot corrosion experiment showed a marked interaction between sulfate-induced hot corrosion and particulate erosion; the rate of metal consumption was much greater than that attributable to the sum of erosion and hot corrosion processes acting alone.

KEY WORDS: erosion-corrosion, coatings, superalloys, oxidation, oxidation-erosion, hot corrosion, erosion-hot corrosion

The term erosion-corrosion is used to denote processes whereby materials degradation occurs simultaneously by mechanical and chemical means. An example is the combination of hot corrosion and particulate erosion anticipated in fluidized bed coal combustion systems for electric power generation. Such systems would involve the expansion of hot gases from the combustor through a gas turbine, and these gases are likely to contain corrosive substances from impurities in the coal as well as particulate

[1]Assistant materials project engineers and senior staff scientist, respectively, Pratt & Whitney Aircraft, Commercial Products Division, Middletown, Conn. 06457.

matter (coal ash and sorbent from the bed) which might significantly affect the oxidation or hot corrosion behavior of the turbine materials.

Individually, hot corrosion and particulate erosion have been extensively studied, and theories attempting to account for these phenomena have been developed [*1-12*].[2] Hot corrosion is accelerated high-temperature oxidation due to the presence of molten salt deposits on materials. The resistance of nickel- and cobalt-base superalloys to hot corrosion and other forms of environmentally induced attack is known to depend on formation of protective scales of aluminum oxide (Al_2O_3) or chromium oxide (Cr_2O_3). Alumina is more protective in simple oxidation, especially in moving airstreams where chromia can be further oxidized to gaseous CrO_3. Chromia scales, however, may be more resistant to some types of hot corrosion conditions where a thin alumina layer would be fluxed or penetrated by acidic or basic salts.

The type of scale formed on nickel- and cobalt-base alloys exposed to oxidizing conditions is a function of composition. The effects of compositional variables, including major constituents chromium and aluminum which render the alloy a chromia- or alumina-former and minor elements (for example, yttrium, lanthanum, or hafnium) which may affect oxidation behavior via an influence on scale adherence, have been widely studied and are sufficiently well defined that the behavior of alloys in simple oxidation is usually predictable from their compositions [*13-15*]. However, since the alloy content for favorable oxidation characteristics is generally not compatible with mechanical property requirements, an extensive coatings technology has evolved for surface protection of high-temperature structural components. Techniques such as pack cementation, plasma spraying, and physical vapor deposition are widely used to modify surface chemistries by diffusion or to overlay oxidation-resistant coatings.

Erosion is mechanical removal of material by a stream of moving fluid, usually with entrained solid particles. Studies of room temperature erosion by gas-entrained particles have defined two fundamentally different types of material behavior, denoted as ductile and brittle erosion [*5-12*]. Ductile erosion is characterized by maximum rate of material removal at low impingement angles. The eroded surface usually exhibits clear evidence of material deformation in the form of particle tracks or micromachining grooves at low angles and impact craters at high angles. Brittle erosion is marked by maximum material loss at normal particle impact; the apparent mechanism is microfracturing and removal of fractured segments by subsequent impacts.

Particulate erosion at elevated temperatures has been studied by directing streams of particles against heated specimens. Recent work has confirmed earlier observations that material loss at high temperature may be either greater or less than at room temperature [*12,16,17*]. Under relatively mild

[2] The italic numbers in brackets refer to the list of references appended to this paper.

erosive conditions, for example, 304 stainless steel was found to experience less weight loss at 500°C than at 25°C, apparently due to formation of an oxide scale which was more erosion resistant than the underlying substrate [*16*]. Similar experiments on type 310 stainless steel, however, showed greater metal consumption at 975°C than at room temperature [*17*]. The difference between the 975°C and room temperature data was most pronounced at low velocities, where the erosive process was confined to the oxide scale; it was much less at high velocities, where the particles penetrated the scale and directly eroded the metallic substrate.

The next step in complexity beyond high-temperature erosion in gaseous reactive environments (that is, air or combustion gases) is simultaneous hot corrosion due to liquid salt deposits plus an erosive or fouling effect of impinging solid particles. Such a situation is possible in the case of coal-fired gas turbines, where liquid salt deposits due to impurities in the coal may form on turbine components operating at elevated temperatures and the high-velocity gas stream may also contain solid particles of fly ash and sorbent from the fluidized bed. The nature of erosion-corrosion interactions under these conditions is difficult to predict, and experimentation is required to define them.

This paper describes an experimental program whose objective is to investigate the behavior of state-of-the-art turbine materials and advanced alloy or coating systems under simultaneously occurring processes of hot corrosion and solid particle impingement. These conditions are being produced in laboratory tests by using a high-velocity dynamic combustor with provision for ingestion of salt and abrasive particles, either individually or simultaneously, into the gas stream. The results presented in this paper involve equipment characterization and oxidation-erosion studies which are a prerequisite for understanding the more complex case of erosion-hot corrosion. Results from an exploratory erosion-hot corrosion experiment are also briefly described.

Equipment and Procedure

Dynamic Combustor

The burner rig used for this work is based on a dynamic combustor designed by Dils [*18*] to provide controlled and well-defined oxidation or hot corrosion test environments. It was operated for this program on aircraft-grade jet fuel and compressed air. It is capable of attaining gas temperatures as high as 1400°C in the vicinity of test specimens which are inserted through the wall of the flame duct as shown schematically in Fig. 1. The combustor was modified for this program such that abrasive powder could be injected into an instrument collar between the primary and secondary combustor. Transport of a controlled amount of powder to the instrument collar was accomplished by means of a variable-speed

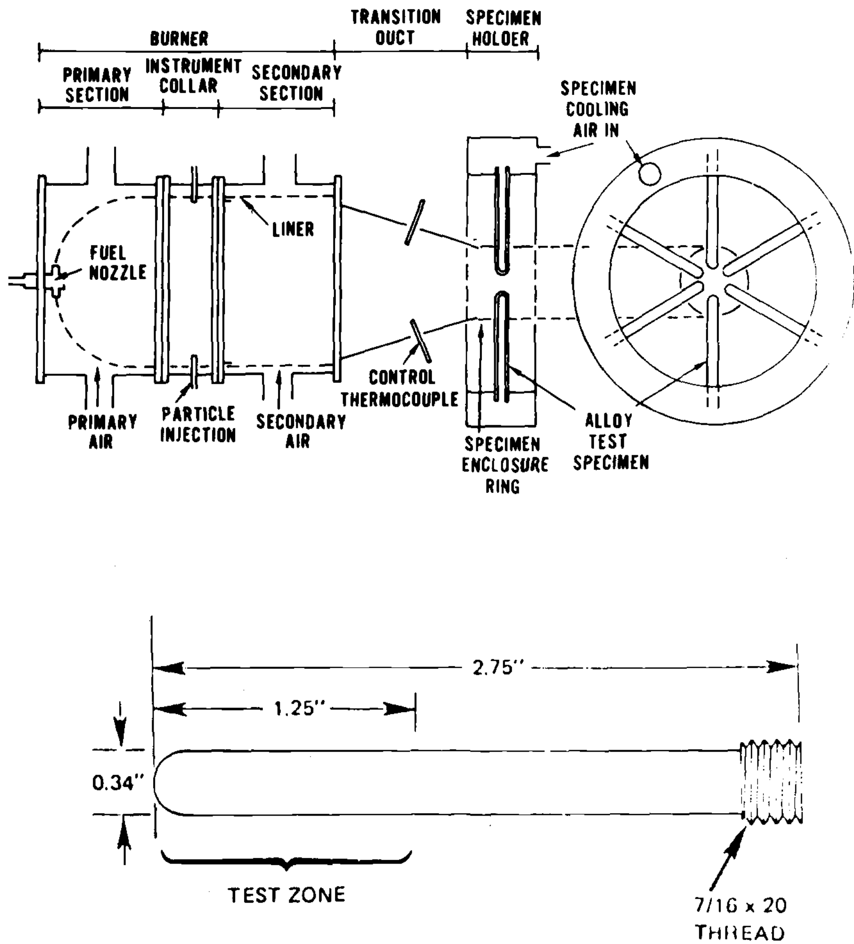

FIG. 1—*Schematic diagram of dynamic combustor and test specimen for oxidation-erosion and erosion-hot corrosion experiments.*

screw feed device and argon carrier gas. Salt for hot corrosion testing was injected as an aqueous solution through a hypodermic needle downstream of the primary fuel swirler plate. The specimen holder was slowly rotated (at approximately 3 rpm) about the rig axis during operation to provide for maximum uniformity of exposure conditions.

Materials and Specimen Preparation

Materials selected for the test program were:

1. IN 738 (Ni-16Cr-8.5Co-3.4Ti-3.4Al-1.75Mo-2.6W-1.75Ta), a cast superalloy which forms Cr_2O_3 protective scales in normal oxidation.

2. Aluminized IN 738, the foregoing alloy treated by a pack cementation process which produces a 75-μm aluminide coating.
3. X-40 (Co-25.3Cr-10.5Ni-7.5W-0.5C), a cast chromia-forming superalloy used for turbine guide vanes.
4. CoCrAlY (Co-25Cr-6Al-0.2Y and Co-17Cr-12Al-0.5Y), overlay coating alloys applied by physical vapor deposition on various superalloys.
5. IN MA-754 (Ni-20Cr-2 volume percent Y_2O_3), a dispersion-strengthened superalloy which forms Cr_2O_3 during oxidation.
6. Haynes 188 (Co-22Ni-22Cr-14.5W-0.1C-0.07La), a wrought chromia-forming alloy containing a rare earth addition to improve oxide adherence.
7. Silicon nitride (Si_3N_4), a hot-pressed ceramic considered to have potential for turbine guide vanes due to its favorable creep properties and oxidation resistance.
8. Yttria-stabilized zirconium oxide, applied as a plasma-sprayed thermal barrier coating on IN 738.

The test specimens were cylinders of dimensions shown in Fig. 1. The uncoated alloys were mechanically polished with 600 grit silicon carbide paper prior to testing; coatings were tested after conventional deposition and heat-treating cycles.

Experimental Procedure

All burner rig tests were run at the same mass flow rate (10.5 kg/min) and air:fuel ratio (32:1) except for minor changes in fuel pressure to adjust the specimen temperature to 871°C (1600°F) at the start of each run. Performance of the specimens in test was evaluated by visual inspection and weight change measurements at appropriate intervals. Weight change per unit area was calculated based on the surface area of the hemispherically capped cylinder exposed to the burner rig flame in the baseline tests and half of this area for the erosion tests (since the material losses from the leading edge were at least an order of magnitude larger than those from the trailing edge). Post-test metallurgical analysis included scanning electron microscopy (SEM) of surface features and conventional metallography of cross sections through the center of the hot zone of all the specimens.

The abrasive powder used for most of the oxidation-erosion testing was α-Al_2O_3. It was selected because of its high hardness (Mohs 9), chemical stability, high melting point, and availability in a range of well-characterized size distributions. Three grades with an average particle size of 20, 2.5, and 0.3 μm, respectively, were used. Tests were also run with magnesium oxide to determine if a powder of similar size, shape, and stability would be less erosive because of its lower hardness (Mohs 4½).

Time in test varied from 20 to 200 h, based on weight change data and visual assessment of sufficient degradation to permit metallurgical analysis of the mechanism of attack.

Results and Discussion

Characterization of Burner Rig and Particle Trajectories

Prior to initiation of materials testing, the burner rig was thoroughly characterized with respect to gas and specimen temperature, particle velocity and spatial distribution, and trajectories of particles in the gas stream.

Temperature measurements were made with thermocouples and an optical pyrometer. Data indicated that temperature variations at the leading edge of the specimens would be less than 10°C during oscillation of the specimen holder and that the trailing edge would be approximately 30°C cooler than the leading edge.

Particle velocity and spatial distribution in the combustor gas stream were determined for the 20, 2.5, and 0.3 μm alumina powders by laser Doppler velocimetry techniques. Figure 2 presents velocity and relative particle flux data for the 20- and 2.5-μm powder in the specimen plane which is perpendicular to the rig axis and 1.3 cm downstream of the burner nozzle. The velocity data indicate that the 20-μm particles were accelerated to approximately 80 percent of the freestream gas velocity, while the less massive 2.5-μm particles reached almost 100 percent of the gas velocity. Data for the 0.3-μm powder were intermediate between velocities of the 20- and 2.5-μm particles, an effect attributed to the tendency of fine particles to agglomerate and behave in the gas stream as effectively larger particles.

Values of relative particle flux (parentheses in Fig. 2) varied more widely than the velocity data. However, since the six-specimen array was slowly rotated through the particle-containing stream as shown on the diagrams

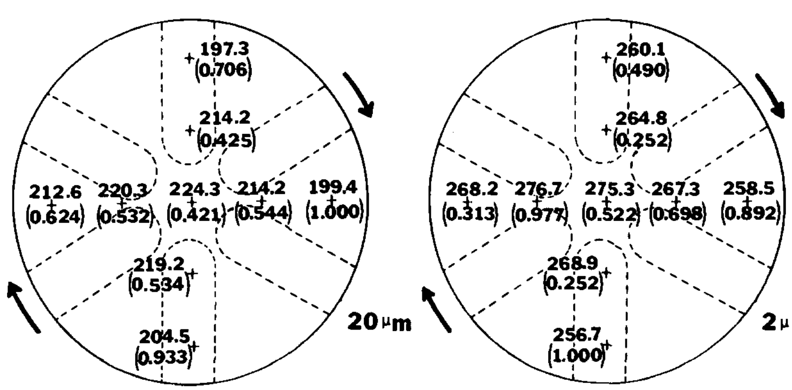

FIG. 2—*Particle velocities (m/s) and relative-number flux data (in parentheses) for 20- and 2 μm Al_2O_3 particles in the transition duct of the dynamic combustor. Dotted lines show position of test specimens; arrows indicate rotation of the specimen holder through flux field.*

in Fig. 2, the variations were the same for all of the specimens. Visual inspection and weight change data are thus an indication of the relative performance of the different test materials exposed to the same average conditions.

The final area of burner rig characterization was calculation of particle trajectories. Such calculations are necessary because particles approaching cylindrical shapes may be strongly deflected by fluid streamlines such that the velocity and impact angle at the point of contact with the specimen may be significantly different than the upstream velocity and the apparent impact angle defined by the freestream flow direction and the tangent to the cylinder [*12*]. Since erosion rate is critically dependent on particle velocity and impact angle, the possibility of particle deflection by fluid streamlines is of paramount importance.

Particle trajectories for the gas conditions and specimen size being used in these tests were calculated for the size range of alumina particles of interest [*19*]. Results are shown qualitatively in the computer-drawn diagrams of Fig. 3. They indicate that particles of >11-μm diameter will be only weakly influenced by fluid streamlines; that is, the trajectory is a straight line up to the point of impact, and impact velocity is negligibly different from that upstream of the specimens. For smaller particles, graphs of true impact angle, normalized impact velocity, and normalized impact number density versus apparent impact angle ($90 - \beta$) are presented in Figs. 4, 5, and 6, respectively.

Figure 4 shows that for small particles the true impact angle is always less than the apparent impact angle and there is a cutoff value of apparent angle below which particles of a given size will be deflected around the specimen and will not impact the surface. Figure 5 reflects the fact that particles approaching the cylinder at high impact angles are decelerated by fluid streamlines, coming to rest at the nose of the leading edge; conversely, particles approaching at intermediate angles must accelerate to travel the

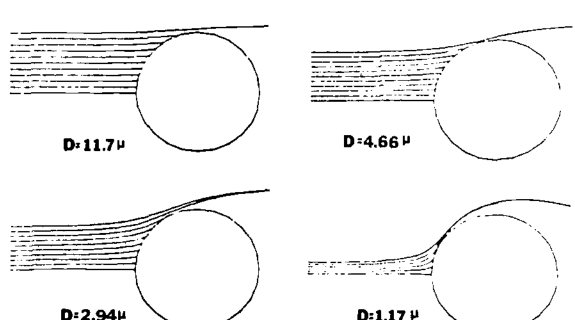

FIG. 3—*Particle trajectories in the dynamic combustor for the size range of alumina powders used in oxidation-erosion testing.*

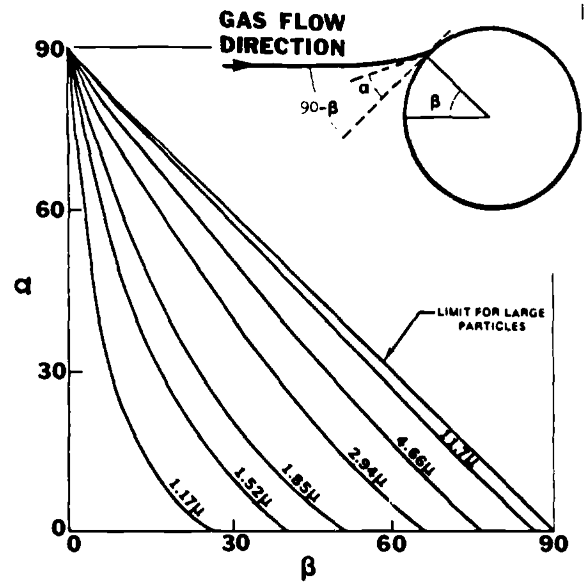

FIG. 4—*True impact angle* (α) *versus apparent impact angle* ($90 - \beta$) *of various particle sizes impinging on cylindrical burner rig specimens.*

greater distance of the curved trajectory. Finally, Fig. 6 shows the variation of impact number density with apparent impact angle due to the cylindrical geometry and curvature of the trajectories.

A possible effect of boundary layers on erosion rate in the burner rig was assessed by computing the response of a particle in a fluid flow where the velocity drops abruptly from one level U_1 to another U_2 [*20*]. It was found that the distance required to decelerate a particle to half its incoming velocity is about 5.5 times the boundary-layer thickness for a 1-μm particle impacting at 90 deg. The deceleration distance is a much larger multiple of boundary-layer thickness for all other impact angles and for larger particles. It was concluded that particles large enough to cause erosion of the burner rig specimens would be negligibly influenced by boundary-layer effects.

Baseline Oxidation

In order to interpret subsequent oxidation-erosion data, it is necessary to know the behavior of the test materials for the gas conditions of the burner rig operated without ingestion of solid particles. As expected, weight change data from a baseline oxidation test at 871°C showed small weight gains for the alumina-forming coatings and slightly larger weight losses for the chromia-forming alloys (Fig. 7). This difference is believed to reflect

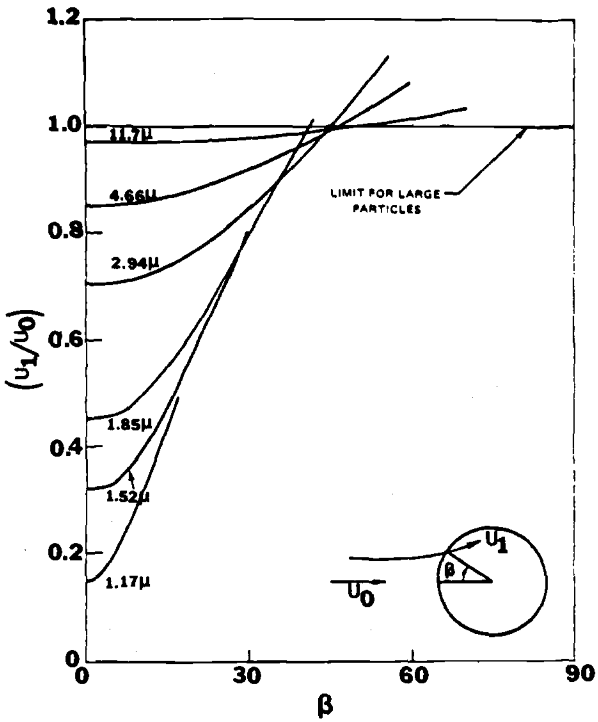

FIG. 5—*Normalized impact velocity (neglecting boundary-layer effects) versus particle size and apparent impact angle (90 − β).*

the stability of alumina scales in simple oxidation and volatilization of chromia as gaseous CrO_3.

In comparison with the metallic specimens, the Si_3N_4 exhibited very little oxidation; the plotted weight loss is primarily due to chipping of the specimen during insertion and removal from the specimen holder.

Oxidation-Erosion with 20-μm Al_2O_3

Addition of 130 ppm of 20-μm alumina to the gas stream resulted in consumption of the metallic materials at a rate approximately three orders of magnitude greater than that observed in the baseline oxidation test (Fig. 8). Also, there was no significant difference between weight change data obtained for alloys which form chromia or alumina scales during oxidation. The aluminide coating on IN 738, for example, was rapidly eroded away in spite of its good oxidation resistance, and MA-754, which experienced the maximum weight loss in the oxidation test, performed essentially the same as CoCrAlY in oxidation-erosion. Finally the silicon nitride expe-

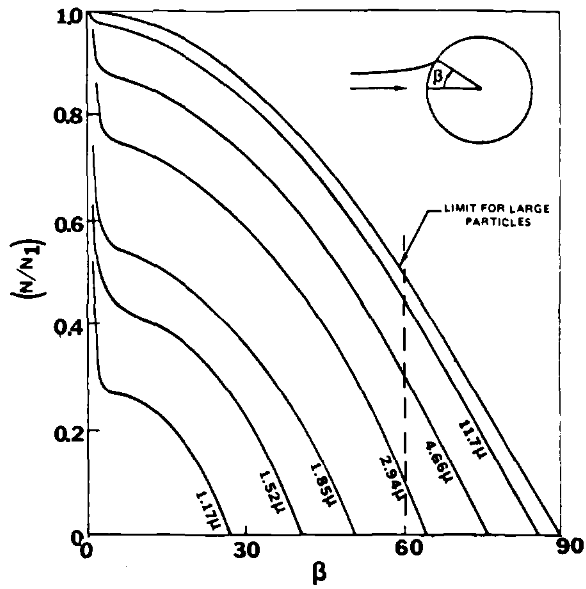

FIG. 6—*Impact number density (number of impacting particles per unit area, normalized with respect to upstream particle flux* N_I*) versus particle size and apparent impact angle.*

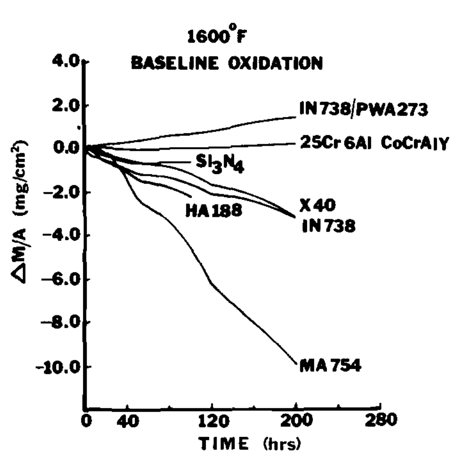

FIG. 7—*Weight changes due to oxidation of test materials in the high-velocity burner rig-operated without ingestion of abrasive or salt. Specimen temperature = 871 °C.*

rienced a very small weight loss, demonstrating good resistance to conditions which caused significant erosion of the metallic systems.

Post-test examination of the oxidation-erosion specimens revealed similar features on all of the metallic materials. Typical observations on visual inspection are illustrated in Fig. 9, where the specimens are positioned to

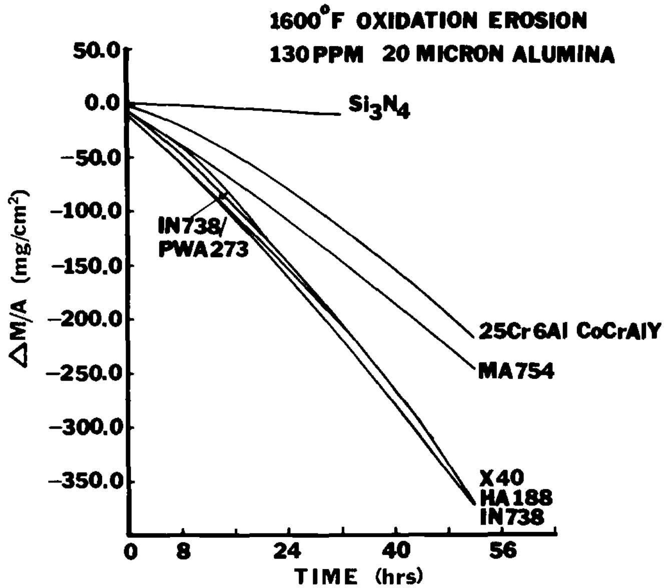

FIG. 8—*Weight losses in 871°C oxidation-erosion test with Al_2O_3 abrasive powder of 20-µm average particle diameter.*

show the changes in contour and surface texture of the exposure zone. The cylindrical section and hemispherical cap were uniformly eroded except for a slight taper attributable to a radial variation in flux density as shown in the data of Fig. 2. A pronounced angular dependence of metal removal rate was evident, with maximum erosion at intermediate impact angles producing a cam-shaped cross section with relatively flat faces on opposite sides of the nose of the leading edge (that is, 90-deg impact). There were no end effects of the hemispherical cap except for a dependence of surface texture and metal recession on impact angle which was apparently similar to that on the cylindrical section.

Typical SEM observations of the eroded surfaces are presented in Fig. 10. Well-defined micromachining marks resulting from individual particle impacts are characteristic of areas corresponding to low and intermediate impact angles (Fig. 10*a*). At approximately normal impact angles, individual particles formed craters with prominent lips at the edges (Fig. 10b). At very high magnifications (× 10 000), features resembling a thin oxide film were evident, consistent with surface discoloration and high electrical resistivity across the specimen surface. However, these features were at least an order of magnitude smaller than the micromachining grooves and impact craters which developed during the erosion process, and hence it is concluded that the oxide scale had no major influence on the rate of metal removal.

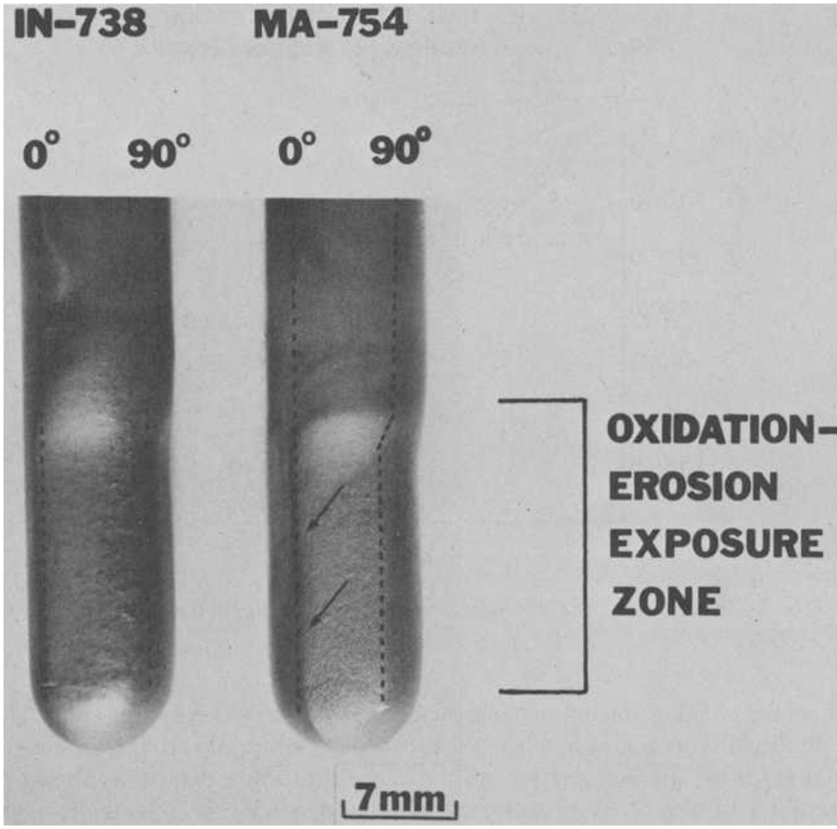

FIG. 9—*Exposure zone of specimens tested 52 h in 871°C oxidation-erosion with 20-μm Al_2O_3. Dotted lines mark 0 and 90-deg particle impact. Note low angle rippling (arrows) on Ma-754.*

After visual and SEM inspection, the specimens were sectioned through the center of the oxidation-erosion exposure zone and mounted for metallographic examination. Except for one specimen (X-40) which inexplicably was more round than the others, the eroded cross sections were all of similar shape with very flat surfaces making the same angle (~50 deg) with the direction of particle impingement (Fig. 11). Microscopic examination of the leading and trailing edges confirmed the SEM observations of minimal oxidation of the surface exposed to the eroding particles. The trailing edge of IN 738, for example, showed the scale morphology and γ' depletion typical of the oxidation behavior of this alloy in the absence of erosion (Fig. 12*a*). The leading edge of the same specimen, however, exhibited no discernable oxide scale or alteration of surface structure (Fig. 12*b*), indicating

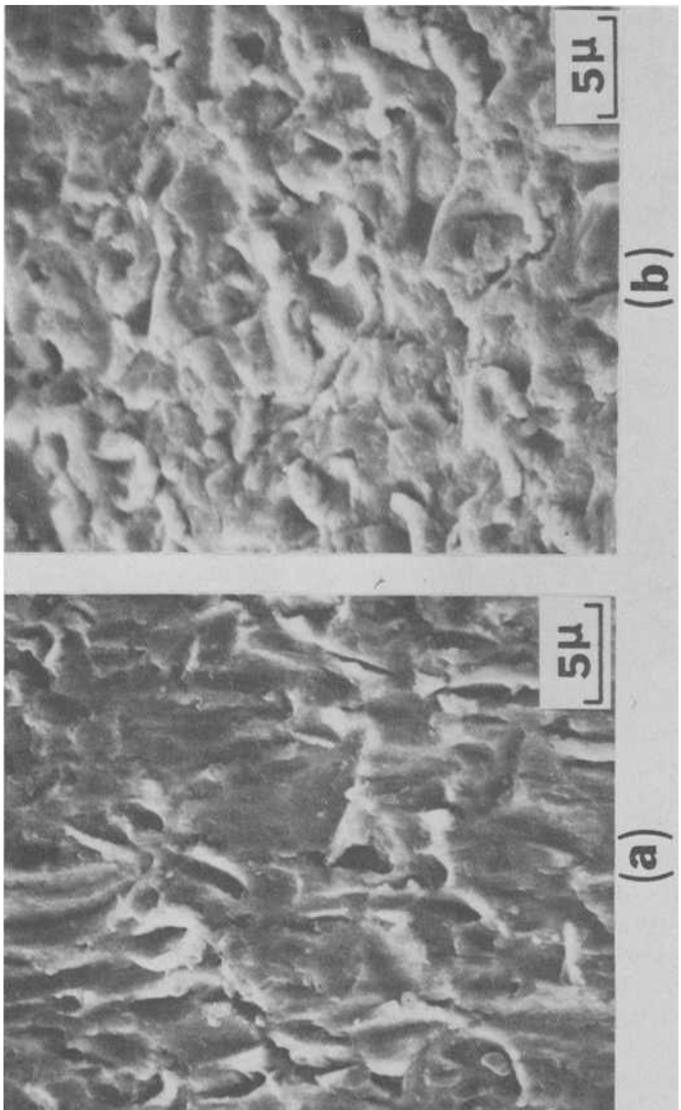

FIG. 10—Surface features of IN 738 after 20 h in 871°C oxidation-erosion test with 20-µm Al_2O_3: (a) ~20-deg impact angle; (b) ~90-deg impact angle.

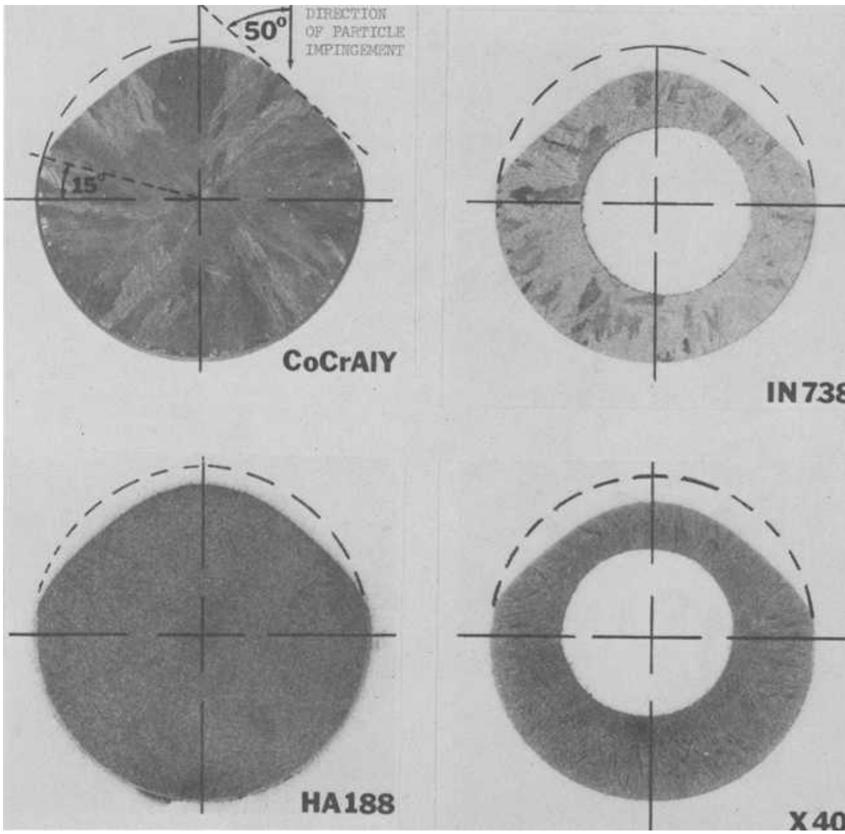

FIG. 11—*Transverse sections through hot zone of cylindrical specimens eroded by 20-μm Al_2O_3 at 871°C.*

that the rate of material removal by mechanical erosion was much faster than any effects produced by oxidation.

The microstructural features of the 20-μm oxidation-erosion specimens indicate material removal by a type of micromachining process similar to that observed by many investigators in room temperature erosion testing of ductile materials. The mechanism of metal removal in ductile erosion has been analyzed by Finnie [*5-7,10,11*], who solved the equations of motion for a particle of mass m and velocity v impacting a planar surface at angle α and removing a volume of material q. If the total volume Q removed by mass M is M/m times that removed by a single particle, Finnie estimated that

$$Q = C\frac{MV^2}{4}\frac{1}{p}f(\alpha)$$

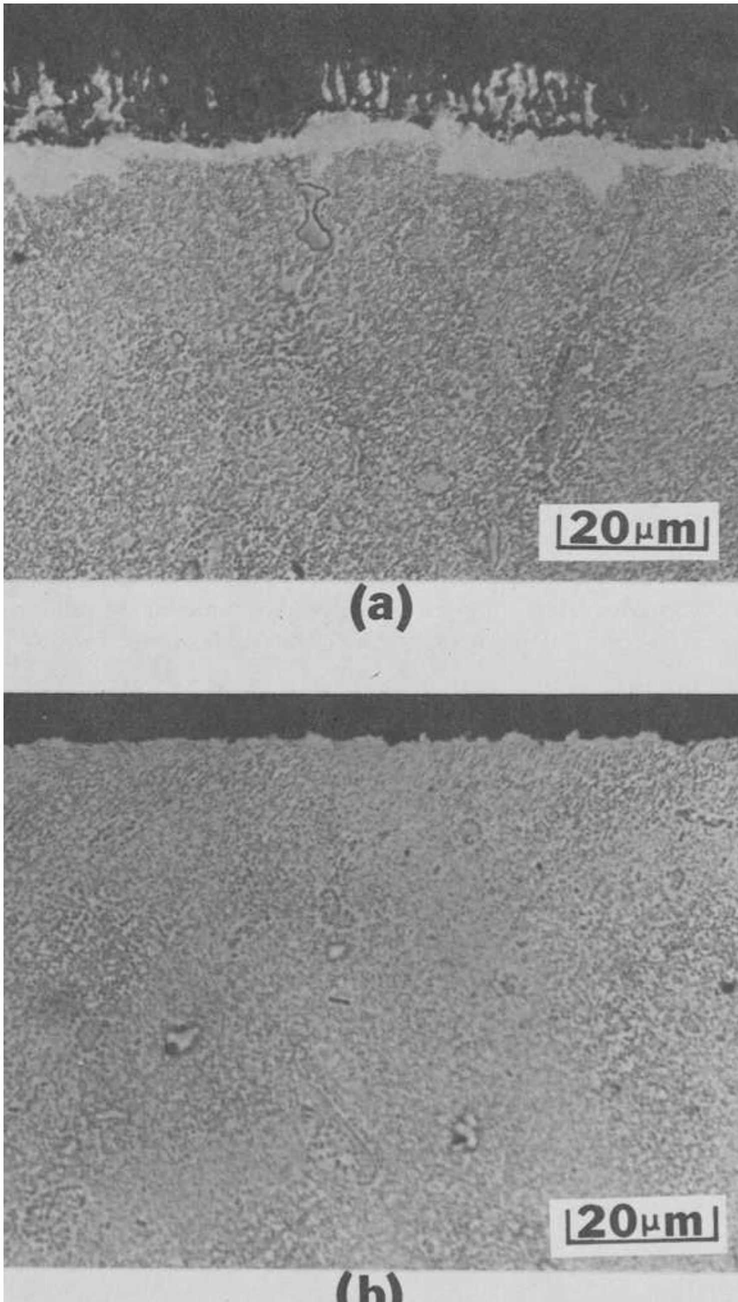

FIG. 12—*Oxidized trailing edge* (a) *and eroded leading edge* (b) *of IN 738 after 52 h in 871°C test with 20-µm Al_2O_3 abrasive.*

where C is the fraction of particles cutting in an idealized manner and p is a flow stress as measured in a tension or compression test. The function $f(\alpha)$ is such that Q varies with impingement angle as indicated by the dashed curve in Fig. 13.

Finnie observed that experimental data obtained by directing streams of abrasive against flat-plate specimens of various metals agreed with the predicted angular dependence of erosion rate at low but not at high angles (for example, the data points for aluminum superimposed on Fig. 13). He reasoned that the discrepancy at high angles was primarily due to surface roughening and applied a semi-empirical correction to the high-angle portion of $f(\alpha)$ to account for the fact that most of the impacting particles see a highly roughened surface left by the previous cut; the correction brought the theoretical and experimental curves into good agreement (Fig. 13).

From a mechanistic point of view, erosion of the cylindrical specimens in these experiments is fundamentally the same as erosion of flat surfaces as analyzed by Finnie. The radius of curvature of the cylinder is a factor of 2000 times the average particle diameter, and the curvature of the cylindrical surface is negligible over the ~10-μm length (see Fig. 10) of the micromachining grooves. Hence a given abrasive grain removes the same volume of material as if it were impinging on a flat plate. However, for a cylindri-

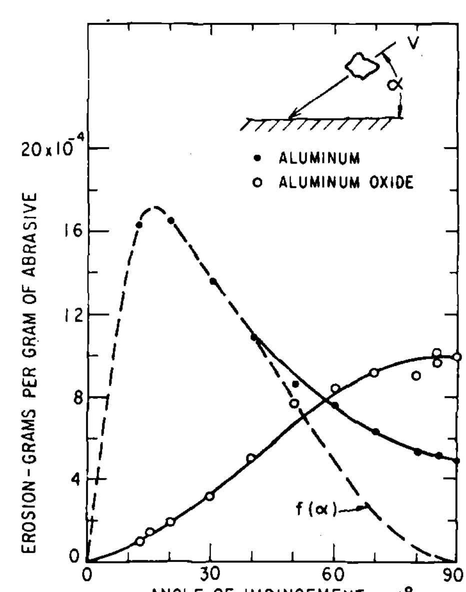

FIG. 13—*General form of mass removal rate versus impingement angle for ductile and brittle erosion. From Ref. 11.*

cal surface in a uniform flux of particles, it is not possible to express weight change of the specimen versus impingement angle as in Fig. 13 because the cylinder is being eroded at continuously varying angles.

The quantity most easily measured as a function of impact angle on a cylindrical shape is surface recession. The magnitude of surface recession reflects the angular dependence of material removal by a single impacting particle as analyzed by Finnie and an angle-dependent correction to account for the variation in number of particle impacts per unit area around the circumference of the cylinder. For linear trajectories the correction is simply $\sin\alpha$. Hence the expected angular dependence of erosion rate of specimens exposed to the 20-μm Al_2O_3 powder is Finnie's function $f(\alpha)$ multiplied by $\sin\alpha$. The parameter $f(\alpha)\sin\alpha$, including the high-angle semi-empirical correction and normalized with respect to its maximum value, is plotted versus impact angle in Fig. 14.

Erosion rate versus impingement angle was determined for the 20-μm oxidation-erosion specimens by measuring the linear recession from the original cylindrical cross section on the photomacrographs of Fig. 11. To limit consideration to angular relationships (that is, to factor out the effect of material properties which caused approximately twofold differences in the amount of metal removal), the data were normalized by scaling the maximum recession of each specimen to a factor of unity. Data points,

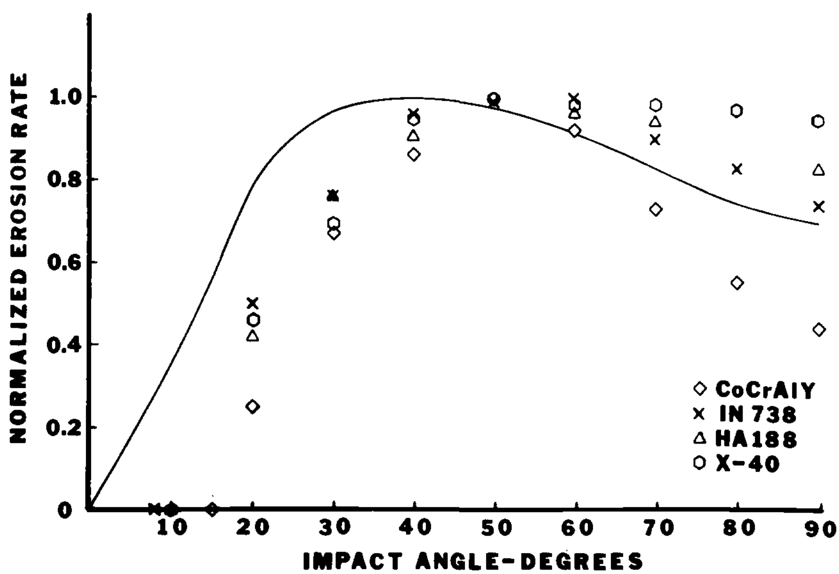

FIG. 14—*Angular dependence of normalized erosion rate of cylindrical specimens by particles (20-μm Al_2O_3) with linear trajectories. Data points are from measurement of metal removal on cross sections shown in Fig. 11.*

plotted in Fig. 14, are generally in agreement with the computed curve, although the measured values are systematically shifted to the right and quantitative agreement of the ratio of maximum erosion with erosion at 90 deg is not good.

The reason for the shift of the experimental data to the right, including a low-angle portion of the cylinder which experiences no detectable erosion in spite of particle impacts, is not evident. The oxide layer, which must be present on any metal exposed to this temperature in an oxidizing environment, may be having a subtle effect on the mechanism of metal removal. Nevertheless, it is apparent that erosion theory developed and tested for room temperature erosion of plate specimens is generally consistent with high-temperature oxidation-erosion of cylinders.

The amount of degradation of the Si_3N_4 in this test was significantly less than that for the metallic alloy specimens. Because the amount of degradation was small, it was not possible to correlate the amount of material loss with impact angle, and features of the eroded area, as revealed by SEM, did not permit a clear definition of the erosion mechanism.

Oxidation-Erosion with 2.5-μm Al_2O_3

Weight losses for metallic specimens exposed to 300 ppm of 2.5-μm Al_2O_3 particles were much smaller than produced by 20-μm Al_2O_3 but significantly greater than for baseline oxidation (compare Figs. 7, 8, and 15). Also, in contrast to the 20-μm test, data for the less-erosive powder can be grouped into alloys forming Al_2O_3 or Cr_2O_3 scales, the alumina-formers consistently losing less weight than the chromia-formers.

Surface features of the alloy specimens were considerably finer than those from the 20-μm test and not as clearly interpretable; no evidence of individual particle impacts or micromachining marks could be found on the eroded surfaces. Typical features, such as those illustrated in Fig. 16*a*, suggest a material removal mechanism involving development of folds and isolated, smeared debris as sketched in Fig. 16*b*. The loosely adhering debris is in turn removed from the surface by subsequent impacts.

Examination of transverse cross sections of the alloy specimens revealed that the rate of metal removal was strongly dependent on impact angle. The most striking example was the aluminide-coated IN 738 specimen shown in Fig. 17. The aluminide layer was eroded away in two symmetrically located arcs bounded by apparent impact angles of approximately 35 and 80 deg. Portions of the leading edge exposed to low-angle and near-normal impact, however, retained the aluminide coating. CoCrAlY-coated specimens, where thickness measurements permitted precise determination of the amount of metal loss, also exhibited maximum thinning of the coating at apparent impact angles near 45 deg.

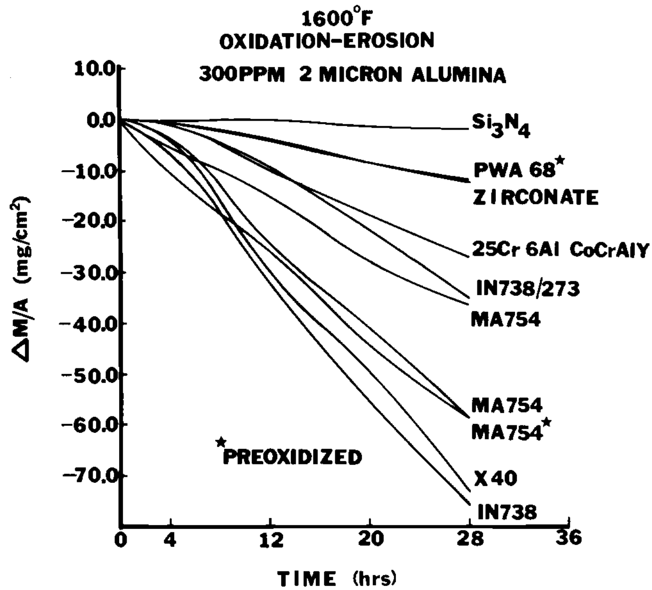

FIG. 15—*Weight losses in 871°C oxidation-erosion test with 2.5-μm Al_2O_3 powder. Data are from two runs at same gas conditions and particle flux.*

To explain this angular dependence of erosion produced by the 2.5-μm powder, the particle trajectory analysis and published erosion rate versus impact angle data were used as follows. Values of the true impact angle, impact velocity, and impact number density versus apparent impact angle ($90 - \beta$) for 2.5-μm particles were read from Figs. 4, 5, and 6, respectively. Metal removal versus true impact angle was then read from Fig. 13. Normalized erosion rate around the circumference of the cylinder was assumed to be proportional to the product of velocity squared, impact number density, and the metal removal versus impact angle data in Fig. 13. This product is listed in Table 1 and plotted versus apparent impact angle in Fig. 18.

The relationship between normalized erosion rate and apparent impact angle predicted by this calculation exhibits a sharp maximum at an apparent impact angle near 45 deg. Examination of Table 1 shows that the high erosion rate at 40 to 50 deg on the cylinder occurs because the true impact angles are approximately 15 to 25 deg, which is the true angular range of maximum ductile erosion. The erosion rate decreases sharply at lower angles due to very low values of impact number density, reaching zero at a cutoff value of apparent impact angle below which no erosion occurs because particles are deflected around the cylinder and do not impact the surface. At angles above

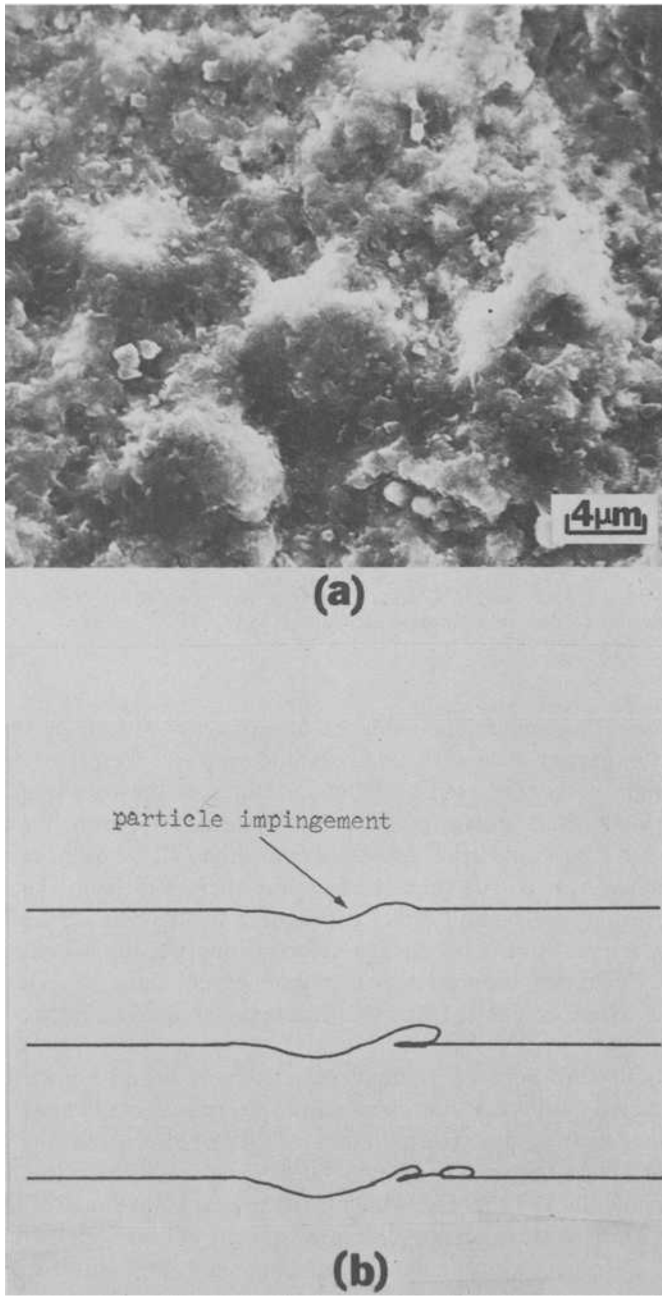

FIG. 16—*Surface features typical of eroded areas and schematic diagram of proposed mechanism of material removal by 2.5-μm Al_2O_3 particles.*

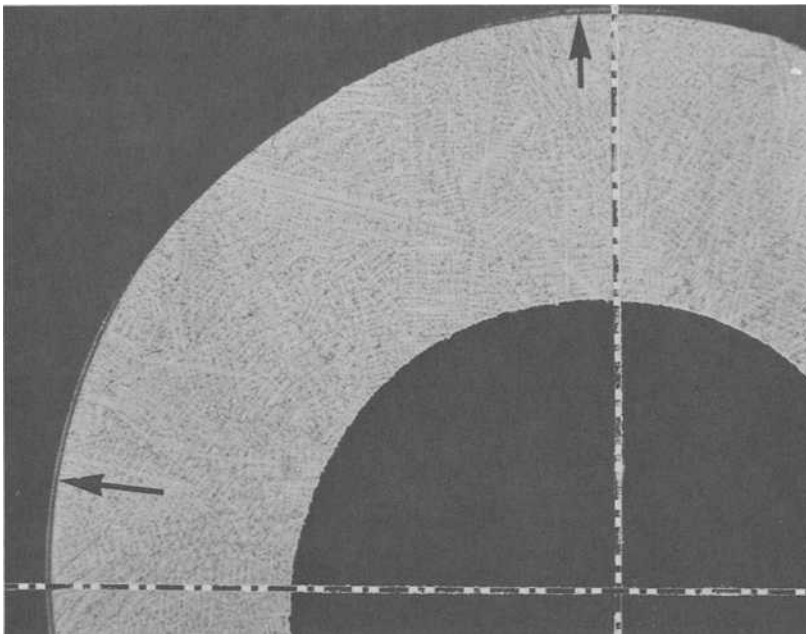

FIG. 17—*Cross section of aluminide-coated IN 738 eroded by 2.5-μm Al_2O_3 particles impinging from top to bottom. Dark-etching border (arrows) is aluminide coating retained at low and near-normal impact angles but eroded away between ~35 and 80 deg.*

TABLE 1—*Calculation of estimated erosion rate of cylindrical specimen by 2.5-μm alumina in the dynamic combustor.*

Apparent Impact Angle	True Impact Angle[a]	Velocity[b]	Impact Number Density[c]	Erosion Rate[d]	Relative Erosion Rate of Cylinder[e]
90	90	0.70	1.00	5.1	0.39
80	70	0.72	0.74	6.4	0.38
70	55	0.77	0.68	8.3	0.52
60	40	0.85	0.59	11.1	0.74
50	27	0.95	0.47	14.2	0.94
45	20	0.99	0.40	16.4	1.00
40	15	1.06	0.32	17.2	0.96
35	9	1.14	0.22	14.2	0.63
30	5	1.18	0.11	9.2	0.22
26	0	...	0.00	0.0	0.00

[a]From Fig. 4.
[b]From Fig. 5.
[c]From Fig. 6.
[d]From Fig. 13, using value of true impact angle.
[e](V^2 × Impact Density × Rate):(V^2 × Impact Density × Rate) at 90 deg.

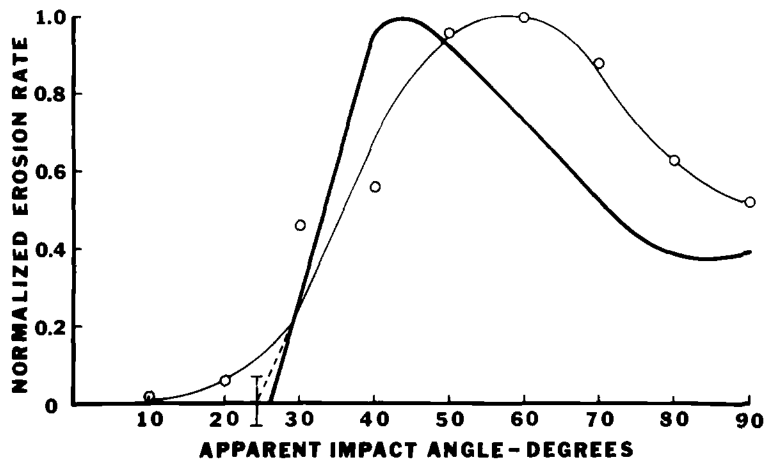

FIG. 18—*Angular dependence of normalized erosion rate of cylindrical specimens by particles (2.5-μm Al_2O_3) with curved trajectories. Data are from thickness measurements on eroded CoCrAlY coating.*

the peak of the curve, an increase in impact number density promotes erosion but is offset by lower particle velocity and lower values of erosion rate versus true impact angle.

Experimental data superimposed on Fig. 18 were obtained by metallographic measurement of reduction in thickness of a CoCrAlY coating versus apparent impact angle. As in the case of the 20-μm powder in Fig. 14, qualitative agreement of the calculated and observed angular dependence appears good, although the data points are systematically to the right of the computed curve.

Also included in the test with the 2.5-μm Al_2O_3 were two ceramic specimens and a preoxidized CoCrAlY coating (weight change data are in Fig. 15). As expected, hot-pressed silicon nitride was not noticeably degraded. However, a plasma-sprayed zirconia thermal barrier coating was significantly eroded; apparently the porous, low-density structure is much less erosion resistant than the fully dense silicon nitride. High-temperature preoxidation (1 h at 1200°C) of one of the CoCrAlY specimens was carried out to provide a thicker oxide (~3 μm) than that which forms in 871°C oxidation-erosion. Weight change data and subsequent metallography suggested that the thicker oxide decreased the rate of material consumption, especially at high impact angles.

Oxidation-Erosion with 8-μm Magnesium Oxide

An oxidation-erosion test was run with 300 ppm of crushed magnesium oxide powder with an average particle diameter of 8 μm. The purpose of the experiment was to determine if the magnesium oxide would be less erosive than alumina because of its lower hardness (Mohs 4½ versus Mohs 9).

All of the specimens tested were found to erode at rates of about one-half to one-sixth that produced by the same loading (in ppm by weight in the gas stream) of 2.5-μm alumina. Considering the difference in particle size, these results indicate a substantial effect of particle hardness under the oxidation-erosion conditions of the experiment. However, the mechanism of metal removal and oxidation-erosion interactions was not discernably different.

Deposition of Fine Alumina and Magnesia Powders

Several grades of alumina and magnesia powders with average particle diameters of <1 μm were found to deposit and build up on the leading edge of the test specimens. Visual observations indicated that deposition started at the nose of the leading edge (that is, at 90-deg impact) and build up from this point to a triangular prism with a well-defined knife edge at 90 deg. This sequence would be expected from the trajectory analysis, which indicates that small, low-momentum particles would be most markedly decelerated at 90 deg (see Fig. 5). Lacking the kinetic energy to cause erosion, they simply become trapped in the stagnant zone or boundary layer and deposit on the surface.

Post-test metallography of specimens exposed to the fine powders showed that no measurable erosion had taken place prior to or during buildup of the deposit.

Hot Corrosion and Erosion-Corrosion

A baseline hot corrosion test was run by injecting an aqueous solution of Na_2SO_4-25 weight percent K_2SO_4 into the primary combustor; concentration and flow rate of the solution were adjusted to produce a deposition rate of approximately 0.05 mg/cm^2/h on an inert platinum probe of the same geometry as the test specimens. Weight change data for this test are plotted in Fig. 19. Comparison with Fig. 7 shows the increased rate of degradation of the metallic materials due to the presence of the salt.

Erosion-hot corrosion was produced by simultaneous ingestion of salt (0.05 mg/cm^2/h) and abrasive particles (300 ppm of 2.5-μm Al_2O_3) into the burner rig. Note that the deposition rate and particle loading are the same as those used individually in baseline hot corrosion and oxidation-erosion experiments. Weight change data for the erosion-hot corrosion test are plotted in Fig. 20. Comparison of the magnitude of these weight changes with those of Fig. 15 (abrasive particles but no salt) and Fig. 19 (salt but

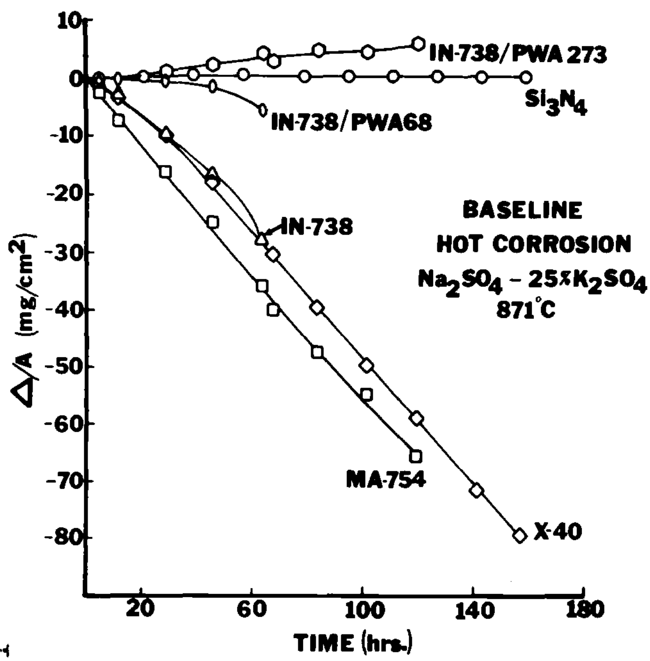

FIG. 19—*Weight losses in 871°C hot corrosion test with Na_2SO_4-K_2SO_4 salt.*

no abrasive particles) indicates a rate of metal consumption significantly greater than the sum of erosion and hot corrosion processes acting alone.

In contrast to the metallic materials, the hot-pressed silicon nitride demonstrated good resistance to conditions which caused severe attack of the other specimens.

The mechanism of rapid metal consumption by erosion-hot corrosion was not evident from initial metallographic examination. The metallography did establish, however, that the eroded surfaces showed substantial evidence of chemical attack (surface scale and formation of subsurface sulfide precipitates), in spite of material loss at a rate much faster than that expected for the diffusion processes necessary to produce the observed effects (Fig. 21). Apparently the erosion-hot corrosion mechanism involves the establishment of conditions extremely favorable for penetration of sulfur into the alloy.

Summary and Concluding Remarks

The behavior of nickel- and cobalt-base superalloys in corrosive, particle-laden gas streams was investigated by injecting salt and abrasive particles into a high-velocity burner rig. Baseline tests were run without

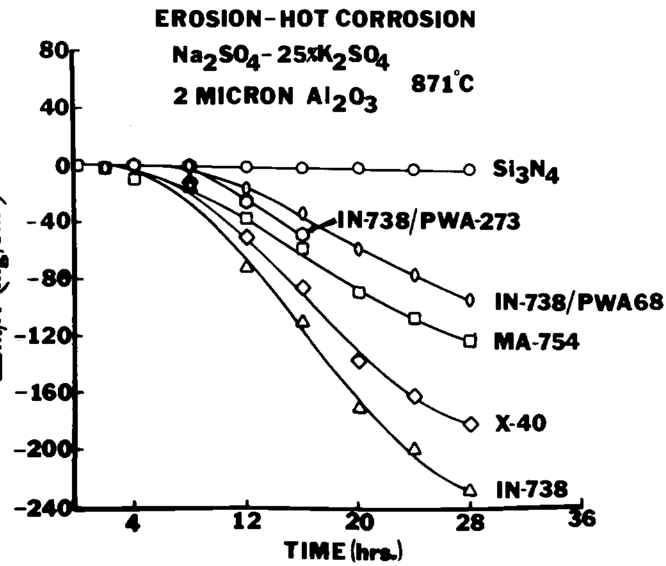

FIG. 20—*Weight losses due to simultaneously occurring processes of sulfate-induced hot corrosion and particulate erosion by 2.5-μm Al_2O_3.*

abrasive particles to isolate the effect of the oxidizing and corrosive environments, and metallurgical analysis of tested specimens was carried out to determine the mechanism of material consumption in each type of test. Results and conclusions were as follows.

1. *Oxidation-Erosion with 20-μm Al_2O_3*—All of the metallic specimens were rapidly consumed by mechanical erosion; oxidation processes did not significantly influence the rate or mechanism of material removal.

2. *Oxidation-Erosion with 2.5-μm Al_2O_3*—Rate of material consumption was about an order of magnitude greater than in baseline oxidation, but alumina-forming alloys consistently performed better than chromia-formers. Alumina scales appeared to reduce erosion, especially at low and near-normal impact angles, while chromia was ineffective due to volatilization in the high-velocity gas stream.

3. *Oxidation-Erosion with 8-μm Magnesium Oxide*—Magnesium oxide was found to be significantly less erosive than aluminum oxide due to its lower hardness.

4. *Deposition of Fine Powders*—Several types of alumina and magnesia powders with average particle sizes of <1 μm were found to deposit on the leading edge of the test specimen, showing that fouling by fine particles may occur under the same gas conditions where larger particles would cause erosion.

5. *Erosion-Hot Corrosion with 2.5-μm Al_2O_3*—A pronounced interaction between simultaneously occurring processes of hot corrosion and partic-

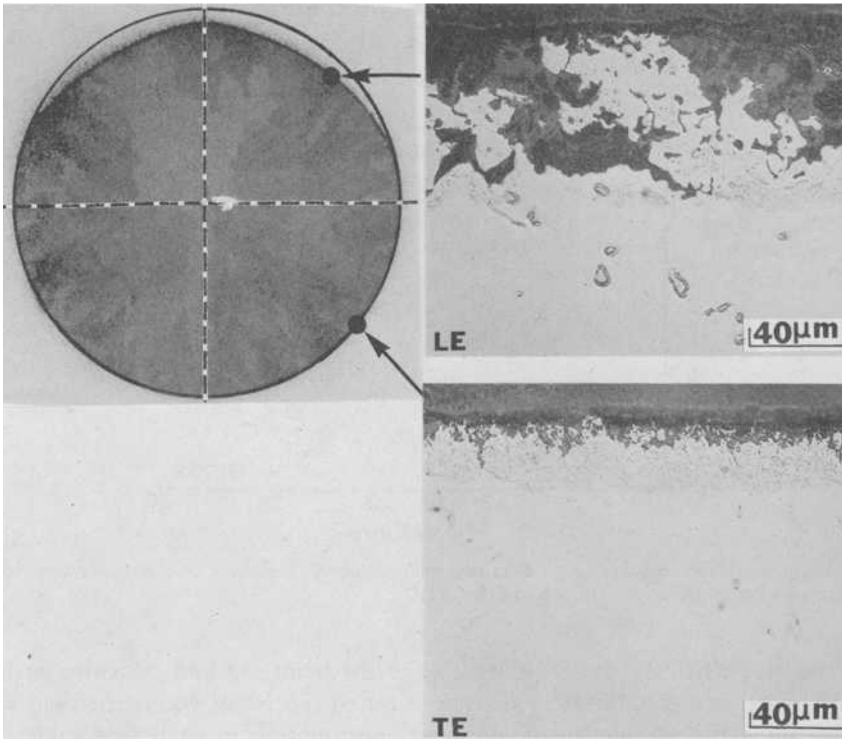

FIG. 21—*Cross section and surface microstructures of IN 738 tested 28 h in erosion-hot corrosion.*

ulate erosion resulted in materials consumption at a rate significantly greater than that attributable to both processes acting alone.

Hot-pressed silicon nitride was not significantly attacked by any of the test conditions which produced severe degradation of the metals.

These results show that the behavior of materials in erosion-corrosion can be dominated by one of the processes or influenced by an interaction between both. An example of the former case is the test results with 20-μm Al_2O_3 abrasive. The observed behavior is completely consistent with well-documented mechanisms of room temperature ductile erosion, including the lack of erosion at low impact angles, which can be accounted for by Bitter's hypothesis that a critical value of the velocity component normal to the surface is required to produce erosion [*8,9*]. In spite of the elevated-temperature oxidizing environment, material removal occurred by a purely mechanical mechanism independent of the very thin oxide film which formed between particle impacts. Surface features were essentially the same as those reported for room temperature erosion, and, after correcting for the cylindrical geometry, erosion rates of the specimens were consistent with erosion rate versus impact angle data obtained for room temperature erosion of plate specimens.

The case of the 2.5-μm powder is considered an oxidation-erosion interaction in that material removal was markedly accelerated by erosion but performance of the alloys was still influenced by the type of oxide scale (that is, alumina or chromia). Although it cannot be proved in the burner rig because of an inability to run an erosion test in the absence of an oxidizing environment, all observations are consistent with the conclusion that alumina scales increased the erosion resistance of the alloys, especially at low and near-normal impact angles. The alumina-forming alloys experienced smaller weight losses because this scale is chemically stable in a simple oxidizing environment (that is, no liquid salt deposit); chromia, on the other hand, is less protective because it volatilizes in the high-velocity gas stream.

The mechanism of material removal by oxidation-erosion interactions was not conclusively established in this work. There was no unequivocal evidence of particulate erosion (that is, micromachining grooves or impact craters) as observed with larger particles, and oxide scales on the impacted surfaces were too thin for convenient examination. It was shown, however, that the angular dependence of erosion rate is similar to that for room temperature erosion of ductile materials in spite of the presence of an oxide layer. It is therefore proposed that the Al_2O_3 scales and the alloy surfaces were eroded as a single entity with the oxide having a significant inhibiting effect.

In contrast to this situation, the observed interaction between erosion and hot corrosion was deleterious; a synergistic effect of the two processes resulted in a markedly increased rate of metal consumption.

Acknowledgment

This work was sponsored by the Electric Power Research Institute (EPRI), Palo Alto, Calif., under Project No. RP543-1; Dr. R. I. Jaffee was the EPRI program manager.

The assistance of C. E. Londin with the experimental work is gratefully acknowledged.

References

[1] Stringer, J., "Hot Corrosion in Gas Turbines," MCIC Report No. 72-08 NTIS, U.S. Department of Commerce, Springfield, Va., 1972.

[2] Goebel, J. A., Pettit, F. S., and Goward, G. W., *Metallurgical Transactions*, Vol. 4, No. 1, 1973, pp. 261–278.

[3] Felten, E. J., Goebel, J. A., and Pettit, F. S., "Initiation and Propagation of Sodium Sulfate-Induced Hot Corrosion and Effects Produced by Sodium Chloride," *Proceedings*,

3rd Conference on Gas Turbine Materials in a Marine Environment, University of Bath, Bath, U.K., 1976.
[4] Stringer, J., *Annual Review of Materials Science*, Vol. 7, 1977, pp. 477-509.
[5] Finnie, I. in *Proceedings* of 3rd National Congress of Applied Mechanics, American Society of Mechanical Engineers, 1958, pp. 527-532.
[6] Finnie, I., *Wear*, Vol. 3, 1960, pp. 87-103.
[7] Finnie, I. *in Symposium on Erosion and Cavitation, ASTM STP 307*, American Society for Testing and Materials 1962, pp. 70-82.
[8] Bitter, J. G. A., *Wear*, Vol. 6, 1963, pp. 5-21.
[9] Bitter, J. G. A., *Wear*, Vol. 6, 1963, pp. 169-190.
[10] Sheldon, G. L. and Finnie, I., *Transactions* American Society of Mechanical Engineers, Vol. 88B, 1966, pp. 387-399.
[11] Finnie, I., Wolak, J., and Kabil, Y., *Journal of Materials*, Vol. 2, No. 3, 1967, pp. 682-700.
[12] Tilly, G. P., *Wear*, Vol. 14, 1969, pp. 63-79.
[13] Giggins, C. S. and Pettit, F. S., *Journal of the Electrochemical Society*, Vol. 118, No. 11, 1971, pp. 1782-1790.
[14] Irving, G. N., Stringer, J., and Whittle, D. P., *Corrosion*, Vol. 33, No. 2, 1977, pp. 56-60.
[15] Pettit, F. S., Giggins, C. S., Goebel, J. A., and Felten, E. J. in *Alloy and Microstructural Design*, J. K. Tien and G. S. Ansell, Eds., Academic Press, New York, 1976, Chapter 10, pp. 349-402.
[16] Young, J. P. and Ruff, A. W., *Transactions* American Society of Mechanical Engineers, Vol. 99H, No. 2, 1977, pp. 121-125.
[17] Ives, L. K., *Transactions* American Society of Mechanical Engineers, Vol. 99H, No. 2, 1977, pp. 126-132.
[18] Dils, R. R. and Follansbee, P. S., *Corrosion*, Vol. 33, No. 11, 1977, pp. 385-402.
[19] Dring, R. P., "Particle Impact on a Cascade of Circular Cylinders," Report No. UTRC77-30, United Technologies Research Center, East Hartford, Conn., 1977.
[20] Dring, R. P., "Particle Impact on a Cascade of Circular Cylinders (Boundary Layer Effects)," Report No. UTRC77-69, United Technologies Research Center, 1977.

DISCUSSION

D. M. Mattox[1] *(written discussion)*—What is the expected chemical environment of the turbine blade?

R. H. Barkalow, J. A. Goebel, and F. S. Pettit (authors' closure)—The test conditions described in this paper are believed to be relevant to two types of schemes being proposed for operation of coal-fired gas turbines. One would involve expansion through a turbine of hot, fully combusted gases from a fluidized bed; the second, combustion in a turbine of low-Btu gas from a coal gasifier. Since excess air will be mixed with the coal or coal gas to promote complete combustion, the gases in the turbine are expected to contain sufficient oxygen to cause oxide scale formation on turbine alloys and coatings even though sulfur, carbon, and chlorine may be present.

[1] Sandia Laboratories, Albuquerque, N. Mex.

Gases entering a coal-fired high pressure turbine are also expected to contain gaseous oxides and molten salts due to contaminants in the coal (sodium, potassium, sulfur, chlorine, and perhaps heavy metals) as well as suspended solid particles of fly ash and sorbent from the fluidized bed. Extensive experience with aircraft, marine, and industrial turbines has shown that ingestion of gaseous impurities can result in accelerated materials degradation (hot corrosion) by a variety of mechanisms involving deposition of liquid salts on the surfaces of turbine components. An influence on the hot corrosion process of mechanical erosion by high-velocity gases and solid particles is not unique to coal-fired turbines (for example, runway dust is ingested into aircraft engines); the unknown regime of materials behavior being addressed in this paper is the possibility of a more significant effect of the erosive component due to a different type and consistently higher flux of solid particles than encountered in other applications of gas turbines.

S. M. Wolf[2] (*written discussion*)—The cylinder exposed to hot corrosion-erosion showed much greater weight loss than its counterpart subjected to oxidation-erosion. Were there differences in erosion behavior (other than weight loss) or microstructural features (in the eroded regions) between the two specimens?

R. H. Barkalow, J. A. Goebel, and F. S. Pettit (*authors' closure*)—Surface microstructures of specimens exposed to oxidation-erosion and erosion-hot corrosion conditions were significantly different. In the former case, surface and metallographic features produced by the oxidation process were lacking, but features evidently developed by the impacting particles were discernable. In the latter case the reverse was observed; microstructural features produced by the hot corrosion process (external scale, precipitates of sulfides and diffusion zones within the alloys) were present, but, except for the cam-shaped cross sections, there were no features which could be attributed to impacting particles.

This difference in features of the surfaces eroded in different environments indicates that erosion is the dominant process in oxidation-erosion whereas hot corrosion appears to be the more critical component in material removal by erosion-hot corrosion. However, since erosion-hot corrosion proceeds at substantially greater rates than hot corrosion alone, the erosion component must play a very important role in the combined process.

Authors' Note Added in Proof

The laser velocity measurements described in the subsection on characterization of the burner rig and particle trajectories were made without the test specimens in place, since the specimen holder precluded line-of-sight

[2]Department of Energy, Washington, D.C.

contact with the particles and use of a quartz window in the nozzle was unsuccessful. It was later recognized that insertion of the six specimens introduces sufficient blockage of the gas path to effect a significant increase in upstream static pressure. The increased pressure increases the density of the hot gases, permitting the constant mass flow of the burner rig (determined by constant settings of fuel flow and upstream pressure on sonic Cox nozzles supplying the compressed air) to be achieved at lower gas velocity. Gas velocity (and consequently the velocity of entrained solid particles) with the specimens in place was calculated to be 0.73 times the values measured in the open duct. The calculation neglected gas leakage at a small gap between the nozzle and the specimen holder and at slightly oversize holes for insertion of the specimens.

The diagram of Fig. 3 and the graphs of Figs. 4, 5, and 6 are corrected for the decrease in velocity due to blockage. The correction was simply a relabeling of particle diameters, since the decreased velocity due to blockage makes a given particle less inertia dominated and the trajectory originally calculated for it is that for a particle of larger diameter (by a factor of 1.17).

The computed angular dependence of relative erosion rate, as listed in Table 1 and presented graphically in Fig. 18, is thus for a particle of 2.9 rather than 2.5 μm diameter. The line of reasoning illustrated by compilation of Table 1 is still considered correct, and the qualitatively good agreement of experimental results with Finnie's analysis of the angular dependence of erosion rate is not affected by the relatively minor modification of the particle trajectory calculations.

M. Menguturk[1] *and E. F. Sverdrup*[2]

Calculated Tolerance of a Large Electric Utility Gas Turbine to Erosion Damage by Coal Gas Ash Particles

REFERENCE: Menguturk, M. and Sverdrup, E. F., "**Calculated Tolerance of a Large Electric Utility Gas Turbine to Erosion Damage by Coal Gas Ash Particles,**" *Erosion: Prevention and Useful Applications, ASTM STP 664,* W. F. Adler, Ed., American Society for Testing and Materials, 1979, pp. 193-224.

ABSTRACT: Erosion damage was estimated for the first stage of a large electric utility gas turbine based on projected particle distributions in the gas leaving the hot gas cleaning system of a pressurized fluidized-bed gasifier system. Based on the assumptions used in making the estimates, cleaning of the turbine expansion gas to a particulate concentration of 0.005 gram per standard cubic metre (0.002 grain per standard cubic foot) with particles larger than 6-μm diameter effectively removed should give satisfactory blade life from an erosion standpoint. Two stages of high-performance cyclone cleanup to 0.1 gram per standard cubic metre (0.5 grain per standard cubic foot) with 0.05 weight percent of 12-μm diameter particles remaining in the gas would wear stator vane trailing edges by 0.25 cm (0.1 in.) thickness (roughly equivalent to full wall thickness in upstream stage vanes) in 10000 h of operation.

The numerical results presented in this paper are based on the estimate that coal ash and sulfur sorbent particles will have, when impacting superalloy turbine materials under turbine conditions, 1/25th of the erosivity of silicon carbide particles impacting a nickel alloy at room temperature. The estimates do not account for the appreciable slowing of the 1- to 3-μm particles in the blade boundary layers before they reach the blading, even though these small particles account for most of the damage. The numerical results are in this way conservative. Actual data on the damage which coal gas particulates do to blade materials under turbine conditions are needed to establish the erosion tolerance of the turbine more accurately.

KEY WORDS: erosion, coal, ash, particles, gas, turbines, fluidized beds, gasification, combustion, trajectories, cleaning, tolerance

[1]Assistant professor, Department of Mechanical Engineering, Boğaziçi University, Istanbul, Turkey; also consultant, Westinghouse Research and Development Center, Pittsburgh, Pa. 15235.

[2]Advisory engineer, Power Generation and Combustion Processes, Energy Systems Division, Westinghouse Research and Development Center, Pittsburgh, Pa. 15235.

Pressurized fluidized-bed combustion systems and low-Btu coal gasification to produce efficient and clean power from coal are being studied. Both of these concepts use combined-cycle power generation systems where part of the power is generated by directing the combusted coal gas through a gas turbine to produce electricity as the end product. The particulate matter and the chemical contaminants contained in the hot gas are likely to cause turbine erosion, corrosion, and deposition.

In this paper, damage to the turbine due to the impact of micrometre-size particles has been estimated. An inviscid gas flow solution was obtained for the first stage of a large transonic gas turbine. The equations of particle motion were solved in this flow field to determine the particle trajectories and the impacts of the particles with the turbine blading. Erosion damage was evaluated by using an erosion model combined with experimental erosion damage data available in the literature.

Materials exhibit different erosion properties at different impact angles. For example, soft steels experience maximum erosion for particle impacts at angles of about 20 deg to the surface. Their erosion resistance increases as the particle angle of attack approaches 90 deg. In contrast, ceramic materials have been observed to suffer the maximum material loss at angles close to 90 deg. The angle at which the erosion resistance of the material becomes minimum is called the maximum erosion angle. The maximum erosion angle is mainly a function of the ductile-brittle nature of the material. However, it may also depend on many other factors such as particle size and shape, velocity, and temperature. In general, materials are reported to have maximum erosion angles varying from 10 to 90 deg.

In this paper a parametric analysis is presented which investigates the effect of maximum erosion angle on turbine erosion damage, with the assumption that the maximum erosion levels are the same for all materials. This provides a direct comparison between materials which have different maximum erosion angles while all other parameters are kept constant. Four specific cases have been treated, corresponding to maximum erosion angles of 10, 20, 30, and 90 deg. Results are presented continuously from 10 to 90 deg by means of curve interpolation. The cumulative damage corresponding to several particle distributions projected to leave the gas cleaning system is obtained.

Analysis of Particle Motion

The numerical calculations pertaining to the gas flows, the particle trajectories, and the erosion assessments were performed for the first stage of an electric utility turbine rated to drive a 65-MW generator. The gas velocities in the stator and rotor channels were calculated by using the Katsanis [*1*][3] computer program that assumes inviscid flow conditions. The

[3]The italic numbers in brackets refer to the list of references appended to this paper.

inviscid flow solution is sufficiently accurate except in the small region near the trailing edge, and thus should be quite appropriate for the particle trajectory calculations.

It must be pointed out that the exclusion of viscous effects, especially the boundary layer formation around the blades, will decrease the accuracy of trajectory calculations for very fine particles. Due to their ability to follow the streamlines closely, the small particles usually approach the blade surface at grazing angles and thus spend considerable time within the decelerating viscous layer. This causes a braking action on the particle motion. As a result, the particle impacts occur at smaller velocities, suggesting a decrease in erosion damage but an increased probability of deposition. In this paper, the particle trajectory and erosion calculations are presented, neglecting boundary layer flows and deposition.

Particle Dynamics

Equations of Particle Motion—Lapple and Shepherd [2] indicate that the only appreciable forces acting on a small solid particle suspended in a low-density, high-velocity fluid flow are the viscous drag force and the particle's own inertia. If the particle is a sphere and the Reynolds number is very small, the drag force is given by Stokes's law

$$\vec{F}_D = 3\pi\mu_g d_p (\vec{V}_g - \vec{V}_p) \tag{1}$$

where

F_D = drag force,
μ_g = gas viscosity,
d_p = particle diameter,
$\vec{V}_g$ = absolute gas velocity vector, and
$\vec{V}_p$ = absolute particle velocity vector.

Equation 1 is modified for large Reynolds number by introducing a correction factor, $f(Re)$

$$\vec{F}_D = 3\pi\mu_g d_p (\vec{V}_g - \vec{V}_p) f(Re) \tag{2}$$

where $f(\mathrm{Re}) = C_D Re/24$. C_D is the drag coefficient for a spherical particle and is equal to $24/Re$ for the Stokes flow. The following series of correlations for the drag coefficient were obtained by Morsi and Alexander [3]

$$\begin{aligned}
C_D &= 24/Re && (0 < Re \leq 0.1)\\
C_D &= 22.73/Re + 0.0903/(Re)^2 + 3.69 && (0.1 < Re \leq 1)\\
C_D &= 38.80/Re - 12.65/(Re)^2 + 0.36 && (1 < Re \leq 10)\\
C_D &= 46.50/Re - 116.667/(Re)^2 + 0.61667 && (10 < Re \leq 100)\\
C_D &= 98.33/Re - 2778/(Re)^2 + 0.3644 && (100 < Re \leq 1000)\\
C_D &= 148.62/Re - 47500/(Re)^2 + 0.35713 && (1000 < Re \leq 5000)
\end{aligned} \tag{3}$$

where Reynolds number is based on the velocity difference by the following relation

$$Re = \frac{\rho_g d_p |\vec{V}_g - \vec{V}_p|}{\mu_g} \tag{4}$$

Here ρ_g is the gas density.

The equations of motion for a spherical particle can be obtained by equating the particle inertia to the drag force. This is done by using the fixed reference frame XYZ of Fig. 1, where only the upper left quadrant of the turbine cross section is shown

$$\begin{aligned} \ddot{X}_p &= G(\dot{X}_g - \dot{X}_p) \\ \ddot{Y}_p &= G(\dot{Y}_g - \dot{Y}_p) \\ \ddot{Z}_p &= G(\dot{Z}_g - \dot{Z}_p) \end{aligned} \tag{5}$$

where

$$G = \frac{18\mu_g}{d_p^2\, \rho_p} f(Re) \tag{6}$$

In these equations, the subscripts g and p refer to the gas and the particle, respectively. The dot denotes the time derivative; for example, $\dot{X}_g$ is the axial component of the gas velocity and $\ddot{X}_p$ is the axial particle acceleration.

It is convenient to write Eq 5 with respect to a coordinate system rotating with the blades. This rotating frame, $xr\theta$, is shown in Fig. 1: x is the axial distance and equal to X of the fixed reference frame; r is the radial distance from the origin, O; and the angular displacement, θ, is measured from the leading edge of the blade. The direction of rotation is assumed to be positive. The following relations exist between the fixed and rotating frames of reference

$$\begin{aligned} X &= x \\ Y &= r \sin(\theta + \omega t) \\ Z &= r \cos(\theta + \omega t) \end{aligned} \tag{7}$$

The gas velocity components are related as follows

$$\begin{aligned} \dot{X}_g &= W_x \\ \dot{Y}_g &= (W_\theta + \omega r) \cos(\theta + \omega t) + W_r \sin(\theta + \omega t) \\ \dot{Z}_g &= (W_\theta + \omega r) \sin(\theta + \omega t) + W_r \cos(\theta + \omega t) \end{aligned} \tag{8}$$

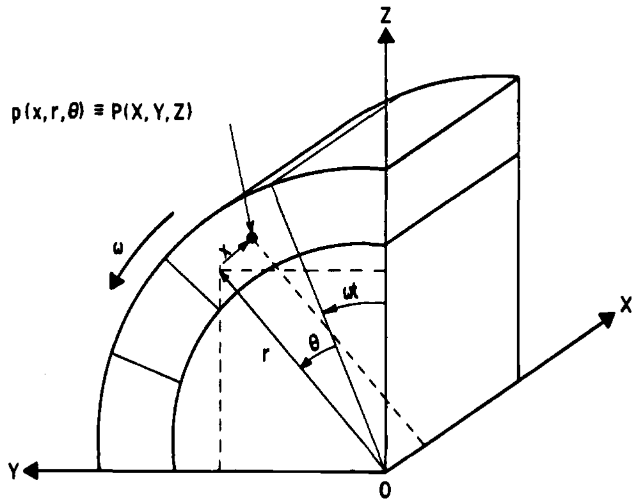

FIG. 1—*Coordinate system for the particle motion in an axial turbomachine.*

where W_x, W_r, and W_θ are the gas velocity components in the rotating reference frame. Substitution of Eqs 7 and 8 in Eq 5 yields

$$\begin{aligned} \ddot{x} &= G\,(W_x - \dot{x}) \\ \ddot{\theta} &= \frac{G}{r}\,(W_\theta - r\dot{\theta}) - \frac{2\dot{r}}{r}\,(\dot{\theta} + \omega) \\ \ddot{r} &= G\,(W_r - \dot{r}) + r\,(\dot{\theta} + \omega)^2 \end{aligned} \tag{9}$$

Similar equations were presented by Hussein [*4*] for two-dimensional gas flows and by Ulke [*5*] for three-dimensional gas flows.

Equation 9 with the variable coefficient G given by Eq 6 can be solved numerically for each particle entering the cascade. The gas velocity components are known from the inviscid flow solution. This solution is not continuous but given at certain points of a finite-difference mesh. For each step of integration, the gas properties and velocities must be interpolated. In this way, the integration can be performed until the particle collides with the blade surface.

The computer model must tell particles which impacted the blade with what velocity and at what angle to leave the blade surface. The velocity of the particle after the collision depends upon the momentum interchange between the particle and the blade surface. In most cases, these velocities must be determined experimentally due to the complexity of the momentum exchange mechanism.

No data are available for the types of particles (coal ash, coal char, and particles introduced by the gas cleaning process), their structure (conditioned by the fuel processing and combustion system used) and size range (smaller than about 10 μm), or for blade and vane surface conditions that are appropriate. Tabakoff and his co-workers have published data on the rebound characteristics of a few specific particles large enough to have their velocities measured by high-speed photographic techniques. The work done by Hussein [*4*] on crushable particles—corn cups and poppy seeds—was used for illustration in this work. Grant and Tabakoff [*10*] published rebound data for "hard" 200-μm silica sand bombarding annealed 2024 aluminum alloy targets where the statistical variation of rebound characteristics was partially explored, but these data are hardly typical of the rebounding of coal gas contaminants from turbine surfaces under operating conditions. To measure the rebound characteristics of the relevant particle sizes will require the use of a technique such as laser anemometry. Figure 2 shows the system being tested in the authors' laboratories for the purpose of gathering the data.

FIG. 2—*The laser Doppler velocimeter and high-speed data collection systems for measuring particle rebound characteristics.*

Data collected by Hussein [4] for poppy seeds and corn cups bouncing off of stainless steel blades are shown in Fig. 3. The data are approximated by the following equations

$$\frac{V_{p2}}{V_{p1}} = \frac{V_{pn2}}{V_{pn1}}\sqrt{\frac{1+\cot^2\beta_2}{1+\cot^2\beta_1}} \tag{10}$$

$$\frac{\beta_2}{\beta_1} = \frac{1}{\beta_1}\cot^{-1}\left(\frac{V_{pt2}}{V_{pt1}}\frac{V_{pn1}}{V_{pn2}}\cot\beta_1\right) \tag{11}$$

$$\frac{V_{pt2}}{V_{pt1}} = 0.95 + 0.00055\,\beta_1 \tag{12}$$

$$\frac{V_{pn2}}{V_{pn1}} = 1.0 - 0.02108\,\beta_1 + 0.0001417 \tag{13}$$

where V_P is the particle velocity and β the acute angle between the velocity vector and the tangent to the surface. Subscripts t and n denote the tangential and normal components with respect to the surface. Subscripts

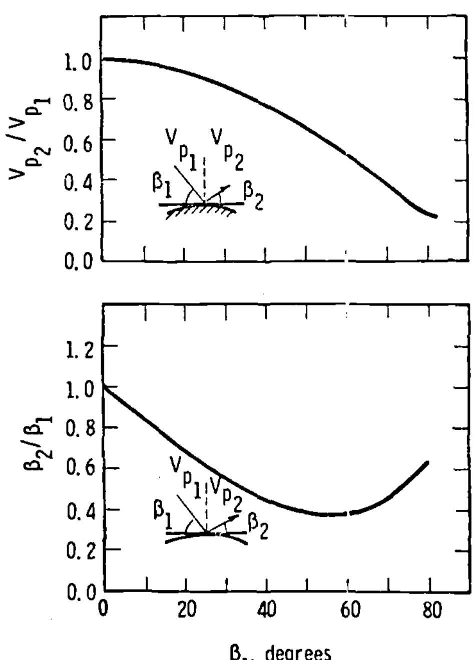

FIG. 3—*Particle rebound data by Hussein* [4].

1 and 2 correspond to the pre-impact and post-impact conditions, respectively.

The solution of Eq 9 can be continued after the particle rebounds from the blade surface with the new initial conditions deduced from Eqs 10–13.

Particle trajectories were calculated for two particle densities (1.5 and 2.5 g/c^3) and five size categories (1, 3, 6, 9, and 12μm). The particle density of 2.5 g/c^3 corresponds to dolomite particles in the expansion gas. The average density of the lighter ash particles is assumed to be 1.5 g/c^3. It was assumed that the concentration of particles above 12-μm size is reduced by the gas cleaning system to such a low level that their contribution to erosion damage can be neglected.

The results are presented for a uniform particle distribution at the turbine stator inlet. Special attention is directed to the particle conditions at the rotor inlet. The position of a particle leaving the stator passage is not exactly known with respect to the rotating blades. In fact, the particle may occupy any circumferential position relative to the rotor blade, depending on the exact locations of the stator and the rotor rows at the time the particle reaches the rotor inlet. It is assumed that any circumferential position has equal probability, provided that sufficiently long time is allowed. This is another way of saying that the circumferential distribution of particles at the rotor inlet is uniform.

The trajectories corresponding to 1- and 12-μm-diameter particles are shown in Figs. 4 and 5. In these figures, the top portion shows the trajectories in the flow channel. The bottom portion is the top view of the axisymmetric blade-to-blade stream surface. In both cases the particle is injected in front of the stator vane leading edge and at the midspan radius. The particle trajectory is calculated throughout the stator passage until the particle enters the rotor passage. At the rotor inlet, the velocity is transformed onto the relative reference frame and nine equally spaced circumferential positions are assigned to the particle. The solution is continued as if nine particles were entering the rotor instead of just one. The particle conditions at the rotor inlet are dependent on the conditions assumed at the stator inlet. Therefore, the same procedure must be followed for every particle entering the stator. If 10 trajectories are considered in the stator passage, then this corresponds to 90 trajectories in the rotor passage. Statistical analysis of these calculations provides excellent impact and erosion data.

It is noted in Fig. 4 that most of the 1-μm ash particles avoid collision with the rotor blades. Less than 10 percent are captured by the blade surface. On the other hand, all of the 12-μm dolomite particles entering the rotor are involved in impacts (Fig. 5). In fact, due to their high inertia, they are turned so little that none of the initial impacts occur on the blade trailing edge. The top portions of Figs. 4 and 5 indicate the radial motions of the particles. Due to their very low inertia, the 1-μm particles display

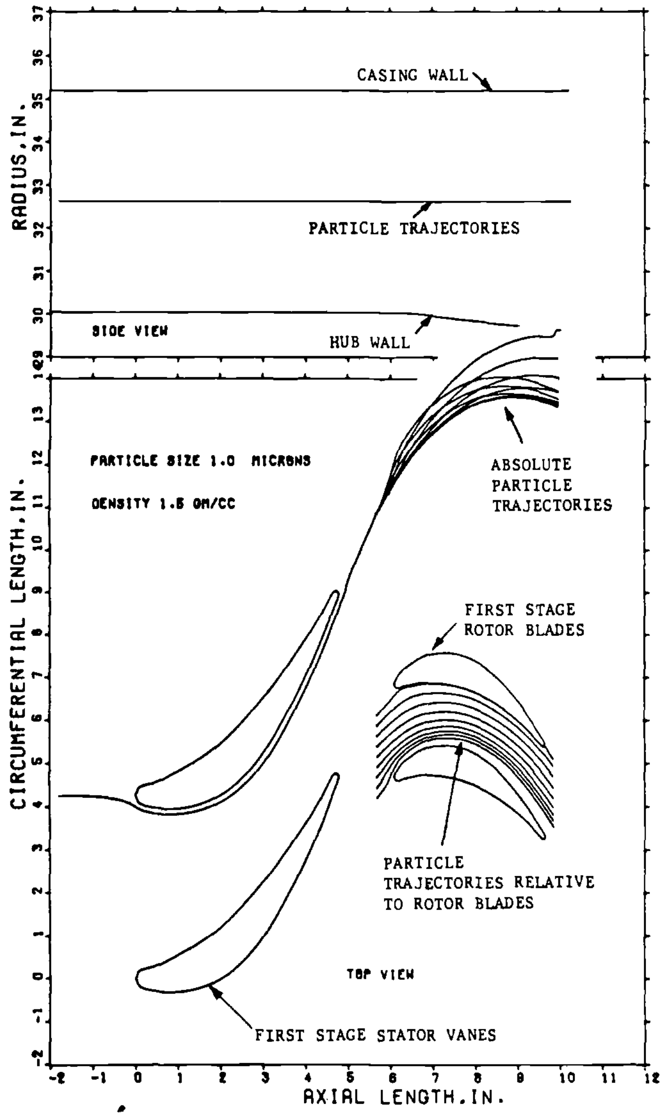

FIG. 4—*Trajectories of 1-μm ash particles through the stator and rotor passages (1 in. = 2.54 cm).*

very little centrifuging. The larger particles are thrown toward the casing wall because of the tangential velocity component. Indeed, the 12-μm dolomite particles shown in Fig. 5 undergo a considerable radial deflection. This centrifuging action is maximum at the stator exit plane, where the tangential velocities reach a maximum.

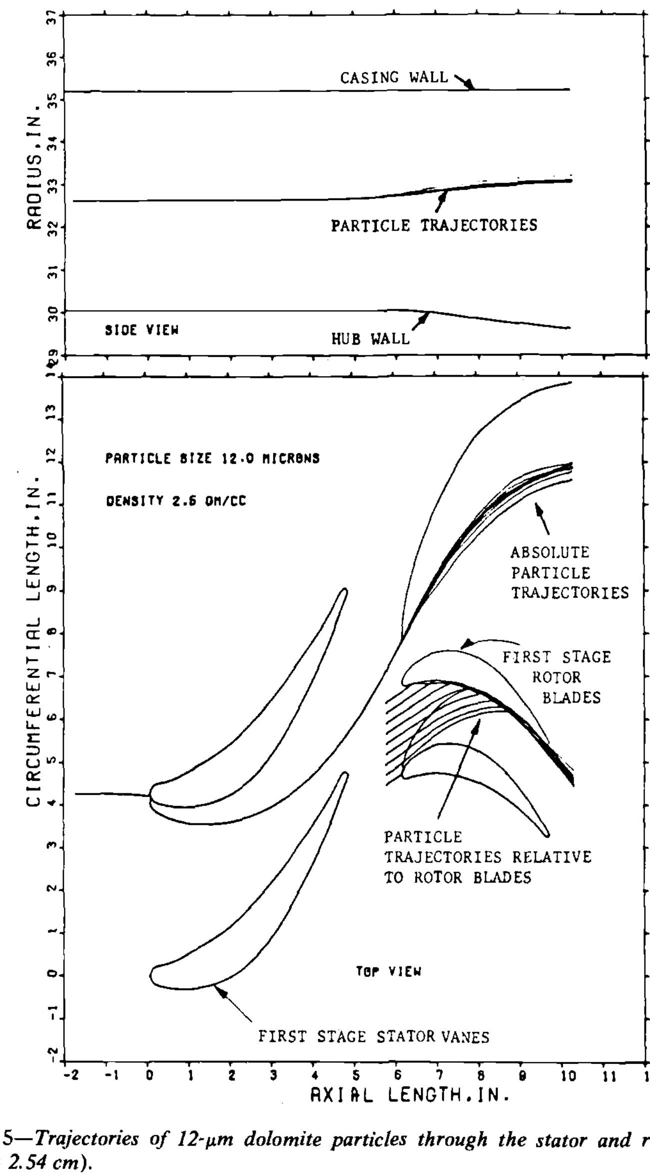

FIG. 5—*Trajectories of 12-μm dolomite particles through the stator and rotor passages (1 in. = 2.54 cm).*

Figures 6 and 7 give the capture efficiencies in the stator and the rotor, respectively. Since greater turning is involved, more particles are captured by the rotor blades than by the stator vanes. Particles of 1 and 3 μm have relatively small capture efficiencies (less than 15 percent in the stator and less than 30 percent in the rotor). For larger particles, the impact percentages increase rapidly. All of the dolomite particles having diameters

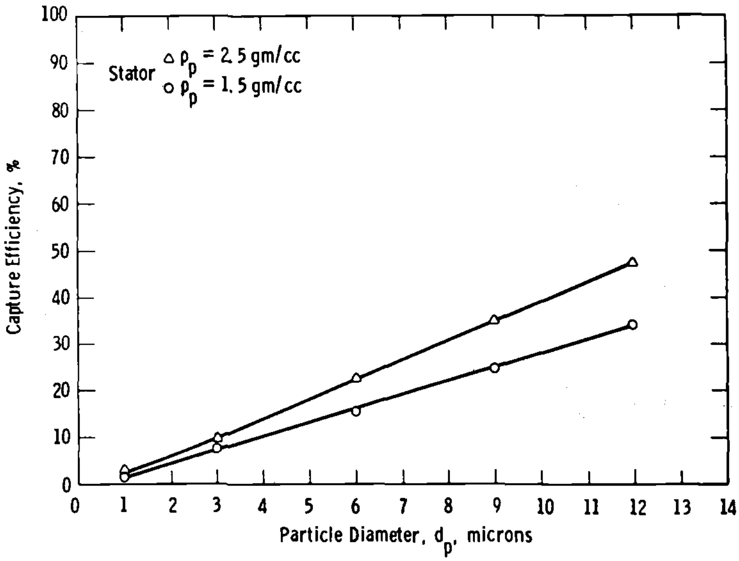

FIG. 6—*Stator capture efficiency as a function of particle size.*

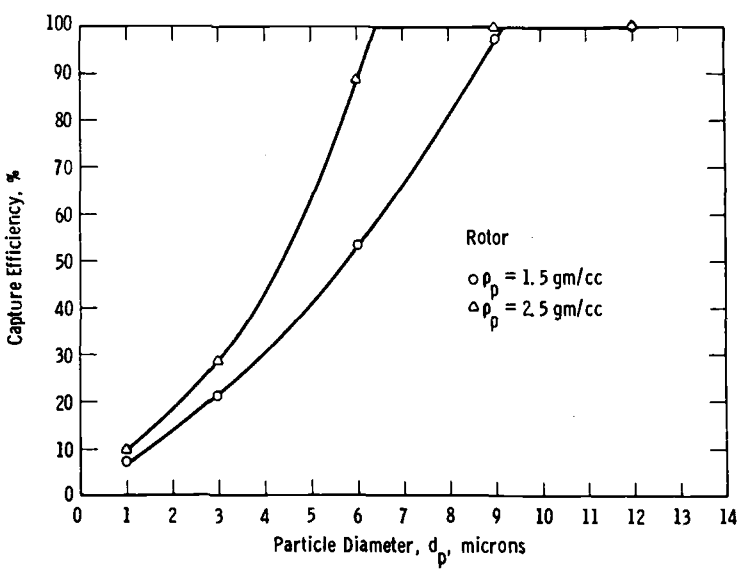

FIG. 7—*Rotor capture efficiency as a function of particle size.*

larger than 6 μm and all of the ash particles having diameters larger than 9 μm collide with the rotor blade's pressure surface. Some of these large particles may hit both surfaces of the blade. Otherwise, the suction surface is essentially impact-free.

Particle velocities corresponding to the first impacts follow trends similar to the pressure surface gas velocities. The deviation increases as the particle size increases. In general, particles hit the blade nose at velocities close to the gas velocity relative to the blade. Very near the leading edge there is a deceleration owing to the stagnation of the gas flow. Following the stagnation region, the impact velocities increase due to the gas acceleration. The particle velocities corresponding to the first impacts in the rotor passage are shown in Fig. 8 as a function of the axial distance from the blade leading edge. The corresponding curves in the stator are similar except that the impact velocities at the vane leading edge are lower [~150 m/s (~500 ft/s)] and the trailing-edge impact velocities are higher [~540 m/s (~1800 ft/s)].

The angle at which particles hit the surface affects the erosion damage. The angles corresponding to the first impacts are shown in Fig. 9 for the rotor pressure surface. It is noted that a small portion of the blade nose is subject to impacts at angles close to 90 deg. As one moves away from the leading edge, the angles corresponding to the first impacts drop sharply, and then they reach a fairly constant value. Figure 10 shows the effect of particle size and density on the trailing-edge angles of impact. The smaller particles (1 and 3 μm size) impact the blade trailing edge at small angles (1 to 4 deg). The larger particles approach the surface at sufficiently large angles so that the effect of boundary layers can be neglected for the first impacts. For instances, the angles corresponding to the first impacts of the 12-μm dolomite particles are everywhere above 30 deg. The repeated impacts following the first one, however, may cause the particles to spend considerable time under the viscous layer and may render them ineffective for erosion after several impacts.

The impact angles in the stator are smaller because the gas is turned through a smaller angle in the stator passage. The trailing-edge impact angles are shown in Fig. 11 as a function of particle size.

Erosion Damage Calculation

Erosion Model

Our analytical model is based on the fact that perfectly ductile materials undergo weight loss by a process of plastic deformation. This type of wear exists if particles strike a body at an acute angle, scratching out some material from the surface. On the other hand, perfectly brittle materials fracture immediately after elastic deformation, and thus they suffer mate-

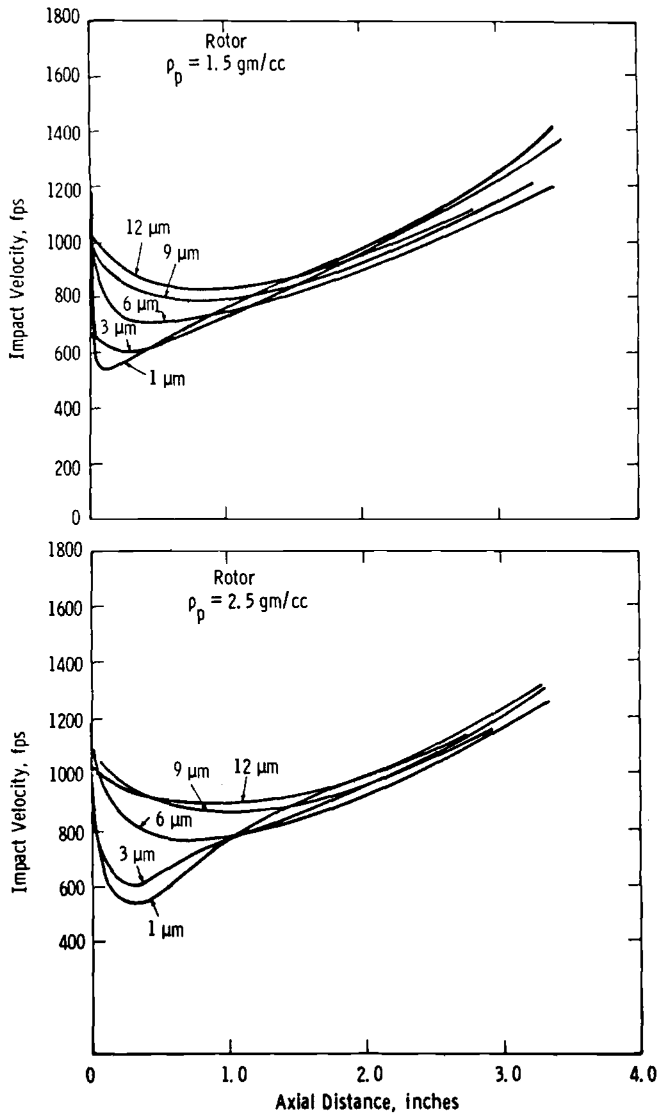

FIG. 8—*Particle impact velocities in rotor as a function of axial position (1 ft/s = 0.3048 m/s; 1 in. = 2.54 cm).*

rial loss through cracking and spalling of surface material at normal impacts. All materials to a certain extent exhibit a combination of ductile and brittle behavior. Nominally *brittle* materials such as glass and ceramics have a maximum erosion angle which is close to 90 deg. The maximum erosion angles for most other materials, however, range from very small

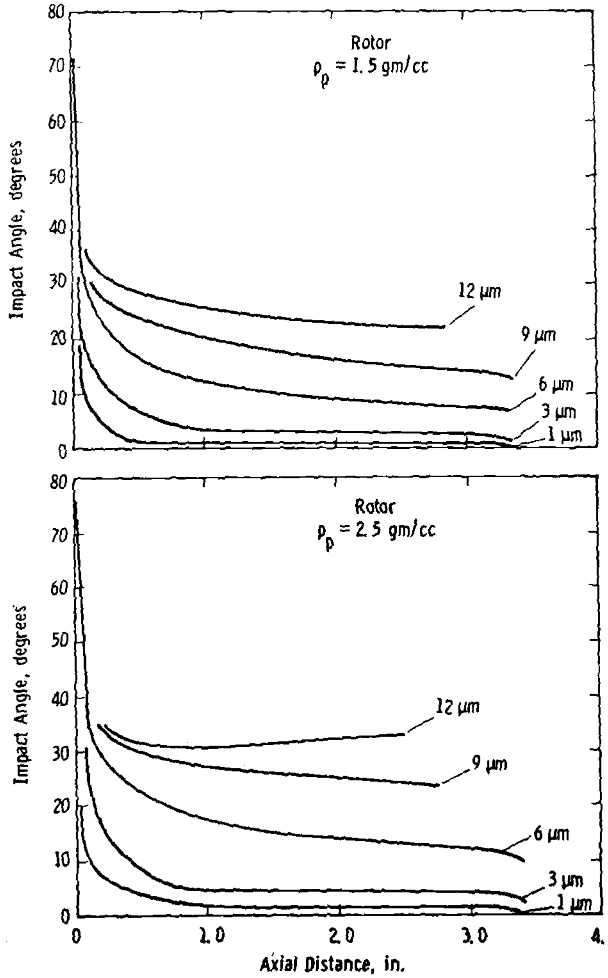

FIG. 9—*Particle impact angles in rotor as a function of axial position (1 in. = 2.54 cm).*

angles to 90 deg, depending on the ductile-brittle nature of the material structure.

According to Bitter [6], erosion damage can be expressed by

$$W = \frac{1}{2} M \frac{(V^2 \cos^2\beta - V_t^2)}{\phi} + \frac{1}{2} M \frac{(V \sin\beta - V_{el})^2}{\epsilon} \tag{14}$$

where

W = volume of material lost due to erosion,
M = total mass of impinging particles,

V_{el} = velocity of a single particle corresponding to elastic deformation,
ϵ = energy needed to remove a unit volume of material from the surface by brittle erosion,
V = particle impact velocity,
ϕ = energy needed to scratch a unit volume of material from the surface by ductile erosion,
β = angle of impingement, and
V_t = residual horizontal component of velocity after impact.

The first term represents the ductile mode of erosion. The second term is the brittle mode of erosion. Generalizing the velocity exponents as m_1 and m_2 and introducing coefficients K_1 and K_2 to define the amplitude of ductile and brittle modes, respectively, we obtain the following expression

$$E = K_1 [(V \cos\beta)^{m_1} - v_t^{m_1}] + K_2 (V \sin\beta - V_{el})^{m_2} \qquad (15)$$

where $E = W/M$, volume removed per unit mass of particles (specific erosion rate). Equation 15 can be rewritten as

$$E = K_1 (V \cos\beta)^{m_1} \left[1 - \left(\frac{v_t}{V \cos\beta} \right)^{m_1} \right] + K_2 (V \sin\beta - V_{el})^{m_2} \qquad (16)$$

In this expression, the term $v_t/V \cos\beta$ is immediately recognized as the tangential restitution ratio. This ratio is very difficult to determine due to

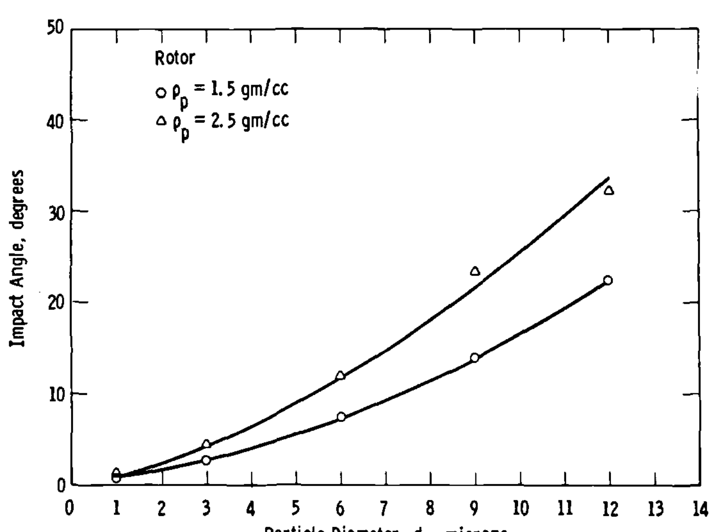

FIG. 10—*Trailing-edge impact angles in rotor as a function of particle size.*

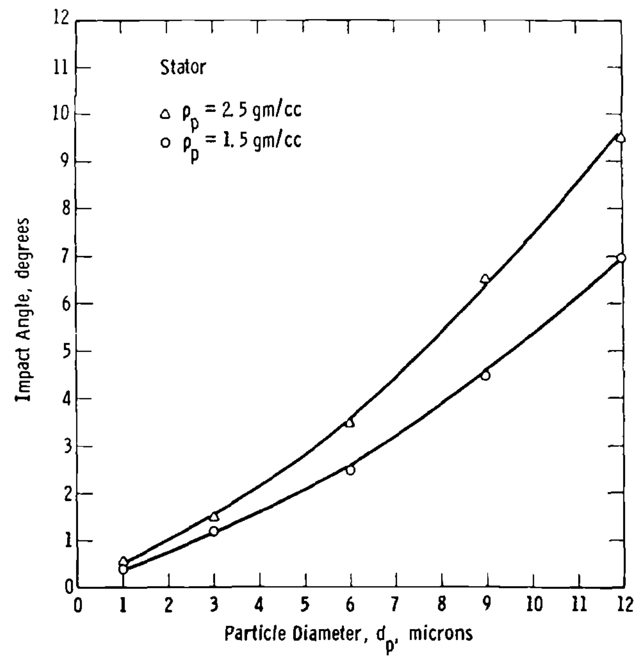

FIG. 11—*Trailing-edge impact angles in stator as a function of particle size.*

the multitude of variables involved. The fact that the particles actually strike a surface which has been roughened by other particles suggests that a wide variety of "true" angles will result even for the particles impacting at the same apparent angle with respect to the previously smooth surface. Therefore, determination of the restitution ratio is a statistical process. For a given erosion system, it is reasonable to assume that the tangential restitution ratio is by and large a function of impact velocity, impact angle, and various material properties. Lumping the material properties into the coefficient K_1 and the velocity into the exponent m_1, the expression in the brackets can be made a function of the impact angle only. Thus

$$E = K_l\,(V\cos\beta)^{ml} f(\beta) + K_2\,(V\sin\beta - V_{el})^{m2} \tag{17}$$

$f(\beta)$ should be chosen in such a way that the resulting curve of erosion rate as a function of angle fits the experimental results. For ductile materials, this curve is zero at $\beta = 0$ and reaches a maximum at an angle β_{max} dictated by the specific erosion conditions. At 90 deg, the only contribution is made by the brittle mode of erosion (deformation wear). A function of angle $f(B)$ that satisfies these conditions can be written as follows

$$f(\beta) = \begin{cases} \sin n\beta \text{ for } \beta \leq \beta_0 \\ 1 \quad \text{for } \beta > \beta_0 \end{cases} \tag{18}$$

where β_0 is the reference angle which is a function of β_{max}, K_1, K_2; and V_{el}; n is equal to $\pi/2\beta_0$.

The energy thresholds for particles smaller than 20 μm were reported by Smeltzer et al [7]. These thresholds are very small compared with the velocities encountered in the gas turbine. Therefore V_{el} can be neglected. Substituting Eq 18 into Eq 17, setting V_{el} equal to zero, and assuming the same velocity exponent for both ductile and brittle modes ($m_1 = m_2 = m$), the following is obtained

$$E = K_1\,(V\cos\beta)^m \sin n\beta + K_2\,(V\sin\beta)^m \text{ for } \beta \leq \beta_0 \tag{19}$$

$$E = K_1(V\cos\beta)^m + K_2\,(V\sin\beta)^m \text{ for } \beta \geq \beta_0$$

A typical erosion curve corresponding to Eq 19 is illustrated in Figure 12. The coefficients K_1 and K_2, the velocity exponent m, and the maximum erosion angle β_{max} must be determined experimentally. First the

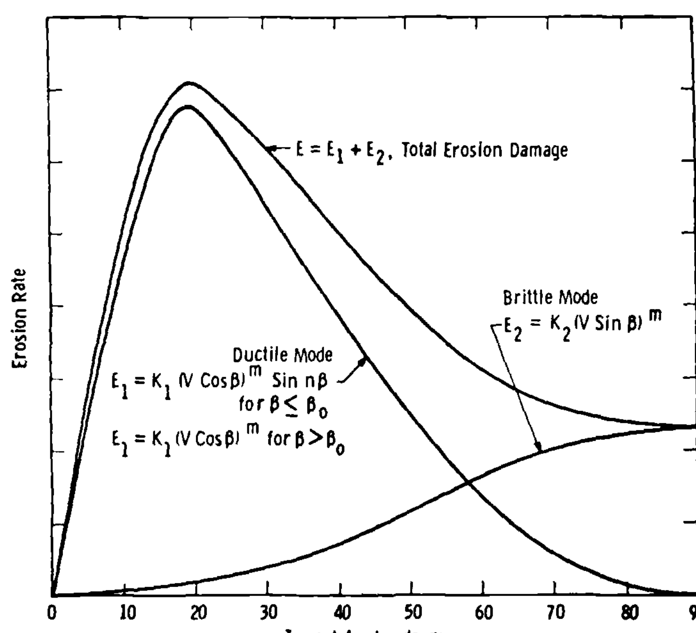

FIG. 12—*Erosion model for ductile materials.*

velocity exponent and the maximum erosion angle are determined. Erosion data at 90 deg are then used to calculate K_2. The remaining parameters K_1, n, and β_0 are all interdependent and can be obtained by a numerical iteration process. For $K_1 > K_2$ (typical for ductile materials), $\beta_{max} < \beta_0$.

The computer model allows the angle of maximum erosion damage to be a parameter so that the sensitivity of erosion damage to the "ductile-brittle" response of the blade and vane materials can be seen. No data on relevant materials, with surface conditions relevant to various stages in the life of the blade, were available at the time the paper was written. Recent work by Dr. Frederick Pettit of United Technology for the Electric Power Research Institute and by Drs. A. Levy (Lawrence Berkeley Laboratory) and I. Wright (Battelle Columbus Laboratories) indicates that the deposit, oxide scale, superalloy structure that the ash particles bombard displays erosion characteristics different from either a ductile metal or a smooth ceramic surface as one might expect. To emphasize this point, Fig. 13 compares the damage done by a distribution of dolomite sulfur-sorbent particles smaller than ~ 5 μm in aerodynamic diameter impacting, at 183 m/s (600 ft/s), a 304 stainless steel target and a turbine blade alloy. The blade target was cut from a Udimet 710 blade removed from a turbine after 9000 h of turbine operation. The difference in the mechanism and amount of damage is apparent.

The experimental data for the numerical erosion predictions of this paper are taken from Finnie et al [*9*]. A velocity exponent of 2.5 was assumed so that the velocity effects will be the same. Table 1 lists the erosion coefficients K_1, K_2, and the reference angle β_0 calculated from the experimental data given for silicon carbide particles eroding a nickel cobalt alloy with 99 percent (Ni + Co). In Table 1 the erosion level corresponding to the maximum erosion angle is kept constant. For the three ductile cases, the brittle mode of erosion (second term on the right-band side of Eq 19) is assumed to be identical. The ductile mode of erosion (first term in Eq 19) is assumed to disappear for the case of $\beta_{max} = 90$ deg.

Comparison of data for silicon carbide erosion in Ref *9* with data for coal ash erosion in Ref *8* shows that silicon carbide particles are approximately 25 times as erosive as ash particles. This ratio was used to extend the predictions to coal ash erosion.

The assumption that coal ash is 1/25th as erosive when bombarding turbine components as silicon carbide bombarding nickel is simplistic. An accurate assessment of the tolerance of a large turbine to particles resulting from a particular coal processing system requires the determination of the erosion damage response of blade materials having the oxide and deposit coatings that are typical of their running condition. These blade materials must be bombarded by particles which have seen temperature-time and chemical concentrations that are typical of the fuel processing and combustion system being considered. The needed data can best be obtained from

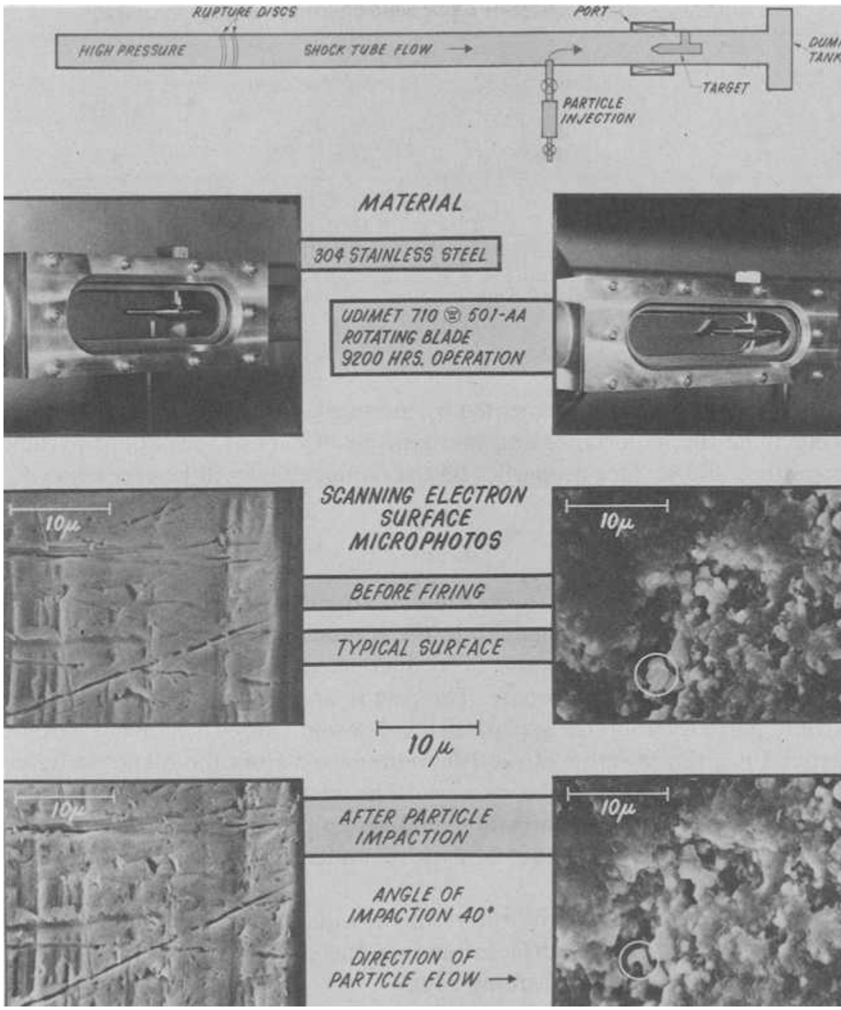

FIG. 13—*Comparison of damage to stainless steel and oxidized turbine alloys caused by impaction by a distribution of dolomite particles smaller than 5 μm in diameter.*

controlled laboratory cascade tests of sufficient length to accurately establish rates of attack. Because the concentrations of "glue forming" chemical contaminants are important to the character of the scale and deposits formed on the blading and because the chemical reactions forming the "glues" are pressure dependent, these tests must be carried out at pressure or with appropriate adjustment of the concentrations of the important chemical reactants (sodium chloride, potassium chloride, sulfur ozide, and hydrogen chloride primarily). These tests are difficult and will be expen-

TABLE 1—*Erosion coefficients for four values of maximum erosion angle.* [a]

β_{max}, deg	β_0, deg	Erosion Coefficient, $\frac{mm^3/g}{(ft/s)^m}$ K_1	K_2
10	10.3	7.44×10^{-8}	2.4×10^{-8}
20	22.7	8.35×10^{-8}	2.4×10^{-8}
30	45.3	1.12×10^{-7}	2.4×10^{-8}
90	90	0	7.18×10^{-8}

[a] Velocity exponent (m) of 2.5 was assumed.

sive. They should be supplemented by incisive laboratory scale experiments to elucidate the importance and mechanisms of deposit formation, particle properties, and surface properties on the damage that will be experienced.

Erosion Damage Results

The erosion predictions in the stator and rotor have been obtained by incorporating the erosion model into the computer program that calculates the particle trajectories. It has been assumed that the dolomite and ash particles have the same erosivity. The results are presented both for silicon carbide particles and coal gas particles. Erosion caused by silicon carbide particles is given in terms of the volume removed from the blade per gram of the particles entering the passage. The results modified for coal gas particles are reported in term of metal recession rates based on an inlet particle concentration of 0.00023 g/m^3 (standard) [0.0001 grain/ft^3 (standard)] of expansion gas.

In both the stator and the rotor, the erosion damage is predominantly confined to the pressure surfaces because the suction surfaces are free of impacts except around the leading edges.

The authors would caution that the simplified two-dimensional model presented in this paper for blade erosion midway between the root and the tip of the first-stage blading is not accounting for the particle concentrating effects of the secondary flows. Work to develop the model to calculate these effects has been reported by Dr. A. Ulke of our laboratories. The extension of this work to quantitative particle concentrations is important to establish an accurate particulate tolerance of a turbine.

Stator Erosion

The stator erosion caused by the 1.5 g/c^3 ash particles, $\beta_{max} = 20$ deg, is shown in Fig. 14 as a function of the axial distance from the leading

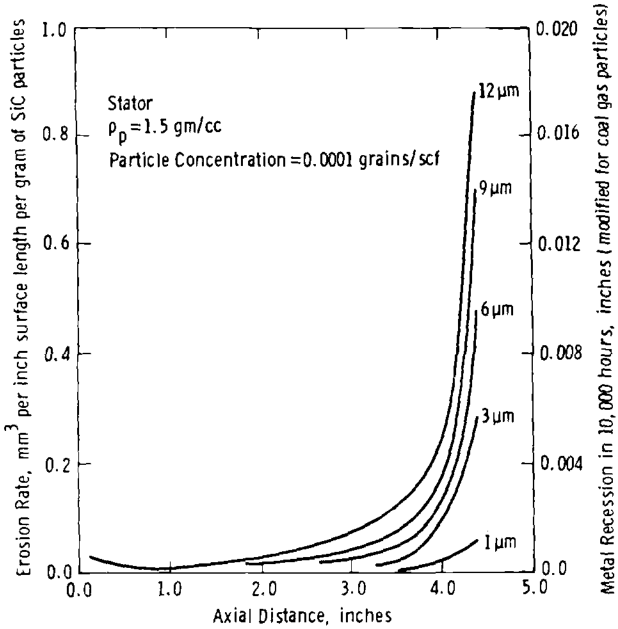

FIG. 14—*Erosion rate in stator as a function of axial position [1.5-g/c³ particles; 1 in. = 2.54 cm; 1 grain/ft³ (standard) = 2.29 g/m³ (standard)].*

edge of the stator vane. Damage caused by the silicon carbide particles is given on the left axis. This damage is expressed as the metal volume (mm^3) removed per inch of vane surface length per gram of particles entering one stator passage. Therefore, each curve integrated over the vane length gives the total material loss per vane (mm^3/g). These results can be readily converted to metal recession rates from the assumed particle concentration of 0.00023 g/m^3 (standard) [0.0001 grain/ft^3 (standard)] and the known geometry of the passage. The axis on the right indicates the amount of metal recession after 10000 h of coal gas operation. It is noted that the erosion magnitudes are strongly dependent on particle size. However, the trends are very much the same. There is very little erosion around the leading edge [less than 0.0025 cm (0.001 in.) of metal recession]. Erosion rates remain low for most of the vane surface, but they sharply increase to critical levels very near the trailing edge. The small amount of damage on the vane nose is not surprising; although the impact angles are large, the velocities are relatively low [~150 m/s (~500 ft/s)] in this region. As one moves away from the leading edge, the impact velocities first decrease and then increase gradually, whereas the impact angles rapidly decrease. The combined result is a net decrease in erosion at first. Farther on near the trailing edge, however, the impact velocities attain very high values [420 to

540 m/s (~ 1400 to 1800 ft/s), depending on size and density], and considerable damage is done. The effect of the maximum erosion angle of the surface material on the trailing edge erosion is shown in Fig. 15 for the ash particles.

Rotor Erosion

The erosion curves of the rotor blades for ash particles are given in Fig. 16 for β_{max} = 20 deg. There is considerable damage on the blade nose due to high impact velocities [~ 300 m/s (~ 1000 ft/s)] and large impact angles (near 90 deg). Following the leading edge, the erosion level drops

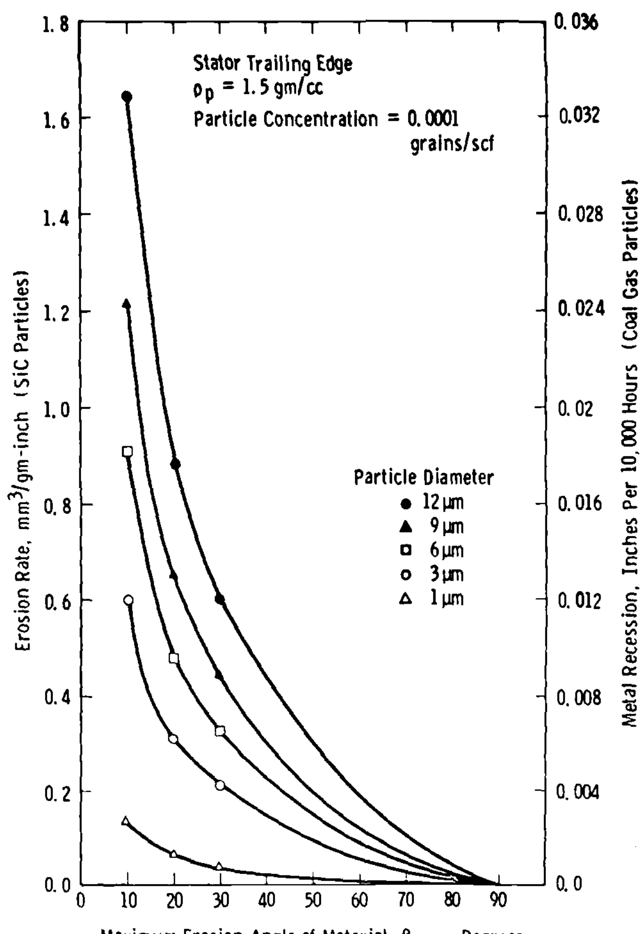

FIG. 15—*Trailing-edge erosion rate in the stator as a function of maximum erosion angle (ash particles) [1 in. = 2.54 cm; 1 grain/ft³ (standard) = 2.29 g/m³ (standard)].*

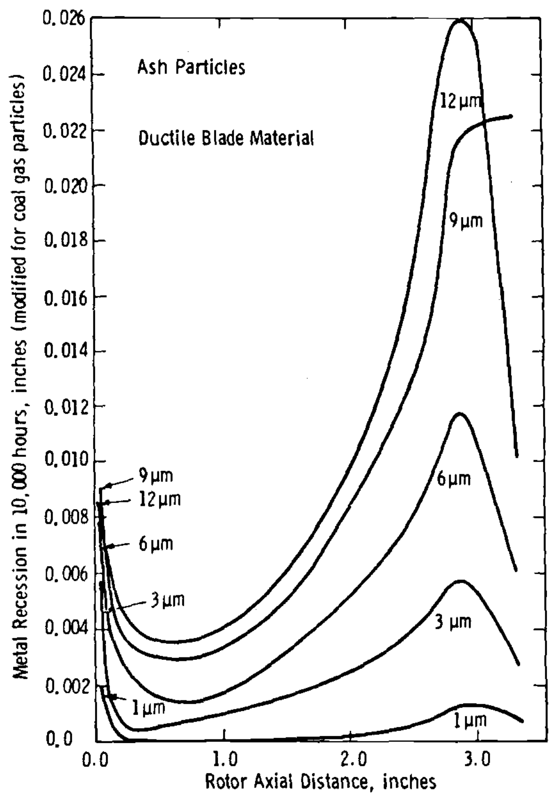

FIG. 16—*Erosion rate in rotor as a function of axial position (1.5 g/c³ particles) [1 in. = 2.54 cm; 1 grain/ft³ (standard) = 2.29 g/m³ (standard)].*

primarily because of a decrease in the number of impacts. For 1- and 3-μm particles (and for 6μm particles to an extent), this drop is more pronounced because the impact angles associated with these particles fall below 10 deg; in addition, there is a considerable decrease in the impact velocities. Farther away from the leading edge, erosion rates start increasing again. This increase is due to increasing velocity and frequency of impacts. It is interesting to see that the location of maximum erosion is rather sensitive to the size and the density of particles. Damage associated with 1- and 3-μm particles peaks slightly ahead of the trailing-edge point because most of these particles, owing to their low inertia, miss the edge of the blade. As the particle size (and thus its inertia) gets larger, the maximum erosion moves right up to the blade edge (9-μm ash particles). Further increases in size or density or both shift the maximum back toward the leading edge. Figure 7 provides an explanation for this behavior. All the ash particles larger than 9 μm hit the blade surface. Therefore additional increase in particle size does not increase the number of impacts but merely pulls the location of the first impact closer to the leading edge.

The rotor erosion primarily occurs at the leading and trailing edges of the blades. The dependence of the leading-edge erosion on the maximum erosion angle and the particle size is illustrated in Fig. 17 for the ash particles. For a given particle size, the erosion rate increases as the maximum erosion angle because the particles hit the blade leading edge at large angles.

In Figure 17, the erosion rates given on the left axis in terms of mm^3 per gram-inch do not provide a direct comparison between the stator and rotor erosion. These erosion rates are obtained per gram of silicon carbide particles entering the passage. Since there are approximately twice as many rotor blades as there are stator vanes, about twice as many particles will be present in each stator passage as in each rotor passage. This must be kept in mind when comparison is made between the stator and rotor blades.

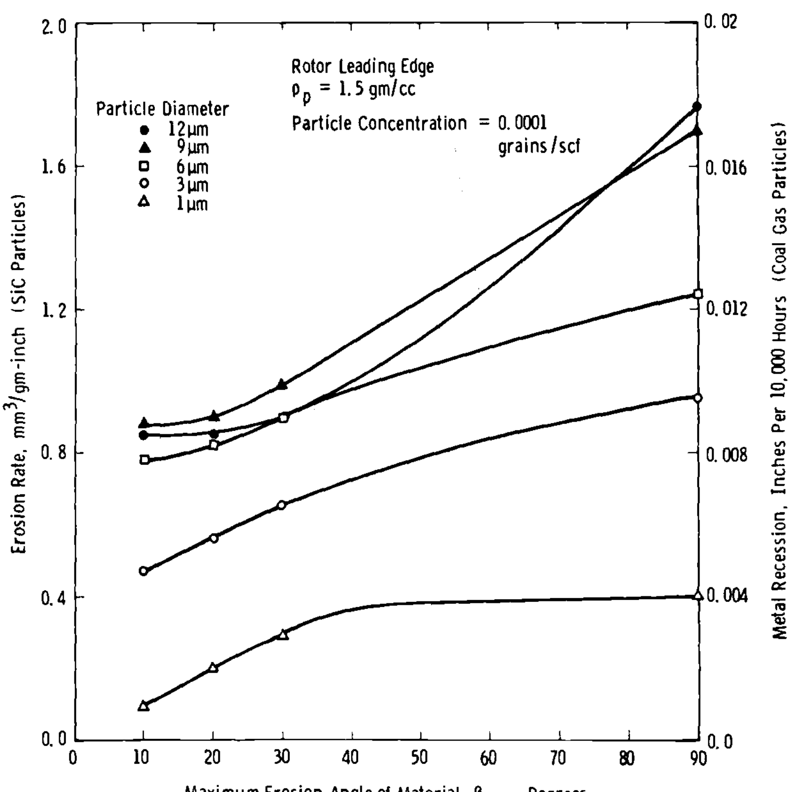

FIG. 17—*Leading-edge erosion rate in the rotor as a function of maximum erosion angle (ash particles) [1 in. = 2.54 cm; 1 grain/ft³ (standard) = 2.29 g/m³ (standard)].*

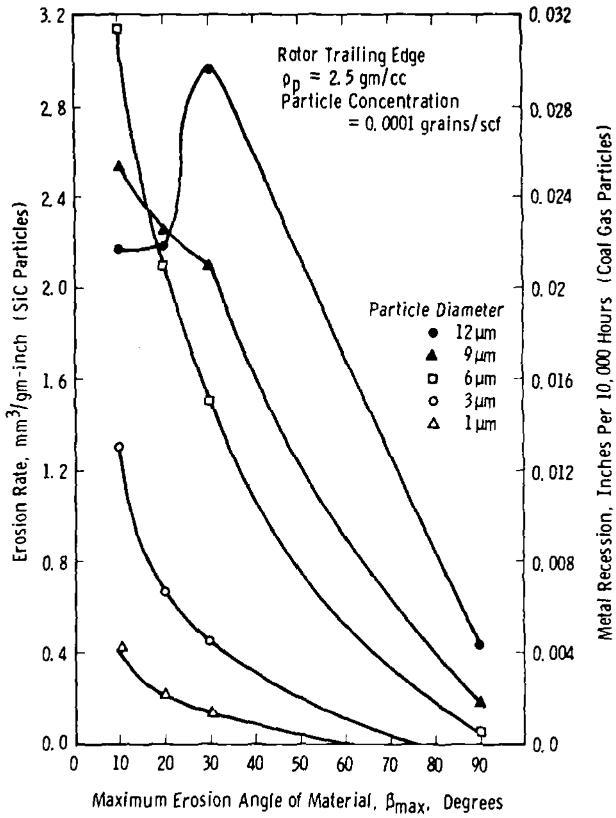

FIG. 18—*Trailing-edge erosion in the rotor as a function of maximum erosion angle (dolomite particles)* [*1 in. = 2.54 cm; 1 grain/(ft³ standard) = 2.29 g/m³ (standard)*].

The metal recession rates indicated on the right axis resolve this problem because they take into account the particle concentration.

The rotor blade trailing-edge damage is illustrated in Fig. 18 for 2.5-g/c³ dolomite particles. These curves are similar to the stator trailing-edge erosion. Since the impact angles are larger, however, the erosion rate corresponding to $\beta_{max} = 90$ deg is higher in the rotor. For the dolomite particles larger than 9 μm, materials with $\beta_{max} < 30$ deg suffer less erosion than materials with $\beta_{max} = 30$ deg because the impact angles for these particles are larger than 30 deg.

Turbine Tolerance to Expected Particle Distributions

In the preceeding pages, erosion predictions have been presented for discrete particle size and particle densities. However, the expansion gas in the actual turbine will contain a continuous spectrum of particles. The damage corresponding to this spectrum can be found by integrating the erosion curves presented earlier, using the particle size and density distribution expected in the expansion gas.

Figure 19 shows the particulate concentrations that are expected to result from various types of particulate cleanup systems based on the assumption that the particle loading at the entrance to the gasifier cyclone would contain 22.9 g/m^3 (standard) [10 grains/ft^3 (standard)].

Figure 20 shows the concentrations as a function of particle size that could be expected from various degrees of gas cleaning following the addition in the combustor of the air required to achieve a nominal turbine inlet temperature of 1100°C (2000°F).

Figure 21 presents the calculated metal recession in 10000 h of operation of the trailing edge of the first-stage stator vanes for these particle size distributions. No data are available to define the angle of maximum erosion damage for superalloys. Metallurgical opinion is that, because of the low ductility of these alloys, this angle might be betweeen 40 and 50 deg. If the assumption is correct, trailing-edge wear from expanding

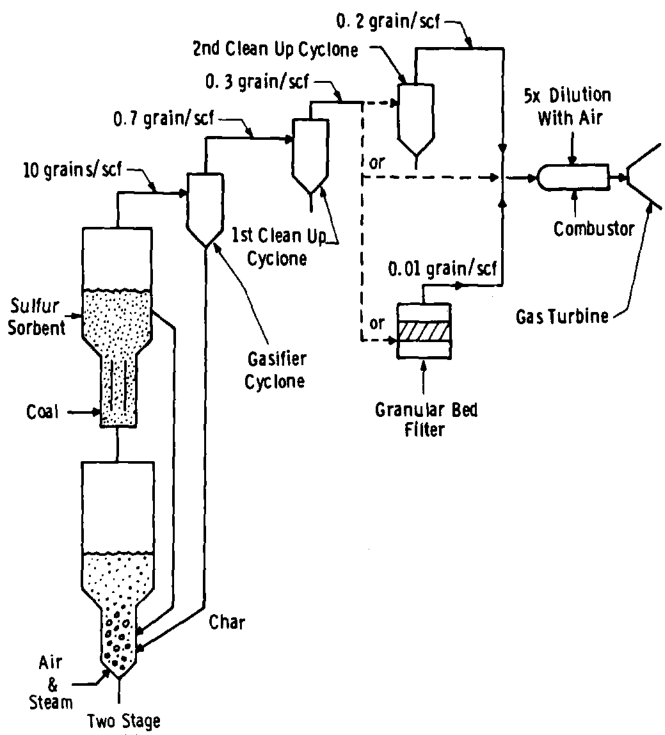

FIG. 19—*Particulate concentrations with various degrees of gas cleaning. (1 grain/ft^3 (standard) = 2.29 g/m^3 (standard)].*

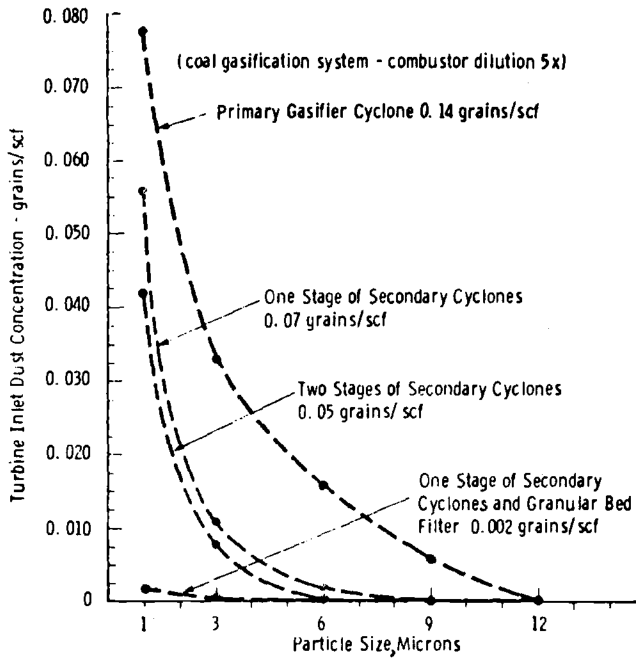

FIG. 20—*Particle size distributions at the gas turbine inlet corresponding to various particle cleanup systems. (1 grain/ft^3 (standard) = 2.29 g/m^3 (standard)).*

the gas cleaned only by the gasifier cyclone would exceed 2.5 cm (1 in.) in 10000 h of turbine operation. [Trailing-edge wall thicknesses in a turbine built to expand clean gas are about 0.25 cm (~0.1 in.) thick.] The first stage of cleanup would reduce wear to 0.5 cm (~0.2 in.) in 10000 h, while two stages of cyclone cleanup would result in 0.25 cm (~0.1 in.) wear in 10000 h. The use of a one-stage cyclone followed by a granular-bed filter would cut trailing-edge wear to about 0.013 cm (0.005 in.) per 10000 h, slightly in excess of the metal losses that occur by oxidation on the first-stage vanes.

The sensitivity of the first-stage rotor nose and the first-stage rotor blade trailing edge to erosion damage is compared with that of the first-stage stator trailing edge in Fig. 22 for a particulate level of 0.0046 g/m^3 (standard) [0.002 grain/ft^3 (standard)]. It appears that cleanup to this level of particulates—0.0046 g/m^3 standard [0.002 grain/ft^3 (standard)] in the turbine expansion gas—is needed for long life.

Conclusion

On the basis of our numerical results, we have shown that, from an erosion standpoint, satisfactory blade life can be obtained by cleaning the

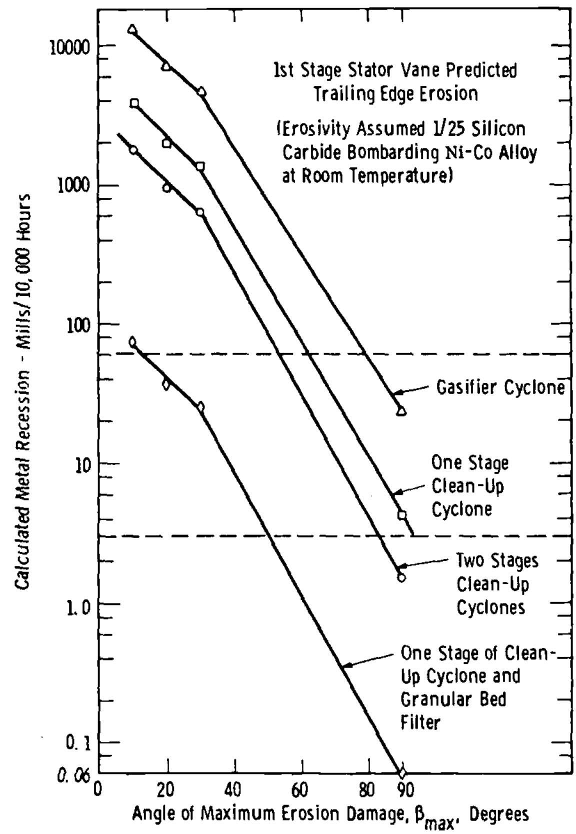

FIG. 21—*First-stage stator vane trailing-edge erosion.* (*1 mil* = *2.54* × *10*$^{-3}$ *cm*)

particulate concentration to 0.0046 g per standard cubic metre (0.002 grain per standard cubic foot), with particles larger than 6-μm diameter effectively removed.

The basic assumption made in the calculations was that coal ash and sulfur-sorbent particles will have, when impacting superalloy turbine materials under turbine conditions, 1/25th of the erosivity of silicon carbide particles impacting a nickel alloy at room temperature. The estimates do not account for the appreciable slowing of the 1- to 3-μm particles in the blade boundary layers before they reach the blading, even though these small particles account for most of the damage. The numerical results are in this way conservative.

Some indication of the sensitivity of turbine components to rebound data can be obtained from Fig. 23, which illustrates the damage done as a function of the number of impacts. For particles larger than about 5-μm

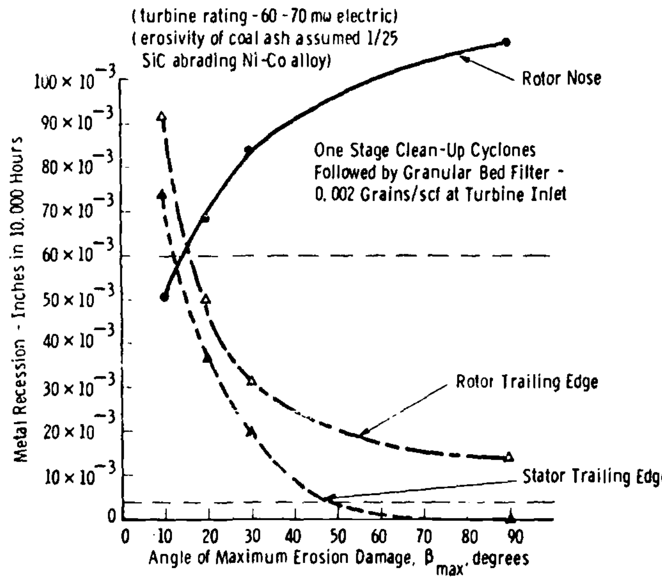

FIG. 22—*Sensitivity of gas turbine first-stage erosion to angle of maximum erosion damage [1 in. = 2.54 cm; 1 grain/ft^3 (standard) = 2.29 g/m^3 (standard)].*

diameter the total number of impacts on the blading is small and erosion damage varies by only a factor of two. The smaller particles effectively roll over the trailing-edge surfaces. These are particles for which this simple model is overpredicting velocity at impact due to boundary layer slowing.

The effect of boundary layer slowing of the small particles and the effect of the erosivity of coal ash relative to silicon carbide have been studied parametrically by Mr. Robert Wolfe of our laboratories for the particle size distributions that could be expected from various granular-bed and fabric filter gas cleaning systems. Figure 24 shows some of the results. Since the boundary layer varies in our turbines from 0 to about 1.27 mm (0.05 in.), it appears that blade life projections neglecting boundary layer slowing may result in erosion rates that are high by a factor of two to ten for particles smaller than 3-μm diameter.

For an accurate assessment of the erosion tolerance of a turbine, of course, actual data on the damage which coal gas particulates do to blade materials are needed.

Acknowledgments

For support of the work reported here, we gratefully acknowledge the Office of Coal Research, U.S. Department of the Interior, and the Energy Research and Development Administration (ERDA). The study was per-

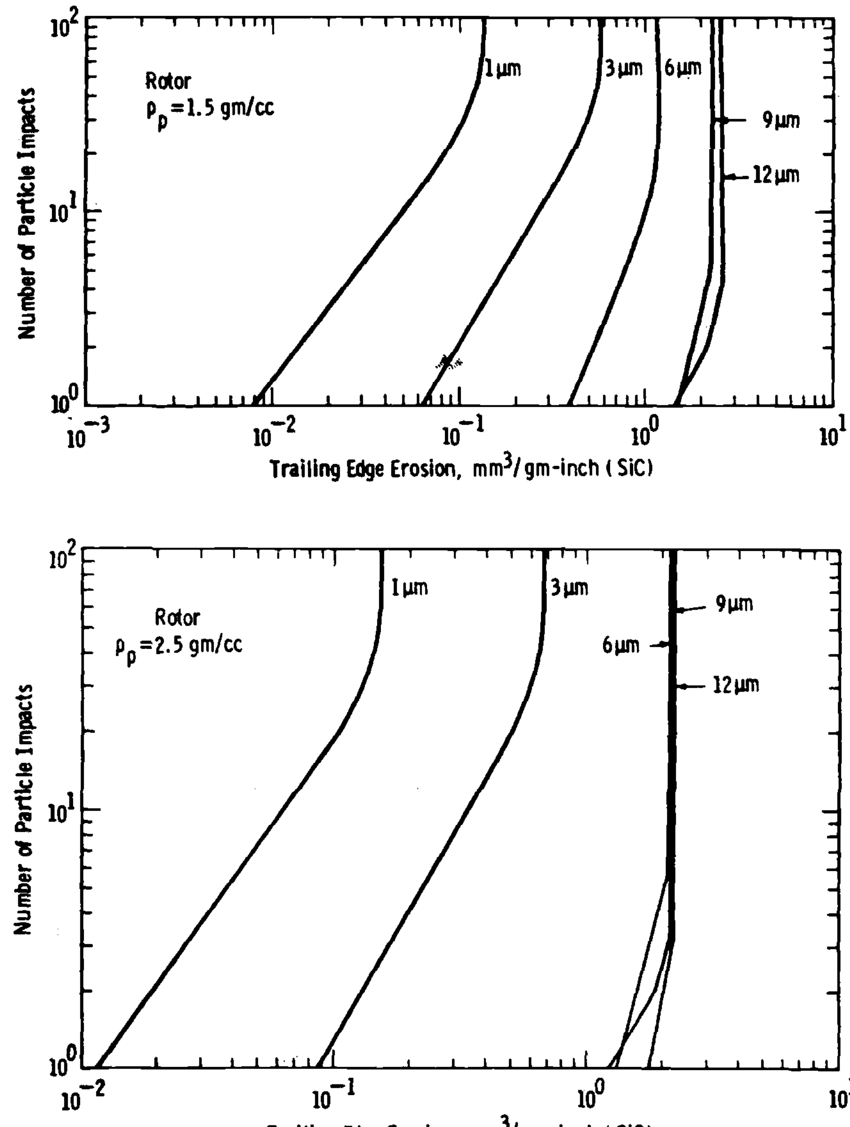

FIG. 23—*Sensitivity of trailing-edge rotor erosion to the number of particle impacts causing erosion damage.*

formed under ERDA Contract E (E9-18-1514), Advanced Coal Gasification System for Electric Power Generation.

The authors would like to acknowledge the pioneering work done by Dr. Tabakoff and his students at the University of Cincinnati demonstrating that modern computing techniques now make feasible the carrying out

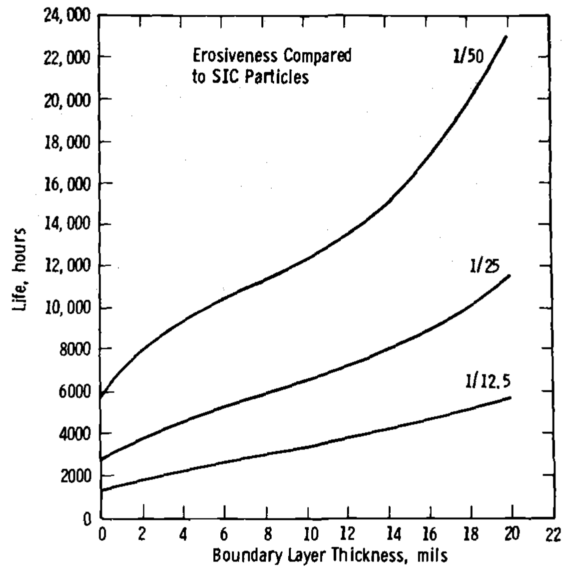

FIG. 24—*Turbine life for a particulate removal system with one stage of granular-bed filters (performance based on Westinghouse bench-scale experiments).*

of the complex calculations of gas flows, particle trajectories, and reaction between the particles and surfaces needed to be able to calculate erosion effects.

The contribution of this paper is in applying these methods to modern gas turbines for the purpose of clarifying the kinds of gas cleaning required for reliable operation of combined-cycle power plants and clarifying the type of experimental data required to calibrate these models so that the predictions are accurate.

Reference

[*1*] Katsanis, T., "Fortran Program for Calculating Transonic Velocities on a Blade-to-Blade Stream Surface of a Turbomachine," NASA T No. D-5427, National Aeronautics and Space Administration, 1969.

[*2*] Lapple, C. E. and Shepherd, C. B., *Industrial and Engineering Chemistry*, Vol. 32, No. 5, 1940, pp. 605-617.

[*3*] Morsi, S. A. and Alexander, A. J., "Theoretical Low Speed Particles Collision with Symmetrical and Cambered Aerofoils," ASME Paper 72-WA/FE-35, American Society of Mechanical Engineers, 1972.

[*4*] Hussein, M. F., "The Dynamic Characteristics of Solid Particles in Particulate Flow in Rotating Turbomachinery," Ph.D. thesis, University of Cincinnati, Cincinnati, Ohio, 1972.

[*5*] Ulke, A., "An Approximate Analysis of the Effect of Secondary Flows on the Motion of Particulates in an Axial Flow Turbine," Westinghouse Research Report (to be published).

[*6*] Bitter, J. G. A., "A Study of Erosion Phenomena," Part I, *Wear*, Vol. 6, 1963, pp. 5-21, and Part II, *Wear*, Vol. 6, 1963, pp. 169-190.
[*7*] Smeltzer, C. E., Gulden, M. E., and Compton, W. A., *Journal of Basic Engineering*. Transactions, ASME, Vol. 92, Series D, No. 3, Sept. 1970, pp. 639-654.
[*8*] Brasinikas, G., "Erosion by Particle Impact—Experiments with Callide Coal Ash," Austrailian Aeronautical Research Laboratories, 1970.
[*9*] Finnie, I., Wolak, J., and Kabil, Y., *Journal of Materials*, Vol. 2, No. 3, Sept. 1967.
[*10*] Grant, G. and Tabakoff, W., *Journal of Aircraft*, Vol. 12, No. 5, May 1975, pp. 471-478.
[*11*] Wolfe, R., "Gas Turbine Erosion Analysis," Westinghouse Research Laboratories, Pittsburgh, Pa., private communication.
[*12*] Ulke, A. and Rowleau, W. T., "The Effect of Secondary Flows on Turbine Blade Erosion," ASME Paper 76-GT-74, American Society of Mechanical Engineers, 1976.

Liquid Drop Impingement

M. Rosenblatt,[1] *Y. M. Ito,*[1] *and G. E. Eggum*[1]

Analysis of Brittle Target Fracture from a Subsonic Water Drop Impact

REFERENCE: Rosenblatt, M., Ito, Y. M., and Eggum, G. E., "**Analysis of Brittle Target Fracture from a Subsonic Water Drop Impact,**" *Erosion: Prevention and Useful Applications, ASTM STP 664,* W. F. Adler, Ed., American Society for Testing and Materials, 1979, pp. 227-254.

ABSTRACT: The erosive damage of an infrared transparent material by a subsonic water drop impact has been numerically simulated. The important early-time pressure loading characteristics from a water drop impact are discussed, and the predicted target damage (in terms of fracture patterns) is presented for variations in material flaw size, material gain size, and impact velocity.

KEY WORDS: fracture, microphysical failure model, subsonic erosion, water drop impact, numerical simulation, erosion

There is a need for substantially improving the resistance of infrared (IR) transparent windows to optical damage resulting from subsonic impacts [$V_0 \leq 366$ m/s (1200 ft/s)] of rain drops. Such damage is usually referred to as subsonic erosion, although it differs from more conventional erosion in that significant optical damage occurs before there is any mass loss from the surface. The apparent reason for the optical damage is internal cracking, which causes loss of transmittance as well as degradation of optical quality.

Erosive damage of optically transparent materials by water drop impacts has been experimentally studied [*1-3*][2] and data have been obtained regarding the optical transmission loss through specific materials subjected to specific erosive environments. However, it is difficult to generalize from the data because of the complex nature of the phenomena involved.

This paper reviews an investigation[3] which had the following specific objectives:

1. To identify the mechanisms responsible for internal crack formation and propagation in IR windows subjected to subsonic rain erosion.

[1] Senior technical staff, California Research & Technology, Inc., Woodland Hills, Calif. 91367.

[2] The italic numbers in brackets refer to the list of references appended to this paper.

[3] The current work has been sponsored by the Air Force Materials Laboratory, Wright-Patterson AFB, Ohio, and the Office of Naval Research, Washington, D.C.

2. To determine the sensitivity of these mechanisms to basic parameters.

The initial phase of the program was reported in Ref *4*. Tensile crack initiation and propagation were treated in that study, and the final predicted crack patterns were used as a measure of target damage. Target damage sensitivity to elastic and tensile failure properties, impact velocity, density, target toughness, and variations in numerical cell size was studied for 21 cases.

In the current study [*5,6*], the primary focus was on identifying the relationship between target damage and *microscopic* material parameters such as grain and flaw size.

The approach is based on developing an analytical loading model of water drop impact and subsequent numerical code solutions of target response using the WAVE-L code with a microphysical crack propagation model. (WAVE-L is a 2-D, Lagrangian, finite-difference code based on the HEMP scheme [*7*].) Figure 1 schematically indicates the general approach.

An analytical pressure loading model for simulating particle impacts has been developed and is discussed in detail in Ref *5*. This impact model specifies the loading pressure on the target surface as a function of radius from the impact point and time, $P(r,t)$. Note that this analytical loading model is based on detailed 2-D WAVE-L numerical calculations of spherical water drops on rigid surfaces. The rigid surface approximation is valid when the target surface deflection is negligible compared with the drop radius. For brittle materials, this condition will be satisfied if the target material impedance (density $\times$ dilatational wave speed) is much greater than the water impedance. The zinc selenide targets described in this report have an impedance which is 14 times greater than water.

The impact loading pressures are used as the loading boundary condition for the axisymmetric numerical solutions in the target. These solutions provide the dynamic stress, strain, and velocity fields, including the effects of crack propagation.

The target material damage is governed by a microphysical crack propagation model involving the flaw size and grain size as material parameters (see Ref *5*). Note that the crack propagation characteristics are an important feature in determining the dynamic stress field. Thus, the stress, strain, and velocity fields are intimately connected to the specific microphysical failure model assumed for the target material.

The important early-time surface pressure loading from a water drop impact is discussed in the following section. Later, the *predicted target damage* (in terms of fracture pattern), is discussed for variations in

1. material flaw size,
2. material grain size, and
3. impact velocity.

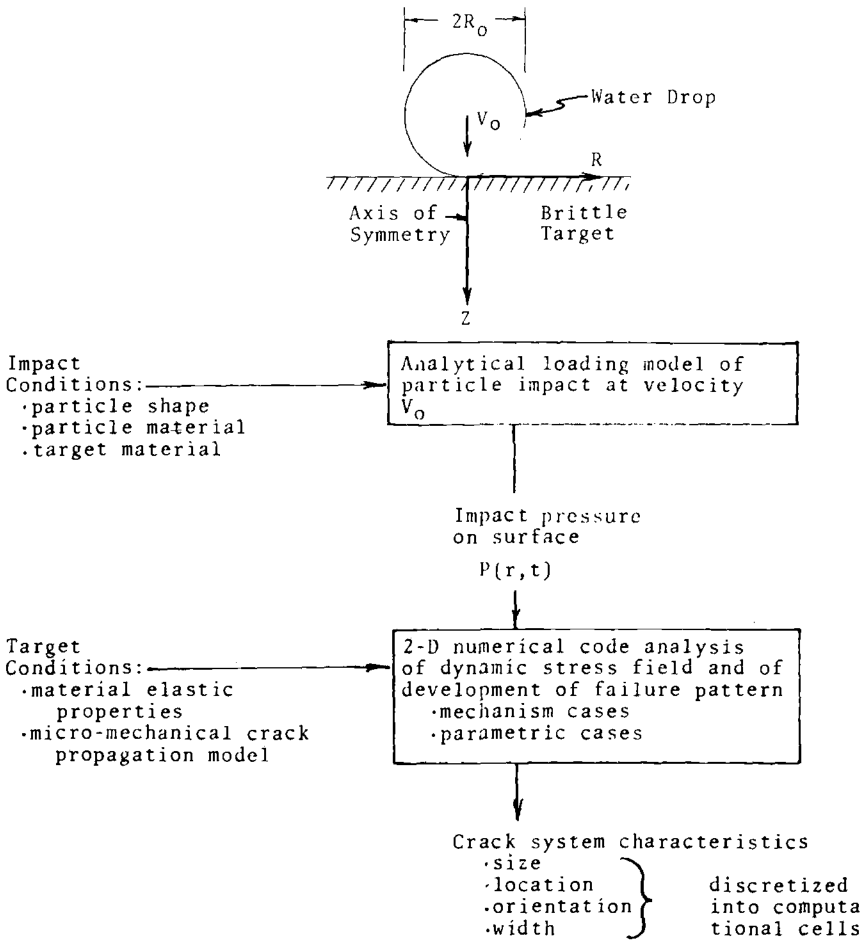

FIG. 1—*Steps involved in analytical approach.*

Water Drop Impact Loading at Early Times

Detailed numerical calculations of 206- and 335-m/s (675 and 1100 ft/s) water drop impact on rigid targets were reported in Ref *4*. These calculations predict the nature of the water drop deformation as well as the pressure loading on the target front surface, $P(r,t)$. For example, Fig. 2 shows the computational grid and velocity field at 0.24 μs for the 335-m/s (1100 ft/s) impact case with a 1-mm-diameter water drop. Figure 3 shows the velocity fields at about 0.5 and 1.2 μs. Figure 4 shows pressure-radius loading profiles on the target surface at various times for the 206-m/s (675

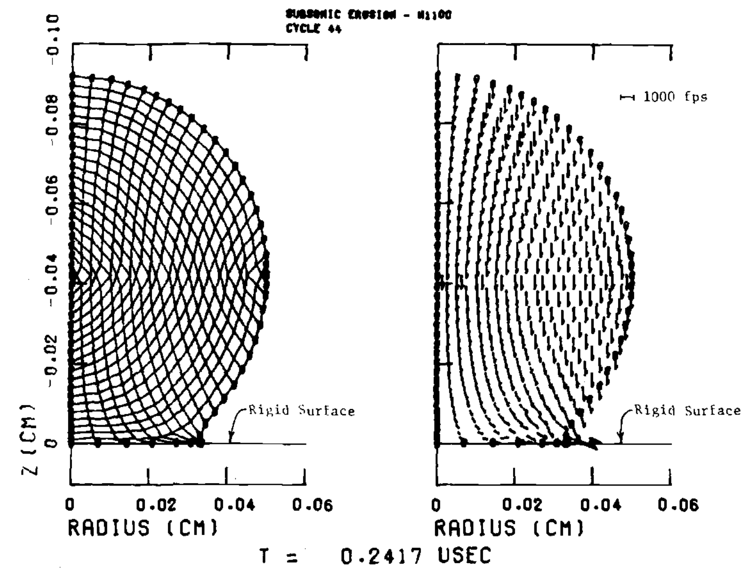

FIG. 2—*Grid configuration and velocity field for 335-m/s (1100 ft/s) impact of a 1-mm water drop on a rigid surface at 0.24 µs.*

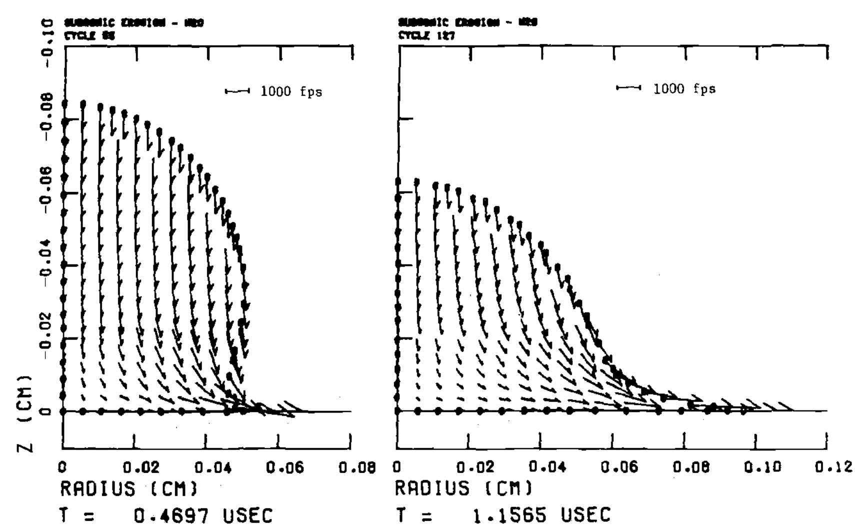

FIG. 3—*Velocity field for 335-m/s (1100 ft/s) impact of 1-mm water drop on rigid surface at 0.47 and 1.16 µs.*

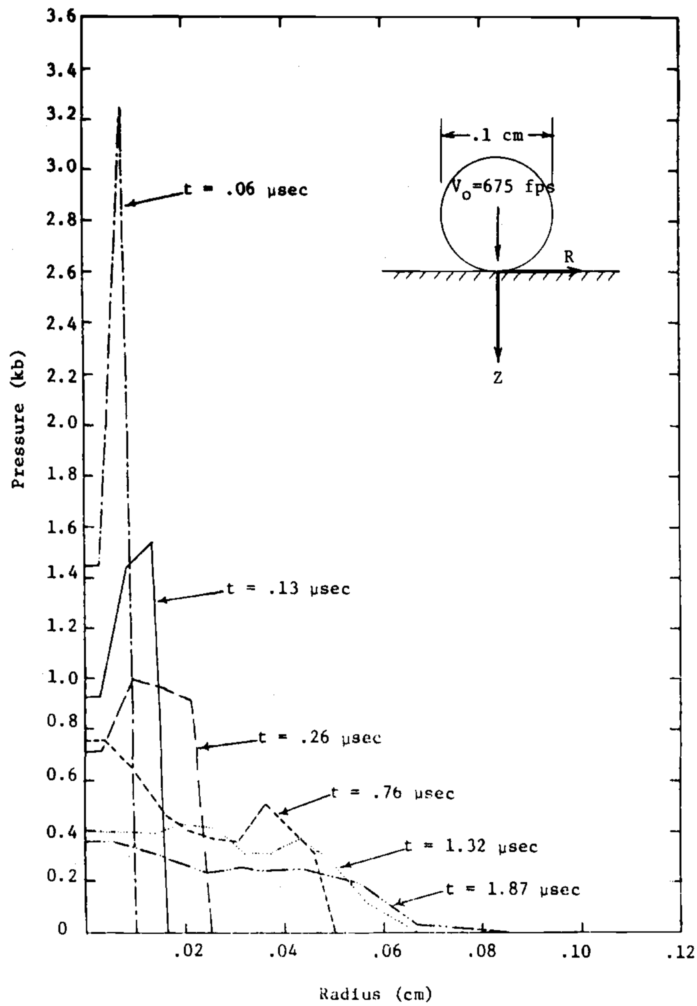

FIG. 4—*Radial pressure profiles on rigid surface for 1-mm water drop impact at 206 m/s (675 ft/s) (1 kbar = 100 MPa).*

ft/s) impact case. (Note that times and distances can be scaled linearly for other droplet diameters at a given impact velocity.)

Due to the spherical geometry of the projectile, an off-axis peak loading pressure occurs at early times which is about twice the plane strain 1-D Hugoniot pressure for the 335-m/s (1100 ft/s) impact velocity case. *The details of the pressure peak formation are important because of its direct relationship to peak tensile stress formation in brittle targets.* The nature of this early-time pressure peak was analyzed using a finely zoned computational grid.

Figure 5 shows the initial computational grid used for describing the 1-mm-diameter water drop impact event. The impact velocity (V_o) is 335-m/s (1100 ft/s). Figure 6 shows the velocity field (using the scale bar shown on the figure) for material in the vicinity of the impact site at 0.02 μs after the impact. The *contact radius* ($\bar{r}$, defined in Fig. 6) is about 0.008 cm (= 80 μm) at this time. Notice the tendency of the velocity vectors in the interaction region to focus toward the contact radius.

Figure 7 shows the velocity field at 0.03 μs. At this time the contact radius is moving outward at a velocity slightly greater than the sound speed (C_o) in undisturbed water. The numerical simulation predicts that the pressure peak occurs near the contact radius and continues to increase in magnitude as long as the contact velocity is greater than about C_o.

Figures 8 and 9 show the velocity fields at 0.05 and 0.09 μs. The convergence of the velocity vectors is still qualitatively apparent; however, the pressure *on* the impact plane has been reduced by relief waves from the droplet-free surface (near the contact radius).

The predicted pressure versus time profiles at several radii on the impact surface are shown in Fig. 10. The peak pressure occurs at a radius of about

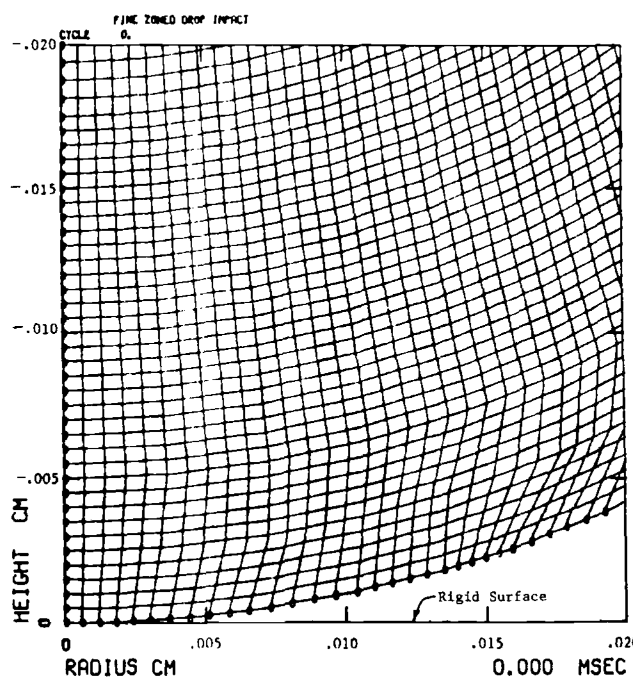

FIG. 5—*Initial computational grid for 1-mm water drop impacting a rigid surface at (335-m/s) 1100 fps.*

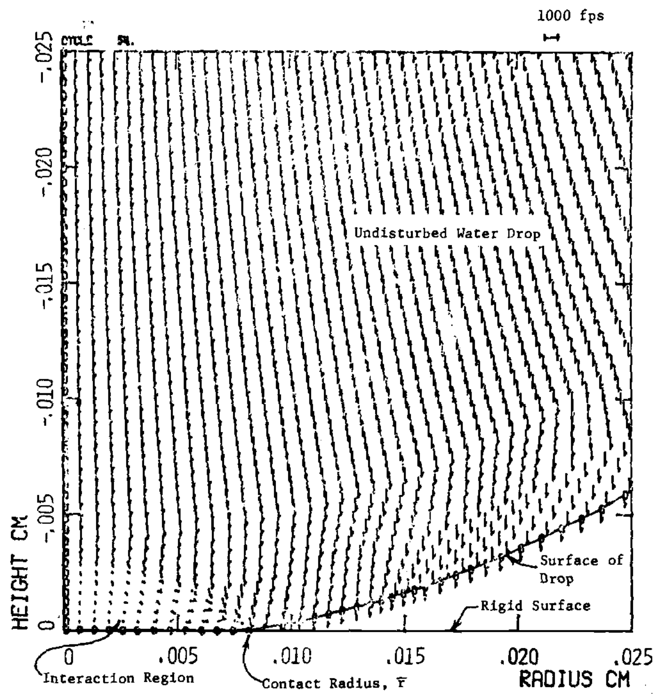

FIG. 6—*Velocity field at 0.02 μs showing the interaction region between the 1-mm water drop and rigid surface for 335-m/s (1100 ft/s) impact.*

0.01 cm or *20 percent of the droplet radius for the 335-m/s (1100 ft/s) water drop impact on a rigid surface.* (Note that this 20 percent value is velocity dependent as discussed in the following.) Beyond this radius, the peak pressure on the surface begins to fall off as indicated in Fig. 11.

The maximum loading pressure on the rigid surface is predicted to be about twice the 1-D shock Hugoniot value for water or 2.7 times the water-hammer pressure of $\rho_o C_o V_o$. This result is in good agreement with the purely analytical plane-strain solution of Heymann [*8*].

Figure 12 summarizes the relationships between contact radius speed ($\dot{\bar{r}}$), water sound speed (C_o), and the *timing* of the maximum pressure predicted in the numerical simulation. The rate of increase of the contact radius ($\dot{\bar{r}}$) as a function of time (t) can be obtained by assuming that the spherical droplet (radius R_o) remains undeformed where it is not in contact with the rigid boundary during the impact (at velocity V_o). The geometry is indicated in Fig. 12 such that

$$\bar{r}^2 + (R_o - V_o t)^2 = R_o^2 \qquad (1)$$

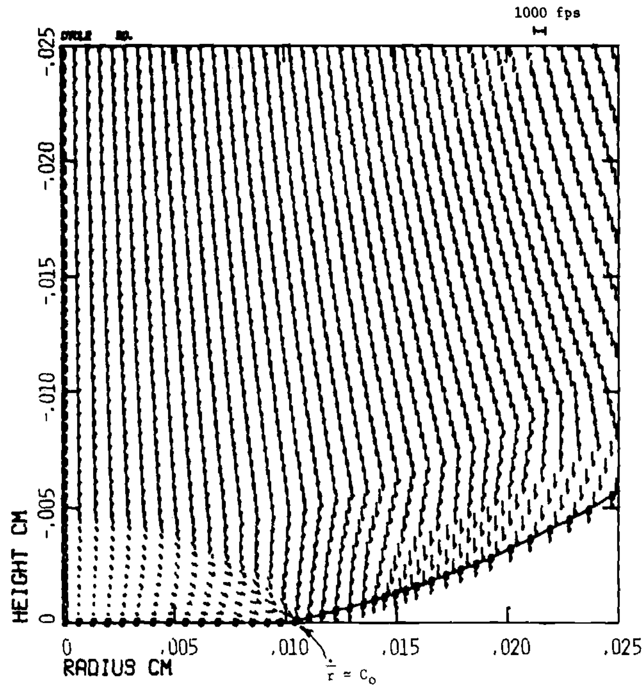

FIG. 7—*Velocity field at 0.03 μs for 335-m/s (1100 ft/s) impact of 1-mm water drop on rigid surface.*

$$\dot{\bar{r}} = \frac{V_o(R_o - V_o t)}{\bar{r}} \tag{2}$$

The $\dot{\bar{r}}$ versus time curve for the calculated case is plotted in Fig. 12 as a solid line. Also shown is the speed of sound in undisturbed water ($C_o = 0.15$ cm/μs or about 5000 ft/s). The dashed curve shows the peak pressure versus time (use right scale) for this solution. The peak pressure attains its maximum at a time of about 0.033 μs, which corresponds to the time when the speed of the contact radius is about C_o. At times greater than 0.033 μs, the peak pressure decreases.

Thus the 335-m/s (1100 ft/s) numerical simulation predicts that the *peak pressure* increases near the contact radius as long as the velocity of the contact radius exceeds the sound speed (C_o) in undisturbed water. We suggest that for *subsonic* raindrops the assumption of $\dot{\bar{r}} \sim C_o$ can be used (in Eqs 1 and 2) as a working estimate for the critical contact radius associated with the maximum pressure. Thus, the predicted critical contact radius ($\bar{r}_c$) occurs at

$$\bar{r}_c = \frac{R_o V_o}{\sqrt{C_o^2 + V_o^2}} = \frac{R_o(V_o/C_o)}{\sqrt{1 + (V_o/C_o)^2}} \tag{3}$$

However, we do not feel this result can be generalized to much higher impact velocities since the parameter C_o is not critical to the interaction dynamics for hypersonic impact.

The importance of the critical radius, $\bar{r}_c$, is demonstrated in the next section by directly relating this contact radius to the onset of tensile failure in brittle targets.

Dynamic Target Response

Figure 13 shows the grid used for the target response predictions of 2-mm-diameter water drop impacts at 222-and-341 m/s (730 and 1120 ft/s). An analytical loading model [5] was used to specify the loading pressure on the target surface.

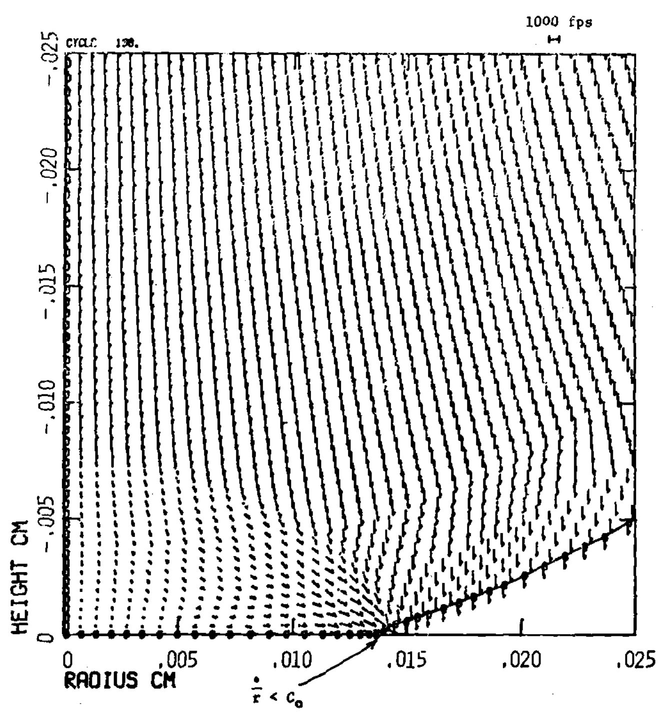

FIG. 8—*Velocity field at 0.05 μs for 335-m/s (1100 ft/s) impact of 1-mm water drop on rigid surface.*

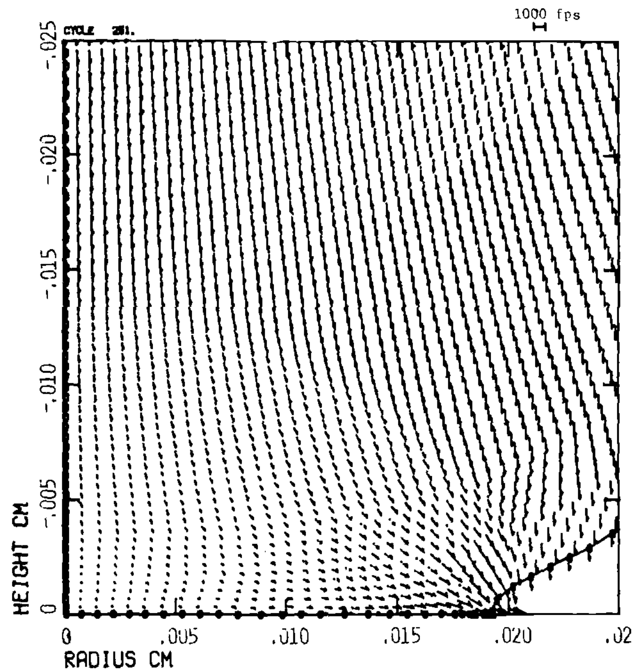

FIG. 9—*Velocity field at 0.09 μs for 335-m/s (1100 ft/s) impact of 1-mm water drop on rigid surface.*

Elastic Analyses

Figure 14 indicates the *elastic response* of a zinc selenide (ZnSe) window in terms of the particle velocity field and principal in-plane (r, z) *tensile stress* field at 0.1 μs. The velocity vectors show the magnitude and direction of the velocity of the particle mass located at the tail of the vector. A 15-m/s (50 ft/s) scale bar is shown in the upper right corner of the figure. The principal tensile stresses are indicated by lines which show their magnitude and direction in the r-z plane. (Hoop tensile stresses are not indicated on these plots.) A tension crack will tend to develop in a direction perpendicular to the plotted principal tensile stress direction. A 1-kbar (14 500 psi) scale bar is shown in the upper left corner of these plots. Thus, at 0.1 μs after the impact, the peak velocities are roughly 15-m/s (50 ft/s) in the target and the peak tensile stresses are about 2 kbar (~30 000 psi).

The region of high tensile stresses occurs in an annular volume near the surface outside the contact area. The material directly under the contact area is in pure compression. Figure 15 shows the corresponding velocity and in-plane tensile stress fields at 0.2 μs. The qualitative features are similar to the 0.1-μs plots; however, the peak velocities and peak tensile stresses have already decayed below the 0.1-μs values.

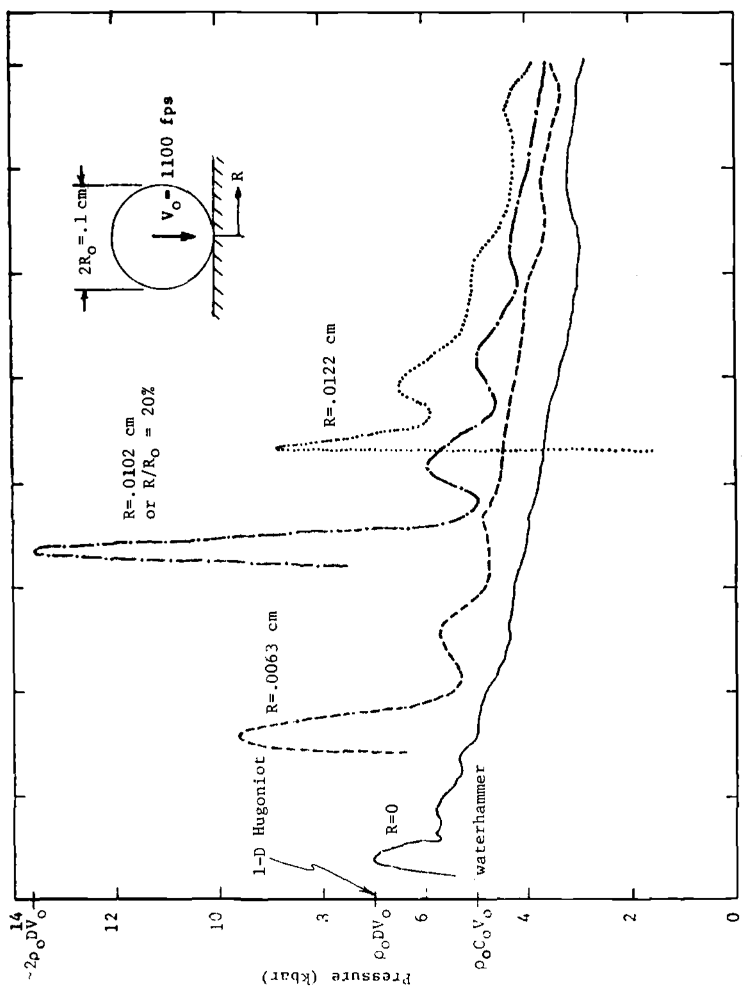

FIG. 10—*Pressure versus time at several radii on rigid impact surface for 335-m/s (1100 ft/s) impact of 1-mm water drop (1 kbar = 100 MPa).*

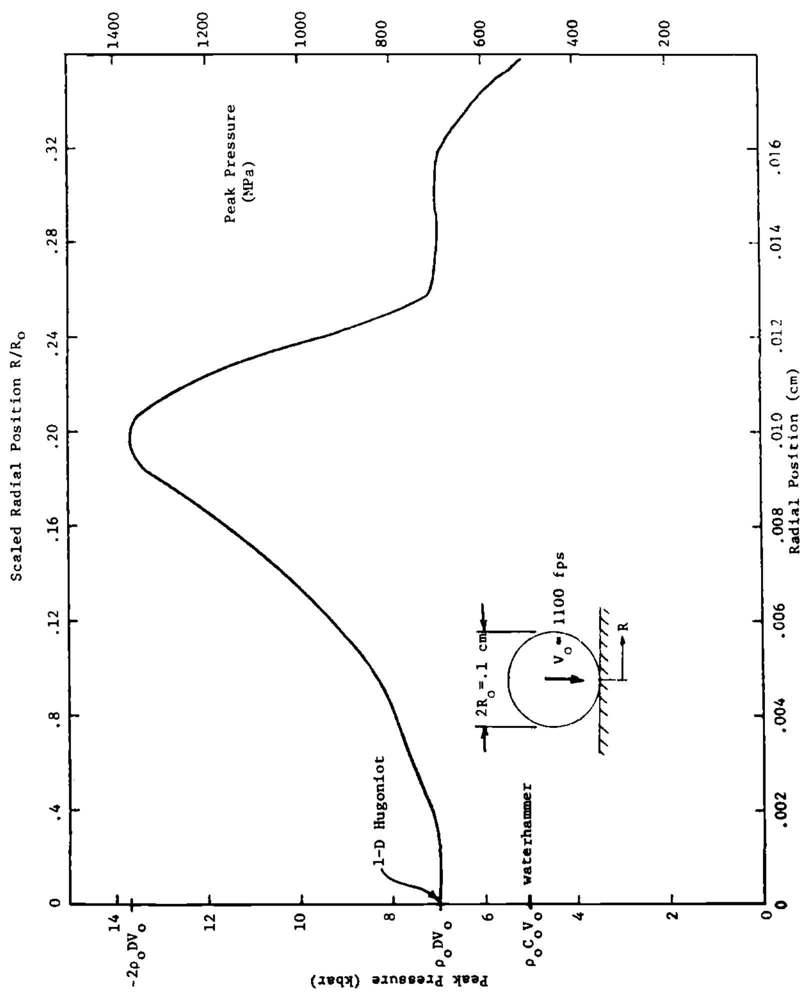

FIG. 11—*Peak pressure on rigid impact surface versus radius for 335-m/s (1100 ft/s) impact of 1-mm water drop.*

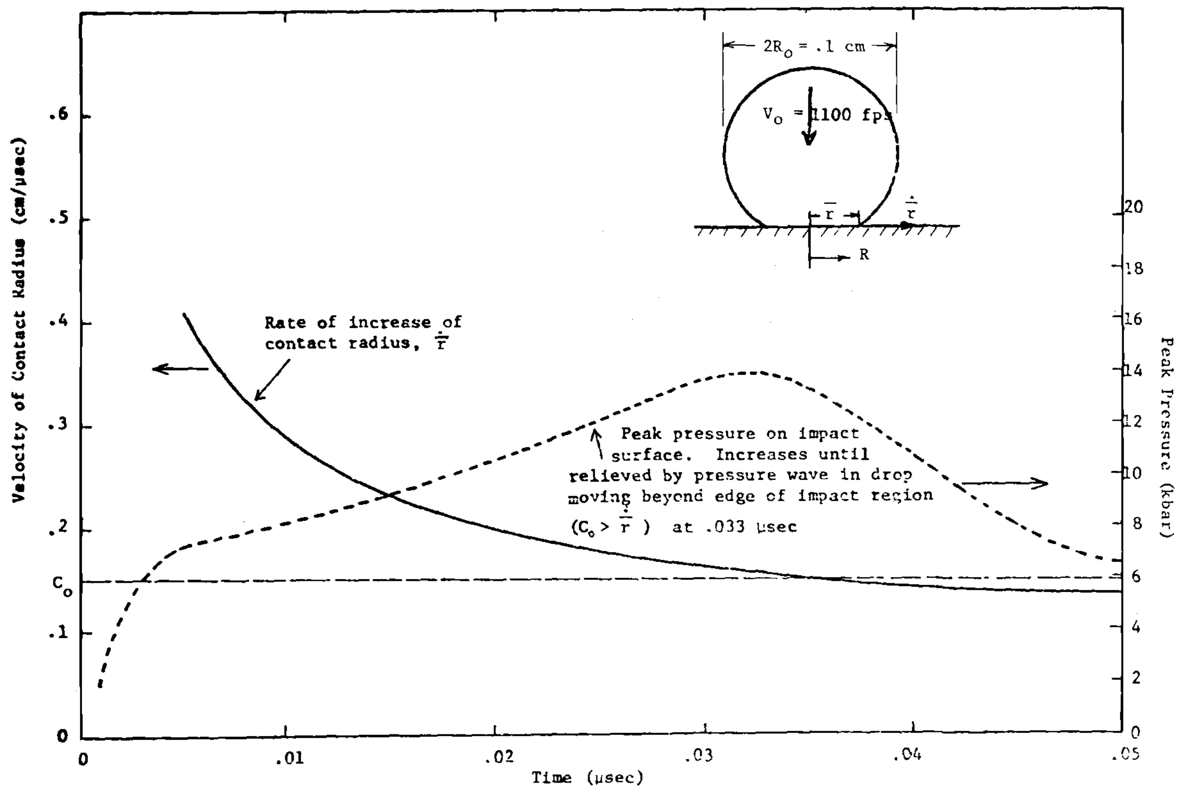

FIG. 12—*Rate of increase of impact radius and peak pressure versus time for 335-m/s (1100 ft/s) of 1-mm water drop on rigid surface (1 kbar = 100 MPa).*

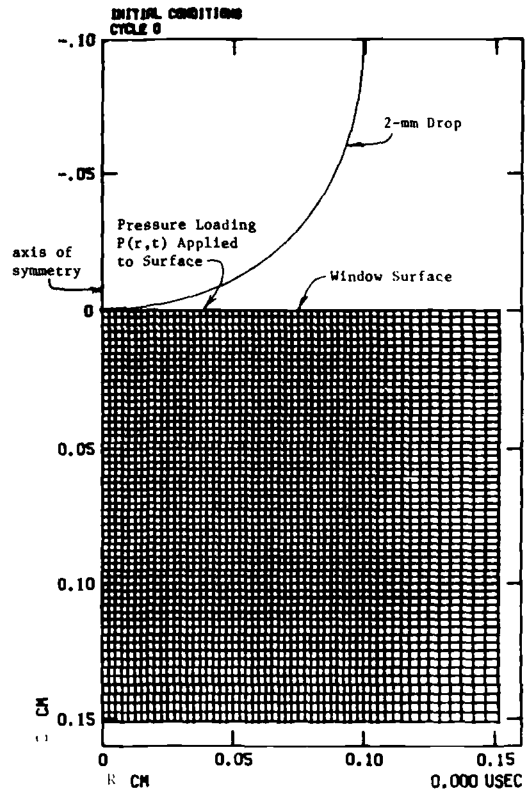

FIG. 13—*Initial computational grid in target window using 80 cells per 2-mm drop diameter.*

Figure 16 is a more quantitative description of the peak tensile stress behavior in the target near the impact point. This figure shows the behavior of the peak tensile stress versus scaled radius near the target front surface. *Note that the location of the off-axis peak loading pressure* ($\bar{r}_c$ *on Fig. 16*) *correlates very well with the radial onset of the tensile response.* The location of the maximum tensile stress is dominated by the impact loading pressure gradients, that is, dP/dt and dP/dR.

Figure 17 shows the peak tensile stress versus scaled depth ($Z/2R_o$) profiles for both the 222-and-341 m/s (730 and 1120 ft/s) impact of 2-mm droplets on ZnSe. Note the very steep stress gradient near the impact surface, $Z/2R_o = 0$. In fact, an analytical solution by Blowers [9] predicts an infinite peak tensile stress at the impact surface for purely elastic targets.

Figure 17 also indicates the peak tensile stress versus depth variation with impact velocity. The peak tensile stress increases substantially with a 50 percent increase in velocity. In fact, when comparing these curves more closely, we see that the maximum tensile stress versus scaled depth

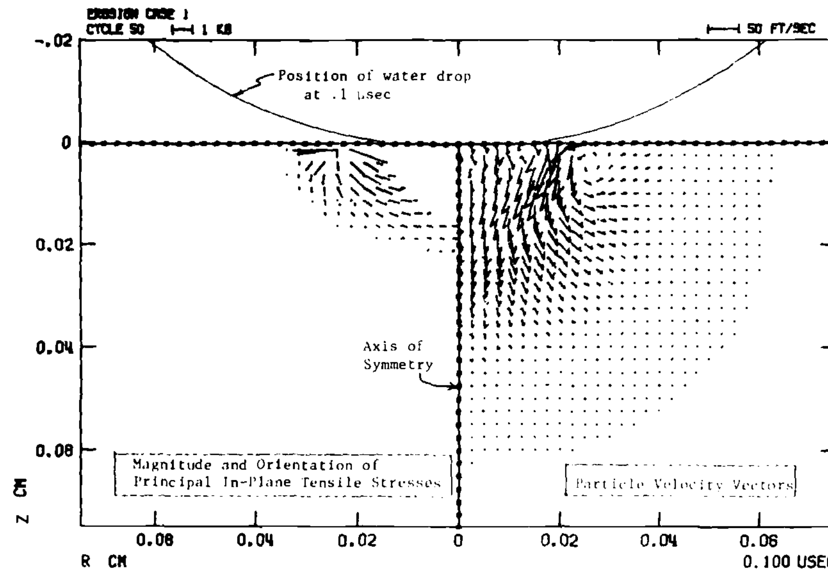

FIG. 14—*Elastic response of ZnSe window for 222-m/s (730 ft/s) impact of 2-mm water drop at 0.1 μs.*

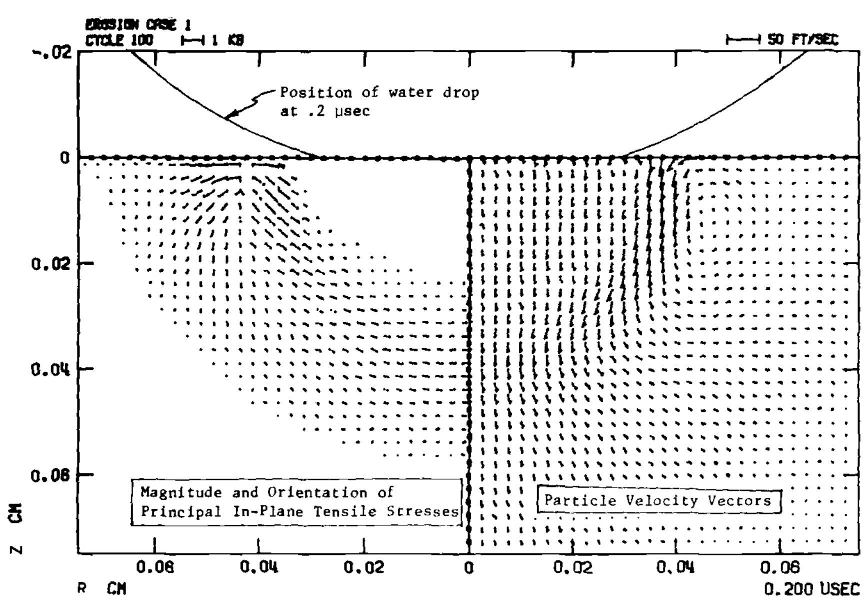

FIG. 15—*Elastic response of ZnSe window for 222-m/s (730 ft/s) impact of 2-mm water drop at 0.2 μs.*

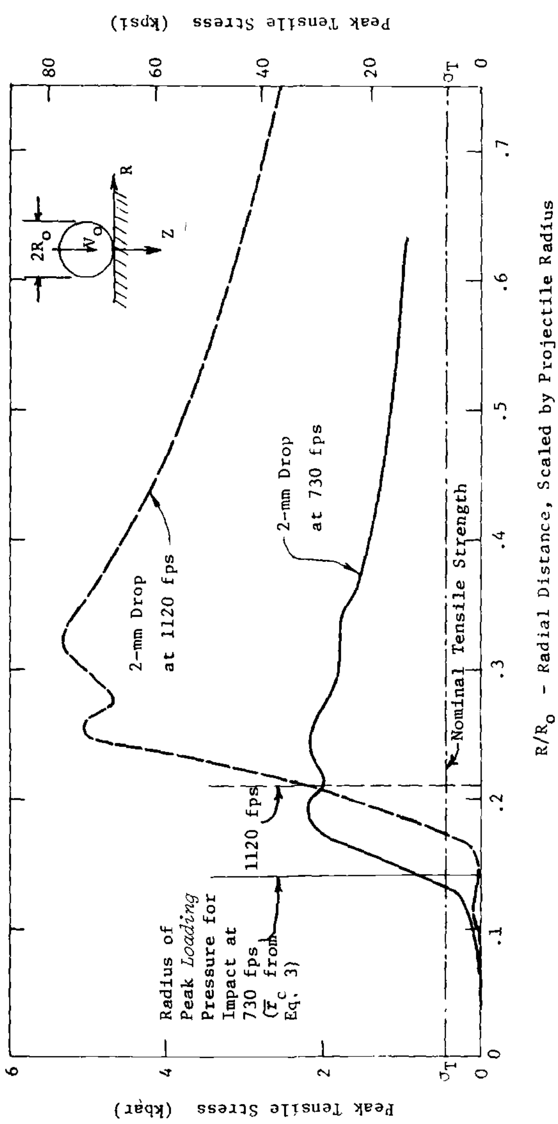

FIG. 16—*Radial variation of peak elastic* tensile *stress at* $Z/R_o = 0.0125$ *for 2-mm water drop impact on ZnSe window at 222- and 341-m/s (730 and 1120 ft/s) (1 kbar = 100 MPa).*

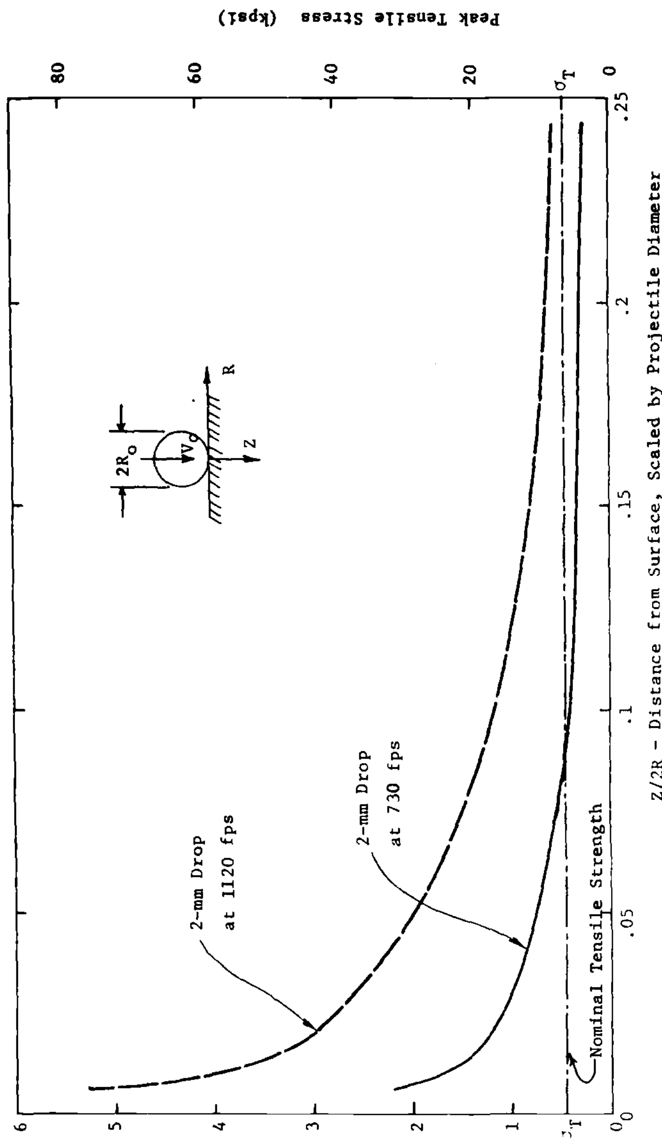

FIG. 17—*Variation of peak elastic tensile stress with depth for water drop impact on ZnSe window at 222- and 341-m/s (730 and 1120 ft/s) (1 kbar = 100 MPa).*

depends on V_o^2. This is illustrated in Fig. 18, which shows the peak tensile stress divided by impact velocity squared (and target density) versus scaled depth for the two impact velocities treated in this study. Thus, velocity-squared scaling works reasonably well for subsonic impact velocities.

Erosion (Tensile Failure) Predictions

Using a microphysical model [5] involving flaw and grain size, predictions of crack configuration (that is, crack orientation, depth, and extent) can be made with the WAVE-L code. This model is based on the interaction between a crack (flaw) and a slip or twin band [*10*] and is consistent with experimental observations [*3,11*] on ZnSe. Figure 19 shows an example (nominal case) of the predicted crack configuration for an impact of a 2-mm water drop on ZnSe at 222-m/s (730 ft/s). Since the microphysical model propagates [*12*] cracks through a cell, the crack configuration plots indicate whether the cell has fractured completely, whether the crack has grown to greater than 50 percent of the cell size, or to greater than 10 percent but less than 50 percent of the cell size. If the cell is completely fractured, the orientation of the crack is indicated.

Figure 19 predicts that the surface should be damaged between radii of roughly 0.02 and 0.05 cm. This agrees very well with experimentally observed data given in Ref *3* and noted in Fig. 19. Also in Ref *3*, the observation is made that for the 222-m/s (730 ft/s) impacts, the cracks appear to extend to a depth of about 1 grain. This is in good agreement with the prediction of Fig. 19.

Figure 20 shows the predicted effect on the final crack configuration of *halving the flaw size* from the nominal case. The effects are large in terms of both reduction in radial extent of the damage region and in the depth of the damage region.

Figure 21 shows the predicted effect of *halving the grain size* as compared with the nominal case. There is an improvement in both the radial extent of the damage region and the depth; however, the improvement is not as dramatic as in the flaw size reduction case.

Figure 22 shows the crack configuration for a 341-m/s (1120 ft/s) impact of a 2-mm water drop impact on ZnSe. The experimental observation of the surface damage region is in good agreement with the predictions. We do not know of any corresponding measurements of the depth and spatial distribution of cracks below the target surface.

Note that Fig. 19 and 22 show the critical contact radius, $\bar{r}_c$, for the peak off-axis impact pressure described in the previous section. The experimental results and numerical simulations of surface damage show a good correlation between the inner radius of damage and $\bar{r}_c$. The impact loading pressure gradients, in time and radius, cause large tensile stresses to develop near $\bar{r}_c$ on the target surface. The elastic properties of the target will certainly

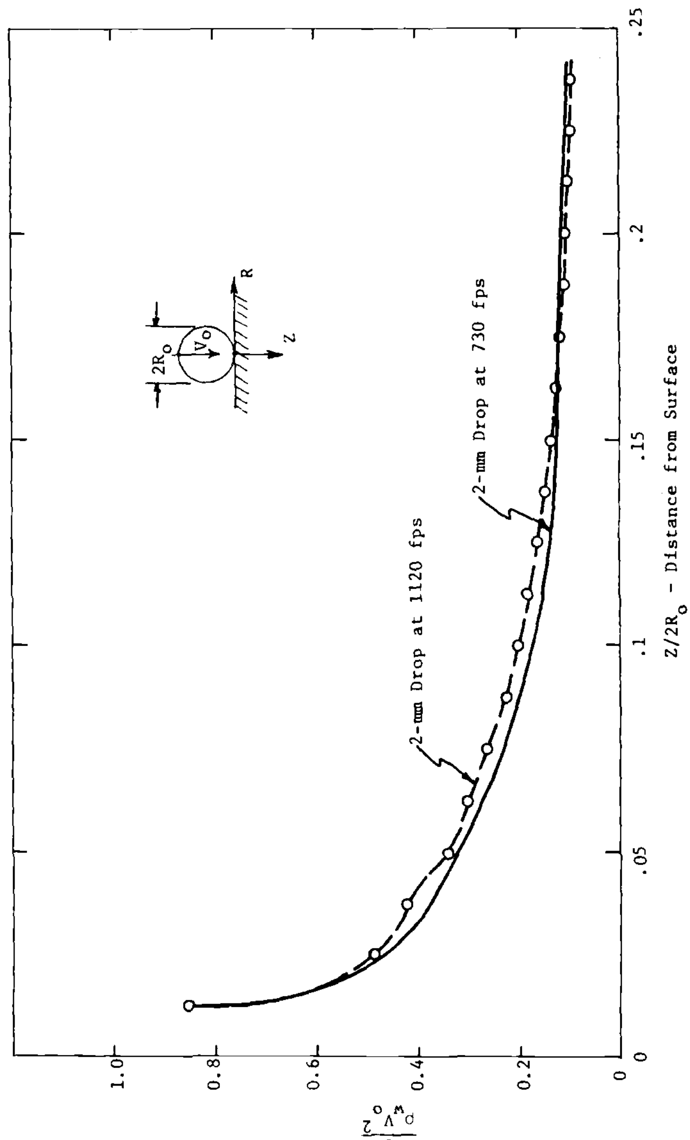

FIG. 18—*Velocity-squared scaling of peak tensile stress variation with depth for 2-mm water drop impact on ZnSe window.*

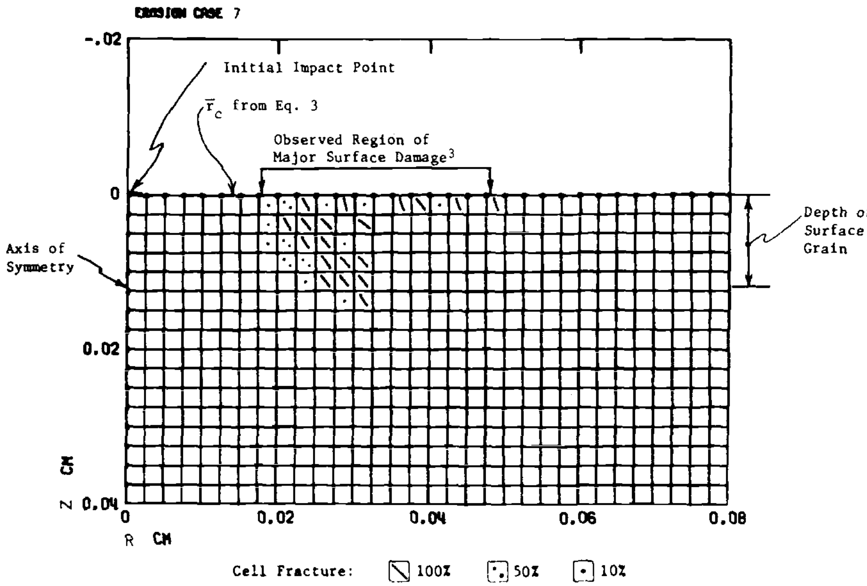

FIG. 19—*Crack configuration for 222-m/s (730 ft/s) impact of 2-mm water drop on ZnSe using nominal microscopic fracture criterion [nominal case with 120-μm (=0.012 cm) grain size and 40-μm initial flaw length associated with each computational cell].*

influence the exact radius of the peak tensile stress on the target surface; however, the results of this study indicate that the dominant mechanism is the large off-axis loading pressure which peaks near $\bar{r}_c$.

Limited experimental comparisons with predicted numerical results for ZnSe *surface* fracture characteristics appear good; however, additional experimental data are needed for the crack spatial distribution predictions, that is, for depth, orientation, and number. Note that the target fracture predictions for ZnSe are based on the microphysical model described in Ref 5. One potentially important aspect of the model is the assumed flaw distribution in the target. In this initial study, a uniform flaw distribution (one flaw associated with each computational cell) has been assumed. This leads to flaw growth over a relatively large volume in the target; for example, Fig. 22 shows complete cell fracture from flaw growth in many cells below the target surface. If the flaw distribution or size or both decreased with depth, then the crack configuration below the surface would obviously be more discrete since *individual* cracks would have to propagate into a target region with fewer or smaller preexisting flaws or both. Currently, the microphysical model and various target flaw distributions are being investigated for use in additional numerical simulations.

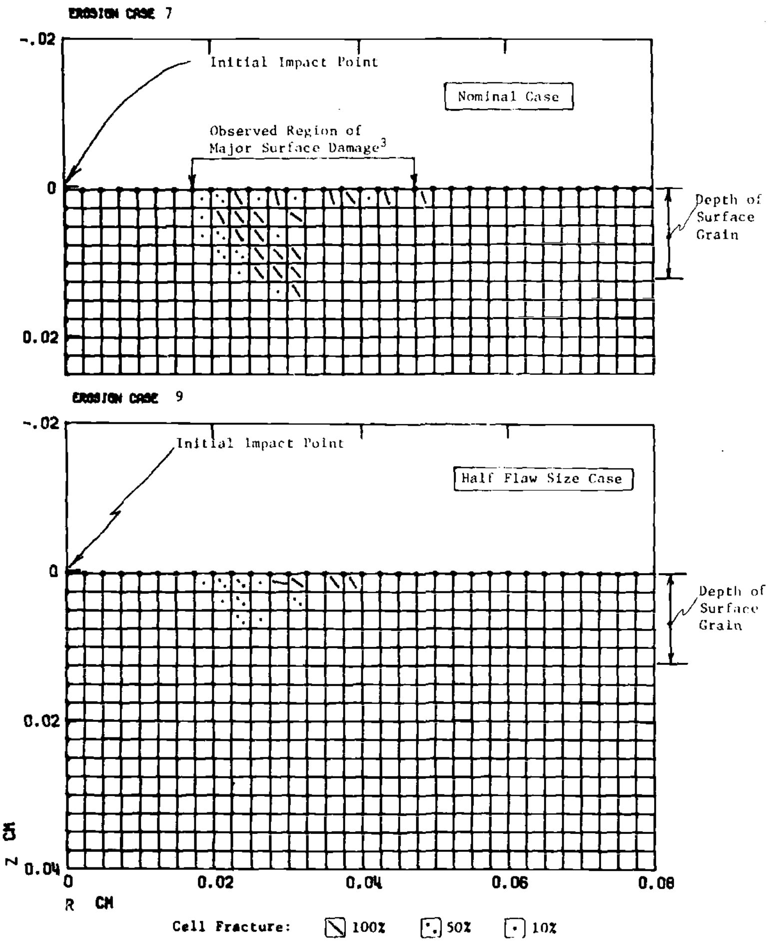

FIG. 20—*Effect of flaw size on crack configuration for 222-m/s (730 ft/s) impact of 2-mm water drop on ZnSe.*

Conclusions and Recommendations

Based on the numerical simulations and experimental comparisons conducted during the present study, the following brittle target damage mechanisms (from a single water drop impact) have been identified:

1. Tensile crack propagation is the primary damage mechanism. Tensile failure occurs behind the shear and Rayleigh waves which are generated in the target by the dynamic impact pressure load, $P(r,t)$. For ZnSe impacted at 222 m/s (730 ft/s) by a 2-mm-diameter water drop, the cracks propagate for $\sim 0.2\ \mu s$.

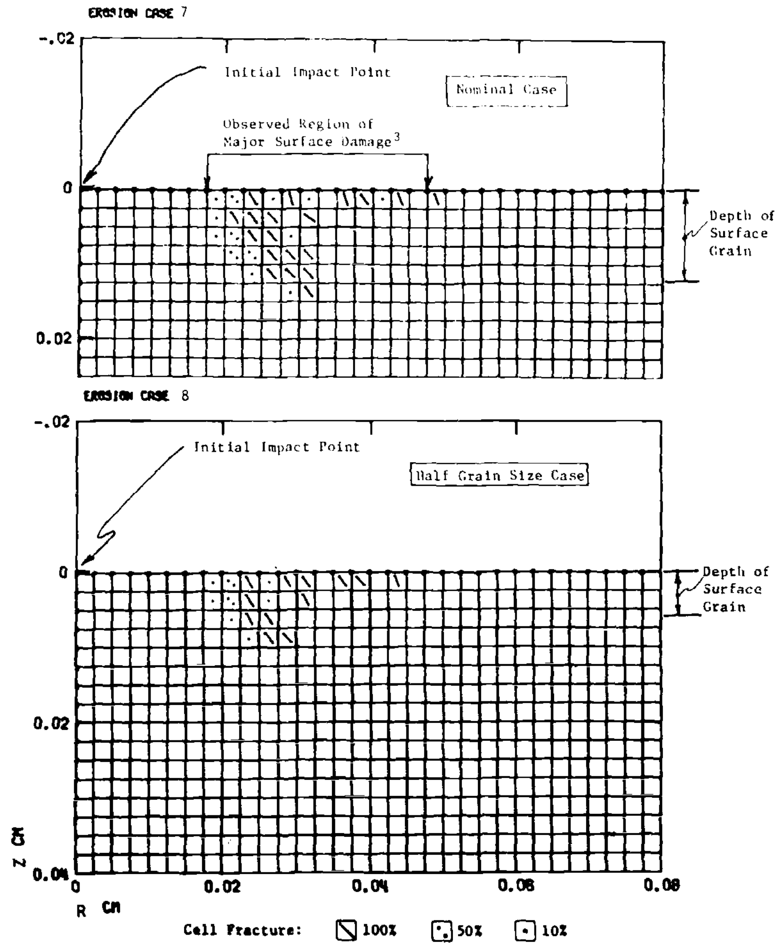

FIG. 21—*Effect of grain size on crack configuration for 222-m/s (730 ft/s) impact of 2-mm water drop on ZnSe.*

2. The tensile stress response near the target surface is directly related to the peak off-axis loading pressure which occurs near the critical radius $\bar{r}_c$ due to the spherical geometry of the drop. This is illustrated in Figs. 16, 19, and 22. For the 335-m/s (1100 ft/s) impact case, this peak surface loading pressure is twice the 1-D shock Hugoniot value and occurs at about 20 percent of the drop radius. As a working estimate for the critical radius ($\bar{r}_c$) corresponding to the peak off-axis surface pressure, we recommend using Eq 3 given herein for subsonic impacts on brittle targets.

3. The water drop has time to interact directly with the tensile cracks generated during the early stages of the drop-target impact. Water may penetrate into a developing crack and enhance damage.

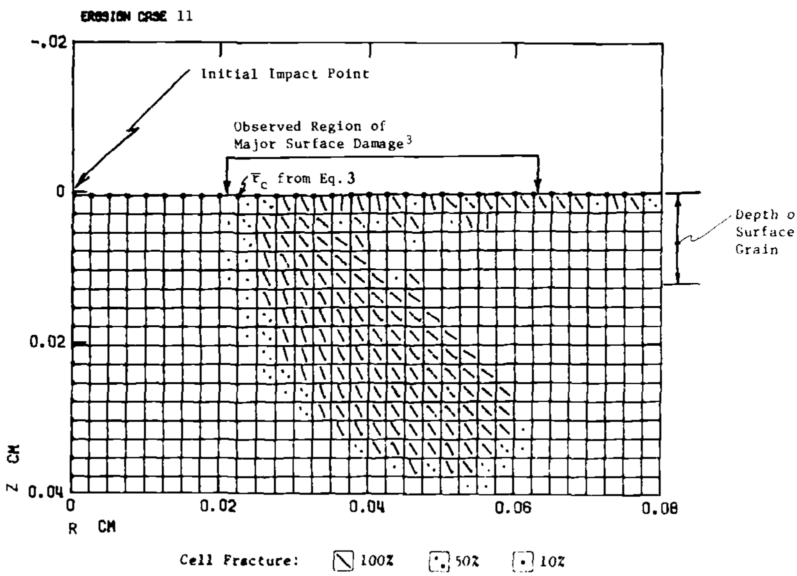

FIG. 22—*Crack configuration for 335-m/s (1120 ft/s) impact of 2-mm water drop on ZnSe using nominal microscopic fracture criterion.*

Limited experimental comparisons with predicted target *surface* damage appear good; however, additional experimental data are needed to evaluate the below-surface target damage predictions. In particular, the microphysical model and assumed target flaw distributions can be improved when additional experimental data become available. Once reliable microphysical models are developed (for prescribed classes of materials), numerical simulations can be performed to optimize the design of material components subjected to dynamic loads.

References

[*1*] Schmitt, G. F., Jr., "Rain Droplet Erosion Mechanisms in Transparent Plastic Materials," *Proceedings*, 4th International Conference on Rain Erosion and Associated Phenomena, Meersburg, Germany, May 1974.

[*2*] Adler, W. F. and Hooker, S. V., "Characterization of Transparent Materials for Erosion Resistance," AFML-TR-76-16. Air Force Materials Laboratory, March 1976.

[*3*] Hackworth, J. V. and Kocher, L. H., "Exploratory Development of Rain Erosion Resistant Infrared Window Materials," AFML-TR-77-84, Air Force Materials Laboratory, May 1977.

[*4*] Rosenblatt, M., Eggum, G. E., DeAngelo, L. A., and Kreyenhagen, K. N., "Numerical Investigation of Water Drop Erosion Mechanisms in Infrared-Transparent Materials," AFML-TR-76-193, Air Force Materials Laboratory, Dec. 1976.

[*5*] Ito, Y. M., Rosenblatt, M., Perry, F. W., and Eggum, G. E., "Analysis of Water Drop Erosion Mechanisms in Infrared-Transparent Materials Using Microphysical Fracture Models." AFML-TR-77-219, Air Force Materials Laboratory, Oct. 1977.

[6] Eggum, G. E., and Rosenblatt, M., "1100 fps Impact of a 1-mm Water Drop on a Rigid Surface at Early Times," CRT 5010-1, Prepared for Prototype Development Associates and Office of Naval Research, Sept. 1975.
[7] Wilkins, M. L.,"Calculation of Elastic-Plastic Flow," UCRL-7322, Rev. I, University of California Radiation Laboratory, Jan. 1969.
[8] Heymann, F. J., *Journal of Applied Physics*, Vol. 40, Dec. 1969, pp. 5113-5122.
[9] Blowers, R. W., *Journal of the Institute of Mathematics and Its Application*, Vol. 5, 1969, pp. 167-193.
[10] Yokoburi, T., Kamei, A., and Konosu, S., *Engineering Fracture Mechanics*, Vol. 8, 1976, pp. 397-409.
[11] Freiman, S. W., Mecholsky, J. J., Rice, R. W., and Wurst, J. C., "Influence of Microstructure on Crack Propagation in ZnSe," *Journal of the American Ceramic Society*, Vol. 58, 1975, pp. 406-409.
[12] Petch, N. J., in *Fracture*, H. Liebowitz, Ed., Vol. I, 1968, pp. 351-393.

DISCUSSION

D. G. Rickerby[1] *(written discussion)*—Does your treatment predict contact areas which are in agreement with those observed experimentally? Also, what insight does it give into a physical understanding of the generation of high edge pressures?

M. Rosenblatt, Y. M. Ito, and G. E. Eggum (authors' closure)—We are not aware of any experimentally determined contact areas. However, the critical contact radius ($\bar{r}_c$) is related to the experimentally determined inner radius of tensile failure in ZnSe targets as discussed in the paper under "Dynamic Target Response." Also, see Ref *8*.

The physical insights concerning high edge pressures are discussed in the "Water Drop Impact..." section of the paper.

N. H. Macmillan[2] *(written discussion)*—If I understand you correctly, you have first calculated (as a function of time and position) the forces resulting from impact of a water drop against a rigid solid, and then *assumed* that these same forces act during impact with a deformable solid. This is obviously not the case, and I therefore wonder if you can give me any idea of the magnitude of the error likely to result from your assumption.

M. Rosenblatt, Y. M. Ito, and G. E. Eggum (authors' closure)—A detailed calculation considering a deformable ZnSe target is described in Ref *4*. The results are very similar to the rigid target case at subsonic [$V_o \leq$ 366-m/s (1200 ft/s)] impact velocities on brittle elastic targets because the target surface deflections are very small compared to the water drop deformations.

For a target material whose acoustic impedance is nearly the same as that of water, the assumption of essentially rigid target behavior is certainly not applicable.

[1] Pennsylvania State University, State College, Pa. 16801.

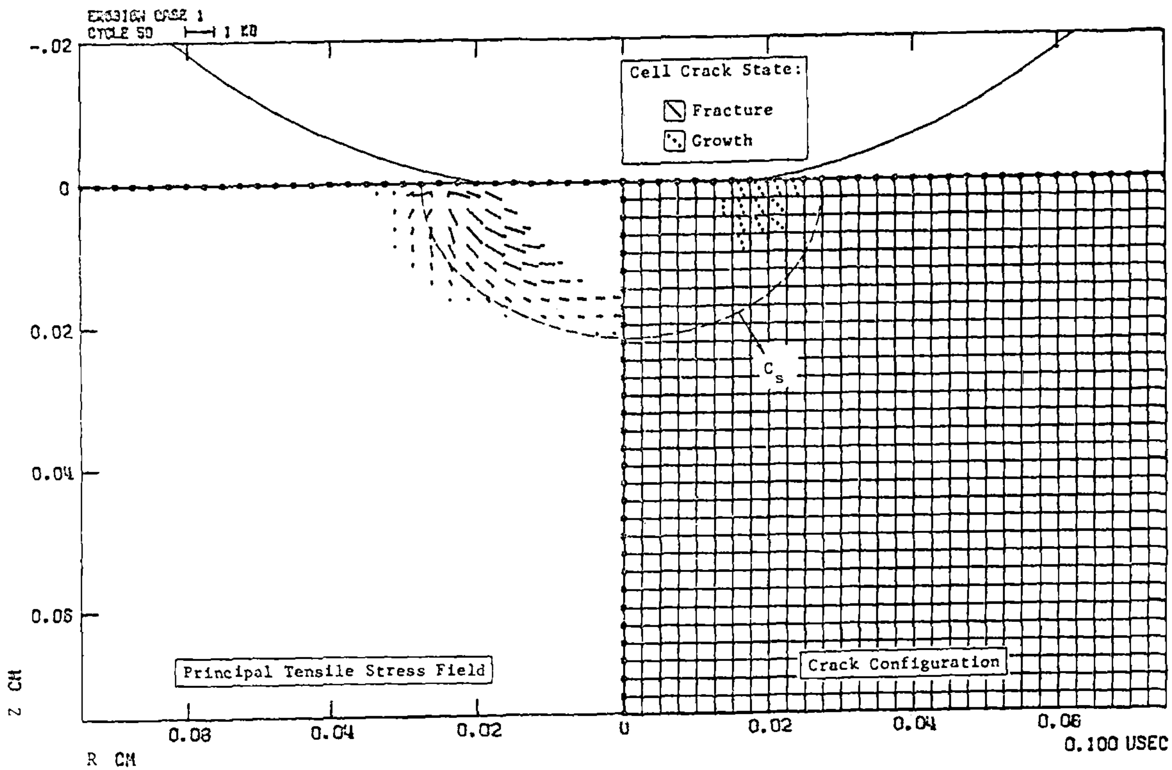

FIG. 23—*Principal tensile stress field and crack configuration behind shear wave front* (C_S) *at 0.1 μs for 222-m/s (730 ft/s) impact of 2-mm water drop on ZnSe window using nominal microscopic fracture criterion.*

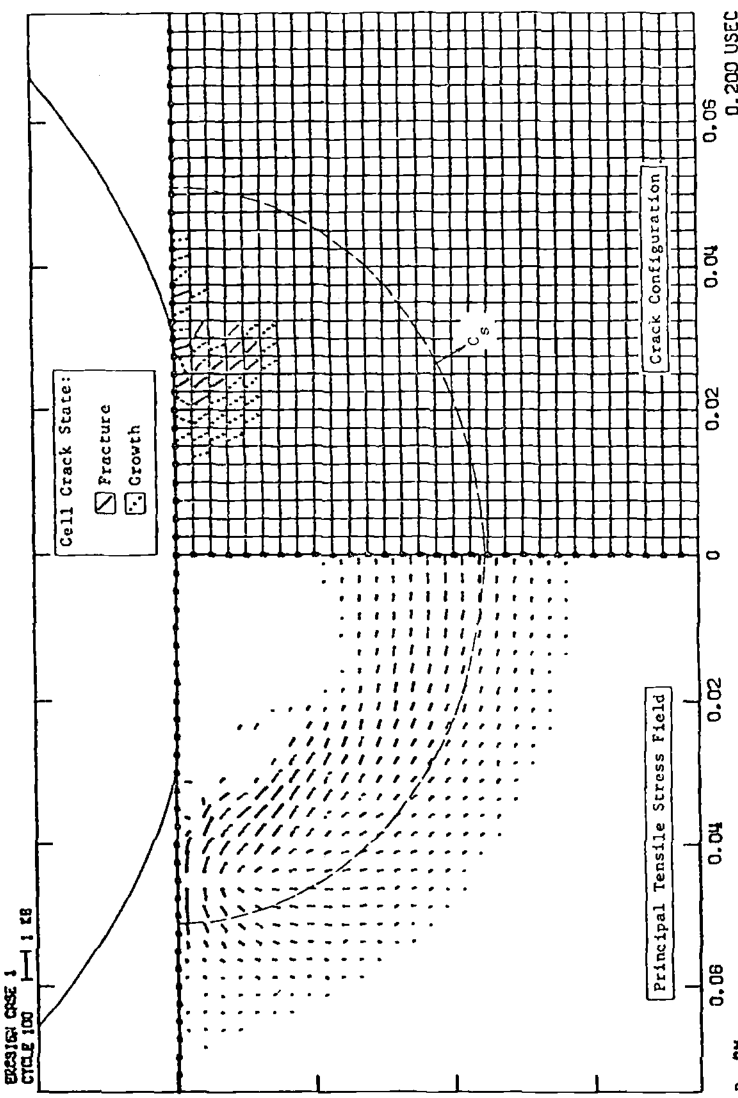

FIG. 24—*Principal tensile stress field and crack configuration behind shear wave front* (C_s) *at 0.2 µs for 222-m/s (730 ft/s) impact of 2-mm water drop on ZnSe window using nominal microscopic fracture criterion.*

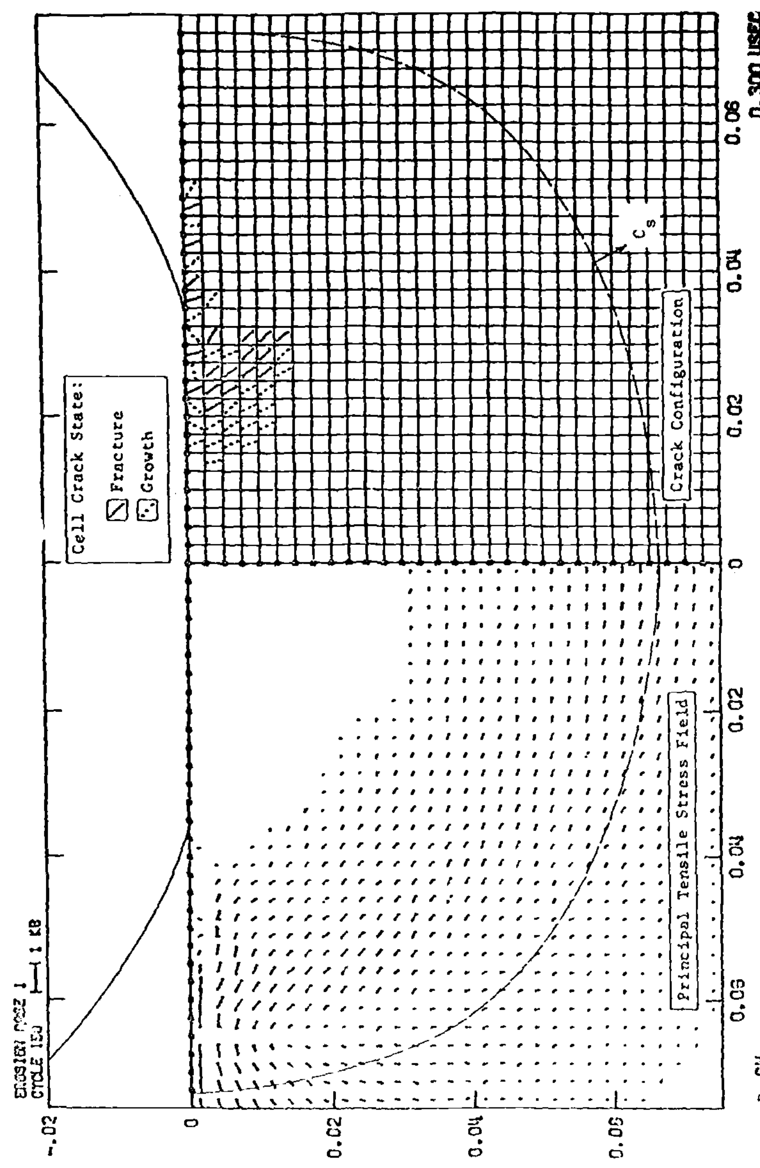

FIG. 25—*Principal tensile stress field and crack configuration behind shear wave front* (C_S) *at 0.3 μs for 222-m/s (730 ft/s) impact of 2-mm water drop on ZnSe window using nominal microscopic fracture criterion.*

N. H. Macmillan[2] (*written discussion*)—Could you explain the significance of the many "fractured cells" shown in Figs. 19-22? Do these represent the formation of multiple concentric Hertzian-type cone cracks, repeated bifurcation of one such crack, or some other mode of fracture?

M. Rosenblatt, Y. M. Ito, and G. E. Eggum (*authors' closure*)—The target response to water drop impact is not a Hertzian response. The dynamic tensile stresses which develop in the target vary both in space and time and are affected by the developing tensile cracks. The tensile response in the target is so great that there is sufficient time for many separate flaws to grow and form the crack patterns seen in Figs. 19-22. We have also included some earlier plots (Figs. 23-25) indicating the nature of the crack initiation and propagation processes.[3] (Note that these figures indicate all crack growth whereas Figs. 19-22 give only cracks with at least 10 percent growth.)

[2] Pennsylvania State University, Materials Research Laboratory, University Park, Pa. 16802.
[3] See Ref 5.

J. V. Hackworth,[1] *L. H. Kocher,*[1] *and I. C. Snell*[1]

Response of Infrared Transmitting Materials to High-Velocity Impact by Water Drops

REFERENCE: Hackworth, J. V., Kocher, L. H., and Snell, I. C., "**Response of Infrared Transmitting Materials to High-Velocity Impact by Water Drops,**" *Erosion: Prevention and Useful Applications, ASTM STP 664,* W. F. Adler, Ed., American Society for Testing and Materials, 1979, pp. 255–278.

ABSTRACT: An experimental and analytical program was performed to investigate the response of zinc selenide, zinc sulfide, and gallium arsenide to water drop impact. The experiments consisted of single-drop impact (0.7, 2.0, and 2.5-mm-diameter drops and impact velocities of 222 and 341 m/s); overlapping drop impacts (2.0-mm drops at 222 m/s); and exposure at 222 m/s to the standard rainfield (1.8-mm drops, 2.54-cm/h rainfall rate). An analytical model was used to compute stresses induced in the materials by a single water drop impact.

Within the conditions tested, each single-drop impact produced a ring fracture pattern characteristic of the material. Resistance to damage increased in the order zinc selenide, gallium arsenide, and zinc sulfide. The superior performance of zinc sulfide with respect to zinc selenide is attributed to the order-of-magnitude smaller grain size of zinc sulfide. Comparison with experimental results showed the analytical model to be a reasonable representation of the drop impact process.

The rainfield test of zinc sulfide showed that transmittance loss at short wavelengths (0.5 to 2.1 μm) was linear with exposure time, indicating a dependence on the extent of subsurface damage. At wavelengths above 2.5 μm, there was an incubation period before loss of transmittance. The end of the incubation period and the start of transmittance loss were associated with the nucleation of surface pits.

KEY WORDS: rain erosion, infrared window materials, single-drop impact, stress waves, erosion mechanisms, multiple-drop impact, erosion

Materials being developed for infrared windows, for example, zinc selenide, zinc sulfide, and gallium arsenide, are all essentially brittle materials which will suffer serious degradation of transmittance when exposed to rainfields at moderate to high subsonic velocities. Knowledge of the mechanisms by which erosion is initiated and the relationship

[1]Principal scientist, chief, Structural Analysis, and principal scientist, respectively, Bell Aerospace Textron, P. O. Box 1, Buffalo, N. Y. 14240.

between the loss of infrared transmission and the progress of erosion is necessary for the development of window materials with improved erosion resistance and for the development of techniques to protect the more susceptible materials. Up to now, only limited work has been done to characterize the response of these materials to raindrop impact.

A complete understanding of the erosion process requires definition of the loads imparted to a surface by water drop impact, determination of the dynamic stresses generated in the material, and establishment of the response of the material to the dynamic stresses. These complex requirements dictate a combined experimental/analytical approach such as was used in the investigation described in this paper.

The experimental part of the investigation consisted of impacting the selected infrared window materials with single and overlapping water drops over a range of drop diameters and impact velocities to define erosion damage mechanisms. The materials were then exposed to multiple-drop rainfields to determine the interaction between erosion damage and infrared transmittance. For the analytical part of the investigation, a computer program developed by Blowers *[1]*[2] was used to calculate the transient stresses induced in the selected infrared window materials by impact with a single raindrop as a function of drop size and impact velocity. The calculated stress patterns were then compared with the results from the microscopic analyses of the single-drop impact sites to verify the validity of the analytical model.

Procedures

Materials

The infrared window materials evaluated were zinc selenide, zinc sulfide, and gallium arsenide. The behavior of zinc selenide was investigated extensively to establish a data base to which the behavior of the other two materials could be compared at selected conditions of drop diameter and impact velocity. Polymethylmethacrylate (PMMA), Type G, was also included as a standard target material to characterize the various water drop environments.

Zinc selenide and zinc sulfide, produced by the chemical vapor deposition (CVD) process, were procured as 0.95-cm-thick plates from the Raytheon Co. Specimens 2.22-cm square by 0.95-cm thick were cut from these plates and optically polished on both sides. Bilayered specimens were also prepared by bonding outer layers of 0.32-cm-thick CVD zinc sulfide, also from Raytheon, to some of the previously polished zinc selenide specimens. Lens cement was used for the bonds so the layers could be separated in a

[2]The italic numbers in brackets refer to the list of references appended to this paper.

decementing solution after the drop experiments. After bonding, the zinc sulfide layers were ground and polished to give three sets of specimens with zinc sulfide layer thicknesses of 0.25, 0.50, and 1.0 mm, respectively. Texas Instruments supplied the gallium arsenide specimens, 3.80 by 2.22 by 0.95-cm thick, from material produced by horizontal gradient freeze from the melt.

Specimens of each material were etched to reveal the microstructure. Zinc selenide and zinc sulfide were etched in a boiling solution of one part hydrochloric acid (concentrated) and one part water by volume. Gallium arsenide was etched in a room-temperature solution of three parts nitric acid (concentrated), one part hydrofluoric acid (48 percent), and four parts water by volume. The zinc selenide had a relatively large grain size with grain diameters as large as 0.10 mm; the grain size of the zinc sulfide was an order of magnitude less. The one specimen of gallium arsenide that was etched was composed of five grains, two of which were quite large. Knoop microhardness (50-g load) of the zinc selenide, zinc sulfide, and gallium arsenide was measured to be 100, 290, and 635, respectively. The elastic properties used for the analytical modeling are presented in Table 1.

Impact Experiments

The experiments as listed in Table 2 were performed in the Air Force Materials Laboratory (AFML)-Bell erosion facility which has been previously described [*2*]. A liquid drop generator was installed in the main chamber of the facility to permit the experimental investigation of the effects of single water drop impact on the target materials. With this single-drop generator, drops having preselected diameters in the range of 0.7 to 2.5 mm could be produced in a controlled and reproducible manner. The standard rainfield used for part of the investigation was produced by spray nozzles and consisted of drops with a mean diameter of 1.8-mm falling at a rainfall rate of 2.54-cm per hour. The specimen to be tested was mounted on the end of a blade and rotated at the desired velocity through the selected environment.

TABLE 1—*Material properties.*

	Zinc Selenide	Zinc Sulfide	Gallium Arsenide
Density, kg/m^3	5270	4080	5310
Young's modulus, MPa	67.2×10^3	74.5×10^3	84.8×10^3
Poisson's ratio	0.3	0.3	0.31
Diltational wave speed, C_1, m/s	4150	4960	4710
Shear wave speed C_2, m/s	2220	2650	2470
Ultimate flexural strength, MPa	58	110	140

TABLE 2—*Experiments performed.*

Material	Impact Velocity, m/s	Single Drop Impact; Drop Diameter, mm	Overlapping Impact by Single Drop; Drop Diameter, mm	Multiple-Drop Impact in Rainfield[a]
ZnSe	222	0.7	0.7	...
ZnSe	222	2.0	2.0	✓
ZnSe	222	2.5	2.5	...
ZnSe	341	2.0	...	...
ZnS	222	2.0	2.0	✓
ZnS	341	2.0	...	...
GaAs	222	2.0	2.0	✓
ZnS layer on ZnSe				
0.25 mm ZnS	222	2.0	2.0	...
0.50 mm ZnS	222	2.0	2.0	...
1.00 mm ZnS	222	2.0	2.0	...

[a]1.8-mm mean drop diameter at 2.54-cm/h rainfall rate.

Analytical Modeling

An analytical method developed by Blowers [*1*] was used to compute the stresses induced in the infrared window materials by impacts with single water drops. This analysis, completely described in Refs *3* and *4*, provides the transient stress distributions within an elastic half-space subjected to a uniform pressure loading distributed over an expanding circular region. The model assumes a perfectly compressible liquid drop colliding with a rigid surface to compute the radius of the loaded region as a function of time. The uniform pressures applied to the expanding loaded regions were computed from a one-dimensional shock-wave relationship for a water drop impacting a deformable solid and are listed in Table 3.

The numerical calculations provide the stresses in cylindrical coordinates at all points within the elastic half-space except in the vicinity of the Rayleigh surface wave, where a nonremovable singularity in the equations

TABLE 3—*Water drop impact pressures predicted from one-dimensional shock-wave relationship.*

Substrate Material	Drop Velocity, m/s	Pressure, MPa
ZnSe	222	429
	341	749
ZnS	222	425
	341	742
GaAs	222	735
	341	761

prevails, and at the surface, where numerical instabilities result during evaluation of transformation integrals. It was found that the stresses were reasonably well behaved at a depth of 5.1 μm or greater below the surface.

Results

Single-Drop Experiments

For all the conditions investigated, the impact of each individual water drop produced a ring fracture pattern on the infrared window materials and an annular indentation on the more readily deformed PMMA. Examples of the sites of impact of 2.0-mm water drops at 222 m/s are shown in Fig. 1 for each material. The ranking of the materials in order of increasing resistance to visible impact damage was zinc selenide, gallium arsenide, and zinc sulfide.

A summary of the effects of drop size and impact velocity on the dimensions of the damaged areas on the three materials is presented in Fig. 2. This figure is based on the average of the measurements of several impact sites for each impact condition. The 2.5-mm drops produced damaged areas almost identical in size and appearance to those produced by 2.0-mm drops. The damaged areas produced by the 0.7-mm drops, although similar in appearance, were considerably smaller than those produced by 2.0-mm drops. The increase in impact velocity from 222 to 341 m/s had a much greater effect on the dimensions of the damaged areas on PMMA than on zinc selenide. Except for their size, the impact sites on zinc selenide were surprisingly similar for both velocities.

Specimens of each material were etched subsequent to single-drop impact to reveal interactions between the ring fractures and the microstructure. The etchants were described in the "Procedures" section. The fractures on zinc selenide were primarily transgranular as shown in Fig. 3, with some intergranular fractures and dislocation etch pits near the inner radius of the damaged area as shown in Fig. 4. This pattern of transgranular cracks at the outer radius of the damaged area with intergranular cracks and dislocation etch pits at the inner radius was typical of all single-drop impact sites formed on zinc selenide at 222 m/s regardless of the drop size. The transgranular fractures were not associated with the twins, which were quite common in this material.

The transgranular nature of the fractures on zinc sulfide are illustrated in Fig. 5; no evidence of intergranular cracks or etch pits was found even with electron microscopic examination of several sites. Examination of the etched gallium arsenide specimen revealed no interaction of the fractures with grain boundaries or twin boundaries; however, preexisting surface scratches served as nucleation sites for damage as illustrated in Fig. 6.

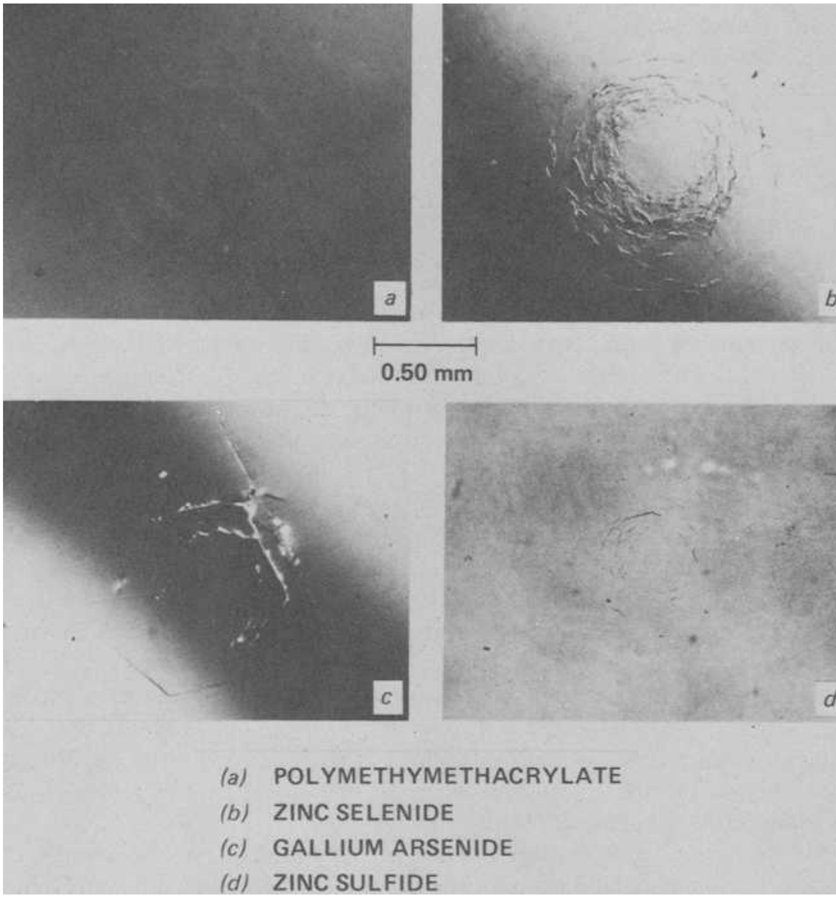

FIG. 1—*Damage produced by impact with 2.0-mm-diameter water drop at 222 m/s.*

Etching also revealed that many of the cracks were associated with particles of a second phase as shown in Fig. 7.

Transmitted light disclosed that considerably more subsurface damage was produced in zinc selenide than in zinc sulfide as shown in Fig. 8. The surface cracks on zinc selenide were found to propagate into the material at an angle of approximately 45 deg to a maximum depth of approximately 0.14 mm as shown in Fig. 9. This depth is somewhat greater than the diameter of the largest grains in the zinc selenide. Etching the cross-sectioned impact site in Fig. 9 showed that the cracks were not restricted to the largest grains; they typically traversed three average-sized grains. Attempts to polish and examine the cross section of an impact site on zinc sulfide were unsuccessful; however, an estimate of the depth of the cracks can be made from their projection at the higher magnification in Fig. 8*c*.

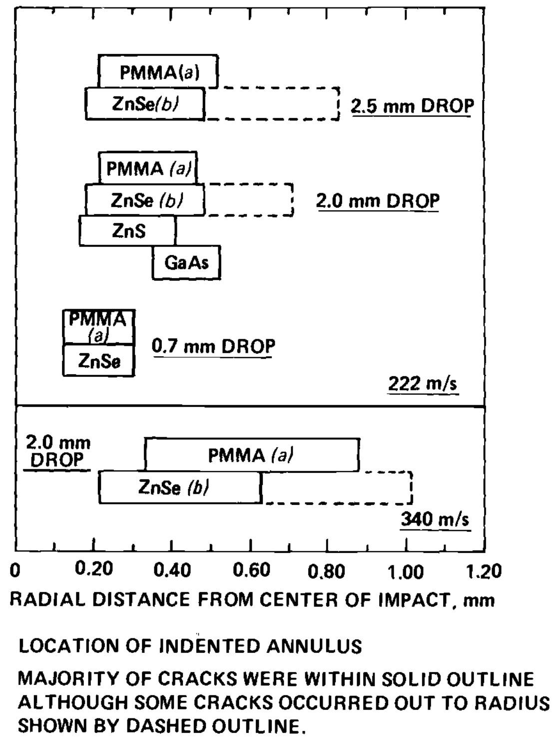

FIG. 2—*Size of damaged area produced by impact with single water drop.*

If it is assumed that the cracks penetrate at a 45-deg angle, their maximum depth would be 0.007 mm. This is somewhat less than the diameter of the largest grains and about one-twentieth the depth of crack penetration on zinc selenide.

Tests were also performed with zinc selenide specimens to determine how material damaged by a drop impact would respond to subsequent drop impacts which overlapped the original ring fracture site. An example of overlapping ring fractures formed by three 2.0-mm drops at 222 m/s is shown in Fig. 10. There was surprisingly little enhancement of damage in the region of overlapping ring fractures in this early stage of erosion; that is, a subsequent drop impact did not appear to significantly increase the extent of subsurface damage caused by the first drop. As revealed visually with transmitted light, subsurface damage at regions of overlap did not appear to be much greater than would be expected from the addition of the damage caused by each drop separately.

Ring fractures formed on the zinc sulfide layers of the bilayered specimens by impact with 2.0-mm drops at 222 m/s are shown in Fig. 11. The ring fractures on the 0.25-mm layer were somewhat more extensive

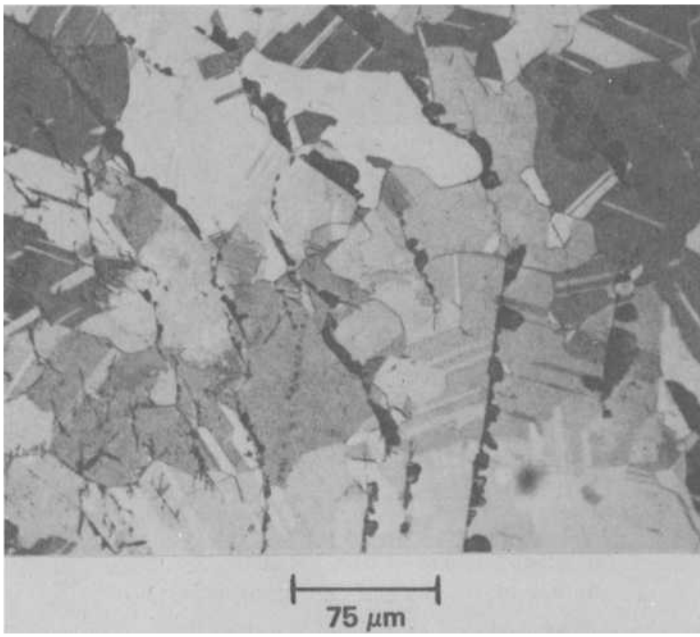

FIG. 3—*Transgranular ring fractures formed on zinc selenide by impact with 2.5-mm drop at 222 m/s.*

than those previously observed on homogeneous zinc sulfide specimens (Fig. 1), while the ring fractures on the 0.50-mm layer were comparable to those on the homogeneous specimens. The ring fractures on the 1.00-mm layer were similar to those on the 0.50-mm layer and therefore are not included in Fig. 11.

There was no evidence that the drop impacts had affected the bond between the layers on any of the bilayered specimens. Examination of the back face of the 0.25-mm zinc sulfide layer after it was removed in the decementing solution showed that the ring fractures had not penetrated through the layer. This observation agrees with the maximum crack depth of approximately 0.007 mm on the homogeneous zinc sulfide specimens.

Rainfield Experiments

The effects of exposure to the standard rainfield upon infrared transmittance at selected wavelengths are listed in Table 4 for zinc selenide, gallium arsenide, and zinc sulfide. These data were taken from, and are representative of, the continuous scans between 0.5 and 2.1 μm and 2.5 and 25 μm which were made for each specimen after each increment of exposure.

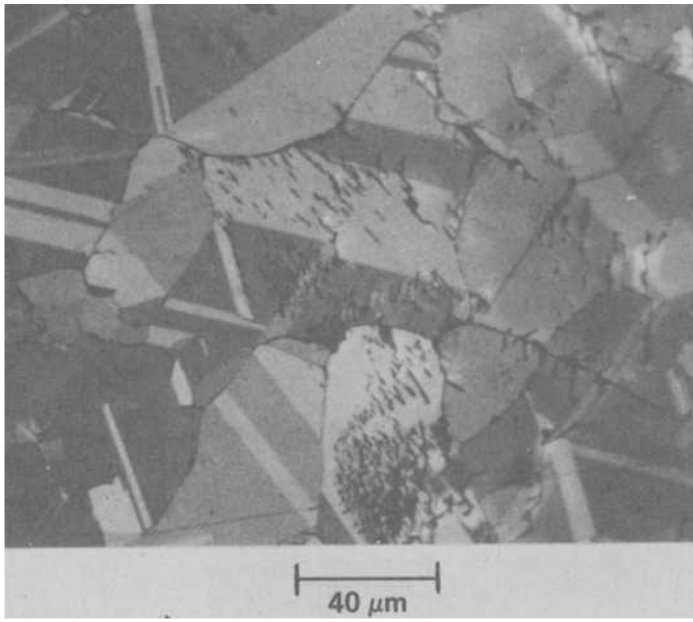

FIG. 4—*Intergranular cracks and etch pits at inner radius of ring fracture zone formed on zinc selenide by impact with 2.0-mm drop at 222 m/s.*

It is obvious from the data in Table 4 that zinc sulfide is the most erosion resistant of the three materials. In the near infrared range of 0.7 to 2.1 μm, the transmittance of all three materials was significantly reduced in the initial stage of erosion. This reduction was almost linear with exposure time. For zinc sulfide, on the other hand, there appeared to be an incubation period before significant loss of transmittance occurred in the longer wavelength band above 2.5 μm. The erosion of zinc selenide and gallium arsenide was too rapid to establish the presence of an incubation period for loss of transmittance at the longer wavelengths. It is thought that these two materials would also exhibit an incubation period if exposed to a less severe rainfield.

The progress of surface damage with exposure time at a selected site on the zinc sulfide specimen is shown in Fig. 12. Nucleation of pits was apparent after 160 s and some of the pits had grown quite large by 240 s. This time range (160 to 240 s) also encompasses the end of the incubation period prior to transmittance loss for the longer wavelengths. Similar large pits were present on the zinc selenide specimen after 20 s and on the gallium arsenide specimen after 40 s, at which times transmittance for the longer wavelengths had decreased significantly.

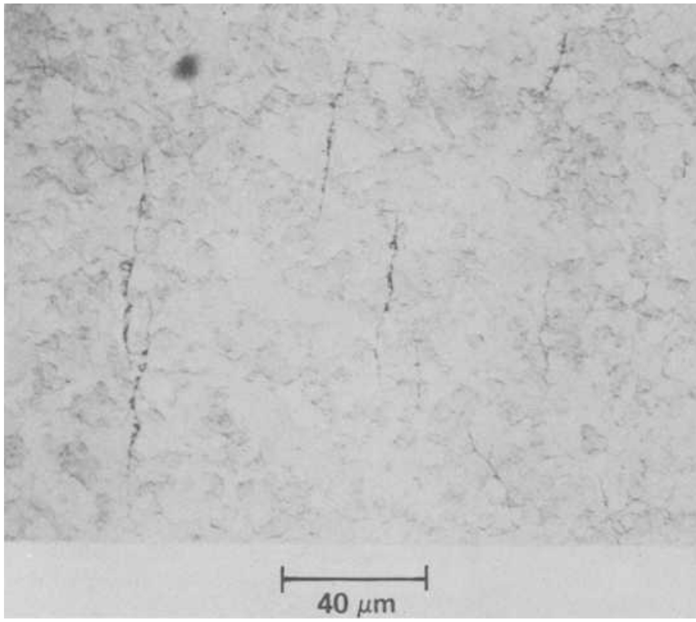

FIG. 5—*Transgranular ring fractures formed on zinc sulfide by impact with 2.0-mm drop at 222 m/s.*

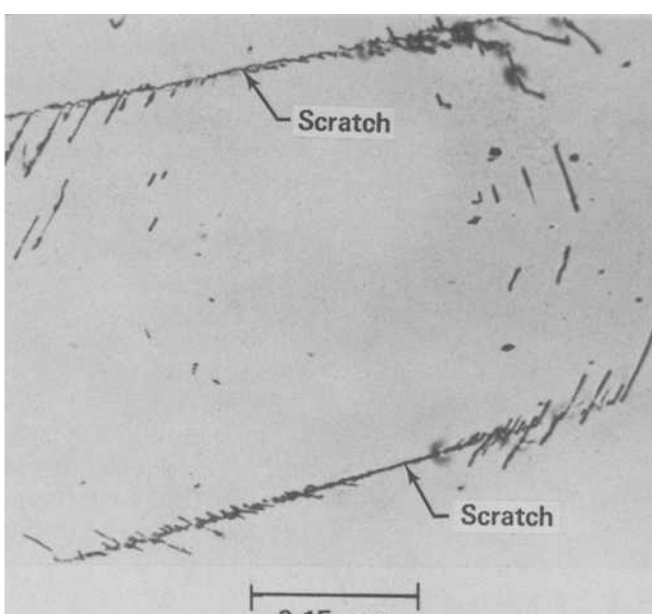

FIG. 6—*Enhancement of damage by scratches on surface of gallium arsenide.*

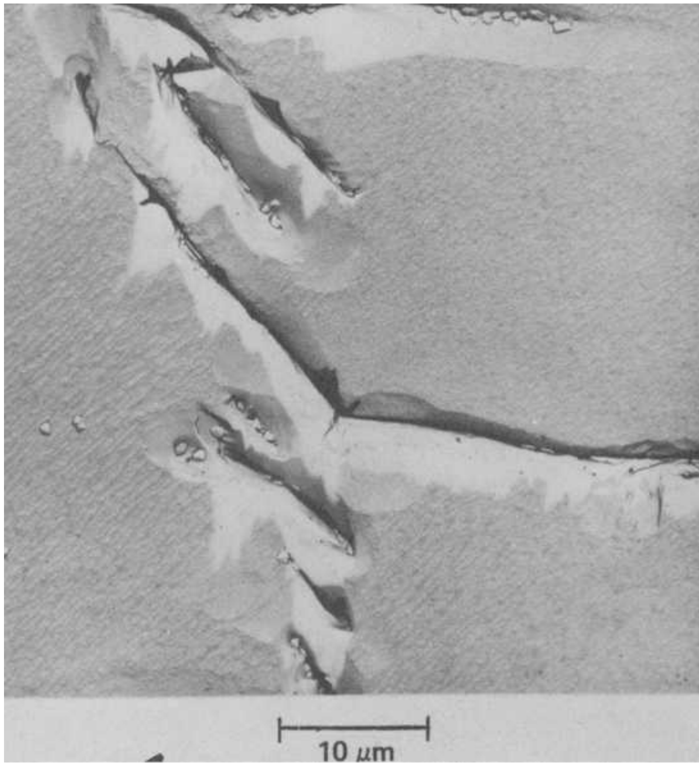

FIG. 7—*Second-phase particles associated with ring fracture cracks on gallium arsenide.*

Analytical Modeling

The radial stress, generally compressive under the loaded region, was found to have significant tensile values outside of the loaded region. It is this stress which causes the ring fracture damage in the impacted material. The remaining stresses were primarily compressive at all points except for small tensile values which occurred just outside the loaded boundary and which are not thought to contribute to failure. Values of the highest radial tensile stress predicted for each impact case are listed in Table 5. As can be seen, the mathematical model predicted stresses which greatly exceeded the ultimate strength of the materials for all conditions.

Selected examples of the plots of computed radial stress, σ_{rr}, are presented in Fig. 13. The magnitudes of the stresses have been normalized and the actual stresses can be found by multiplying the normalized values by the appropriate impact pressures, P_o, in Table 3. The radial distance, r, in the stress plots is measured from the center of impact.

Examination of Figs. 13*a-d* reveals that both the radial location at

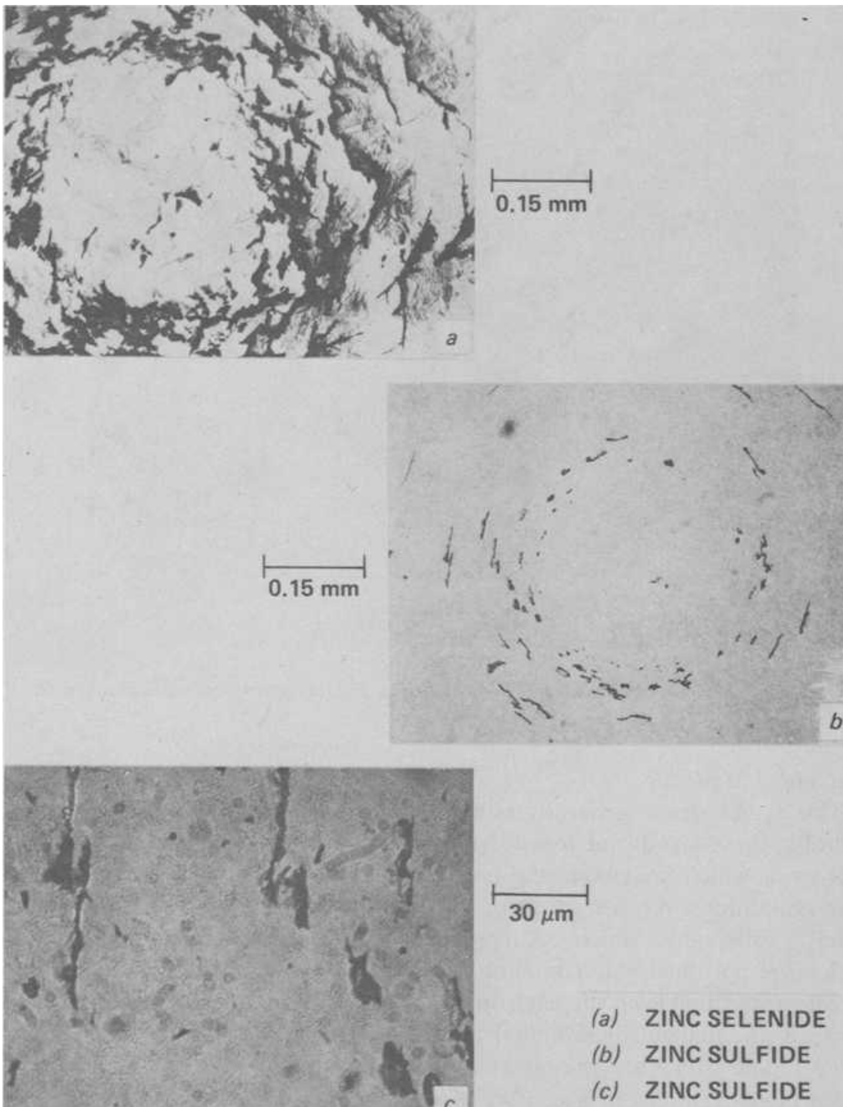

FIG. 8—*Subsurface damage at impact sites formed by impact with 2.0-mm drops at 222 m/s as revealed by transmitted light.*

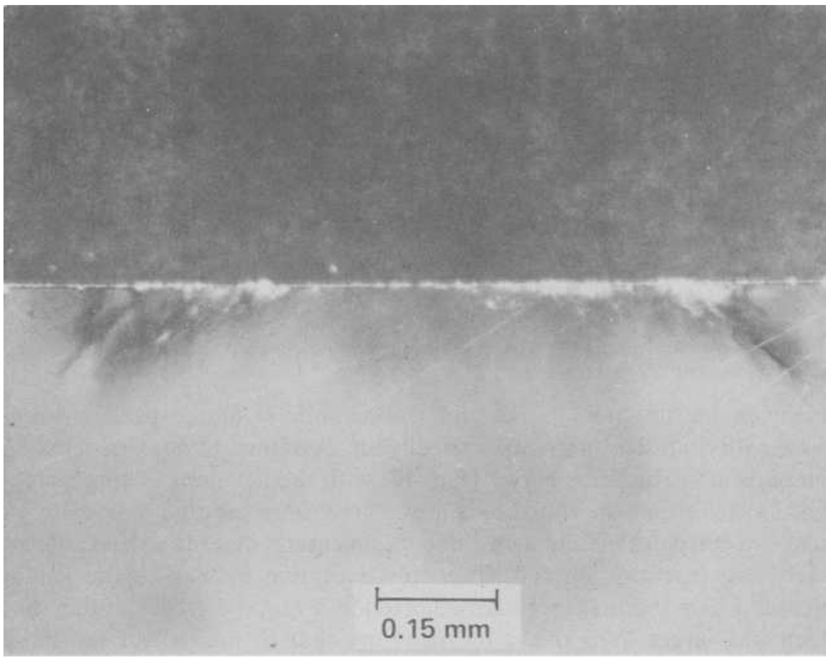

FIG. 9—*Cross section of site on zinc selenide where 2.5-mm drop impacted at 222 m/s.*

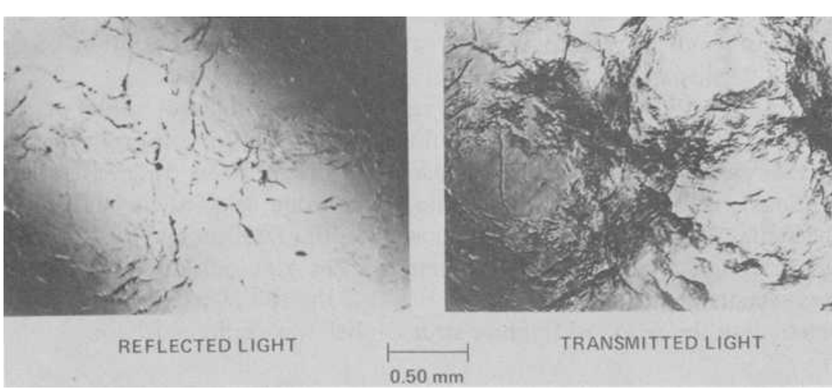

FIG. 10—*Overlapping triplet ring fractures on zinc selenide impacted by 2.0-mm drops at 222 m/s.*

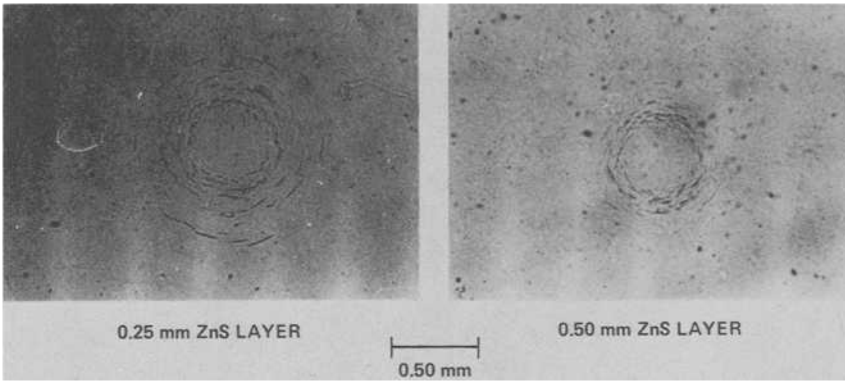

FIG. 11—*Damage produced on zinc sulfide/zinc selenide bilayered specimens by impact with 2-mm drop at 222 m/s.*

which the tensile stress peaks and the magnitude of the peak stress increase with drop size and impact velocity for a given material (zinc selenide). Comparison of the stress curves (Fig. 13) with the locations of ring fracture (Fig. 2) shows that the radial locations where the computed tensile stresses peaked correspond closely with the experimentally determined locations at which ring fractures formed. The only exception appears to be gallium arsenide where the first fractures occurred at a radial distance of 0.35 mm, which was larger than the radial distance of 0.20 mm where the tensile stress reached its maximum peak value. The predicted wave forms at a distance of 0.20 mm were triangular spikes for all three materials. The fact that gallium arsenide was the only material which did not fracture at this location, even though the maximum stress was greatest, suggests the possibility that the fracture of gallium arsenide is more sensitive than that of zinc selenide or zinc sulfide to stress rate or to the duration of the applied tensile stress.

Figure 14 shows the maximum value of the computed radial tensile stress as a function of depth below the surface for a 2.0-mm drop impacting zinc selenide at 222 m/s. For each depth, the stress at several radial locations was computed and the maximum value selected for this curve. The radial stress falls off rapidly below a depth of 25 μm and by 100 μm is less than the reported fracture strength. For zinc sulfide, which has a stress-versus-depth curve similar to Fig. 14, the radial tensile stress would be less than the reported fracture strength below a depth of 50 μm.

Discussion

Single-Drop Experiments

The superior erosion resistance of zinc sulfide as compared to zinc

TABLE 4—*Loss in transmittance versus exposure time in standard rainfield (2.54-cm/h, 1.8-mm drops) at 222 m/s.*

Material	Cummulative Exposure, s	2 μm Trans-mittance, %	2 μm Loss,[a] %	5 μm Trans-mittance, %	5 μm Loss,[a] %	7 μm Trans-mittance, %	7 μm Loss,[a] %	10 μm Trans-mittance, %	10 μm Loss,[a] %
ZnSe	0	74	0	74	0	75	0	75	0
	20	40	46	56	24	58	23	60	20
	30[b]	14	81	30	59	32	57	34	55
GaAs	0	55	0	54	0	59	0	60	0
	20	41	25	50	8	56	5	58	3
	40	26	53	44	18	50	15	52	13
	60[c]	...	...	...	...	...	...	...	...
ZnS	0	74	0	65	0	67	0	70	0
	20	72	3	69	+6	70	+4	72	+3
	40	68	8	70	+8	72	+7	73	+4
	80	63	15	72	+11	72	+7	73	+4
	160	54	27	72	+11	72	+7	73	+4
	240	41	45	56	14	59	12	63	10
	320[d]	29	51	45	31	47	30	50	29

[a] Loss is percent decrease in transmittance from initial value at 0-s exposure; + indicates apparent gain in transmittance.
[b] Specimen broke into two pieces.
[c] Specimen shattered.
[d] Specimen intact.

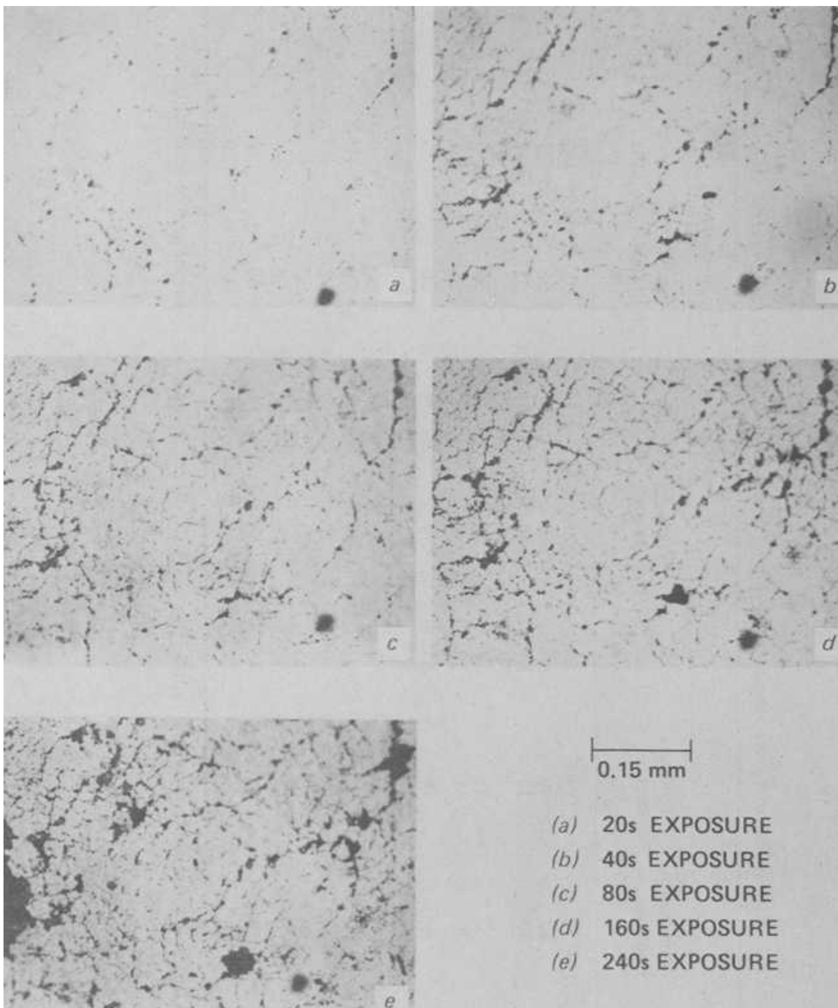

FIG. 12—*Progress of surface damage on zinc sulfide exposed to standard rainfield (2.54-cm/h, 1.8-mm drops) at 222 m/s* (×88).

TABLE 5—*Predicted peak radial tensile stresses for 222- and 341-m/s water drop impacts.*

Material	Drop Diameter, mm	Stress, MPa, at $z = 12.7\ \mu m$ [a]		Stress, MPa, at $z = 5.1\ \mu m$ [a]	
		$V_0 = 222$ m/s	$V_0 = 341$ m/s	$V_0 = 222$ m/s	$V_0 = 341$ m/s
ZnSe	0.7	103	240	188	464
	2.0	214	524	369	973
	2.5	240	614	442	...
ZnS	0.7	79	207	...	...
	2.0	196	475	285	757
	2.5	230	...	...	...
GaAs	0.7	...	...	...	...
	2.0	200	456	374	...
	2.5	...	...	...	...

[a] z is the depth below the impacted surface of the material.

selenide was evidenced by the shallower depth of the ring fractures on zinc sulfide. This shallow depth is undoubtedly related to the smaller grain size of the zinc sulfide, an order of magnitude less than that of the zinc selenide. The small grains would limit the depth of penetration of the fractures, which must cross grain boundaries and undergo directional changes in neighboring grains with different crystallographic orientations. It is probable that a decrease in the grain size of zinc selenide would increase its resistance to damage from water drop impact.

Gallium arsenide was less resistant than zinc sulfide to water drop impact damage even though it had greater hardness and was somewhat higher in strength. Unlike zinc selenide and zinc sulfide, gallium arsenide appeared to exhibit an interaction between the ring fractures and material defects which were resolvable with optical and electron microscopy. The extent of the cracking was enhanced by the presence of scratches on the surface and second-phase particles within the grains, both of which would intensify the stresses generated by water drop impact. It is probable that a water drop impact would have produced ring fractures even without the presence of scratches and second-phase particles; however, these microstructural defects certainly contributed to the low erosion resistance of gallium arsenide by increasing the extent of ring fractures formed by a water drop impact.

The lack of significantly enhanced damage at sites of overlapping drop impact on zinc selenide was somewhat unexpected based on the results of an investigation by Adler [5] on the erosion of glass specimens impacted with glass beads. Adler observed that pits were nucleated at triplet impact sites by the ejection of material which was undermined by the juncture of the conical ring fractures formed by the three impacts. He used this observation as the basis for establishing the pit nucleation criterion for a pit nucleation and growth model of erosion of brittle materials by rain-

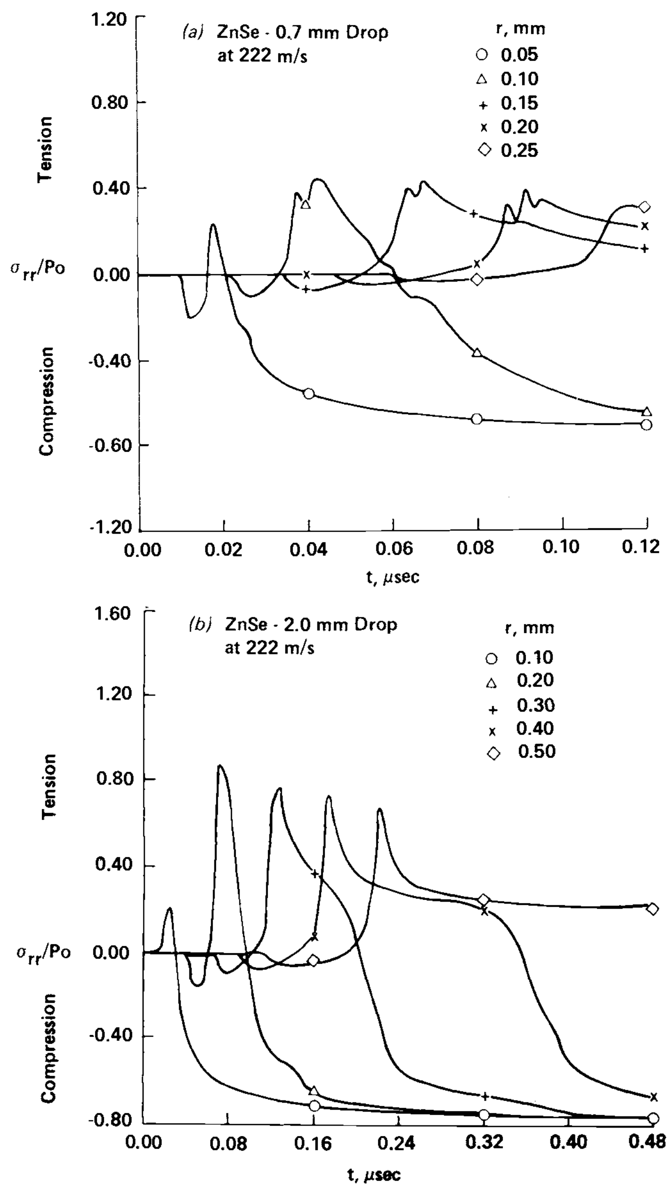

FIG. 13—*Distribution of radial stress at depth of 5.1* μm *below the surface.*

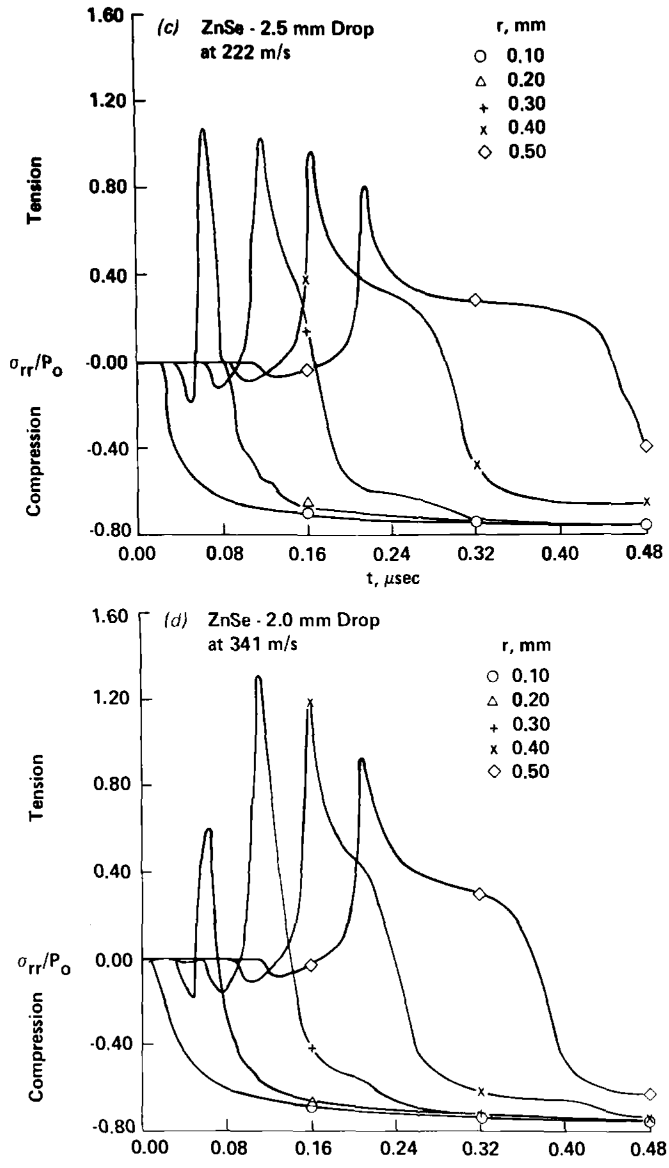

FIG. 13—*Continued.*

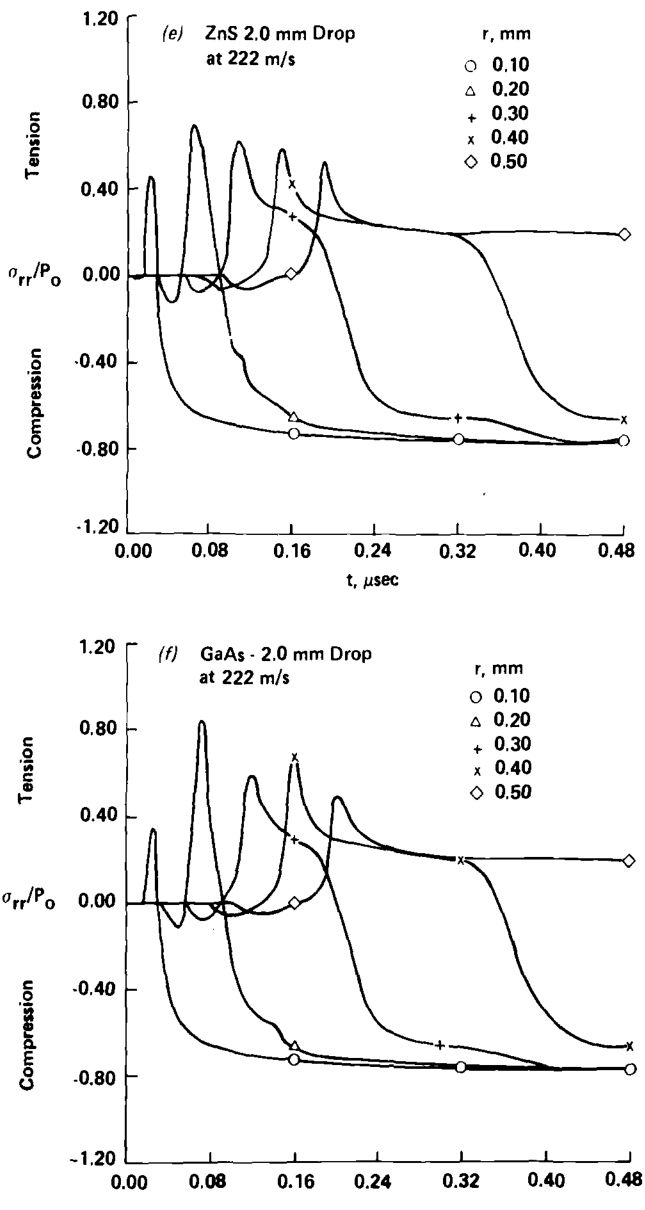

FIG. 13—*Continued.*

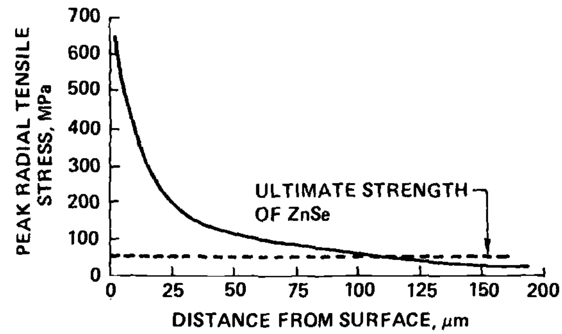

FIG. 14—*Variation of peak radial stress (at* t = *0.1 μs) with depth for a 2.0-mm water drop impacting zinc selenide at 222 m/s.*

drops and by solid particles. The experimental results from this program indicate that triplet water drop impacts do not nucleate a pit on the surface of zinc selenide. Although no triplet water drop impact sites were obtained on zinc sulfide or gallium arsenide, the examination of doublet impact sites makes it appear unlikely that the impact of a third drop would nucleate a pit on these materials. The performance of zinc sulfide in the rainfield experiments also demonstrated that a large number of overlapping impacts is required before significant material removal occurs.

The single-drop experiments with the bilayered specimens demonstrated the promise of using a relatively thin layer of erosion-resistant material to protect a less erosion-resistant substrate. The basic nature of the water drop impact damage on thin zinc sulfide protective layers with a thickness of 0.50 mm and greater was comparable to that on a thick, homogeneous zinc sulfide specimen. The presence of the interface and the different mechanical and physical properties of the zinc selenide substrate did not significantly affect the response to water drop impact of zinc sulfide layers having a thickness of 0.50 mm and greater. These experimental results substantiated the analytical model, which showed that the stresses generated by drop impact decay rapidly with depth below the surface (Fig. 14). In practice, the thickness of the zinc sulfide protective layer will be controlled by the progress of erosion in a rainfield. The surface pits which produced loss of transmittance for bulk zinc sulfide were found to increase in depth as they grew laterally upon continued exposure to the rainfield. The rate at which these pits deepen will dictate the required thickness of the protective layer.

Rainfield Experiments

The series of experiments in the rainfield provided information on the operative erosion mechanisms for the three materials and the correlation between erosion and loss of transmittance. For zinc sulfide, transmittance of the shorter wavelengths (0.5 to 2.1 μm) began to decrease with the subsurface damage caused by the initial drop impacts and continued to decrease almost linearly with exposure time as the amount of subsurface damage increased with additional drop impacts. On the other hand, there was an incubation period before loss of transmittance occurred for the longer wavelengths above 2.5 μm. Actually, the transmittance for the longer wavelengths increased during the incubation period (Table 4). The incubation period lasted for somewhere between 160 and 240 s, which also corresponded to the time for nucleation of relatively large surface pits as illustrated in Fig. 12.

The loss of transmittance for the two wavelength ranges appears to be caused by different types of damage. The formation and subsurface extension of the ring fractures which occur prior to nucleation and growth of large surface pits appear to be the major contributors to transmittance loss at wavelengths between 0.5 and 2.1 μm. The transmittance loss at this shorter wavelength range may be controlled by the area of the ring fractures projected perpendicular to the beam. This would account for the observed linear decrease in transmittance with increase in time of exposure to the rainfield, that is, with the number of drop impacts per unit area.

Surface pits, rather than surface or subsurface cracking, appear to be the primary cause of transmittance loss at the longer wavelengths above 2.5 μm. Transmittance of longer wavelengths does not decrease during the initial incubation stage, while the extent of subsurface cracking increases. Once surface pits have nucleated and started to grow in lateral area, transmittance of longer wavelengths starts to decrease and is inversely proportional to the percentage of total pitted area.

Zinc selenide and gallium arsenide eroded too rapidly in the rainfield to provide a sufficient number of exposures for a complete analysis of the relationship between transmittance and erosion damage. Large pits had formed and started to grow laterally on zinc selenide in 20 s and on gallium arsenide in 40 s. These times corresponded to the times at which transmittance of wavelengths above 2.5 μm began to decrease significantly. It is likely that the relationship between transmittance and erosion for these two materials is similar to that proposed in the foregoing for zinc sulfide, although fewer overlapping impacts would be required to nucleate a surface pit and terminate the incubation period.

Analytical Modeling

The predictive capability of the analytical model appears reasonable when the computed stresses are compared with the results obtained from the single-drop impact experiments. For the materials considered and for the ranges of drop sizes and velocities investigated, the mathematical model predicted that stresses would exceed the published ultimate flexural strengths of the materials. The materials, in fact, did fracture upon single-drop impact for all conditions tested.

Zinc sulfide (Fig. 13*e*) provides an interesting case since the radial locations where stresses were computed bracketed the region of ring fractures observed in the experiments. At radial distances of 0.10 and 0.50 mm, predicted peak stresses were 196 and 225 MPa, respectively, and fracture did not occur. Fracture occurred at in-between radial locations where the predicted peak stress ranged from 243 to 285 MPa. These values are 2.2 to 2.6 times higher than the published fracture strength of 110 MPa. For the case of zinc selenide impacting 0.7-mm-diameter drops at 222 m/s (Fig. 13*a*), fracture did not occur at a predicted stress of 99 MPa (r = 0.05 mm) but did occur at a predicted stress of 145 MPa (r = 0.25 mm). This latter value is 2.5 times higher than the published fracture strength of 58 MPa.

It is not surprising that the predicted stresses where ring fractures occurred were considerably higher than the published fracture strengths of the materials. The fracture strength of brittle materials is controlled by the tail of the size distribution curve at large flaw sizes. In the normal flexural test, the stress is distributed within a large volume of material so the largest flaws will inherently limit the strength. The stress generated by a water drop impact samples a relatively small volume of material where the defects are primarily at the microstructural level, resulting in a higher fracture strength.

Caution must be used, however, in correlating the predicted stresses with measured fracture strengths—for two reasons. First, the assumptions inherent in the model probably introduce errors into the values of the computed stresses. For example, no provision is made for pressure decay as the contact area expands, so the predicted stresses are probably somewhat high at the larger radial locations. Secondly, the use of the quasi-static ultimate strength of the material as the failure criterion for the dynamic case of water drop impact is undoubtedly an oversimplification, but at this time no better criterion is felt to exist.

The analytical model also showed that ring fracture from single-drop impact is a surface phenomenon (Fig. 14). The computed depth of 100 μm at which the radial stress generated in zinc selenide, by impact at 222 m/s with a 2.0-mm drop, fell below the ultimate strength correlated well with the 140-μm depth of the actual fractures shown in Fig. 9. Figure 9 is the site of impact by a 2.5-mm drop; however, the site of impact by a 2.0-mm drop is quite similar. Again, this correlation between the predicted stress pattern and the experimentally determined fracture pattern verifies the validity of the analytical model.

Conclusions

Impacting specimens with single water drops proved to be an excellent method to study the behavior of zinc selenide, zinc sulfide, and gallium arsenide in the early incubation stage of erosion before significant material removal. The rainfield experiments, in turn, proved the importance of the incubation stage in the overall erosion process.

Lengthening the incubation period appears to be the most promising method to improve the overall performance of the infrared window materials. The length of the incubation period is controlled by the response to drop impact of a relatively shallow surface layer. Thus, techniques to form compressive layers on the outer surfaces of infrared window materials should be a fruitful area for investigation.

The analytical model provided valuable insight into the transient stress patterns produced by drop impact. Comparisons between the predicted stress patterns and the experimentally induced ring fractures verified the basic validity of the approach used in the formulation of the model. For future applications, the model can be made even more representative of the actual impact event by incorporation of a timewise decay of the impact pressure and allowance for compressibility of the liquid drop.

Acknowledgments

This research was supported by the Air Force Materials Laboratory under Contract No. F33615-76-C-5125.

References

[1] Blowers, R. W., *Journal of the Institute of Mathematics and Its Application*, Vol. 5, 1969, pp. 167-193.

[2] Wahl, N. E., "Supersonic Rain and Sand Erosion Research; Part 1—Design, Construction, and Operation of a Mach 3 Rotating Arm Apparatus," Technical Report AFML-TR-69-267, Part 1, Air Force Materials Laboratory, Dayton, Ohio, 1969.

[3] Adler, W. F. and Hooker, S. V., "Characterization of Transparent Materials for Erosion Resistance," Technical Report AFML-TR-76-16, Air Force Materials Laboratory, Dayton, Ohio, 1976.

[4] Hackworth, J. V. and Kocher, L. W., "Exploratory Development of Rain Erosion Resistant Infrared Window Materials," Technical Report AFML-TR-77-84, Air Force Materials Laboratory, Dayton, Ohio, 1977.

[5] Adler, W. F., "Analysis of Multiple Particle Impacts on Brittle Materials," Technical Report AFML-TR-74-210, Air Force Materials Laboratory, Dayton, Ohio, 1974.

T. L. Peterson[1]

Multiple Water Drop Impact Damage in Layered Infrared Transparent Materials

REFERENCE: Peterson, T. L. "**Multiple Water Drop Impact Damage in Layered Infrared Transparent Materials,**" *Erosion: Prevention and Useful Applications, ASTM STP 664,* W. F. Adler, Ed., American Society for Testing and Materials, 1979, pp. 279-297.

ABSTRACT: The influence of materials and construction variables on the rain erosion behavior of layered infrared window materials has been investigated at 210 m/s in the simulated rain environment (1.8 mm drop diameter, 2.5 cm/h rainfall rate) of the Air Force Materials Laboratory rotating-arm apparatus.

Outer-layer materials included chemical vapor deposited (CVD) zinc sulfide, hot-pressed zinc sulfide, and CVD gallium arsenide. These materials were either deposited directly onto CVD zinc selenide substrates or adhesively bonded to the zinc selenide.

In general, damage mechanisms and relative rates of degradation were predictable from studies of the erosion behavior of homogeneous specimens. The effect of layer thickness on erosion behavior was determined for outer layers of CVD zinc sulfide. For outer layers thicker than approximately 1.0 mm, damage in the layered specimens was comparable to that in homogeneous CVD zinc sulfide specimens. The amount of multiple impact damage in layers thinner than 1.0 mm compared with that in thicker layers depended upon the technique of fabrication. Damage was more severe for thinner layers bonded to zinc selenide but was somewhat reduced for thinner layers deposited directly on zinc selenide.

The effect of grain size on erosion resistance was demonstrated by comparison of the behavior of layers of CVD gallium arsenide bonded to zinc selenide with that of gradient-freeze grown gallium arsenide. The CVD material was more resistant to impact damage because of its much smaller grain size.

Thin films deposited on zinc sulfide and gallium arsenide as antireflection coatings were susceptible to removal by drop impacts and the subsequent radial outward flow of water away from the impact site. However, more durable antireflection coatings on zinc sulfide have been developed.

KEY WORDS: rain erosion, infrared window materials, zinc sulfide, drop impact, erosion mechanisms, gallium arsenide, erosion

Materials which are transparent to infrared radiation are susceptible to

[1]Materials engineer, Air Force Materials Laboratory, Air Force Wright Aeronautical Laboratories, Wright-Patterson AFB, Ohio.

rain erosion damage after relatively short exposures to rain at moderate to high subsonic velocities. Since lattice absorption generally shifts to shorter wavelengths as physical properties improve [*1*],[2] the few materials which transmit radiation between 8 and 12 μm are generally more susceptible to erosion damage than other transparent materials. Of the materials which transmit in this region, the leading candidates for high-velocity infrared window applications are zinc sulfide, zinc selenide, and gallium arsenide.

The rain erosion behavior of these materials has been investigated at the Air Force Materials Laboratory (AFML), as well as at other laboratories [*2,3*]. Exposure of these brittle materials to multiple water drop impacts at subsonic velocities produces mechanical and optical degradation. Fracture initiates at or near the window surface in the vicinity of a drop impact due to the large transient tensile stresses which occur there. Once a crack is nucleated by a drop impact, it is propagated during subsequent loading cycles. The network of internal fracture surfaces which is produced by this crack nucleation and propagation process causes the infrared transmission through these materials to be greatly reduced before significant removal of material from the window surface occurs.

Of the three materials listed in the foregoing, zinc selenide is the most desirable window material because of its excellent optical properties over all required wavelengths from 0.5 to 12 μm. However, its rain erosion resistance is much less than that of gallium arsenide or zinc sulfide. Zinc sulfide is the most erosion resistant of the materials, but its usefulness is limited by scatter at visible wavelengths and intrinsic absorption beyond 10.5 μm. Therefore, in order to produce an infrared window with the optimum optical properties and rain erosion resistance currently possible, layered or composite window constructions are being developed. A zinc selenide substrate with a thin outer layer of zinc sulfide is one of the more promising structures of this type because it combines the erosion resistance of zinc sulfide with the optical properties of zinc selenide.

Single or multilayer thin films applied as antireflection coatings on infrared windows are a special case of layered materials. In infrared applications, these coatings are required because of the large transmission losses which occur due to reflection at the surfaces of zinc selenide, zinc sulfide, and gallium arsenide. Because removal of these coatings significantly degrades the effectiveness of the infrared system, their durability in a rain environment is critical.

Procedure

The material specimens investigated in this program were all obtained from Air Force research and development contracts. Two techniques for

[2]The italic numbers in brackets refer to the list of references appended to this paper.

fabricating layered window materials were evaluated. The first technique was chemical vapor deposition of zinc sulfide directly onto a polished substrate of chemical vapor deposited (CVD) zinc selenide. This technique is described in Ref *4*. The second technique involved adhesively bonding the outer layer material to the CVD zinc selenide substrate. Outer-layer materials used in the second technique included CVD and hot-pressed zinc sulfide and CVD gallium arsenide. Zinc sulfide has been bonded to zinc selenide with no degradation in optical properties, using a chalcogenide glass from the arsenic-sulfur-selenium (As-S-Se) system as the adhesive. Fabrication of windows using this technique is described in Ref *5*. Other specimens for evaluation of rain erosion behavior only were fabricated using an optical cement, such as Loctite 307, as the adhesive. Additional information characterizing the materials as required to properly interpret the results is provided in later discussions.

The erosion experiments were performed in the AFML rotating-arm facility, which has been previously described [*6*]. Specimens 3.8 by 1.3 by 0.5 cm thick, with top and bottom surfaces optically polished, were mounted at the end of a blade and rotated at a velocity of 210 m/s through the rain environment. The rain environment was produced from hypodermic needles located above the arm. The environment consisted of water drops with a mean drop diameter of 1.8 mm falling to produce a rainfall rate of 2.54 cm/h. The drops impacted the specimens at an angle of 90 deg with respect to the surface, except in a few cases where the impingement angle was 78 deg.

Results

Zinc Sulfide Bonded to Zinc Selenide

Composite windows of zinc sulfide and zinc selenide were formed by first inserting a thin slide of As-S-Se glass between the optically polished mating surfaces of the two window components. The assemblage was then heated and compressed between hot platens so that the glass wetted the materials to be joined and flowed to form a thin layer. The glass layer was uniform and typically 10 μm thick. Final polishing of the outer faces was performed after the joining process.

Damage mechanisms due to rain drop impacts in the CVD zinc sulfide layers were the same as those previously observed in homogeneous zinc sulfide specimens; that is, cracks forming broken concentric rings initiated at the surface and propagated into the specimen. Although complete ring cracks were generally not formed by a single drop impact on zinc sulfide at 210 m/s, several complete rings were observed after multiple impacts had occurred in the area. These cracks were initiated possibly by impacts of somewhat larger drops which might occasionally be present in the rainfield.

Figure 1 illustrates the type of damage observed in CVD zinc sulfide after 20 min exposure to 2.54-cm/h rainfall at 210 m/s. The reflected light micrograph in Fig. 1*a* and the transmitted light micrograph in Fig. 1*b* reveal the extent of surface damage and subsurface damage, respectively. Notice that most of the damage which results in the transmittance loss is subsurface, and that only a small amount of surface pitting has occurred at cracks. Cracks have propagated to a maximum depth of about 1.0 mm.

Although a network of transgranular cracks has been formed by the many drop impacts which have occurred, the original ring crack formations are still indicated. This is not surprising since examinations of overlapping single impacts indicate a tendency for the central undamaged region at the first impact site to resist damage from subsequent impacts.

CVD zinc sulfide layers of various thicknesses from 0.38 to 2.1 mm bonded to zinc selenide were investigated to determine the influence of thickness on the rate of multiple impact damage. Figure 2 shows erosion damage after 20 min at 210 m/s in specimens with 0.38- and 1.5-mm-thick layers of CVD zinc sulfide bonded to zinc selenide.

The damage in the 1.5-mm layer of CVD zinc sulfide was very similar to that in homogeneous zinc sulfide. Damage was confined to the zinc sulfide layer, and no delamination occurred at the bond line. Average crack depths were on the order of 0.3 mm with some crack depths as large as 1.0 mm. Considering these results, one would expect cracks to propagate through the 0.38-mm layer of zinc sulfide and into the zinc selenide. This was indeed the case, and extensive cracking in the zinc selenide results in large dark areas as shown in Fig. 2*c*. The total depth of these cracks was significantly greater than 1.0 mm because crack propagation occurs at lower stress in the zinc selenide than in the zinc sulfide layer.

In general for these exposure conditions, the erosion resistance of the layered specimens was as good as that of homogeneous CVD zinc sulfide if the thickness of the outer layer was greater than 1.0 mm. Similar results were obtained for specimens exposed for 3 min at 257 m/s. Although the effect of velocity on optimum layer thickness should be further investigated, it appears that for practical purposes the thickness should be somewhat greater than the maximum depth of cracks which could be tolerated by the infrared imaging system.

In addition to CVD zinc sulfide, hot-pressed zinc sulfide was also briefly investigated as an outer-layer material which could be bonded to zinc selenide. Although the hot-pressed and CVD material have similar mechanical properties, their erosion behavior was significantly different. Hot-pressed zinc sulfide was more susceptible to damage by multiple water drop impacts than was CVD zinc sulfide. The difference in behavior is shown by the transmitted light micrographs in Fig. 3. Both specimens were exposed for 30 min at a velocity of 210 m/s and an impingement angle of 78 deg. CVD zinc sulfide showed essentially no surface pitting while

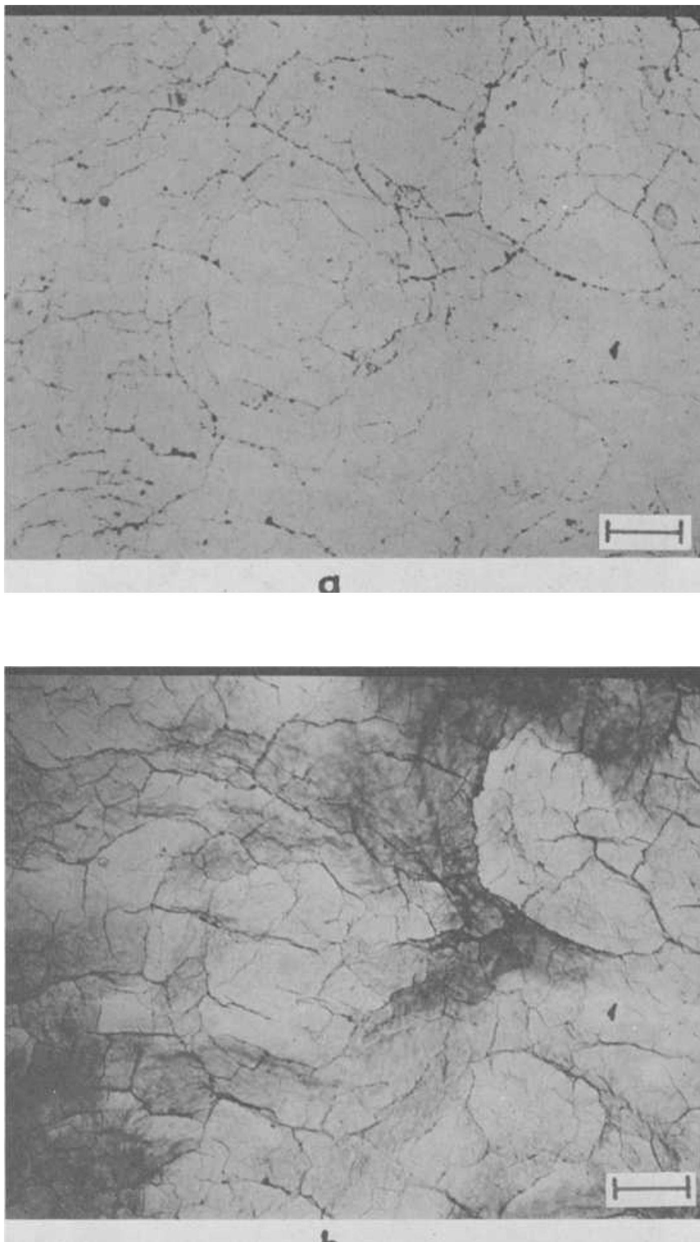

FIG. 1—*Micrographs of multiple water impact damage in CVD zinc sulfide using* (a) *reflected light and* (b) *transmitted light (scale marks indicate 200 μm).*

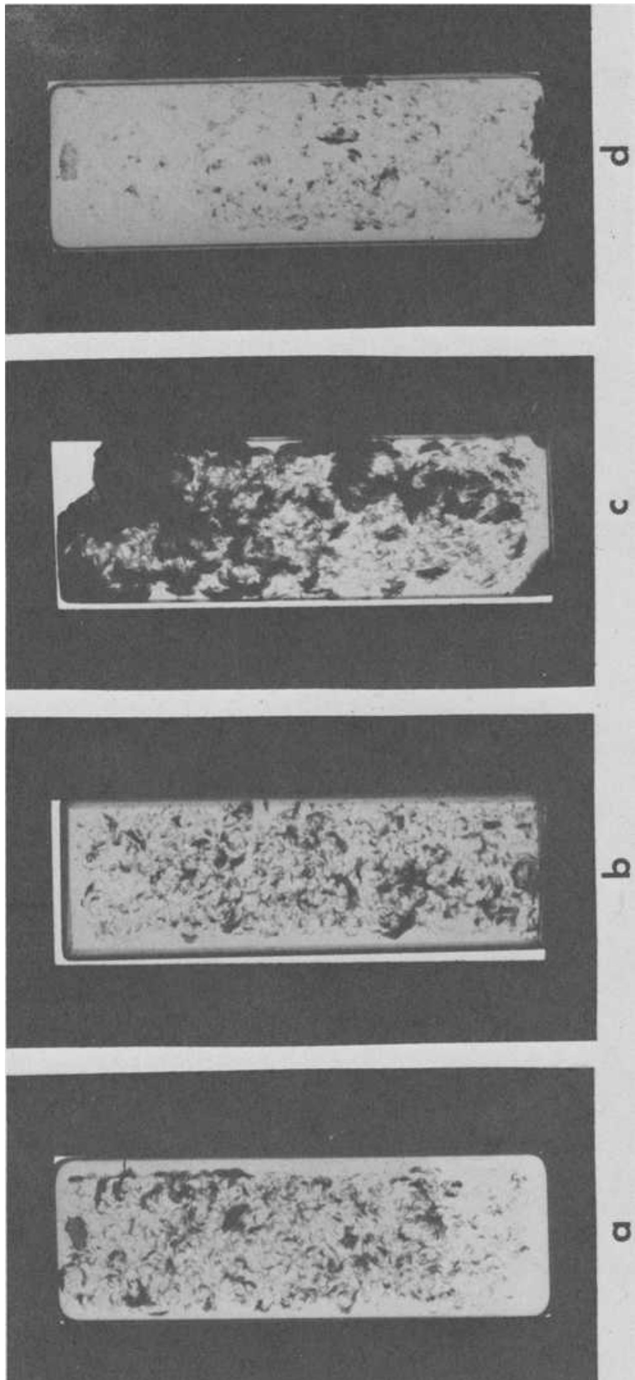

FIG. 2—*Photographs comparing erosion damage in (a) CVD zinc sulfide, (b) 1.5-mm zinc sulfide/glass/zinc selenide, (c) 0.38-mm zinc sulfide/glass/zinc selenide, and (d) 0.5-mm zinc sulfide/zinc selenide after 20 min at 210 m/s.*

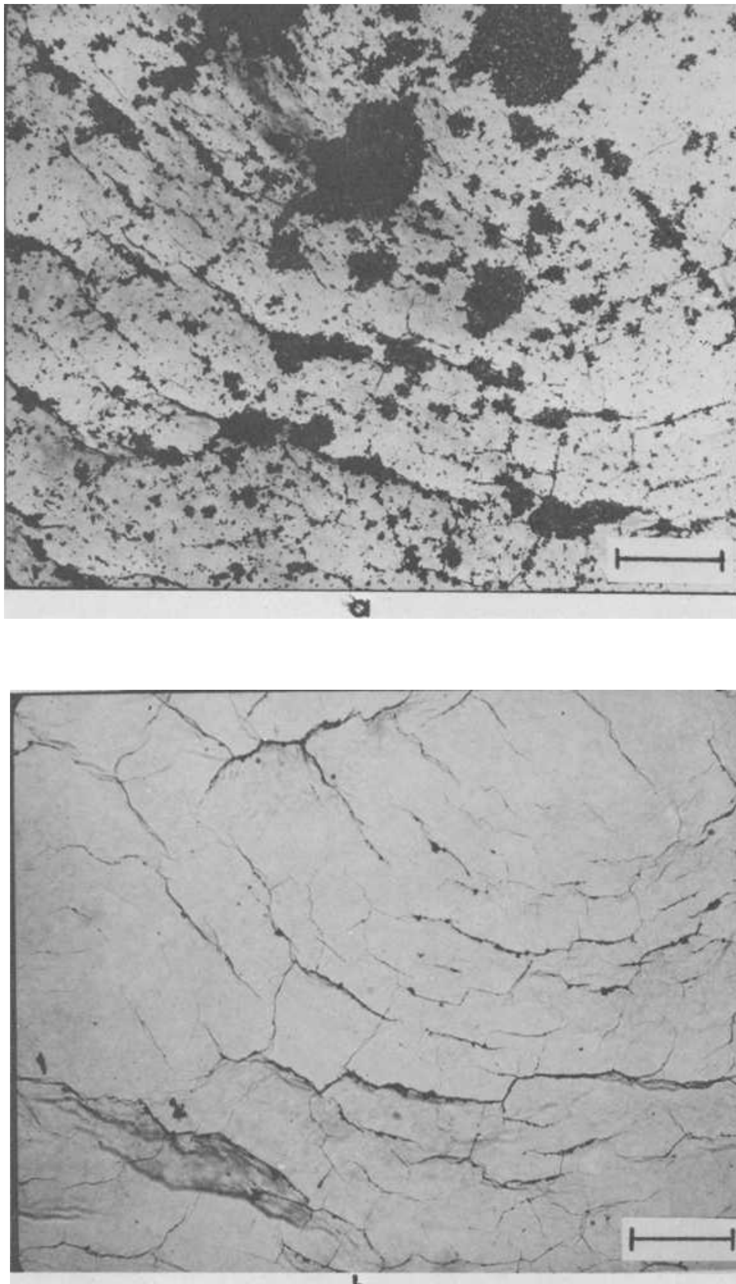

FIG. 3—*Comparison of rain erosion behavior of* (a) *hot-pressed zinc sulfide and* (b) *CVD zinc sulfide (scale marks indicate 100 μm).*

there was extensive surface pitting in the hot-pressed zinc sulfide outer layer. The ring cracks penetrated to approximately the same depth in both materials but to a significantly lesser depth than those shown in Fig. 1 for zinc sulfide impacted at a 90-deg angle.

The microstructure and mechanisms of erosion of hot-pressed zinc sulfide were examined. The microstructure was equiaxed with pronounced twinning and a mean grain size of 5 μm. The erosion pits, as illustrated by Fig. 4, were formed by intergranular fracture which resulted in the removal of whole grains. There was virtually no evidence of the transgranular fracture which occurred in CVD zinc sulfide, indicating relatively poor bonding between the zinc sulfide grains. Because of its lack of erosion resistance, hot-pressed zinc sulfide was not investigated further as an outer-layer material for composite windows.

Zinc Sulfide Deposited on Zinc Selenide

Composite zinc sulfide-zinc selenide windows may also be prepared by depositing zinc sulfide directly onto polished zinc selenide substrates. Specimens prepared using this technique were investigated to again de-

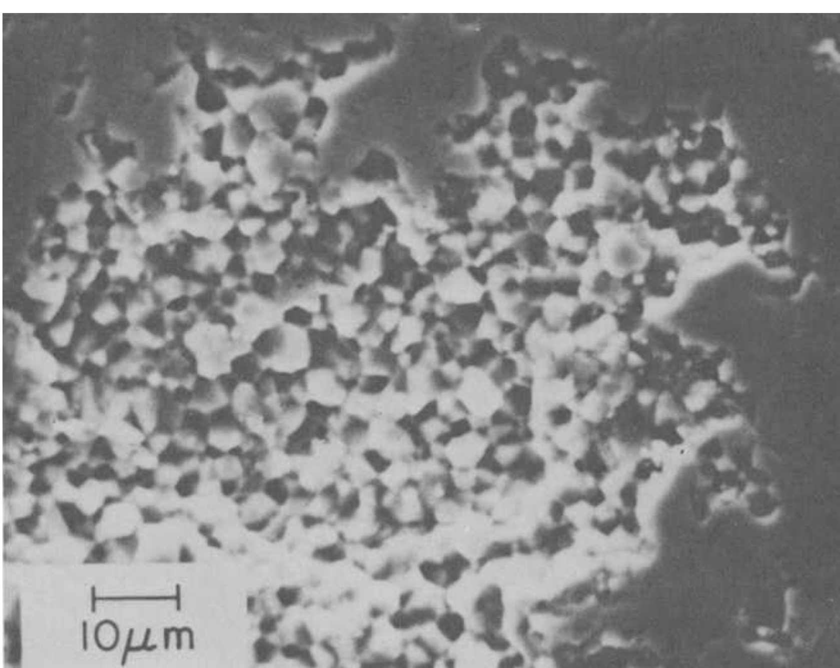

FIG. 4—*Erosion pitting in hot-pressed zinc sulfide by intergranular fracture.*

termine the effect of thickness of the zinc sulfide layer on erosion behavior. Outer-layer thicknesses from 0.5 to 3.0 mm were obtained by varying the depth of grinding and polishing on the top and bottom surfaces of these composite specimens.

The mechanisms of erosion damage in these layers were once again similar to those in homogeneous zinc sulfide. Figure 5 shows the microstructure and cracking in a 0.5-mm zinc sulfide layer which had been etched after a 20-min exposure to the rainfield. The transgranular nature of the cracks which initiated at the surface is characteristic of CVD zinc sulfide. The fine, equiaxed microstructure with a mean grain size of 6 μm is also typical of homogeneous zinc sulfide specimens.

As was the case for the adhesively bonded composites, the damage in zinc sulfide layers thicker than 1.0 mm was the same as that in homogeneous zinc sulfide. However, for all specimens with outer layers of 0.5 and 0.65 mm, the amount of damage after 20 min at 210 m/s did not increase, but was noticeably less than that in homogeneous zinc sulfide. The amount of damage in a specimen with an outer layer of 0.5 mm shown in Fig. 2*d* may be compared with the damage in a homogeneous zinc sulfide specimen in Fig. 2*a*. The density of transgranular cracks on the surfaces of the

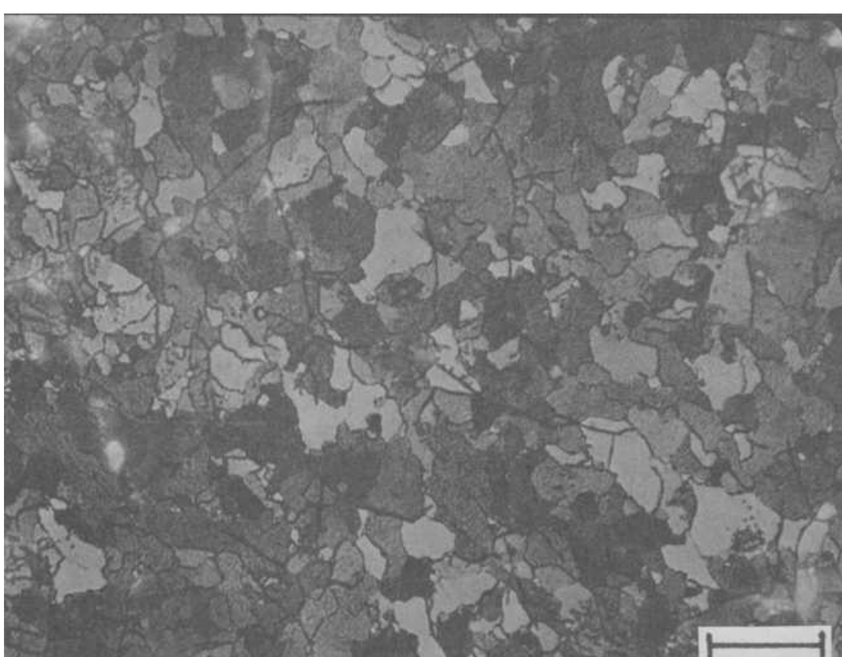

FIG. 5—*Microstructure and transgranular cracking of CVD zinc sulfide layers; reflected light (scale mark indicates 20 μm).*

two specimens was approximately equal, but the cracks propagated much shorter distances into the thin zinc sulfide layer. Average crack depths in the layer were only 0.05 mm, and the maximum depth to which cracks propagated was not more than 0.15 mm. This contrasts with a maximum depth of 1.0 mm in homogeneous zinc sulfide. Besides the depth of crack propagation, there was nothing to distinguish the damage in thin zinc sulfide layers deposited on zinc selenide from that in thicker layers or in homogeneous zinc sulfide.

CVD Gallium Arsenide Bonded to Zinc Selenide

The erosion resistance of gallium arsenide produced by a horizontal gradient-freeze technique is greater than that of CVD zinc selenide but less than that of CVD zinc sulfide. One reason for the low resistance of gallium arsenide grown from the melt is its large grain size. With the CVD process, gallium arsenide with a much finer microstructure may be produced. The rain erosion behavior of two specimens, one with a 0.5-mm outer layer of CVD gallium arsenide and the other with a 1.0-mm outer layer bonded to zinc selenide, was investigated.

Figure 6 compares the erosion damage in the 1.0-mm CVD gallium arsenide layer with that in a homogeneous gradient-freeze gallium arsenide specimen. Both specimens were exposed for 10 min at 210 m/s.

The gradient-freeze specimen contained a few large grains several millimetres in size. Fracture occurred along preferred cleavage planes with relatively long straight cracks visible on the surface. After these cracks initiated, they propagated into the specimen, forming internal fracture surfaces which have been observed using an infrared microscope. This internal damage and the surface pitting which occurred at intersecting cracks were responsible for a significant loss in transmission.

The relatively small grain size of 40 μm of the CVD gallium arsenide shown in Fig. 6*a* tended to limit the transgranular crack length. The propagation of cracks, which had to cross grain boundaries and undergo directional changes in neighboring grains of different orientation was reduced. Short straight cracks, approximately equal in length to the grain size, were observed on the surface. These cracks formed broken concentric rings similar to those observed in zinc selenide and zinc sulfide.

The optimum thickness for the gallium arsenide layer was not determined. The damage after 5 min exposure in the 0.5-mm layer was approximately equal to that in the 1.0-mm layer after 10 min exposure. The damage in layers greater than 1.0 mm was not determined.

Thin-Film Antireflection Coatings

The importance of a durable antireflection coating for infrared windows

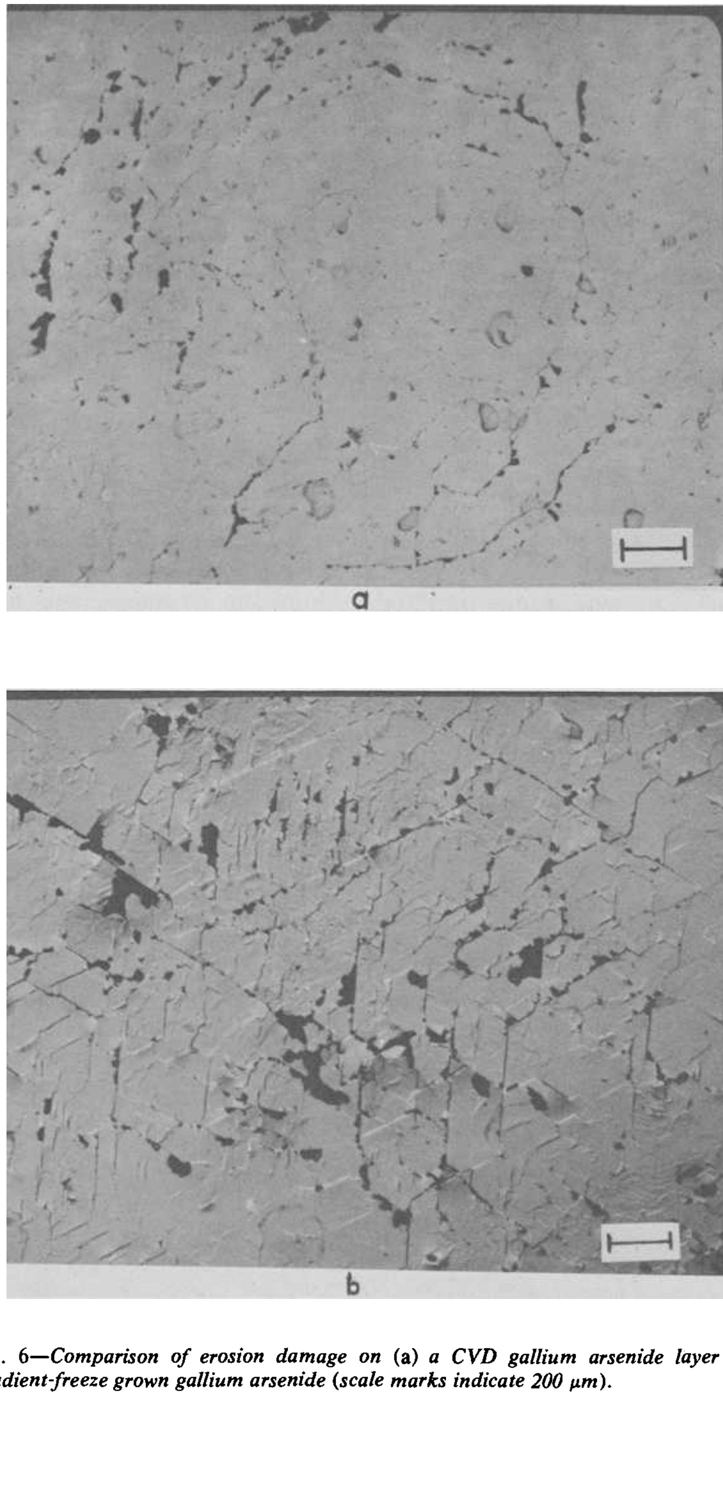

FIG. 6—*Comparison of erosion damage on* (a) *a CVD gallium arsenide layer and on* (b) *gradient-freeze grown gallium arsenide (scale marks indicate 200 μm).*

with high indexes of refraction has been pointed out. Many coating materials and combinations only micrometres thick have been investigated. Results for two coatings on zinc sulfide and one on gallium arsenide are presented to characterize the erosion behavior of these thin films.

The coating shown in Fig. *7a* was typical of antireflection coatings on zinc sulfide before rain erosion resistance was emphasized as an important property. This five-layer coating, consisting of alternating zinc selenide and thorium fluoride layers with an outer layer of cerium fluoride, was exposed for 10 min at 210 m/s and a 78-deg impact angle. Removal initiated at ring cracks in the coating, occurred in layers, and became significant after 10 min. Flow of water over the surface was responsible for lifting and tearing away of the coating at imperfections such as cracks or at exposed edges of the coating. The coating did not affect the erosion behavior of the zinc sulfide substrate.

The durability of the coating shown in Fig. *7b* is typical of that which has been obtained for antireflection coatings on zinc sulfide by adjusting deposition parameters for optimum erosion resistance. This two-layer coating, consisting of a neodymium fluoride layer over a zinc selenide layer, was exposed for 30 min at 210 m/s and a 78-deg impact angle. High substrate temperature during deposition and post-deposition annealing increased the erosion resistance of this coating. Good adhesion was obtained between the neodymium fluoride and the zinc selenide films, as well as between the zinc selenide film and the zinc sulfide substrate. Although small areas of removal initiated at pinholes in the coating and at ring cracks, the coating was quite resistant to large-scale removal.

This same neodymium fluoride-zinc selenide coating was also deposited on gallium arsenide and is shown in Fig. 8. This coating was exposed for 5 min at 210 m/s and a 78-deg impact angle. Its durability was typical for antireflection coatings on gallium arsenide. Coating removal again occurred at cracks in the coating and also occurred at scratches on the surface of the gallium arsenide.

Notice that the nature of damage in the coating depended upon the damage in the substrate, that is, ring cracks in the coating on zinc sulfide and long straight cracks in the coating on gallium arsenide. We therefore conclude that for these thin films crack initiation primarily occurred on the substrate surface and was followed by crack propagation into the coating. Cracking in the substrate was always accompanied by cracking in the coating above.

Discussion

Because these transparent materials are used as infrared windows, the effect of exposure to multiple raindrop impacts on their infrared transmittance must be evaluated. The loss in transmittance expressed as a

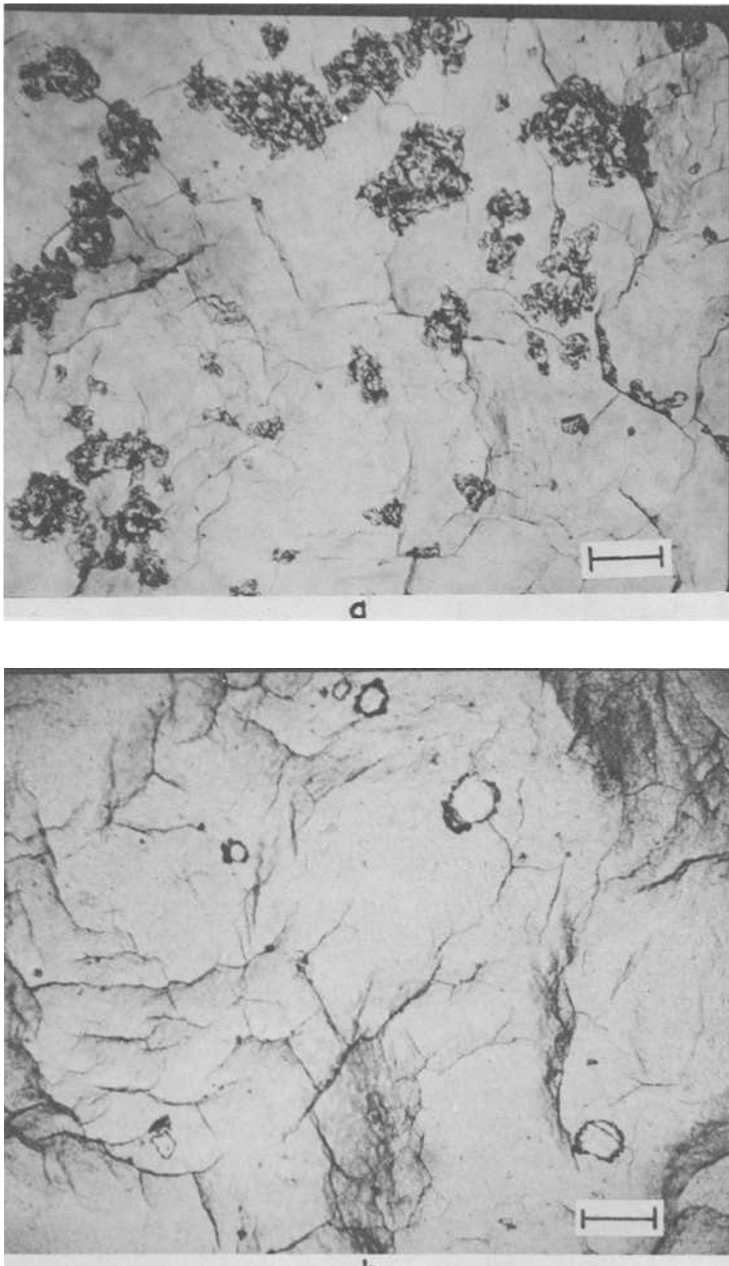

FIG. 7—*Removal of antireflection coatings on zinc sulfide by multiple-drop impacts. Coating* (a) *has been exposed for 10 min and coating* (b) *for 30 min at 210 m/s (scale marks indicate 200 μm).*

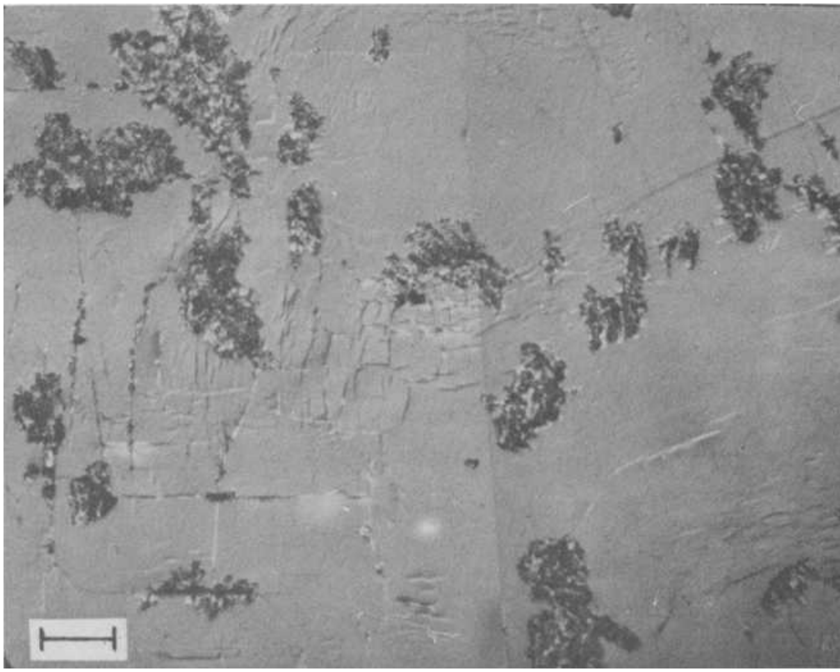

FIG. 8—*Removal of antireflection coating on gallium arsenide by multiple-drop impacts (scale mark indicates 200 μm).*

percentage of the initial transmittance is compared in Table 1 for various materials at wavelengths of 2.5 and 10 μm. All specimens were exposed to 2.54 cm/h rainfall at 210 m/s and a 90-deg impact angle for 20 min. Notice that in addition to being a function of exposure conditions, transmittance loss is also a function of wavelength with the loss increasing for shorter wavelengths.

The superior rain erosion resistance of CVD zinc sulfide compared with that of CVD zinc selenide is readily apparent from the table. The data also show that the resistance of the 1.5-mm layer of CVD zinc sulfide bonded to zinc selenide was approximately the same as that of homogeneous CVD zinc sulfide. The similarity in transmittance loss for both of these specimens is consistent with the similarity in erosion damage shown in Fig. 2. The transmittance loss in the specimen with a 0.38-mm layer of zinc sulfide bonded to zinc selenide was greater than that in zinc sulfide. However, the transmission loss was less in the specimen with a 0.5-mm layer of zinc sulfide deposited directly on zinc selenide.

The rain erosion behavior of the specimens of zinc sulfide bonded to zinc selenide is reconcilable with the behavior of homogeneous zinc sulfide

TABLE 1—*Comparative transmittance loss for various specimens exposed to 2.54 cm/h rainfall at 210 m/s and 90-deg impact angle for 20 min.*

	Loss in Transmittance	$\frac{T_i - T_f}{T_i} \times 100$
Specimen	at 2.5 μm	at 10 μm
CVD ZnSe	96	85
CVD ZnS	9	2
ZnS (0.38 mm)/glass/ZnSe	20	5
ZnS (1.5 mm)/glass/ZnSe	11	2
ZnS (0.51 mm)/ZnSe	6	2

specimens. The radial tensile stress in zinc sulfide due to a drop impact falls off rapidly below the surface. For a 2.0-mm drop impacting zinc sulfide at 222 m/s, the radial tensile stress below a depth of 0.05 mm has been calculated to be less than the reported fracture strength [*3*]. Layers on the order of a millimetre thick and homogeneous zinc sulfide would therefore be expected to respond similarly to a drop impact. Because these cracks continue to propagate for multiple impacts, the response of zinc sulfide layers to extended rain exposure was investigated experimentally.

It was shown that erosion damage in layers thicker than 1.0 mm was comparable to that in homogeneous zinc sulfide. This was undoubtedly related to the fact that cracks propagated no more than 1.0 mm into zinc sulfide exposed to the same multiple impact conditions. Similarly, the increase in damage for layers thinner than 1.0 mm was not unexpected.

The depth of crack propagation, and thus the required thickness of the outer layer, will depend upon the drop size, impact angle, impact velocity, and number of impacts, as well as upon the properties of the material. The effect of these impact conditions on optimum layer thickness should be investigated further. However, it appears that for practical purposes the thickness of the outer layer should be somewhat greater than the maximum depth of cracks which could be tolerated by the imaging system.

Based upon the erosion behavior of the bonded composite specimens, the similarity in erosion behavior of homogeneous zinc sulfide and 1.0- to 2.0-mm-thick layers of zinc sulfide deposited on zinc selenide was expected. However, the increase in erosion resistance observed in thinner layers was contrary to the decrease which was expected. Each of the three possible explanations which have been explored to explain this increase is discussed.

First, numerical code calculations were performed to examine the possible effect of stress wave interactions in thin zinc sulfide layers on zinc selenide for 2.0-mm-diameter drop impacts at 210 m/s [7]. The tension buildup was reduced somewhat in a 0.25-mm zinc sulfide layer when the reflected dilatational wave was allowed to interact with the impact surface as the peak tensions were increasing behind the shear wave front. However, since zinc sulfide and zinc selenide behave so similarly in the elastic regime, the reduction in peak tensile stress was not significant. Therefore, the stress wave interaction argument cannot explain the observed behavior unless the material properties at the interface and in the outer layer are altered by the deposition process to give a greater impedance mismatch than was used in the calculations.

Second, the microstructure of the zinc sulfide layers was examined. The surface microstructure of the zinc sulfide layers was the same as that of homogeneous zinc sulfide specimens. However, examination of cross sections of layered windows in many cases revealed a very-fine-grained zinc sulfide structure adjacent to the interface. The thickness of this region was approximately 0.05 mm. Beyond this region, the grain structure became elongated with an aspect ratio of approximately 6 to 1 and an equivalent equiaxed mean grain size of 6 to 8 μm. This elongated grain structure was also typical of cross sections of homogeneous zinc sulfide specimens. Although the thickness of the fine-grained structure at the interface was only about one tenth of the thickness of the 0.5-mm zinc sulfide layer, the existence of these fine grains could affect crack propagation in this thin layer.

The third and most likely explanation is that of a residual compressive stress in the zinc sulfide layer. A compressive stress in this layer near the interface would increase the resistance of the zinc sulfide to crack propagation for thin outer layers. Zinc selenide has a larger coefficient of thermal expansion than zinc sulfide, and the coefficients for both materials increase slightly with temperature. A compressive stress is therefore predicted in the zinc sulfide layer when it cools to room temperature after deposition at about 650°C. The magnitude of this stress can be estimated using the following equation adapted from Ref *8*

$$\sigma = (1 - 3t + 6t^2)(\alpha_{\mathrm{ZnS}} - \alpha_{\mathrm{ZnSe}})E_{\mathrm{ZnS}}\Delta T$$

where

σ = stress,
t = thickness of ZnS/thickness of ZnSe,
α = thermal expansion coefficient,
E = Young's modulus, and
ΔT = temperature change.

From Ref *9*, $\alpha_{\mathrm{ZnS}} = 7.85 \times 10^{-6}/°\mathrm{C}$ and $\alpha_{\mathrm{ZnSe}} = 8.53 \times 10^{-6}/°\mathrm{C}$ over the range from room temperature to 500°C, and $E_{\mathrm{ZnS}} = 74.5 \times 10^9$ N/m^2.

Therefore, a compressive stress of approximately 23 MN/m^2 is predicted in the zinc sulfide layer. This stress is small compared with the peak tensile stresses predicted at the surface for drop impacts at 206 m/s. However, these tensile stresses diminish rapidly at short distances from the surface, and this residual compressive stress could effectively limit crack propagation in these zinc sulfide layers.

The greater erosion resistance of CVD gallium arsenide compared with that of gallium arsenide grown by the gradient-freeze process demonstrated the importance of grain size. Damage in the CVD gallium arsenide was greater than that in zinc sulfide, but the grain size was still an order of magnitude larger than that in zinc sulfide. Transmission loss in the CVD gallium arsenide layers could not be measured because of absorption in the cement used to prepare the composite specimen.

Progress has been made in the development of durable, thin antireflection coatings on zinc sulfide. Erosion-resistant coatings remain on the surface even though significant cracking has occurred in the coating and the zinc sulfide substrate. High substrate temperatures during deposition and post-deposition annealing have been shown to be beneficial to increased coating durability in a rain environment. It is also obviously important to choose materials which adhere well to each other for adjacent layers in a multilayer coating. Removal of the coating is also strongly affected by the amount of erosion damage in the substrate and the surface finish of the substrate.

Conclusions

When resistance to rain erosion must be maximized without sacrificing broadband transmittance capability, a composite window is a logical and technically feasible approach. CVD zinc sulfide-zinc selenide windows can be readily fabricated by adhesive bonding or direct deposition. Composite windows have excellent optical properties and are as erosion resistant as zinc sulfide.

As long as the zinc sulfide cladding which is bonded to zinc selenide is thick enough, fracture can be confined to the cladding when it does occur. This suggests that a damaged cladding could be replaced periodically, allowing the window to be maintained at a relatively low cost. Although the required thickness is probably somewhat greater than 1 mm for practical applications, optimum thicknesses for various impact conditions need to be more accurately determined.

The erosion behavior of thin layers of zinc sulfide deposited directly on zinc selenide needs to be investigated further. This technique offers the possibility of improving the overall performance of infrared windows. Further improvements in erosion resistance should be obtainable by increasing the residual compressive stress in the outer layer. This could be accomplished by using a material with a lower coefficient of expansion than zinc sulfide. Deposition of thin layers of gallium phosphide and gallium arsenide directly on zinc selenide should therefore be pursued.

Durable thin films on infrared windows can be developed by selecting optimum materials and deposition parameters. Antireflection coatings have been developed which resist removal by multiple raindrop impacts even though significant damage has occurred in the substrate.

References

[1] Hilton, A. R., *Journal of Electronic Materials*, Vol. 2, No. 2, 1973, pp. 211-223.

[2] Hoff, G. and Rieger, H. in *Proceedings*, Eleventh Symposium on Electromagnetic Windows, Georgia Institute of Technology, Atlanta, Georgia, Aug. 1972, pp. 93-97.

[3] Hackworth, J. V. and Kocher, L. W., "Exploratory Development of Rain Erosion Resistant Infrared Window Materials," Technical Report AFML-TR-77-84, Air Force Materials Laboratory, Dayton, Ohio, 1977.

[4] Swanson, A. et al, "Development of Low-Cost Hardened Zinc Selenide for IR Windows," Technical Report AFML-TR-77-22, Air Force Materials Laboratory, Dayton, Ohio, 1977.

[5] Kramer, W. E. et al, "Development of Multispectral Sandwich-Type IR Windows," Technical Report AFML-TR-77-53, Air Force Materials Laboratory, Dayton, Ohio, 1977.

[6] Hurley, C. J. and Schmitt, G. F., "Development and Calibration of a Mach 1.2 Rain Erosion Test Apparatus," Technical Report AFML-TR-70-240, Air Force Materials Laboratory, Dayton, Ohio, 1970.

[7] Ito, Y. M. et al, "Analysis of Water Drop Erosion Mechanisms in Infrared-Transparent Materials Using Microphysical Material Models," Technical Report AFML-TR-77-219, Air Force Materials Laboratory, Dayton, Ohio, 1977.

[8] DiBenedetto, B. A. and Pappis, J., "Chemical Vapor Deposition of Multispectral Domes," Technical Report AFML-TR-75-27, Air Force Materials Laboratory, Dayton, Ohio, 1975.

[9] Swanson, A. et al, "Chemically Vapor Deposited Semiconductors for Laser and Infrared Window Applications," Technical Report AFML-TR-77-34, Air Force Materials Laboratory, Dayton, Ohio, 1977.

DISCUSSION

J. Zahavi[1] (*written discussion*)—Besides the mechanical damage observed in infrared materials exposed to rain erosion conditions, one would expect to find evidence for corrosion processes taking place at the damage area resulting in additional corrosion damage. I wonder whether the authors looked into the aspect of corrosion attack? I would think that one should look into this problem by means of electrochemical methods, electron microscopy, and electron probe microanalysis techniques.

T. L. Peterson (*author's closure*)—The aspect of corrosion attack in infrared transparent materials exposed to raindrop impacts has not been specifically investigated. However, the damage which results from multiple

[1]University of Illinois at Urbana-Champaign, Urbana, Ill. 61801.

drop impacts is believed to be entirely mechanical. No evidence of corrosion damage has been observed in electron microscopy studies of impact-damaged materials.

The presence of water at tips of cracks may, however, influence the fracture characteristics of these materials. For example, fracture mechanics studies have shown that CVD zinc selenide does exhibit moisture-dependent slow crack growth, suggesting a stress corrosion mechanism.[2]

[2]Evans, A. G. and Johnson, H., *Journal of the American Ceramic Society*, Vol. 58, 1975, pp. 244-249.

J. E. Field,[1] *D. A. Gorham,*[1] *and D. G. Rickerby*[1]

High-Speed Liquid Jet and Drop Impact on Brittle Targets

REFERENCE: Field, J. E., Gorham, D. A., and Rickerby, D. G., "High-Speed Liquid Jet and Drop Impact on Brittle Targets," *Erosion: Prevention and Useful Applications, ASTM STP 664*, W. F. Adler, Ed., American Society for Testing and Materials, 1979, pp. 298–319.

ABSTRACT: Two methods are described for producing high-velocity liquid impacts. The first involves projecting a jet of liquid at a stationary target while in the second specimens are fired at suspended drops. An objective of the study was to place the jet method on a *quantitative* basis. Detailed studies of jets, using high-speed photography, allowed the conditions for producing stable and reproducible jets to be obtained for a range of jet velocities (up to ~ 1000 m s^{-1}) and jet diameters (0.4 to 3.2 mm). The relation between jet impact and drop impact damage was achieved after experiments in which high-speed photography, pressure measuring techniques, and damage studies played important roles. The quantitative establishment of the jet method has practical implications since it has advantages in its ease of operation, its ability to simulate large drops, and in having the target stationary. Finally, a hydrostatic test apparatus for measuring the residual strength of brittle specimens following impact and examples of measurements on glasses and silicon nitride are described. Factors affecting the shape of residual strength curves are discussed.

KEY WORDS: erosion, liquid impact, rain erosion, jet method, high-speed photography, fracture, mechanical properties, residual strengths, pressure measurements, glasses, polymers, silicon nitride

It is well known that the impact of a liquid and a solid has important consequences in the rain erosion of aircraft, the erosion of steam turbines, and in cavitation phenomena. The work described in this paper was primarily concerned with the damage produced by the impact of large water drops. This kind of work is important since it is known that a large mass of liquid in a single drop can cause much more damage than the same mass divided into smaller drops. Thus although a rain field may contain only a relatively few large drops, it can be these which determine the catastrophic failure of a component, for example a glass radome. It is worth emphasizing that it is

[1] Physics and Chemistry of Solids, Cavendish Laboratory, Madingley Road, Cambridge, U.K.

the radius of curvature of the drop in the impact region that is important rather than the average drop radius. Thus an oblate drop can behave effectively as a drop of much larger radius.

We used two methods for simulating the collision with large water drops. The first was the technique first devised by Bowden and Brunton [*1,2*][2] for projecting a *jet* of liquid at a stationary target. The second was a gas gun which can fire 25.4-mm-diameter specimens at stationary drops. Both of these methods have their advantages. The first method has the drawback of shooting a jet of liquid but has distinct advantages in its ease of operation, low construction cost, and the velocity range that can be covered. The second is nearer the practical situation, since a spherical drop is struck, but has disadvantages as regards the size of specimen which can be projected and the deceleration (without further damage) of the specimen after impact. The suspension of spherical water drops of diameter greater than 2 mm is also a problem.

One of the objectives of the present project was to see if the jet method could be put on a sounder *quantitative* basis. This has involved extensive studies of jet production and impact (aided greatly by high-speed photography at microsecond framing rates) and the measurement of pressures produced by liquid impact. We have also attempted to put damage assessment on a more quantitative basis. This has involved measuring the residual strengths of specimens following impact. Strength was measured using a hydraulic testing technique. As is shown later, curves of residual strength versus impact velocity (for a constant jet size) show a sharp fall of strength when a critical velocity region is reached. This loss of strength comes at velocities *below* those which give visual (as viewed by eye) impact damage. Clearly this is a point of practical interest. The factors controlling the shape of these curves are now reasonably well understood.

As will become clear later, one of the conclusions from the research is that reproducible, stable jets can be produced which can simulate *drop* impact. For this reason the paper includes experimental details and references so that any of our apparatus can be readily reproduced. For example, there will be details of (1) the jet production method, (2) the gas gun, (3) the hydraulic strength tester, and (4) pressure measuring techniques. All of the foregoing are relatively low-cost items which any laboratory with a well-equipped workshop and electronics section could construct. We have also used high-speed cameras extensively and these are expensive items. However, although high-speed framing photography giving several sequential pictures was essential for our work, in which we had to establish conditions of jet stability, etc., it was not so necessary for future work using the jet method. A brief section is included therefore to describe how spark photography and photocell

[2]The italic numbers in brackets refer to the list of references appended to this paper.

methods could be used to observe jet shapes and velocities in a simple and inexpensive manner.

Experimental and Results

Jet Production

The basic method for jet production was worked out by Bowden and Brunton [1,2]. A projectile is fired into a stainless steel chamber containing a small quantity of water sealed in by a neoprene disk. The projectile and neoprene drive forward as a piston and extrude the water through a narrow orifice. The ratio of waterjet velocity to projectile velocity is typically 3 to 5 times. Figure 1*a* shows schematically the design of the stainless steel chambers which we found most suitable. A range of jet diameters is obtained by varying the dimension *d*. The back surface of the disk should be flush with the rear surface of the chamber. A convenient way to load the chamber is through the nozzle using a hypodermic syringe. Care has to be taken to ensure that the chamber liquid does not contain particles or air bubbles and that the liquid/air interface is convex outward. The chamber is *not* optimized for producing high jet velocity to projectile velocity ratios, since our jets adequately cover the range required in rain erosion applications. If the application had been to produce high-velocity liquid jets for mining or rock cutting, more suitable chamber design could give jet velocity to projectile velocity ratios of 10 to 12 times (see, for example, Ref *3*).

In the original apparatus a commercial spring-operated air gun was used to fire the lead projectile. This basic arrangement has now been modified and the lead slugs are propelled by compressed gas. The compressed gas is typically nitrogen but helium is useful for high-velocity work. The gas bottle is used to load a chamber with gas, and the gun is then fired by triggering a

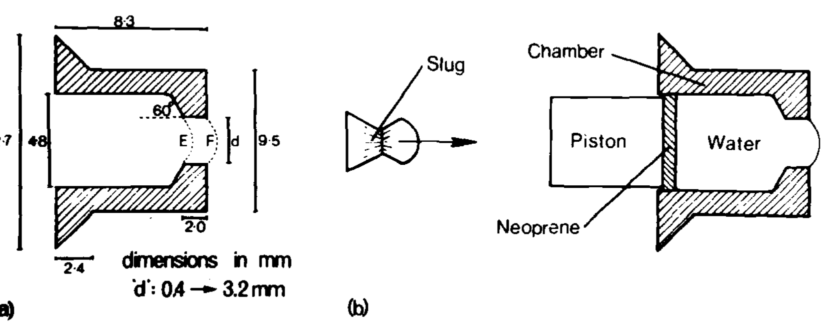

FIG. 1—*Liquid jet apparatus:* (a) *Dimensions of the steel extrusion chamber, filled with water to Positions E or F;* (b) *momentum exchanger piston for low jet velocities.*

fast-acting solenoid valve. A problem which we had at the start of this particular project was obtaining jet velocities *below* a few hundred m s^{-1}. (There were no problems in obtaining higher values up to a few thousand m s^{-1}.) This was eventually overcome by using the arrangement illustrated in Fig. 1*b*; the added piston effectively acts as a momentum exchanger.

Chamber Characteristics

Chambers with jet orifice diameter, d, in the range 0.4 to 3.2 mm have been fully tested. Calibration curves have also been obtained of jet velocity versus gas gun pressure for all the various values of d. The variation in the conversion ratio, that is, the value of V_j/V_s (V_j = jet velocity, V_s = slug velocity), is given in Fig. 2 for three chamber sizes (all loaded to Position F with convex-outward liquid/air interfaces). The ratio is not constant throughout this velocity range for the smaller diameters, but in the larger ones it is approximately constant. When the chambers were loaded to Position E, the velocity ratios were increased by about 7.5 percent for the 0.8-mm nozzle and about 5 percent for the 1.6- and 2.4-mm nozzles. The peaking of

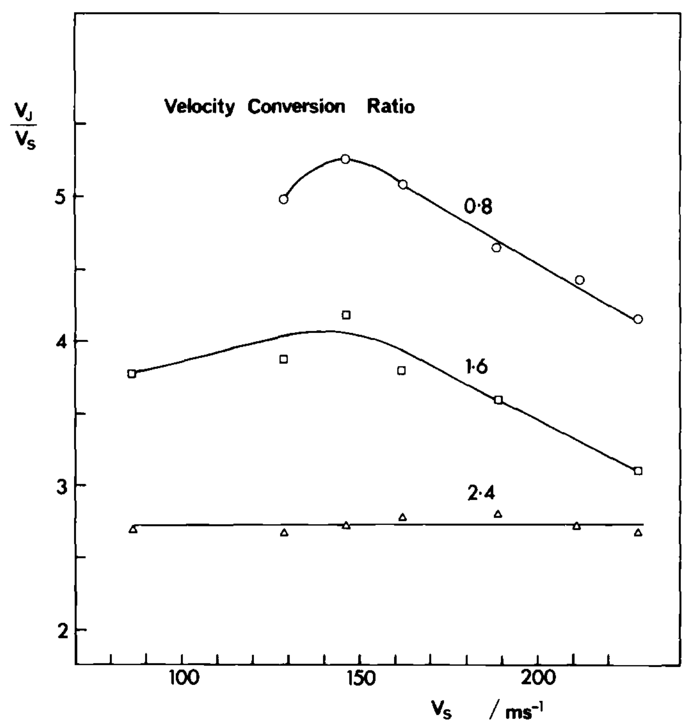

FIG. 2—*Velocity conversion ratio for three exit orifice diameters.* V_j = *jet velocity;* V_s = *slug velocity. Nozzle sizes are 0.8, 1.6, and 2.4 mm.*

the V_j/V_s curves for the 0.8- and 1.6-mm nozzles indicates that there are mechanisms for reducing the conversion efficiency which become more effective both for high velocities and for low velocities. The low-velocity limit of V_j/V_s, that is, the ratio of chamber area to nozzle area, is 36 for the 0.8-mm, 9 for the 1.6-mm, and 4 for the 2.4-mm nozzles. Hydrodynamic effects reduce the efficiency of the nozzles below these ideal figures, but less so the larger the nozzle diameter.

The detailed shape of the curves is quite complex. The main point, however, from a practical outlook is that for given conditions the jets have reproducible velocity and form.

High-Speed Photography of Jet Behavior

Early photographic work on impact in our laboratory was with a Cranz-Schardin system [*2*], a Beckman and Whitley (Model 189) rotating mirror camera [*2,4-6*], and a Beckman and Whitley 501 single-frame image converter camera [*7*]. All these systems have drawbacks which limit their usefulness for the present application. Our Cranz-Schardin system provides very high resolution over a limited area, but it is difficult to set up and successive frames suffer from parallax. The Beckman and Whitley 189 rotating mirror camera also has good resolution and a high framing rate. However, liquid jet production is difficult to trigger on a microsecond scale unless expensive means are used, and so with a rotating mirror camera of limited access (film over only part of the cycle) the success rate is low. The Beckman and Whitley image converter is a single-frame camera, and to obtain a sequence involves several cameras, with the inherent problems of light loss or parallax errors. The camera recently adopted for our work, the Imacon[3] framing image converter, overcomes these disadvantages at the expense of a slightly inferior resolution capacity. It has three basic advantages over the other high-speed photographic systems available: (1) it is synchronizable *from* the event, (2) it is sensitive enough to record scattered light from opaque objects, using conventional light sources, and (3) the use of Polaroid film facilitates large numbers of sequences being taken, thus improving calibration data and allowing reproducibility of the waterjets to be investigated.

The camera was triggered by detecting, with a photomultiplier, reflected laser light from the waterjet. The signal from the photomultiplier was fed through suitable delay units to the xenon flash light source and the camera. Single flash pictures were taken with the same synchronization arrangement, and were illuminated by a 150-ns spark source.

An Imacon sequence, using shadowgraph photography, of a 750 m s^{-1} jet impacting a polymethylmethacrylate block is shown in Fig. 3. Such pictures

[3]J. Hadland P. I. Ltd., Bovingdon, Herts, U. K.

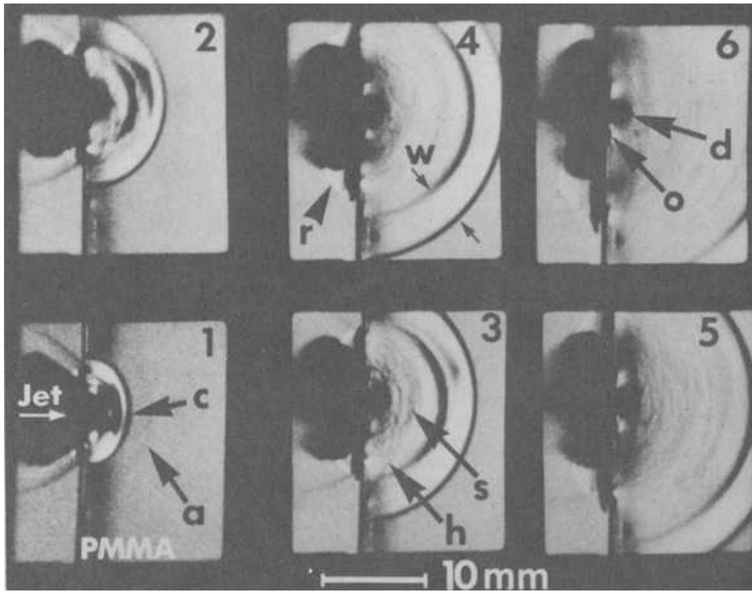

FIG. 3—*Shadowgraph sequence of the impact of a 750-m s*$^{-1}$ *waterjet onto a PMMA block. 1 μs per frame:* (a) *stress front induced by detached air shock;* (r) *reflected air shock;* (c) *main compressive stress pulse of width* w; (h) *head wave;* (s) *shear front (poorly defined because of the nature of the optical system*); (d) *subsurface 'shear' failure;* (o) *main ring crack.*

can give information about the jet velocity and head profile, associated air shocks, the sideways flow of liquid after impact, the various stress waves in the target block, and the growth of damage.

Figure 4 illustrates the kind of data which can be obtained about jet stability (only two frames from each sequence are given). The figure gives information for three chamber sizes, and in each case for both empty and full loading of the exit portion of the chamber (Positions E and F of Fig. 1*a*). In all examples a central 'core' of liquid is surrounded by a 'bag' of spray; this spray has a negligible effect on the damage. For liquid impact erosion studies the jets of Fig. 4*a, c, d,* and *f* would be suitable provided the specimens were within 10 mm of the nozzle. The jet in Fig. 4*b* emerges with a hydrodynamic instability and this is rapidly magnified by the air drag. It is important to realize that, even if a jet is initially stable, aerodynamic forces can exceed the restoring forces provided by the liquid's surface tension. So-called Taylor instability arises when the disruptive forces cause surface waves to develop. For jets of a few hundred m s^{-1}, Taylor instability takes place a few centimetres from the nozzle plane. A full discussion of the way high-velocity liquid jets behave can be found in Ref *8*.

In Fig. 4*e* a precursor jet has formed; with an empty end section (Position

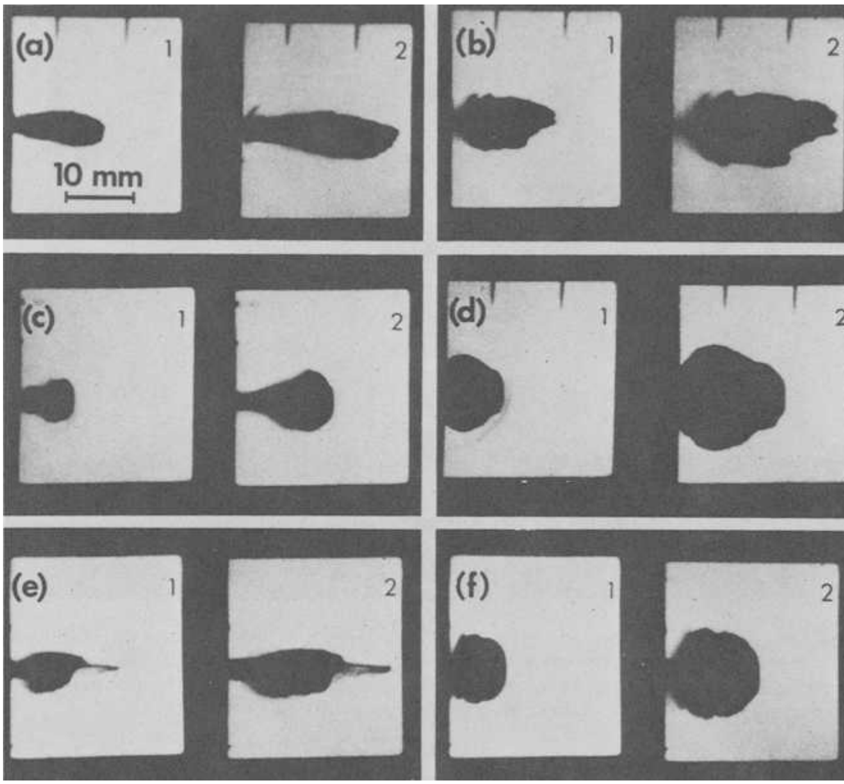

FIG. 4—*Frames selected from Imacon sequences of various jet sizes, all at 10 μs per frame. Slug velocity 175 m s*$^{-1}$ *for each sequence.* (a), (c) *and* (e) *are jets produced with the exit portion of the chamber left empty* (*Position E*); (b), (d) *and* (f) *are with it full* (*Position F*); (a) *0.8-mm nozzle, exit empty, 980 m s*$^{-1}$; (b) *0.8-mm nozzle, exit full, 910 m s*$^{-1}$; (c) *1.6-mm nozzle, exit empty, 735 m s*$^{-1}$; (d) *1.6-mm nozzle, exit full, 700 m s*$^{-1}$; (e) *2.4-mm nozzle, exit empty, main jet 550 m s*$^{-1}$, *'Munroe' jet 800 m s*$^{-1}$; (f) *2.4-mm nozzle, exit full, 525 m s*$^{-1}$.

E in Fig. 1) of the larger orifice chambers, this took place whether the liquid/air interface was convex or concave. With a full chamber a precursor or Munroe jet developed only when the liquid/air interface was concave inward (Fig. 5). The production of the precursor jet can be explained in terms similar to that of a jet from a shaped charge (see, for example, Ref. *9*).

The use of single-shot photography is illustrated in Fig. 6. In Fig. 6*a* ablation from the head of the jet forms the 'bag' of spray; note that it is possible to make out the central high-density core of liquid. Figure 6*b* shows a later stage with another jet which has developed Taylor instability.

In cases where hydrodynamic or aerodynamic instability modes develop, the jets are not suitable for erosion studies. However, we now understand reasonably well the conditions which produce these instabilities. Jets which

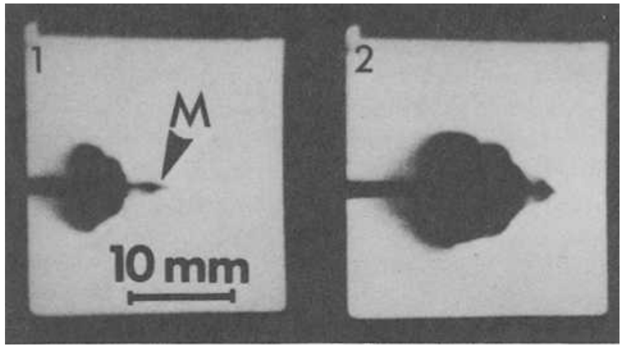

FIG. 5—*'Munroe' jet, M. 1.6-mm-diameter nozzle with the liquid/air interface concave inward. 10 μs per frame. Main jet velocity 740 m s*$^{-1}$.

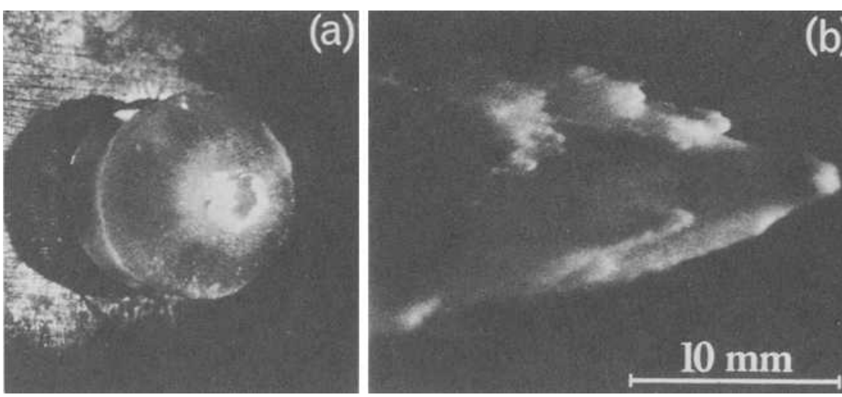

FIG. 6—*Single flash pictures of 450-m s*$^{-1}$ *waterjets. 2.4-mm nozzle. Flash duration 150 ns. Distances of jet from chamber:* (a) *10 mm,* (b) *110 mm.*

would be suitable for erosion studies would be those illustrated in Fig. 4*a, c, d,* and *f* at a standoff distance of about 10 mm. The bag of spray which develops has been shown to be made up of micrometre-sized drops and these do *not* contribute to the damage [*8*]. The jets have a rounded nose; this can be counted as an advantage since it makes simulation of impact with a rain drop more realistic. The following table summarizes the loading conditions required for reproducible, stable jets of various diameters.

Nozzle diameter/mm	Liquid Interface
0.4	Position E (see Fig. 1)
0.8	Position E
1.6	Position E or position F, convex outward
2.4	Position F, convex outward

Recording with Photocells; Spark Photography

We have used high-speed framing photography extensively. The question arises as to how important such camera equipment is for anyone constructing our jet apparatus and wanting to make erosion studies. The answer is that although a camera like the Imacon would be beneficial, it is not essential. The slug (projectile) velocity can be measured very easily in a number of ways, of which probably the simplest is to interrupt light beams falling on photocells spaced at measured distances apart. Once projectile velocities are known and the gun is calibrated in terms of firing pressure, stable jets of various sizes and velocities can be obtained. The ratios of V_j/V_s discussed earlier could then be used to calculate the jet velocities. However, with very little further expenditure it would be possible to measure the jet velocity directly, again using photocells or 'spark' photography. For a full discussion of commercial light sources and spark photography, see the book by Früngel [*10*].

Comparison of Jet and Drop Impact

This comparison involves answering two questions. First, Can impact with jets give similar damage patterns to those produced by spherical drops? Then, if the answer to that is yes, What jet size gives damage comparable to a particular-sized drop impacting at the same velocity? The reasons that the answers are not easy to settle are varied. In the first place, the impact of a perfect cylinder gives a water-hammer pressure over a small central area which depends on drop radius and impact pressure [*5*]. Secondly, there is the fact that perfect cylinders with radius equal to the orifice diameter are not easy to produce. The reasons for this are discussed in detail in the following. It means that the jets we recommend using have, at the 'standoff' distance of 10 mm, a head diameter which is larger than the orifice diameter. This head diameter depends on the chamber loading and jet velocity. Data are given later for four jet sizes.

Our approach was a multiple one: (1) We made detailed studies of the damage produced by both jet and drop impact on aluminium, Polymethylmethacrylate (PMMA), and glass targets[4]; (2) we photographed the impact of jets and drops, and in the particular cases of transparent targets and 2-D drops, we observed stress wave propagation in them; and (3) we took pressure records.

Impact with Drops

Specimens of PMMA and aluminium were mounted in projectiles and

[4]The work is now being extended to a wider range of materials. The results support the view that jet impact can simulate drop impact with reasonable accuracy.

fired at suspended drops using a gas gun of 25.4-mm barrel diameter.[5] The impact process was recorded with the Imacon so that it was possible to measure impact velocity in each case within ± 3 percent. High-magnification photographs were taken of the drop immediately prior to firing the gun. The photographic records allowed accurate values (± 2 percent) of drop size and curvature to be taken. This was important since drops evaporate quite rapidly after suspension, and misleading answers can be produced if firing is delayed.

Water drops of greater than 2 to 3 mm in diameter are difficult to suspend. The range of drop sizes was extended up to 6 mm by using a mixture of gelatine and water. The amount of gelatine used was kept as low as possible consistent with obtaining spherical drops of the required size. Impact 'crater' dimensions were measured by taking profilometer traces and by microscopic observation. A typical set of results of impact mark dimensions versus velocity for PMMA is shown in Fig. 7. This material forms an annular crater; the insert shows the quantities *a*, *b*, and *c* which were measured. The results have been plotted nondimensionally by dividing by the drop diameter d'. Note that if the line for c/d' is extrapolated back, it passes through the origin. Figure 8 gives a plot of *c* versus drop diameter for an impact velocity

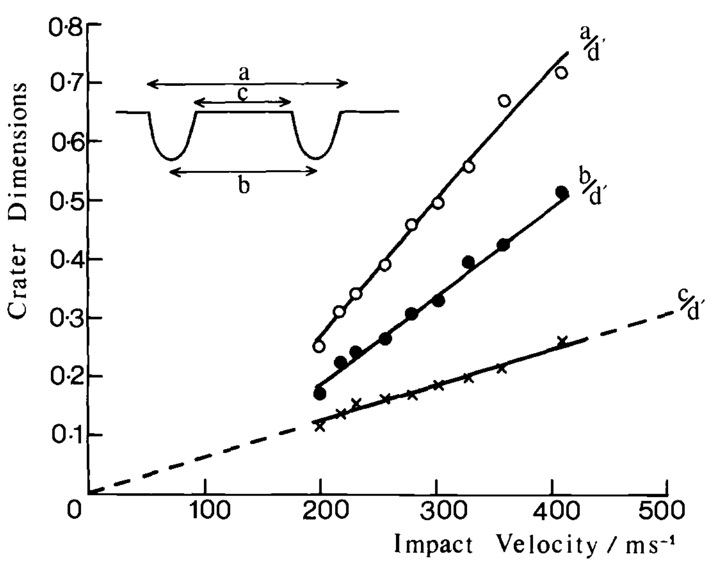

FIG. 7—*Liquid drop impact on PMMA, showing crater dimensions (plotted nondimensionally in terms of drop diameter,* d'*) versus impact velocity. The various crater dimensions are given in the insert.*

[5]The gun was based on a gun built in the authors' laboratory for solid-particle erosion studies and described in Ref *11*.

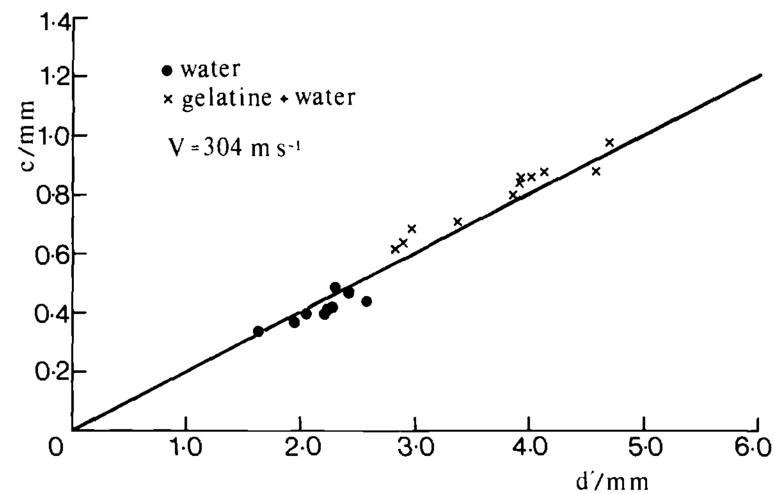

FIG. 8—*A plot of* c *versus drop diameter,* d′. *Impact velocity of 304 m s*$^{-1}$. *Note that* c *increases approximately linearly with* d′ *and that both the water and gelatine/water drops fall on the same line.*

of 304 m s^{-1}. Note that the water and the gelatine/water drops all fall near the same straight line of slope ~0.2, and within the statistical spread of results. This is reasonable since the changes to the viscous and surface tension forces caused by adding the gelatine are small compared with the impact forces. The simple expedient of adding a small quantity of gelatine to the water has thus doubled the range of drop diameter which can be conveniently studied, without introducing significant errors into the results.

Liquid Jet Impact

The damage parameters a, b, and c (see insert on Fig. 7) were also measured for waterjet impact. Results were obtained for 0.4, 0.8, 1.6, and 2.4-mm nozzles at the standoff distance of 10 mm. Nozzles 0.4 and 0.8 were loaded to Position E (see Fig. 1*a*) and the larger two to Position F. Figure 9 shows how c varies with velocity for damage marks on PMMA for all four nozzles; the results are plotted in dimensionless form (that is, crater dimension over nozzle diameter, d). If the waterjets had maintained the nozzle dimensions up to the 10 mm standoff, then there should have been no change in c with velocity. However, as our photographic work has shown, when a chamber is loaded to Position F (Fig. 1*a*), the jet has a 'mushroom' head (see insert Fig. 12). This 'head' is a consequence of two effects: (1) the liquid in the final section of the chamber (that is, the liquid between Positions E and F) which is pushed aside by the faster-moving liquid which has been forced through the tapering section of the chamber, and (2) air drag, which would

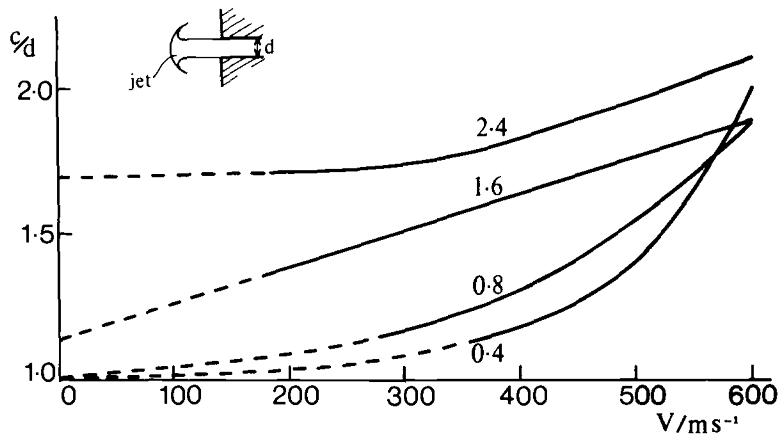

FIG. 9—*The variation of* c/d *with jet velocity for four nozzles, in nondimensional form. Insert: cross section through typical jet, showing 'mushroom' head which is larger than the nozzle diameter.*

be expected to be some function of jet velocity. The measurements can be used to give equations for c for each nozzle [*12*]. The results plotted in Figs. 7 and 9 can be replotted to give the equivalent drop size in millimetres that the four chambers produce (Fig. 10).

One of the objects of the work was to simulate impact with large water drops; this has clearly been achieved. The two large nozzles cover impacts with large masses of water, equivalent to drop sizes in the range 10 to 30 mm. The 0.4-mm nozzle is particularly useful for simulating impact with 2-mm diameter drops since the ratio of drop diameter to orifice diameter is almost exactly constant (that is, close to 5) for velocities in the range 300 to 600 m s^{-1}. The 0.8-mm nozzle simulates drops of diameter ~4.5 mm for a similar range. If 3-mm drops had to be simulated, a nozzle with an orifice diameter of 0.6 mm would suffice. As mentioned earlier, if a drop is distorted so that it impacts with a high radius of curvature, it will act effectively as a larger drop. The jet method is therefore particularly advantageous in being able to simulate very large drops.

Crater Shape

Craters have been measured by taking profilometer traces and by microscopic observation [*12–15*]. It appears from present results that our jets do produce damage patterns similar to equivalent-sized drops. The reason for this is basically that the initial water-hammer pressure in both cases controls the amount of damage. Damage extension during the later stages of flow (when the liquid is behaving incompressibly) is relatively small and not significantly different for drop and jet impact in the velocity range we have

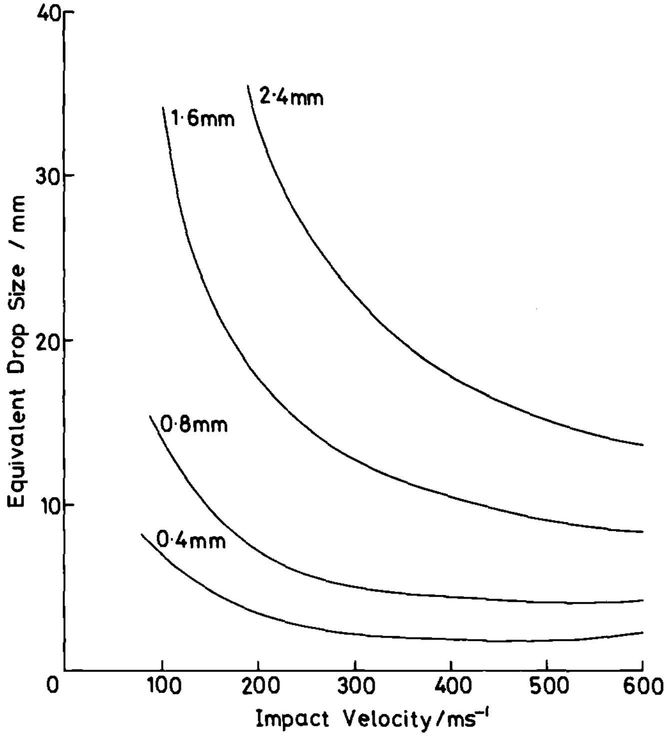

FIG. 10—*Equivalent drop size produced by the four chambers versus velocity. The 0.4-mm chamber, for example, simulates 2-mm drop impact for a wide velocity range. Very large drops can readily be simulated.*

studied. This conclusion has support from pressure transducer measurements [*12,13*] taken with the system illustrated in Fig. 11. The initial water-hammer pressure is followed by a tail a factor 10 to 20 times lower in magnitude.

Residual Strength After Impact

Assessment of impact damage in brittle materials is most realistically carried out by measuring the residual strength after impact. This is particularly important in the low-velocity range, where significant strength losses can occur before the induced damage reaches visible dimensions [*12*]. Residual strength testing is only entirely satisfactory for brittle targets if the specimen is stationary when impacted. If the specimen is the moving body, the deceleration forces after impact could cause further crack growth. Our residual strength tests are therefore based on jet impact experiments. The data shown in Figs. 9 and 10 can be used to obtain equivalent drop sizes.

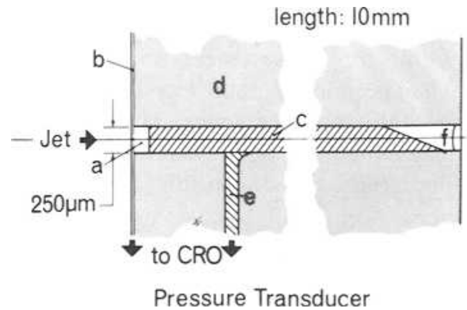

FIG. 11—*Schematic diagram of the pressure transducer mounting.* (a) *0.25-mm-diameter, 0.1-mm-thick transducer;* (c) *backing rod;* (b) *and* (e) *electrodes to cathode ray oscilloscope (CRO);* (f) *adhesive;* (d) *holder.*

In our work the residual strength of specimens following a single liquid impact has been determined using a uniform hydrostatic loading system to produce a biaxial stress distribution on the surface of the specimens. The specimens are disks of diameter 51 mm and nominal thicknesses 3 and 6 mm. These are centrally impacted, and then tested to failure in the pressure tester (Fig. 12), the damaged surface being in tension. Advantages are that edge failures can be minimized and the test region extends almost to the edge of the specimen, in contrast to the ring-on-ring test where only a small area within the inner ring is suitable. A full description of the apparatus has been published [*16*].

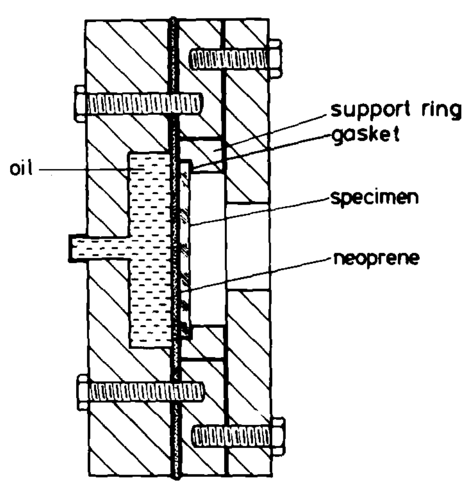

FIG. 12—*Section of pressure test apparatus for 51-mm glass disks. Overall diameter 133 mm; thickness 55 mm. Constructed from mild steel.*

Results of residual strength curves are given in Figs. 13-17. It is important to realize the statistical nature of these results. A wide variation in observed strength values is found for measurements made under similar conditions. For this reason, each experimental point was determined by taking the mean of at least six, and usually more, readings. The error bars in the figures are $\pm 2\sigma_m$ (that is, 95 percent confidence) where σ_m is the standard error in the mean. With some materials, the silicon nitride for example, only a limited number of specimens were available. A significant point is that when strength reduction first occurs, it does so only in some of the specimens. As the impact velocities are further increased, there is a greater probability that a given specimen will suffer a reduction in strength, so that at higher velocities all specimens show some strength degradation. In the intermediate region, specimens fall into two groups: those which fail at lowered stresses due to impact damage, and those which fail at stresses comparable to the original strength of the glass. This does not necessarily indicate that no damage has occurred, only that the crack extension due to impact loading is within the distribution of initial flaw sizes for the as-received surface. As the velocity of impact increases, the proportion of specimens in the reduced-strength group increases. Results may be presented in several different ways in order to demonstrate this more clearly.

1. Averaging all fracture stresses at a given impact velocity irrespective of the group into which they fall (Figs. 13, 14, 16, 17). However, points in the transition region are not physically meaningful in the sense that they represent observed fracture stresses; rather they are the combined averages of two different statistical distributions.

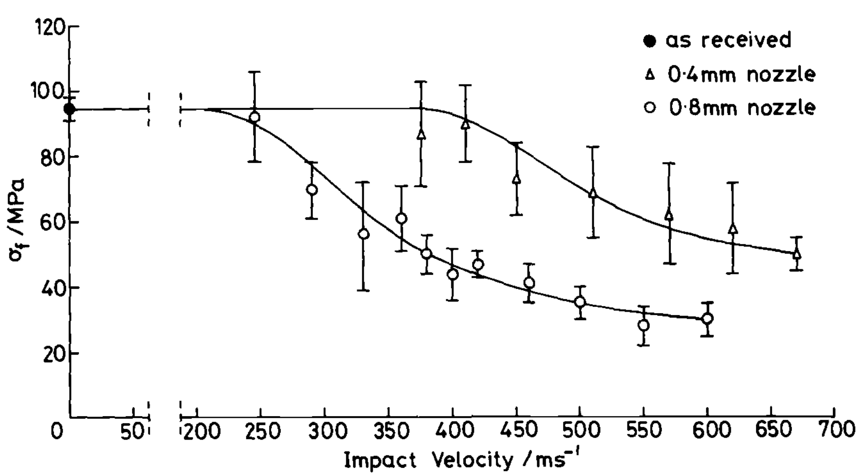

FIG. 13—*Residual strength of '3-mm' soda-lime sheet glass following liquid impact with a jet from the 0.4- and 0.8-mm nozzles.*

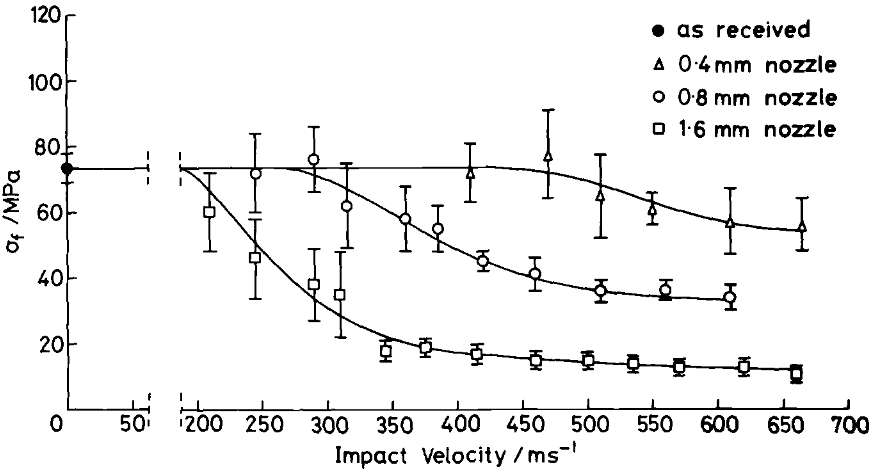

FIG. 14—*Residual strength of '6-mm' soda-lime float glass following liquid impact with a jet from the 0.4, 0.8, and 1.6-mm nozzles.*

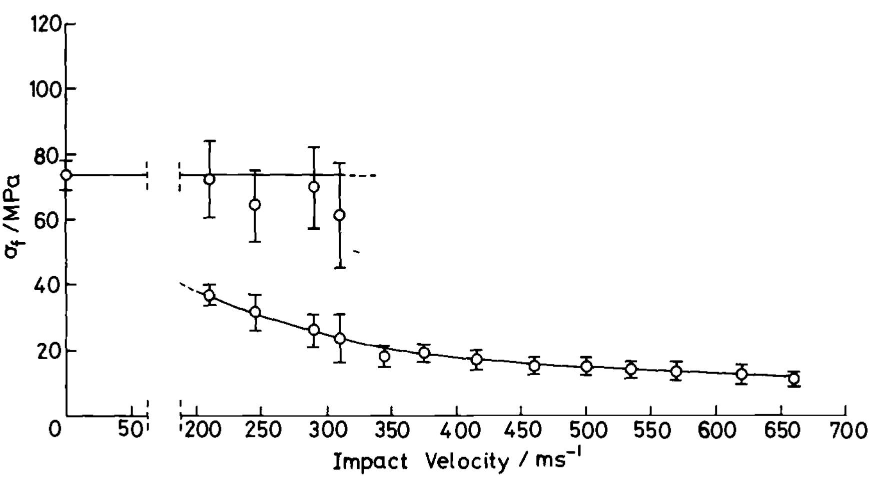

FIG. 15—*Residual strength of '6-mm' soda-lime float glass after impact with a liquid jet from the 1.6-mm nozzle. Results in the transition region are plotted as two separate values in order to indicate the bimodal nature of the distribution of strength values.*

2. Plotting the two groups separately with an overlap in the velocity region where fracture stresses may fall into either group (Fig. 15). This gives a truer indication of failure stresses likely to be realized in practice, but gives no idea of their relative probabilities.

3. A plot of fracture stresses obtained from individual experiments. Two types of failure are found: from a noncentral fracture origin corresponding to

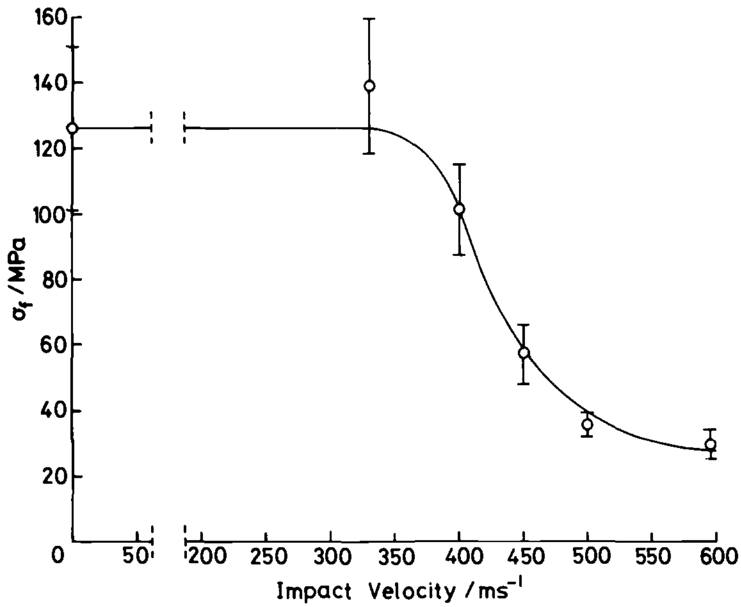

FIG. 16—*Residual strength of calcium aluminate glass of 3-mm nominal thickness after impact with a liquid jet from the 0.8-mm nozzle.*

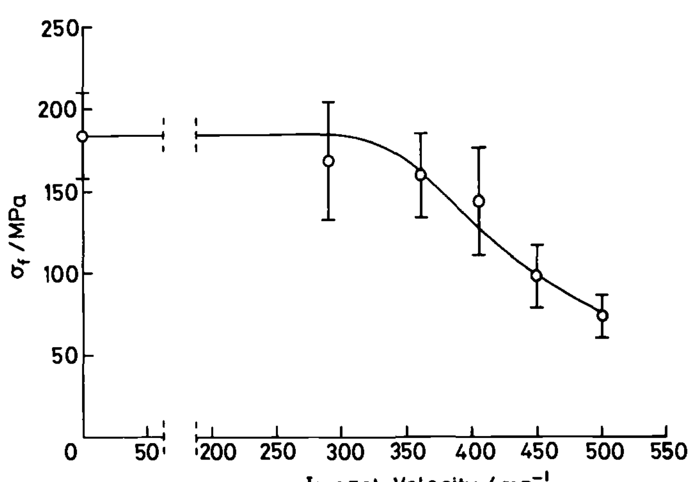

FIG. 17—*Residual strength of reaction-bonded silicon nitride of 3-mm nominal thickness after impact with a liquid jet from the 0.8-mm nozzle.*

a negligible strength reduction, and from a central origin indicating strength degradation due to impact damage. The proportion of central fracture origins increases with increasing impact velocity.

Results are given in Fig. 16 for 3-mm specimens of polished calcium aluminate glass. The 0.8-mm nozzle was used, so that an impact with an approximately 5-mm-diameter drop was modeled. The initial strength of the glass was found to be 126 ± 25 MPa compared with 94.5 ± 3.5 MPa for the 3-mm-thick soda-lime glass. Comparison of the results for calcium aluminate with those for soda-lime silicate may be made by reference to Fig. 13. It is clear that the transition region is displaced to the right and is steeper in the case of the calcium aluminate; the effect of the superior polish given to the glass has been to reduce the number and severity of surface flaws, resulting in an increase in the impact velocity required to cause strength degradation. The much smaller spread in values for the soda-lime glass is partly a result of the many specimens studied and partly a result of a uniform distribution of serious flaws. For velocities in excess of 400 m s^{-1}, however, the residual strength levels of both types of glass are practically identical. The conclusion is that an improved surface finish increases the resistance of the glass to the initial onset of damage, but once damage has occurred the residual strength levels are comparable with those for unpolished surfaces. Under in-service conditions, however, surfaces are unlikely to be preserved in their highly polished state for very long, so that polishing treatments have not to date proved a solution to the practical problem of rain impact damage.

Disk specimens of reaction-bonded silicon nitride were subjected to a series of liquid impact residual strength tests (Fig. 17). Young's modulus and Poisson's ratio for silicon nitride are functions of ρ, the density of the material. This was slightly variable within the batch of specimens used in the tests, but typical values of these quantities were $E = 185$ GPa and $\nu = 0.243$, for $\rho = 2550$ kg m^{-3}. The mean fracture strength for as-received disks was found to be 184 ± 26 MPa using the hydraulic pressure test technique. Availability of specimens permitted investigation of velocities up to 500 m s^{-1} only. The position of the transition region is roughly the same as that for polished calcium aluminate specimens. At impact velocities of 450 and 500 m s^{-1}, for which all specimens tested were found to undergo strength reduction, the residual strength of the ceramic was found to be of the order of *twice* that of the glasses at the same impact velocities.

The shape of the residual strength curves is interesting. Their characteristic features are the low-velocity plateau, the drop of strength over a narrow transition region, and then the slowly decreasing high-velocity region. There is only space to discuss these features briefly. The damage around the loaded area in brittle targets is caused by the Rayleigh surface wave interacting with defects [5]. The initial plateau continues until the wave causes a defect to extend to a length greater than others in the region. Defect extension takes place in this dynamic situation when $\sigma^2\tau$ exceeds a critical value, where σ is the amplitude of the stress pulse and τ its duration [15,17]. Once a defect begins to grow, it extends rapidly toward its maximum velocity (about 1500 m s^{-1} for glass); the greater the stress, the more rapid is this acceleration. Taking as an example a 0.8-mm-diameter jet impacting glass of strength about 100 MPa at around 500 m s^{-1}, calculation shows that τ is about 0.2 μs and that defects of about 50 μm length are extended to about 350 μm. This corresponds to a strength decrease of approximately 2.6 times, which is close to what is observed (Fig. 13).

The foregoing suggests that the important factors in choosing a brittle material for rain erosion situations are (1) a high critical stress intensity factor K_{Ic}, since this determines the height and extent of the initial plateau, and (2) a low maximum fracture velocity, since this controls the transition 'step.' Maximum crack velocities are related to stress wave velocities, but tend to be a higher fraction of them for solids with well-defined cleavage planes [18]. Both K_{Ic} and maximum crack velocity depend on the square root of a modulus, so this cancels. We are left with the conclusion that we need a solid with high fracture surface energy and density. Ignoring the question of composite materials, isotropic solids giving conchoidal fractures are likely to be better than those failing by cleavage. Of the materials illustrated in Figs. 13-17, silicon nitride fits these requirements best.

Conclusions

This paper shows that it is possible to obtain a reasonably accurate simulation of drop impact using waterjets. No claim is made that the simulation is perfect since there is always the possibility of small differences in pressure distribution or duration. By suitable scaling, however, jets and drops can be related so that, at a particular velocity, water-hammer pressures are produced over similar-sized areas and for similar durations.

Advantages of the jet method are ease of operation, the ability to simulate large drop sizes, and the fact that the target specimen is stationary. Having a stationary target is important with brittle specimens, with specimens of complex shape, and when residual strength measurements are required.

Details are given for producing a gun apparatus for firing jets. If chambers are designed and loaded to the specifications given, then reproducible stable jets are obtained. These jets can simulate drops from ~1 to ~30 mm in the velocity range up to ~1000 m s^{-1}. It is possible to produce jets of even higher velocity by using higher projectile velocities or by making the chamber design more efficient (the ratio of jet velocity to projectile velocity can be made ~10× by careful design; see, for example Ref *3*). A gas gun was used for firing specimens at suspended drops with velocities up to ~400 m s^{-1}. This apparatus was simple to construct and has proved versatile and useful [11].

An image converter camera, the Imacon, was used extensively for jet and impact studies. Its advantages were that it was synchronizable from the event, could be used with conventional light sources, and gave records on Polaroid film. However, although such a camera was essential for this project, less-sophisticated methods could be used for future erosion studies using the jet method. Suggestions were made as to how projectile and jet velocities could be recorded using photocells and spark photography.

When a drop impacts, the size of the damage region depends on both drop size and velocity. This is of great importance in explaining why the large drops in a rain field are the most damaging (the water-hammer pressures cover a larger area and last longer). If a drop is oscillating, the important dimension is the radius of curvature at the impact surface. This means that a drop can act effectively as a much larger drop. This needs to be remembered when assessing the hazard of collisions with large rain drops; it is not the *mean* size of the largest raindrop that is important, but the largest radius of curvature that this drop can reach when oscillating. Water drops of diameter greater than ~2 mm are difficult to suspend. This problem was overcome by using gelatine/water drops for the size range 2 to 6 mm.

If the jet method had produced perfectly cylindrical jets of diameter equal to the orifice dimension, then the specimen area subjected to water-hammer pressures would have remained constant for all velocities. In practice, the jets produce a mushroom-shaped head and its dimension is a function of velocity and orifice size. However, at a standoff distance of 10 mm the jets behave reproducibly. Curves are given for the size of damage patterns produced by the jets. The fact that the jets produce a mushroom head with a slightly curved front face is almost certainly beneficial in allowing the jets to simulate the drop impacts accurately. An important point for the range of velocities considered is that the water-hammer pressures greatly exceed the stagnation pressures produced by incompressible flow. Thus it is always the first instant of impact which is of prime importance with *both* jet and drop impact. Pressure traces taken with very small pressure transducers confirm these conclusions.

The importance of *quantitatively* assessing damage is emphasized in this paper. A hydraulic test apparatus for measuring residual strengths is described and residual strength data for various solids discussed.

The results also have application to steam turbine erosion where impact with large drops can also occur. Very-high-velocity jet impact is also being considered for mining applications. A combined theoretical and experimental study of high-velocity liquid jet production has recently been published [8].

Acknowledgments

The research was supported by grants from the Science Research Council and the Ministry of Defence, Procurement Executive.

References

[1] Bowden, F. P. and Brunton, J. H., *Nature*, Vol. 181, 1958, p. 873.
[2] Bowden, F. P. and Brunton, J. H., *Proceedings of the Royal Society*, Vol. A263, 1961, p. 433.
[3] Rhyming, I. L., *Journal of Applied Mathematics and Physics*, Vol. 24, No. 10, 1973, p. 150.
[4] Brunton, J. H. in *Proceedings*, 5th International Congress on High-Speed Photography, Cologne, Germany, 1961, p. 503.
[5] Bowden, F. P. and Field, J. E., *Proceedings of the Royal Society*, Vol. A282, 1964, p. 331.
[6] Brunton, J. H. and Camus, J.-J. in *Proceedings*, 3rd International Conference on Rain Erosion and Allied Phenomena, Farnborough, England, 1970, p. 327.
[7] Camus, J.-J., Ph.D. Thesis, University of Cambridge, Cambridge, England, 1971.
[8] Field, J. E. and Lesser, M. B., *Proceedings of the Royal Society*, Vol. A357, 1977, p. 143.
[9] Birkhoff, G., MacDougall, D. P., Pugh, E. M., and Taylor, G. I., *Journal of Applied Physics*, Vol. 19, 1948, p. 563.
[10] Früngel, F. B. A., *High-Speed Photography*, Vol. 2, Academic Press, New York, 1965.
[11] Hutchings, I. M. and Winter, R. E., *Journal of Physics 'E'*, Vol. 8, 1975, p. 84.
[12] Field, J. E., Camus, J.-J., Gorham, D. A., and Rickerby, D. G., "High-Speed Liquid Impact Studies," Directorate of Materials Report 203, H. M. Stationery Office, London, 1976.
[13] Field, J. E., Camus, J.-J., Gorham, D. A., and Rickerby, D. G. in *Proceedings*, of 4th International Conference on Rain Erosion, Meersburg, Germany, 1974.
[14] Gorham, D. A., Ph.D. Thesis, University of Cambridge, Cambridge, England, 1974.
[15] Rickerby, D. G., Ph.D. Thesis, University of Cambridge, Cambridge, England, 1977.
[16] Gorham, D. A. and Rickerby, D. G., *Journal of Physics 'E'*, Vol. 8, 1975, p. 794.
[17] Steverding, B. and Lehnigk, S. H., *Ceramic Bulletin*, Vol. 49, 1970, p. 1057.
[18] Field, J. E., *Contemporary Physics*, Vol. 12, 1971, p. 1.

DISCUSSION

M. M. Vijay[1] *(written discussion)*—How far was the target from the nozzle in terms of the nozzle diameter? In my own case, using continuous jets, if the distance between the nozzle and the target is less than 5 nozzle diameters, no erosion was observed. Could you comment on this or could you try this in your laboratory? I would like to see pictures of your specimens at *very close distances.*

J. E. Field, D. A. Gorham, and D. G. Rickerby (authors' closure)—In most of our experiments the distance between the nozzle and the target was 10 mm. For the largest nozzles this is about three diameters, and for the 0.8-mm nozzle the distance represents over 12 diameters. The 0.4-mm nozzle required a standoff distance of less than 5 mm.

After the jets have left the lateral confining pressure of the nozzles they slowly expand, and varying the standoff distance causes the damage site dimensions to change. At too great a distance, above about 12 diameters, instabilities arising from aerodynamic and inertia forces are causing the jet to

[1]National Research Council of Canada, Ottawa, Ont., Canada.

fragment. At this stage the core of liquid loses its coherence, and the damage marks become irregular and unrepresentative of liquid drop impacts. In our experiments it is necessary to retain a smooth leading surface to the jet in order to simulate a drop impact. In the case of a continuous jet the mechanisms of material removal are different, and it may well be that the break-up and instabilities that are enhanced by using a large standoff distance are accelerating material removal. It is difficult to comment further about your observations without knowing details of your apparatus and the velocity regime of your jets.

D. A. Gorham,[1] *M. J. Matthewson,*[1] *and J. E. Field*[1]

Damage Mechanisms in Polymers and Composites Under High-Velocity Liquid Impact

REFERENCE: Gorham, D. A., Matthewson, M. J., and Field, J. E., **"Damage Mechanisms in Polymers and Composites Under High-Velocity Liquid Impact,"** *Erosion: Prevention and Useful Applications, ASTM STP 664,* W. F. Adler, Ed., American Society for Testing and Materials, 1979, pp. 320-342.

ABSTRACT: This paper presents results from recent liquid impact studies of a variety of glass and carbon fiber reinforced and nonreinforced thermoplastic and thermosetting polymers. Basic damage modes from single impacts in the velocity range 500 to 1000 m s^{-1} are described and the mechanisms of failure are analyzed. The thermosetting resins studied are essentially brittle, in contrast to the very ductile thermoplastics, and these fundamental differences are emphasized when fibrous reinforcement is added. The effects of matrix properties, reinforcement geometry, the condition of the impacted surface, and impact angle are illustrated and discussed. The main conclusion is that, although no ideal solution exists to withstand all impact situations, it is possible to establish general rules which assist in the design of composites for specific purposes. In particular, reinforced thermoplastic resins are found to have considerable advantages over reinforced thermosetting resins for many practical situations, particularly when the postimpact material strength needs to be maximized.

KEY WORDS: erosion, rain erosion, impingement, impact, liquid impact, composite materials, fiber reinforcement, glass fibers, carbon fibers, polymers, thermoplastics, thermosets

The use of nonmetallic materials in situations involving a risk of high-velocity liquid impingement is of increasing importance. This paper presents recent results from a study of the failure processes in reinforced and nonreinforced thermoplastic and thermosetting polymers under high-velocity impact from liquid cylinders. Other work has shown that these cylinders can be a good model for the impact of spherical liquid drops. The various damage mechanisms are discussed in terms of the properties

[1]Physics and Chemistry of Solids, Cavendish Laboratory, Madingley Road, Cambridge, England.

of the materials, and the effects of composite reinforcement geometry, surface condition, and impact angle are illustrated.

The high-velocity waterjets used in this study were produced by the technique of Bowden and Brunton [*1*].[2] In this technique, a lead air-gun pellet is fired at a steel chamber which contains a small quantity of water sealed in by a neoprene disk. The projectile and neoprene drive forward as a piston and extrude a jet of liquid through the narrow orifice. All the impacts illustrated in this paper are with jets from a 1.6-mm-diameter orifice. In this case, the waterjet velocity is approximately four times the slug velocity, and because of jet expansion the head diameter at the point of impact (10 mm from the chamber end) is ~3.5 mm. A variable-velocity gas gun produces jets over a continuous velocity range of 200 to 1000 m s^{-1}. More information about the properties of the jets may be found in Refs 2–4.

The basic mechanics of liquid-solid impact are well known. On impact the liquid is compressed and a very high pressure is developed, of the order of ρCV where, ρ is the liquid density, C the appropriate shock velocity, and V the impact velocity. This pressure is relieved by release waves propagating in from the free surface toward the axis, and then the rest of the jet or drop flows stably against the solid surface, developing much lower stresses ($\sim \frac{1}{2}\rho V^2$). For the typical impact conditions in this paper, a jet of 3.5 mm diameter impinging at 800 m s^{-1}, the initial pressure peak is 1.5 GPa and lasts for 1 μs. High-speed photography has confirmed that most of the solid damage occurs during this time, and that the rest of the jet flows harmlessly on to the surface [*2,5*].

Experiments in which solid specimens are fired at liquid drops have shown that there are close similarities between the impact of drops and of jets from the Brunton apparatus [*6*]. The equivalent size of drop which will produce the same damage dimensions as a given jet has also been established over a wide range of conditions [*4*], showing that the jets can simulate the impact of drops ranging in size from 2 to over 30 mm. The materials of the present study have been impacted over most of this size range, but the illustrations in this paper are from a single nozzle that is equivalent above 500 m s^{-1} to a 10-mm drop. This nozzle produces damage modes that are similar to those found with both larger and smaller sizes. The reinforcement fibers, typically <10 μm diameter, are so much smaller than impact site dimensions that they do not produce a dependence of damage upon drop size over this range. Therefore, most of the damage analysis in the present work is of direct relevance to a wide range of liquid impact situations, and has significance in solid impact and explosive loading involving similar pressure histories. In the case of rain erosion simulation, a concentration upon the effect of drops which are somewhat larger than the average size is desirable for two basic reasons:

[2]The italic numbers in brackets refer to the list of references appended to this paper.

1. The few largest drops in a distribution of sizes will cause overwhelmingly the greatest amount of damage in the high-velocity situations where single impacts are important. In particular, a single impact from a large drop can cause catastrophic failure of a component that is merely suffering gradual erosion by the multiple impact of smaller liquid masses.
2. In practice, a liquid drop will be distorted by aerodynamic effects, such as the oscillation of a falling drop and the flattening of a body of liquid as it passes through a shock wave attached to a rapidly moving solid object.

Both these effects lead to a high proportion of drops which have an increased radius of curvature of the impacting surface, and which produce pressure histories that are characteristic of spherical drops of larger diameters. Contact area and duration of pressure are both increased markedly by quite small distortions of a spherical drop.

Thermoplastic Polymers

The damage pattern in polycarbonate at 860 m s^{-1} is shown in a general view in Fig. 1*a*, where five principal regions may be distinguished. Region 1 is a large plastic crater of maximum depth ~ 500 μm, and it is bounded by a relatively sharp transition to an undamaged annulus, Region 2. The surface profile of this site (Fig. 2*a*) illustrates the pileup around the crater, where Region 2 is defined by a smooth section of the upper slope. The lower slope is roughened to form Region 3, shown in more detail in Fig. 1*c*. Sectioning has provided no evidence of this surface deformation penetrating into the material, in contrast to Region 4, which consists of circumferentially oriented cracks extending beneath the surface up to 50 μm. Many of these cracks have been eroded (Fig. 1*c*) by the rapid outward flow of the jet in the later stages of the impact, which has caused material to be plucked out in a relatively brittle manner. Region 5 consists of material piled up into ridges or rucks in response to a radial surface shear stress. The surface profile shows the generally raised level of this area and the detail view in Fig. 1*d* illustrates the regularly spaced ridges of plastic deformation.

These damage modes may be explained as follows. The jet contacts the surface over an area extending to roughly the boundary between Regions 3 and 4. The water is behaving compressibly at this stage and to a first approximation the pressure may be considered to be constant over the contact area. The magnitude is given by the water-hammer equation

$$P = \frac{VZ_1Z_2}{Z_1 + Z_2}$$

where V is the impact velocity and Z_1 and Z_2 the shock impedances

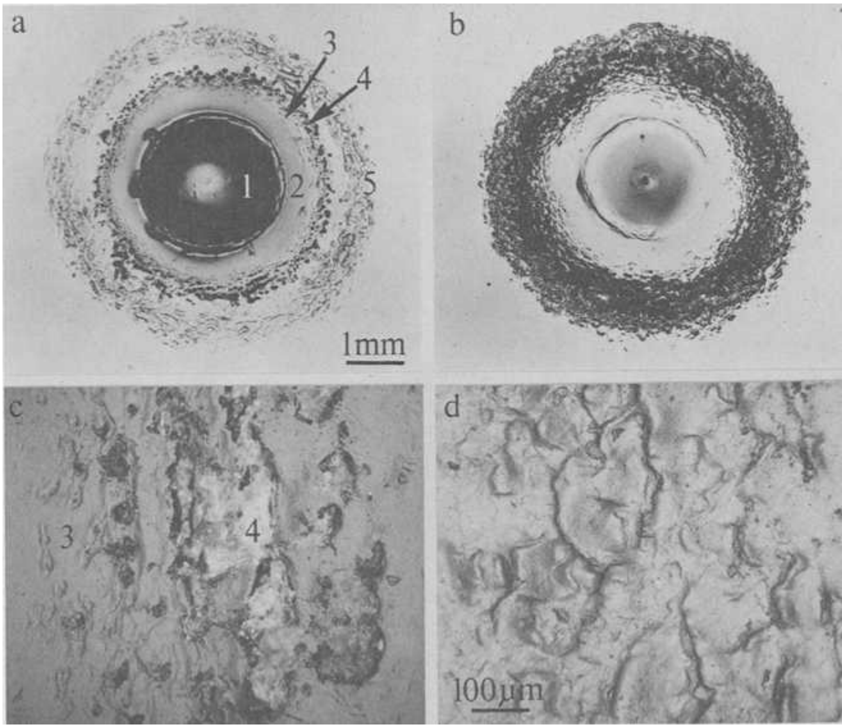

FIG. 1—*Water impact damage on ductile thermoplastic polymers.* (a) *860-m s^{-1} water cylinder impact upon polycarbonate. Regions marked correspond to those in Fig. 2* a. (b) *860-m s^{-1} water cylinder impact upon polyethersulphone. Same scale as* (a). (c) *Detail from* (a) *showing Regions 3 and 4, same scale as* (d). (d) *Detail from* (a) *showing Region 5.*

(evaluated at the impact pressure) of the fluid and solid. For water impinging upon polycarbonate at 860 m s^{-1}, $P = 1.3$ GPa. The constant pressure over the circular contact area would lead to a maximum shear stress of 400 MPa being developed at a depth of 1.2 mm below the surface, assuming a value of Poisson's ratio of 0.4. The compressive flow stress of polycarbonate under slow loading at room temperature is 85 MPa. At a strain rate of about 10^5 s^{-1}, typical of the liquid impact situation, the theory of Bauwens-Crowet, Bauwens, and Homes [*7*] estimates a compressive yield stress of 250 MPa, equivalent to a shear strength of ~170 MPa. This will be enhanced slightly by the hydrostatic pressure component under the impact site, and, using the data of Raghava, Caddell, and Yeh [*8*], the final value of shear strength is estimated to be ~200 MPa. The possible shear stresses were shown above to be considerably in excess of this figure, and so gross plastic deformation is not surprising. At a velocity of 550 m s^{-1}, however, at which no shear deformation is found in the

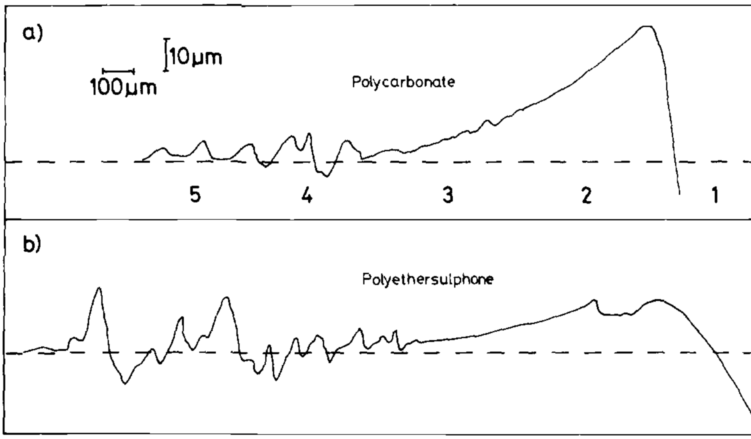

FIG. 2—*Surface profiles of liquid impact damage of Fig. 1.* (a) *Polycarbonate, regions correspond to Fig. 1* a; (b) *polyethersulphone.*

center of the impact site, the shear stress is calculated to be 230 MPa, but the yield becomes only ~190 MPa. Since the threshold velocity for which plastic deformation occurs varies with jet size, that is, with impact duration, it is probable that a time-dependent yield criterion must be introduced. Work on this problem is in progress.

While the impinging liquid is behaving compressibly and the central area is under a roughly uniform pressure, there is a radial tension in the surface around the contact periphery. This is analogous to the stress which forms the Hertzian ring-crack in ball indentation of brittle materials, and in the present case it opens up many circumferential fractures in the surface of the polycarbonate (Region 4). The regime of high-pressure loading by the compressed liquid is progressively terminated from the periphery of the jet by high-velocity lateral jetting. High-speed photographic observation of various liquid impact situations [*1,9*] has demonstrated that this lateral jetting is several times the normal impact velocity, and it therefore causes a severe shearing of the surface. It forms the surface roughening of Region 3, erodes the tensile fractures in Region 4 and extends them by stretching the surface, and causes the cumulative pileup of material in Region 5.

The damage site from a similar impact on polyethersulphone (ICI grade 300P) also shows a large but well-defined area of plastic deformation surrounded by an annulus of surface damage (Fig. 1*b*). This annulus is also divisible into regions, but the differences are not as marked as in the case of polycarbonate. The surface profile (Fig. 2*b*) illustrates the change from small-scale irregularities on the inside edge to larger ones toward the periphery.

Thermosetting Resins

Impact damage to two nonreinforced thermosetting polymers, polyester and epoxy resins, is shown in Fig. 3. At 550 m s^{-1} the brittle polyester (Crystic 625) develops damage in the form of short circumferential cracks which are eroded by the rapid radial jetting. These cracks are similar to those found in inorganic glasses under liquid impact and are formed by the intense surface stress wave that propagates outwards from the impact site [*10*]. The long straight marks are scratches left by the polishing process that have been eroded by the radial jetting; surface discontinuities as small as 0.1 μm can be eroded in this way [*11*]. At the same velocity the tougher example of epoxy resin (MY778), shown in Fig. 3*c*, has damage in the form of an annulus from which material has been plucked to leave many small irregular cavities. There are no short circumferential cracks, and polishing marks have not been eroded. Although the low strain-rate properties of these two materials are not widely differing (the epoxy is tougher by a small factor), the unusual loading condition of an

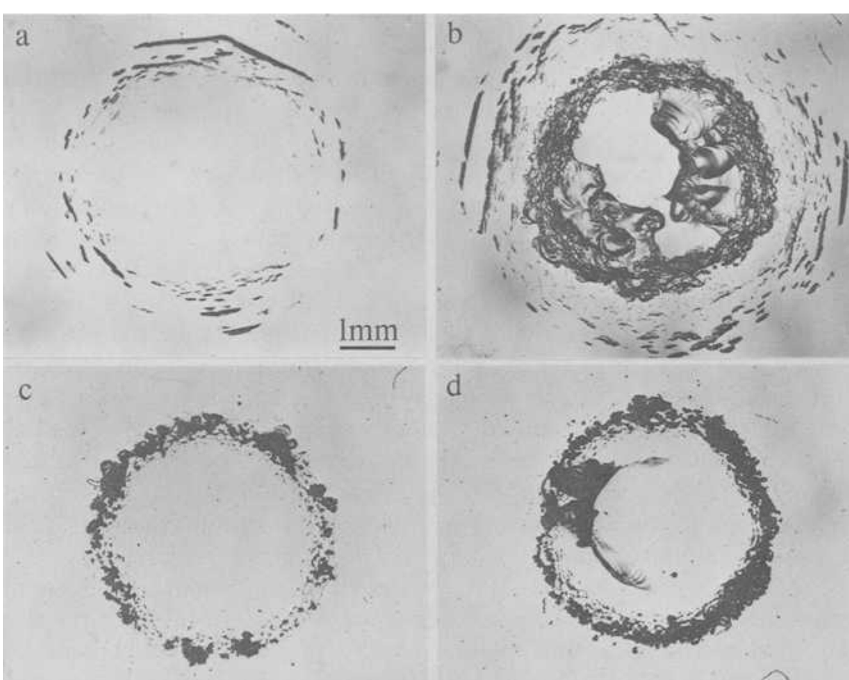

FIG. 3—*Water impact damage on brittle thermosetting polymers.* (a) *Polyester, Crystic 625, 550 m s* $^{-1}$; (b) *polyester, 860 m s* $^{-1}$; (c) *epoxy, MY778, 550 m s* $^{-1}$ (d) *epoxy, 860 m s* $^{-1}$.

extremely high pressure acting for a very short time has caused the fracture behaviors to diverge.

At a higher velocity, 860 m s^{-1}, the polyester also develops an annular region of brittle material removal that extends under the contact area in the form of gross chipping failure (Fig. 3*b*). The circumferential cracks are more numerous and are more heavily eroded. The epoxy resin displays an enhanced annulus of material removal at the higher velocity (Fig. 3*d*) and in addition a crack has formed within the central region. In other sites on the epoxy resin the circular crack in this position has been observed to vary from fully formed to nonexistent. Slight surface rippling in the vicinity of this crack and in the damage annulus is the only indication of any plastic deformation, and it is much less pronounced than in the previous examples of thermoplastics. The polyester shows no visible evidence of surface or subsurface flow.

Reinforced Polyester and Epoxy Resins

The largely ductile response of the thermoplastics and the almost entirely brittle failure in the thermosetting polymers are carried over into composites made from these materials. Typical damage sites from 700-m s^{-1} liquid jets impinging upon reinforced thermosetting resins are shown in Figs. 4 and 6. Figure 4*a* is a unidirectional carbon reinforcement (Type III) in LY 558 epoxy resin. The characteristic features of surface damage on such materials at this velocity are penetration of at least one fiber layer and comparatively large-scale splitting and delamination. The site in Fig. 4*a* has a central, almost circular region that is relatively undamaged, surrounded by a ring of failure. This annulus consists of surface resin removal, matrix failure, fiber fracture, and some fiber removal. As the jet of water arrives in contact with the surface, the 'Hertzian' ring of tension will cause cracks to form along the fiber direction, tangentially to the contact area ("L" in Fig. 5); very similar behavior is found in static Hertzian indentations of composite specimens. A strip of unbroken fibers is then further deformed until the radial tension increases to the level at which the fibers will break by transverse cracks (in Region T of Fig. 5). These cracks will occur at random positions outside the contact area as the distribution of weaknesses and stress concentrators falls within the field of tension, and this produces the 'smeared out' zone of fractures, Region 2 in Fig. 4*a*. Region 3 in this figure is caused by the rapid radial flow of water occurring after the compressible-behavior phase. The fractures and deformation as well as the original surface profile form discontinuities which are eroded by this radial jetting, removing some of the penetrated plies over this area and initiating longitudinal splits and delamination. More material is lost from those areas where the radial jetting is perpendicular to the fiber direction. Internal damage is visible in the section of

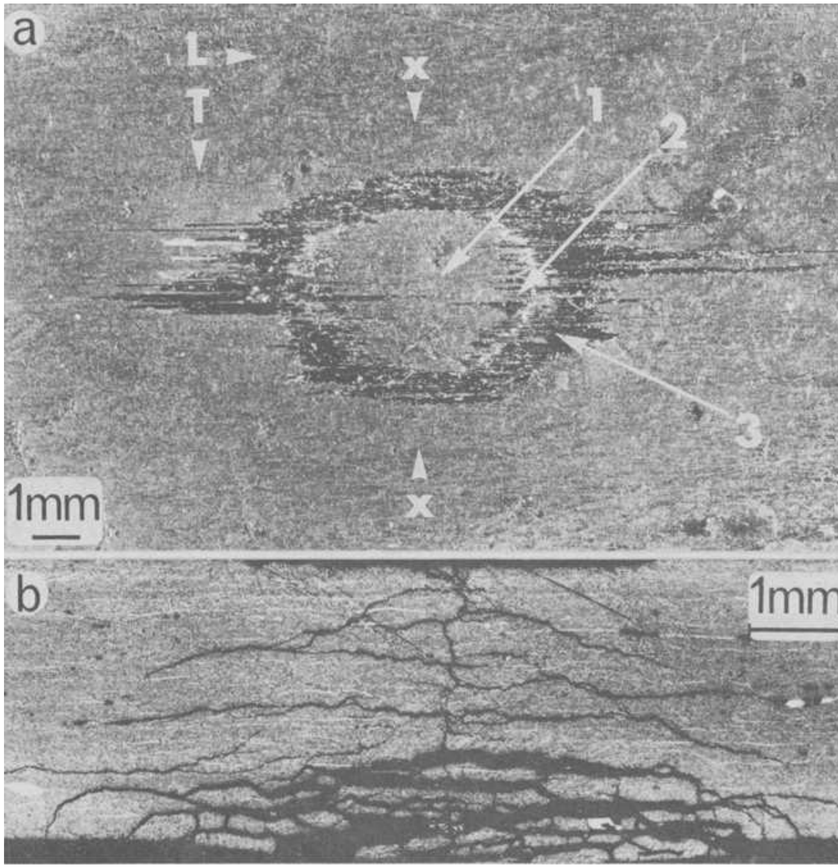

FIG. 4—*Single 725-m s*$^{-1}$ *impact on a 3-mm unidirectional carbon fiber laminate in epoxy resin.* (a): *L, longitudinal direction;* T, *transverse direction;* 1, *central region;* 2, *region of transverse cracking;* 3, *annulus of a subsurface ply exposed by the removal of material.* (b): *Section through* x-x *of* (a).

this site (Fig. 4*b*). The 3-mm plate was thin enough for the bending response to dominate the failure pattern, producing a complex region of spalling and delamination. The inhomogeneous nature of the material also leads to many microscopic failure sites formed by the main compressive loading pulse.

Figure 6*a* is the impacted surface of a 3-mm-thick laminate of woven glass mat in epoxy resin (MY 753). The surface damage consists of resin failure and fiber exposure around the edge of a central undamaged region. The light ring consists of this surface failure together with an area of subsurface delamination, debonding, and matrix fragmentation. The surrounding diamond shape is the internal delamination, which can be seen

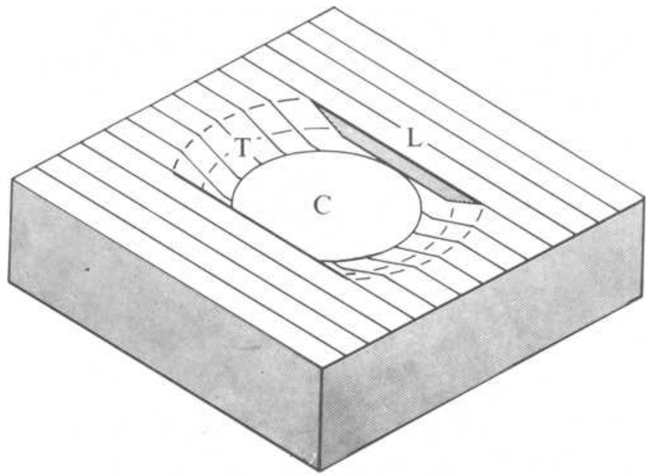

FIG. 5—*Impact of a cylindrical jet on a unidirectional composite.* C, *contact area;* L, *longitudinal cracking;* T, *transverse failure region. After impact, the contact area returns to the level of the undisturbed surface, but the longitudinal and transverse failures remain; see Fig. 4*a.

more clearly in Fig. 6*b*, a rear view of the same specimen. This feature consists of a circular spall, and a larger delamination with characteristic square symmetry situated on a level slightly nearer the front surface. In general, both stress waves and the interlaminar failure find their preferred propagation direction to be along fiber bundles rather than oblique or transverse to them, and this can cause the characteristic diamond shape.

Figure 6*c* is the result of five impacts on a 12-mm-thick plate of similar material, and Fig. 6*d* is a section through this site (along the line XX). This section illustrates the region of multiple spalling (Sp), and delamination (D). Region C is under the main compressive loading of the impact, and isotropic materials fail because of the large shear components set up. However, the inhomogeneous structure of the composite material provides mechanisms for tensile failure of the fibers, the matrix, and their interface. The dimensions of the fibers in the types of composite under consideration are associated with stress wave propagation times which are very much smaller than the ~ 1-μs duration of the main pressure pulse. Therefore, from the point of view of individual fibers, the stress distribution is quasi-static and the results of conventional stress analysis may be applied. The analysis for a cylindrical inclusion in an elastic matrix is well known [*12, 13*]. Significant local stress concentrations, both positive and negative, occur under an applied uniform stress; the stress concentrations become more serious when inclusions are in close proximity [*14,15*]. This leads to

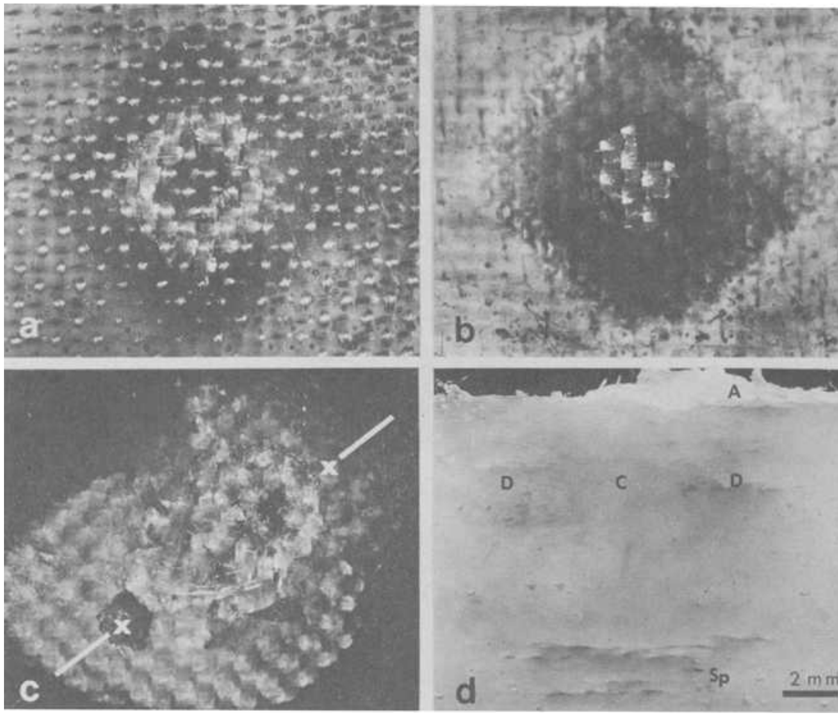

FIG. 6—*700 m* s^{-1} *impacts on glass fiber laminates in epoxy resin.* (a), (b) *Front and rear surfaces of a single impact on a 3-mm plate;* (c) *five impacts on a 12-mm plate;* (d) *section along* X-X *of* (c) *showing:* A, *water penetration and delamination;* C, *region of compression failure;* D, *frontal delamination; and* Sp, *multiple spall fractures.*

an area of local failure sites directly under the impact. These are not visible in Fig. 6*d*, but a clear example is presented in Ref *16*.

Similar impacts onto the identical reinforcement in a polyester resin (Crystic 625) show the same type of damage features of debonding, delaminating, and spalling but to a more marked extent. For example, the area of internal delamination in a 3-mm plate of reinforced polyester is approximately twice that of the epoxy. This is an indication of the higher fracture toughness of the latter. It is in the surface damage on woven laminates, however, that aspects of the behavior of nonreinforced matrix material modify the erosion mechanisms. Unlike a unidirectional or crossply construction, the top surface of a woven cloth is uneven, and to produce a composite with a flat surface there must be a matrix layer of nonuniform thickness above it. This varies in a typical material from areas where the fibers are intersecting the surface to regions where the reinforcement is covered by several hundred micrometres of matrix. Figure 7*a* illustrates part of an impact site on a very coarse weave of glass cloth in brittle polyester resin, where most of the damage has occurred in a region where the matrix was $>100\ \mu m$ thick. 'R' is part of an annulus from which resin has been removed by a process similar to that shown in Fig. *3b*. Although not visible in this picture, fibers have been exposed by this resin removal. Outside the annulus are short circumferential cracks, many of which are associated with voids that intersect the surface. A typical void is shown in Fig. *7b*. The cracks have in addition been stressed by the radial jetting, leading to material fracture in the downstream direction. Figure *7c* is an enlargement of a group of these cracks and the direction of radial jetting is arrowed. Cracks which have not nucleated at voids show similar erosion behaviour.

Parts of the annulus of Fig. *7a* are shown in greater detail in Fig. *8a* and *b*, being, respectively, where the radial direction (arrowed) is perpendicular or parallel to the local fiber direction. Where it is perpendicular (Fig. *8a*), the matrix has been chipped away from the fibers, which themselves may be lifted and broken by the radial jetting. Material removal at this stage is limited by the strength of the fibers. The matrix fracture surfaces are similar to the nonreinforced case of Fig. *3b*. When the radial direction is parallel to the fibers (Fig. *8b*), however, much less material has been removed, and the fibers themselves remain undamaged. In this orientation, the stiffness of the fibers has inhibited the formation of tension cracks that lead to chipping. Also, fibers exposed in this situation are obviously not severely stressed by the fast radial flow of the jet along their length, and thus fewer fibers are fractured.

A thick layer of a tougher resin will offer good protection to the fibers; the chipping of material is obviously an undesirable fracture mode for this purpose. The example of Fig. 4 has only a few micrometres of resin covering the outermost fiber layer, and quite extensive fiber fracture has resulted. In Fig. *6a* fibers are fractured at the high points of the weave, where they are close to the surface. The "valleys" are filled with resin which protects the lower parts of the weave, and so failure points are unconnected. A more serious situation develops if these valleys are not filled, as can happen if resin is not able to completely wet the fabric during the molding process. Figure *7d* shows the result of an impact onto an area of a few square millimeters in which the outermost layer of glass cloth was not covered in resin. Penetration has occurred early in the impact and water has been forced in between the top two laminae to cause very extensive delamination. Fiber breakage is quite widespread and the residual strength of the specimen has been seriously degraded. By comparison, Fig. *7e* is a similar impact onto a correctly formed part of the same specimen where the resin surface layer was complete. Penetration, fiber fracture, and material removal are all considerably reduced. Similar gross frontal delamination of a number of defect-free glass-mat-reinforced thermosetting polymers has also been found in this velocity range for multiple impact

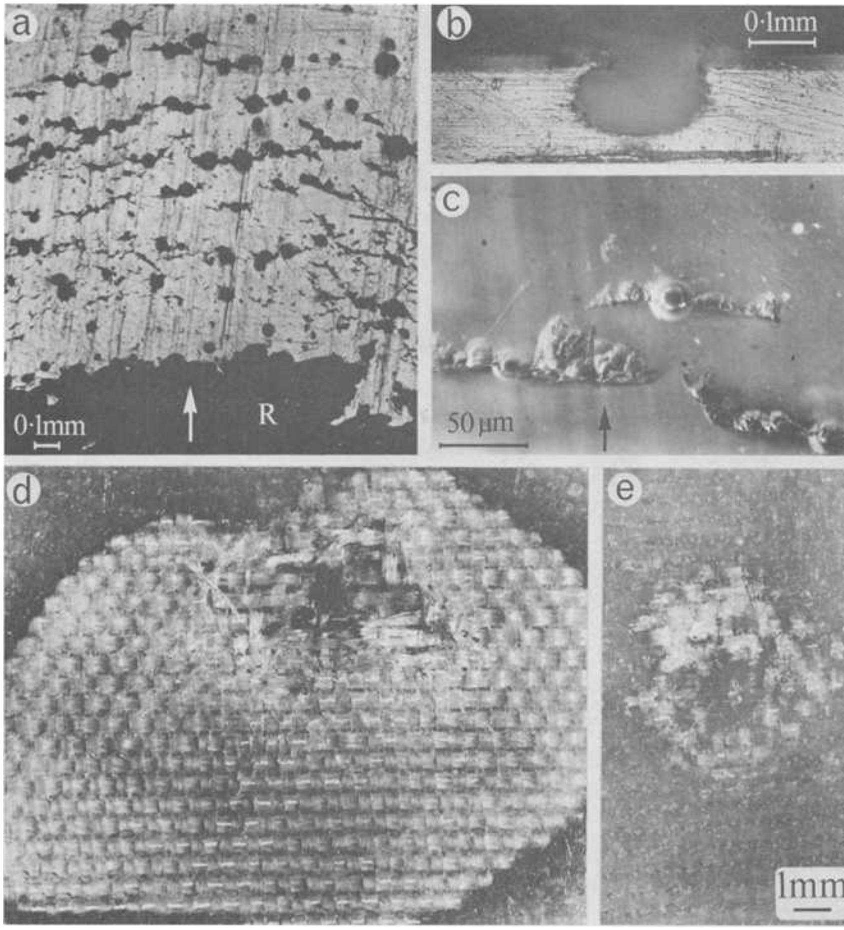

FIG. 7—*700 m s*$^{-1}$ *impacts onto glass cloth in polyester resin.* (a) *Nucleation of circumferential cracks.* R, *part of annulus of resin removal. Direction of radial jetting is arrowed.* (b) *Typical void from* (a). (c) *Erosion of cracks in the "downstream" direction (arrowed).* (d) *Delamination arising from impact upon a defect in the surface resin. See text.* (e) *Impact onto a defect-free part of the same specimen as* (d).

(see Fig. 6) and oblique impact [*17*], and also under very-high-velocity normal impacts (>1000 m s^{-1}). It has not been observed with any unidirectional-ply reinforcements.

Reinforced Polyethersulphone

Some examples of 860 m s^{-1} impacts on a reinforced thermoplastic matrix are presented in Fig. 9. The annulus of surface damage seen in Fig. 9*a* consists of rippling and tearing of the thin matrix layer, which

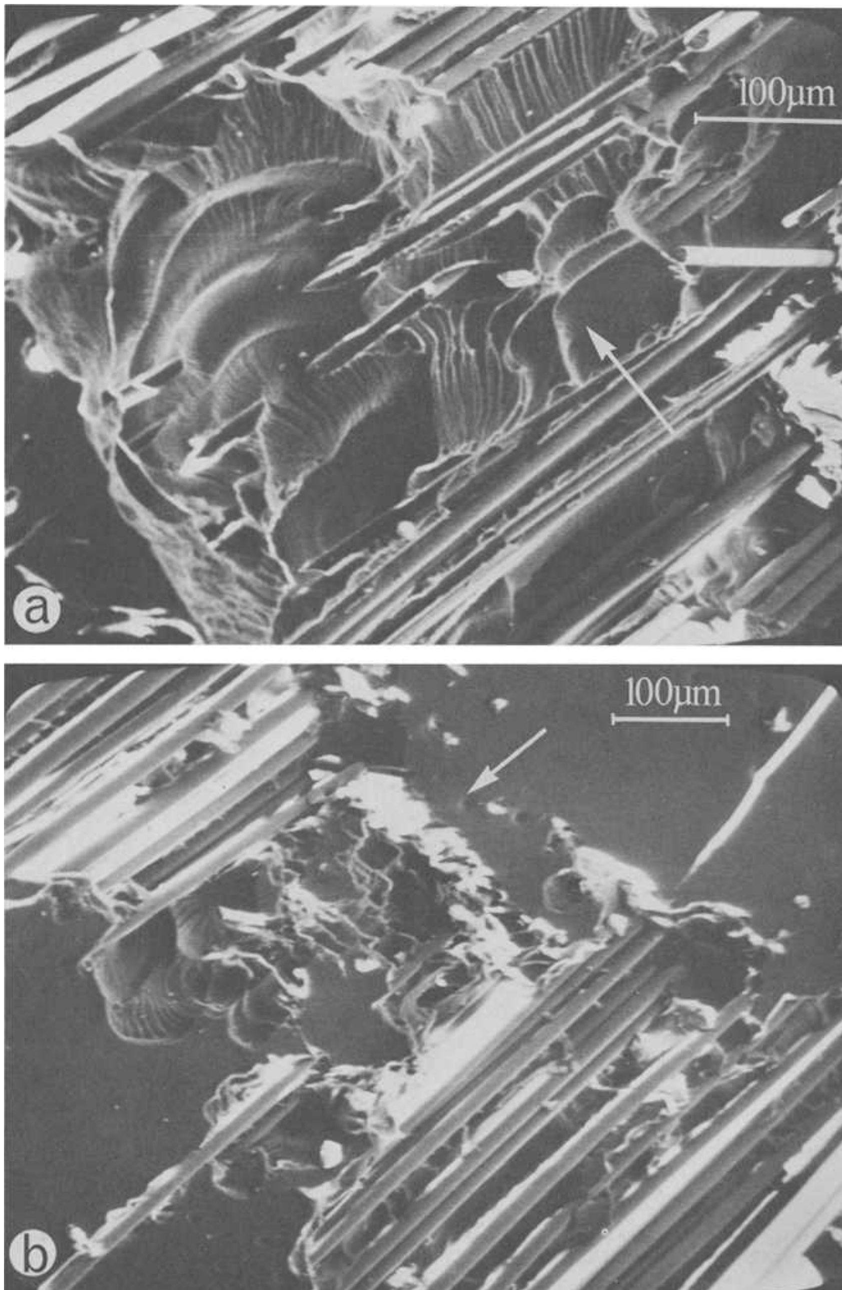

FIG. 8—*700-m s^{-1} impact upon glass cloth laminated in polyester resin.* (a) *Radial direction (arrowed) is perpendicular to the fibers;* (b) *radial direction is parallel to the fibers.*

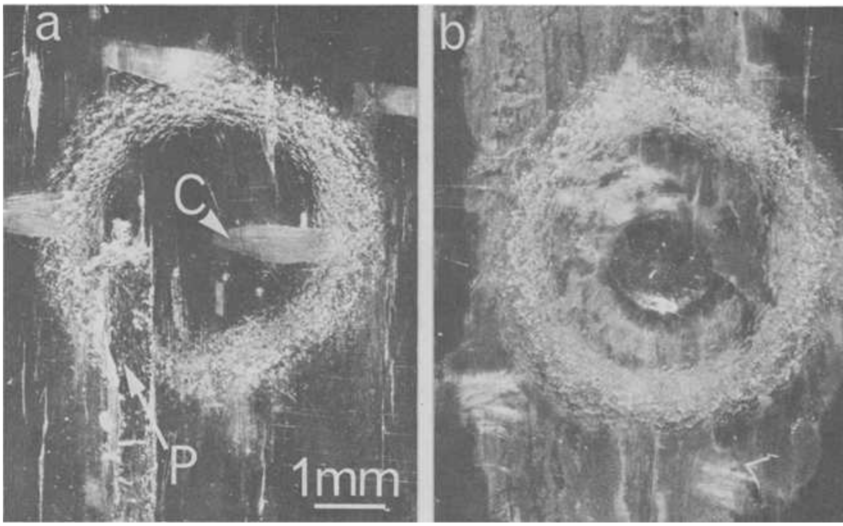

FIG. 9—*860-m s^{-1} impacts upon unidirectional layers of Type II carbon fibers in polyethersulphone.* (a) *Noncoated specimen.* C, *cross-stitching in fiber plies;* P, *region of fiber and matrix removal.* (b) *Specimen with 400-μm surface coating of matrix material.*

varies between <10 and ~ 50 μm thick. The surface deformation is severe, but the underlying fiber arrangement is largely undisturbed. There are regions where a section of fibers is plucked out, such as Area 'P' marked in Fig. 9*a*, and some small-scale fiber breakage is present. Also, distortion of the linear fiber arrangement occurs because of the flow of the matrix, but in general this type of deformation is inhibited by the high stiffness of the reinforcement. Distortion and fracture of the fibers seems to be maximized when the direction of radial jetting is ~ 60 deg to the fiber axis, in contrast to the area of maximum damage with thermosetting matrices, which occurs when these directions are perpendicular. Compared to this latter example, the effect of high-velocity liquid impact on reinforced thermoplastics is much less serious in terms of material removal and in particular with regard to the residual strength of the specimen. Internal damage is less severe, both delamination and spalling being considerably reduced. The most serious damage mode with thin plates of reinforced thermoplastic is longitudinal splitting, which can easily lead to complete penetration with one impact.

The annulus of surface damage in the foregoing examples is quite similar to that observed with nonreinforced thermoplastic material. Less material has been plucked out, but the plastic deformation is enhanced. The large plastic crater that dominates the deformation of the latter case is, however, almost entirely suppressed by the stiff support given by the fibers. The crater depth in Fig. 9*a* is 16 μm, compared with >150 μm for the nonreinforced matrix. If an additional thick surface layer of matrix is provided, plastic deformation occurs within this layer. Figure 9*b* shows this situation where deformation to a depth of 100 μm has occurred in a surface layer of depth ~400 μm. The coating has been delaminated by the impact, this failure being more extensive in the longitudinal fiber direction. At much lower velocities, the delamination consists of two separate areas situated underneath opposite sides of the annulus at the ends of a diameter that is parallel to the fibers. This suggests that the delamination is a shear failure resulting from the lateral displacements in the coating caused by the plastic deformation. The modulus mismatch between coating and substrate is greater in the longitudinal than in the transverse direction. A dynamic illustration of this mechanism, using high-speed photography, is given in Ref *18*.

Variation of Impact Conditions

As the jet size or velocity is increased, the damage to composite materials from a single impact is rapidly accelerated. This variation has been quantified by measuring damage areas in two materials: a woven glass cloth in epoxy resin and a chopped glass reinforcement in a polysulphone matrix. Detailed results, to be published, have been obtained over a range of jet sizes from 0.4 to 6.5 mm, and of velocities from 250 to > 1000 m s^{-1}.

Figure 10 illustrates the variation of subsurface delamination in the glass/epoxy material with angle of impact for three impact velocities. 0 deg represents normal impact. It is a commonly found rule in liquid impact that normal impingement is the most damaging. However, this example shows a situation in which the rule does not apply. At each velocity, maximum delamination occurs at a moderately oblique angle. It is seen that the damage area becomes smaller as the angle deviates slightly from 0 deg, and then peaks again as obliquity is further increased. This behavior was first observed in a different glass-cloth/epoxy system by Gorham and Field [*17*] where illustrations of the change in damage pattern are given. In that case the peak corresponded to delamination of the type illustrated in Fig. 7*d*, where water penetrates the surface and then is forced between layers of reinforcement. In the present results, however although this is influencing the damage variation at the highest velocity, at the lowest one there is no surface penetration, and the anomalous behavior is a consequence of the differing stress distribution and history of oblique solid-liquid impact.

Discussion

The examples presented in this paper represent only a small sample of the component material types, reinforcement arrangements, and impact

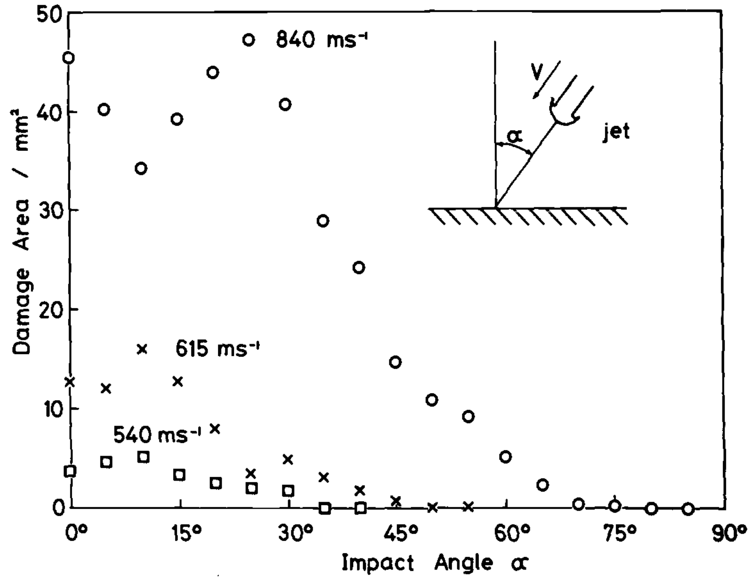

FIG. 10—*Damage variation for single oblique impacts: 9-mm plate of glass cloth in MY720 epoxy resin. Area of subsurface delamination measured for three impact velocities as a function of impact angle.*

conditions that we have studied. A few more examples of various reinforcements in polyester and epoxy resins are presented in Ref *16*. However, a number of general points which have arisen in the work are illustrated by these present examples. Composite materials have a very wide variation of mechanical properties, depending critically on the nature of the components and their mutual adhesion, and the conditions which determine the extent of a particular damage mode are complex. Great variability can be found between impacts at different positions on a single composite plate, due to the inherent inhomogeneity of construction and properties. Macroscopic properties, such as fiber volume fraction, are not necessarily significant for predicting the effects of impacts, which are sampling the local variation of these parameters. The stress created by an 800-m s^{-1} water impact are much higher than the strengths of the matrix, the interfaces, and often also of the fibers. Therefore, exact measurements of these properties, particularly the average values for a composite specimen, are of secondary importance. Some damage to a composite plate is inevitable; the extent of damage is dependent upon such factors as strength and toughness. However, a qualitative analysis of damage modes and mechanisms has a general relevance to many types of composite material. The main characteristics of liquid impact under the present conditions are the high pressures (typically 1.5 GPa at 800 m s^{-1}) applied for a short time

(~ 1 μs). Therefore, the analysis of damage applies not only to a wide range of liquid impact situations, but also to the similar effects of high-velocity small solid particles and to explosive loading.

The impact energy of this type of loading must be dissipated by some means, and the stresses are high enough so that if one failure mode is inhibited, then another will probably be enhanced. The best practical solution is to attenuate the stresses quickly by a nondestructive method, such as an elastomeric coating in which the impact energy is absorbed as elastic deformation energy and as heat. However, this cannot always be achieved successfully because of practical considerations. Also, in the event of coating failure the composite is unprotected. Therefore, a study of the failure modes and mechanisms in composite materials is relevant.

The Presence of Reinforcement

The very nature of a composite material renders it liable to severe damage from high-velocity liquid impact. The inhomogeneity of structure arising from the presence of a second mechanically dissimilar component produces complex local stress states from simple compressive loading, and there are many possible points of failure initiation distributed throughout the material. In practice a composite material is designed and used in order to withstand a particular working stress state most efficiently. This usually means that the strength properties are nonisotropic, and the resulting weak planes or directions between layers or within the reinforcement fail easily under the triaxial stress state of an impact and form spall fractures, delamination, and splits.

In this way the impact damage to the tough but essentially brittle epoxy resins that have been illustrated here is worsened by the presence of reinforcement. At the velocities studied, significant internal damage of debonding and matrix failure is found within the composite, whereas very little damage is found with pure matrix material. The fractures of splitting, delaminating, and spalling that are a result of the structural inhomogeneity can be quite widespread. However, at velocities which are low enough for the reinforcement not to break, the very brittle polyester resin is protected by the reinforcement. Fibers limit the brittle chipping away of the nonreinforced matrix. This agrees with the results of subsonic erosion tests reported by Schmitt [*19*], where material removal was caused by multiple impact. Material loss from a very brittle resin is reduced by the presence of reinforcement, although residual strength may not be maintained. A nonreinforced plate of this brittle resin, a few millimetres thick, will shatter under a single impact of sufficiently high velocity, as the propagation of stress waves causes failure at quite large distances from the impact site. With reinforcement present, the long bending cracks are inhibited, spallation does not cause gross material removal, and stress wave propagation is attenuated. In this case the resistance of the composite to withstand impact is a dramatic improvement over the matrix alone.

The ductile thermoplastic matrices are less affected by the presence of reinforcement, and it is again not possible to generalize upon whether or not the changes are beneficial. In terms of material loss and residual strength, these largely ductile materials withstand high-velocity impact to a much better degree than their brittle counterparts. However, the presence of stiff reinforcement tends to inhibit plastic flow and to encourage the brittle failure modes of splitting, etc. This is particularly important with thin plates, and residual strength can be catastrophically reduced by a single impact. However, if a composite with a ductile matrix is designed to minimize these undesirable failure modes, then the overall response may be an improvement on the nonreinforced case because of the reduced deformation.

Effect of Component Material Properties

When designing a composite material to be used in a given erosive situation, it is usually necessary to impose certain criteria on the postimpact behavior, such as minimizing material loss, maintaining a surface profile, or maximizing residual strength. With this in mind, it is useful to discuss the impact behavior of a composite material in terms of the properties of its components.

A very brittle matrix, illustrated in this paper by a polyester resin, allows comparatively large-scale material removal by chipping, resulting in exposure and fracture of the reinforcement. Tensile failure under the compressive components of the loading history arises from the inhomogeneity of the two-component structure, causing matrix fracture and fiber debonding. Weak planes or directions between layers or within the reinforcement encourage comparatively large-scale splitting, delamination, and spalling. The surface chipping can be greatly reduced by using a tougher material such as an epoxy resin, but internal failure is still of a similar order. Tensile strength is then severely reduced by fiber fracture and debonding; bending stiffness and strength are also impaired by delamination and splitting.

Ductile matrices are much more successful at protecting the reinforcement, particularly against surface damage. However, the stiffness of the fibers suppresses the ductility of the matrix material, and some impact energy is therefore dissipated in the brittle failure modes already described. There is very little removal of material from the surface, but the plastic deformation does disturb the surface profile. Fiber fracture is much less apparent. If the large-scale splits and delaminations are inhibited, possibly by use of a thick plate, then the residual strength will be only slightly impaired.

The mechanical properties of the fibers are not as important as those of matrix in determining the overall damage. The stiffness will determine the deformation of a ductile matrix composite, and strength will determine the amount of fiber breakage and removal with brittle matrices. Within the comparatively limited range of modern glass and carbon fibers, however, the differences in damage patterns that we have found for single impacts are not large, although the geometry of the reinforcement can produce very significant differences. Unidirectional fibers suffer from long splits and cracks in the longitudinal direction. A woven reinforcement contains the damage more successfully, but more fibers are fractured at the high stress concentrations of crossover points and at high points of the weave. Crossply laminates are very susceptable to delamination, while short fiber reinforcements do not limit the removal of large pieces of a brittle matrix. Therefore, certain mechanical properties may be retained better than others after impact. The effect of various geometries is illustrated in Ref *16*.

These examples show that it is sometimes possible to predict the type of response that a particular combination of matrix type and reinforcement geometry will have. However, it is necessary to know the properties of the component materials at the strain rate of the impact situation, which is typically $>10^5$ s^{-1}. At this strain rate the response of polymeric materials in particular cannot always be predicted from low-strain-rate data. Many change their behavior from ductile to brittle modes as the strain rate is increased, and some localize shear deformation into narrow bands above a critical rate. Either change will increase the impact damage. However, quite accurate prediction of the performance of a composite can be made from impacts on the nonreinforced matrix material. The presence of reinforcement produces more uniform changes within a particular group of matrices. The waterjet technique used in the present investigation is an experimentally convenient and very rapid method for quickly assessing the properties of materials in order for their composite ability to be predicted.

Conclusions

A wide variety of failure modes have been observed in the materials studied, and the severity of each is strongly dependent upon impact conditions and upon local material properties. Nonreinforced polymers have shown behavior ranging from fully brittle to largely ductile. Qualitative prediction of the behavior of a given composite can be made from knowledge of the matrix properties at high strain rate. Although there is no ideal material to withstand impact in all applications, it is possible to establish rules which assist in the design of composites for specific purposes. In general it is better to absorb the impact energy by ductile failure, in which strength reduction and mass loss are both miminized. By this criterion, the brittle thermosetting resins, epoxy and polyester, are less successful than the ductile thermoplastics such as polycarbonate and polyethersulphone.

Acknowledgments

We thank the Science Research Council and the Ministry of Defence (Procurement Executive) for grants to the laboratory.

References

[1] Bowden, F. P. and Brunton, J. H. in *Proceedings of the Royal Society,* Series A, Vol. 263, 1961, pp. 433-450.
[2] Gorham, D. A., "High Velocity Liquid Jets and Their Impact on Composite Materials," Ph.D. Thesis, University of Cambridge, Cambridge, England, 1974.
[3] Gorham, D. A. and Field, J. E. in *Proceedings,* 11th International Congress on High-Speed Photography, London, 1974, Chapman and Hall, London, pp. 442-447.
[4] Field, J. E., Gorham, D. A., and Rickerby, D. G., this publication, pp. 298-319.
[5] Gorham, D. A., in *Proceedings,* 10th International Congress on High-Speed Photography, Nice, France, 1972, Association Nationale de la Recherche Technique, Paris, pp. 438-444.
[6] Field, J. E., Camus, J.-J., Gorham, D. A., and Rickerby, D. G. in *Proceedings,* 4th International Conference on Rain Erosion, Meersburg, Germany, 1974; Royal Aircraft Establishment, Farnborough, England, pp. 395-420.
[7] Bauwens-Crowet, C., Bauwens, J.-C., and Homes, G., *Journal of Materials Science,* Vol. 7, 1972, pp. 176-183.
[8] Raghava, R., Caddell, R. M., and Yeh, G. S. Y., *Journal of Materials Science,* Vol. 8, 1973, pp. 225-232.
[9] Fyall, A. A. in *Proceedings,* 2nd International Conference on Rain Erosion, Meersburg, Germany, 1967; Royal Aircraft Establishment, Farnborough, England, pp. 593-603.
[10] Bowden, F. P. and Field, J. E., *Proceedings of the Royal Society,* Series A, Vol. 282, 1964, pp. 331-352.
[11] Field, J. E. in *Proceedings,* 2nd International Conference on Rain Erosion, Meersburg, Germany, 1967; Royal Aircraft Establishment, Farnborough, England pp. 593-603.
[12] Sezawa, K. and Nishimura, G., *Reports, Aeronautical Research Institute,* Tokyo, Vol. 6, 1931, pp. 25-43.
[13] Goodier, J. N., *Applied Mechanics, Transaction,* American Society of Mechanical Engineers, Vol. 55, 1933, pp. 39-44.
[14] Shelley, J. F. and Yu, Y.-Y., *Journal of Applied Mechanics,* Vol. 33, *Transactions,* American Society of Mechanical Engineers, Vol. 88, Series E, 1966, pp. 68-74.
[15] Hill, J. L., *Journal of Applied Mechanics,* Vol. 33, *Transactions,* American Society of Mechanical Engineers, Vol. 88, Series E, 1966, pp. 715-718.
[16] Gorham, D. A. and Field, J. E., *Journal of Physics, D: Applied Physics,* Vol. 9, 1976, pp. 1529-1541.
[17] Gorham, D. A. and Field, J. E., *Wear,* Vol. 41, 1977, pp. 213-222.
[18] Gorham, D. A. and Field, J. E., *Nature* (London), Vol. 257, 1975, pp. 216-217.
[19] Schmitt, G. F. in *Proceedings,* 3rd International Conference on Rain Erosion, Elvetham Hall, England; Royal Aircraft Establishment, Farnborough, England, 1970, pp. 107-128.

DISCUSSION

J. V. Hackworth[1] (*written discussion*)—Why does damage on PMMA and composites created by water-jet impact tend to maximize at impact direction/specimen angles of 15 to 20 deg? Was this angle effect checked with specimens shot into suspended drops?

We have recently impacted zinc selenide into 2.0-mm drops at 222 m/s with the zinc selenide surface tilted 30 deg from the normal, and we find the extent of ring fractures drastically reduced from that on specimens with the surface normal to the impact direction. Within the next few weeks, we will test at 15 deg from the normal. Data from this test should be available for this comment before the *STP* is printed.

D. A. Gorham, M. J. Matthewson, and J. E. Field (*authors' closure*)—It is commonly observed that damage due to liquid impact does decrease as the angle of incidence deviates from the normal. We have described (Ref *17*) two exceptions to this rule in which damage is maximized at slightly oblique angles. In the case of PMMA, the maximum occurred because two separate failure regions, the ring crack and the subsurface failure, were brought into contact by the noncircularly symmetric stress field of the oblique impact. The total extent of failure was not enhanced, but mass loss increased because a greater amount of failure was accessible to a free surface. In the case of the composite, the amount of visible damage increased because of a new failure mode, namely, wide-spread delamination, which occurred under oblique impact. In both examples a critical velocity had to be exceeded in order for these effects to appear. For PMMA, a velocity of >580 m s^{-1} was necessary to cause the subsurface shear failure, and penetration of the top ply of the composite took place with only an impact at >550 m s^{-1}. We have not checked these effects by firing specimens into suspended drops, but we do expect that the anomalies would be found under impact conditions that are similar to those of the illustrated jet impacts. (See reply to question by A. F. Conn.)

A. F. Conn[2] (*written discussion*)—This question relates to the ability of your liquid jets to simulate the material-removal aspects of liquid droplet impact for those materials wherein you observe considerable removal due to the outwashing action. The jets have considerably more liquid available, relative to the drops, for this outwashing. Thus, my question is, Have you run the suspended drop tests, and compared the material removal with that observed for the jets, or is there other evidence that has convinced you that the jets are indeed a good simulation for the material-removal action?

[1] Bell Aerospace Textron, Buffalo, N.Y. 14221.
[2] Hydronautics, Inc., Laurel, Md. 20810.

D. A. Gorham, M. J. Matthewson, and J. E. Field (authors' closure)—Removal of material due to lateral outlfow of the liquid, whether a drop or jet, may be considered in two stages. Firstly, the high-pressure regime of liquid impact loading, that is when the liquid is compressed, is terminated by extremely high-velocity jetting from the free surface of the liquid. This jetting is typically 2 to 3 km s^{-1} for the conditions discussed in the paper. Irregularities in the surface (for example, steps as small as 0.1 μm) are subjected to extremely large stresses. Therefore, cracks are eroded, and, if the surface layer of a laminate has been penetrated, delamination failure is initiated. High-speed photography has shown that most damage occurs within this early time when the liquid is compressed and is exerting a high pressure upon the solid. However, this regime does not last for long. When the compressed liquid has been relieved by the release waves from the free surface, the rest of the liquid impinges stably against the solid surface. Therefore, after a time of typically 1 μs, the lateral flow velocity has been reduced to a value that is less than the original impact velocity. Most of the liquid contained in the jet or drop impinges on the surface in this way.

The two stages of behavior have been observed with the impact of both liquid drops and jets. The initial high-velocity jetting is similar for both cases, occurring only during the "water-hammer" stage of the impact. However, the stable flow of the remaining part of the jet may differ from that of a drop, depending on how long the jet is. In the examples illustrated in the paper where the contact area is 3 mm across, the volume of water contained in the extrusion nozzle is equivalent to a cylindrical jet 3 mm in diameter and about 12 mm long. A 10-mm-diameter drop would produce a similar size of damage mark, and in this case the column of water behind the contact area is 10 mm long. Of course, the total volume of the equivalent drop is much larger than that of the jet, although much of the drop will be impacting around the initial compressively loaded area of contact. Therefore, in the present work the quantities of water involved in the low-velocity outflow of the jet are not considerably more than in the impact of an equivalent drop. Although we have not carried out the suspended-drop tests, we do expect that the same anomalies in angular impact will be seen. In general we have not seen any difference between suspended-drop damage and jet impact damage that is due to differences in the lateral flow. Most damage occurs during the initial water-hammer phase of impact, and most of the liquid flows harmlessly against the solid. The total quantity of water does not affect the results.

G. A. Savanick[3] *(written discussion)*—In recent years a new uranium mining technology, called solution mining, has evolved in the United States. In solution mining a solvent is injected through a well into the

[3]U.S. Bureau of Mines, Twin Cities Mining Research Center, Twin Cities, Minn. 55111.

uranium-bearing rock, where it takes the uranium into solution. The solution bearing the uranium then flows into another well from whence it is pumped into a processing plant. The wells into which the solution is injected or recovered are typically cased with Schedule 40 polyvinyl chloride (PVC) casing. The Bureau of Mines has been using a 69-N/m^2, 26.6-litres/min (10 000 psi, 7 gal/min) continuous waterjet to cut perforations through the PVC in order to effect communication between the wellbore and the adjacent rock. The waterjet performs very well in PVC; that is, it cuts a clean hole through the PVC and surrounding grout terminating in the adjacent rock.

Recently, a need has arisen to use casing that is stronger than PVC but less expensive than steel. Casings composed of a fiber glass composite have been shown to fill this need. Unfortunately, perforation of these casings with the 69-N/m^2, 26.6-litres/min (10 000 psi, 7 gpm) continuous waterjet has been accompanied by severe delamination manifested by blisters forming on the inside of the casings. Do the authors have any suggestions as to how perforation operations can be applied to avoid this delamination?

D. A. Gorham, M. J. Matthewson, and J. E. Field (authors' closure)— All our experiments with laminated composites have shown that in situations where there is significant damage or penetration, delamination is unavoidable. The interlaminar surfaces are planes of weakness, and failure resulting from various mechanisms (see Ref *16*) is directed along them. The problem does not arise with short random fiber reinforcements, although these produce a material with different mechanical properties that may or may not be suitable for your application. This type of reinforcement in a ductile thermoplastic matrix will fail by a simple penetration; a brittle matrix will cause widespread failure. If mechanical strength was not important, then elastomers, which fail by a single narrow penetration, may also have been a solution to your problem.

Hypervelocity Erosion

W. F. Adler[1] *and A. G. Evans*[2]

Erosion Damage in Carbon-Carbon Composites at Hypersonic Impact Velocities

REFERENCE: Adler, W. F. and Evans, A. G., "**Erosion Damage in Carbon-Carbon Composites at Hypersonic Impact Velocities,**" *Erosion: Prevention and Useful Applications, ASTM STP 664*, W. F. Adler, Ed., American Society for Testing and Materials, 1979, pp. 345–375.

ABSTRACT: The damage to three-dimensional orthogonal carbon-carbon composites created by particle impacts ranging from 1800 to 6000 ms^{-1} has been characterized for three weave constructions at both ambient and temperatures up to 3600°C. The subsurface damage modes in the vicinity of the impact crater are described for the range of conditions investigated. Hypotheses are advanced concerning the failure modes and kinetics for the material ejected from the crater based on examination of sectioned specimens and high-speed photographic sequences.

Kinking of the longitudinal and lateral fiber bundles is found to be the primary damage mode. Kinking of the longitudinal fiber bundles under the impact site (which controls the depth of the impact crater) displays a relatively minor dependence on the bundle dimensions. The lateral extent of the impact crater is dependent on the longitudinal fiber bundle content—decreasing as the bundle dimensions increase. It is hypothesized that kinking of the longitudinal fibers leads to this removal, which is related to kinking of the adjacent lateral fiber bundles which increases with the particle impact velocity.

KEY WORDS: carbon composites, impact, erosion, damage modes, fracture, kinking, hypervelocity impact, penetration mechanics, shock waves, stress waves

Investigation of the erosive response of fibrous composites exposed to natural (rain/ice) and induced (dust) particulate environments is stimulated by the need for reentry vehicle protection materials. The erosion performance of existing system materials has been evaluated using ground-impact simulation testing and verification flight tests [*1–6*].[3] In the evaluation of materials

[1]Director, Materials Science Section, Effects Technology, Inc., 5383 Hollister Ave., Santa Barbara, Calif. 93111.

[2]Professor, Department of Materials Science and Engineering, University of California at Berkeley; formerly, Group Leader, Structural Ceramics, Structural Materials Department, Rockwell International Science Center, Thousand Oaks, Calif. 91360.

[3]The italic numbers in brackets refer to the list of references appended to this paper.

fabricated for improved erosion resistance, all material evaluation has been directly related to erosion test performance. Little attention has been given to information for material development activities. It has thus been difficult for material manufacturers to relate erosion test results, such as mass loss ratios, to material construction or processing variables.

Mass loss determinations have been performed either by single-particle impact procedures [*6*] or by continuous erosion testing in ballistic range facilities [*1-3*]. Mass loss laws have then been derived for specific materials based on experimental correlations. However, the single particle studies have not adequately represented the effects of multiple collisions, while the laws derived from the continuous erosion studies have focused on the result and not the process of erosion. In both cases extrapolation to service conditions has been made from a limited data base without consideration of the physical processes by which cratering occurs. A program is underway to extend the existing data base and to interrelate many aspects of the erosion process on a macroscopic scale for the purpose of predicting material removal rates [*7*].

Each single-particle impact causes substantial subsurface damage in addition to mass loss [*8-9*]. Furthermore, after many sequential single-particle impacts on one specimen, the average mass loss for each test is considerably higher than the baseline single-particle value. It has been postulated that this increase in average mass loss is due to subsurface interaction of damaged material. This increase is frequently referred to as "damage enhancement," and a damage enhancement factor has been defined as the ratio of the mass loss obtained for a predamaged surface to that obtained for a virgin surface. Damage enhancement is possibly the most sensitive parameter in erosive mass loss; experimental values of up to 3.3 have been recorded [*7*]. It is also a complex function of extrinsic variables (such as velocity, particle size, particle type, and temperature), as well as intrinsic variables (such as material properties and material failure modes).

The present work is directed toward quantifying the extent and nature of the subsurface damage produced by a variety of impact conditions and toward assessing the contribution of the most significant aspects of the subsurface damage to damage enhancement. The ultimate objective will be to suggest viable microstructural modifications that would improve the erosion resistance of carbon composites. For this purpose, detailed post-test examination of crater formation and subsurface damage has been performed for three carbon-carbon materials (Table 1) impacted by glass, nylon, or water projectiles in the velocity range 1800 to 6000 ms^{-1} at temperatures from 20 to 3600°C. These observations have been correlated with information obtained from high-speed photography, concerning the material removal sequence, and from selected quasi-static experiments which provide ancillary data concerning both the conditions for damage formation and the physical properties of the composite constituents. These correlations permit preliminary postulates to be constructed about the details of the cratering process from initial contact to damage completion.

TABLE 1—*Characteristics of carbon-carbon composites investigated.*

Material Designation	Reinforcing Fibers	Processing	Number of Ends			Unit Cell Dimensions,[a] mm			Bulk Density,[b] g/cm^3	Manufacturer
			X	*Y*	*Z*	*X*	*Y*	*Z*		
2-2-3	T50	CVD + pitch	2	2	3	0.76	0.76	0.84	1.87	General Electric
1-1-5	T50	CVD + pitch	1	1	5	0.76	0.76	0.76	1.86	General Electric
1-1-13	T75	pitch/CVD/pitch	1	1	13	1.02	1.02	0.56	1.96	McDonnell Douglas

[a] Preform dimensions for ideal conditions, not measured values from specimens examined.
[b] Approximate values since billet-to-billet variations occur as well as spatial differences within a billet.

Damage Observations

The conditions used in this work for damage analysis are primarily single-particle impacts produced by 1-mm glass beads using a high-energy capacitor discharge exploding foil system [*4–6*]. Tests can be performed on carbon-carbon materials at temperatures up to 3600°C in this facility. A commercial induction heating unit is used to heat a 12-mm-diameter by 12-mm-long specimen to 3600°C in less than 10 s.

The craters produced at hypersonic particle impact velocities are examined using both optical and electron microscopy. Initially, plan views of the craters are obtained using scanning electron microscopy (SEM) to provide a general comparison of the nature of the damage from one test condition to another and for the various carbon-carbon systems. Then the crater is scanned for details of the surface fracture modes. Subsequently the specimens are sectioned. The preferred sectioning method involves impregnation of the specimen with epoxy to preserve the details of the microstructure during subsequent sectioning operations (the epoxy resin can be made to completely permeate the interior of the specimen by using an outgassing procedure). A wire saw at the lowest possible cutting rate is used to section the specimen, which is then metallographically polished. Optical microscopic observations are made on progressive cross sections to establish a three-dimensional picture of the extent and nature of the subsurface damage and its relation to the damage observed on the crater surface. The general nature of the damage produced for a range of impact conditions will be described.

Damage Perspectives

A sequence demonstrating the development of the impact damage at low temperature (0 to 2500°C) as a function of projectile velocity (for 1-mm glass projectiles) is presented in Fig. 1. The crater mass loss is typically the same or greater than the room temperature value over this temperature range. At velocities below $\sim$2000 ms^{-1}, the projectile is retained by the target (Fig. 1*a*) and the crater consists primarily of a central zone that accommodates the penetration of the projectile. At higher velocities (Fig. 1*b*), however, the projectile is ejected, and the crater contains an outer ledge in addition to a more deeply penetrating central zone. Surface spallation, manifested as the stripping of the lateral bundles exposed to the surface, is also apparent (Fig. 1*c*). A longitudinal bundle is defined as a bundle oriented in the direction of the applied force (dynamic or quasi-static)—usually the bundles normal to the surface—while the bundles orthogonal to the applied force are referred to as lateral bundles. The surface of the specimen in Fig. 1*c* was photographed prior to impact. Comparison of the pre- and post-impact conditions show that the surface damage is localized and that no fine-scale damage occurs

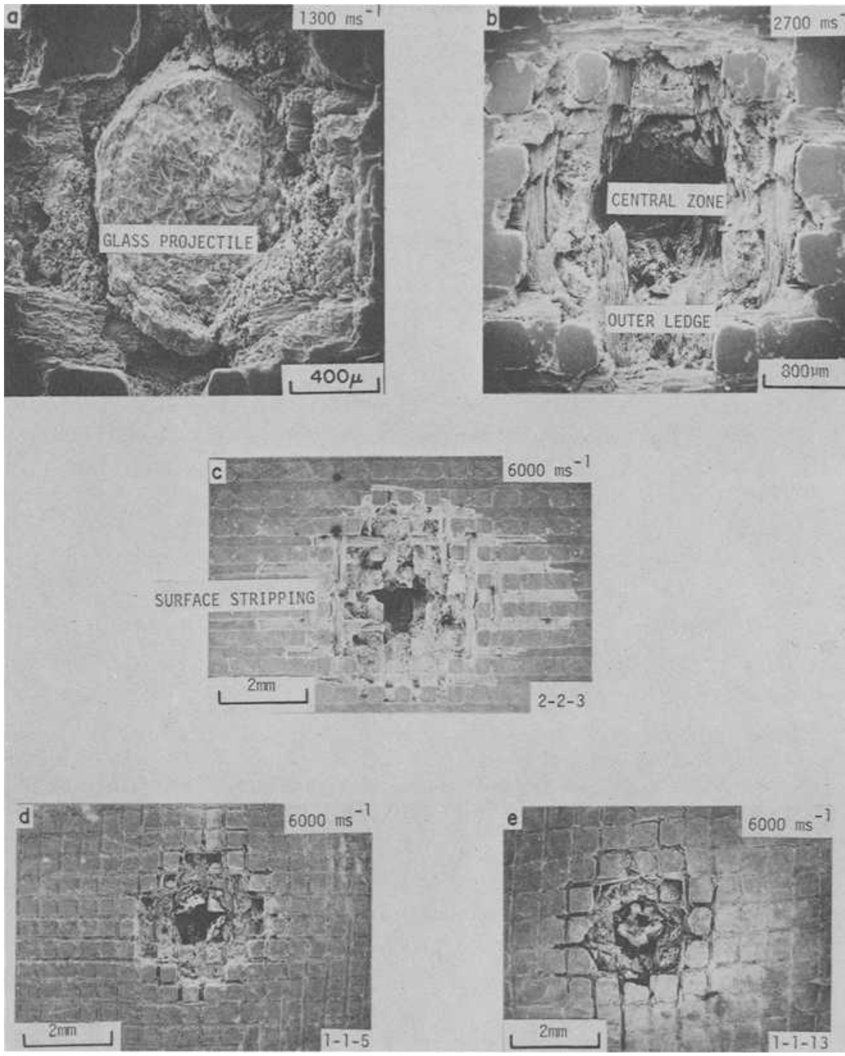

FIG. 1—*SEM overview of craters formed by 1-mm glass projectile impacts.*

beyond the area encompassed by the fiber stripping boundary. An initial evaluation of the effect of the yarn bundle geometry (see Table 1) on the damage morphology (Fig. 1*c*,*d*,*e*) indicates that as the proportion of longitudinal bundles increases, the central penetration zone tends to increase slightly in depth, while the outer ledge diminishes in width. Although this comparison also involves processing and fiber variations, it is believed that this general trend is accurate. Close inspection of the central zone (Fig. 2*a*)

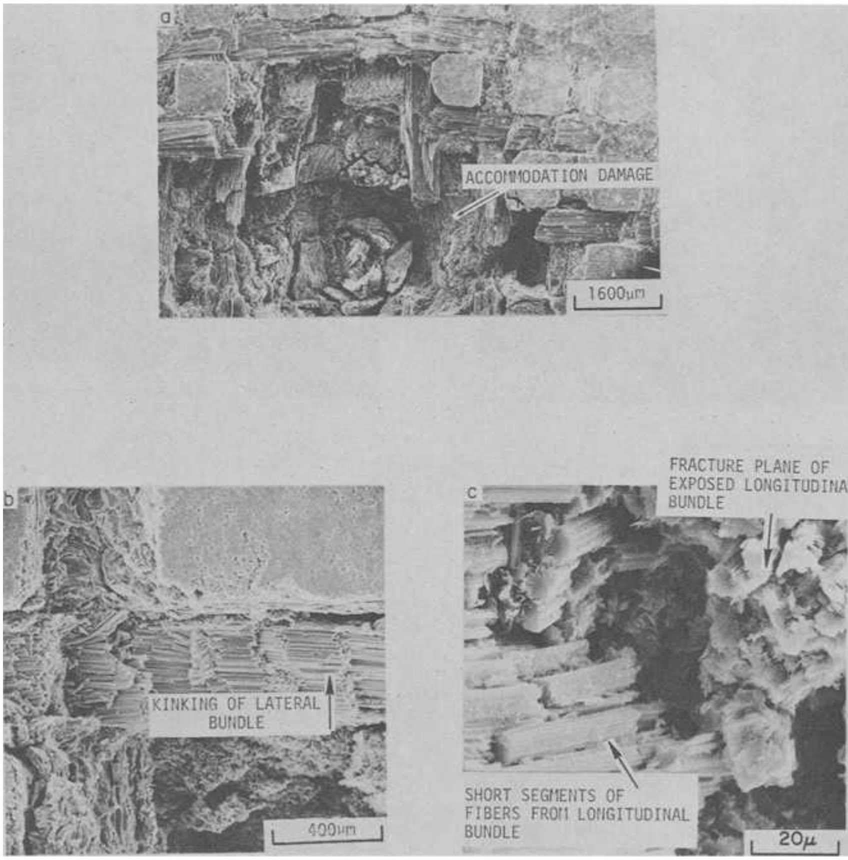

FIG. 2—*SEM's of details of impact craters in 2-2-3 material.* (a) *Accommodation damage at base of central zone;* (b) *kinking of a lateral bundle at crater edge;* (c) *short fiber segments on a longitudinal bundle at outer ledge.*

indicates the existence of accommodation damage, manifested as exposed fibers conforming to a spherical boundary. This suggests that the central zone is formed by the direct penetration of the projectile as at the lower velocities. Kinking of the lateral fiber bundles near the crater periphery is also apparent in certain microstructures (Fig. 2*b*), and the presence of short lengths of longitudinal fibers laterally displaced away from the impact center (Fig. 2*c*) is commonly observed on longitudinal bundles at the crater ledge.

The damage created by deformable projectiles (water or nylon) has most of the same features (Fig. 3), although there is little evidence of accommodation damage in the central zone. Linking of the outer edge damage zones is observed for closely spaced impacts; however, relatively minor interaction

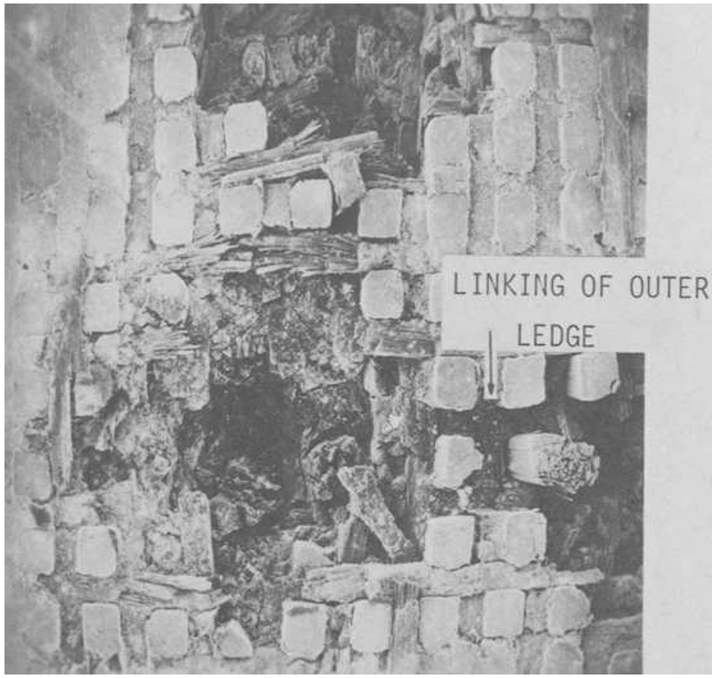

FIG. 3—*Impact damage on 2-2-3 created by 1-mm nylon beads at 4000 ms* $^{-1}$

between the subsurface damaged produced is seen for adjacent impacts. The microscopic development of the damage enhancement effect is still unknown.

At high temperatures ($\gtrsim 2500\,°C$) the impact damage is again quite similar (Fig. 4), except that the impact is accompanied by permanent distortion of the fibers adjacent to the central zone (Fig. 4*a*) and by the creation of permanent interbundle separations (Fig. 4*b*). The crater mass loss for a 2-2-3 carbon-carbon steadily decreases from its maximum value at temperatures in excess of 2500 °C.

Damage Details

The detailed nature of the impact damage has been obtained from sectioned specimens. The principal modes of damage identified in this study are summarized in schematic overviews (Fig. 5*a,b,c*). Sections close to the center of impact obtained from low-temperature impacts ($<2500\,°C$) show that the longitudinal bundles directly beneath the central penetration zone (Fig. 5*a*) are extensively kinked (Fig. 6) and that the out-of-plane lateral bundles are vertically displaced. No clear relation between the kink mode (in-

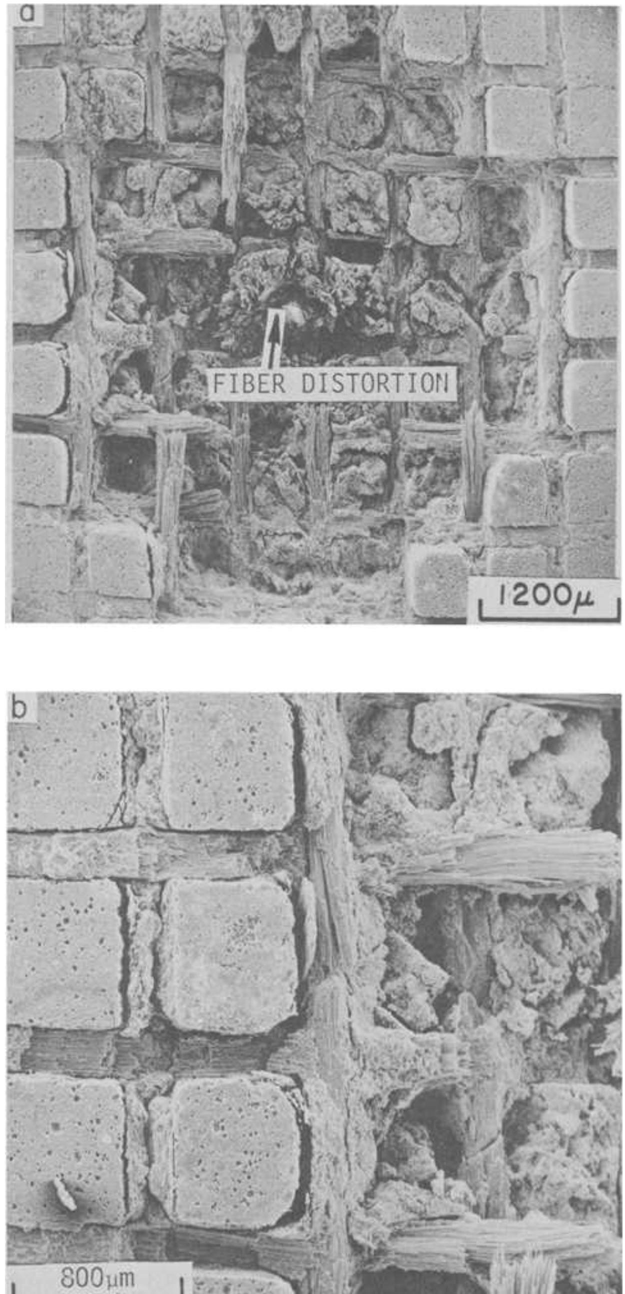

FIG. 4—*SEM's of high temperature (3500°C) impact damage in 1-1-5 material impacted by a 1-mm glass projectile at 6000 ms*$^{-1}$*, indicating* (a) *distortion of longitudinal fibers in central zone, and* (b) *separation between lateral bundles and matrix at outer edge.*

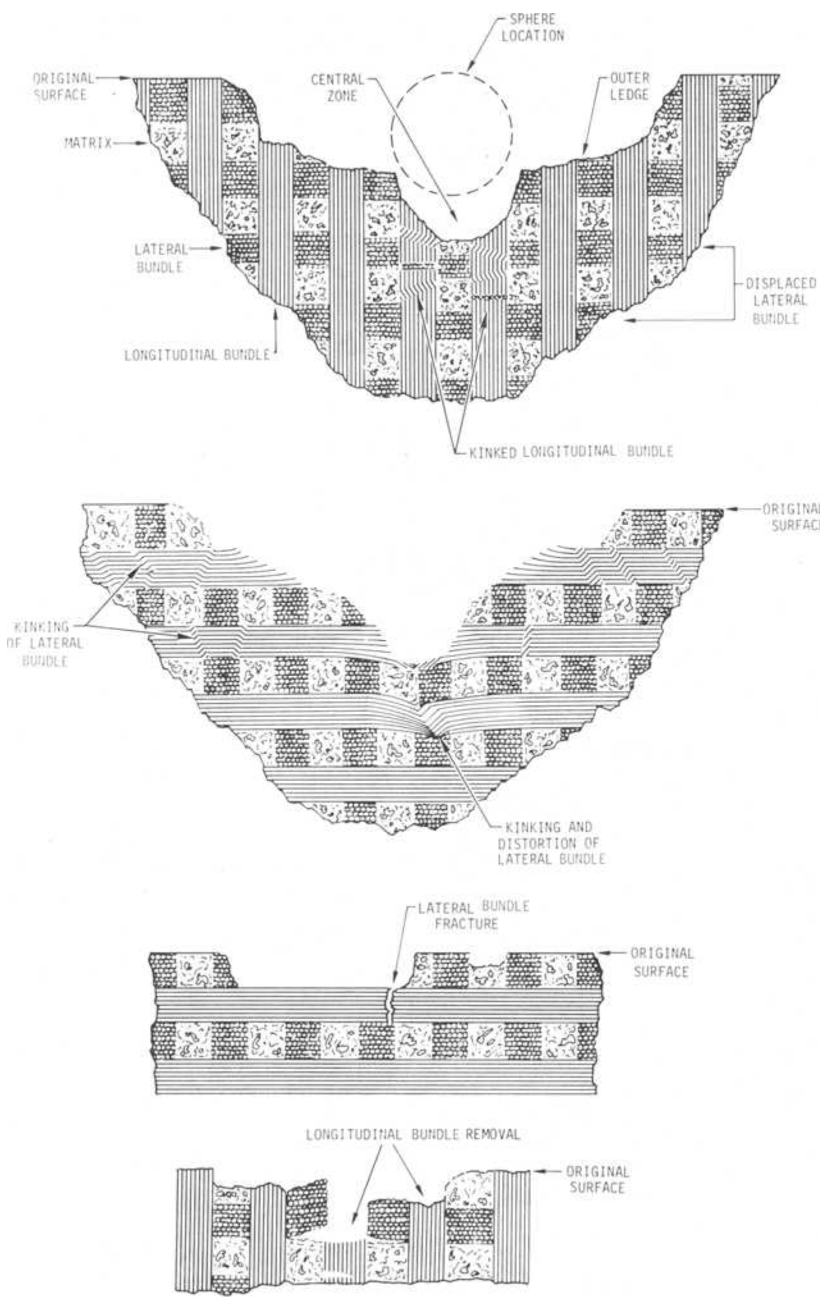

FIG. 5—*Schematics of damage created by projectile impact.* (top) *Section near the impact center revealing longitudinal bundles;* (middle) *section near impact center revealing lateral bundles;* (bottom) *section near crater periphery.*

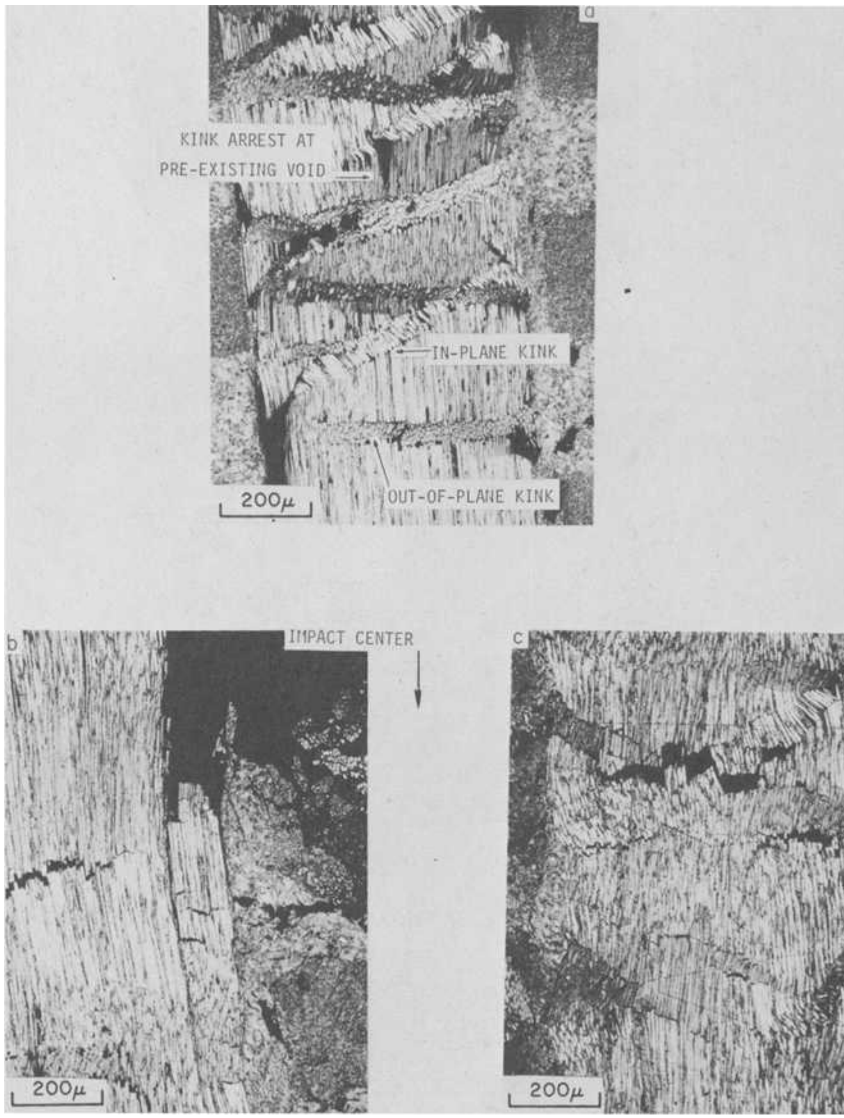

FIG. 6—*Optical micrographs of polished sections near impact center revealing longitudinal bundles.* (a) *Kinking damage beneath center of impact;* (b) *bundle fracture beside crater;* (c) *Partial separation of bundle at kink boundaries.*

plane or out-of-plane), the initiation site, or the location of the adjacent out-of-plane lateral bundles could be discerned (Fig. 6*a*). Microfracture is invariably observed at the kink boundaries (Fig. 6*a*), while independent macrofracture (Fig. 6*b*) and partial separation of the kink boundaries (Fig.

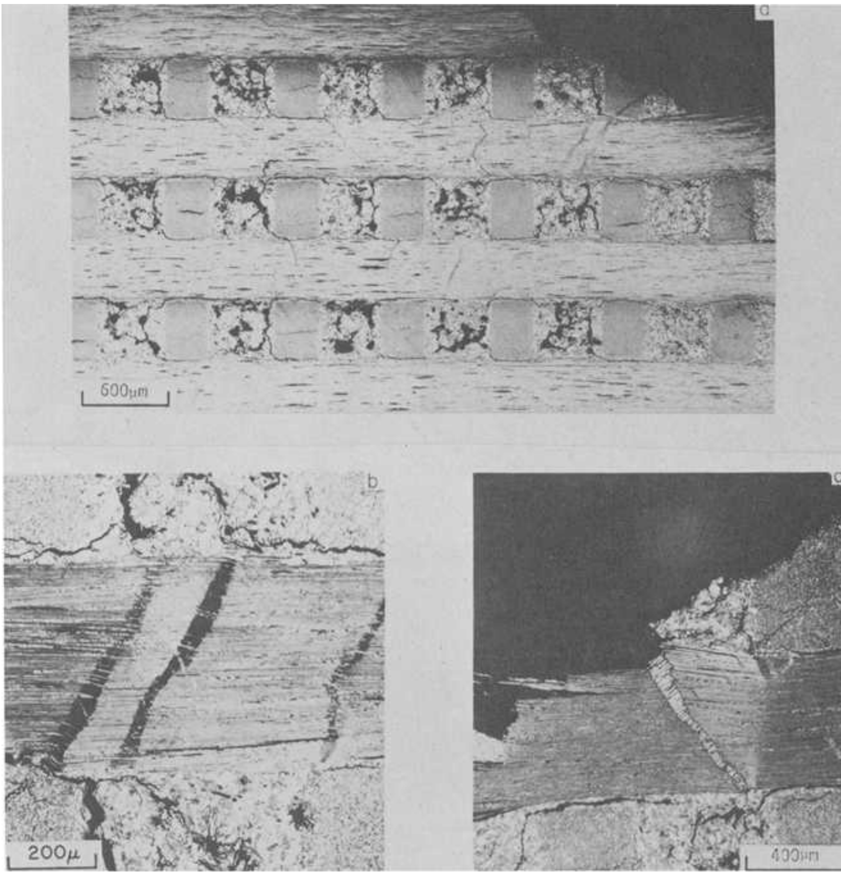

FIG. 7—*Optical micrographs of polished sections near impact center revealing lateral bundles.* (a) *Overview of kink locations;* (b) *detail showing local consistency of kink morphology;* (c) *detail showing kink beside crater wall.*

6*c*) are apparent in some longitudinal bundles near the crater boundary. Several layers of in-plane lateral bundles (Fig. 5*b*) also exhibit kinking that extends well beyond the periphery of the crater (Fig. 7*a*). These kinks are mostly in-plane (Fig. 7*b*,*c*) and generally narrower than the kinks in the longitudinal bundles. There is often a distinct fiber orientation relation (Fig. 7*a*): positive near the crater, mixed at a distance $\sim 7d_b$ from the center of impact (where d_b is the bundle thickness), and then predominately negative at larger distances. This kinking often initiates at sites close to the corner of out-of-plane lateral fiber bundles. A more complex mode of kinking is apparent in the lateral bundles directly beneath the impact center (Fig. 8). Inspection of these fiber failures indicates mixed-mode kinking, usually on a plane between the opposite corners of the adjacent out-of-plane lateral

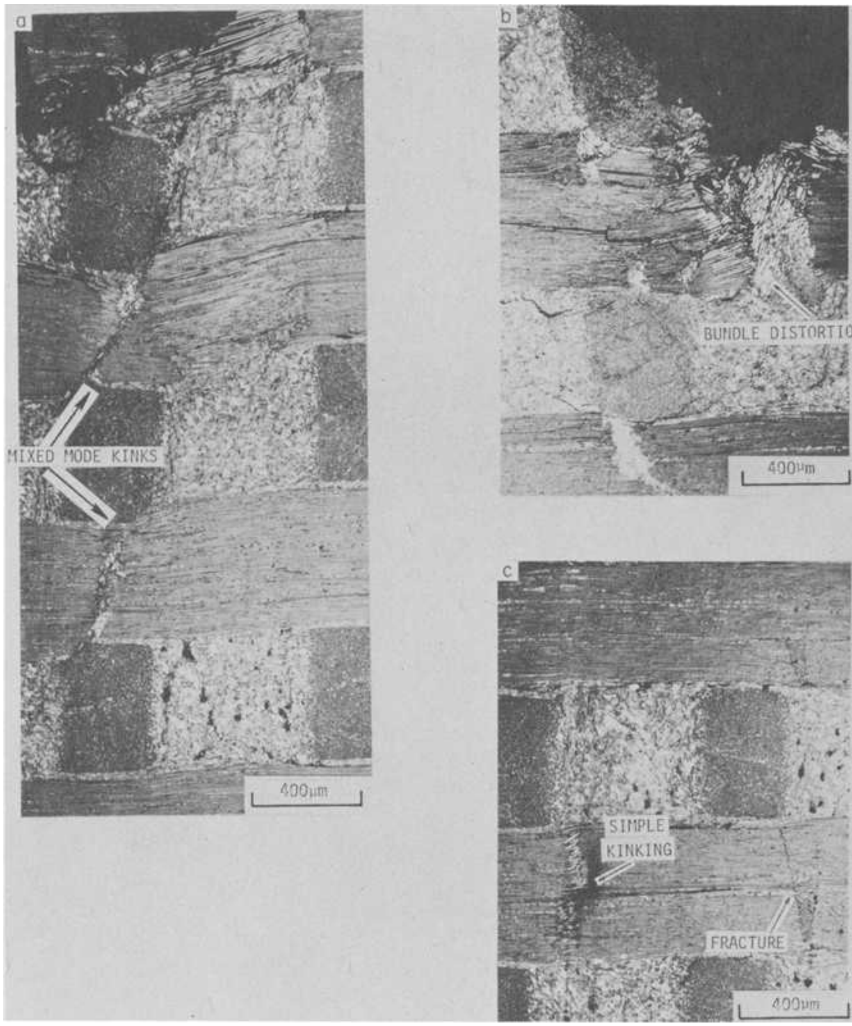

FIG. 8—*Optical micrographs of section near impact center showing compressional damage in lateral bundles beneath impact zone.* (a) *Mixed mode kinks adjacent to out-of-plane lateral bundles;* (b) *distortion at crater base;* (c) *simple kinking and fracture remote from crater.*

bundles (Fig. 8*a*). However, some tensile fractures (Fig. 8*b*) and simple kinking adjacent to the matrix (Fig. 8*c*) can also be detected.

The effects of varying the dimensions of the longitudinal bundles or the projectile velocity on the extent and morphology of the kinking are summarized in Figs. 9 and 10. Preliminary measurements of kinking in the longitudinal and lateral bundles show the general nature of the increase in the damage with the projectile velocity. A strong velocity dependence is seen

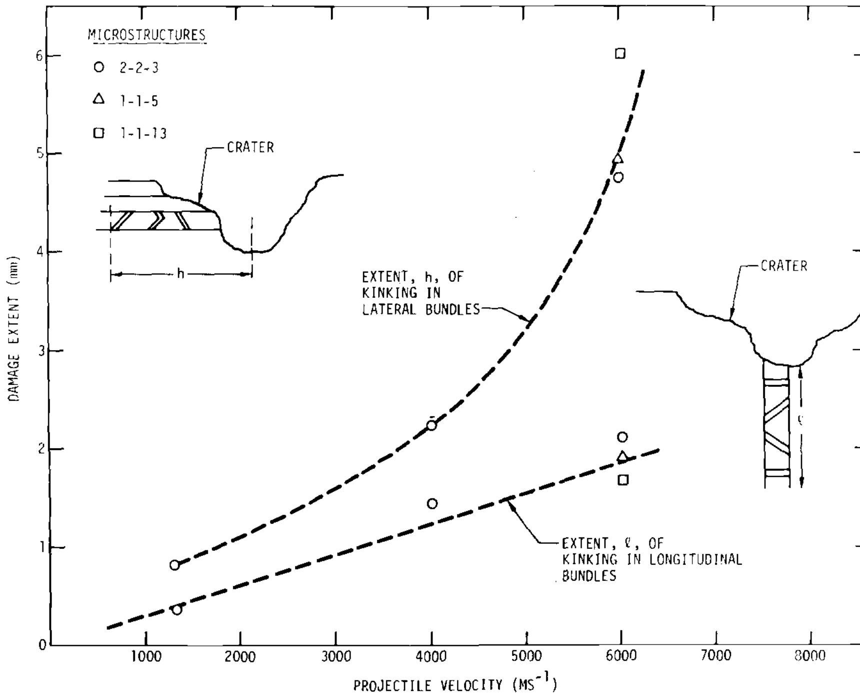

FIG. 9—*Maximum extent of kinking in longitudinal and lateral bundles as a function of projectile (1-mm glass sphere) velocity for three microstructures.*

for the kinking damage in the lateral fibers (Fig. 9). However, the density of the kinks formed on the lateral bundles is much less than the densities observed for the longitudinal bundles. The detailed morphology of the kinking in the longitudinal bundles does vary with bundle geometry (Fig. 10). For relatively large bundle diameters, the kinking is confined primarily to an intensely damaged single bundle, with some partial kinking of the adjacent bundles. For smaller bundles the kinking is usually less intense and distributed over two or more adjacent bundles.

Near the crater periphery (Fig. 5*c*) lateral bundle fracture is typical (Fig. 11*a,b*). Occasionally, subsurface kinks can be detected in longitudinal bundles (Fig. 11*c*) at the lateral bundle/matrix interface. It is also apparent from the fiber configuration at the crater surface (Fig. 11*d*) that the fractures in the longitudinal bundles that lead to material ejection are relatively planar in character and usually occur in the plane of the lateral bundle/matrix interface. Some isolated fractures in the longitudinal bundles are also evident.

The impact damage at elevated temperatures (>2500°C) exhibits some important differences from that discerned at low temperatures. Extensive permanent distortion of the bundles near the crater surface (Fig. 12) in-

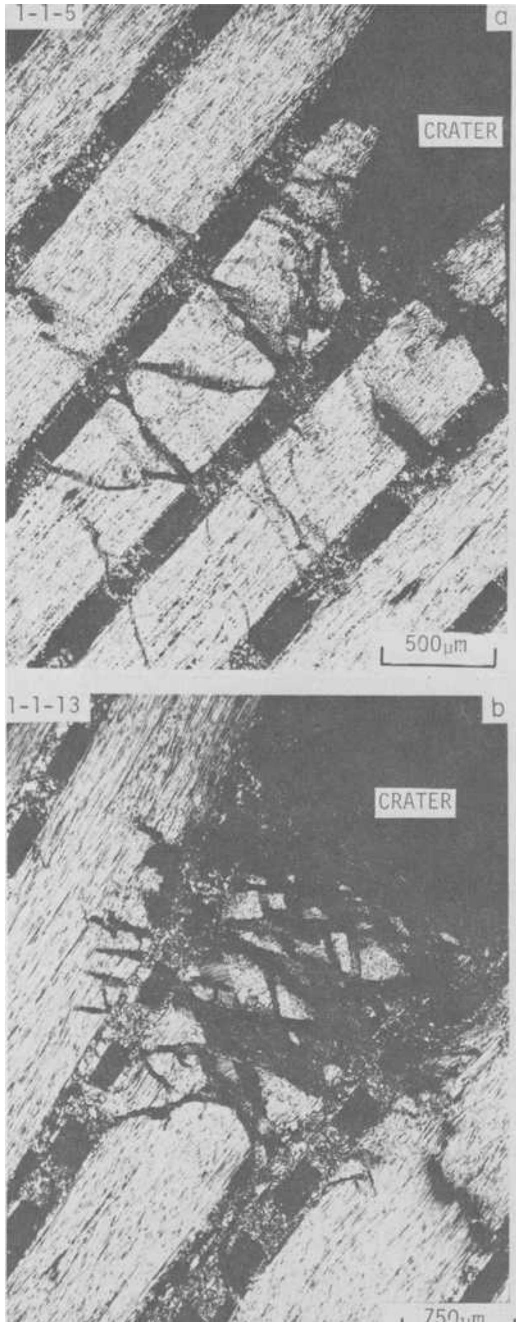

FIG. 10—*Optical micrographs of sections near impact center revealing longitudinal bundles, illustrating the effects of bundle dimensions on kink morphology: 1-mm glass sphere impacts at 6000 ms*$^{-1}$

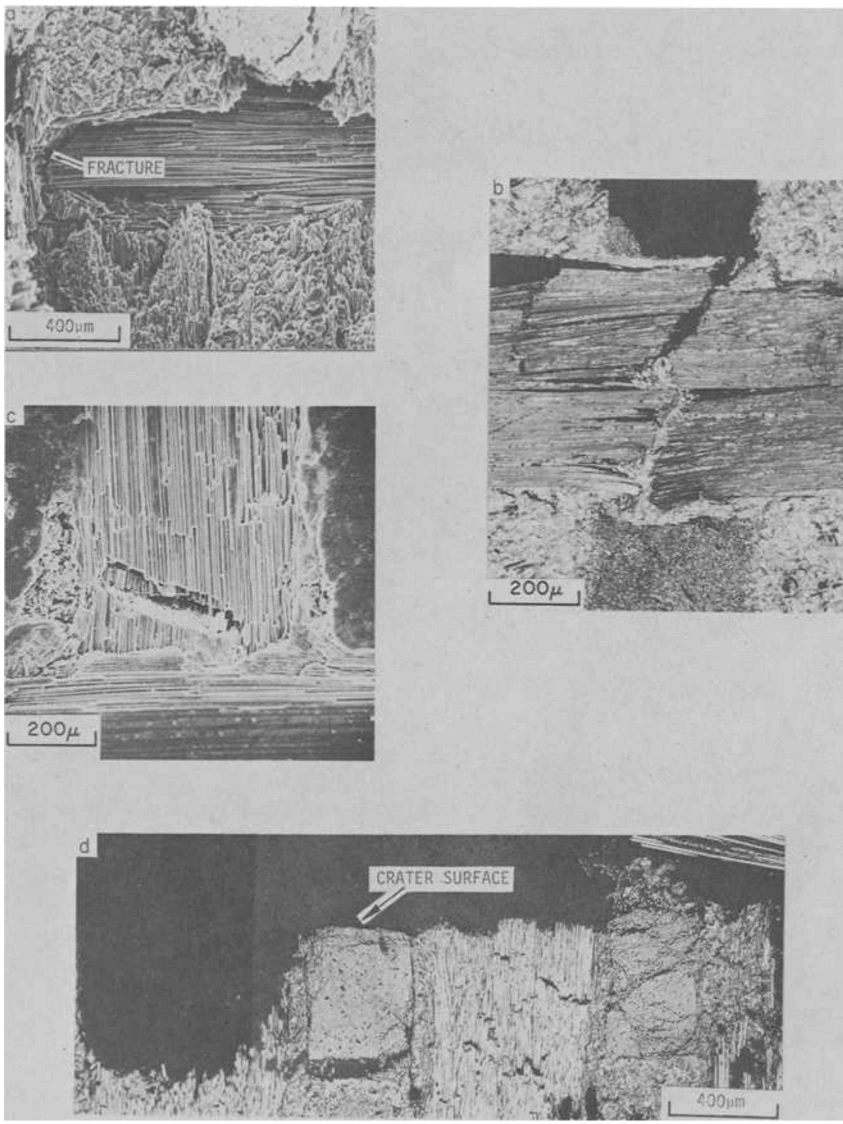

FIG. 11—*Micrographs of fractures near crater periphery.* (a) *SEM of a fractured lateral bundle;* (b) *optical micrograph of a polished section showing a lateral bundle fracture;* (c) *SEM of a polished section showing a subsurface kink in a longitudinal bundle;* (d) *optical micrograph of a polished section showing morphology of longitudinal bundle fractures.*

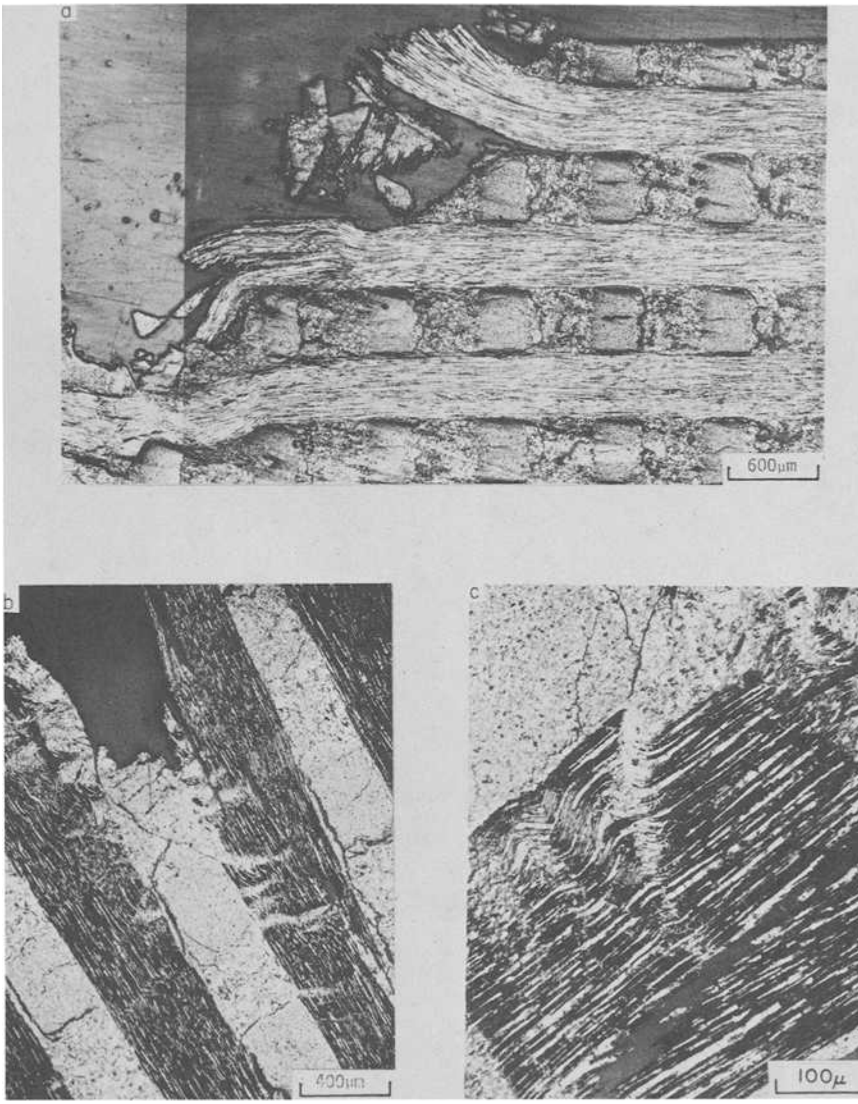

FIG. 12—*Optical micrographs of sections through a 2-2-3 material impacted at 3500°C by a glass projectile at 6000 ms*$^{-1}$. (a) *Overview showing lateral bundle distortion;* (b) *overview of longitudinal bundle kinking;* (c) *detail of a kink in a longitudinal bundle.*

dicates that the fibers are capable of limited plastic extension prior to fracture. The kinking is less extensive, especially along the lateral bundles, and the kinks usually arrest before they propagate through the fiber bundles (Fig. 12*b*). Fiber fracture does not invariably occur at the kink boundary (Fig.

12*b*); rather, the kink strain is accommodated in a significant proportion of fibers by a permanent distortion mechanism.

Material Ejection

High-speed photographic sequences have been taken of a limited number of impacts on the 2-2-3 material. A sequence obtained for a 1-mm glass projectile impacting at 2440 ms^{-1}, shown in Fig. 13, indicates the existence of an initial conical spray of material ejection, followed by the primary ejection phase, consisting of material ejected normal to the specimen surface as a central plume rising out of the crater. (Note that the diameter of the base of the plume is approximately equal to the particle diameter, 1 mm.) By tracing the temporal changes in the location of a distinctive feature in the plume, the approximate time at which it was freed from the crater can be reconstructed by plotting the location of identifiable elements in the ejecta as a function of the framing time increment. It is evident that although the penetration phase was completed within less than a few microseconds, the material ejection time exceeds 200 μs—over an order of magnitude longer. The primary material ejection thus occurs well after full penetration.

Crater Mechanics

The extent of the damage in carbon-carbon composites created by small-projectile impacts is dictated by the stresses that develop due to the impact event and the material's resistance to the important modes of damage. Since damage can derive from both the compressive and shear stresses (kinking) and tensile and shear stresses (fracture), some idea of the general nature of the stresses involved in the entire impact cycle is needed to interpret the damage sequence. Then, knowledge of the conditions for initiating the various modes of damage is required in order to correlate the dynamic stresses with both the incidence of damage and material removal. A precise and detailed analysis of this complex process can be performed only by numerical methods. However, a perspective of the process can be obtained from simplified analyses which allow elucidation of several important principles for material improvement with respect to erosive environments.

A possible failure sequence which reproduces the final crater morphology and subsurface damage as observed in the previous section is constructed in Fig. 14. The assumed conditions in the failure sequence are for a rigid particle with the density of glass impacting a target approximating the 2-2-3 fiber bundle construction at 3600 ms^{-1}. The details of the failure sequence depend on the impact site. The location of the impact is shown in Fig. 14*a*. The conditions which may prevail during the penetration phase along the cross sections denoted A-A and B-B are illustrated in Fig. 14*b* and *c*. The three-dimensional nature of the carbon-carbon composite was taken into account

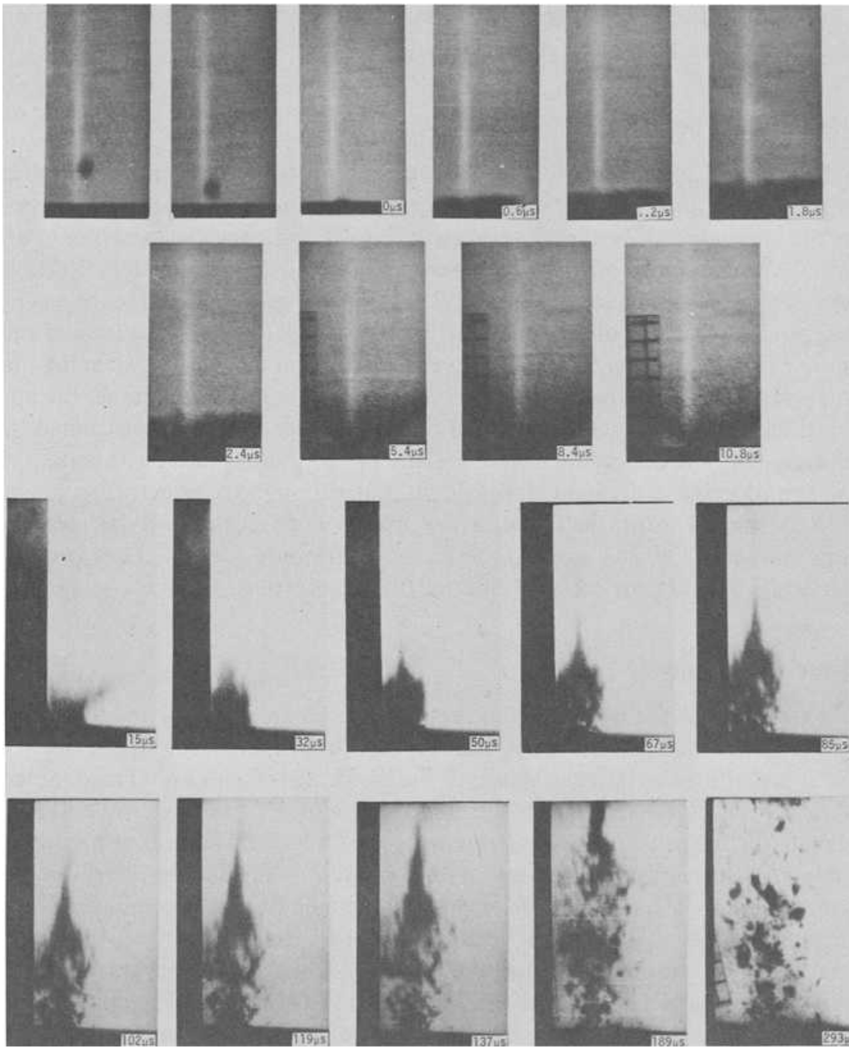

FIG. 13—*High-speed photographic sequence of a 1-mm glass sphere impact at 2400 ms^{-1}.*

in constructing these figures (although some modification in the artistic endeavor should be made to better reflect the material properties). The known data pertaining to the final crater cross sections, the subsurface damage, and the dynamics of the crater formation process (Fig. 13) are all correlated in this schematic construction of the failure sequence. This condensation of our investigative observations can now be used as a guide to focus on critical areas for micromechanical modeling which will be productive in establishing physically realistic correlations between the material removal process and the mechanical and microstructural properties of three-dimensional carbon-carbon materials.

Impact Stresses

Following the initial contact of the projectile with the target, stress waves initiate and propagate away from the contact zone in both the target and the projectile. The actual character of the propagating waves is quite complex due to the inhomogeneous nature of the carbon-carbon target material. For the three-dimensional weaves investigated here, preferred directions exist along the lateral and longitudinal fiber bundles, intersecting a region about the diameter of the impact particle centered at the initial impact site. The wave fronts actually become quite irregular as they propagate since every propagation direction radiating in a quadrant of a hemisphere centered at the point of contact in the three-dimensional carbon-carbon composite represents a different set of material properties and surfaces of discontinuity.

In the idealized case of normal impact by a rigid spherical particle on a homogeneous, isotropic material, an essentially spherical wave is initiated which degenerates with distance from the impact site, due in part to the geometric attenuation of the expanding area for the propagating spherical front and due in part to the inherent dispersion and attenuation of the material. The same effects prevail for the carbon-carbon materials except that the intensity and development of the dynamic stresses will be dependent on the abrupt changes in the material properties; on the reflection of waves from the discontinuous surfaces existing between fibers in the bundles, bundle/matrix interfaces, pores, and cracks in the composite; and on the penetration of the target by the projectile.

While knowledge of the general propagation characteristics of the wave fronts is important, this is only a part of the necessary information relevant to failure of the material. It is also necessary to evaluate the temporal evolution and magnitude of the transient stresses generated in the material. These stresses are related to the magnitude and direction of the forces applied to the material during projectile penetration.

Upon initial contact with the surface of the target, a spherical glass bead imparts an essentially normal pressure with relatively weak compressive waves propagating in the lateral directions. A one-dimensional analysis indicates that the magnitude of the instantaneous normal pressure is 9.7 GPa for a glass bead and 4.6 GPa for a spherical water drop impacting a carbon-carbon target at 2000 ms^{-1}. The normal pressures for a particle impact velocity of 6000 ms^{-1} are 44.2 GPa for glass and 26.6 GPa for water. The magnitudes of these instantaneous pressures are sufficient to produce shock fronts in both the target material and the impacting body. The relation between the pressures generated in these bodies and the associated material

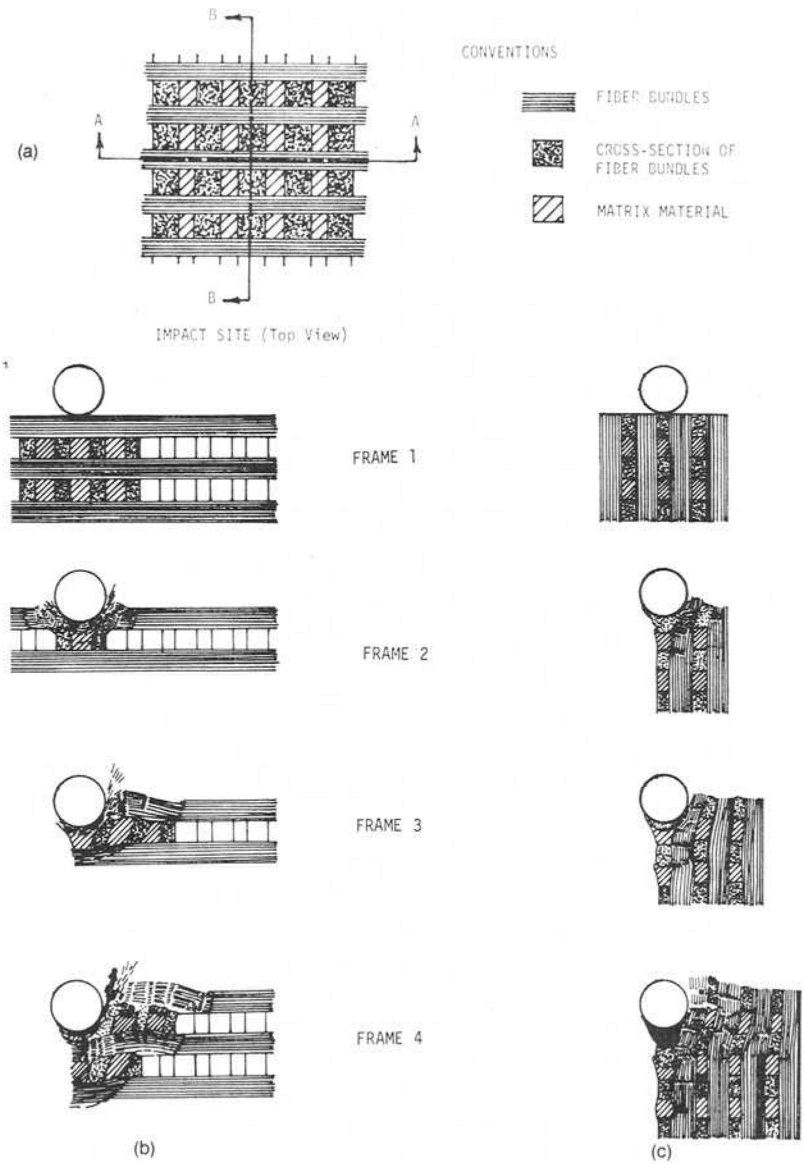

FIG. 14—*Schematic of cratering process in three-dimensional carbon-carbon composite with a 2-2-3 weave geometry.*

velocities is expressed in terms of their shock Hugoniot (hydrodynamic equations of state).

The mechanics of the particle penetration process describe the magnitude and the temporal variation of the forces loading the material which govern

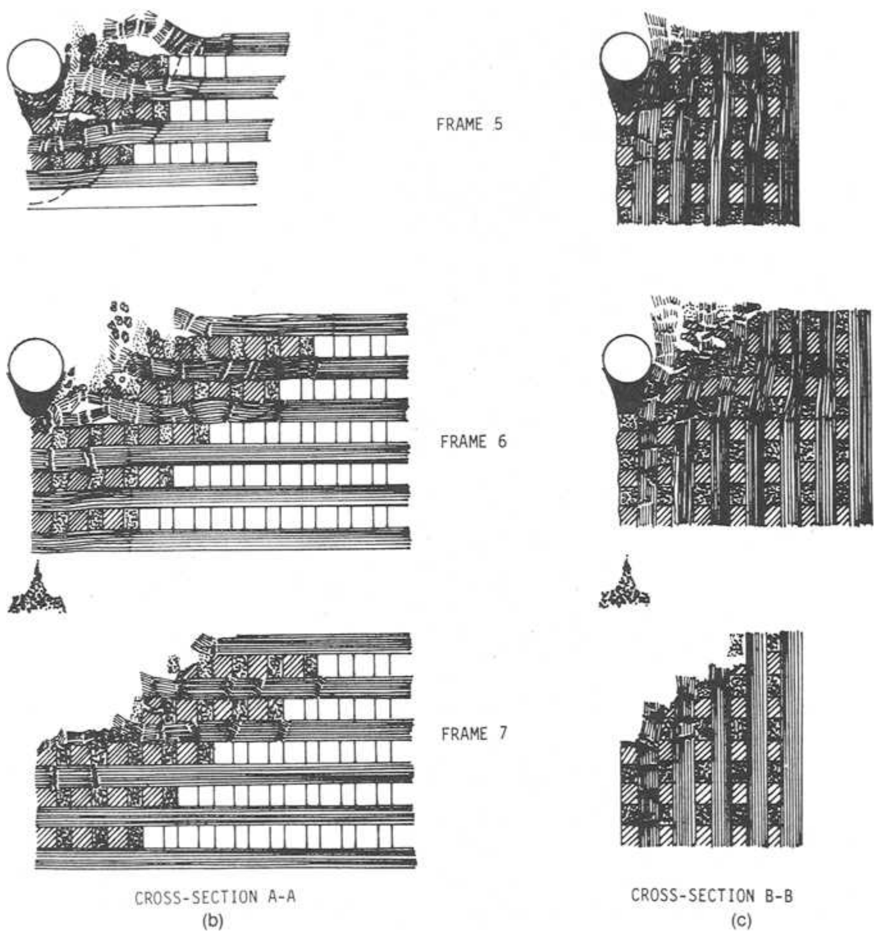

FIG. 14—*Continued.*

the character of the stress waves propagating away from the impact site. The general nature of these waves is represented by the Hugoniot relations. The analysis of the dynamic stresses is quite complex and it is conceptually very difficult to follow the course of the waves which develop behind the irregular wave forms as indicated in Fig. 14. It is important to note that these waves, in contrast to the usual one-dimensional case, involve all six components of the stress tensor. However, the fiber bundles serve as wave guides. The bundles along the preferred X, Y, and Z-directions are loading primarily along their longitudinal axes. These are the wave propagation conditions most amenable to analysis and are the major contributors to the observed failure modes.

Shock-related phenomena comprise only the very earliest stages of the penetration process. The expanding shock fronts quickly attenuate as they move out of the primary damage zone. As penetration continues, the shock wave is succeeded by elastic/plastic waves. (The term plastic wave is used here to denote the relatively slow-moving waves that encompass the nonlinear zone of material response. The nonlinearities are attributed to matrix densification, matrix and fiber plasticity, and viscoelastic effects.) Penetration proceeds as the projectile decelerates, even though it may be highly fractured or extensively deformed. This process, coupled with the inertia of the expanding boundary, continues to impose a direct pressure on the surrounding material; the particle velocity and pressure at the actual target/sphere interface are correspondingly complex functions of the depth of penetration. As the shock wave propagates, a rarefaction develops due to reflections from the target surface as well as due to deformation and fracture of the impacting particle. The dynamic stresses are complicated further by the presence of the penetration crater, which introduces a second free surface.

Damage Mechanisms

The character of the residual damage observed in impacted specimens, the observed material ejection sequence, and the likely states of stress developed during impact, combined with known wave propagation characteristics of three-dimensional carbon materials [*10*], suggest the following evolution of damage.

The fiber stripping of the lateral fiber bundles at the target surface extending well beyond the crater dimensions (Fig. 1) is conjectured to be due to low-pressure elastic precursor waves traveling down the surface fiber bundles. The preferential nature of the material removal is clearly seen. These weak compressive waves will propagate at the elastic wave velocity along the set of lateral bundles exposed at the surface. The evolution of the stresses associated with the stress waves in the vicinity of the target's free surface have been considered elsewhere [*11*]. This analysis shows that significant tensile normal stresses occur in a region behind the compressive wave front, and it appears that these stresses, which diminish rapidly with depth, are sufficient to remove a narrow band of fibers from the exposed lateral bundles.

As the projectile penetrates the target material, stress waves will propagate away from the damage zone; however, the loading cycles described previously will be modified by the compaction and crushing of material in the vicinity of the particle/target interface and precipitously terminated by removal (ejection) of a portion of the intervening material. This phase of the ejection process can be seen in the high-speed photographic sequences of the impact event (Fig. 13) as the expulsion of pulverized material first as a conical spray and then normal to surface of the target. The maximum velocity of the crushed material occurs at the periphery of the evolving crater; however, this cylinder of ejected material is overtaken by a central plume of finely pulverized material moving at a considerably higher velocity. The difference in the expulsion velocity associated with the observed ejection sequence is due to the nature of the driving force in each case. The conical spray is due to penetration of the particle, and the ejected cylinder of material is due to the crushed material which is forced around the penetrating particle. The central plume, with a maximum velocity along the normal to the surface passing through the initial contact point, occurs as a result of all the material along this axis being carried down to the full depth of particle penetration. The recovery forces for this material and the volume of material involved are considerably greater than those involved in material motion around the particle as it penetrates.

The initial contact pressures are quite high for particle impacts above 2000 ms^{-1} (6500 ft/s) and shock waves will be propagated along the *Z*-fiber bundles. The extent and sequencing of the shock wave generated are intimately associated with the constituent properties and the particle penetration mechanics. Large-amplitude wave fronts will precede the particle/target interface once the velocity of this interface falls below the shock velocity. The propagating wave will precondition the material ahead of the moving particle/target interface. The constituents engulfed by the wave front may be deformed in the manner shown in Figs. 14*b* and *c*. The actual deformations, the available dissipation mechanisms, and subsequent reflections from the internal surfaces of discontinuity are all related to the properties of the constituents. The penetration of the rigid bead will be affected to some extent by these characteristics of the composite.

The extent of the damage parallel to the surface of the target is dependent on the force that is transmitted across the crushed and ultimately removed interfacial layer between the particle and the target material. The changing magnitude and orientation of the pressures which develop at the moving particle/target interface control the general nature of the propagating stress waves, the initiation of rarefaction waves, and the near-field damage. Enlargement of the penetration crater occurs by the direct deformation of the matrix and fiber bundles. The free surface of the target presents an essentially unsupported face which permits large flexural deformations of the in-plane lateral fiber bundles, which are assumed to respond as simple beams. The flexural modes are illustrated in Fig. 14*b*.

Kinking in the lateral fiber bundles may result from the off-axis dynamic pressure components. Waves are then propagating in axial and near-axial directions along the fiber bundles to produce tension and compression zones as these waves are reflected off the fiber bundle boundaries. Only the second and third layers of lateral fiber bundles in Fig. 14*b* are situated such that the finite-amplitude waves are capable of producing damage in this manner before they are attenuated to insignificant levels. The dynamic stresses which can be transmitted at a near-axial direction in the fourth and subsequent lateral fiber bundles are fairly well attenuated with distance before they reach the critical orientation, so that only the kinking produced by transverse shearing in the vicinity of the impact site is found along these lateral bundles.

The propagation of waves ahead of the advancing particle/target interface produces extensive deformation of the constituents lying along the *Z*-axis. The longitudinal fiber bundles are pushed laterally to allow passage of the highly compacted zone of material as seen in Fig. 14*c*. Simultaneous with this action, the adjacent lateral fiber bundles are undergoing flexure and are being removed from the lattice. This constraint is therefore removed. Progressively fragmented sections will be removed from the exposed *Z*-bundles. Kinking in the longitudinal bundles will take place in a manner analogous to that described for the lateral bundles. It should be observed that finite deformations are generated in the material below the crater so that when the kinking process takes place the location of the adjacent composite elements will be different than what is observed in the relaxed state. This may provide an explanation for the lack of correspondence between the location of kinks and the relative stiffnesses of the adjacent elements observed in post-test microscopic examinations. However, kinking is probably related to both the adjacent constraints and the wave propagation modes which develop along the length of the fiber bundles.

Frame 6 in Fig. 14*b* and *c* is the point of maximum penetration. Rarefaction processes have already begun, but now the elastic energy in the deformed and compressed material will rapidly act to restore the material to its initial state. This dynamic relaxation process is responsible for ejection of the central plume of material rising from the crater as shown in Fig. 13 and depicted in Frame 7 in Fig. 14*b* and *c*. If a glass bead is used as the impacting particle, it will be highly fragmented during the penetration process and these small fragments will be ejected from the crater with the carbonaceous debris.

The final crater geometry and mass removal will be dependent on the properties of the impacting particle, whether it is water, ice, glass, or nylon. However, the general features of the material removal process and the form of the residual damage will be essentially identical to that described here, using the simplifying assumption of a rigid impacting particle—the difference being only a matter of degree. Idealized test conditions are quite useful and generally sufficient for suggesting ways in which the erosion resistance of the material can be improved; however, the details of the particle/target interactions and quantification of the critical failure conditions are necessary if mass loss predictions are desired.

The construction in Fig. 14 clearly defines the types of deformation modes and fractures to which a three-dimensional carbon-carbon composite may be subjected. In general the constituents in a three-dimensional carbon-carbon composite do not appear to respond to localized impacts in an integrated manner, but the individual constituents (primarily fiber bundles) are free to undergo predictable modes of deformation. This is an important observation in the development of analyses to be undertaken in conjunction with microscopic observations of the final crater morphologies and residual damage. This approach provides a physical basis for the development of failure models and identification of those properties of the elements in the composite which control the crater dimensions. The observations summarized in Fig. 14 indicate that failures occur by flexure and transverse shearing of the fiber bundles, transverse tensile failure of the lateral fiber bundles, and interfiber shearing. Other studies have indicated the influence of the porosity of the composite on the matrix shear strength and propagation of the stress waves generated during the particle penetration process.

Summary and General Implications

The considerable differences in the extent and character of the kinking damage beneath and beside the penetration zone have important implications for the interpretation of the damage process and for designing more damage-resistant materials.

Kinking of the longitudinal fiber bundles beneath the penetration zone is reproduced under dynamic and quasi-static conditions; its extent is probably dictated by the stress state near the final stages of penetration, when the projectile is moving relatively slowly and the applied pressure is comparable to the quasi-static penetration pressure. The effects of the bundle dimensions and the matrix and fiber properties on the resulting impact damage should thus be related to their separate effects on the critical stress for kinking and the penetration pressure—the latter through its influence on both the penetration distance and the dynamic stresses. It is already apparent that kinking is suppressed by increasing the matrix yield strength and elastic modulus [12] (an immediate implication for materials development), whereas the observed lack of correlation of kinks in adjacent bundles suggests that the influence of the bundle dimensions on the kink formation condition is small. Similarly, the penetration pressure should be enhanced by increasing the matrix flow strength, while the effect of the bundle dimensions, although uncertain, is probably quite small. However, it is not immediately obvious that the extent of the kinked zone is decreased by increasing the penetration pressure. This ambiguity arises because the diminution in penetration distance is counteracted by an increase in the amplitude of the dynamic stresses. Further work is clearly needed to develop a detailed picture of the role of the penetration pressure on the extent of longitudinal fiber bundle kinking and its dependence on microstructure.

The kinking of the lateral fiber bundles beside the penetration zone is detected only under fully dynamic conditions, and its extent is strongly dependent on the impact velocity. Presumably, therefore, the conditions that encourage this kinking develop earlier in the penetration process, perhaps because the pressure applied to the bundles declines before penetration is complete. The morphology of the kinks also suggests that the free surface has an important influence on the kinking process.

The longitudinal fiber bundles beside the penetration zone must also be damaged during the impact cycle, to account for the observed occurrence of the outer ledge (Fig. 1*b*). Since there is no systematic evidence of residual damage in these bundles, suggestions concerning the nature of this damage can only be speculative. There is much supportive evidence for the speculation that these bundles are damaged by kinking during the penetration phase and that the severity of kinking leads to the subsequent full ejection of the damaged zone. The regularly spaced kinks (that initiate at the matrix/bundle interface) observed adjacent to the impact center in the penetration tests indicate that the relative displacements that accompany penetration can generate in-plane shear stresses, as indicated schematically in Fig. 15. Then, the sequence of kinks required to accommodate an applied in-plane shear stress, when the restraint provided by the orthogonal bundles has been removed by prior kinking, suggests that a series of shear kinks could develop beside the penetration zone.

In support of the foregoing hypothesis we note that the relatively planar character of the fractured longitudinal bundles at the base of the outer ledge is typical of kink boundary fracture, while the common occurrence of these bundle fractures at a lateral bundle/matrix interface is typical of shear induced kinks. Also, the short fiber segments sometimes observed on the longitudinal bundles, Fig. 2*c*, could be the remnants of the kinked zone. Should this damage process pertain, the extent of the damage normal to the impact direction would exhibit (in addition to the prevading influence of the matrix flow stress and modulus) a significant dependence on the proportion of longitudinal fibers in the sense that the damage zone will decrease as the content of longitudinal fibers increases [*12*]. This effect is consistent with the observations of the effect of the longitudinal fiber content on the extent of the outer ledge. It is also noted, however, that kinking of the restraining lateral bundles is a necessary precursor to the damage process; this requirement implies an upper limit on the zone size that might be encountered for relatively small longitudinal fiber contents.

Acknowledgments

The authors appreciate the financial support provided by the Office of Naval Research under Contract N00014-76-C-0854 and the funding allocated for W. F. Adler during the initial phases of this work from the Space and Missile Systems Organization Contract F04701-76-C-0069 with Effects Technology, Inc. The specimens for investigation within this program were obtained from the SAMSO program and an Air Force Materials Laboratory program, Contract F33615-75-C-5214, with Effects Technology, Inc. The authors also acknowledge helpful discussions pertaining to stress wave propagation in carbon-carbon composites with W. M. Isbell and M. E. Graham.

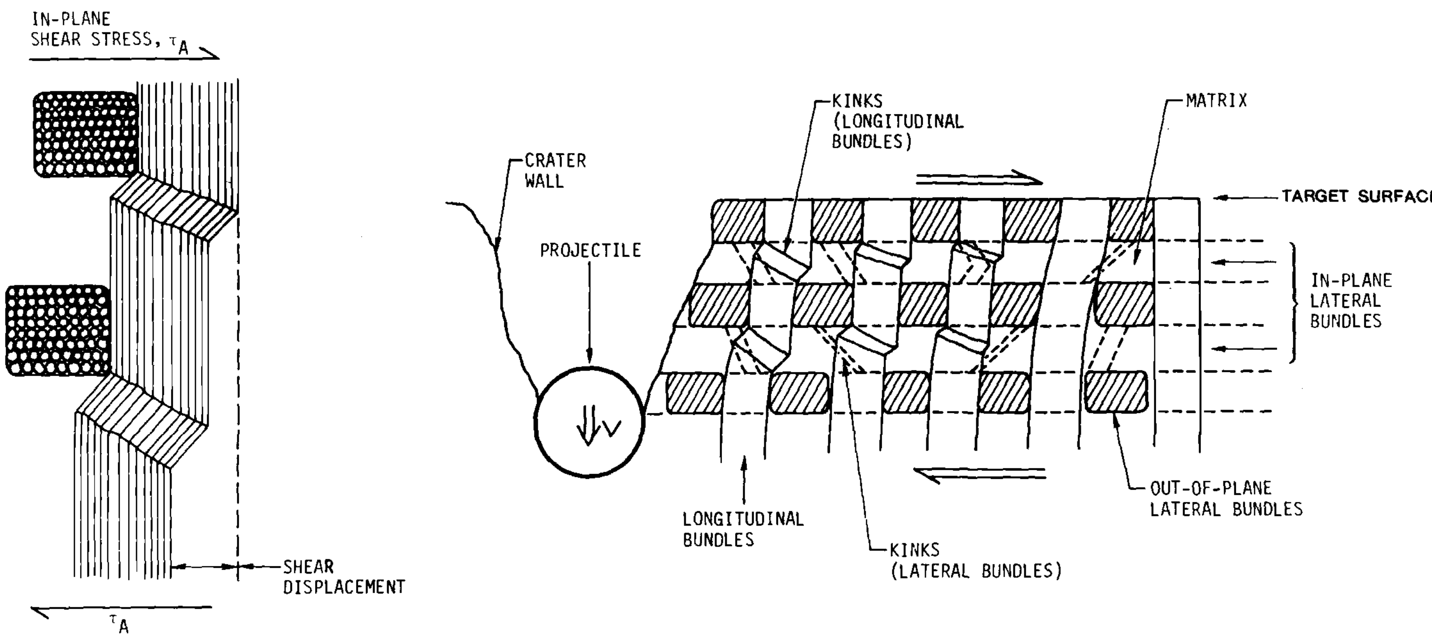

FIG. 15—*Schematic indicating possible development of kinks in longitudinal bundles at outer ledge.*

References

[1] Sullivan, R. J. and Hockridge, R. R., "Simulation Techniques for Hypersonic Erosion Phenomena," *Proceedings*, Fourth International Conference on Rain Erosion and Associated Phenomena, A. A. Fyall and R. B. King, Eds., published by the Royal Aircraft Establishment, England, 1974.

[2] Mortensen, R. B., "Advanced Erosion Test Facilities," *Proceedings*, Fourth International Conference on Rain Erosion and Associated Phenomena, A. A. Fyall and R. B. King, Eds., published by the Royal Aircraft Establishment, England, 1974.

[3] Reinecke, W. G., "Rain Erosion at High Speeds," *Proceedings*, Fourth International Conference on Rain Erosion and Associated Phenomena, A. A. Fyall and R. B. King, Eds., published by the Royal Aircraft Establishment, England, 1974.

[4] Carlyle, J. D., Graham, M. E., and Menna, T. L., "Development of the Particle Impact Test Facility," Effects Technology, Inc., Presented at the 25th Meeting of the Aeroballistic Range Association, Naval Ordnance Laboratory, Oct. 1974.

[5] Carlyle, J. D., Graham, M. E., and Menna, T. L., "Particle Impact Calibration Test Results," Effects Technology, Inc., Presented at the 25th Meeting of the Aeroballistic Range Association, Naval Ordnance Laboratory, October 1974.

[6] Carlyle, J. D., Graham, M. E., and Menna, T. L., "Facility for High Speed Particle Impact Testing," *Review of Scientific Instruments*, Vol. 46, 1975, pp. 1221-1225.

[7] Effects Technology, Inc., "Erosion Modeling Program," Space and Missile Systems Organization Contract F04701-76-C-0069, 1976.

[8] Kratsch, K. et al, "Exploratory Development and Investigation of Carbon-Carbon Composite Materials Having Improved Hypersonic Particle Erosion Resistance—CHIP (Carbon Hypersonic Impact Program)," AFML-TR-75-157, Air Force Materials Laboratory, Sept. 1975.

[9] Rubin, L., "Impact Damage Mechanisms of 3-D Carbon-Carbon Material," Space and Missile Systems Organization TR-76-142, July 1976.

[10] Tuler, F. R., Graham, M. E., and Ferdman, M. A., "Stress Wave Response of Carbon Composite Materials," Army Materials and Mechanics Research Center Report CTR74-2, Jan. 1974.

[11] Adler, W. F., "Liquid Drop Collisions on Deformable Media," *Journal of Materials Science*, Vol. 12, 1977, pp. 1253-1271.

[12] Evans, A. G. and Adler, W. F., "Kinking as a Mode of Structural Degradation in Carbon Fiber Composites," *Acta Metallurgica*, Vol. 26, 1978, pp. 725-738.

DISCUSSION

L. Rubin[1] *(written discussion)*—Would you please explain the criteria by which you distinguish "kinking" from "column buckling"? Horizontal shear dislocations have been observed and documented in both axial and transverse fiber bundles of 3-D carbon-carbon composites as well as in unidirectional composites. It appears that column instability as a result of transverse shear dislocations, in any plane, might qualify as column buckling and not require the introduction of a new term.

It might also be of interest to note that a hypervelocity impact end-on to a unidirectional fiber bundle carbon-carbon composite produced subsurface shear dislocations in planes radiating approximately 45 deg from the base of

[1]The Aerospace Corp., P.O. Box 92957, Los Angeles, Calif. 90009.

the impact crater, somewhat analogous to Hertzian cracks in brittle materials.

W. F. Adler and A. G. Evans (*authors' closure*)—Dr. Rubin's comment is a very interesting one. There is little doubt that the bundle damage, which we have referred to as "kinking," is usually a consequence of a buckling instability (except under conditions of applied shear), be it elastic or elastic/plastic in character. However, it is important to recognize that buckling refers to a mode of material response which does not invariably lead to damage or local failure of the type we have described. Thus, we have introduced the term kinking to describe the specific damage mode that is the consequence of the buckling instability, in the situation of present interest. To further illustrate the need for a term other than buckling, we shall briefly describe two examples of buckling instabilities that lead to very different types of damage: (1) Buckling of an elastic beam on an elastic foundation leads to a series of uncorrelated fractures in the beam, the spatial relation between these fractures being determined by the character of post-buckling elastic deformation and the statistical distribution of fracture initiating flaws; in this instance the *damage* is simple *fracture*. (2) Plastic buckling of a beam leads to the formation of intense slip bands in the zone of initial instability; in this instance the *damage* consists of small cracks, etc. in the bands of *intense* (adiabatic) *shear*.

Finally, we point out that the 45-deg trajectories of the shear failures found by Dr. Rubin exhibit a different orientation than Hertzian cracks (22-deg to the surface). The Hertzian cracks follow the quasi-static principal tensile stress trajectory and commence outside the contact area. The planes at 45-deg probably coincide with maximum shear stress trajectories, which exhibit a 45-deg symmetry in the immediate vicinity of the penetration axis for the Hertzian theory of impact.

L. K. Ives[2] (*written discussion*)—Could you comment on the nature and differences in the damage associated with elastic-plastic and shock waves?

W. F. Adler and A. G. Evans (*authors' closure*)—Dr. Ives's question addresses a central issue in hypervelocity impact damage analyses, especially in brittle materials. Some physical understanding of the formation of spherical shock waves, their propagation, and degeneration into elastic-plastic waves has been evolving for isotropic elastic, perfectly plastic materials.[3] Although the details will be different for anisotropic materials, or for materials which undergo more complex forms of inelastic deformation, similar trends are to be anticipated. However, the stresses that accompany these waves and cause the observed damage are not well characterized. Numerical solutions are usually resorted to, in order to obtain stress information, but these are only

[2]National Bureau of Standards, Materials, B118, Washington, D.C. 20234.

[3]A reasonably coherent review is given by P. Chadwick, "Spherical Waves in Elastic-Plastic Materials," *Inelastic Behavior of Solids*, M. F. Kanninen, W. F. Adler, A. R. Rosenfield, and R. I. Jaffee, Eds., McGraw-Hill, New York, 1970.

meaningful if they contain the correct physics. Problems of interpretation thus invariably arise and these have to be worked out through iterations between numerical computation and damage observations. This stage is just beginning to be attained for the carbon-carbon composites, but at the present time one can only speculate on the respective damage modes associated with the shock and elastic/plastic waves.

We note the possibility that the deviatoric components of stress associated with the shock wave may not exceed the critical shear stress for kinking. If this is indeed correct, kinking will be associated with the succeeding elastic/plastic wave rather than with the shock wave. The other mode of compressional damage seems to depend primarily on the principal normal stress, and there is no reason to believe that this damage could not be associated with the shock wave, the elastic-plastic wave, or even the elastic precursor, which would have an amplitude sufficient to initiate kink formation. In any event, the passage of the shock wave will tend to precondition the material, by producing essentially nondestructive finite deformations, which is then acted upon by possibly more damaging transient stress states. Some of these effects are described in the "Crater Mechanics" section of the paper.

A. F. Conn[4] *(written discussion)*—You are using glass and nylon beads to simulate the damage caused by water droplets at hypersonic velocities. Will you please comment on what you feel are the strengths and weaknesses of this usage of solid spheres for your experiments?

W. F. Adler and A. G. Evans (authors' closure)—It is very difficult to impact water drops at hypervelocities in a laboratory facility, so alternative test procedures are resorted to in order to achieve a comparable effect. The amount of material removed by a single particle is normally used for comparing one test condition with another. The argument usually introduced to justify the mass loss as a meaningful parameter for comparison is that the target material is in the hydrodynamic state and therefore no differentiation will be made in the effect of the impact conditions as long as the applied pressures, computed on the basis of the Hugoniot relations, are equal in magnitude. Using this approach, the mass removal will be comparable for nylon, glass, and water particles as long as the impact velocity is adjusted so that the same impact pressure is imparted to the target for each particle type. This approach is based on a one-dimensional approximation of the impact conditions and does not account for the deformability of the impacting particle and penetration of the target material.

The descriptions of the damage modes associated with cratering in carbon-carbon composites presented in the paper suggest that differences in the subsurface damage around a crater will definitely depend on the particle characteristics. It was noted in the text that the shock-wave effects are rapidly attenuated and that the strength of the target material becomes impor-

[4]Hydronautics, Inc., Pindell School Road, Laurel, Md. 20810.

tant before completion of the loading cycle. We therefore cannot support the popular hydrodynamic analogy for the hypervelocity impact conditions investigated here. It is our view that any alternative to water drop impacts has to be viewed with considerable caution and understanding, and in no way do we mean to imply that glass beads or even nylon beads (whose Hugoniot approximates that for water) at impact velocities in the range of from 2000 to 6000 ms^{-1} will reproduce the details of a water drop collision. It is our contention, as stated in the paper, that the damage modes produced by water drops, nylon and glass beads, and the material removal sequence are similar. The differences in the qualitative aspects of the particle impact are only a matter of degree; that is, the quantity of the damaged material removed and the extent of the subsurface damage produced will depend on the particle/target interactions. The failure modes can therefore be adequately identified and modeled using glass beads to represent the impact conditions for rounded particles in general, whether they are rigid or deformable. An independent modeling effort is required to quantitatively evaluate particle-type effects; however, general material failure models will be available from the approach used here.

We trust that this answer to Dr. Conn's question provides adequate perspective on our erosion studies.

G. F. Schmitt, Jr.[1]

Influence of Materials Construction Variables on the Rain Erosion Performance of Carbon-Carbon Composites

REFERENCE: Schmitt, G. F., Jr., "**Influence of Materials Construction Variables on the Rain Erosion Performance of Carbon-Carbon Composites,**" *Erosion: Prevention and Useful Applications, ASTM STP 664,* W. F. Adler, Ed., American Society for Testing and Materials, 1979, pp. 376–405.

ABSTRACT: The influence of materials construction variables and environmental parameter effects on the rain erosion behavior of carbon-carbon reentry vehicle nosetip thermal protection materials has been investigated at velocities of 1220 to 1675 m/s by firing rocket sleds equipped with special specimen holders through the artificial rainfield at Holloman Air Force Base.

A high percentage of axial reinforcement (fibers end-on to the surface) is desirable in carbon-carbon composites for improved erosion resistance. One-dimensional reinforcement of this type would provide maximum erosion resistance, but the need for structural properties in reentry vehicle applications requires a combination of this high axial loading with fine-weave orthogonal 3-dimensionally reinforced construction for enhanced erosion-resistance and balanced performance. The small unit cell size is essential for good resistance. Increased in-plane isotropy in these composites by rotating the *X-Y* plies reduced the macroroughness development which is typical of the carbon-carbon composites in the multiple rain environment.

Improvements in weaving, impregnation, pyrolysis, and graphitization are reflected in a reduction in the mass loss ratio of composites which have similar *Z* bundle area fractions, but were made at different chronological times.

It was determined that Thornel 50 fiber composites gave better performance than Thornel 75, C-1000, C-3000, and other fibers. The introduction of intermediate chemical vapor deposition (CVD) of carbon coupled with low- or high-pressure pitch processing provided matrices for composites with improved erosion resistance compared with pyrolyzed resin or pitch-only processes.

Empirical relationships were determined to govern the erosion rate as a function of velocity and impingement angle.

KEY WORDS: rain erosion, carbon-carbon composites, rocket sled testing, multiple impact, materials construction variables, supersonic velocity, erosion

[1]Materials research engineer, Air Force Materials Laboratory, Wright-Patterson Air Force Base, Ohio.

The rain erosion fixtures which have been previously used for assessing the erosion behavior of materials were utilized for these investigations. They are described in detail in an earlier paper [*1*].[2]

The three particular fixtures are shown in Figs. 1–3. The small rain erosion wedge holds 48 specimens of dimension 3.175 by 3.175 by 1.27 cm thick (16 each at angles of 13.5, 30, 45, and 60 deg). In this wedge the specimens are covered by stainless steel face plates so that a 2.54- by 2.54-cm surface is exposed through the face plate window. The four-angle stepped wedge is utilized at speeds of 1375 m/s and below. The 13.5-deg

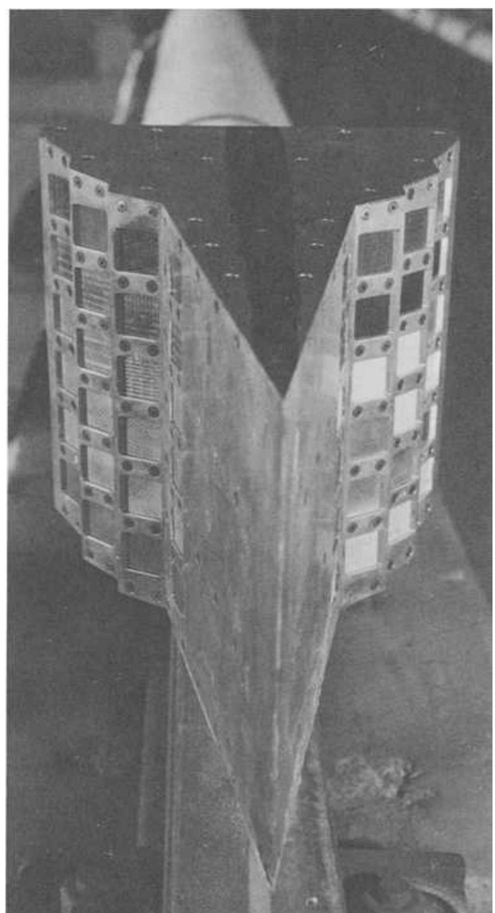

FIG. 1—*AFML rain erosion wedge for Mach 4.0 tests.*

[2]The italic numbers in brackets refer to the list of references appended to this paper.

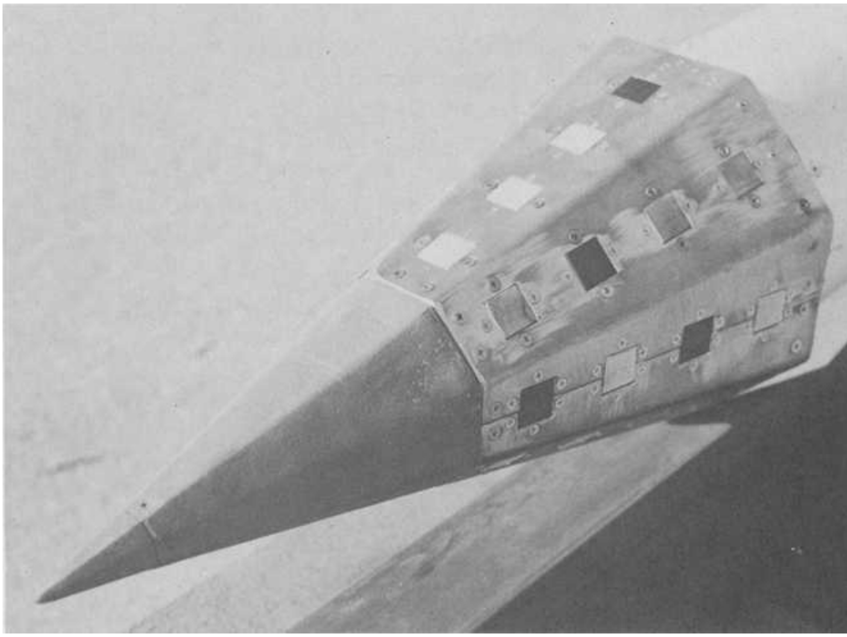

FIG. 2—*13.5-deg cone for Mach 5 rain erosion tests.*

cone (Fig. 2) holds 32 specimens of similar dimensions except for a 0.229-cm shoulder, 0.3175 cm wide around the edges, giving it a 2.54- by 2.54-cm raised face which flush mounts into the cone. The 30-deg cone holds 16 identical specimens (Fig. 3).

The Holloman Track Facility

Track Description

The Holloman rocket sled track used for these tests has been described in detail in Ref *2*. The track has been extended to 15240 m in length but all other details are the same as previously reported. Currently, 5486 m of the track are equipped with nozzles for rain simulation. However, only 610 m of rainfield were used in these tests because of the degree of damage experienced by the specimens. Monorail sleds are used for rain erosion tests with braking accomplished by water-filled polyethylene bags or frangible plastic water trays laid directly on the track.

Most firings are made during the night to take advantage of calm night air on the desert. Wind conditions for rain runs are restricted to three knots or less crosswind to prevent distortion of the rain pattern.

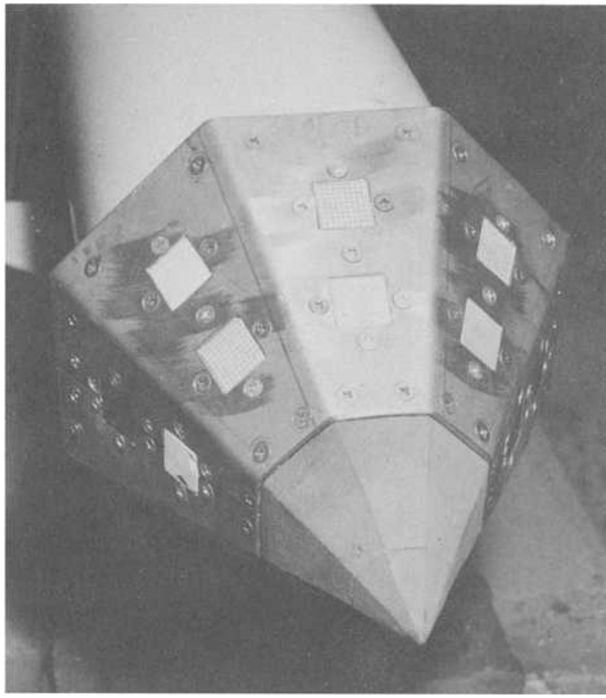

FIG. 3—*30-deg cone for Mach 5 rain erosion tests.*

Rocket Sleds

All rocket sled hardware and motors were provided by the Holloman Test Track Directorate. To accelerate to peak velocity and to sustain the desired Mach numbers in the 610 m of rain, staging with several combinations of rocket motors was used to achieve the required velocity profile, which peaked out as the sled entered the rainfield and decreased from there, providing a flat enough profile for valid analysis.

A sled was used in which the wedge or 13.5- or 30-deg cones were mounted directly on the front of the last-stage Gila IV booster motor. Satisfactory velocity profiles were achieved at all velocities through proper selection of firing points, stages, and combinations of booster and sustainer motors. A complete history of the four sled firings with dates, firing times, wind conditions, average velocities in the rain, and specimen designations is given in Table 1.

The Holloman Rainfield

These tests utilized 610 m of the new rainfield installation, described in Ref *3*, and resulted in rainfall rates of 60.2 to 69.6 mm/h or approximately

TABLE 1—*Run record—for high-velocity series.*

Nominal Velocity	Test Fixture	Holloman Run No.	Date	Time of Day	V_{avg}, m/s	Exposure Time, s	Length of Rainfield, m	Average Rainfall Rate, mm/h	Wind	Specimens
Mach 4.0	small wedge	30R-M5	10 June 1975	0420	1274.60	0.4809	610	69.59 σ = 22.38	1.5 mph-W (1.3 knots)	T-15, T-16, T-17, T-18, T-19 T-20, T-21, T-22, T-23, T-24 H-10, H-11, H-12, H-13 H-14, H-15, H-16, H-17 H-18, A-45, A-46, A-47 A-48
Mach 5.0	13.5-deg cone	30R-N5A	18 Dec. 1975	1730	1619.35	0.3345	610	60.19[a] σ = 28.52	calm	T-7, T-13, T-14, T-15, T-16 T-17, T-18, T-19, T-20, T-24 H-10, H-11, H-13, H-14, H-15, H-16, H-17, H-18, H-22, H-23, A-45, A-46, A-47
Mach 5.0	30-deg cone	30R-04	15 June 1976	0403	1617.14	0.3935	610	67.56 σ = 16.46	1.3 knots-W 4.3 knots-N	T-7, T-13, T-14, T-15, T-16 T-17, T-18, T-19, T-20 T-24, T-25, T-27, T-28 H-13, H-18, A-52
Mach 4.0	small wedge	30R-MGA	16 June 1976	0400	1264.72	0.4780	610	67.06 σ = 21.41	1.6 knots-E 1.7 knots-N	T-25, T-26, T-27, T-28, H-25 H-26, H-27, H-28, H-29 H-30, A-49, A-50, A-51 A-52

[a]Due to cold conditions, rainfield rain calibration may be slightly low compared with actual intensities (by as much as 20 percent).

3 g/m^3 of rain concentration. The mean drop size is 1.37 mm diameter. See Fig. 4 for the drop size distribution with the new rainfield.

The influence of debris shielding has been investigated in comparing this new reduced-concentration rainfield with the old installation and found to not be a factor for the range of concentrations and velocity in these tests [*4*].

Analysis Method

Mean Depth of Penetration Rate/Velocity/Impingement Angle Equation

The determination of erosion rate-velocity dependence has received considerable emphasis by numerous investigators because velocity is the most significant environmental parameter associated with rain erosion.

In the Air Force Materials Laboratory (AFML) analysis, a mean depth of penetration rate, *MDPR*, has been defined in which erosion has been assumed uniform across the entire specimen area. This *MDPR* is calculated from the weight loss, density, known surface area, and time of exposure as obtained from microsecond readings on the Holloman instrumentation. The expression

$$MDPR = KV^{\alpha} \sin^2 \theta \tag{1}$$

where

$MDPR$ = mean depth of penetration, cm/s,
K = empirical constant,
V = velocity, ft/s, and
θ = impingement angle, (90 deg is normal incidence, for example).

was previously found to provide the best fit to the data for the reinforced 2-D plastic laminate radome and some monolithic ceramic (where appropriate) materials [*5,6*].

However, in this series of tests, analysis of the data with the expression

$$MDPR = KV^{\alpha} \sin^m \theta \tag{2}$$

where m = 1, 2, 2.5, 3, and 4, determined that the best fit for the data occurred with $MDPR = KV^{\alpha} \sin^3 \theta$ for the carbon-carbon composite materials, implying a stronger angular dependence than previously postulated.

Furthermore, the monolithic graphites were best correlated by the expression

$$MDRP \sin \theta = K(V \sin\theta)^{\alpha} \tag{3}$$

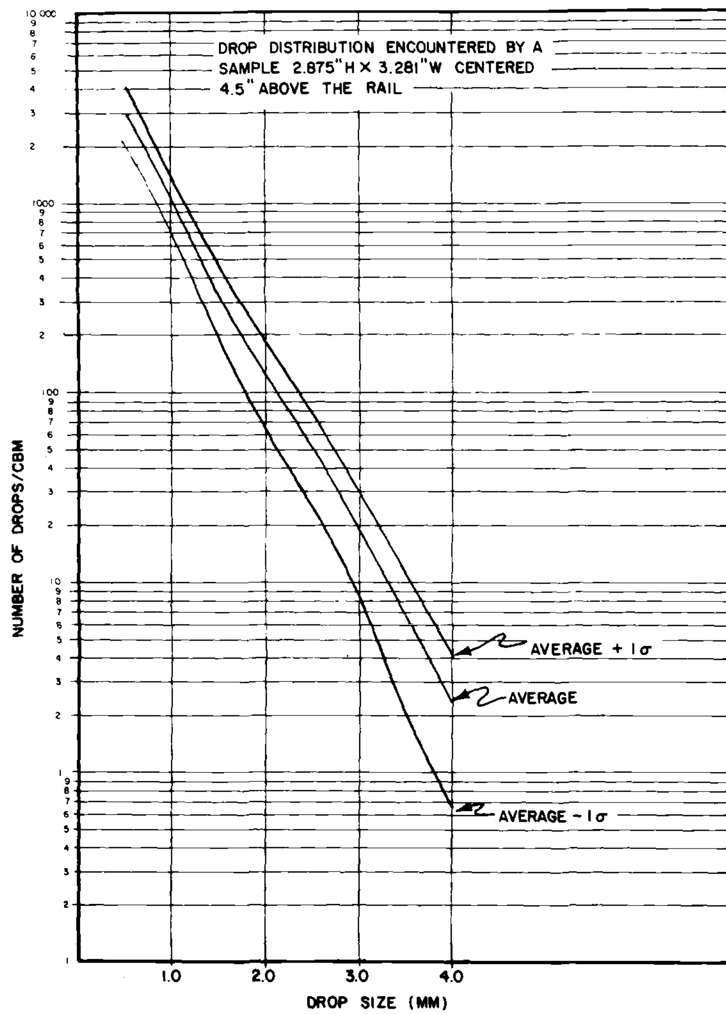

FIG. 4—*New Holloman rainfield drop size distribution.*

The expression had formerly been used [*1*] but abandoned in favor of the sine-squared expression which fit the resin composite materials best. Equation 3, which correlates the erosion response of the monolithic graphite materials, depends on the impact pressure and it is a direct function of the normal component of the velocity ($V \sin\theta$). Obviously, the carbon-carbon composite erosion response also depends on impact pressure, but the introduction of fibrous reinforcement increases the angular dependence to $\sin^3\theta$ as determined by this analysis (see Table 2). The good fit obtained for the erosion data for the carbon-carbon composites with Eq 3 (see Table 3) also

TABLE 2—*Rain erosion equation constants:* MDPR = $KV^{\alpha}\sin^3\theta$; *nose tip materials.*

No.	Material	α	Correlation Coefficient, r	K	($MDPR/\sin^3\theta$ for V = 305 m/s), cm/s	Number of Data Points
Carbon-carbon composites						
T-15	GE orthogonal 3-D (CCAP)	6.652	0.977	7.82×10^{-25}	7.06×10^{-5}	5
T-16	Philco Ford fine weave 3-D (CCAP)	5.243	0.849	1.53×10^{-19}	8.19×10^{-4}	5
T-17	MDAC orthogonal 34-7 3-D (CCAP)	8.242	0.999	1.24×10^{-30}	6.61×10^{-6}	5
T-18	GE polar weave (CCAP)	13.319	0.992	3.53×10^{-49}	3.20×10^{-9}	4
T-19	MDAC 4-4-2 3-D (CERA)	9.777	0.842	2.53×10^{-36}	5.04×10^{-7}	6
T-20	GE 1-1-3 3-D (CERA)	8.719	0.861	1.44×10^{-32}	2.06×10^{-6}	6
T-21	MDAC 1-1-2 3-D (CHIP)	insufficient data		...	...	1
T-22	MDAC 2-2-4 3-D (CHIP)	insufficient data		...	...	1
T-23	MDAC 1-D T-50/TaC (CHIP)	insufficient data		...	...	1
T-24	AVCO 1-1-5 3-D (CERA)	8.302	0.939	5.75×10^{-31}	4.65×10^{-6}	6
T-25[a]	GE 1-1-5 3-D (CERA)	6.914	0.883	6.55×10^{-26}	3.62×10^{-5}	5
T-26	GE 1-1-5 3-D (CERA)	insufficient data		...	...	2
T-27[a]	MDAC 1-1-5 4-D (CERA)	9.315	0.791	6.81×10^{-35}	5.99×10^{-7}	5
T-28[a]	MDAC 1-1-13 3-D (CERA)	8.696	0.921	1.29×10^{-32}	1.59×10^{-6}	5
Graphites						
T-7	ATJ-S graphite	9.491	0.882	5.09×10^{-35}	1.51×10^{-6}	10
T-13	994 improved strain-to-failure graphite	11.103	0.915	3.98×10^{-48}	8.12×10^{-8}	7
T-14	TS-1276 uniform-properties graphite	10.975	0.871	8.53×10^{-41}	7.16×10^{-8}	7

[a] Mach 4.0 and Mach 5.0, 30-deg cone only; all others are based on at least three runs.

TABLE 3—*Rain erosion equation constants:* MDPR $sin\theta = K(V\ sin\theta)^{\alpha}$; *nose tip materials.*

No.	Material	α	Correlation Coefficient, r	K	$(MDPR/\sin^3\theta)$ for $V = 305$ m/s), cm/s	Number of Data Points
Carbon-carbon composites						
T-15	GE orthogonal 3-D (CCAP)	3.573	0.973	1.23×10^{-13}	6.46×10^{-3}	5
T-16	Philco Ford fine weave 3-D (CCAP)	3.824	0.962	2.24×10^{-14}	6.65×10^{-3}	5
T-17	MDAC orthogonal 347 3-D (CCAP)	3.097	0.953	5.68×10^{-12}	1.12×10^{-2}	5
T-18	GE polar weave (CCAP)	2.408	0.692	1.62×10^{-9}	2.71×10^{-2}	4
T-19	MDAC 4-4-2 3-D (CERA)	3.315	0.850	5.95×10^{-13}	5.23×10^{-3}	6
T-20	GE 1-1-3 3-D (CERA)	3.535	0.900	9.14×10^{-14}	3.67×10^{-3}	6
T-21	MDAC 1-1-2 3-D (CHIP)	insufficient data		...	...	1
T-22	MDAC 2-2-4 3-D (CHIP)	insufficient data		...	...	1
T-23	MDAC 1-D T-50/TaC (CHIP)	insufficient data		...	...	1
T-24	AVCO 1-1-5 3-D (CERA)	3.796	0.944	1.50×10^{-14}	3.65×10^{-3}	6
T-25[a]	GE 1-1-5 3-D (CERA	4.415	0.972	1.09×10^{-16}	1.92×10^{-3}	5
T-26	GE 1-1-5 3-D (CERA)	insufficient data		...	...	2
T-27[a]	MDAC 1-1-1-5 4-D (CERA)	5.943	0.986	4.74×10^{-22}	3.20×10^{-4}	5
T-28[a]	MDAC 1-1-13 3-D (CERA)	4.488	0.956	3.81×10^{-17}	1.11×10^{-3}	5
Graphites						
T-7	ATJ-S graphite	3.010	0.821	1.47×10^{-11}	1.57×10^{-2}	10
T-13	994 improved strain-to-failure graphite	3.737	0.871	2.98×10^{-14}	4.85×10^{-3}	7
T-14	TS-1276 uniform-properties graphite	3.307	0.834	5.75×10^{-13}	4.80×10^{-3}	7

[a]Mach 4.0 and Mach 5.0, 30-deg cone only; all others are based on at least three runs.

confirms a strong dependence on normal velocity component (impact pressure).

Mass Loss Ratio

The mass loss ratio, G, was used in part for analysis of the data as described in a later section of the paper. It was obtained by dividing the weight loss of any particular specimen by the rain mass encountered, which was determined from the rain intensity data (liquid water content approximately 3 g/m^3) and the swept volume that that specimen encountered in traversing the 610-m rainfield.

The *MDPR* is a recession rate as determined and may be related to the mass loss ratio as follows. If the speed through the Holloman rainfield is constant, which is approximately true, then

$$G = \frac{\rho}{w(V \sin\theta)} MDPR$$

where ρ is the material density (g/cm^3) and w the rain concentration or liquid water content (g/cm^3). Note that *MDPR* varies as $V \sin\theta$ to one power higher than G. This occurs because *MDPR* is a rate of material removal, and, as encounter speed and $\sin\theta$ increase, the rate of the rain mass encountered increases in direct proportion. Note that this difference from G in speed and angle dependence holds for any erosion rate, or any total recession (measured normal to the local surface) that occurs in a fixed duration at constant rate.

Results on Reentry Vehicle Nosetip Materials

The results herein are based upon the four runs described in Table 1, which consisted of two Mach 4.0 tests with the stepped wedge (30R-M5 on 10 June 1975 and 30R-M6 on 16 June 1976), a Mach 5.0 test with the 13.5-deg cone (30R-N5A on 18 Dec. 1975), and a Mach 5.0 test with the 30-deg cone (30R-04 on 15 June 1976). All of these tests were conducted through the new 60 to 90 mm/h rainfield.

For these carbon-carbon and graphite materials which erode (do not catastrophically fracture), the values of K (the constant), α (the velocity exponent), r (coefficient of correlation from a regression analysis), F (the value of $MDPR/\sin^3\theta$ at $V = 305$ m/s), and the number of data points which were used for the analysis are also provided in Tables 2 and 3. The value of $MDPR/\sin^3\theta$ or $MDPR \sin\theta$ at $V = 305$ m/s is an arbitrary selection of velocity at which to compare the erosion (*MDPR*) as computed from the correlations obtained. Since these relationships are based upon only a few data, the ranking of materials based upon the calculated value and those actually measured in the 30-deg, Mach 5.0 run (V normal = 808 m/s) or the 60-deg, Mach 4.0 specimens (V normal = 1102 m/s) differs somewhat. For purposes of discussion in this paper, the rankings based upon measured mass loss/*MDPR* will be utilized.

The number of data points indicated are those from all runs from Mach 4.0 to Mach 5.0 which could be used in developing the *MDPR-V* relationships. If no values for K, α, r, or F are shown, insufficient data were obtained to develop the velocity-erosion rate relationship. Note that the data on the last three Carbon-Carbon Erosion Resistance Assessment (CERA) carbon-carbons was obtained at Mach 4.0 and Mach 5.0, 30 deg only since a Mach 5.0, 13.5-deg cone run has not been made since these materials were completed.

These graphites and carbon-carbon composite materials which are particularly suited for very high heating conditions and high-performance maneuvering or other advanced reentry vehicles were obtained from the Air Force- and Navy-sponsored Carbon-Carbon Assessment Program (CCAP), Carbon Hypersonic Impact Program (CHIP), and CERA program that developed these materials.

Carbon-Carbon Composites—Prior to discussing the ranking of materials, a description of the nomenclature is in order. The carbon-carbon materials are described by three numbers. For example, the T-19 composite is labeled MDAC 4-4-2. The 4-4-2 designation for this material and similar designations for others (1-1-3, 1-1-5, etc.) refers to the number of fiber yarns per site or per layer in the X-Y-Z directions, respectively, so that the 4-4-2 material had 4 Thornel 75-X yarns and 4-Y yarns per layer and 2 Thornel 75-Z yarns per site. Figure 5 describes the unit cell dimensional

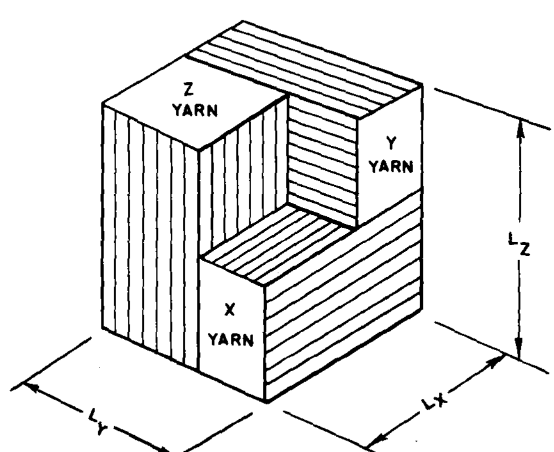

FIG. 5—*Unit cell dimensional nomenclature in 3-D orthogonal weave.*

nomenclature in 3-D orthogonal weaves. Typical damage to one of these carbon-carbons after the Mach 5.0, 30-deg exposure is shown in Fig. 6*a*; note the large degree of roughness developed.

The ranking of these nosetip materials based upon their mean depth penetration at 30 deg, Mach 5.0, wherein all were exposed to identical conditions on the same run, was as given in Table 4. Note that since the density of all these materials is 1.8 to 2.0 (see Table 5), Table 4 also gives the mass loss ratio ranking.

If the ranking is made based upon higher angle exposures (60-deg) at Mach 4.0, only a slight change in the positions of the top ranking materials occurs while the relative position of the other materials varies considerably. The polar weave ranks second in these conditions, where it was lowest at Mach 5.0, 30-deg, due to complete loss of the specimen. This complete failure may have been caused because the specimen was undersized and had been potted in plastic to fit the cone. The 60-deg, Mach 4.0 ranking is given in Table 6.

The effect of data scatter on these rankings can be considered in the following manner. The relative performances of all materials under the two test conditions can be compared as in the list given in Table 7. It is noted at once that the ratio of performance at M5/30-deg to performance at M4/60 deg is relatively uniform; the value of the ratio falls within ± 18 percent (1σ) of the average for all except two of the materials (MDAC 1-1-1-5 and TS-1276). In view of the fact that two tests (two sources of error) are involved, it is somewhat unlikely that changes in ranking could be determined with certainty. However, this also provides confidence in the comparability of the rankings obtained under these two conditions.

Of the two materials which showed large deviations from average behavior, one (MDAC 1-1-1-5) exhibited relative insensitivity to test condition, and the other (TS-1276) showed exceptionally strong sensitivity to test condition. The graphites appear to be somewhat more sensitive to test conditions than the carbon-carbon. Previous investigations of impact damage in monolithic graphite materials [7] have shown a relative insensitivity to multiple impact, and the differences between the numbers of drops impacting at 60 deg versus the number at 30 deg with their respective damage cannot explain this sensitivity. Perhaps it may be attributed to data scatter.

The rankings given in Tables 4 and 6 demonstrate the improvement which has occurred in the weaving and processing of the carbon-carbon composites from the time of the CCAP materials fabrication (1972) until the time of the CERA materials (late 1974 to spring 1976). These improvements coupled with the understanding of the influence of *Z*-reinforcement percentage, and other weave geometry, have enabled reduction in the erosion mass loss of approximately 30 to 40 percent.

Thus, it has been demonstrated that the beneficial influence of a high percentage of fibers oriented end-on to the surface of a composite can be

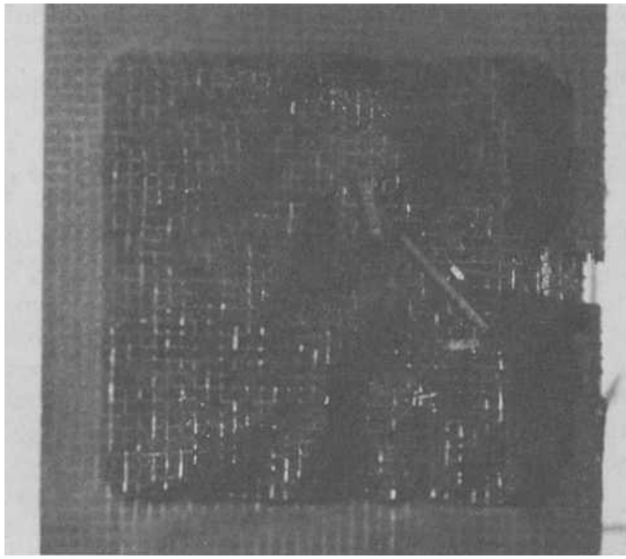

FIG. 6a—*Rain erosion damage to carbon-carbon composite after 30-deg, Mach 5 exposure.*

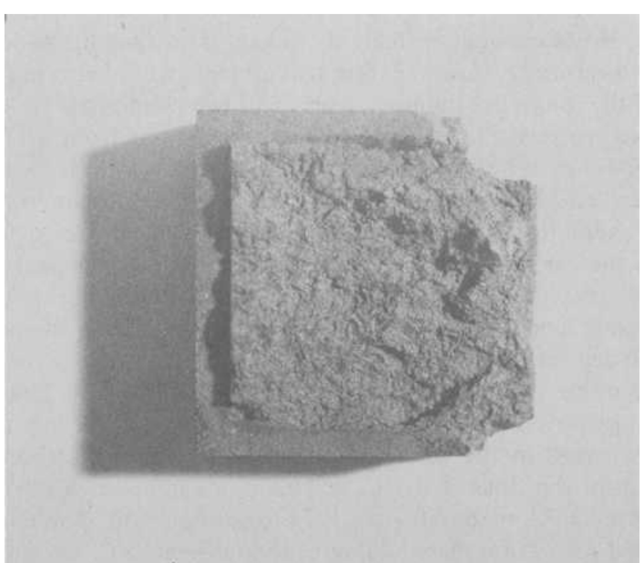

FIG. 6b—*Rain erosion damage to ATJ-S graphite after 30-deg Mach 5 exposure.*

TABLE 4—*Nosetip materials ranking at Mach 5.0, 30 deg.*

No.	Material	Source	*MDPR*, cm/s
T-28	MDAC 1-1-13 T-75/pitch + CVD + pitch	CERA (Group 2)	0.531
T-27	MDAC 1-1-1-5 T-50/pitch + CVD + pitch	CERA (Group 2)	0.575
T-25	GE 1-1-5 T-50/CVD + pitch	CERA (Group 2)	0.584
T-20	GE 1-1-3 T-50/CVD + pitch	CERA (Group 1)	0.677
T-19	MDAC 4-4-2 T-75/pitch	CERA (Group 1)	0.773
T-24	AVCO 1-1-5 T-50/resin	CERA (Group 1)	0.785
T-15	GE high axial orthogonal C-3000/C-1000/pitch	CCAP	0.829
T-16	Philco-Ford fine weave orthogonal T-75/resin	CCAP	0.919
T-17	MDAC orthogonal (347) T-50/pitch	CCAP	0.978
T-14	TS-1276 graphite	...	1.055
T-7	ATJ-S graphite	...	1.233
T-13	994 graphite	...	1.302
T-18	GE polar weave T-50/ CVD + pitch	CCAP	completely gone

extended to carbon-carbon nosetip thermal protection materials. However, thermostructural requirements on the nosetip materials make an extremely high-percentage *Z*-reinforcement (for example, MDAC 1-1-13) impractical because of inability to withstand *g* forces and because of high nosetip ablative recession rates due to high thermal conductivity. Therefore, orthogonal 3-D reinforcement is the state of the art for these composites.

These tests demonstrate the desirability of fine-weave spacing in confining the extent of cratering. These conclusions are further borne out in the work of Reinecke et al [*8*] and Kratsch et al [*9*].

The construction parameters of all of the carbon-carbon composites are summarized in Table 5.

Graphites—Three graphites were also investigated, including ATJ-S graphite as a baseline material, 994 improved strain-to-failure graphite, and TS-1276 uniform-properties graphite. They were included in the 13.5-deg, Mach 5.0 (30R-N5A) and Mach 5.0, 30-deg cone (30R-04) runs, which not only provided an intercomparison of the three but also a comparison with all of the carbon-carbon composites.

The TS-1276 uniform properties graphite ranked slightly better than the ATJ-S whereas the 994 improved strain-to-failure was definitely poorer in erosion resistance as borne out by the 13.5-deg Mach 5.0 and 30-deg Mach 5.0 exposures. A comparison is made in Table 8.

On the basis of this test the graphites ranked below all of the carbon-carbons except the polar weave, which was completely lost. If the Mach 4.0

TABLE 5—*Carbon-carbon materials for Holloman testing.*

AFML No.	Material Designation (Billet No.)	Yarn	Matrix	Yarn Spacings, mm		Volume Fractions			Yarn Ends per Bundle			Density, g/cm
				$X(Y)$	Z	$X(Y)$	Z	Total	X-	Y-	Z-	
T-15	GE 3D (CCAP)	C-3000 (2) C-1000 (X)	pitch	0.686	1.067	0.114	0.042	0.452	2	2	2	1.932
T-16	PF 3D (CCAP)	Thornel 75	resin	0.609	0.762	0.139	0.222	0.500	2	2	4	1.846
T-17	MDAC 3D (347)	Thornel 50	pitch	0.711	1.016	0.116	0.162	0.394	2	2	4	1.859
T-18	GE Polar Weave	Thornel 50	AVD-pitch	...	...	...	...	...	...	...	...	1.90
T-19	MDAC 4-4-2 (316)	Thornel 75	pitch	0.711	1.016	0.179	0.063	0.421	4	4	2	1.941
T-20	GE 1-1-3 (320)	Thornel 50	CVD + pitch	0.432	0.762	0.149	0.149	0.254	1	1	3	1.878
T-21	MDAC 1-1-2 (220)	Thornel 50	pitch	0.584	0.584	0.123	0.246	0.492	1	1	2	1.92
T-22	MDAC 2-2-4 (327)	Thornel 50	pitch and CVD + pitch	0.584	1.016	0.154	0.160	0.468	2	2	4	1.87
T-23	1-D Tac/Graphite	Thornel 50 and chopped filaments	TAC	0.254	0.762	TaC 0.878	T-50 0.122	...	...	...	...	8.63
T-24	Avco 1-1-5 (508)	Thornel 50	resin	0.229	1.27	0.169	0.153	0.492	1	1	5	1.948
T-25	GE 1-1-5 (115-2)	Thornel 50	CVD + pitch	0.762	0.762	0.085	0.42	0.594	1	1	5	1.883
T-26	GE 1-1-5 (115-3)	Thornel 50	CVD + pitch	0.762	0.762	0.085	0.42	0.594	1	1	5	1.883
T-27	MDAC 1-1-1-5 (4D 844)	Thornel 50	Lo Press pitch + Hi Press pitch	UV, W direction 0.965	0.991	U. V. W. 0.05	0.26	0.41	1-1	1-	5	1.9825
T-28	MDAC 1-1-13 (845)	Thornel 75	Lo Press pitch + Hi Press pitch	0.559	1.092	0.05	0.444	0.544	1	1	13	1.9633

TABLE 6—*Nosetip materials ranking at Mach 4.0, 60 deg.*

No.	Material	Source	*MDPR*, cm/s
T-28	MDAC 1-1-13 T-75/pitch + pitch	CERA	0.313
T-18	GE polar weave T-50/CVC + pitch	CCAP	0.339
T-22	MDAC 2-2-4 T-50/pitch + CVD + pitch	CHIP	0.382
T-25	GE 1-1-5 T-50/CVD + pitch	CERA	0.395
T-7	ATJ-S graphite	...	0.717[a]
T-14	TS-1276 graphite	...	0.437
T-21	MDAC 1-1-2 T-50/pitch	CHIP	0.454
T-20	GE 1-1-3 T-50/CVD + pitch	CERA	0.456
T-24	AVCO 1-1-5 T-50/resin	CERA	0.482
T-27	MDAC 1-1-1-5 T-50/pitch + pitch	CERA	0.491
T-15	GE high axial orthogonal C-3000/C-1000/pitch	CCAP	0.501
T-19	MDAC 4-4-2 T-75/pitch	CERA	0.505
T-16	Philco-Ford fine weave orthogonal T-75/resin	CCAP	0.557
T-17	MDAC Orthogonal (347) T-50/pitch	CCAP	0.595
T-13	994 graphite	...	0.659
T-23	MDAC 1-D T-50/TaC matrix	CHIP	0.131[b]

[a]Data on ATJ-S graphite from a Mach 4.0 run in the old 140- to 165-mm/h rainfield (twice the intensity).
[b]Specimen cracked through the thickness into several pieces, which implies catastrophic failure although mass loss was low.

TABLE 7—*Relative performances of materials.*

Material	$M_1 = MDPR$ (M5/30 deg)	$M_2 = MDPR$ (M4/60 deg)	$R = \dfrac{M_1}{M_2}$
T-28	0.531	0.313	1.70
T-27	0.575	0.419	1.17
T-25	0.584	0.395	1.48
T-20	0.677	0.456	1.48
T-19	0.773	0.505	1.53
T-24	0.785	0.482	1.63
T-15	0.829	0.501	1.65
T-16	0.919	0.557	1.65
T-17	0.978	0.595	1.64
T-14	1.055	0.437	2.41
T-7	1.233	0.717	1.72
T-13	1.302	0.659	1.98
T-18	...	0.339	...
			$\bar{R} = 1.67 \pm 0.30$

data are used for comparison, the ATJ-S and TS-1276 rank intermediately among the carbon-carbons but the 994 graphite is still very poor. A typical condition of the ATJ-S graphite is shown in Fig. 6*b* after 30-deg, Mach 5.0 exposure.

TABLE 8—*Erosion resistance comparison.*

No.	Material	[a]*MDPR*, cm/s	[a]G(Mass Loss Ratio)
T-7	ATJ-S graphite	1.233	8.45
T-13	994 graphite	1.302	8.73
T-14	TS-1276	1.055	7.19

[a]30 deg, Mach 5.0, 67.6 mm/h rainfall.

Discussion

The comparison of carbon-carbon composite nosetip thermal protection materials demonstrates the superiority of materials which have a high percentage of Z-fibers end-on to the surface. The CERA 1-1-13 composite was deliberately constructed to maximize the area percentage of Z-fibers (k_z) and the CERA 4-4-2 construction was included because it was just the opposite, that is, mostly transverse X-Y bundles. The other CERA materials fall in between.

Figure 7 shows the mass loss ratio (mass removed/mass impacted) for the CCAP and CERA composites from the 30-deg, Mach 5.0 exposure (where all were exposed to the identical environment) plotted versus k_z (area percent Z fiber). As previously determined for radome construction (see Refs *5* and *6*, for example), the benefit of high axial fiber content is clear with a reduction of 50 percent in mass loss ratio by increasing Z-fiber area percentage from 20 to 45 percent. Small unit cell size is also important and partially responsible for the improved behavior of the GE 1-1-5 (0.762-mm cell) and compared with the Avco 1-1-5 (1.27-mm cell). Therefore, a combination of high Z-fiber loading coupled with small cell dimensions should provide optimum erosion performance. As can be seen in Fig. 7, this was achieved in part on the GE 1-1-5 composites, which would be anticipated to have better ablative properties (lower recession rate) and thermostructural performance (due to fine X-Y layer spacing and more uniform reinforcement) than the 1-1-13 construction, which exhibited a similar erosion resistance.

The influence of processing is considerable within these two 1-1-5 composites in that the GE 1-1-5 composite had chemical vapor deposition (CVD) impregnation pitch matrix material and was based upon a woven 3-D preform, while the Avco 1-1-5 composite had no CVD pyrolyzed resin matrix, and was a 2-D weave with Z-direction fibers inserted. However, the spacing of the Z-fibers and the percentage of X-Y fibers in the unit cell determine the extent of the crater damage area. A fine spacing tends to limit this damage and reduce the mass loss.

Figure 8 also compares mass loss ratio versus k_z for the CCAP and the first group of CERA composites from the 60-deg, Mach 4.0 exposures

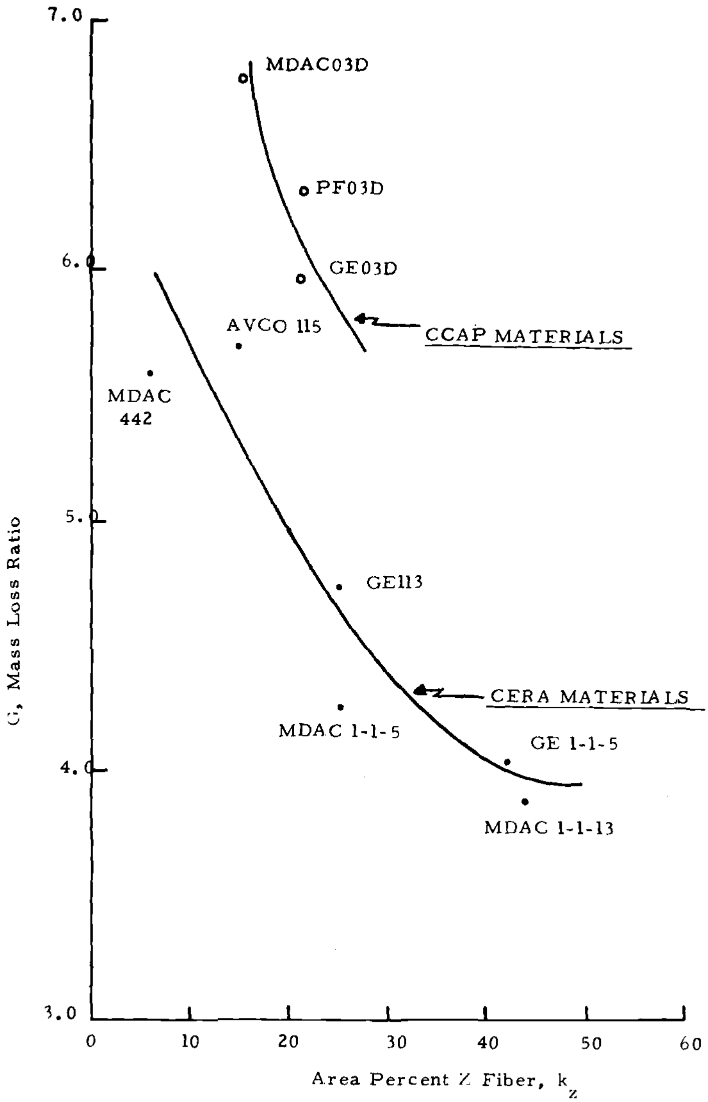

FIG. 7—*Mass loss ratio versus area percent Z-fiber—30-deg, M5.0 data.*

(three different tests) and the 13.5-deg, Mach 5.0 exposures (two different tests). In both cases, the higher *Z*-fiber content materials resulted in reduced erosion even at the very low 13.5-deg impingement angle where the data scatter is greater.

If a plot of mass loss ratio versus total fiber volume fraction, K_t is made for these composites, no correlation is evident, as can be seen in Fig. 9. Since the size of the unit cell is important and the matrix is significantly

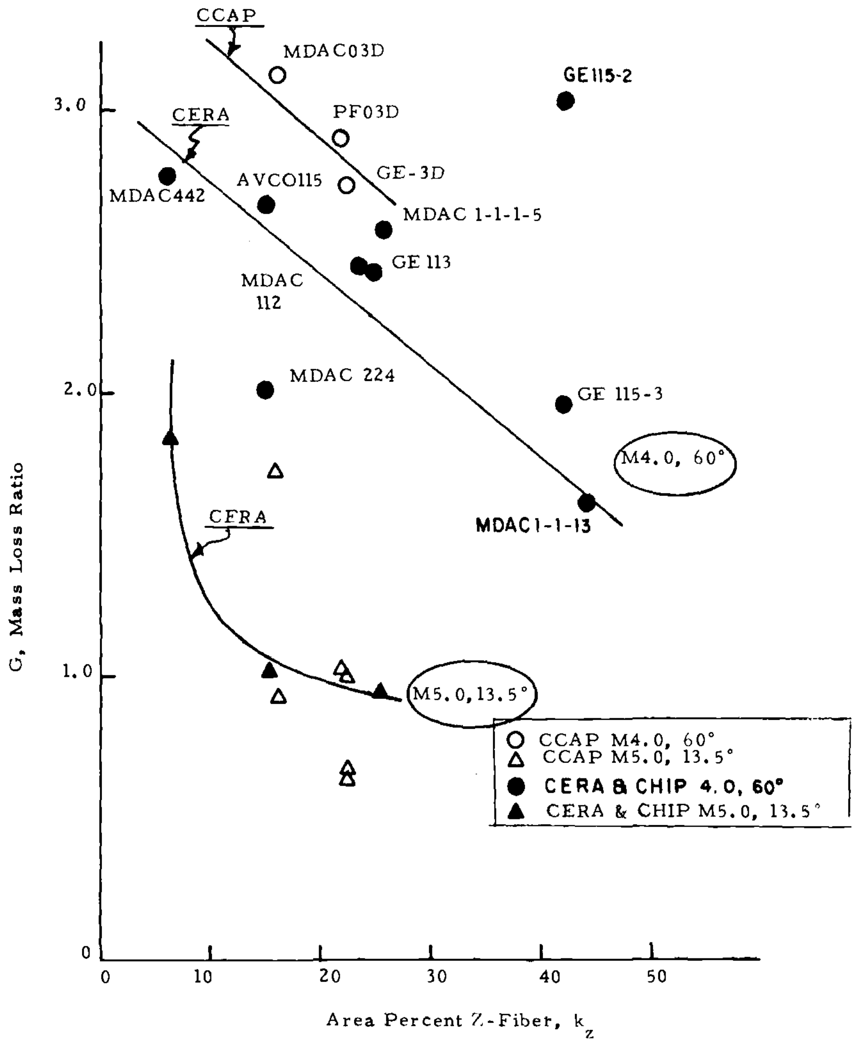

FIG. 8—*Mass loss ratio versus Area Percent Z-fiber—13.5-deg, M5.0 and 60-deg, M4.0 data.*

weaker, one might expect the total fiber content to govern the mass loss behavior. However, the relationship is more complex as shown by the scatter and lack of trends in this figure.

If the CCAP composites in Figs. 7 and 8 are compared with the CERA composites, the improvements in weaving and processing are clearly evident. The CCAP materials are of vintage 1972 to 1973 while the CERA materials date from late 1974 to spring 1976. During this time, substantial advances in the state of the art for fabrication of carbon-carbon composites have

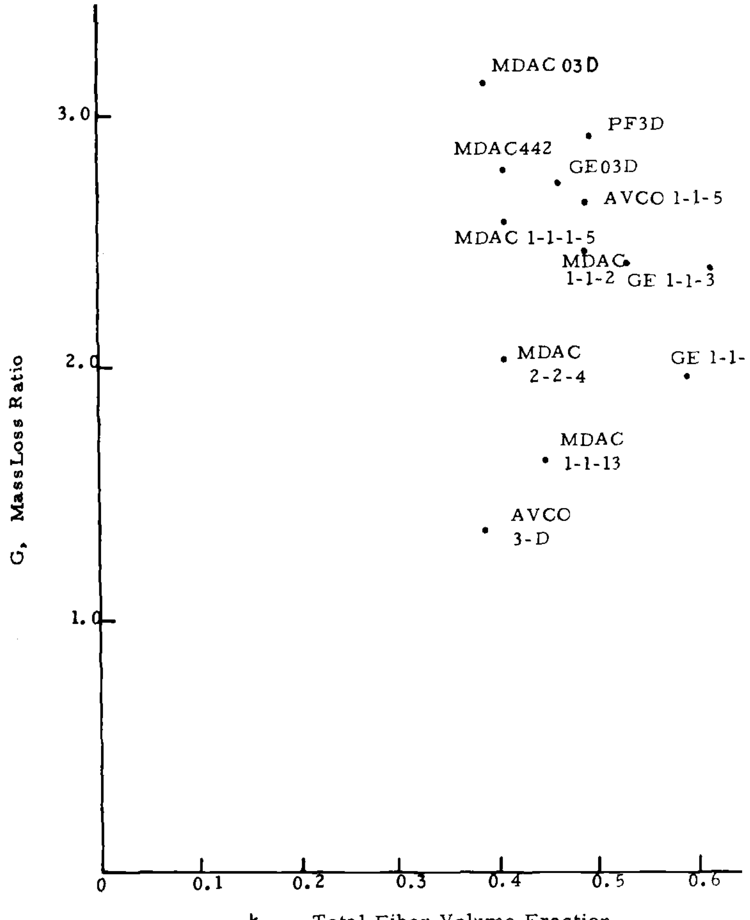

FIG. 9—*Mass loss ratio versus total fiber volume fraction—60-deg, M4.0 data.*

occurred and this has resulted in approximately 15 to 20 percent reduction in erosive mass loss.

A comparison of the mass loss ratio rankings of the various composites may be found in Fig. 10 for the CCAP and CHIP materials and in Fig. 11 for the CERA materials as a function of the normal component of the velocity ($V \sin\theta$). The rankings, from the various angle/velocity combinations, are quite consistent in terms of those materials which exhibited the poorest erosion resistance (MDAC 347 0-3D CC and Philco Ford 0-3D from CCAP or Avco 1-1-5 and MDAC 4-4-2 from CERA). Thus, these screening tests would eliminate them from further development. The superiority of the high axial CERA composites is generally shown in Fig. 11 with the T-27

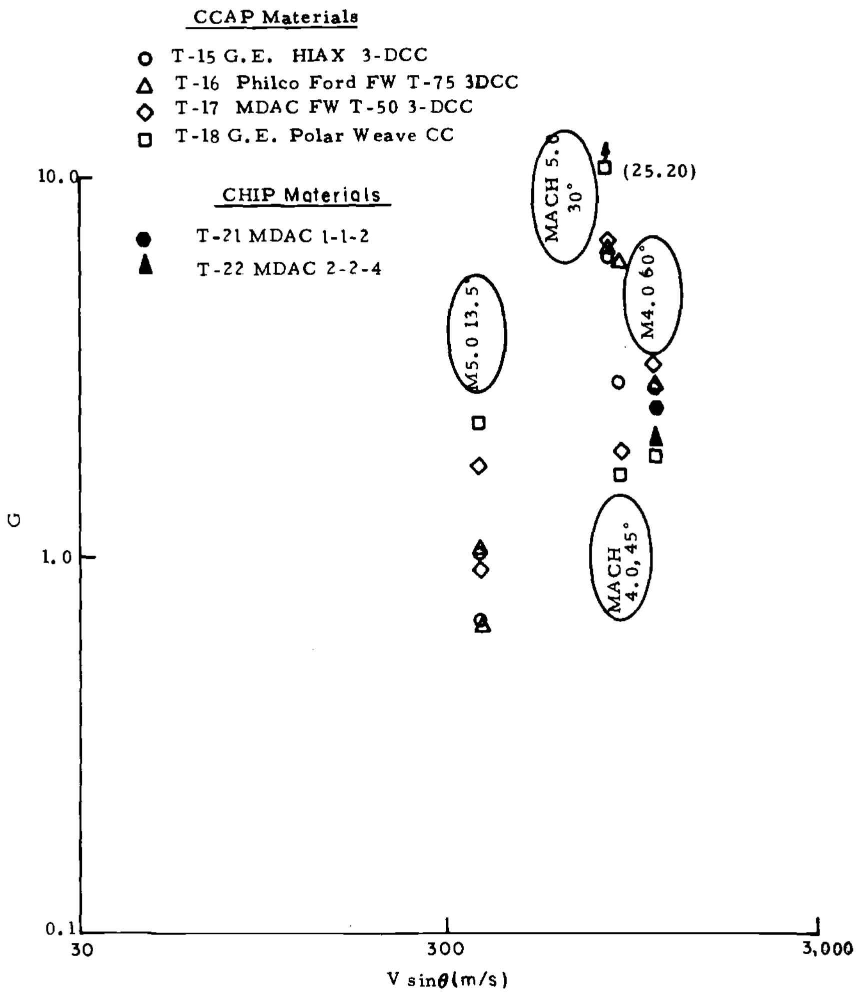

FIG. 10—*Mass loss ratio versus normal component of velocity—CCAP and CERA materials.*

(MDAC 1-1-1-5), T-25 (G. E. 1-1-5), and T-28 (MDAC 1-1-13) exhibiting less mass loss at most angle conditions compared with the others.

Based upon the results for all carbon-carbon composites, specific processing conditions in terms of graphitization temperatures or numbers of impregnation cycles cannot be recommended, but the utilization of CVD to improve matrix-fiber bonding, pitch matrix compared with pyrolyzed resin, and T-50 or T-75 continuous rayon filaments for reinforcement, is indicated.

Plots of mass loss ratio versus normal velocity components are shown in Figs. 12–17 for the six CERA carbon-carbon composites with the ve-

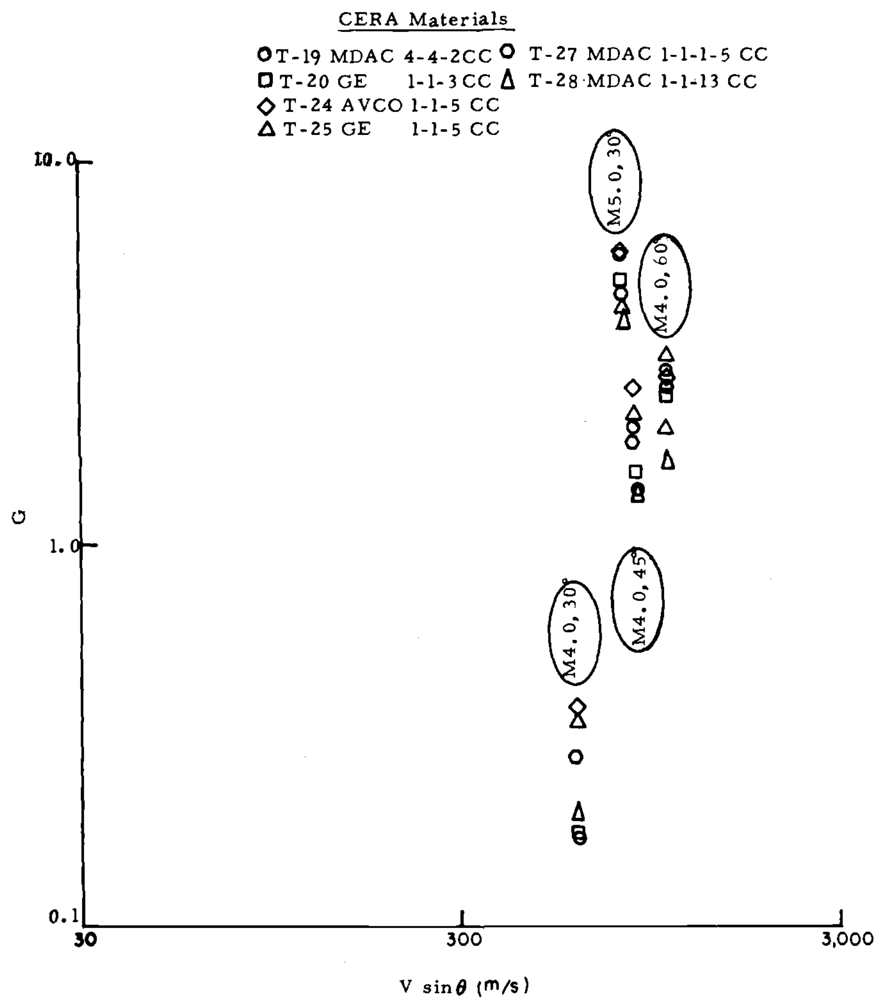

FIG. 11—*Mass loss ratio versus normal component of velocity—CERA materials.*

locity exponent as determined from the computer regression analysis indicated. In the case of the first group of CERA composites, the high values of the 13.5-deg, Mach 5.0 mass loss ratios partially offset the low values of the 30-deg, Mach 4.0 (where shock-layer effects reduce the mass loss), and the exponents are 2.3 to 2.8. With the second group of CERA composites, no 13.5-deg, Mach 5.0 data have been obtained yet and the 30-deg, Mach 4.0 data result in higher-velocity exponents 3.4 to 4.9 being determined for these materials.

An attempt was made to relate the ranking of materials as obtained at Holloman to those obtained at other facilities. Past experience [*11*] has

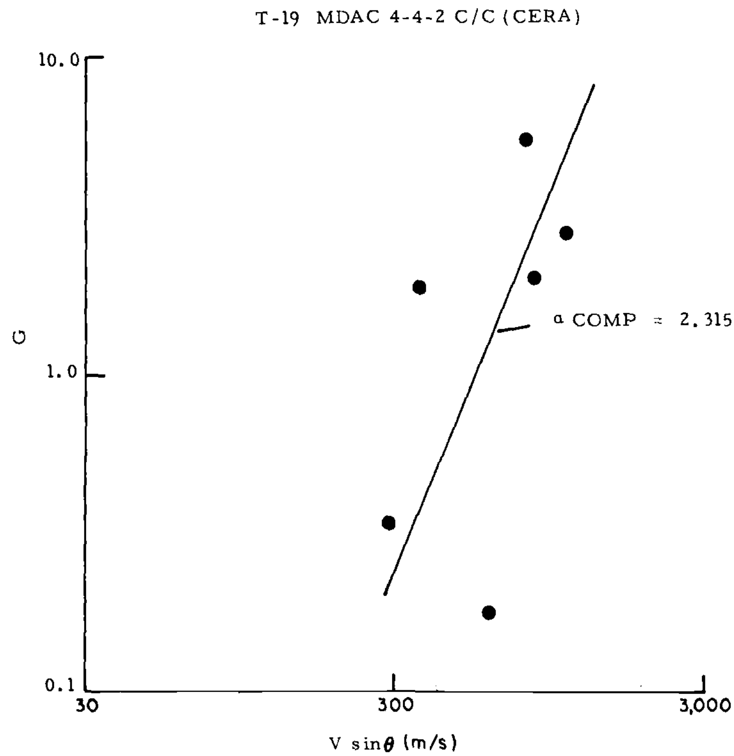

FIG. 12—*Mass loss ratio versus normal component of velocity—MDAC 4-4-2 carbon-carbon.*

shown that the influences of materials parameters determined in these sled tests have in general held true in higher-velocity multiple-impingment erosion conditions.

Comparison of rankings of the CCAP and CERA materials from the Science Applications, Inc. (SAI) and Effects Technology, Inc. (ETI) single glass particle impact facilities, the Avco graupel ice ballistics range tests, the Arnold Engineering Development Center (AEDC) dendritic ice crystal tests, and the multiple impingement rain tests are given in Table 9.

As can be seen in this table, the single-particle ranking of materials showed disagreement with the multiple-impingement ranking but the better materials (MDAC 1-1-13, GE 1-1-5, GE 1-1-3) were typically grouped near the top in all facilities and the same was true for the poorer materials (MDAC 4-4-2, graphites, polar weave). The sensitivity of the composite materials to residual damage and multiple-impingement effects in a real-time sense, such as in the rocket sled tests or the ballistics range tests, is

[3]The author is indebted to Mr. Marlyn E. Graham of Effects Technology, Inc. for this suggestion.

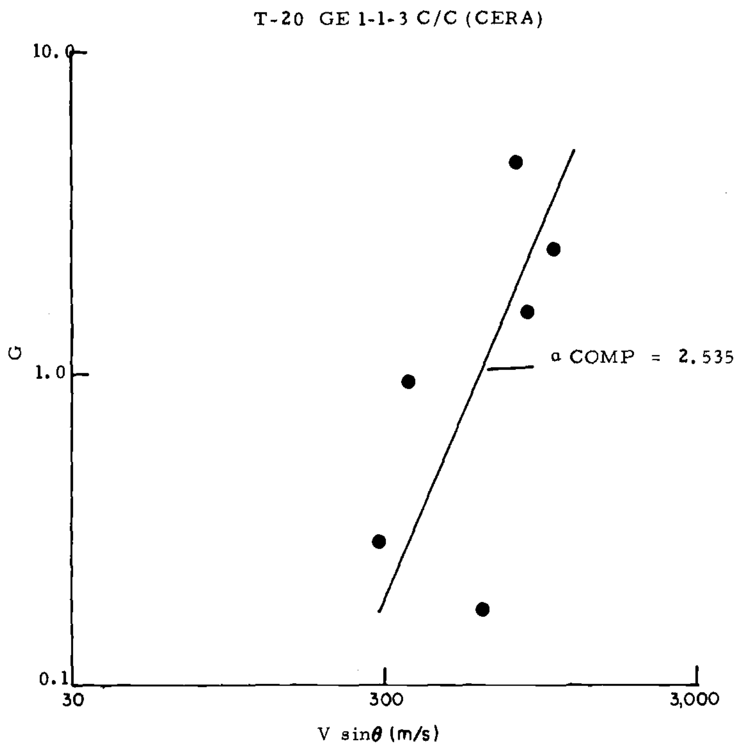

FIG. 13—*Mass loss ratio versus normal component of velocity—GE 1-1-3 carbon-carbon.*

difficult to determine since only post-test integrated damage is obtained. Comparison with single-particle tests is only a curiosity because the velocity is low on the sled tests, aerodynamic effects can influence mass removal in both sled and ballistics range tests (and this is not simulated in single-particle tests), the effects of mechanical vibration and stopping are unknown (but believed to be minor on the sled because of the condition of eroded specimens which are recovered with many pieces remaining), and because of the uncertainties associated with a multiple-impact experiment through a precalibrated environment. A multiple-impact experiment in the single-particle facility would provide a much more valid comparison but those data are not available on these composites.

The benefit of the increased in-plane isotropy obtained with rotating the *X-Y* plies in an orthogonal construction was subtle, but important. The 1-1-1-5, 4-D construction was similar dimensionally to the GE 1-1-5 orthogonal construction and both ranked similarly in the multiple-impingement rain and ice environments. The 4-D construction exhibited the least mass loss in the AEDC ice crystal tests, which were the only ones on actual sphere-cone shapes. Whether this good performance can be directly tied

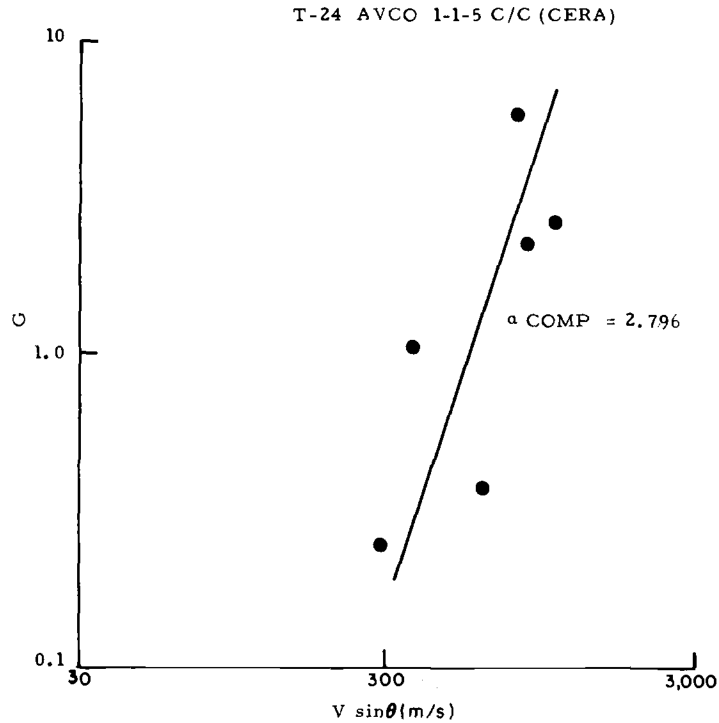

FIG. 14—*Mass loss ratio versus normal component of velocity—AVCO 1-1-5 carbon-carbon.*

with the reduced tendency for macroroughness development by the 4-D materials and, hence, with less ablation and ablation-erosion coupling, is only speculative at this point, but is believed to be plausible.

Conclusions

1. A high percentage of axial reinforcement (fibers end-on to the surface) is desirable in carbon-carbon composites for improved erosion resistance.
2. The fine-weave (small unit cell size) orthogonal construction coupled with high axial fiber loading provides increased erosion resistance for nose-tip applications.
3. Improvements in processing and weaving of carbon-carbon composites, including the use of initial CVD impregnation and pitch for the matrix and continuous rayon-based fibers, can significantly increase their high-speed erosion performance.
4. The carbon-carbon composites exhibit macroscopic roughness after exposure to the multiple-impingement rain environment. The use of in-

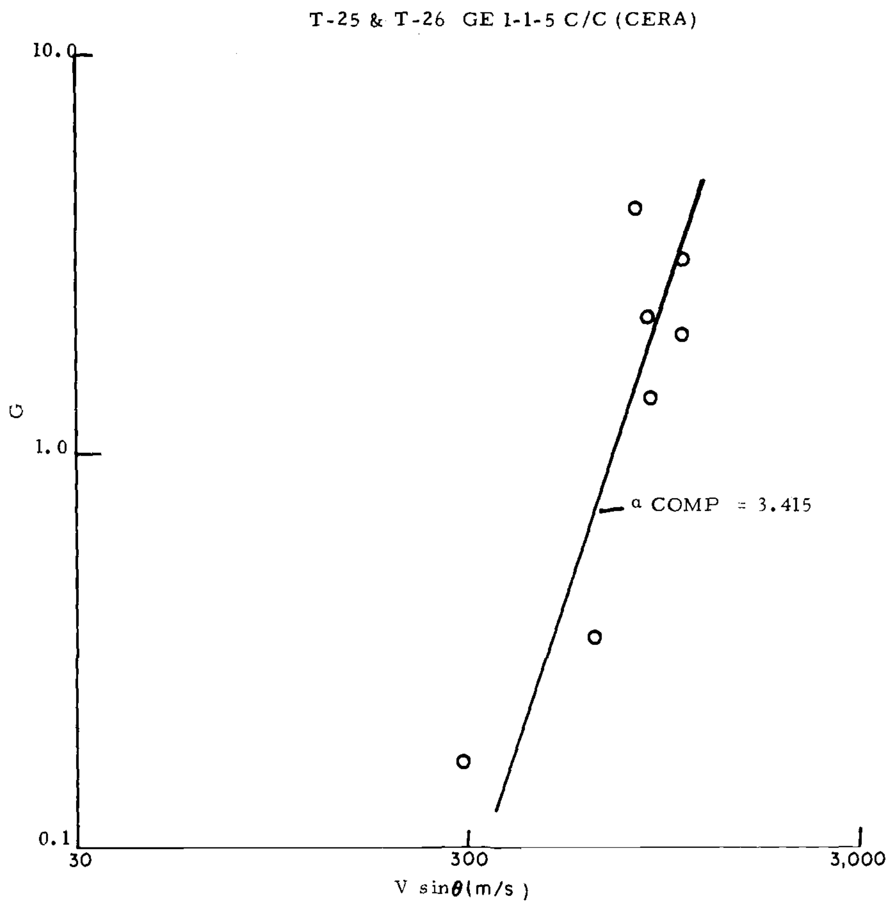

FIG. 15—*Mass loss ratio versus normal component of velocity—GE 1-1-5 carbon-carbon.*

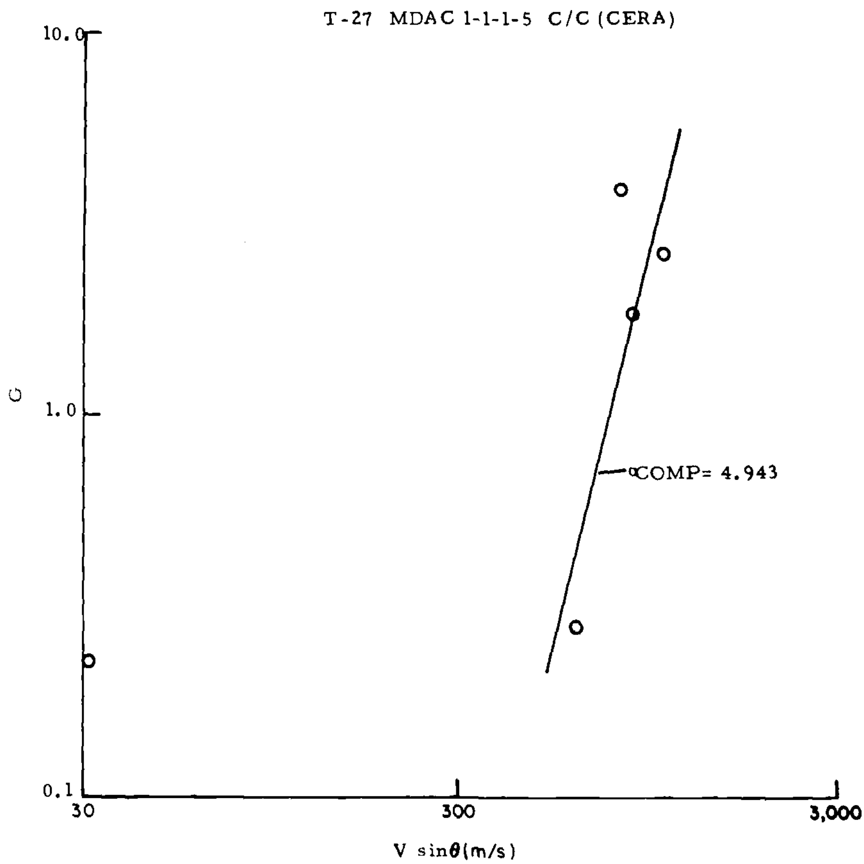

FIG. 16—*Mass loss ratio versus normal component of velocity—MDAC 1-1-1-5 carbon-carbon.*

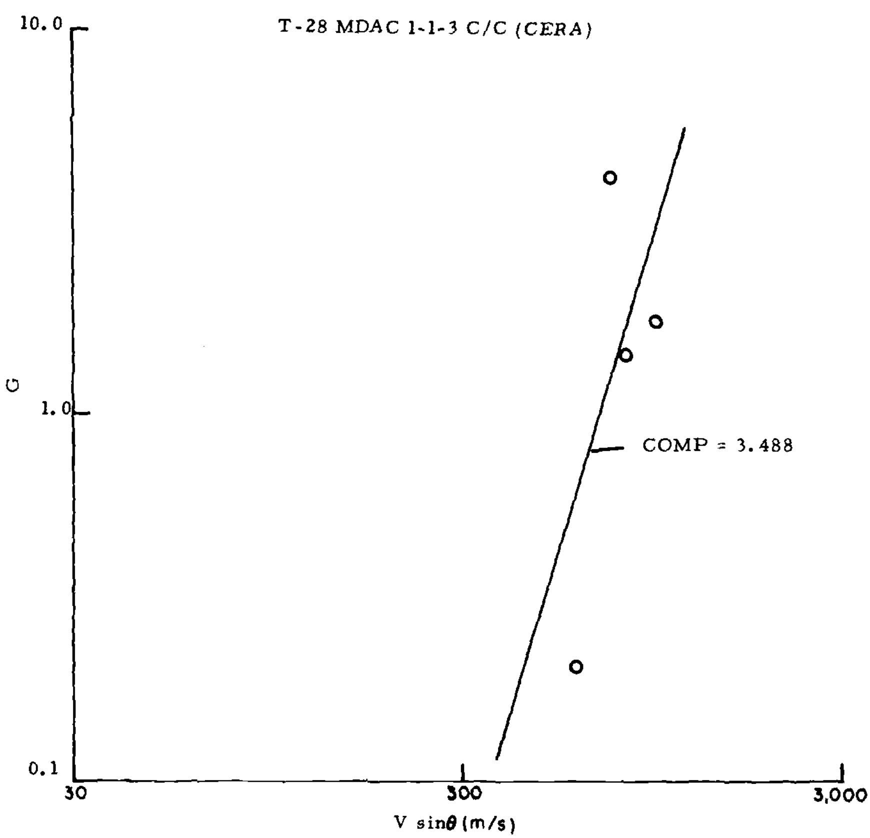

FIG. 17—*Mass loss ratio versus normal component of velocity—MDAC 1-1-3 carbon-carbon.*

TABLE 9—*Ranking of CERA and CCAP carbon-carbon materials from various investigations.*

Material		Holloman Multiple Rain Erosion, 30 deg, 1675 m/s	Holloman Multiple Rain Erosion, 60 deg, 1280 m/s	Single Particle[a] (SAI and ETI), 1000-μm 3658 m/s Glass Spheres	Reinecke[b] Ranking, Multiple-400-μm Ice, 1524-m/s, RADEF Ballistics Range	Jones Ranking,[c] Multiple Dendritic Ice, 5486 m/s, AEDC Ballistics Range
MDAC 1-1-13 T-75/pitch + CVD + pitch	CERA (Group 2)	1	1	2	not run yet	4
MDAC 1-1-1-5 T-50/pitch + CVD + pitch	CERA (Group 2)	2	8	5	not run yet	1
GE 1-1-5 T-50/CVD + pitch	CERA (Group 2)	3	3	3	not run yet	2
GE 1-1-3 T-50/CVD + pitch	CERA (Group 1)	4	6	4	not run yet	6
MDAC 4-4-2 T-75/pitch	CERA (Group 1)	5	10	8	not run yet	11
AVCO 1-1-5 T-50/resin	CERA (Group 1)	6	7	8	not run yet	5
G. E. Hi Axial orthogonal C-3000/C-1000/pitch	CCAP	7	9	1	2	7
Philco-Ford fine weave orthogonal T-75/resin	CCAP	8	11	1	5	9
MDAC orthogonal (347) T-50/pitch	CCAP	9	12	6	1	10
TS-1276 graphite	...	10	5	not run	not run	not run
ATJ-S graphite	...	11	4	8	4	8
994 graphite	...	12	13	6	3	3
GE polar weave T-50/CVD + pitch	CCAP	13	2	7	not run	12

[a]Ref *9*.
[b]Ref *8*.
[c]Ref *10*.

creased in-plane isotropy (such as in the 4-D construction with rotated X-Y plies) provides a technique for reducing this roughness development.

5. Rankings of materials from single-particle and multiple-particle ground-based facilities show general agreement in materials classes (construction) which exhibit the most erosion resistance and those which rank poorest.

6. Velocity exponents in the speed regime from 1220 to 1675 m/s were determined to range from 5.2 to 9.7 for carbon-carbon composites' *MDPR* as a function of velocity. These are based upon impingement angles of 13.5, 30, 45, and 60 deg. Other velocity and $\sin\theta$ combinations could represent the erosion behavior of these materials approximately equally well.

7. For the carbon-carbon composites, the *MDPR* varied with the sine cubed of the impact angle within the velocity regime and specific angles employed in these tests.

References

[1] Schmitt, G. F. in *Characterization and Determination of Erosion Resistance, ASTM STP 474*, American Society for Testing and Materials, 1970, pp. 323-352.
[2] Schmitt, G. F., Reinecke, W. G., and Waldman, G. D. in *Erosion, Wear, and Interfaces with Corrosion, ASTM STP 567*, American Society for Testing and Materials, 1974, pp. 219-238.
[3] Rasmussen, H. J., *Journal of Environmental Sciences*, July/Aug. 1977, pp. 15-25.
[4] Schmitt, G. F., *Journal of Aircraft*, Vol. 12, No. 10, Oct. 1975, pp. 761-762.
[5] Schmitt, G. F., *Journal of Aircraft*, Vol. 10, No. 12, Dec. 1973, pp. 705-709.
[6] Schmitt, G. F., *High Temperature-High Pressures*, Vol. 6, No. 2, 1974, pp. 177-188.
[7] Rubin, L., in *Proceedings*, Fourth International Conference on Rain Erosion and Associated Phenomena, Vol. 2, Royal Aircraft Establishment, Farnborough, England, 8-10 May 1974, pp. 887-925.
[8] Reinecke, W. G., unpublished results, Avco Corp., Lowell, Mass., 15 March 1976.
[9] Kratsch, K. M., private communication, Science Applications, Inc., Santa Ana, Calif., 10 Nov. 1975.
[10] Jones, G. R., unpublished results, ARO, Inc., Tullahoma, Tex. 22 Aug. 1976.
[11] Reinecke, W. G., in *Proceedings*, Fourth International Conference on Rain Erosion and Associated Phenomena, Vol. 1, Royal Aircraft Establishment, Farnborough, England, 8-10 May 1974, pp. 209-233.

Cavitation Erosion

C. M. Preece,[1] *S. Vaidya,*[2] *and S. Dakshinamoorthy*[3]

Influence of Crystal Structure on the Failure Mode of Metals by Cavitation Erosion

REFERENCE: Preece, C. M., Vaidya, S., and Dakshinamoorthy, S., "**Influence of Crystal Structure on the Failure Mode of Metals by Cavitation Erosion,**" *Erosion: Prevention and Useful Applications, ASTM STP 664,* W. F. Adler, Ed., American Society for Testing and Materials, 1979, pp. 409–433.

ABSTRACT: The cavitation-induced deformation and erosion of metals of the three common crystal structures, face centered cubic, body centered cubic, and hexagonal close packed (fcc, bcc, hcp), have been investigated. It is shown that the shock-loading conditions encountered by the metal during cavitation enhances the effects of different deformation modes and strain-rate sensitivity arising from differences in crystal structure. This, in turn, results in a complex crystal orientation and grain size dependence of erosion rates.

These factors, which are highlighted under cavitation conditions and minimized under quasi-static loading, are considered responsible for the lack of any correlation between erosion rates and conventional mechanical properties such as strength and hardness.

KEY WORDS: cavitation erosion, nickel, brass, iron, zinc, cobalt, slip, twinning, grain size, brittle fracture, ductile rupture, erosion

Many investigations during the past 30 years [*1–11*][4] have attempted to obtain a correlation between rates of erosion of materials by cavitation and some single bulk mechanical property, or combination of properties, of the material. These properties include ductility, hardness, yield or ultimate strength, strain energy, ultimate resilience, and fatigue life. Unfortunately, all such attempts have been unsuccessful. Consequently, at the present time, there is no simple parameter which can be used by an engineer to select an appropriately erosion-resistant alloy or to gauge the potential lifetime of a part exposed to cavitation.

[1]Member of the technical staff, Bell Laboratories, Murray Hill, N. J. 07974.

[2]Graduate student, Department of Materials Science, State University of New York at Stony Brook, N. Y. 11794.

[3]Process engineer, General Instrument Corp., Hicksville, N. Y.

[4]The italic numbers in brackets refer to the list of references appended to this paper.

If one considers the dynamic nature of the stressing produced by cavitation, however, the reasons for the lack of any correlation with quasi-static mechanical properties become readily apparent. In metallic materials tested at ambient temperatures under normal quasi-static loading conditions, differences in deformation modes and strain-rate sensitivity arising from differences in crystal structure have relatively little effect on the failure mode. Under the dynamic, localized loading conditions experienced by a metal exposed to cavitation, however, such differences are manifested in markedly different failure mechanisms. The purpose of this paper is to illustrate the role played by the crystal structure of metals and alloys in determining the mechanism by which they absorb the cavitation energy and, hence, in influencing their erosion rates.

Experimental Procedure

Specimens of nickel, copper-zinc (Cu-30Zn), iron, zinc, and cobalt were prepared from rolled sheet and mechanically polished and heat treated under vacuum to give the grain sizes listed in Table 1. They were then exposed to cavitation generated in distilled water at room temperature by an ultrasonic system described elsewhere [*12*]. This system is similar to that used in the ASTM Vibratory Cavitation Erosion Test G 32-72, but with a 12.7-mm diameter horn and a specimen held stationary 2.5 mm below the horn tip. The frequency and amplitude of the horn are 20 KHz and 50 μm, respectively,

TABLE 1—*Mechanical and heat treatments.*

Material	Mechanical Treatment	Heat Treatment	Grain Diameter	
Nickel	20% cold rolled	1150°C, 8 days, air-cooled	360	
	5% cold rolled	900°C, 6 days, air-cooled	120	
	50% cold rolled	900°C, 1 h, air-cooled	50	
	50% cold rolled	900°C, ½ h, air-cooled	46	
	75% cold rolled	900°C, ½ h, air-cooled	40	μm
	90% cold rolled	900°C, ½ h, water-quenched	10	
Cu-30Zn	0% cold rolled	200°C, 30 min, air-cooled	20	
	40% cold rolled	300°C, 120 min, air-cooled	67	
	40% cold rolled	300°C, 240 min, air-cooled	110	
Iron	66% cold rolled	800°C, 15 min, air-cooled	3.6	
	33% cold rolled	850°C, 24 h, furnace-cooled	2.9	
	66% cold rolled	1200°C, 2.5 h, cooled 50°C/h	0.4	
	60% cold rolled	900°C, 5 min, air-cooled	0.1	
Zinc	50% hot rolled	320°C, 18 h	1.5	mm
	10% reduction in area, swaged	300°C, 1 h	1.0	
	10% reduction in area, swaged	25°C, 3 months	0.1	
Cobalt	hot rolled	900°C, 2 h, furnace cooled to 300°C, 24 h	25μm	

and under these operating conditions the stress produced in the specimen is approximately 250 MPa. The progression of erosion was monitored by mass loss measurements (reproducible to ± 0.2 mg) and by scanning electron microscopy (SEM) to determine the influence of crystal structure and of grain size.

Results and Discussion

Face Centered Cubic Metals

Face centered cubic (fcc) metals and alloys are isotropic and, of the three common metallic structures, the least sensitive to strain rate. Consequently, their response to cavitation is similar to their ambient temperature behavior in that they are highly ductile and fail by a void growth and coalescence mechanism [*13*] or a ductile rupture mechanism [*14*].

The specific response of nickel has been described in detail elsewhere [*14*]. Its surface becomes heavily distorted on exposure to cavitation and, for grain sizes greater than ~ 50 μm, the craters produced by the deformation are independent of grain orientation, the presence of grain boundaries, and the grain size. Figures 1*a* and 1*b* show the craters formed on specimens of 150 and 50 μm grain size, respectively, after 3 h exposure and illustrate the similarity in crater size. The erosion rate of nickel is, therefore, also independent of grain size, d, for values of $d \leq 50$ μm. For finer grain sizes, however, there is a marked difference in the character of the eroded surface, Figs. 1*c* and 2*b*, and a very rapid increase in erosion resistance, as indicated by the incubation periods, t_o, and rate of mass loss, $\dot{M}$, plotted in Fig. 3. This behavior may be explained as follows. For large-grained specimens, the formation of craters requires macroscopic deformation of only a few grains. Thus, the resistance to crater formation in such specimens depends on the deformation characteristics of the individual grains; that is, the response is like that of a single crystal. In fine-grained specimens, on the other hand, large numbers of grains must be deformed to produce a similar crater and, thus, the erosion behavior would be a reflection of the deformation characteristics of the polycrystalline material, requiring increased stress (or, in the present case, increased time) for a given degree of deformation in decreasing grain-sized specimens. In fact, however, in the very-fine-grained material, craters such as those described previously for nickel, aluminum, and copper [*15*] do not develop. Instead, the erosion occurs predominantly at the grain boundaries in a manner similar to that observed in α-brass and described in the following.

The response of Cu-30Zn (α-brass)—which is also fcc—is grain size dependent over the whole range examined. Figure 4 shows that the surface distortion occurs predominantly at the grain boundaries, the interior of the grains remaining relatively flat. This behavior has been attributed to the very

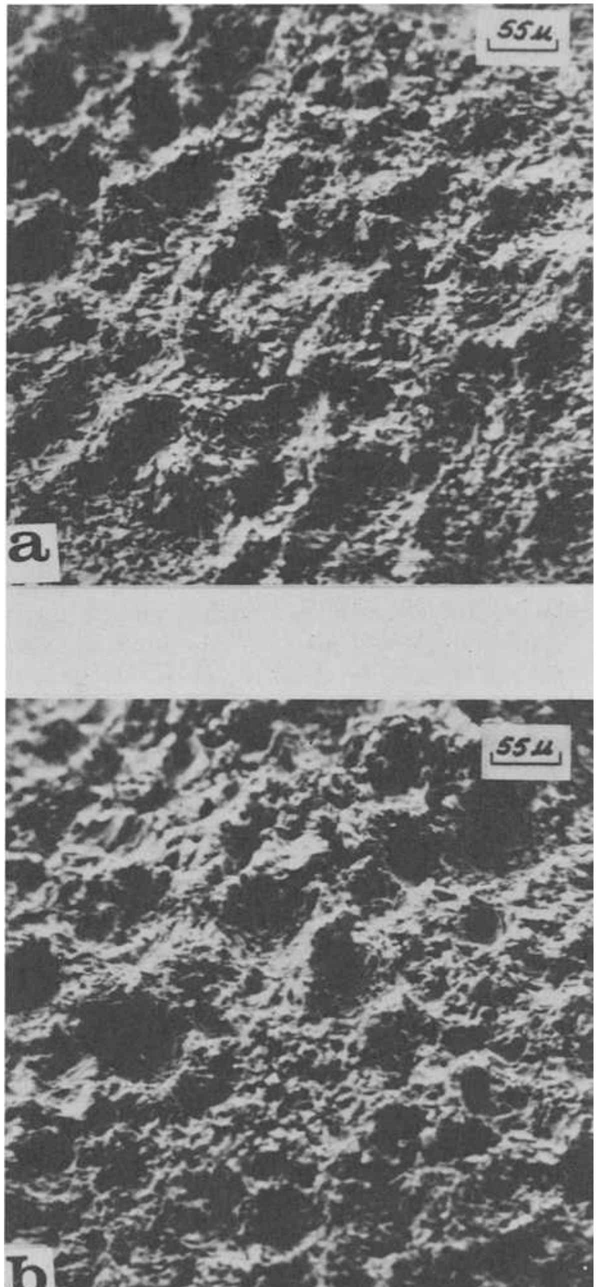

FIG. 1—*SEM's of deformation and erosion of nickel after 3-h exposure to cavitation:* (a) *150-μm* grain size, (b) *50 μm grain size, and* (c) *10-μm grain size.*

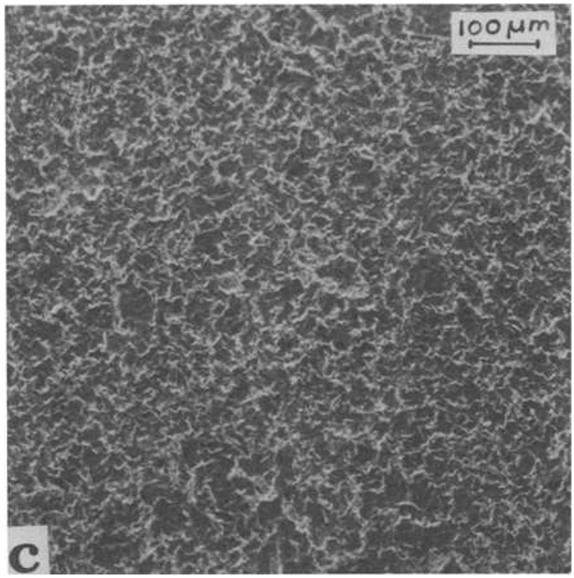

FIG. 1—(*Continued.*)

low stacking fault energy and the resultant planar slip mode of the brass (0.006 J/m^2 compared with 0.08 J/m^2 for nickel) [*13*]. Since the dislocations in Cu-30Zn are restricted to their original slip plane by the large stacking faults, there is relatively little interaction between dislocations, and the major barriers to slip are the grain boundaries. Thus, it is at the grain boundaries that sufficiently high stress concentrations to allow cross slip occur, thereby producing the surface distortion which subsequently results in ductile rupture.

Since the material loss occurs at the surface protuberances and these are confined to the grain boundary areas in brass, there is a significant effect of grain size on the erosion rates as indicated by the data in Fig. 5. One might intuitively expect the erosion to decrease with increasing grain size on the basis that large-grained specimens have a smaller grain boundary area than fine-grained specimens in contrast to the observed trend of increasing erosion with increasing grain size. However, the surface distortion requires a high degree of multiple slip, which, in the case of a low stacking fault energy material, requires a high effective shear stress to enable the dislocations to cross slip. The effective shear stress produced by a pileup of dislocations at a barrier (for example, at a grain boundary) is given by

$$\tau_e = (\tau_a \text{-} \tau_f)\left(\frac{d}{x}\right)^{1/2} \tag{1}$$

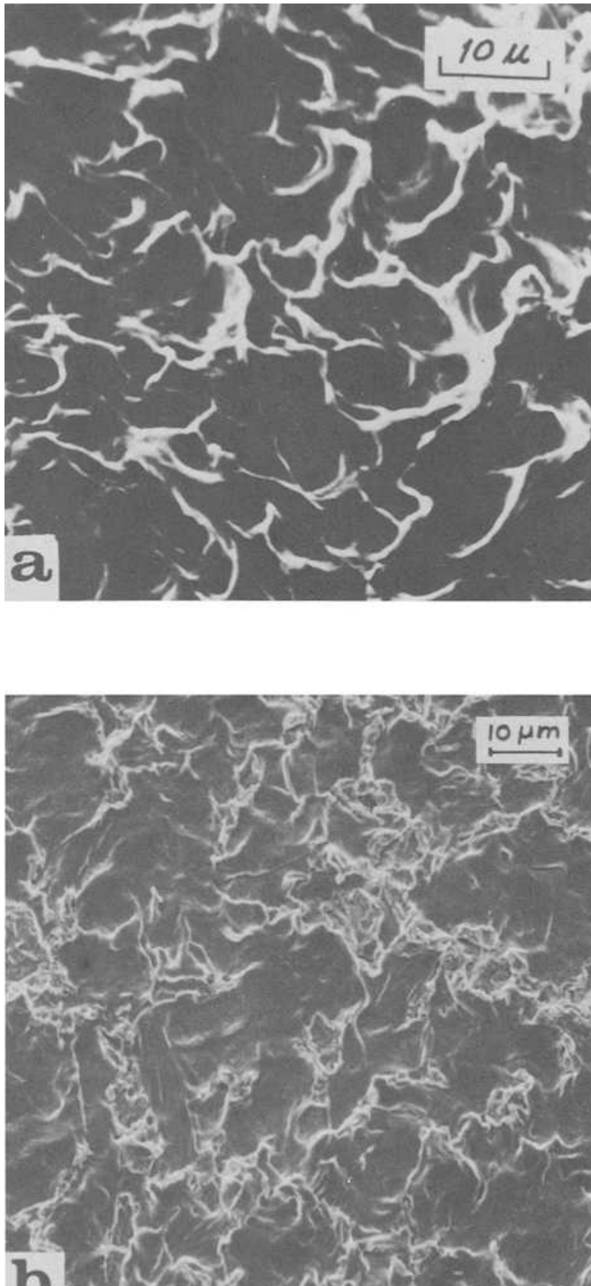

FIG. 2—*SEM's of* (a) *craters formed in 150-µm grain size nickel by cavitation and* (b) *grain boundary erosion in 10-µm grain size nickel.*

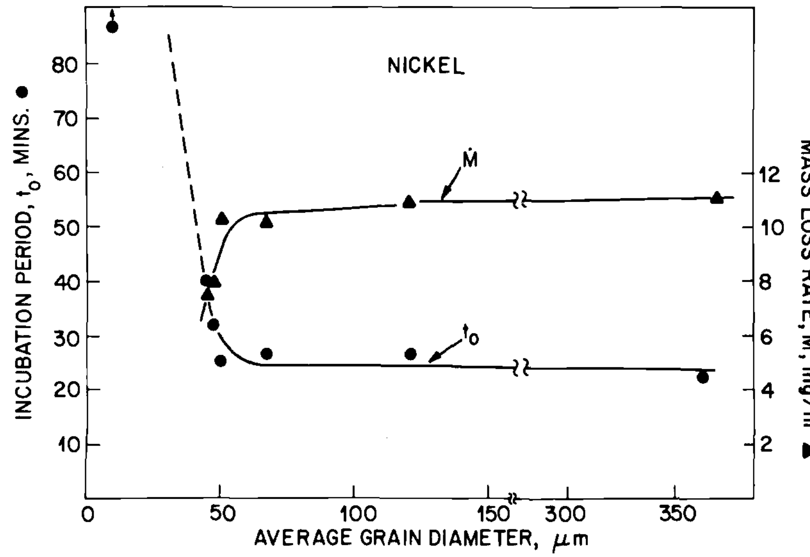

FIG. 3—*Incubation period,* t_o, *and rate of mass loss,* M, *of nickel as a function of its grain size,* d.

where

τ_a = applied shear stress acting of the pileup,
τ_f = lattice friction stress,
d = distance between dislocation source and barrier, and
x = distance between leading dislocation and barrier [16].

The maximum value of d is the grain diameter, and thus the maximum effective shear stress for a constant applied stress will increase with increasing grain size. Both the time necessary to produce a measurable mass loss (t_o) and the subsequent rate of mass loss ($\dot{M}$) will obviously be related to the stress level produced by deformation, explaining the observed trends in t_o and $\dot{M}$. The plot of t_o versus $d^{1/2}$ is, in fact, linear as shown in Fig. 6, thereby confirming the relationship in Eq 1.

Body Centered Cubic Metals

The body centered cubic (bcc) metals are also isotropic but, unlike the fcc metals, their deformation is highly strain-rate sensitive. The response of any material to an applied stress is always a competition between flow (deformation) and fracture and, as the temperature is decreased or the strain rate increased, flow, which is thermally activated, becomes more difficult so that there is an increased tendency toward brittle fracture. It appears from the present experiments on zone-refined iron that the strain rate produced by

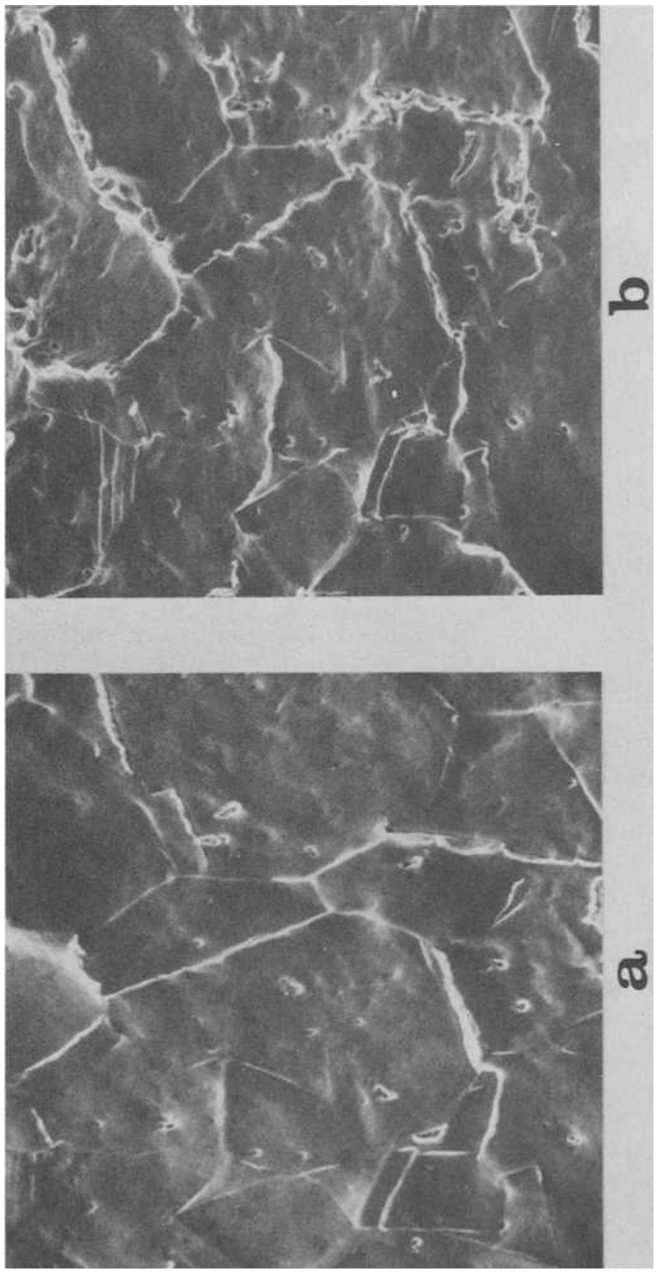
a
b

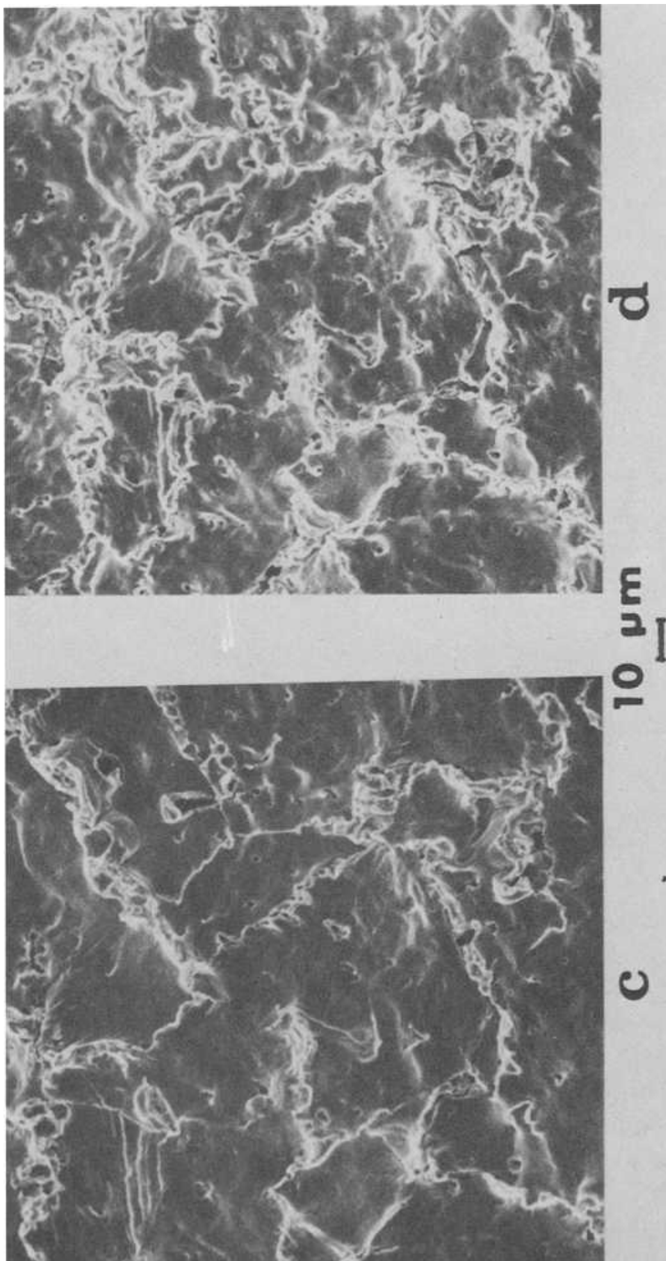

FIG. 4—SEM's of development of erosion of Cu-30Zn by increasing exposure to cavitation for (a) 48 min, (b) 81 min, (c) 109 min, and (d) 144 min.

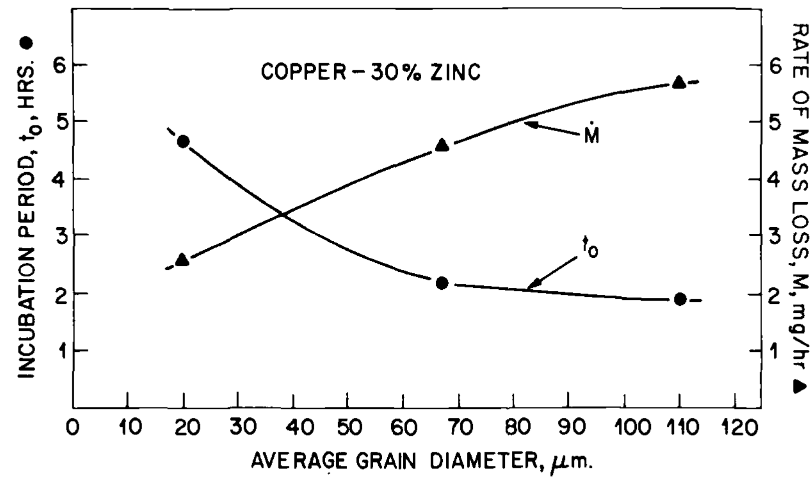

FIG. 5—*Incubation period,* t_0, *and rate of mass loss,* $\dot{M}$, *of Cu-30Zn as a function of its grain size,* d.

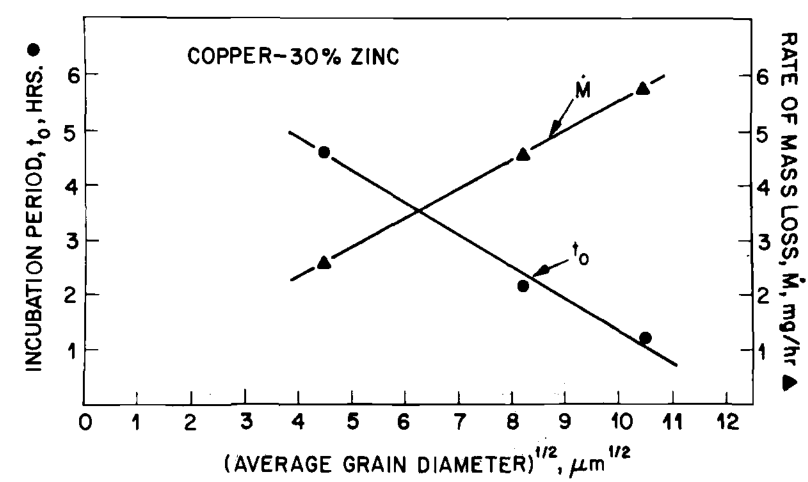

FIG. 6—*Incubation period and rate of mass loss of Cu-30Zn plotted as a function of* $d^{1/2}$.

cavitation approximates the transition from ductile to brittle behavior. The intriguing result of this is that two different modes of material removal occur in the same specimens, as illustrated in Fig. 7. The iron exhibits a high degree of deformation, predominantly by twinning, which is also characteristic of high strain rates. Then, usually, the first detectable material loss occurs by a ductile mechanism, similar to that produced in fcc metals. This loss is initiated at twins and grain boundaries, Fig. 8, and results in the severe surface distortion shown in Fig. 7*c*. While the deformation occurs uniformly

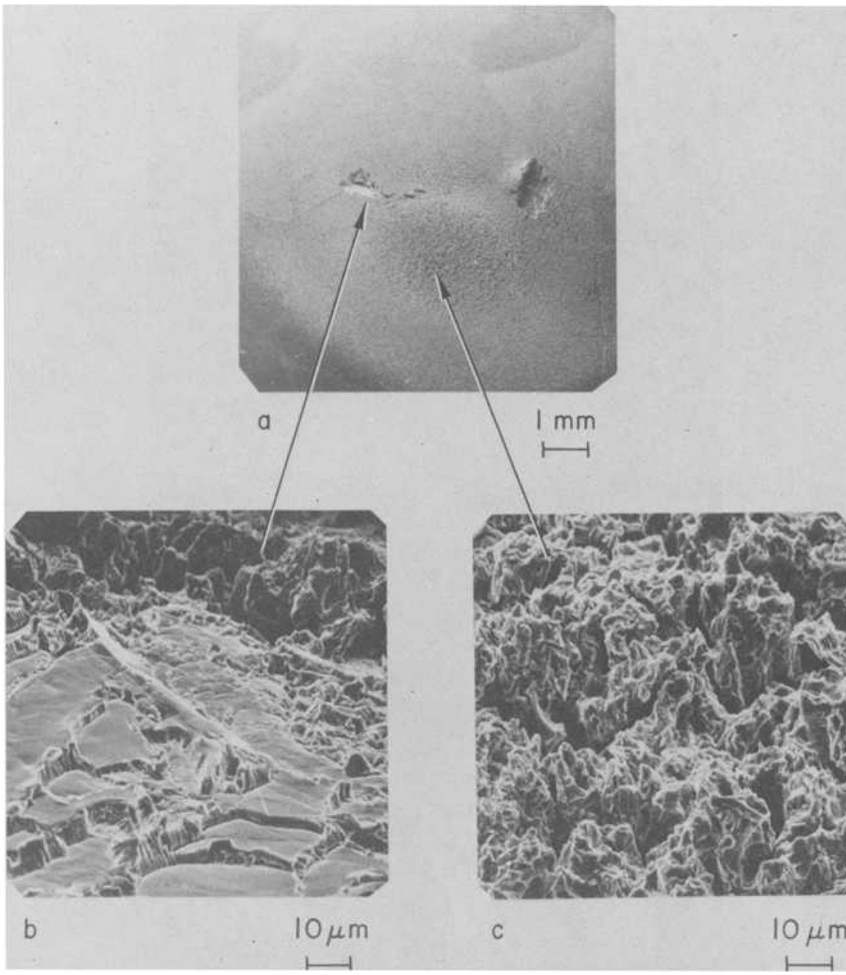

FIG. 7—*SEM's of* (a) *surface of iron after 4½-h exposure to cavitation, showing two modes of erosion* (b) *by brittle fracture and* (c) *by ductile rupture.*

over the whole surface of a grain, the degree of distortion appears to be somewhat orientation dependent, resulting in slightly different degrees of erosion in different grains. This effect can be seen in the large-grained specimen in Fig. 7*a*, but at later times is no longer visible. Therefore, the grain orientation effect would not be likely to produce any significant dependence of erosion rates on grain size.

The second mode of material removal, which results in a greater rate of erosion, is the formation of pits by a cleavage mechanism. The latter are invariably initiated at grain boundaries and propagate rapidly across the grain.

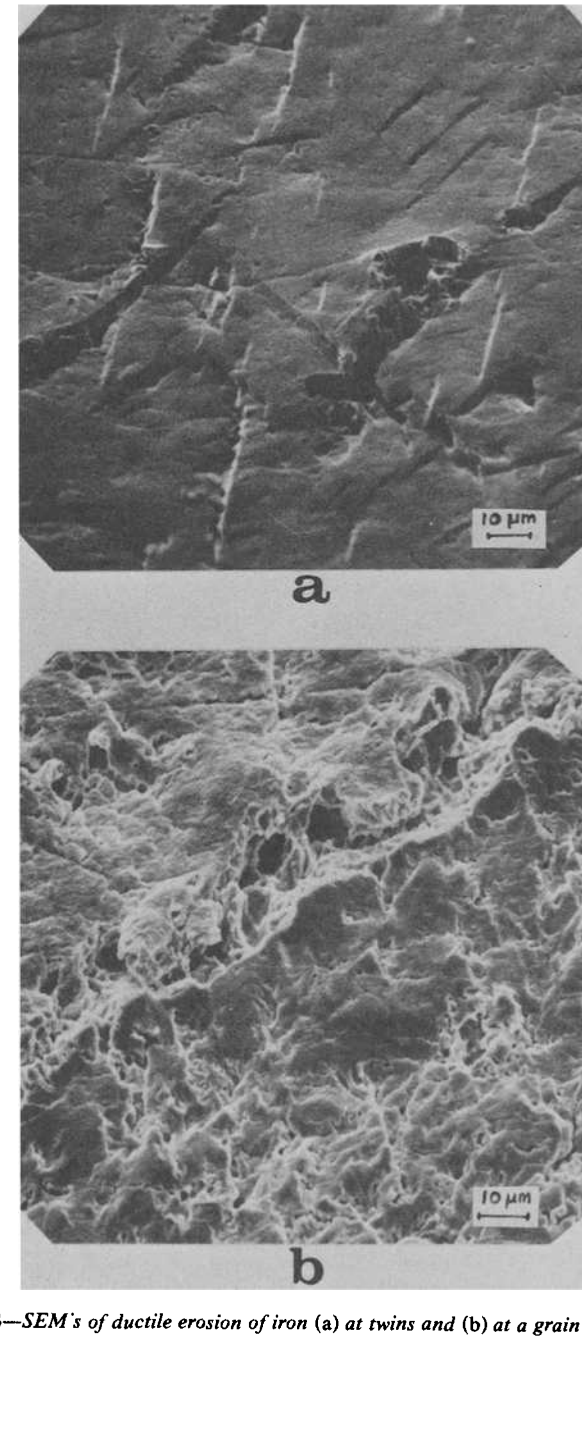

FIG. 8—*SEM's of ductile erosion of iron* (a) *at twins and* (b) *at a grain boundary.*

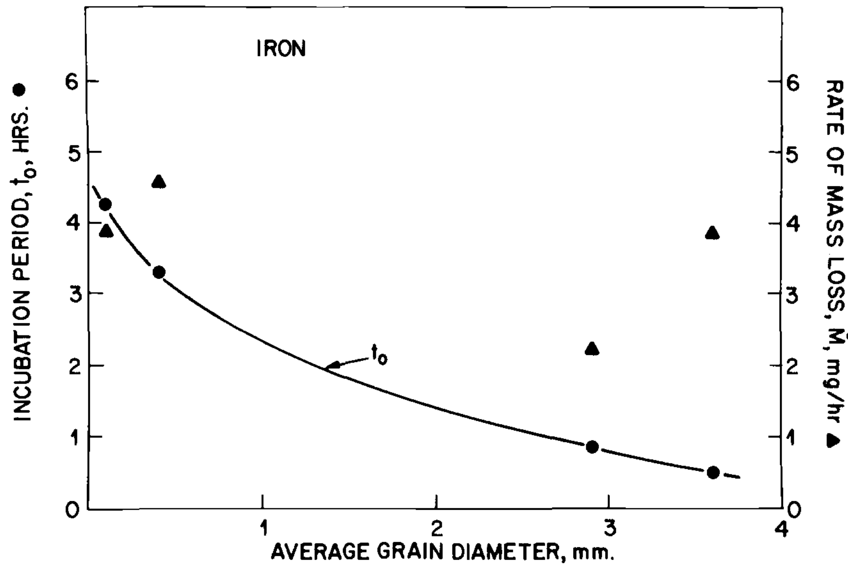

FIG. 9—*Incubation period,* t_0, *and rate of mass loss,* M, *of iron as a function of its grain size,* d.

Erosion by cleavage would, therefore, be expected to be strongly grain size dependent—t_o decreasing with increasing d (for the same reasons as those discussed earlier for brass) and $\dot{M}$ increasing, because of the distance a cleavage crack can propagate before having to change direction at a grain boundary. However, the proportion of mass loss attributable to cleavage varies from specimen to specimen and is not a function of grain size. Thus, a simple grain-size relationship, such as that observed for brass, is not observed. The data in Fig. 9 show that there is a general trend of decreasing t_o with increasing d, but the scatter in the mass loss rate data is so high that no trend is discernable.

Hexagonal Close Packed Metals

Hexagonal close packed (hcp) metals are crystallographically anisotropic to varying degrees, and can be strain rate sensitive, depending on the particular metal. Zinc has an axial ratio of 1.856 compared with that of 1.633 for ideal close packing and is, thus, highly anisotropic. Easy dislocation motion in zinc occurs only on the basal system, $(0001)\langle 11\bar{2}0\rangle$, although other slip modes do become operative if basal slip is inhibited [17]. Cleavage also occurs quite readily on the basal plane and, because of the limited number of basal slip systems and the high critical stresses for pyramidal and prismatic slip which increase further with decreasing temperature [18], zinc undergoes a ductile-to-brittle transition at low temperatures or high strain rates. Consequently, one would expect a highly brittle response of zinc to cavitation, rather than the combination of ductile and brittle erosion described earlier for iron. Nevertheless, although the material removal is always brittle, high densities of slip and twinning are observed in favorably oriented grains, while other grains do not exhibit any deformation or work hardening, Fig. 10. Erosion of zinc occurs by the nucleation of cracks at grain boundary triple points and grain boundary/twin intersections and their propagation across the grain, Fig. 11. The ease of propagation of the crack across the next grain boundary is, of course, dependent on the relative orientation of the two adjacent grains. In many cases the crack is arrested at a grain boundary and does not grow

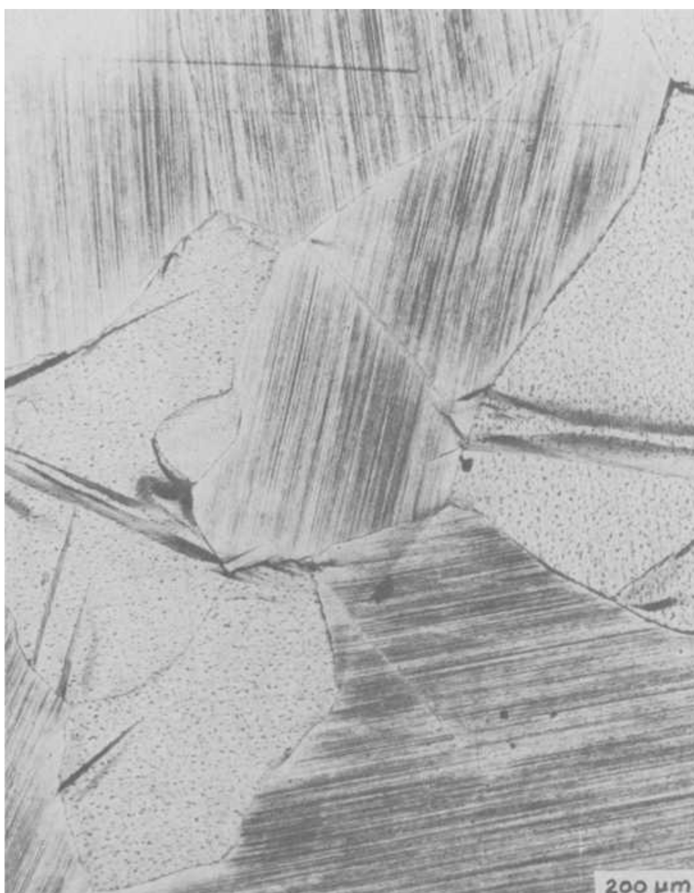

FIG. 10—*Optical micrograph of zinc showing slip in some grains and twins in other grains.*

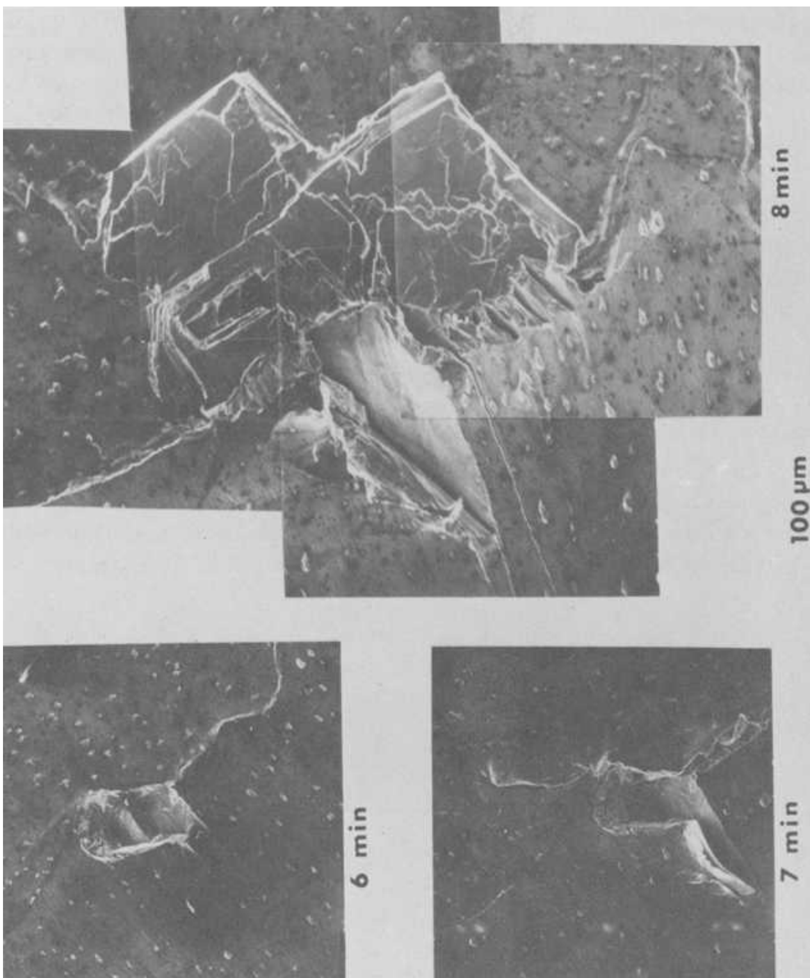

FIG. 11—*SEM's of zinc polycrystal showing the development of erosion by brittle cleavage.*

with continued exposure to cavitation. Continued erosion, therefore, requires the initiation of new cracks.

The reflection of this behavior on erosion rates is illustrated in Fig. 12. In contrast to the trends observed in iron, there is negligible grain size dependence of the incubation period, while the rate of mass loss increases consistently with increasing grain size. This behavior may be explained as follows. In this highly brittle metal, the crack nucleation is not as dependent on prior plastic flow as it is in iron and, therefore, cracks can readily nucleate at any point of local stress concentration. Thus, there are fewer cracks nucleated in large-grained specimens than in fine grained material because the number of such sites, for example, grain boundary triple points, is larger in the latter. However, by the time a reproducibly detectable amount of material removal has occurred, the few cracks in the large grains have grown more than those in the fine-grained specimens, as illustrated in Fig. 13. Thus, the time taken to obtain 0.5 mg mass loss[5] is approximately the same for all specimens. Moreover, this trend continues and, because the cracks generally propagate rapidly across one grain, the rate of mass loss at later times increases with increasing grain size.

The equilibrium structure of cobalt at room temperature is also hcp, but the metal undergoes a phase transition to the fcc structure at 417°C. There is always some of the metastable fcc phase retained in polycrystalline cobalt at room temperature, but it has been shown [*19*] that this phase rapidly transforms to the equilibrium hcp structure on exposure to cavitation and that the erosion rate of cobalt is not affected by the initial fcc content.

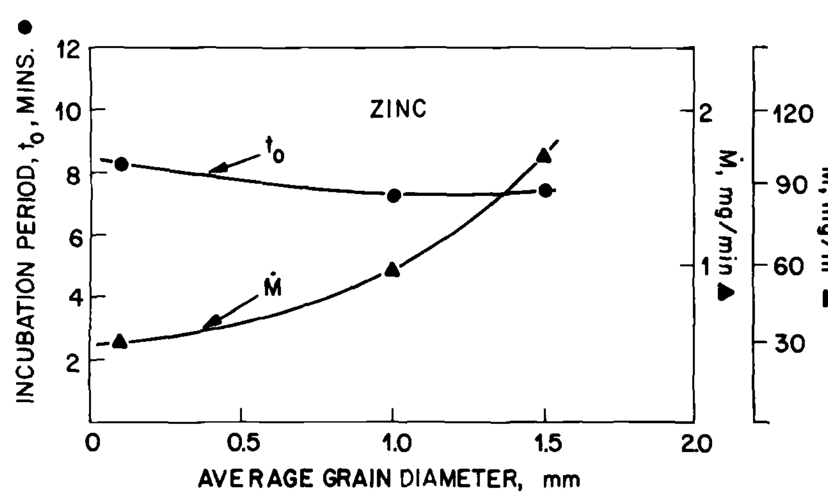

FIG. 12—*Incubation period,* t_0, *and rate of mass loss,* $\dot{M}$, *of zinc as a function of its grain size,* d.

[5]Which is used to denote the incubation period, t_0.

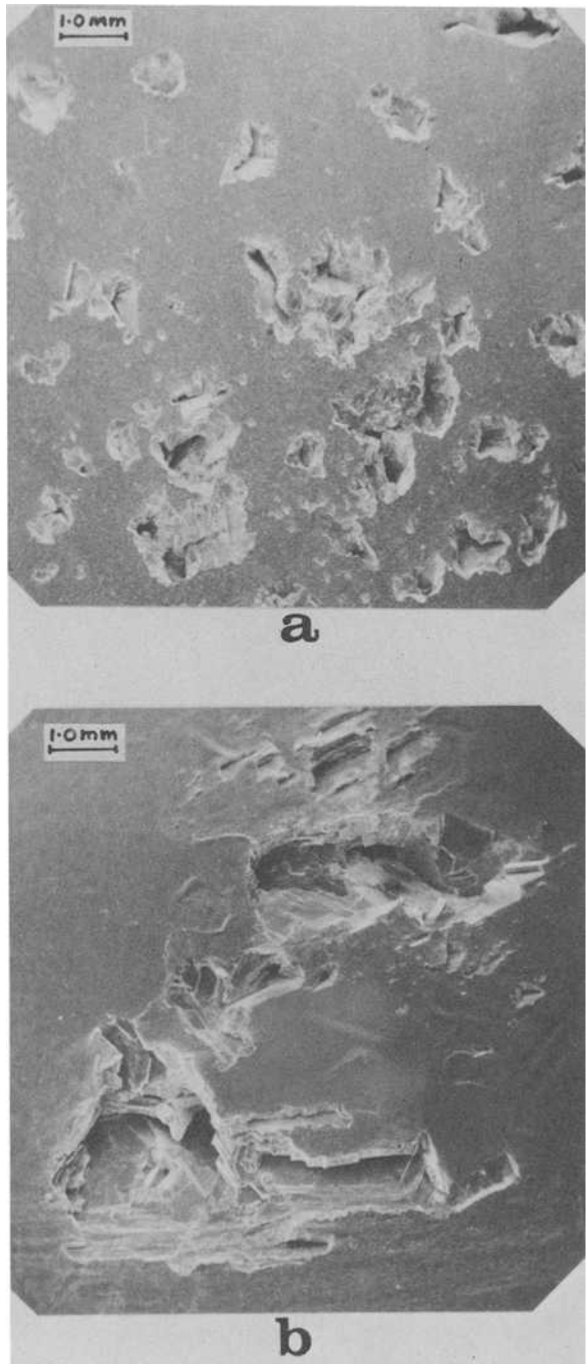

FIG. 13—*SEM's of pits formed in zinc of grain size* (a) *0.1 mm and* (b) *1.5 mm after 40-min exposure to cavitation.*

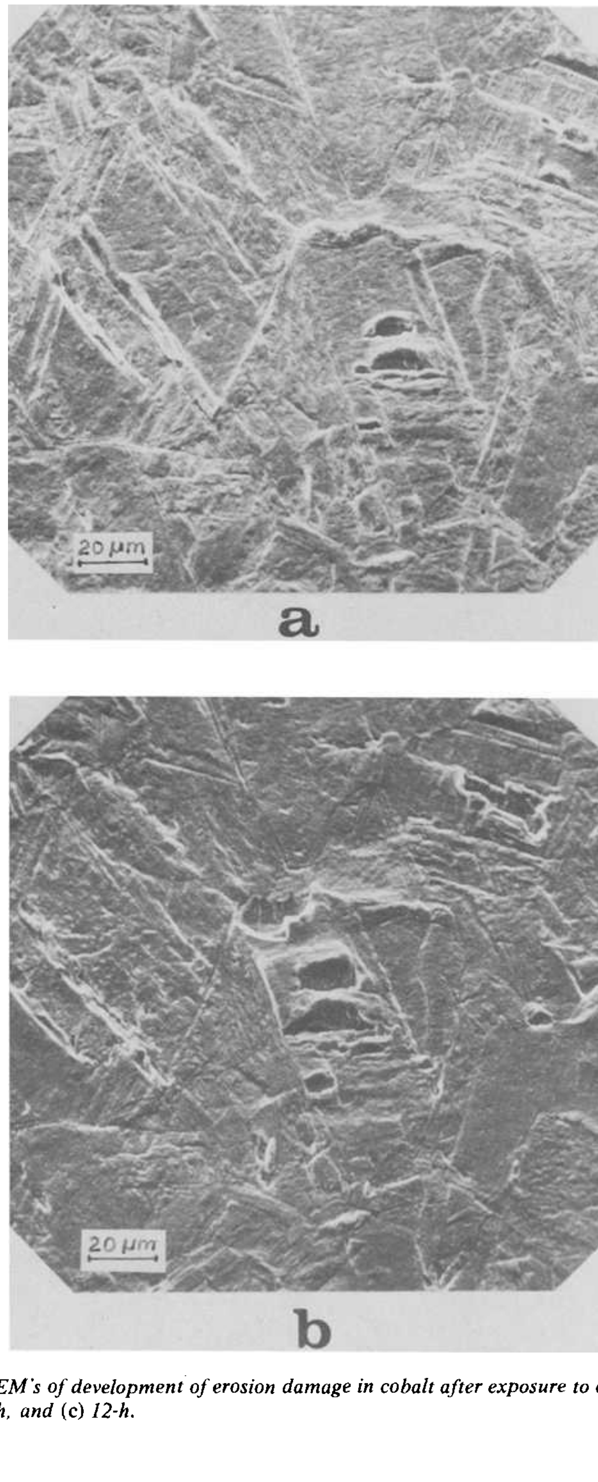

FIG. 14—*SEM's of development of erosion damage in cobalt after exposure to cavitation for* (a) *6-h,* (b) *9-h, and* (c) *12-h.*

FIG. 14—(*Continued.*)

The cobalt hcp phase has an almost ideal axial ratio (1.623) and, as a result, it can slip readily on six systems (basal and second-order pyramidal) and can also twin on six systems. Consequently, cobalt has many more mechanisms of absorbing and dissipating the energy of the cavitation stress pulses than does zinc. Moreover, cobalt apparently does not undergo a ductile-to-brittle transition at low temperatures or high strain rates. The erosion of cobalt is, therefore, by a ductile mechanism as illustrated in Figs. 14 and 15. While the incubation period of the specimens tested was only ~5 h, that is, comparable to that of iron, the subsequent rate of the mass loss was exceptionally low: ~0.097 mg/h. The grain size of these specimens was ~25 μm but the effective grain size was considerably finer. As Figs. 14 and 15 illustrate, the surface of cobalt rapidly develops a high density of surface markings which, because of their orientation and the fact that they are still visible after the surface has been polished, have been identified as twins. Unlike the few large twins which develop in selected grains in zinc, the twins in cobalt appear quite uniformly over the whole surface of the specimen, and their width is too small to be resolved by SEM. Previous transmission electron microscopy (TEM) studies [*19*] indicate that they are in the 0.01- to 0.1-μm range. The twins have the effect of dividing the grains into smaller segments, 0.1 to 1.0 μm in size, and, because of the different orientation of twins relative to the matrix, these segments can be regarded as the effective grain

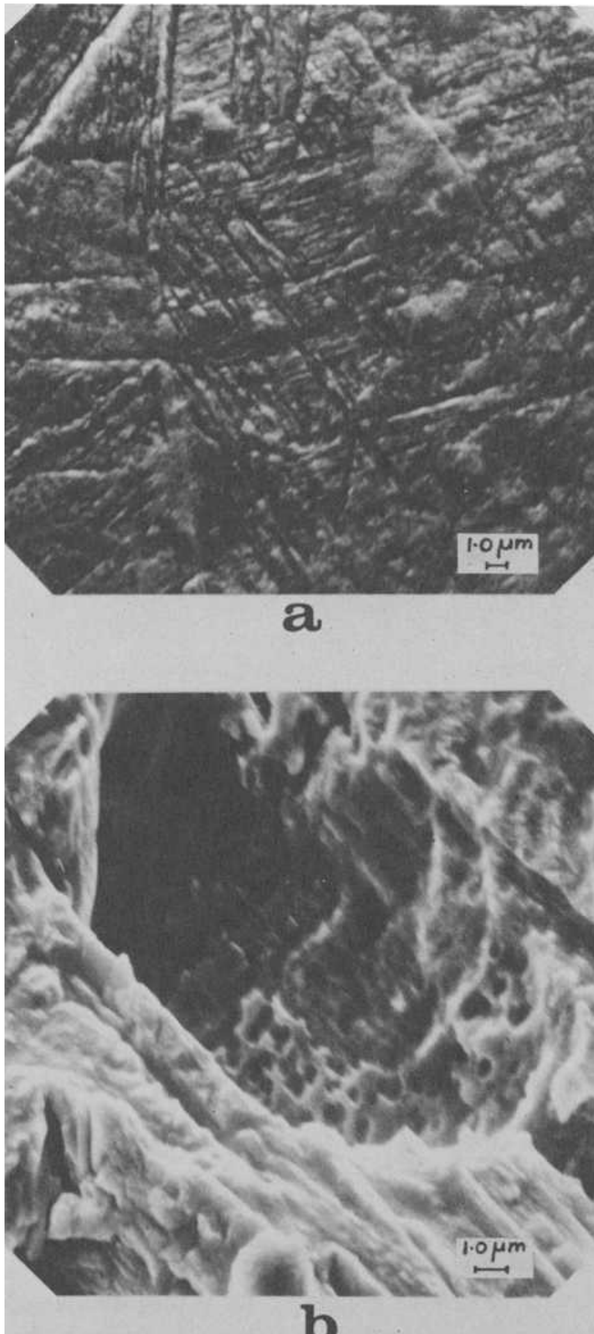

FIG. 15—*SEM's of cobalt showing* (a) *twin formation after 4-h exposure and* (b) *dimpled surface of an erosion pit after 9-h.*

size of the specimen. This very fine structure is presumably responsible for the high erosion resistance of this metal. No attempt has been made to determine whether there is any effect of the original grain size in cobalt because the deformation twin structure produced by cavitation appears to dictate the response of the metal and is independent of initial grain size.

Summary and Conclusions

This investigation has illustrated the importance of three factors—namely, deformation mode, strain rate sensitivity, and grain size—in determining the specific cavitation erosion rates of metals.

The deformation mode determines the ease of absorption of the cavitation impact energy. In the fcc metals, which have 12 easy slip systems, deformation occurs readily. In the nickel, easy cross slip can occur because of its high stacking fault energy. In the large-grained specimens, this results in extensive work hardening leading to local stress concentrations and, hence, to surface distortion throughout the whole surface area. In the fine-grained nickel and the α-brass, on the other hand, the grain boundaries provide the major regions of stress concentration and thereby limit the surface distortion and subsequent erosion to these regions.

In the bcc and hcp metals, extensive twinning occurs but the morphology and subsequent effect of the twins on erosion rates vary from metal to metal. The iron is considerably more ductile than zinc because of its large [*48*] number of possible slip systems. The twins in iron are needle-like or lenticular with very large aspect ratios, and they are not observed to grow in length or thickness with increased exposure to cavitation. The major effect of the twins is to produce surface relief, which in turn becomes the site for erosion by ductile rupture. The twins in zinc are also lenticular but are broader than those in iron and grow in thickness with increased exposure to cavitation. In addition, secondary twins develop within the primary twins. The limited number of slip and twin systems in zinc results in a few very large twins growing in the favorably oriented grains, with other grains deforming only by slip. The high stress concentrations developed at twin/grain boundary intersections and at triple points between grains with differing degrees of deformation readily lead to brittle cracking in this highly strain-rate-sensitive metal.

In contrast, cobalt, which has more slip and twinning modes than zinc, and is relatively strain-rate insensitive, is highly ductile. However, the fragmentation of the grains to a submicrometre level by the twins confines the development of surface asperities to this scale and also precludes the buildup of the requisite stress concentrations for crack nucleation.

It is apparent from the present results that grain size can play a major role in determining erosion resistance. In all structures examined, there is a general trend of increasing resistance with decreasing grain size, but the

TABLE 2—*Erosion data for comparable grain-size materials.*

Material	Structure	Grain Diameter, μm	t_o, h	$\dot{M}$, mg/h	Mechanism
Nickel	fcc	120	0.40	9.00	ductile
Cu-30Zn	fcc	110	1.88	5.76	ductile
Iron	bcc	100	4.25	3.58	mixed
Zinc	hcp	100	0.14	30.00	brittle
Cobalt	hcp/fcc	25	5.00	0.097	ductile

specific increase is dependent on the actual mechanism of erosion as indictated by the t_o and $\dot{M}$ values in Table 2. It is obvious from the data for zinc and, to a lesser extent, for iron, that a highly brittle response is extremely detrimental. This is because brittle cracks can propagate at the stress wave velocity of the solid, and erosion by this mechanism involves the removal of large particles of metal.

In the very-fine-grained nickel and cobalt, however, the dimensions of any surface distortion are severely limited by the grain (or effective grain) size. Thus, erosion is by the removal of very tiny particles, and the corresponding erosion resistance is, consequently, very much higher.

In summary, it is obvious from these results that any simple correlation between bulk quasi-static mechanical properties and cavitation erosion resistance is highly unlikely. The response to cavitation is much more dependent on deformation mode and strain-rate sensitivity than are most mechanical properties, and it has a more complex grain size dependence than do the latter. However, it may be concluded that a highly ductile material, with a high critical stress for dislocation motion and a very fine effective grain size, will exhibit the greatest erosion resistance.

Acknowledgments

The author would like to thank the International Nickel Corp. for the nickel, the Olin Corp. for the brass, Battelle Columbus Laboratory for the iron, and the Stellite Division of Cabot Corp. for the cobalt used in this investigation. The second author wishes to express her appreciation to Zonta International for the Amelia Earhart Aerospace Fellowship. This work was supported in part, by the National Science Foundation under Grant No. DMR 72-03227A01.

References

[1] Hobbs, J. M. in *Erosion by Cavitation or Impingement, ASTM STP 408,* American Society for Testing and Materials, 1967, pp. 159-185.

[2] Rheingans, W. J., *Transactions*, American Society of Mechanical Engineers, Vol. 72, 1950, p. 705.

[3] Garcia, R. and Hammitt, F. G., *Transactions*, American Society of Mechanical Engineers, Vol. 89D, 1967, p. 753.
[4] Lichtman, J. Z. and Kallas, D. H. in *Proceedings*, Symposium on Cavitation Research Facilities and Technology, American Society of Mechanical Engineers, 1964, p. 185.
[5] Gould, G. C. in *Characterization and Determination of Erosion Resistance, ASTM STP 474*, American Society for Testing and Materials, 1970, pp. 182-211.
[6] Tickler, J. W., Vander Elsen, J. B., and deGee, A. W. J., *Transactions*, American Society of Mechanical Engineers, Vol. 92F, 1970, p. 220.
[7] Thiruvengadam, A., *Transactions*, American Society of Mechanical Engineers, Vol. 88B, 1966, p. 332.
[8] Marriot, J. B. and Bowden, G., *Philosophical Transactions of the Royal Society*, London, Vol. 260A, 1966, p. 144.
[9] Eisenberg, P., *Transactions*, Society of Naval Architects and Marine Engineers, Vol. 73, 1965, p. 241.
[10] Busch, H., Hoff, G., and Langbien, G., *Philosophical Transactions of the Royal Society*, London, Vol. 260A, 1966, p. 168.
[11] Thiruvengadam, A., *Transactions*, American Society of Mechanical Engineers, Vol. 85D, 1963, p. 365.
[12] Vyas, B. and Preece, C. M., *Journal of Applied Physics*, Vol. 47, 1976, p. 5133.
[13] Vyas, B. and Preece, C. M. in *Erosion, Wear, and Interfaces with Corrosion, ASTM STP 567*, American Society for Testing and Materials, 1974, pp. 77-105.
[14] Dakshinamoorthy, S., M. S. thesis, Department of Materials Science, State University of New York at Stony Brook, N.Y., 1975.
[15] Vyas, B. and Preece, C. M., *Metallurgical Transactions*, Vol. 8A, 1977, p. 915.
[16] Cottrell, A. H., *Dislocations and Plastic Flow in Metals*, Clarendon Press, Oxford, U.K., 1963, p. 107.
[17] Bell, R. L. and Cahn, R. W. in *Procceedings of the Royal Society*, London, Vol. A239, 1957, p. 494.
[18] Salita, O., *Soviet Materials Science*, Vol. 31, 1971, p. 190.
[19] Chandrasekeran, S., M.S. thesis, State University of New York at Stony Brook, N.Y., 1974.

DISCUSSION

D. A. Summers[1] (*written discussion*)—Do you have any information on the bubble size in the test you ran and the potential effect on your results were this size to change? I would relate this particularly to the work reported in this publication (p. 320) by Gorham from Cambridge on the effect of droplet size on threshold pressure and also to the earlier work on cavitation bubble size done at Cambridge and reported at the Royal Aircraft Establishment Rain Erosion Conference.[2]

During the course of the discussion, Frank Heymann commented that a rough calculation of reentrant jet diameter from cavitation bubbles is about

[1]Rock Mechanics and Explosives Research Center, University of Missouri-Rolla, Rolla, Mo. 65401.

[2]Brunton, J. H., *Proceedings*, 3rd International Conference on Rain Erosion and Allied Phenomena, A. A. Fyall and R. B. King, Eds., Royal Aircraft Establishment, Farnborough, U.K., 1970.

60 μm. How does the reentrant jet diameter change with cavitation bubble diameter?

C. M. Preece, S. Vaidya, and S. Dakshinamoorthy (*authors' closure*)—We have not attempted to determine the bubble size in these experiments because of the difficulty of focusing on the bubbles in the interior of the cloud rather than on those on the periphery (which are often those which have grown to supercritical size and "escape" to the surface instead of collapsing). However, experiments by Professor Hammitt and others suggest that they are of the order of 10 to 25 μm in diameter. The jet diameter from such bubbles should be no more than about one tenth of the bubble diameter, that is, $\simeq 1$ to 2.5 μm. The experiments on single bubbles involve much larger, artificially produced bubbles, and I assume that these are the ones which Mr Heymann was considering with a jet diameter of 60 μm.

Regarding the effect of bubble size on erosion damage (compare Gorham's work on droplet size), this would be considerable in situations in which the individual bubbles and their jets are the major cause of damage, for example, in a low-intensity flow system. In the present experiments, in which the concerted collapse of large numbers of bubbles is the dominant cause of erosion, the answer is not so simple. While the shock-wave pressures from a single bubble are proportional to the cube of its maximum radius, those from a cloud of bubbles will also depend on the number and spacing of the bubbles. Dr. K. A. Mørch of the Technical University of Denmark is currently working on this problem and we hope to have the results of his efforts shortly.

G. Mayer[3] (*written discussion*)—If your argument about the level of stresses and cross slip etc. at or near grain boundaries in the cavitation of brass specimens is valid, I would expect the presence of large deformation twins, with a material of such low stacking fault energy. Are they there? Do they contribute to reducing or enhancing cavitation resistance?

If cobalt is very effective in its cavitation resistance, and Cu-30Zn is not, it seems that the ability to *nucleate* twins, rather than to *propagate* them, may be an important factor.[4]

Also, in comparing cavitation resistance, perhaps some sort of homologous temperature should be considered.

C. M. Preece, S. Vaidya and S. Dakshinamoorthy (*authors' closure*)—Yes, we do observe large deformation twins in brass and they probably contribute to the erosion in several ways. Firstly, their actual formation will absorb some of the incident cavitation energy. Secondly, they subdivide the grains, reducing the effective grain size, but since they are relatively few and quite coarse they do not have as significant an effect as do the numerous

[3]Army Research Center, Research Triangle Park, N. C. 27709.

[4]It is probably easier to nucleate twins by deformation in cobalt, whereas it is difficult to nucleate twins by deformation in many brasses but easy to propagate them.

fine twins in cobalt. Thirdly, the surface relief produced by the twins, together with the dislocation barriers created by their boundaries, results in the twins being preferred sites for erosion.

In fact, both the brass and the cobalt are more erosion resistant than expected from their mechanical properties, which suggests that a low stacking fault energy and the ability to twin may both be important properties. The fact that cobalt is so much more erosion resistant does, however, imply that ease of nucleation of twins rather than their growth may be significant, as you suggest. This is a subject which we are continuing to investigate.

Regarding the homologous temperature suggestion, we considered this factor also, but, in cavitation in water, the useful temperature range ($\simeq 10$ to $90\,^\circ C$) is too small to be significant.

Masanobu Matsumura[1]

Influence of Test Parameters in Vibratory Cavitation Erosion Tests

REFERENCE: Matsumura, Masanobu, "**Influence of Test Parameters in Vibratory Cavitation Erosion Tests**," *Erosion: Prevention and Useful Applications, ASTM STP 664*, W. F. Adler, Ed., American Society for Testing and Materials, 1979, pp. 434–458.

ABSTRACT: A series of tests on iron and steel in a water tunnel system, which simulated field conditions quite closely, showed that each material has its own process of erosion, and that in general the fracture of metals by cavitation turns from ductile to brittle with the lapse of testing time.

Fractures of iron and steel in the vibratory method turned, as in the water tunnel, from ductile to brittle. It was found also that the ductile-brittle transition is decisively influenced by experimental parameters such as temperature of the test liquid, frequency of the vibration, and corrosiveness of the test liquid.

Based on these experimental results, it was concluded that, in the vibratory test, the process of damage of a material can be changed to a great extent by choosing appropriate conditions of the test.

KEY WORDS: cavitation erosion, corrosion, water tunnel, vibratory method, iron and steels, ductile fractures, brittle fractures, erosion

The magnetostriction vibratory method is one of the testing methods used to evaluate the resistance of various materials to cavitation erosion. Test specimens are vibrated vertically with high frequency in liquid to induce cavitation on their surfaces. The apparatus and specimens, as well as power consumption for this method, are smaller than those for other methods. The quantity of liquid needed for the test is also so little that tests in molten salt can be carried out relatively easily. Therefore, this method has been widely used as an accelerated test for screening materials. This testing method, however, involves so many parameters (frequency of vibration, amplitude of vibration, temperature of test liquid, etc.) that in 1972 ASTM Committee

[1]Associate professor, Department of Chemical Engineering, University of Hiroshima, Sendamachi, Hiroshima, Japan.

G-2 [*1*][2] recommended a standard procedure and standard parameters of the method in order to correlate and utilize the test results of various investigators. Another disadvantage of the method is that the process of the damage on the test specimen may be different from that observed in practical machines and apparatus, because cavitation is produced in a particular way in this testing method.

The resistance of materials to cavitation erosion is generally described in terms of cumulative weight loss of the test specimen plotted against total time of exposure to cavitation. The fact that the rate of weight loss is not uniform in time was pointed out independently by Thiruvengadam and Preiser [*2*] and Varga and Sebestyén [*3*] at nearly the same time. The authors of Ref *2* divided the cavitation damage process according to the superficial rise and fall of weight loss rate as follows: incubation, acceleration, attenuation, and steady state. Thiruvengadam [*4*] later introduced the "time-scale law" wherein the relation between the relative erosion rate and relative exposure periods for several materials can be reduced to the same curve. Thus, he suggests that the rate-time curves exhibit essentially the same shape with a single narrow peak. Plesset and Devine [*5*] related the attenuation of erosion rate to the phenomenon of hole formation. They showed that the decrease in erosion rate, which is characteristic for the attenuation period, is due to the hydrodynamic damping effect of a stationary gas bubble which had settled in each of the deep holes. Suezawa et al [*6*] also recognized the damping effects of bubbles on the decrease in rate of erosion. Moreover, they proposed four characteristic regions in the damage process according to the growth rate of the holes. Tichler et al [*7*] distinguished between a resistance against uniform material removal and resistance against pit (hole) formation and found a good correlation between these resistances and the mechanical properties of the materials. Thus, the significance of the hole (pit) formation on the rate of erosion is recognized. Hobbs [*8*] found that the maximum erosion rate persists as a steady-state rate for some time rather than forming a narrow peak, as described by Thiruvengadam, and that whereas the less-resistant materials pass straight from the constant-rate period into the final period of decreasing rate, the more resistant Monel metal and stainless steel first show a slight increase in erosion rate before the final falloff. Heymann [*9*] simulated the rate-time curve by a mathematical model, assuming many "surface elements" which are detached from the surface due to subsurface fatigue, and demonstrated that subsequent peaks in the rate-time curve may occur if the distribution of individual times required for their removal has little dispersion. Thus, it is implicitly anticipated that peaks and valleys in the rate-time curves will be closely related to destruction phases, such as the formation of holes, and to the mechanical properties of the material.

[2]The italic numbers in brackets refer to the list of references appended to this paper.

In this paper the relation between the rate-time pattern and the damage process in field conditions was first investigated using a water tunnel.

Process of Damage in Practical Machines and Apparatuses

Experimental Apparatus and Materials

The experimental apparatus chosen was a water tunnel system which simulates closely the state of damage by cavitation in structural materials in the field. The structure and characteristics of the water tunnel system, which was developed by Professor Erdmann-Jesnitzer at the University of Hannover, have already been reported in detail [*10,11*].

The following are the main technical data for the water tunnel:

Cross section of tunnel	40 by 30 mm
Surface area of specimen	30 by 30 mm
Type and dimensions of cavitation exciter	semicolumns of 15-mm radius
Maximum flow rate	~40 m/s
Liquid	tap water: temperature, 20°C ± 1 (68°F)

The chemical compositions and mechanical properties of Armco iron, mild steel (0.15C), and nodular graphite cast iron (NGCI) used as experimental materials are similar to those given in ordinary textbooks and handbooks.

Change in Rate of Erosion with Lapse of Testing Time

The erosion rate R (weight loss of the specimen per unit time) obtained by differentiating a figure of weight loss of the specimen (W) versus testing time (t) is shown in Fig. 1. The R increases initially and decreases after reaching its maximum value. There exist two maximum values in the R-t curve of Armco iron.

Observation of Damaged Surface

The surface of the specimen eroded was observed under a scanning electron microscope (SEM).

Armco Iron—Figure 2*a* shows the appearance at the testing time of 1 h, that is, just after the incubation period. The surface is considerably deformed plastically. A smooth surface seemingly identical to the polished one obtained on preparing the specimen still exists. No sharp crack is observed. Figure 2*b* shows a specimen after the testing time of 4 h, corresponding to

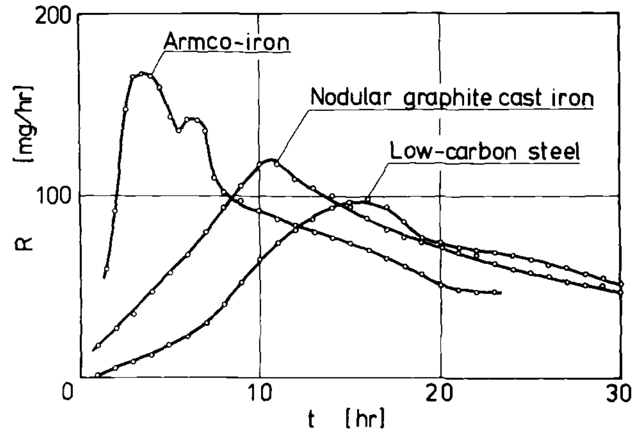

FIG. 1—*Effect of test duration on rate of erosion for iron and steel.*

the vicinity of the first maximum peak in the R-t curve. The appearance of the damaged surface changes drastically. Many small fractured surfaces, small irregular cracks, and cracks of big width are observed. Narrow and smooth fractured surfaces appear on the damaged surface of the specimen exposed to cavitation for a longer time. Figure 2*c* (12 h) shows the smooth fractured surfaces as black spots, one of which, existing in the center, is magnified and shown in Fig. 2*d*. This smooth surface is a "cleavage facet," which is considered to show a typical brittle fracture in the fractography.

Mild Steel—Figure 3*a* shows a specimen after 1 h of incubation, in which large plastic deformation is observed, as in the case of Armco iron, and Fig. 3*b* shows a specimen after 17 h of testing, in which many small fractured surfaces and large and small irregular cracks are observed, as in the case of Armco iron. However, no cleavage facets are observed during all the period of the testing.

NGCI—This material has structure in which spheroidal graphite is surrounded by ferrite surrounded by pearlite. Being attacked by cavitation, graphite, which is mechanically weak, is separated from the surface of the specimen, leaving a small pit there, Fig. 4*a*. From the initial stage of the damage (t = 1 h), smooth fractured surfaces with no plastic deformation appear in ferrite surrounding the small pit, Fig. 4*b*. These smooth fractured surfaces appeared during all the period of the testing, and the many small fractured surfaces observed in Armco iron and mild steel also appeared during nearly all the period of the testing, Fig. 4*c*.

Distribution of Hardness

The distribution of hardness (Vickers hardness, Hv) in a cross section of a specimen after finishing the test is shown in Fig. 5. The testing times are 25 h

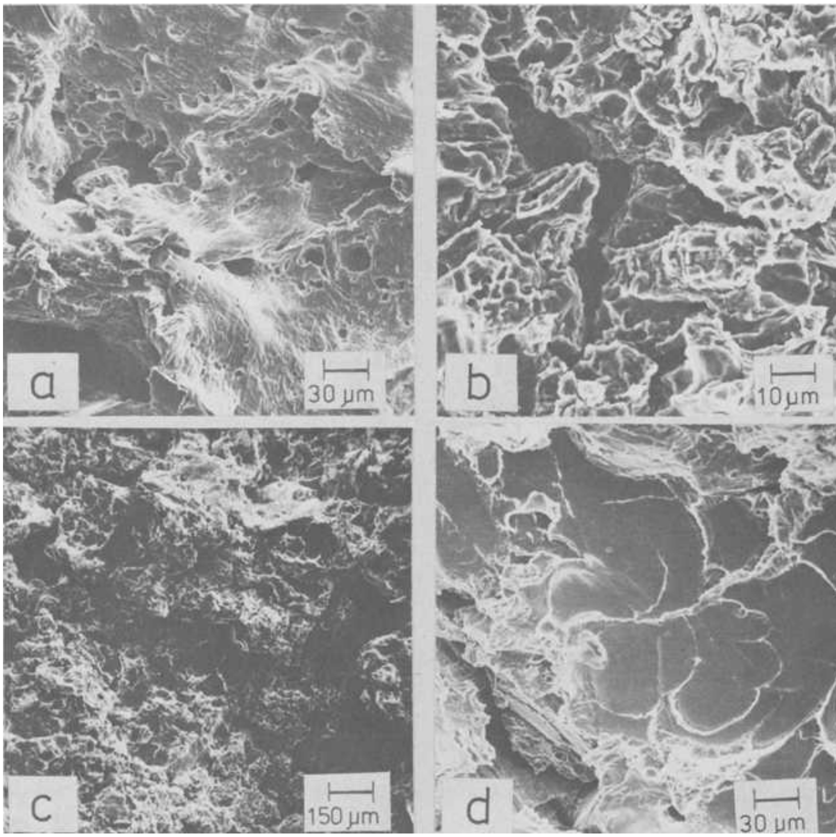

FIG. 2—*SEM's of cavitation damages on Armco iron after different loading times:* (a) *1 h,* (b) *4 h,* (c) *12 h, and* (d) *12 h.*

for Armco iron, 45 h for mild steel, and 30 h for NGCI. In the cases of mild steel and NGCI, hardness was measured in the region of ferrite.

Comparing hardness at places deep inside the specimen not affected by the cavitation, that of ferrite of cast iron is higher than that of other materials. This is due to silicon atoms dissolved in ferrite. The silicon contents revealed by means of X-ray analysis are 0.03 percent by weight in Armco iron, 0.04 in mild steel, and 0.5 in NGCI. The increases in the hardness near the damaged surface are due to the strain hardening caused by the plastic deformation through cavitation attack [*6,12-14*]. The rate of increase in the hardness in the damaged surface of Armco iron is much higher than that of mild steel and that of NGCI, which is in fact nearly negligible. The depths of strain hardening are 800 μm in Armco iron, 700 μm in mild steel, and about 300 μm in NGCI.

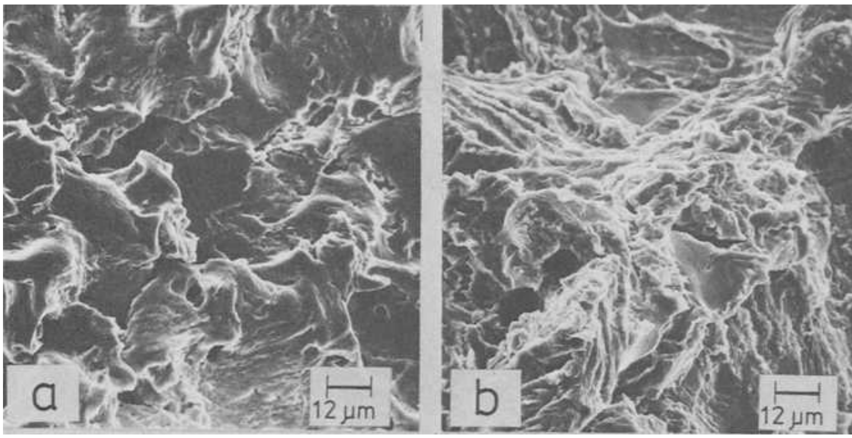

FIG. 3—*SEM's of cavitation damages on low-carbon steel (0.15C) after different loading times:* (a) *1 h and* (b) *17 h.*

The distribution of hardness in a cross section of a specimen of Armco iron tested for only 35 min (before finishing of the incubation period) was measured, Fig. 6. Comparing Figs. 6 and 5, there is not much difference in their rates of increase in the hardness in the damaged surfaces, but the depth of strain hardening is 300 μm after 35 min, which is considerably shallower than 800 μm after 25 h.

Process of Erosion

Because ferrite in NGCI is hard and brittle, the destruction due to cavitation is consistently brittle fracture that shows smooth fractured surfaces. Because Armco iron is ductile metal, its destruction is initially (mainly during the incubation period) ductile with large plastic deformation; then it becomes more brittle with many small fractured surfaces, and thereafter most brittle with relatively large smooth fractured surfaces as in the case of NGCI. The reason that the destruction changes gradually from ductile to brittle is that the material to be destructed becomes harder and more brittle by strain hardening.

Mild steel shows ductile fracture during the incubation period and less-ductile fracture in which many small fractured surfaces appear, but it does not show the stage of the most brittle fracture. The reason for this is revealed by Fig. 7, which shows a crack running along a cross section in a specimen of mild steel (Fig. 7*b* was obtained by etching the same place as in Fig. 7*a*). The crack penetrates about 300 μm deep inside from the left damaged surface. This is deeper than cracks in Armco iron (below 100 μm). It is observed that there are two holes on the line of the crack, that is, the line of the crack runs

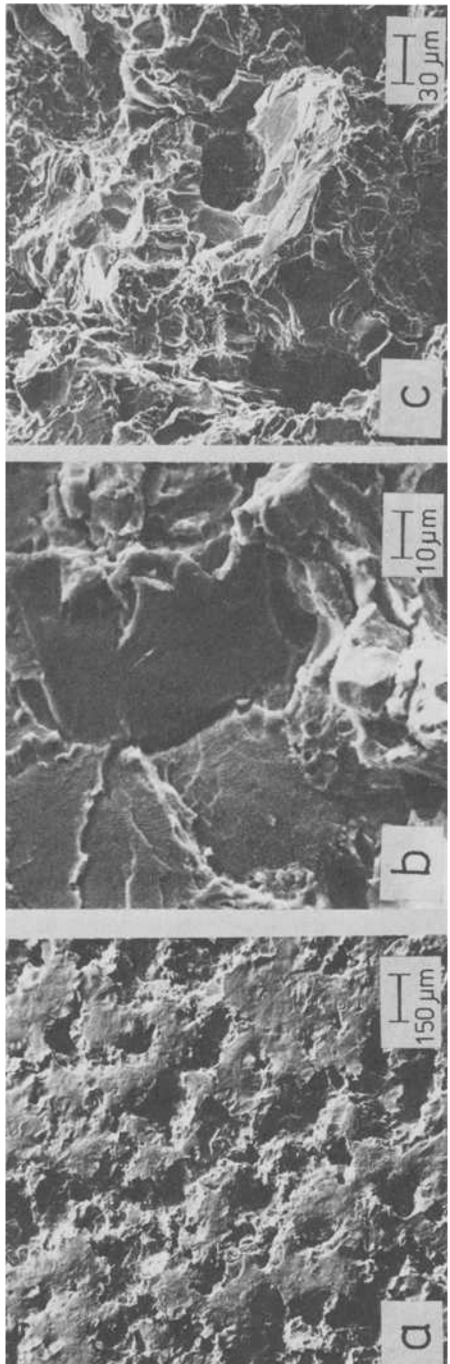

FIG. 4—*SEM's of cavitation damages on NGCI after different loading times:* (a) *1h,* (b) *1 h, and* (c) *4 h.*

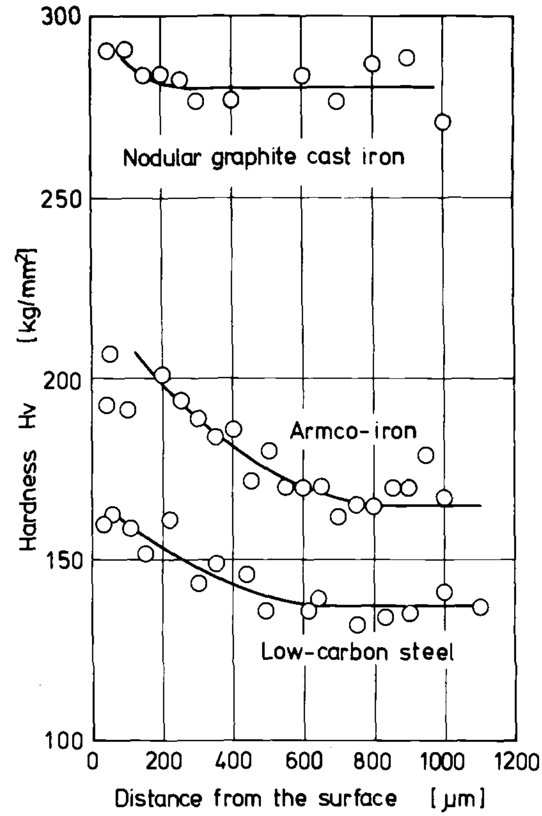

FIG. 5—*Change in hardness of specimens after cavitation test.*

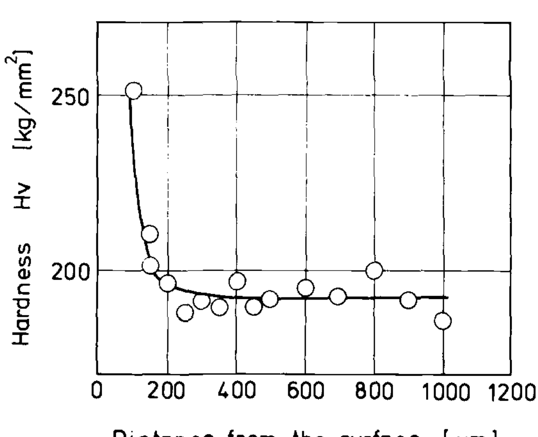

FIG. 6—*Change in hardness of Armco iron specimen after a loading time of 35 min.*

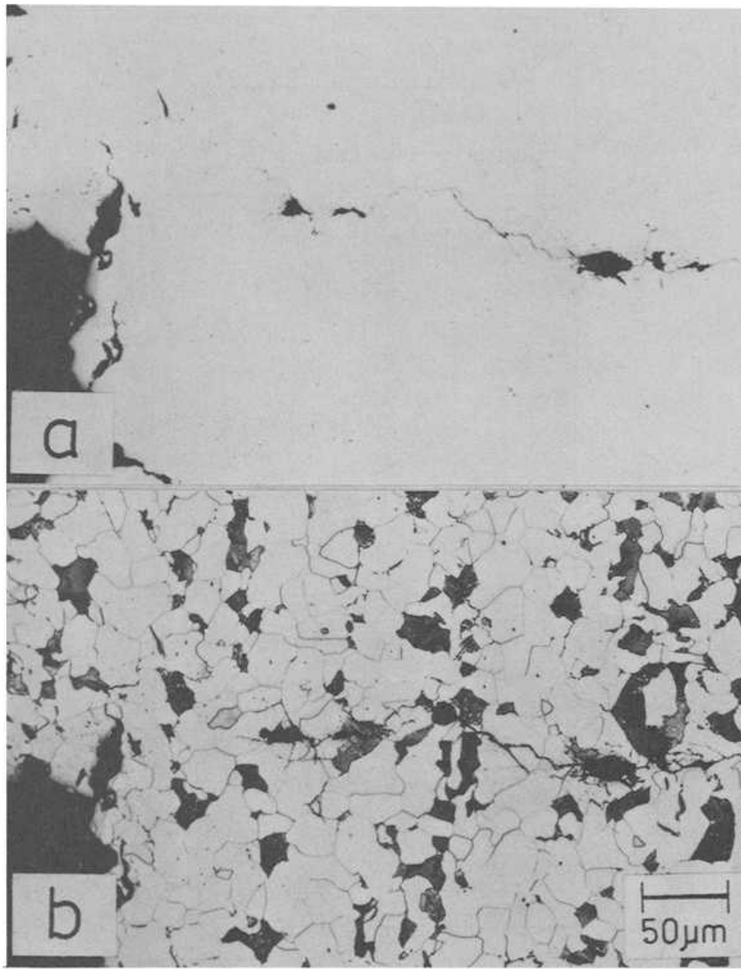

FIG. 7—*Optical micrographs of cavitation damage on low-carbon steel (0.15C).*

passing the holes. Such deep cracks passing holes are observed at various places in the cross section of the specimen. Besides, holes without cracks are also observed. SEM observations have revealed that the holes are in the region of pearlite crystal. Pearlite deep inside the material disintegrates from the attack of cavitation, and crack runs passing the disintegrated pearlite cause the separation of the material. Therefore, the material is less hardened than Armco iron and the stage of the most brittle fracture is not attained in this material.

From the facts described in the foregoing, it is known that the process of erosion of metallic materials, in the case of ductile metals, changes gradually from ductile to brittle fracture and that the characteristics of the materials such as hardness, strain hardenability, and metallographic structure determine how the process of erosion changes.

A fact worthy of remark is that, after having passed the incubation period, two maximum peaks appear in the R-t curve of Armco iron, which has two stages of fracture, and one maximum peak appears in those of NGCI and mild steel, which have one stage of fracture.

Process of Damage in the Magnetostriction Vibratory Test

Experimental Apparatus and Procedures

The details of the experimental apparatus and procedures have been reported previously [15]. The main technical data of the magnetostriction vibratory apparatus are as follows:

Vibration frequency and amplitude	6.5 kHz: 69 μm, 10.1 kHz: 55 μm, 19.9 kHz: 28 μm
Diameter of specimen	16 mm
Submersion depth of a specimen into a liquid	3mm
Liquid	deionized water of specific resistance over 5 by 10^6 Ω cm; temperature, 40 °C ± 1 (104 °F)

Change in Rate of Erosion with Lapse of Time

Figure 8 shows the relation between the rate of erosion, R, and the time of the test, t, obtained at a constant temperature of 40°C (104°F). Aluminium of 0.35 percent by weight was added to the Armco iron mentioned previously, which was designated as iron here. Cast iron used here is gray cast iron. As stainless steel, 18Cr-9Ni steel is used. Unlike the case of the water tunnel, the R-t curve of mild steel (0.13 °C) has two maximum peaks and that of iron

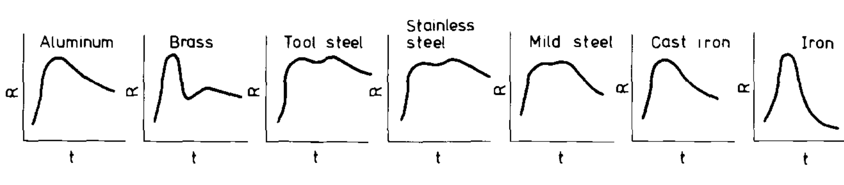

FIG. 8—*Rate-time curves for different materials [frequency: 19.9 kHz, amplitude: 28 μm, test liquid: water, 40°C (104°F)].*

has only one peak. This fact suggests that the process of damage in the magnetostriction vibratory method is different from that of the water tunnel method.

Change in Damaged Surface with Lapse of Time

As already reported by the present author and other investigators, in the magnetostriction vibratory test the roughness of the damaged surface increases initially and then many small holes of diameters smaller than 1 mm appear on the surface [*5,6,14*]. Figure 9 shows a relationship between the total area of small holes, *a*, on the surface of an iron specimen tested at 40°C and the time of testing, *t*. The curve of *a* versus *t* can be divided into four stages, at each of which the curve can be expressed approximately by a straight line. During the first period (a), only the roughness of the damaged surface increases but no holes appear. In the (b) period, a few small holes appear in the central region of the specimen, but the number does not increase rapidly. In the (c) period, the number of the holes as well as the area of each hole increases rapidly and the surface of the specimen becomes covered nearly completely with the holes. In the last period, (d), the generation and growth of holes nearly stop.

Comparing the *a-t* relationship with the *R-t* relationship (expressed by a dot-dash line in Fig. 9), the rate of erosion, *R*, reaches the maximum in the (c) period, where the number and area of the holes increase rapidly, and decreases in the (d) period. The relationship between the rate of erosion and the process of generation and growth of small holes is exactly identical to that for the case reported previously in which the frequency of the vibration was

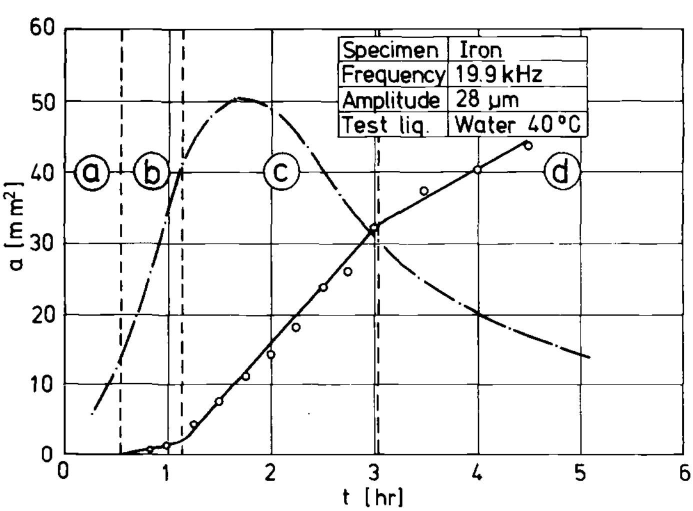

FIG. 9—*Comparison between* R-t *and* a-t *curve for iron.*

10.1 kHz and the amplitude was 55 μm [*6,14*]. In other words, the process of the growth of the small holes affects to a great extent the rate of erosion regardless of the frequency of vibration.

Process of Growth of Small Holes

The process of the growth of a hole generated on the damaged surface of an iron specimen was observed by SEM. Figure 10 [*1*] shows the generation of a small hole at 25 min after starting the test. The surface surrounding the hole shows the damage produced in the *a* period (Fig. 9); namely, small complex fractured surfaces deformed plastically overlap each other. Figure 10 [*2*] shows the state at 30 min, where the small hole has grown in the directions of right and upper left. The grown part consists of a few relatively large smooth fractured surfaces. Large smooth surfaces are observed both at the bottom and the sidewall of the hole at 45 min, Fig. 10 [*3*], and at 50 min, Fig. 10 [*4*]. At 55 min, Fig. 10 [*5*], a bump protruding from the upper part of the hole is separated, leaving a smooth fractured surface larger than ones in the vicinity. Figure 10 [*6*], 100 min, shows that the bottom is covered with small fractured surfaces accompanied by plastic deformation, similar to the surrounding damaged surface outside the hole, while brittle fractured surfaces still remain at the rim of the hole (indicated by an arrow). Figure 10 [*7*] and [*8*], corresponding to 140 and 180 min, respectively, show states in the *d* period. It is seen that during this 40 min the shape of the hole did not change and the growth nearly ceased.

From observations described in the foregoing, it is known that, on the surface damaged in the *a* period, small fractures with plastic deformation overlapped each other complicatedly, indicating the fracture to be ductile. Also, the growth of the hole in the *c* period showed smooth surfaces, indicating brittle fracture where large lumps separated themselves. In the *b* and *c* periods, although the damaged surface, excepting holes, shows ductile fractured surfaces as does *a*, most of the damage was considered to be brittle fracture, judging from the appearance of the growth of the holes.

Process of Damage of Metals in Magnetostriction Vibratory Test

Figure 11 shows a comparison between the *R-t* and *a-t* of stainless steel, which was selected as a typical material to have two maximum peaks on the *R-t* curve in Fig. 8. Of the two peaks that appear, taking a certain interval between themselves, the latter one appears in the *c* period. This fact suggests that the peaks (only one for each curve) appearing in the *R-t* curves of iron and cast iron are of the same kind as the latter one of the two peaks for stainless steel, etc., and that the former peak for iron and cast iron is negligibly small. On the other hand, in the case of aluminum, only the degree of roughness of the specimen surface increased from the start of the test with

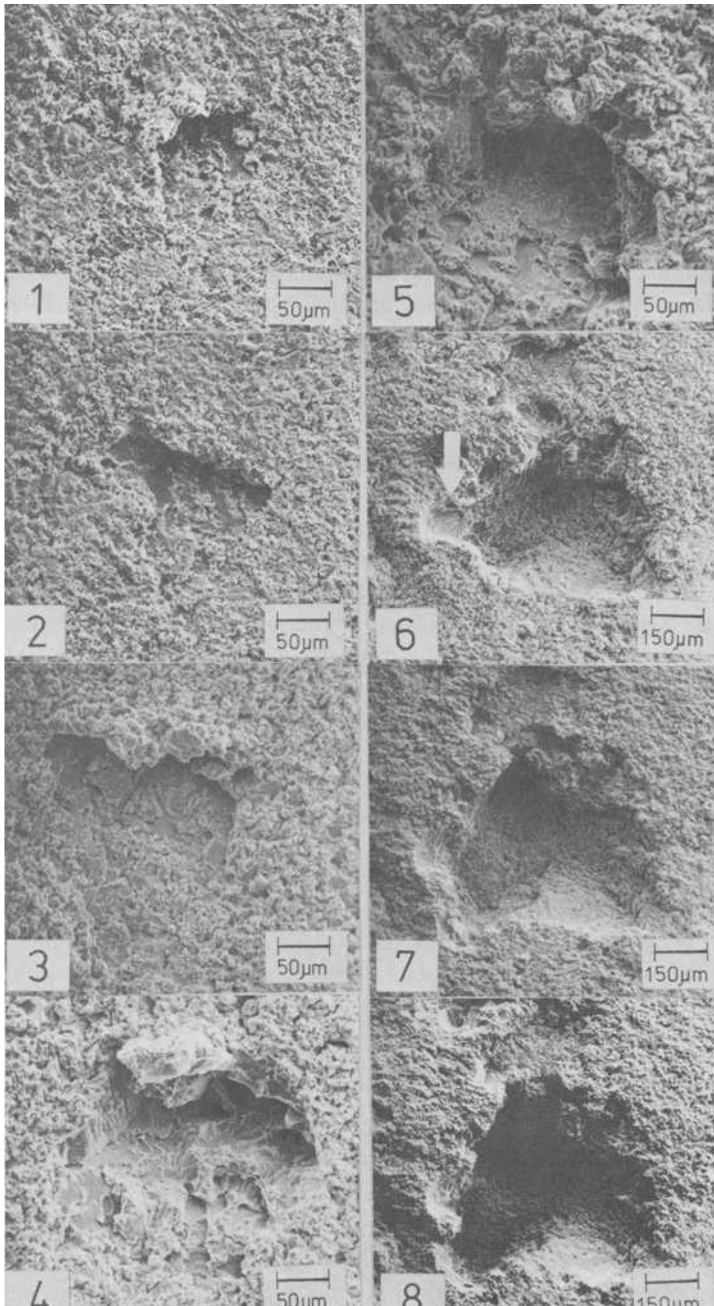

FIG. 10—*SEM life history of an eroded hole in an iron specimen.*

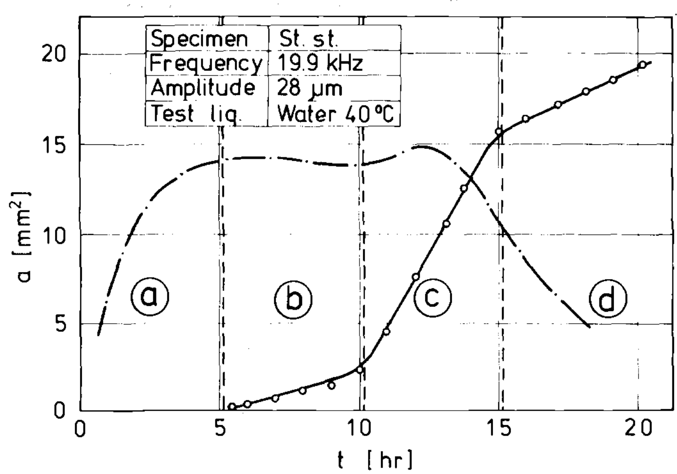

FIG. 11—*Comparison between* R-t *and* a-t *curve for stainless steel.*

the lapse of time, and no definite hole appeared. Therefore, the only one peak in the R-t curve of aluminum is considered to correspond to the former one of the two peaks for stainless steel, etc.

Taking into consideration the process of growth of the hole observed by SEM, the universal damage process of metallic materials in the vibratory test may be described as follows. In the initial period of damage the surface is attacked uniformly and material is removed by relatively ductile fracture. This is followed by the formation of holes which grow by a relatively brittle fracture. The characteristics of materials determine, if other conditions are the same, how much damage occurs in each period. Maximum peaks appear on the curves of rate of erosion versus time if the amount of damage is sufficiently great.

In order to prove the theory just described concerning the process of damage, specimens of iron that had only one peak to correspond to brittle fracture on the R-t curve were tested at a more ductile condition, that is, at higher temperatures, to see if peaks corresponding to ductile fracture would appear. Test temperatures were 5°C (41°F), 40°C (104°F), 90°C (194°F), 150°C (302°F), and 200°C (392°F); the frequency and the amplitude of vibration were 19.9 kHz and 28 μm, respectively. As liquids for the tests, glycerin was used for 150 and 200°C (302 and 392°F), and deionized water for tests below 150°C (302°F).

Characteristics of the R-t curves obtained at various temperatures are shown in Fig. 12. On the R-t curves, only one peak appears at room temperature, but another peak appears before it as temperature is elevated. The rates of erosion at the two peaks are nearly equal at 200°C (392°F).

This result supports without doubt the theory mentioned earlier that the

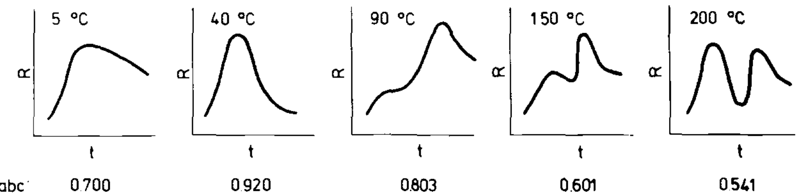

FIG. 12—*Effect of temperature on rate-time curve of iron (frequency: 19.9 kHz, amplitude: 28 μm).*

only one peak existing on the *R-t* curve of iron at room temperature corresponds to the second peak of the *R-t* curve of stainless steel, etc., the first peak for iron being negligibly small and the damage corresponding to the first peak being due to a relatively ductile fracture.

Expression of Process of Damage by a Coefficient

In order to compare quantitatively the damage caused by the two kinds of the damaging stages which appear on the *R-t* curves, a coefficient

$$W_c{}^*/W_{abc}$$

is introduced. Here, W_{abc} is the total of the damages in the periods ⓐ, ⓑ, and ⓒ, and $W_c{}^*$ is the amount of damage in the c^* period. c^* period is the period between the time $t_a{}^*$ obtained by extending the *a-t* line and the finishing time of ⓒ period, Fig. 13. This coefficient shows the ratio of the amount of damage in the c^* period to the total amount of damage, namely, the ratio of the contribution of brittle fracture to the total damage.

The reason that the total amount of damage here does not include the damage in ⓓ period is, as reported before, that the change in *R* in ⓓ period is caused by the change in the behavior of cavitation bubbles on the surface of the specimen and is not related to the characteristics of the materials [*5,6,14*].

ⓑ period is considered to be a period of mere transition from ⓐ to ⓒ; therefore, $W_c{}^*$ is adopted instead of W_c. Each hole has its own time of generation; some holes that generate before the average time of generation appear at the beginning of ⓑ period. In other words, some parts of the damaged surface in ⓑ period enter ⓒ period, and the rest still belong to ⓐ period. In the latter half of ⓑ period, nearly the whole damaged surface enters ⓒ period. This corresponds to the time, $t_a{}^*$, when c^* period starts. Furthermore, the positions of the second peaks of tool steel (1.17C) and mild steel as well as stainless steel shown in Fig. 11 belong to c^* period rather than to ⓒ period.

The values of $W_c{}^*/W_{abc}$ are given below the *R-t* curves in Figs. 8 and 12.

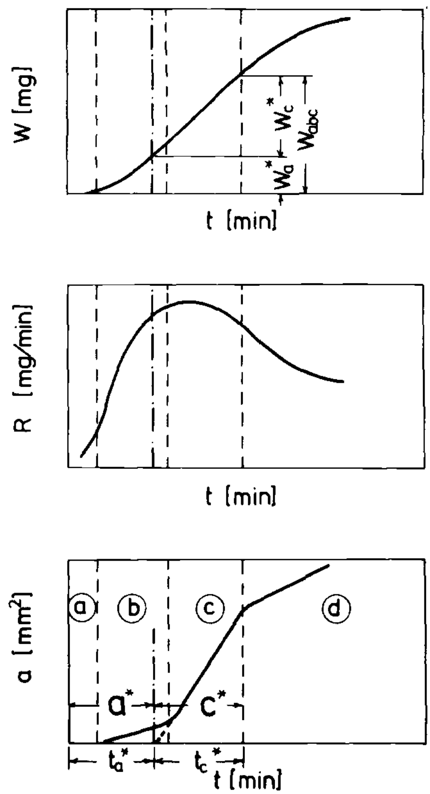

FIG. 13—*Definitions of* t_a*, t_c*, W_{abc}, W_a*, *and* W_c*.

In all cases, the value of the coefficient increases as the ratio of the second peak to the whole increases, expressing very well the characteristic to be seen in the *R-t* curve.

Influences of Conditions of Test on Process of Damage

Influence of Amplitude and Corrosion

The influence of amplitude and corrosiveness of the liquid on the process of damage was studied using iron specimens. The frequency of the vibration was 19.9 kHz; the amplitude was 13 to 28 μm, and the pH of the liquid for the test was adjusted from 2 to 5.7 by aqueous solution of hydrochloric acid at 40°C (104°F). Figure 14 shows the results obtained. When the pH of the liquid is constant, W_c*/W_{abc} is also constant, even if the amplitude changes; that is, the amplitude has no influence on the process of damage expressed by this coefficient.

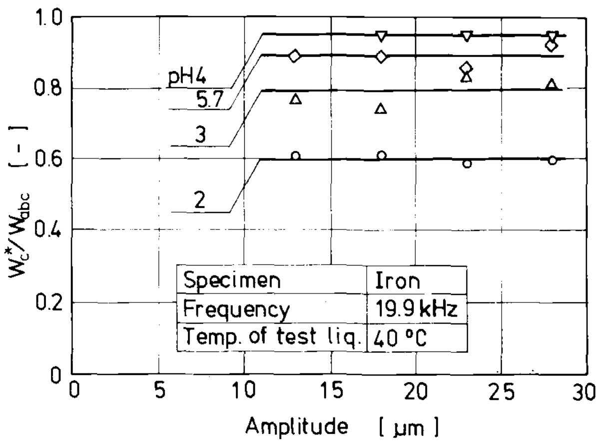

FIG. 14—*Effects of amplitude and pH of test liquid on* W_c*/W_{abc}.

On the other hand, the amplitude affects greatly the velocity of damage. Figure 15 shows the influence of the amplitude on the average velocity of damage in the stages of $a*$ and $c*$. Because t_a* and t_c* are the length of $a*$ period and $c*$ period (durations of each period), respectively, W_a*/t_a* and W_c*/t_c* are the average velocity of damage in $a*$ period and $c*$ period, respectively. It is observed that the velocity of damage in $c*$ period is more affected by the amplitude than that in $a*$ period.

The corrosiveness of the liquid for the test has a great influence on W_c*/W_{abc}. As shown in Fig. 14, when the value of pH is low, namely, when the corrosiveness of the liquid is great, the value of W_c*/W_{abc} is small. Figure 15 shows the influence of the corrosiveness on the velocity of damage; when the corrosiveness of the liquid changes, the average velocity of damage changes to a great extent in the $a*$ period, but hardly at all in the $c*$ period. This means that the corrosiveness of the liquid for the test affects to a great extent the velocity of damage in the $a*$ period, while it has scarcely any effect on that in the $c*$ period.

Influence of Frequency of Vibration

Table 1 shows the influence of the frequency of vibration on W_c*/W_{abc}. This series of tests was carried out in deionized water at 40°C (104°F), with the frequency and amplitude being varied simultaneously—an amplitude of 28 μm at frequency of 19.9 kHz, 55 μm at 10.1 kHz, and 69 μm at 6.5 kHz. Consequently, the values of W_c*/W_{abc} in Table 1 can contain the influence of the amplitude as well as that of the frequency. However, the change in W_c*/W_{abc} of the same material shows only the influence of the frequency, because the amplitude does not affect at all W_c*/W_{abc}, as shown before.

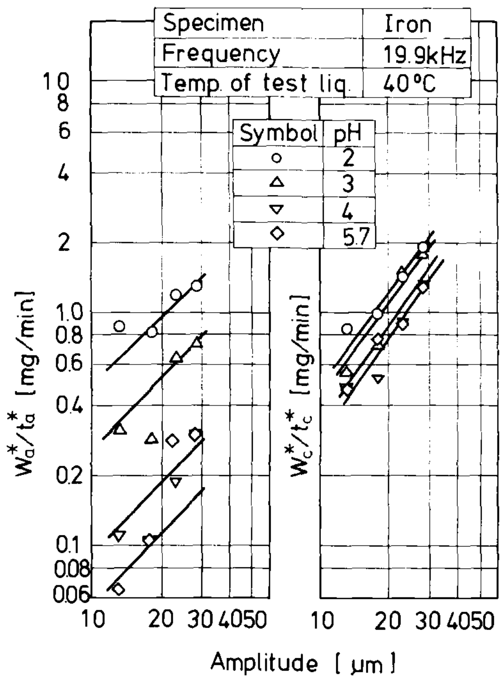

FIG. 15—*Effects of amplitude on erosion rate in* a* *and* c* *periods.*

The differences between the W_c^*/W_{abc} values of brass and iron listed in Table 1 are ~0.6 at 19.9 kHz, ~0.4 at 10.1 kHz, and below 0.1 at 6.5 kHz. That the difference among the W_c^*/W_{abc} values of various materials decreases with the decrease in frequency means that the processes of damage of all materials are the same at low frequencies, regardless of the characteristics of the materials. From this fact it is known that frequency has a great influence on the process of damage.

On the other hand, as for the influence of the frequency on the velocity of damage, the velocity of damage of a material (for instance, brass) in Table 2 shows little change when conditions are changed. This means that the change in the velocity of damage due to the change in the amplitude is compensated for by the change in the frequency. Frequency is a factor that affects the velocity of damage as well as the process of damage.

Discussion

The water tunnel method shows that the fracture of metallic material caused by cavitation erosion follows, in general, a transition from ductile to brittle fracture with the lapse of time. A principal cause for the transition of the mechanism of fracture is the hardening of the metallic materials due to

TABLE 1—*Effects of frequency and amplitude on* W_c^*/W_{abc} [*test liquid: water, 40°C (104°F)*].

Frequency, kHz	Amplitude, μm	Brass	Tool Steel	Stainless Steel	Mild Steel	Cast Iron	Iron (Ferrite)
6.5	69	0.588	0.627	0.649	0.667	0.679	0.662
10.1	55	0.423[a]	0.487	0.598	0.564[a]	0.755	0.816
19.9	28	0.337	0.374	0.460	0.484	0.838	0.920

[a]Amplitude; 45 μm.

TABLE 2—*Effects of frequency and amplitude on erosion rates in* a* *and* c* *period [test liquid: water, 40°C (104°F)].*

Frequency, kHz	Amplitude, μm	W/t, mg/min	Brass	Tool Steel	Stainless Steel	Mild Steel	Cast Iron	Iron (Ferrite)
6.5	69	W_a^*/t_a^*	0.880	0.291	0.226	0.365	1.15	0.683
		W_c^*/t_c^*	0.940	0.374	0.392	0.496	1.51	1.18
10.1	55	W_a^*/t_a^*	0.880[a]	0.180	0.315	0.346[a]	0.343	0.707
		W_c^*/t_c^*	0.875	0.219	0.335	0.383	0.551	1.55
19.9	28	W_a^*/t_a^*	0.901	0.183	0.209	0.402	0.264	0.300
		W_c^*/t_c^*	0.851	0.192	0.228	0.361	0.575	1.30

[a] Amplitude; 45 μm.

plastic deformation. Characteristics of the materials such as mechanical properties, chemical compositions, and metallographic structures also have influence on the transition.

In the magnetostriction vibratory test, the fracture of metals observes the transition from ductile fracture to brittle, as in the water tunnel method. A characteristic of the process of damage of each material due to this transition appears in the correlation between the rate of erosion and time.

It is meaningless, however, to discuss whether the magnetostriction vibratory test stimulates better the process of damage by the water tunnel method or in practical machines and apparatuses—comparing Figs. 1 and 8—because it has been verified that the process of damage changes to a great extent depending on the conditions of the test in the magnetostriction vibratory test. Therefore, it can be naturally expected that the process of damage in practical machines and apparatuses depends to a great extent on the conditions of operation. Figures 1 and 8 show only one example of various processes of damage to the same material.

Although it is quite feasible to make the vibratory method simulate actual service damage by chosing parameters adequate for the purpose, there are still some delicate problems in correlating directly the condition of the vibratory test to that of actual service damage. For example, frequency of vibration has an effect not only on the intensity of each cavitation blow but also on the repetition of attack. Besides, it causes a very high acceleration on the test specimen, the effect of which on the destruction of the materials has not yet been made clear. On the other hand, any reliable measure of the intensity of cavitation attack on materials under field conditions has not yet been attained; even the cavitation number, for example, has a limit as a measure of dynamic similarity of flow [*16*]. What can be concluded so far is that, in the vibratory test, the process of damage of a material can be changed to a great extent by choosing appropriate conditions for the test, as the conditions of the test can be relatively easily changed.

When the magnetostriction vibratory test is applied, it must be taken into consideration that stages of damage of different mechanisms of fracture should occur within the range of time in which the weight loss of the specimen can be observed. The reason is that, in the case, for instance, of study of the influence of corrosion on erosion, different experimental results will be obtained depending on the time of the test, as the influence in a^* period is different from that in c^* period. Furthermore, it can be expected that there may exist stages of damage other than a^*, c^*, and ⓓ and some even in the incubation period. This fact must be taken into consideration when experiments to develop more erosion-resistant materials are performed.

Conclusions

1. In the cavitation damage of metallic materials, in general, the mechanism of fracture changes from ductile to brittle with the lapse of time.

2. This transition of the mechanism of fracture depends on the material characteristics, such as strain hardenability, mechanical properties, and metallographic structures, as well as on the conditions of the test.

3. In the magnetostriction vibratory test, the process of damage of a material can be changed to a great extent by choosing appropriate conditions of the test.

Acknowledgment

The water tunnel experiments were carried out at the Institut für Werkstoffkunde (B) of the Technical University of Hannover, Hannover, West Germany, while the author was there as a Humboldt scholarship student. The author is much indebted to Prof. F. Erdmann-Jesnitzer and Dr. H. Louis of the university and Alexander von Humboldt Stiftung. Thanks are also due to Dr. Tsuda of the Tokyo Institute of Technology, who supported the experiments in the magnetostriction vibratory test, and to the chief director of the Hiroshima Research Institute of the Technical Center of Mitsubishi Heavy Industries Ltd., who allowed the author to use the scanning electron microscope.

This work was supported by the science research expenditure of the Ministry of Education of Japan (055216, 1975).

References

[1] *Annual Book of ASTM Standards*, 1974, Part 10.
[2] Thiruvengadam, A. and Preiser, H. S., *Journal of Ship Research*, Vol. 8, No. 3, Dec. 1964, pp. 39-56.
[3] Varga, J. and Sebestyén, Gy., *Periodica Polytechnica*, Budapest, Vol. 8, No. 3, 1964, pp. 343-352.
[4] Thiruvengadam, A. in *Proceedings*, 3rd International Conference on Rain Erosion and Allied Phenomena, Royal Aircraft Establishment, Farnborough, England, 1970.
[5] Plesset, M. S. and Devine, R. E., *Journal of Basic Engineering, Transactions*, American Society of Mechanical Engineers, Series D, Vol. 88, No. 4, 1966, pp. 691-705.
[6] Suezawa, Y., Matsumura, M., Nakajima, M., and Tsuda, K., *Journal of Basic Engineering, Transactions*, American Society of Mechanical Engineers, Series D, Vol. 94, No. 3, 1972, pp. 521-532.
[7] Tichler, J. W., de Gee, A. W. J., and van Elst, H. C. in *Erosion, Wear, and Interfaces with Corrosion, ASTM STP 567*, American Society for Testing and Materials, 1974, pp. 56-76.
[8] Hobbs, J. M. in *Erosion by Cavitation or Impingement, ASTM STP 408*, American Society for Testing and Materials, 1967, pp. 159-179.
[9] Heymann, F. J. in *Erosion by Cavitation or Impingement, ASTM STP 408*, American Society for Testing and Materials, 1967, pp. 70-110.
[10] Erdmann-Jesnitzer, F. and Louis, H. in *Erosion, Wear, and Interfaces with Corrosion, ASTM STP 567*, American Society for Testing and Materials, 1974, pp. 171-196.
[11] Matsumura, M., Erdmann-Jesnitzer, F., and Louis, H., *Kagaku Kogaku Ronbunshu*, Vol. 1, No. 4, 1975, pp. 432-438.
[12] Erdmann-Jesnitzer, F. and Borbe, P. C., *Werkstoff und Korrosion*, Vol. 20, No. 7, 1969, pp. 583-595.
[13] Endo, K. and Nishimura, Y., *Transactions*, Japan Society of Mechanical Engineers, Vol. 38, No. 309, 1972, pp. 924-932.
[14] Suezawa, Y., Matsumura, M., and Tsuda, K., *Journal of the Materials Science Society of Japan*, Vol. 6, No. 2, 1969, pp. 86-93.

[15] Matsumura, M., *Kagaku Kogaku Ronbunshu*, Vol. 2, No. 4, 1976, pp. 399-404.
[16] Knapp, R. T., Daily, J. W., and Hammitt, F. G., *Cavitation*, McGraw-Hill, New York, 1970, p. 43.

DISCUSSION

F. G. Hammitt[1] (*written discussion*)—This paper is of special interest because of the comparison between flowing system venturi cavitation damage results and vibratory results, particularly with regard to the "characteristic curves" of time-versus-volume loss rate. However, it would be helpful to the reader not familiar with the Erdmann-Jesnitzer work in Hannover, Germany, where this work was accomplished, if at least a schematic of the flow path geometry used were included.

It would also be helpful, in applying and interpreting the results, if a table were included providing full mechanical property data on the materials tested. Incidentally, in this regard, what specifically is the material NGCI? As a nonmetallurgist, I at least am not familiar with that designation.

Masanobu Matsumura (*author's closure*)—The author is grateful to Professor Hammitt for his kind comments. A schematic of the chamber used for the flow cavitation erosion tests is shown in Fig. 16. Fuller details may be found in Refs *10* and *11*.

The mechanical properties of the materials used in the vibratory tests are listed in Table 3. The NGCI used in the flow cavitation erosion tests consists of nearly the same chemical composition as the cast iron in Table 3 except

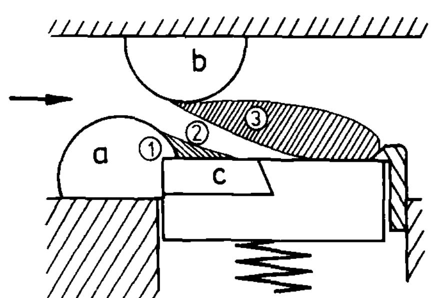

FIG. 16—*Schematic diagram of chamber for flow cavitation erosion test.* (a) *and* (b) *barricades;* (c) *test specimen;* 1 *and* 3 *stream of bubbles;* 2 *liquid, devoid of bubbles.*

[1]Professor of mechanical engineering, University of Michigan, Ann Arbor, Mich. 48109.

TABLE 3—*Mechanical properties of specimens.*

	Lower Yield Point, MN/m^2	Upper Yield Point, MN/m^2	Tensile Strength, MN/m^2	Elongation, %	Reduction of Area, %	Hv, kg/mm^2
Iron (ferrite)	160	. . .	283	59.0	78.0	108
Mild steel	326	331	462	35.5	66.9	146
Tool steel	365	371	734	21.7	27.5	229
Cast iron	. . .	. . .	212	0.5	0.7	171
Stainless steel	. . .	. . .	667	64.7	73.2	195
Brass	. . .	. . .	391	15.2	29.1	144
Aluminum	. . .	. . .	61.4	58.0	92.9	94

that some magnesium is added to make graphite spherical, which usually forms itself into flake. Consequently, NGCI has a higher strength than the usual cast iron. In the flow cavitation erosion tests, special attention was paid to the behavior of ferrite, which is commonly contained in Armco iron, mild steel, and NGCI.

R. P. M. Proctor[2] (*written discussion*)—In both the text and Figs. 14 and 15, the author shows quite clearly that the pH of the environment and hence, by implication, its corrosivity can have a very marked effect on cavitation damage to iron; in particular, as the pH goes from 5.7 to 2, and the environment therefore becomes more corrosive to iron, the author's parameter $W_c{}^*/W_{abc}$ increases by 50 percent while the parameter $W_a{}^*/t_a{}^*$ increases by almost an order of magnitude. Unfortunately the author nowhere discusses the implication of these results or attempts to interpret them in mechanistic terms. This is a notable omission, particularly in view of the fact that the author interprets his data as indicating that cavitation damage occurs initially by a ductile fracture process and eventually, after a transition, by a brittle fracture process. Yet ductile fracture by microvoid nucleation, growth, and coalescence, and brittle fracture by cleavage, are generally accepted as being environment-insensitive processes, and it is very difficult to envisage them being so markedly affected by a change in pH. In summary, I believe that the author's model of the damage process as consisting of ductile or brittle fracture or both is inconsistent with his experimental data on the effect of environmental pH and corrosivity on the rate of cavitation damage.

Masanobu Matsumura (*author's closure*)—The general opinion[3] to date on the interaction of corrosion with erosion is that cavitation erosion is a pure mechanical process and can be accelerated by corrosion. The main effect of corrosion is the weakening of the properties of material and rendering it more susceptible to erosion. The author agrees with this opinion.

[2]Lecturer in corrosion science, University of Manchester Institute of Science and Technology, Manchester, England.

[3]Kallas, D. H. in *Erosion, Wear, and Interfaces with Corrosion, ASTM STP 567*, American Society for Testing and Materials, 1974, pp. 5–17.

Liquid Jet Technology

D. L. Eddingfield[1] *and M. Albrecht*[1]

Effect of an Air-Injected Shroud on the Breakup Length of a High-Velocity Waterjet

REFERENCE: Eddingfield, D. L. and Albrecht, M., "**Effect of an Air-Injected Shroud on the Breakup Length of a High-Velocity Waterjet,**" *Erosion: Prevention and Useful Applications, ASTM STP 664,* W. F. Adler, Ed., American Society for Testing and Materials, 1979, pp. 461-472.

ABSTRACT: Air-injected shrouds are used to create an airflow parallel to a high-speed waterjet to examine the effect of the air velocity on the breakup length of the waterjet. Eight shrouds having four different lengths and two different diameters are employed in this study. The air velocity was varied from zero to approximately twice the velocity of the waterjet. The waterjet has an exit diameter of 0.766 mm (0.030 in.) and an exit velocity of 266 m/s (874 ft/s) for all the experimental runs.

Of the shrouds tested, the shortest shroud with the smaller diameter produced the best results for the entire air velocity ranges. The breakup length of the waterjet with a shroud compared to that of a waterjet without a shroud ranges from 1.2 for an air-to-water velocity ratio of zero up to a value of approximately 1.7 for a velocity ratio of 2.0.

Cutting tests on a representative material are planned to establish firmly the benefit of utilizing an air-injected shroud in conjunction with a high-velocity waterjet.

KEY WORDS: waterjet, coaxial jets, breakup length, coherent length, standoff distance, erosion

The ability to cut or fragment materials using high-speed waterjets at relatively large standoff distances is desirable for many applications, for example, borehole mining of coal and other minerals. In such cases, the task is usually one of maximizing the effective cutting length of the jet for a given nozzle design and given operating pressure.

There exists an extensive amount of reported work in the literature dealing with nozzle design and operating characteristics. Summers and Zakin[2] give a

[1] Assistant professor and graduate student, respectively, Engineering Mechanics and Materials Department, Southern Illinois University, Carbondale, Ill. 62901.

[2] Summers, D. A. and Zakin, J. L., "The Structure of High Speed Fluid Jets and Their Use in Cutting Various Soil and Material Types," Final Report, USAMERDC Contract No. DAAKO2-74-C-0006, Rock Mechanics and Explosives Research Center, University of Missouri-Rolla, Rolla, Mo.

summary of the work of previous investigators who examined the effect of nozzle shape and diameter, fluid properties, and pressure on the coherent length of a liquid jet. In addition, results of their work on jet structure are presented. In an attempt to put the design of a nozzle on a theoretical basis, Lohn and Brent[3] have examined the flow equations governing both the boundary layer and core development in the nozzle.

It is generally accepted that the effective cutting length of a high-speed continuous waterjet is a function of the coherent length of the jet. In this paper the coherent length will be taken as the distance from the nozzle exit plane to the location downstream where the jet becomes discontinuous across its entire cross section. The phrases "coherent length" and "breakup length" will be considered to be synonymous.

At low Reynolds numbers, the breakup of a liquid jet is due primarily to capillary breakup (footnote 2). Above a Reynolds number of approximately 60 000, however, the jet breakup is due primarily to aerodynamic effects. Aerodynamic breakup is the result of the interaction of the liquid jet with the ambient air, which strips off a portion of the surface of the liquid jet and thereby creates a spray surrounding a coherent liquid core. This spray decelerates rapidly and aids little in the cutting process.

This paper examines the possibility of minimizing or delaying the aerodynamic breakup by creating a coaxial airjet around the waterjet.

Equipment

Pressure Intensifier

The pressure intensifier system consisted mainly of a 0.2-m-diameter (8 in.) hydraulic cylinder whose 0.089-m-diameter (3.5 in.) shaft is used to pressurize a cylindrical stainless steel container. The cylindrical container is 0.15 m (6 in.) outside diameter, approximately 0.089 m (3.5 in.) inside diameter, and 0.97 m (38 in.) long. The system operates as a one-shot pressure intensifier which will give a test duration of 20 s with a 266-m/s (872 ft/s) flow from a 0.762-mm-diameter (0.030 in.) nozzle.

Nozzles

All the nozzles used for this work are fabricated from brass and constructed according to the Leach and Walker design, which has a 13-deg conical contraction followed by a three-diameter length straight section as shown in Fig. 1. The exit diameter of the nozzle is 0.762 mm (0.030 in.) and the outside surface of the nozzle has a 13-deg taper down to a 3.95-mm-diameter

[3]Lohn, P. D. and Brent, D. A., "Nozzle Design for Improved Water Jet Cutting," Third International Symposium on Jet Cutting Technology, May 1976, Paper A3.

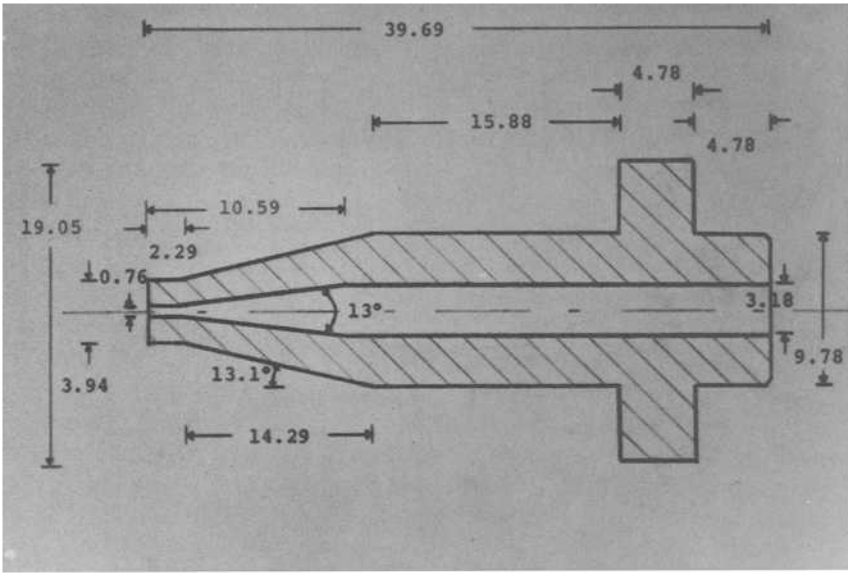

FIG. 1—*Water jet nozzle. All lengths are in millimetres.*

(0.155 in.) straight portion. The taper aids in guiding the airflow when a shroud is attached.

Air Shroud and Shroud Mounting Base

The air shrouds and shroud base shown in Fig. 2 are machined from brass stock. The shroud mounting base has four air ports equally spaced around its perimeter. The ports terminate in a chamber which supplies the airflow to the air shrouds. This air chamber has an outer diameter of 31.75 mm (1.25 in.).

All of the air shrouds have an initial inside diameter of 22.2 mm (0.875 in.) with a 38.7-deg conical contraction which terminates at the straight section of the shroud. A total of eight air shrouds is employed in this investigation. The shrouds are divided into two groups which have different values of the diameter of the straight section. The dimensions of the shrouds are given in Table 1.

Experimental Procedure

For each shroud, the air velocity is adjusted to the desired value without a water flow. The air velocity in the shroud without a water flow is assumed to be the same value as that which exists when the water flow is present. Since the waterjet cross-sectional area at the nozzle exit is only approximately 2.5

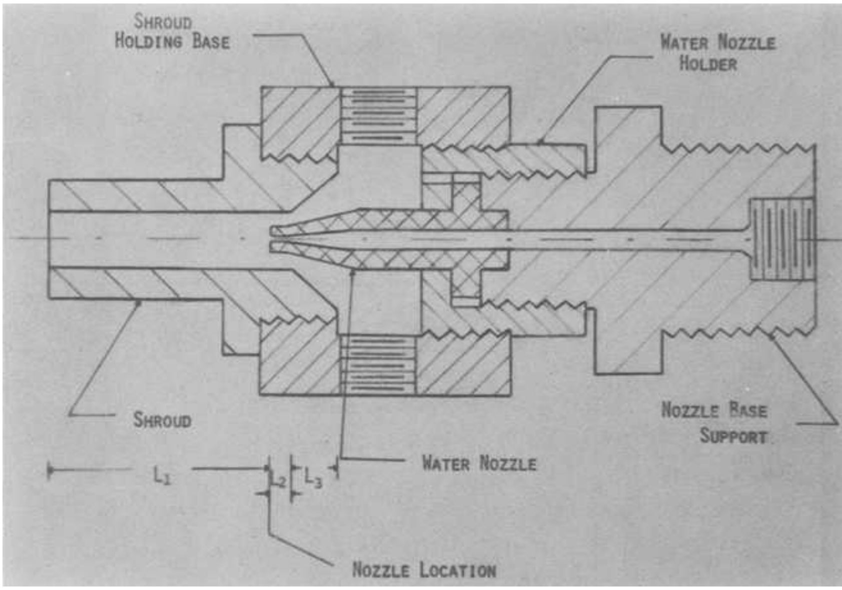

FIG. 2—*Water jet nozzle, shroud mounting base, and shroud assembly.*

percent of the shroud cross-sectional area for the 4.75-mm-diameter (0.1875 in.) shroud and 0.64 percent for the 9.52-mm-diameter (0.375 in.) shroud, it is felt that this assumption is justified.

The air velocity values vary from 0 to 450 m/s (1476 ft/s) but the waterjet velocity is held constant at a value of 266 m/s (872 ft/s) for all the experimental runs.

For each air shroud and each value of the air velocity, a minimum of three photographs is taken with a 35-mm camera. The camera is positioned so that the field of view is from approximately 5.08 to 43.18 cm (2 to 17 in.) downstream of the waterjet nozzle. Diffused backlighting is employed using two slaved strobes which provide a high-intensity flash of duration 8.0 μs.

The photographs are analyzed to determine the downstream location at which the coherent core of the waterjet can no longer be detected. The values determined from the three photographs for each test condition are averaged to give the breakup length of the waterjet, $L_{b,r}$.

Results and Discussion

The results of the experimental runs are plotted in Figs. 3 and 4. $L_{b,s}/L_{b,r}$ represents the ratio of the measured breakup length of the waterjet with an air-injected shroud to a reference breakup length. The reference breakup length $L_{b,r}$ is defined as the measured breakup length of the waterjet without

TABLE 1—*Air-injected shroud dimensions (refer to Fig. 2 for notations).*

Shroud No.	Inside Diameter, mm	(in.)	L_1, mm	(in.)	L_2, mm	(in.)	L_3, mm	(in.)
1A			8.46	(0.333)				
2A	9.53	(0.375)	38.63	(0.375)	2.67	(0.105)	7.93	(0.312)
3A			76.73	(3.02)				
4A			144.83	(4.52)				
1B			8.46	(0.333)				
2B	4.76	(0.188)	38.63	(1.52)	~0		10.90	(0.429)
3B			76.73	(3.02)				
4B			144.83	(4.52)				

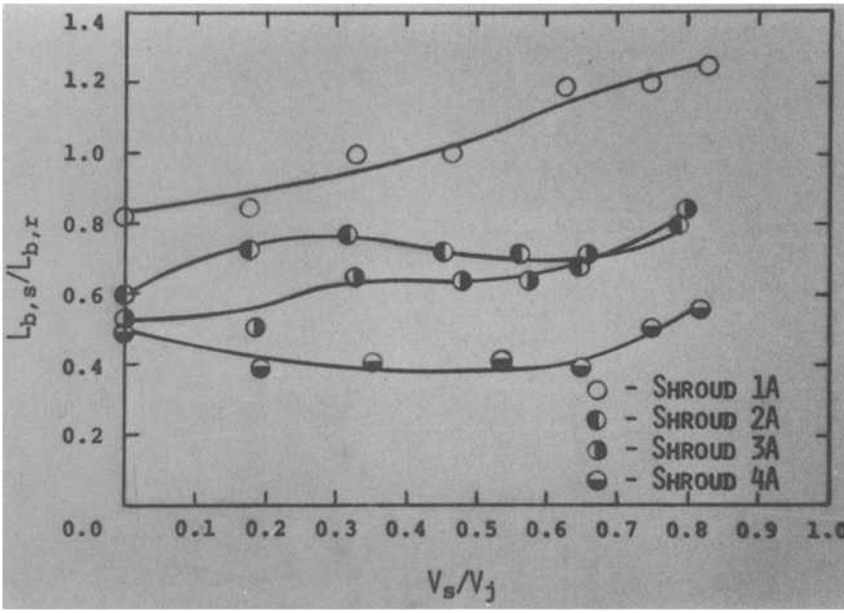

FIG. 3—*Breakup length ratio versus air-to-water velocity ratio for four shroud lengths. Shroud diameter = 9.52 mm.*

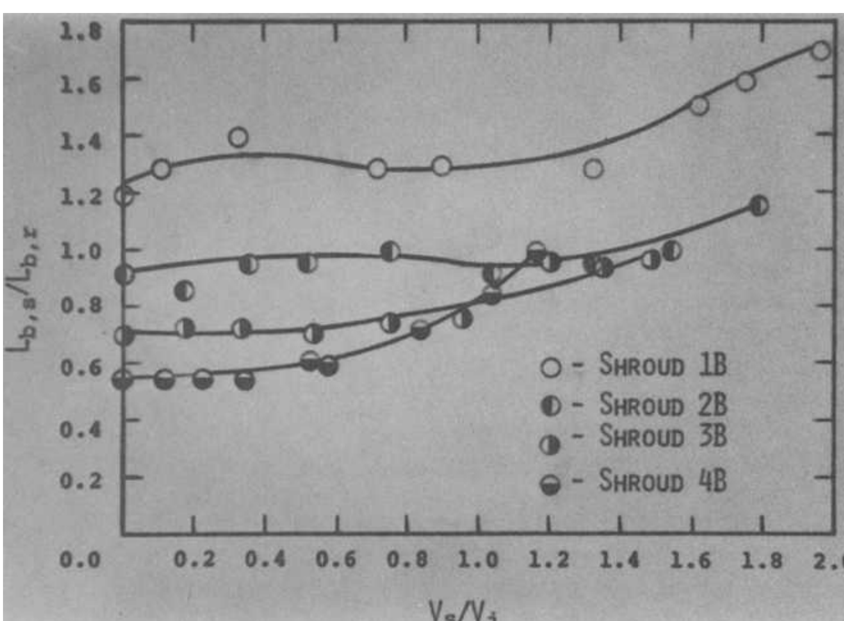

FIG. 4—*Breakup length ratio versus air-to-water velocity ratio for four shroud lengths. Shroud diameter = 4.76 mm.*

a shroud. $L_{b,r}$ is measured from the exit plane of the nozzle, whereas $L_{b,s}$ is measured from the exit plane of the shroud. Thus, in each case, the breakup length is measured from the position of zero standoff distance. Note that an improvement in the breakup length is indicated when the value of the ratio $L_{b,s}/L_{b,r}$ exceeds one. V_s/V_j represents the ratio of the velocity of the air in the shroud to the velocity of the waterjet at the exit plane of the nozzle. Both $L_{b,r}$ and V_j are constant for all the data collected. $L_{b,r}$ for the waterjet is 140 nozzle diameters.

The data for $V_s/V_j = 0$ are slightly misleading and require an explanation. These data are for the case where no external air supply was connected to the shroud. Consequently the airflow in the shroud is being aspirated by the water flow and the velocity is nonzero but probably very low.

Representative photographs of the waterjet are presented in Figs. 5*a*-5*i*. Due to space limitations, only photographs showing the highest relative velocity ratio are presented.

For both series of shrouds, the figures show that the shortest shroud length gives the best results. In Series A, an improvement in the breakup length results for a velocity ratio greater than approximately 0.5. In Series B, the improvement is noted for all values of the velocity ratio.

For Series A, all the shrouds yield a relative breakup length less than one with the singular exception of Shroud 1A, which gives an improvement in the relative breakup length for values of V_s/V_j greater than 0.5, as mentioned previously. Little significance should be given to the crossing of the curves for Shrouds 2A and 3A. This may be due to some extraneous conditions present in these particular experimental runs which altered the jet structure of Shroud 2A to produce lower values of the relative breakup length for the three highest values of the velocity ratio. This is only speculation, however, which must be confirmed by further tests.

For Series B, with the exception of the longest shroud, 4B, the breakup length is insensitive to the velocity ratio up to a value of approximately one. It is interesting to note that for the shortest shroud, 1B, the relative breakup length increases approximately 20 percent even for the case of an aspirating shroud. The rapid increase in the breakup length of Shroud 4B cannot be explained at this time. Unfortunately, the maximum value of the velocity ratio obtainable with this shroud is approximately 1.2 due to the maximum pressure limitations of the compressed-air supply.

One effect of the air-injected shroud is to produce a spray plume surrounding the coherent core which is dispersed more radially but less densely than the plume of the waterjet without a shroud. Alpinieri[4] found in his experiments with coaxial jets of an inner carbon dioxide jet and an outer airjet that the larger the velocity of the outer jet with respect to that of the inner jet,

[4]Alpinieri, L. J., *American Institute of Aeronautics and Astronautics Journal*, Vol. 2, No. 9, Sept., 1964, pp. 1560-1567.

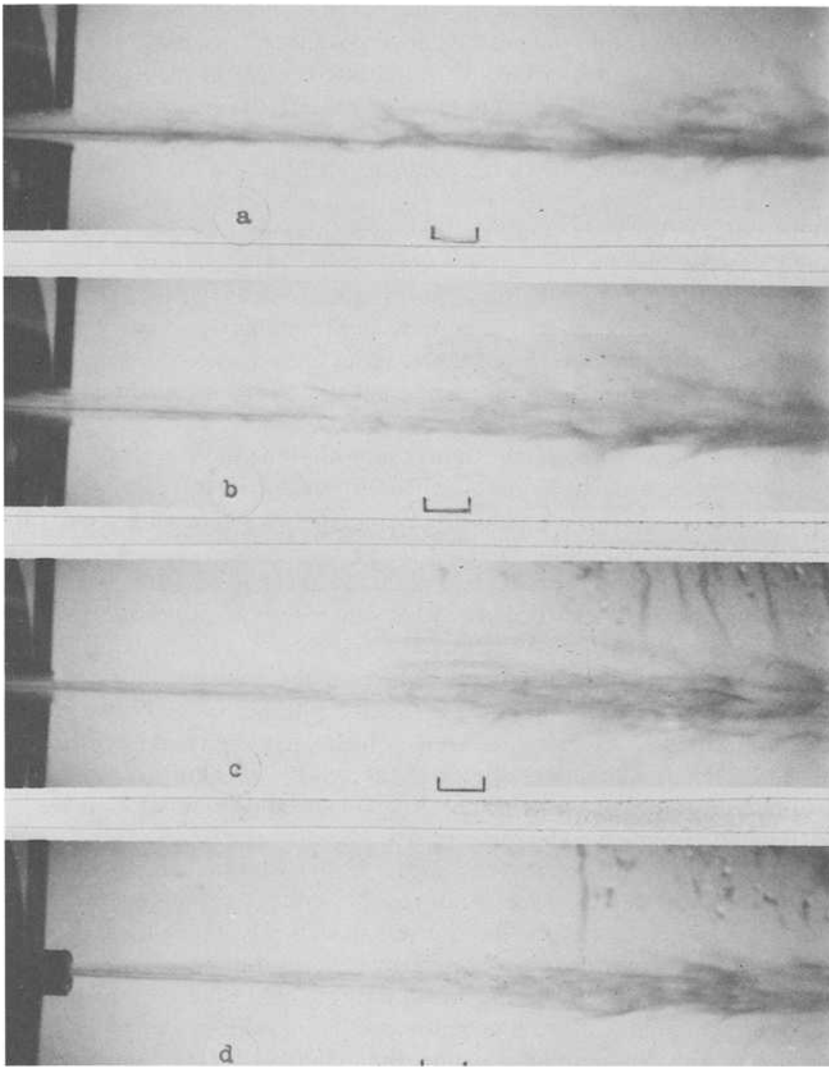

FIG. 5—*Photographs of water-jet* V_j = *266 m/s. The scale indicates a 2-cm length.* (a) *Water-jet without Shroud (5 cm downstream from nozzle exit).* (b) *Water-jet with Shroud 1A,* V_s = *224 m/s (4.4 cm downstream from shroud exit).* (c) *Water-jet with Shroud 2A,* V_s = *210 m/s (0.8 cm downstream from shroud exit).* (d) *Water-jet with Shroud 3A,* V_s = *213 m/s (shroud exit is shown).* (e) *Water-jet with Shroud 4A,* V_s = *717 m/s (shroud exit is shown).* (f) *Water-jet with Shroud 1B,* V_s = *524 m/s (3.5 cm downstream from shroud exit).* (g) *Water-jet with Shroud 2B,* V_s = *477 m/s (2.3 cm downstream from shroud exit).* (h) *Water-jet with Shroud 3B,* V_s = *395 m/s (shroud exit is shown).* (i) *Water-jet with Shroud 4B,* V_s = *311 m/s (shroud exit is shown).*

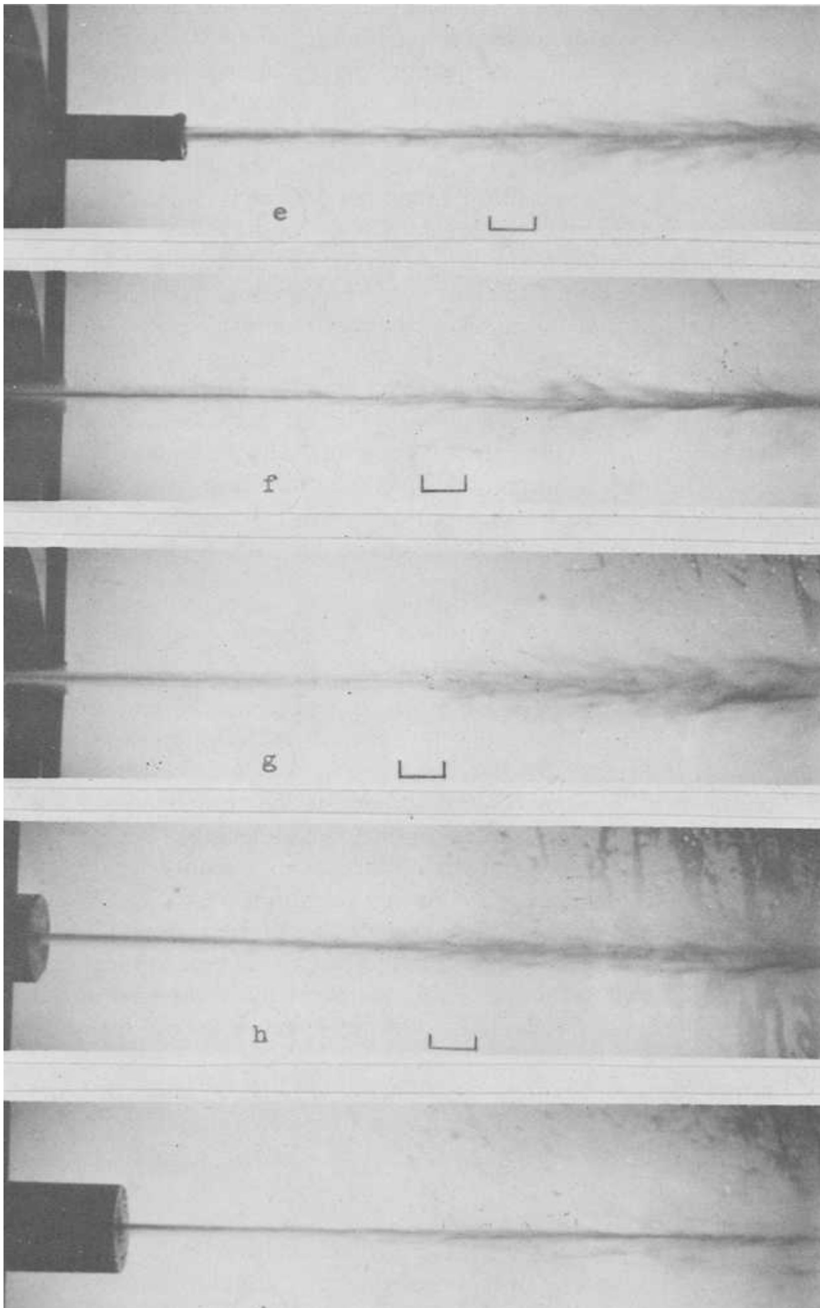

FIG. 5—*Continued*

the larger will be the amount of air entrained. He reasoned that any turbulent fluctuation present in the outer jet is a fluctuation that would not exist if the outer jet was at rest. Consequently, the use of an air-injected shroud probably introduces two interacting and conflicting effects. Additional turbulent fluctuations are introduced in the radial direction which act to disrupt the jet, but, on the other hand, the shear stresses at the surface of the waterjet are reduced. Which mechanism dominates determines whether or not the air-injected shroud increases the breakup length of the waterjet.

The photographic evidence indicates that the air-injected shroud produces a waterjet which has a smaller-diameter core. However, this smaller core is found to persist farther downstream than that of the waterjet without a shroud.

The benefit of utilizing an air-injected shroud for cutting and fragmentation can be firmly established only by actual tests on representative materials. Such tests are currently being conducted by the authors. However, the results of the work reported in this paper indicate that a modest increase in standoff distance can be achieved using air-injected shrouds. Also, a redesign of the shroud based on the results of this study is planned.

Conclusions

1. In general, the breakup length ratio $L_{b,s}/L_{b,r}$ has its largest values for the shroud which has the shortest internal straight section. Therefore, the internal straight section of the shroud appears not only unnecessary, but detrimental.

2. For the two diameters of the shrouds tested, the smaller-diameter shroud produces the largest increase in the breakup length.

3. For the shortest shroud, increasing the ratio of the air velocity relative to the water velocity increases the breakup length ratio $L_{b,s}/L_{b,r}$. However, even when the air supply is disconnected, the shortest shroud with the smaller diameter produces a 20 percent increase in the breakup length.

4. The air-injected shroud probably increases the transverse turbulent fluctuations of the waterjet but delays the aerodynamic drag of the ambient air on the waterjet.

5. Cutting tests on a representative material must be made in order to firmly establish the usefulness of adding an air-injected shroud to a waterjet.

Acknowledgments

The financial support of the Southern Illinois University Coal Extraction and Utilization Research Center for this research is gratefully acknowledged.

DISCUSSION

F. J. Heymann[1] *(written discussion)*—Why is your air shroud nozzle designed with a conical instead of rounded entry? Do you deliberately want to create a vena contracta smaller than the shroud diameter? One difference between the short and long shrouds might then be that for the longer ones the airjet reattaches and for the short one it does not, resulting in an effectively smaller-diameter air shroud.

D. L. Eddingfield and M. Albrecht (authors' closure)—The conical cross section of the air shroud was chosen for ease of machining. Because these were the initial experiments, it was the simplest geometry to use even though the best cross-sectional shape will probably be of a more streamlined shape.

Your comment about reattachment of the airjet is pertinent and bears further investigation.

B. P. Selberg[2] *(written discussion)*—Your data indicates that the greatest increase in jet coherence occurs after the shrouded airflow chokes. Once choking occurs at $M = 1$, further increases in stagnation pressure will cause both a favorable shear gradient and an increase in the air exit pressure. This increased air pressure will tend to confine the jet. Do you have a physical feeling as to whether the velocity shear effect or the pressure effect is dominating in the measured improved jet coherence?

D. L. Eddingfield and M. Albrecht (authors' closure)—By speculation, the velocity shear effect is the dominant mechanism. Note that Shroud 1B for the aspirating case ($V_s/V_j \simeq 0$) gave approximately 20 percent improvement over that of the waterjet without a shroud. For this case, the air exit pressure is atmospheric.

J. P. Barber[3] *(written discussion)*—The basic premise of your program appears to be that jet breakup is dominated by Helmholtz instabilities. Have you done any analyses of Helmholtz instability growth in waterjets? Are the results of your experiments in agreement with classical Helmholtz predictions?

D. L. Eddingfield and M. Albrecht (authors' closure)—No, we have not performed any analyses of Helmholtz instability growth in conjunction with our experiments.

A. F. Conn[4] *(written discussion)*—What was the length, in terms of nozzle diameters, for your baseline jet breakup distance?

[1]Westinghouse Electric Corp., P. O. Box 9175, Mail Stop A204, Philadelphia, Pa. 19113.
[2]University of Misssouri-Rolla, Mechanical and Aerospace Engineering, Rolla, Mo. 65401.
[3]University of Dayton, Research Institute, 300 College Park Ave., Dayton, Ohio 45469.
[4]Hydronautics, Inc., Pindell School Road, Laurel, Md. 20810.

D. L. Eddingfield and M. Albrecht (authors' closure)—Approximately 140 diameters.

A. Lichtarowicz[5] *(written discussion)*—Looking at your Fig. 4 showing the effect of a small-diameter shroud on the velocity ratio, it appears that the increased in the effectiveness of the shortest shroud starts to rise at the point where the airflow becomes sonic. Is this so?

I would be interested in seeing your result when the airflow becomes supersonic. The nozzle arrangement as shown in Fig. 2 indicates that you have a rather crude convergent-divergent nozzle.

D. L. Eddingfield and M. Albrecht (authors' closure)—Yes, this is true. We are currently pursuing further studies with a supersonic air shroud.

P. D. Lohn[6] *(written discussion)*—With regard to the possibility of supersonic effects: the air-water interface is a two-phase region where the sound speed may be extremely small. Supersonic effects must be suspected on the edge of any waterjet in air whether or not the jet is shrouded.

[5]University of Nottingham, University Park, Nottingham, U. K. NG7 2RD.
[6]TRW System and Energy, Inc., Redondo Beach, Calif. 90278.

M. Mazurkiewicz,[1] *C. R. Barker,*[2] *and D. A. Summers*[2]

Adaptation of Jet Accumulation Techniques for Enhanced Rock Cutting

REFERENCE: Mazurkiewicz, M., Barker, C. R., and Summers, D. A., "**Adaptation of Jet Accumulation Techniques for Enhanced Rock Cutting,**" *Erosion: Prevention and Useful Applications, ASTM STP 664,* W. F. Adler, Ed., American Society for Testing and Materials, 1979, pp. 473–492.

ABSTRACT: The velocity of a waterjet can be increased when the jet impacts a target material or another waterjet. A theory describing such augmentation in terms of velocity, mass, and energy change is considered. The phenomenon is sensitive to jet structure and the jet velocity profile. Jet velocity profiles do not remain constant over great distances from the nozzle, and ultimately disrupt into droplets. Within the droplet the profile is more regular and the velocity constant. The theory is extended to cover the case of droplet collisions, and experimental evidence of jet augmentation and its effects is presented.

KEY WORDS: impact pressure distribution, fluid jet augmentation, droplet impact, erosion, rock, converging nozzle

The use of the high-pressure waterjet as a cutting tool has, within the past five years, become a commercial reality. The range of application has covered a spectrum from cardboard and wood through coal and rubber to metal.

Research investigators have carried out test programs at pressure levels up to 40 kbar, well above the 2.5 to 4 kbar level of commerically available equipment. Such research has shown that under certain circumstances, there can be benefits to working at these higher pressures. Equipment for this type of work is, however, generally only of the "one-of-a-kind" research tool variety, and results of test findings at the higher pressure levels have indicated relatively short lives for the generating pressure systems and particularly the nozzles in which the transition to cutting speed occurs.

[1] Assistant professor, Instytut Technologii Budowy Maszyn, Politechnika Wroclawska, Poland.

[2] Senior investigator and director, respectively, Rock Mechanics and Explosives Research Center, University of Missouri-Rolla, Rolla, Mo.

Because of the problems associated with creating pressures within a piece of equipment, consideration has turned to the possibility of generating high velocities beyond the nozzle by the use of interacting jets or jet impact on a solid surface.

This approach has already proved successful in the development of shaped charges, particularly for military applications during World War II [*1-3*].[3] Theoretical and experimental analysis of this phenomenon has shown that directional cumulative jet accelerations to velocities of the order of 1000 to 2500 m/s can be achieved. The velocity achieved is a function of the charge size and the shape and material composition of the liner which, upon collapse, will create the cutting jet.

This paper examines the related field where an augmented velocity jet or "fast jet" is produced by the impact between two identical waterjets or of a single waterjet with a rigid flat surface. The paper extends the existing theory developed for shaped explosive charges to describe the formation and nature of the secondary waterjets formed when two identical jets meet. The secondary jets move in opposing directions along the line bisecting the angle between the original jets. The motion of the secondary jets must satisfy the principles of conservation of mass, energy, and momentum. Calculations are thereupon described which govern the mass and velocity of these secondary jets.

Particular considerations are given to the case where one of the secondary jets is of sufficient velocity to have the capability of cutting a target material.

In the passage of a waterjet from the nozzle into a surrounding fluid, the effect on the jet of the surrounding fluid is to cause a change in the pressure profile (velocity profile) of the jet (Fig. 1). The initial condition with a constant velocity across the profile changes to a Gaussian distribution with increasing distance from the nozzle as the water on the outside of the core is removed. The initial analysis is based on those portions of the curve where the primary jet still retains a constant velocity across the profile, and finally the case where the jet is broken into droplets is considered.

Analytical Model

Consider an original primary fluid jet in the region close to the nozzle where it retains an even pressure profile across its section. Let such a jet have a square cross section of area $b \times b$ with a leading edge which is a flat surface, and consider the initial stages of impact. If it is assumed that all portions of the original jet are approaching a rigid flat surface with the same velocity vector inclined at angle α relative to the flat surface and with the leading edge of the primary jet inclined at angle γ to plane A_1A_2, the first portion of the leading edge of the primary jet will contact the plane 00 at

[3] The italic numbers in brackets refer to the list of references appended to this paper.

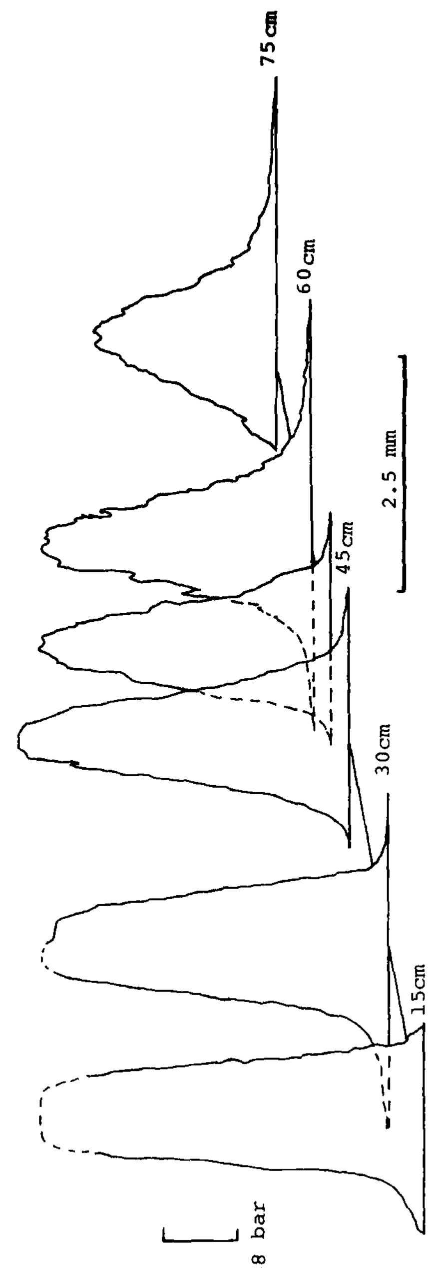

FIG. 1—*Impact pressure profiles at various distances along a waterjet issuing from a 1.5-mm nozzle diameter at 545 bar.*

Point A_1 (Fig. 2). This simulation is equivalent to the intersection of two similar jets approaching a common plane of symmetry 00 at angle γ (Fig. 3).

If the flow were a continuous laminar flow, then the primary jet would divide to produce two streams flowing in opposite directions along the surface 00. Each stream would have a velocity magnitude V_o, where V_o is the magnitude of the inflow velocity. Such a condition is nontypical and a more generalized case will be considered.

Velocity of the Secondary Jets

Sims [4] used a control volume approach to determine the velocity relationship between the primary and secondary jets for the special case $\gamma = 90$ deg. He concluded that, as the jet contact point A_1 moves along plane 00 at a speed V_A, jets created at the plane would have velocity magnitudes (V_{fj} to the right, herein referred to as the "fast jet," and V_{sj} to the left, herein referred to as the "slow jet") given by the equations

$$\begin{aligned} V_{fj} &= |\overline{V}_R + \overline{V}_A| = V_R + V_A \\ V_{sj} &= |\overline{V}_A - \overline{V}_R| = V_A - V_R \end{aligned} \tag{1}$$

where V_R is the relative velocity of the primary jet to the jet contact point. From the velocity polygon in Fig. 2 we can derive the following

$$\begin{aligned} V_R &= \frac{V_o \sin\alpha}{\sin(\alpha + \gamma)} \\ V_A &= \frac{V_o \sin\gamma}{\sin(\alpha + \gamma)} \end{aligned} \tag{2}$$

If Eq 2 is substituted into Eq 1, then

$$V_{fj} = V_o \left[\frac{\sin\alpha + \sin\gamma}{\sin(\alpha+\gamma)} \right] \tag{3}$$

$$V_{sj} = V_o \left[\frac{\sin\gamma - \sin\alpha}{\sin(\alpha+\gamma)} \right] \tag{4}$$

Hence, the speed of the secondary jets depends only on V_o, α, and γ.

Mass of the Secondary Jets

The mass of the secondary waterjets can be estimated by applying the equations for conservation of momentum and mass at Point A_1 (Fig. 2)

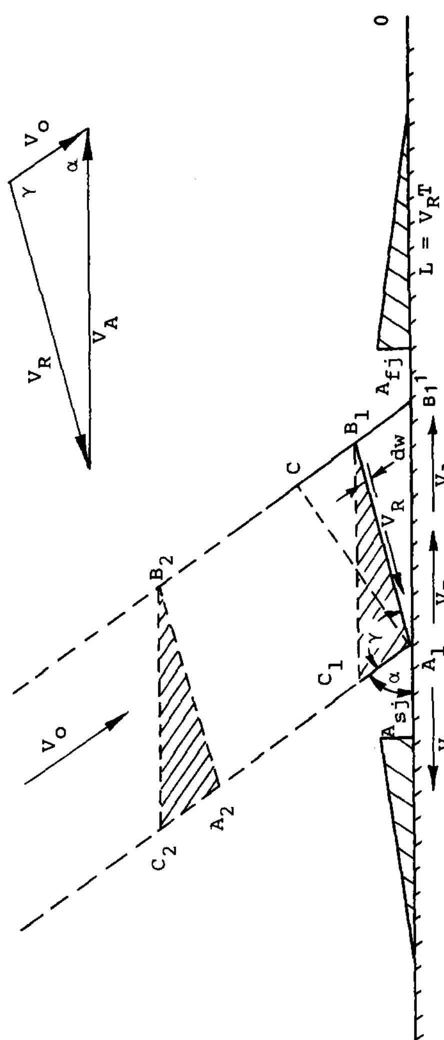

FIG. 2—*Geometric representation of the stages of impact of a flat-faced waterjet on an oblique plane.*

$$\int \rho V_R^2 \cos[180 \text{ deg} - (\alpha + \gamma)]\, dA_{in} = -\int \rho V_R^2\, dA_{fj} + \int \rho V_R^2\, dA_{sj} \quad (5)$$

and

$$\int \rho V_R dA_{in} = \int \rho V_R dA_{fj} + \int \rho V_R dA_{sj} \quad (6)$$

where

dA_{in} = elemental vertical cross section of inflow jet,
dA_{fj} = elemental vertical cross section of fast jet, and
dA_{sj} = elemental vertical cross section of slow jet.

$$\begin{aligned} dA_{in} &= b\, dw \\ dw &= V_o \sin(180 \text{ deg} - \gamma)\, dt \end{aligned} \quad (7)$$

substituted into Eqs 5 and 6 give

$$\begin{aligned} (A_{fj})_{\max} &= \int_0^{\max} dA_{fj} = \frac{b^2[1 + \cos(\alpha + \gamma)] \sin(\alpha + \gamma)}{2 \sin\alpha} \\ (A_{sj})_{\max} &= \int_0^{\max} dA_{sj} = \frac{b^2[1 - \cos(\alpha + \gamma)] \sin(\alpha + \gamma)}{2 \sin\alpha} \end{aligned} \quad (8)$$

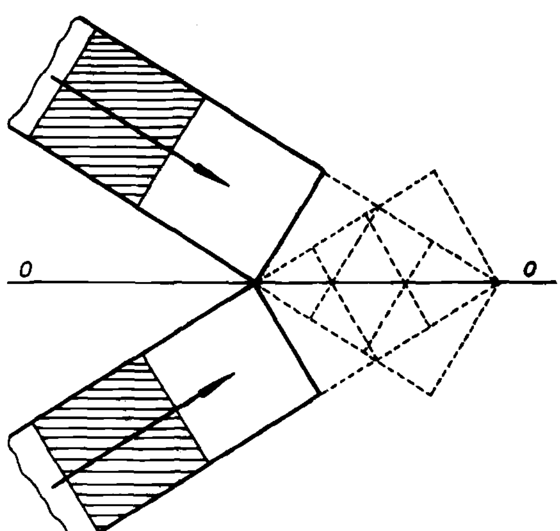

FIG. 3—*Collision of two flat-faced square jets.*

The area of the vertical cross section of the secondary waterjet impacting on the surface increases linearly from 0 to the value $(A_{fj})_{max}$. This occurs during the time T that Point B_1 moves to $B_1{}^1$. If we let distance $B_1B_1{}^1$ be x and consider triangles A_1CB_1 and $A_1B_1B_1{}^1$, then

$$T = \frac{x}{V_o} = \frac{b \sin(\alpha + \gamma)}{V_o \sin\alpha \sin\gamma} \tag{9}$$

The length of the secondary jet is therefore

$$l = V_R T \tag{10}$$

From Eqs 2 and 9 this gives

$$l = \frac{b}{\sin\gamma} \tag{11}$$

Secondary jets will have a wedge shape with an area of the base of $(A_{sj})_{max}$ and $(A_{fj})_{max}$, width b, and length l. Letting the mass density of the water be ρ, the mass of the secondary jets will be

$$\begin{aligned} (M_{fj})_{max} &= \frac{\rho b^3}{4} \frac{[1 + \cos(\alpha + \gamma)]\sin(\alpha + \gamma)}{\sin\alpha \sin\gamma} \\ (M_{sj})_{max} &= \frac{\rho b^3}{4} \frac{[1 - \cos(\alpha + \gamma)]\sin(\alpha + \gamma)}{\sin\alpha \sin\gamma} \end{aligned} \tag{12}$$

The total mass that participates in the formation of the secondary waterjets is the sum of $(M_{fj})_{max}$ plus $(M_{sj})_{max}$

$$M_{in} = \frac{\rho b^3}{2} \frac{\sin(\alpha + \gamma)}{\sin\alpha \sin\gamma} \tag{13}$$

Energy of the Secondary Jets

Using Eqs 3, 4, and 12, the kinetic energy of the secondary waterjets can be derived

$$\begin{aligned} EK_{fj} &= \frac{\rho b^3 V_o^2}{8} \frac{[1 + \cos(\alpha + \gamma)]\,(\sin\alpha + \sin\gamma)^2}{\sin\alpha \sin\gamma \sin(\alpha + \gamma)} \\ EK_{sj} &= \frac{\rho b^3 V_o^2}{8} \frac{[1 - \cos(\alpha + \gamma)]\,(\sin\alpha + \sin\gamma)^2}{\sin\alpha \sin\gamma \sin(\alpha + \gamma)} \end{aligned} \tag{14}$$

The kinetic energy of the secondary jets is a function of V_o, b, and angles α and γ.

Concentration of Energy

Even more significant than the energy ratio is the concentration of energy. This information, important in estimating the cutting potential of the secondary jets, is obtained by dividing the kinetic energy by the cross-sectional area of the secondary jets. Hence

$$
\begin{aligned}
K_{fj} &= \frac{EK_{fj}}{(A_{fj})_{\max}} = \frac{\rho b V_o^2}{4} \frac{(\sin\alpha + \sin\gamma)^2}{\sin\gamma \sin^2(\alpha+\gamma)} \\
K_{sj} &= \frac{EK_{sj}}{(A_{sj})_{\max}} = \frac{\rho b V_o^2}{4} \frac{(\sin\alpha - \sin\gamma)^2}{\sin\gamma \sin^2(\alpha+\gamma)}
\end{aligned}
\tag{15}
$$

The concentration of energy for the primary jet can be written as

$$K_{in} = \frac{EK_{in}}{A_{in}} = \frac{\rho b V_o^2}{4} \frac{\sin(\alpha+\gamma)}{\sin\alpha \sin\gamma} \tag{16}$$

where $A_{in} = b^2$, the area of the cross section of the primary jet. The concentration of energy ratio is then obtained from Eqs (15) and (16) as

$$
\begin{aligned}
\frac{K_{fj}}{K_{in}} &= \frac{(\sin\alpha + \sin\gamma)^2 \sin\alpha}{\sin^3(\alpha+\gamma)} \\
\frac{K_{sj}}{K_{in}} &= \frac{(\sin\alpha - \sin\gamma)^2 \sin\alpha}{\sin^3(\alpha+\gamma)}
\end{aligned}
\tag{17}
$$

Analysis of the Theoretical Results

It is obvious from studying the foregoing equations that the values of α and γ are very important in determining the characteristics of the secondary jets. Figure 4 was computed by dividing Eq (3) by V_o. Note that the actual value of α and γ is not as critical as the sum $(\alpha + \gamma)$. The velocity ratio is high as $(\alpha + \gamma)$ approaches 180 deg.

The potential to generate extremely high velocities with a relatively low driving pressure can be illustrated by the following example. Suppose that $\alpha = 80$ deg and $\gamma = 90$ deg and that the driving pressure P_o is 1000 bar. Then from the relation $V_o \simeq 14\sqrt{P_o}$, V_o is 440 m/s. But the velocity augmentation from Eq 3 is 11.4, so that V_{fj} is 5000 m/s. To produce a jet velocity of this magnitude by conventional extrusion methods would require a driving

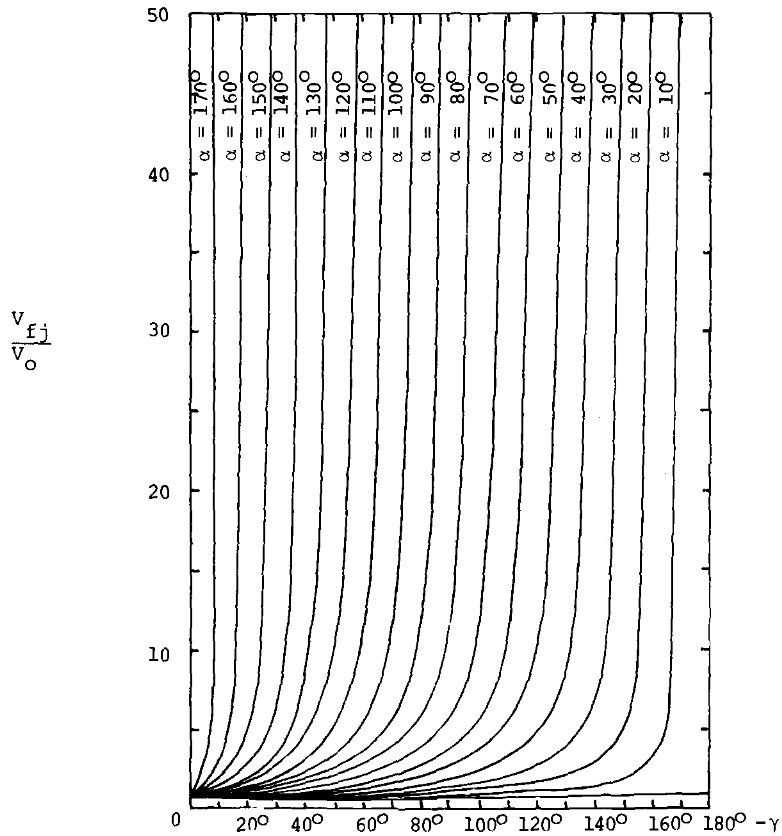

FIG. 4—*Velocity augmentation ratio as a function of the impact angles α and γ.*

pressure of 130 000 bar, 130 times that required if the augmentation is produced.

Figure 5 is a plot of the kinetic energy ratio EK_{fj}/EK_{in} for various values of α and γ. From this figure it can be seen that the kinetic energy ratio is at a maximum value of 1 when α and γ are equal. Three types of flow can be identified based on the relationship between α and γ (Fig. 5). When $\gamma = \alpha$, all the energy is possessed by the fast secondary jet and the slow jet has none. In the region where $\gamma < \alpha$, the slow secondary jet moves to the left. In the region where $\gamma > \alpha$, the secondary slow jet moves to the right along with the fast secondary jet. Figure 6 is a plot of the concentration of energy ratio. This figure is very similar to Fig. 4 and the same comments apply. Based on the information that the kinetic energy ratio is maximum for $\alpha = \gamma$ (Fig. 5), the optimum condition for energy concentration can be plotted as a dashed line on Fig. 6.

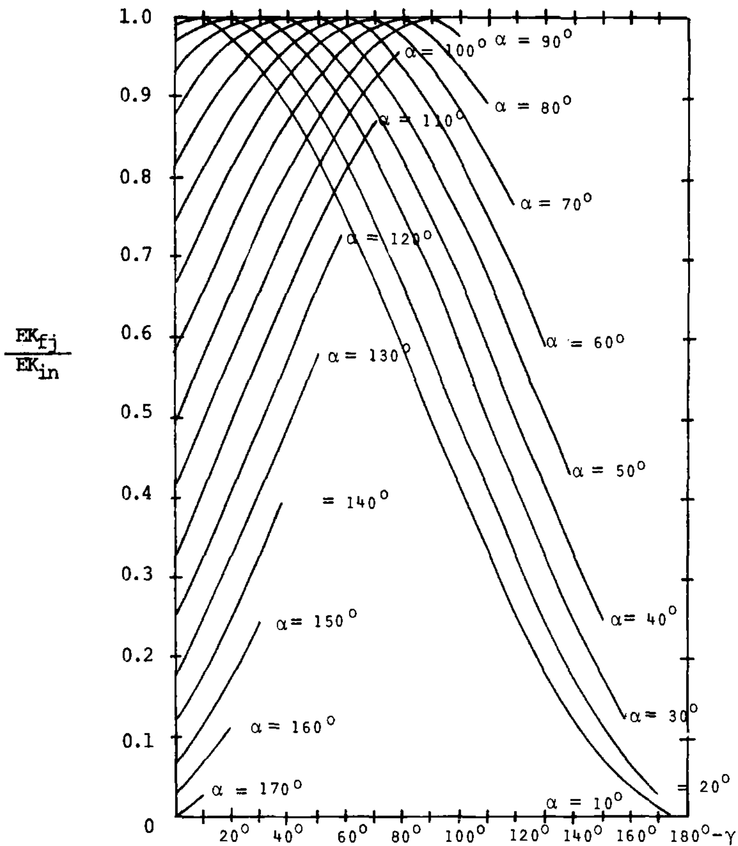

FIG. 5—*Kinetic energy augmentation ratio as a function of the impact angles α and γ.*

Experimental Applications

Under normal circumstances it is extremely difficult to obtain a flat leading edge to a waterjet or to maintain a uniform velocity across the jet profile. The surface or profile is generally curved (Fig. 1) or more severely distorted by jet movement relative to the surrounding medium.

At the point where the jet breaks into droplets, however, the contour of the leading surface will stabilize and the velocity will be sensibly constant within the droplet. This set of conditions allows the foregoing analysis to be extended to cover this case. Analysis of this phenomenon has been carried out in Cambridge [5] and therefore only a comparative relation will be made.

Figure 7 shows a central element sliced from a spherical droplet, of radius R and moving at speed V_0 toward the flat surface 00 at an angle α. Every phase of the collision can be considered using the previously derived equa-

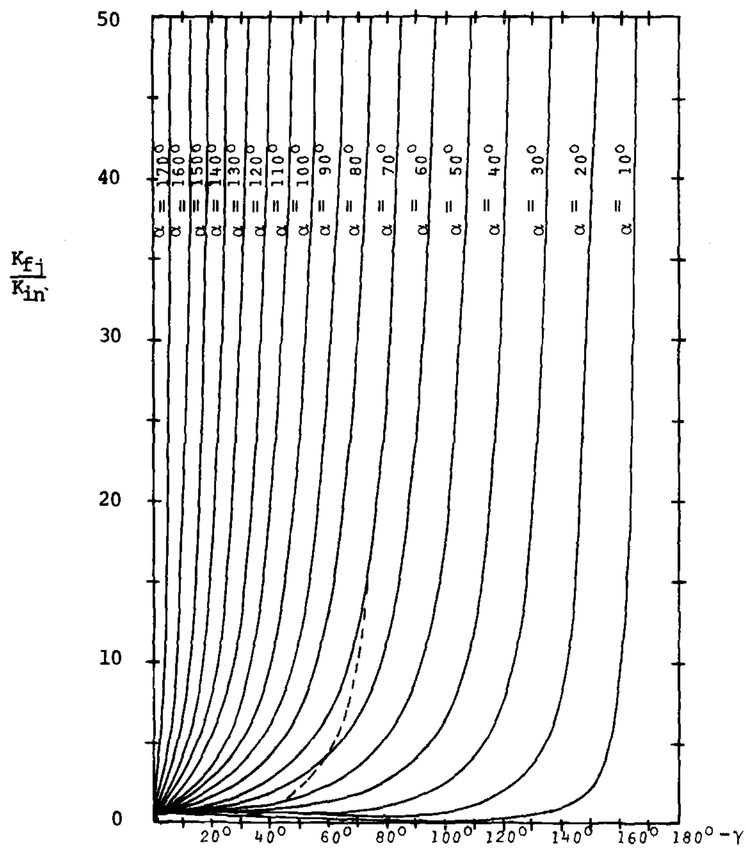

FIG. 6—*Energy intensification ratio as a function of the impact angles α and γ.*

tions with suitable transformations to adapt them to the present geometry. For example, when the face of the element from M' to M'' contacts the flat surface, the geometry is the same as that of Fig. 2. The droplet first contacts the plane 00 at M_1 and the analysis ends when the contact point moves along the arc to the point M_n. The value of β will vary from α to 180 deg in the interval

$$0 \leq t \leq \frac{R(1 + \sin\alpha)}{V_o \sin\alpha}$$

and

$$\gamma = 180 - \beta$$

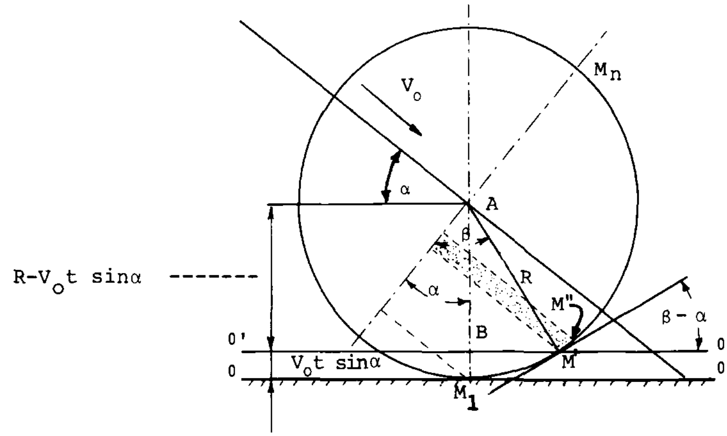

FIG. 7—*Geometric representation of the impact of a bubble with an oblique surface.*

which can be substituted into Eqs 3, 14, 16, and 17 to give a new set of equations valid for the central portion of the droplet

$$\frac{V_{fj}}{V_o} = \frac{\sin\alpha + \sin\beta}{\sin(\beta - \alpha)} \tag{18}$$

$$\frac{EK_{fj}}{EK_{in}} = \frac{[1 - \cos(\beta - \alpha)]\,(\sin\alpha + \sin\beta)^2}{2\sin^2(\beta - \alpha)} \tag{19}$$

$$\frac{K_{fj}}{K_{in}} = \frac{(\sin\alpha + \sin\beta)^2 \sin\alpha}{\sin^3(\beta - \alpha)} \tag{20}$$

Representative values obtained using these equations are shown in Fig. 8, 9, and 10.

Discussion of Results

The fast-jet velocity ratio (Fig. 8) when plotted as a function of the angle α and β indicates that the curves for various values of α are similar in shape but displaced as a function of β. In every case the velocity ratio becomes very large as the angle α approaches the value of β. For practical considerations, the range of β that leads to the formation of satisfactory fast jets is considered to be $\alpha \leq \beta \leq \alpha + 15$ deg.

From the curves in Fig. 9 which show the kinetic energy ratio as a function of the angles β and α, the same conclusions can be drawn as for the earlier case of a flat impact shown in Fig. 5. The highest energy ratios occur when α and γ are equal ($\gamma = 180 - \beta$).

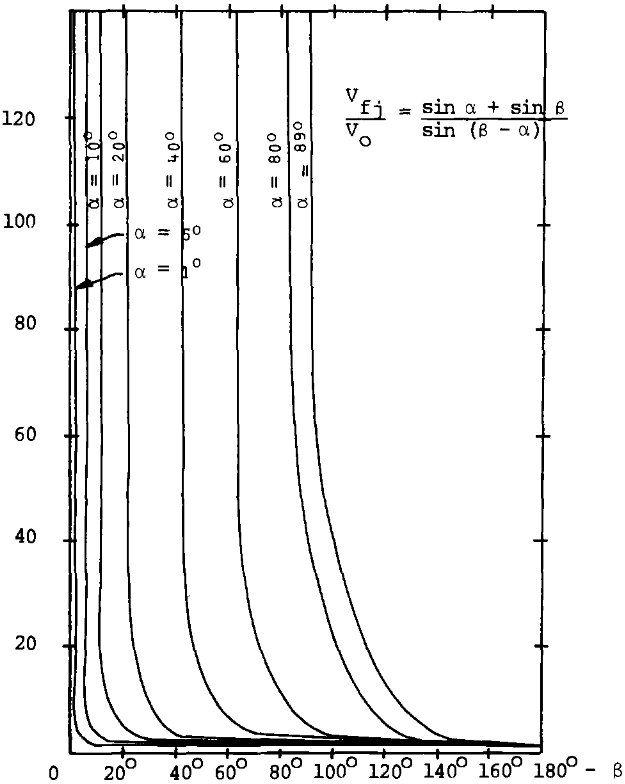

FIG. 8—*Velocity augmentation ratio for a droplet impact as a function of the angles α and β.*

The concentration of energy ratio shown plotted in Fig. 10 is similar to that for a flat-faced jet (Fig. 6). It is again found that, as α approaches β, so the energy ratio tends to infinity. Where values of α are small, the range of β over which the jet energy is highly concentrated is also small, but as α increases, so the width of the angle β over which a highly intensified jet is produced is also increased. It is interesting to note that the kinetic energy augmentation is at an optimum where $\alpha = \gamma$ and that the energy intensification is at an optimum where $\alpha = \beta$. Since $\gamma = 180 - \beta$, this suggests that the optimum energy augmentation with the most concentrated jet might occur when $\alpha = \beta = \gamma = 90$ deg. Under such circumstances the fast jet would be at greatest damage potential when the vertically impacting drop is at its maximum contact diameter. In this regard, investigators at Cambridge [5] have found that damage from impacting droplets is confined to the periphery of the droplet impact zone. The equivalence of the relationship between droplet flow and continuous jet flow is suggested by a corresponding result obtained at Rolla with a high-pressure continuous jet directed at an aluminum target located

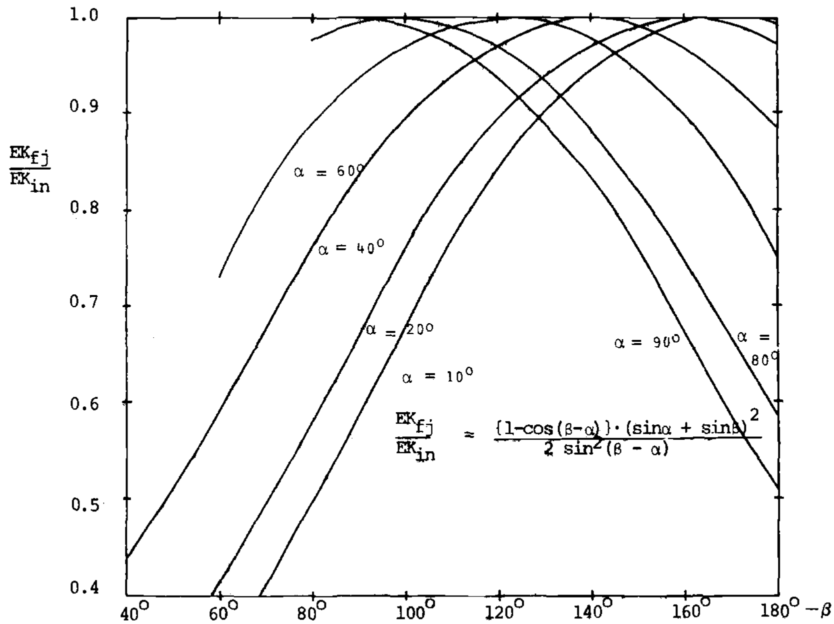

FIG. 9—*Kinetic energy augmentation ratio as a function of the impact angles α and β for a droplet.*

2.5 cm from the jet nozzle (Fig. 11), where damage is also confined to the region at and beyond the jet impact periphery.

Experiments have, however, concentrated on examining the zone of jet interaction farther down the jet stream where the flow has disrupted into droplets. Figure 12 shows a photograph of such a jet collision with an impact angle of $\alpha = 10$ deg at 4 bar obtained by the strobe flash technique [*10*]. All the droplet components of each jet do not impact other droplets since there is no control over their spatial distribution and velocity. When two droplets do collide, however, the shock wave generated by the fast jet is clearly visible. The results are similar to those of a collapsing cavitation bubble, which produces a Monroe jet with accompanying shock waves [*6*]. It is similar to the photographs obtained by Edney [*7*] of the explosive extrusion of the waterjet in a vacuum.

In practice the structure of a high-pressure waterjet, particularly at velocities of the order of 300 m/s, is extremely sensitive to interference from adjacent bodies. For this reason, while waterjet impact on solid bodies can be used to generate augmented velocities, the diffuse structure around two continuous jets will interfere with the jet structure prior to impact and negate much of the proposed augmentation. Conversely, once the jet has disintegrated into droplets, this is no longer the case, although the target

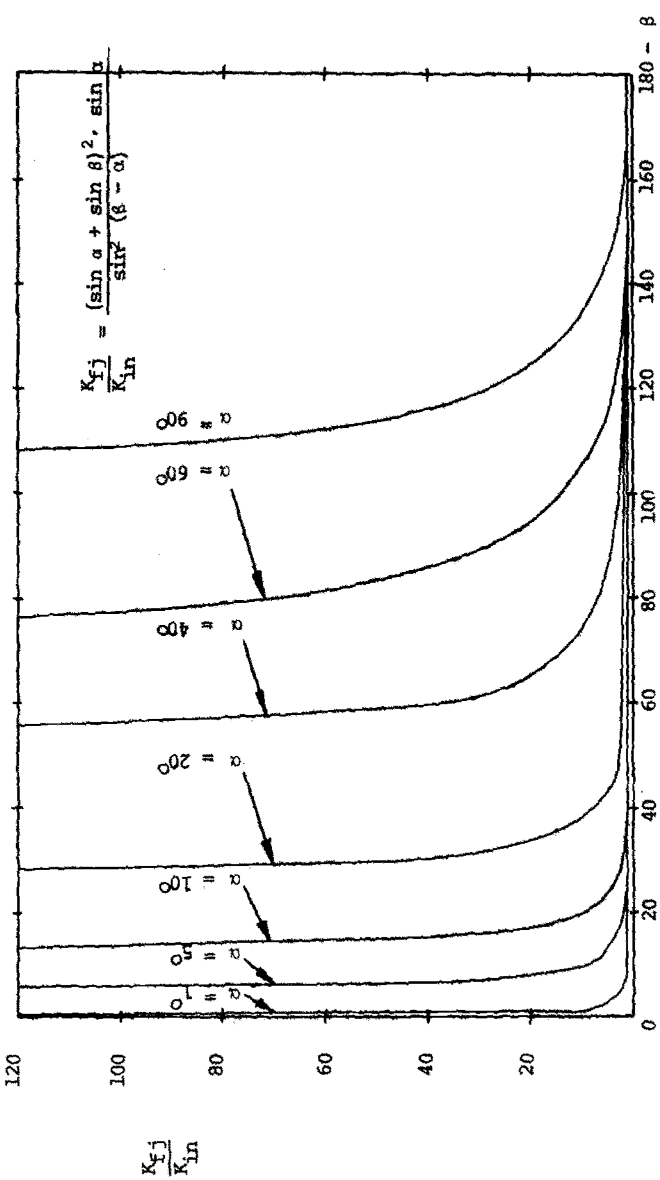

FIG. 10—*Energy intensification ratios as a function of the impact angles α and β for a droplet impact.*

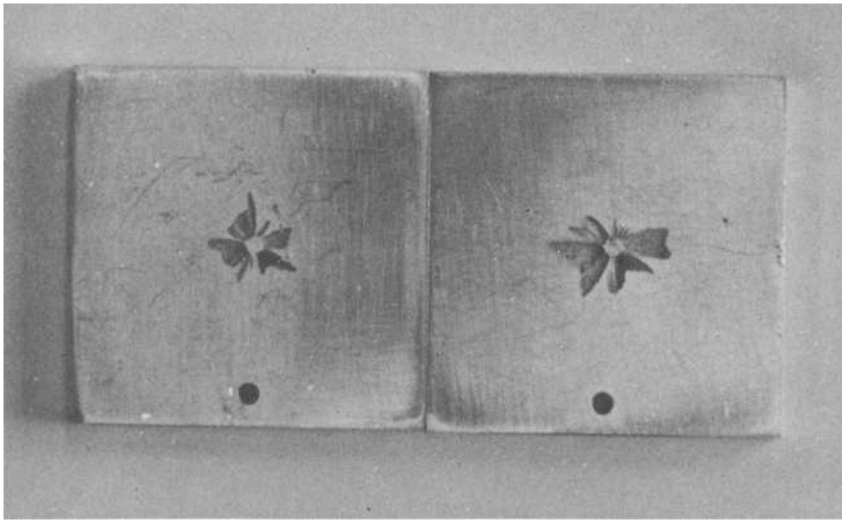

FIG. 11—*Aluminum targets after continuous jet impact at 680 bar stagnation pressure; damage is confined to an area on the periphery of the jet and beyond.*

location should be in the immediate vicinity of the impact point since the fast jets produced are extremely small and thus rapidly disrupted. Further research on the effectiveness of interfering jets, designed to interact beyond the jet collapse distance, is therefore required.

Rock Cutting Experiments

As a practical test of the potential effectiveness of converging jets, an experiment was carried out on Berea sandstone specimens, 15 cm diameter and 30 cm long, with test nozzles placed 1.25 cm above the specimen. The jet pressure was 680 bar for this study, in which approximately 20 different nozzle geometries were examined. Nozzles were constructed to produce two parallel jets of diameter 1 mm, separated by distances of 1.27, 1.78, and 3.0 mm. Nozzles were also constructed to produce converging jets at included angles 1, 2, 5, 10, 15, and 20 deg. All the nozzles were machined from brass and the inside surfaces of the nozzles were lapped.

The best results were obtained with the parallel nozzles having the 1.27- and 1.78-mm spacing and the convergent nozzles with 1- and 2-deg included angle. The results from the 5, 10, 15, and 20-deg angle were poor, no cumulative effect being observed. The sandstone specimens were split after an exposure time of 10 to 15 s when either the 1- or 2-deg nozzles were tested (Fig. 13).

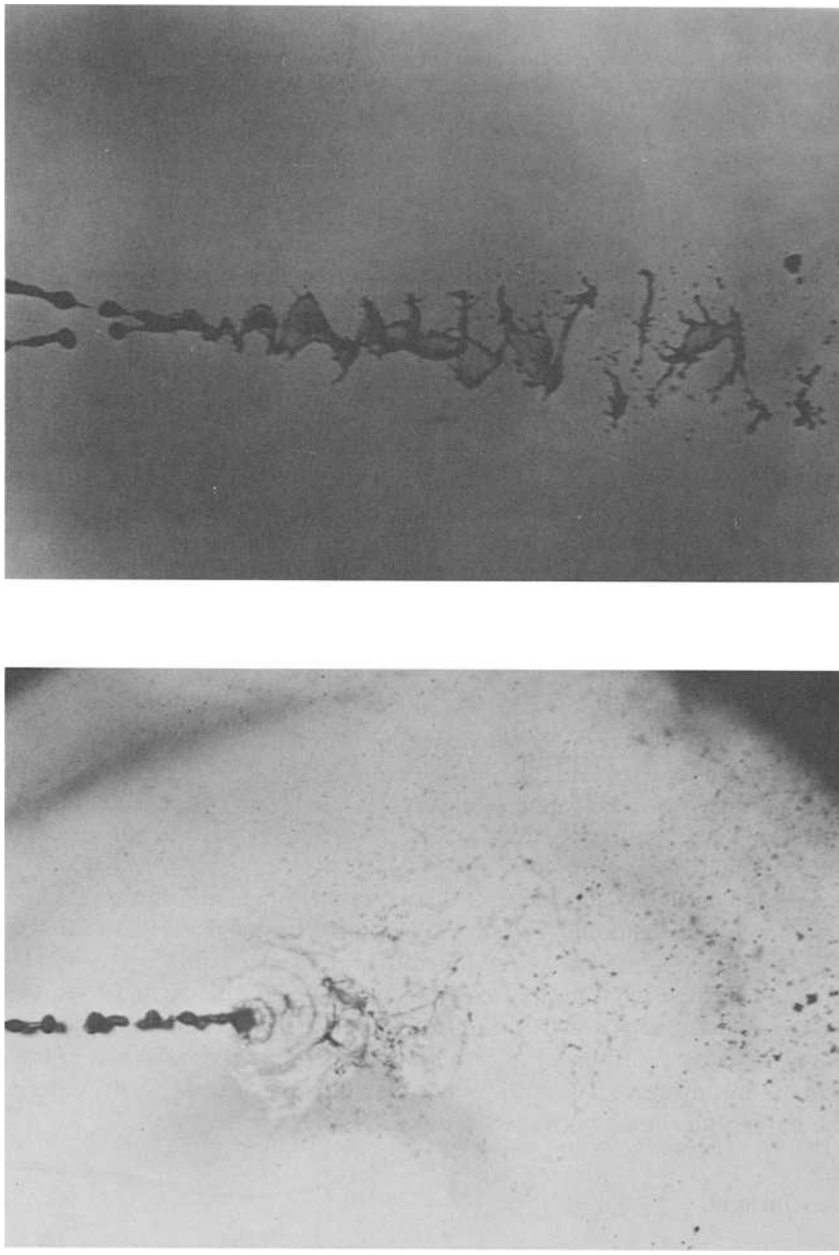

FIG. 12—*Views of water jets at a pressure of 4 bar converging at an angle of 10 deg at the point where the jet turns into droplets:* (a) *top view showing the angle of impact,* (b) *side view showing shock waves generated by the small augmented jet velocity.*

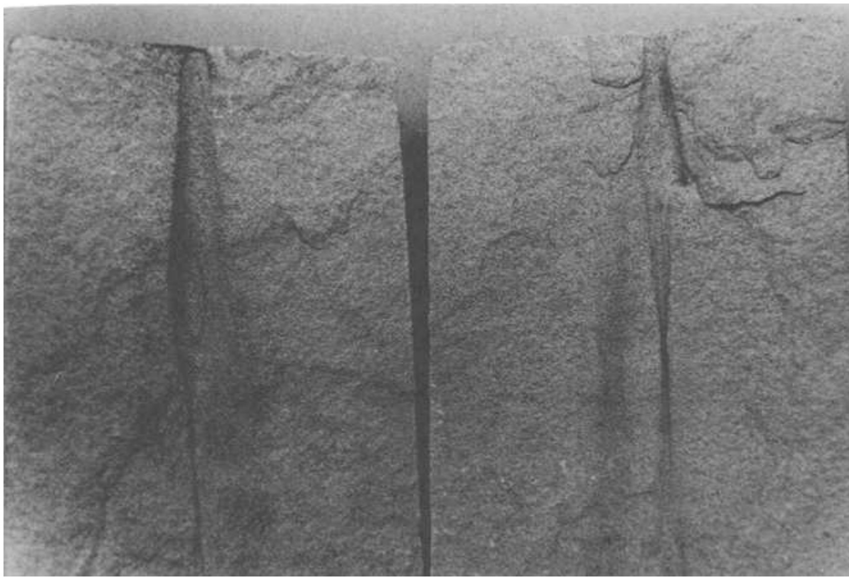

FIG. 13—*Cavity cut into Berea sandstone by a converging jet showing the narrow cut made by secondary jet action.*

Figure 14 shows one of the convergent nozzles located just above the sandstone. Using the parallel nozzles with 1.27- and 1.78-mm spacing gave results similar to those of the 1- and 2-deg convergent nozzles. One reason postulated for this is the Coanda effect by which two jets flowing close together tend to merge into one jet [*9*].

Subsequent to the conclusion of this experiment the authors were engaged in research on a hydraulic mining unit in a surface mine in northern Missouri [*8*]. The seam of coal was being mined by waterjets at a pressure of 680 bar when it was discovered that the coal was interlayered with pyrite lenses, with a compressive strength of the order of 2000 bar. Under normal conditions the jets would not cut this material, so a set of converging jet nozzles was inserted into the cutting head. The jets produced cut the pyrite satisfactorily, allowing the mining machine to advance at a rate of 1.7 m/min.

Conclusions

The use of external augmentation techniques to improve waterjet cutting ability has been demonstrated to be an effective way of improving the cutting of rock and is a means of generating higher pressures than those extant within the preexisting flow. Because of the problems which arise in bringing two flat-ended jets together exactly symmetrically, it is proposed herein that

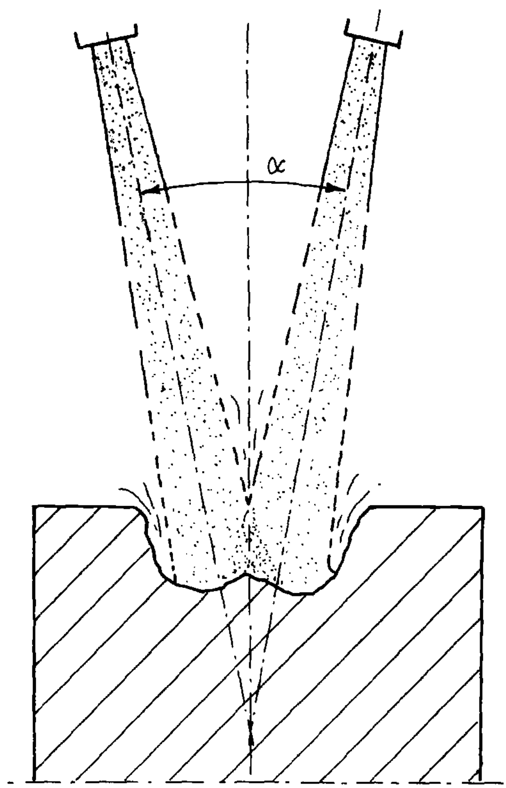

FIG. 14—*Proposed geometry for augmented cutting using the enhanced velocity effects from colliding droplets.*

a more effective technique would be to converge the jets at a point where they have just broken into droplets. Photographic evidence of such an event shows that large velocity augmentation is possible.

References

[*1*] Birkhoff, G. et al, *Journal of Applied Physics*, Vol. 19, June 1948.

[*2*] Walsh, T. M. et al, *Journal of Applied Physics*, Vol. 27, No. 3, March 1953.

[*3*] Eichelberg, R. J. and Pugh, E. M., *Journal of Applied Physics*, Vol. 23, No. 5, May 1952.

[*4*] "Externally Augmented Hypervelocity Jet Program," Bowles Engineering Corporation, Final Report R-10-31-69, Contract DOT-FR-9-0015, Silver Springs, Md. 1969.

[*5*] Brunton, J. M., *Philosophical Transactions of the Royal Society*, Series A, Vol. 260, pp. 79-85, 28 July, 1966.

[*6*] Summers, D. A. and Bushnell, D. J., *Proceedings*, Workshop on the Application of High Pressure Water Jet Cutting Technology, University of Missouri-Rolla, Rolla, Mo., 1975.

[*7*] Edney, B. E., "Experimental Studies of Pulsed Water Jets," 3rd International Symposium on Jet Cutting Technology, Chicago, May 1976.

[*8*] Summers, D. A., Barker, C. R., and Mazurkiewicz, M., "Development of a Longwall

Water Jet Mining Machine," Phase III Report, University of Missouri-Rolla, Rolla, Mo., 1977.

[9] Metral, A. and Zerner, F., *The Coanda Effect*, United States Atomic Energy Commission Publication AEC-TR-3386.

[10] Summers, D. A. and Zakin, J. L., "The Structure of High Speed, Fluid Jets and Their Use in Cutting Various Soil and Material Types," Final Report on USA Mobility Equipment Research and Development Center Contract DAAK 02-74-C-0006, April 30, 1975.

B. P. Selberg[1] and C. R. Barker[1]

Dual-Orifice Waterjet Predictions and Experiments

REFERENCE: Selberg, B. P. and Barker, C. R., "**Dual Orifice Waterjet Predictions and Experiments**," *Erosion: Prevention and Useful Applications, ASTM STP 664,* W. F. Adler, Ed., American Society for Testing and Materials, 1979, pp. 493–511.

ABSTRACT: A simplified dual-orifice circular jet analysis is developed to predict maximum velocity and pressure profile capabilities of waterjets. The analysis is applied to nozzles having total exit diameters of 1.016 mm operating at stagnation pressures of 2.812 MN/m^2. These conditions result in flow rates of less than 2.27×10^{-1}m^3/s of water. Dual-orifice converging nozzles with 2- and 10-deg included convergence angles are analyzed as well as dual-orifice diverging nozzles with 8, 10, and 20-deg included divergence angles. The control-volume form of the conservation of mass and the conservation of momentum equations is applied to the converging dual-jet case. Velocity profiles prior to jet mixing, after Schlichting and Tollmien, are used as profile input to the conservation equations. Profile shapes after Schlichting are used downstream of the jet mixing process. Linear jet diameter growth laws are applied to predict jet diameters before and after the mixing process. The merged jet profiles are calculated downstream of the nozzle at representative stations and compared with a single-orifice jet profile of the same energy input. Diverging dual-orifice jet profiles are generated using the same profile and diameter growth equations as for the converging dual-orifice nozzle jet. Velocity and pressure profiles, generated at representative stations downstream of the nozzle exit, are compared with single-orifice nozzle profiles of the same total energy input. Experimental comparisons are made with 2- and 10-deg included-convergence-angle converging nozzles and with 8, 10, and 20-deg included angle diverging nozzles at 2.812 MN/m^2 stagnation pressure. All nozzle shapes consist of a 13-deg converging cone followed by a straight section of length 2.5 exit diameters. A pressure transducer, fixed to the traveling carriage of a lathe and oriented so that the nozzle axis is in line with the transducer axis, is used for profiling studies. A hardened steel shield with a 5.00×10^{-1} mm central hole protects the transducer for the pressure profile studies. These pressure profile measurements are made at the same representative stations as the analytical results. Discussion of the agreement between analytical and experimental results is made with emphasis on limitations of the analytical model, the experimental tests, and on suggested improvements in nozzle design which will bring the analytical predictions and experimental results closer together.

KEY WORDS: waterjets, dual-orifice jets, converging jets, diverging jets, nozzle surface roughness, jet coherence, jet cutting, erosion

[1] Associate professor of aerospace engineering; associate professor of mechanical engineering and research associate, respectively, University of Missouri-Rolla, Rolla, Mo. 65401.

Many researchers have investigated both theoretically and experimentally single-orifice waterjets [*1-8*].[2] From this work the most widely accepted nozzle has a conic convergent section with a 13-deg angle followed by a straight section of length 2.5 exit diameters. Generally, these single-orifice nozzles are capable of producing waterjets that remain coherent for a distance of 100 to 250 nozzle diameters [*9*]. Some improvement in these jet coherence lengths can be obtained by adding long-chain polymers to the water [*10*] or by changing nozzle geometry [*3,11*].

Whereas single-orifice nozzle design is well understood, there has been comparatively little work conducted on dual- or multiple-orifice design. Some work has been carried out by Nikonov [*12*] and Summers [*13*] et al. Nikonov found that a 15-deg-included-angle dual-orifice nozzle gave the most effective jet action whereas Summers et al obtained the best results with a 20-deg-included-angle dual-orifice diverging nozzle. It is the purpose of this paper to further develop the multiple-orifice nozzle base by investigating dual-orifice nozzles that are being fed by the same supply pipe.

Theoretical Analysis

A simplified turbulent-jet theory, due first to Tollmien [*14*], was applied to axisymmetric circular jets. This theory is for an airjet into air or a waterjet into water and does not take into account the two-phase flow which will occur at the waterjet-air boundary. However, the application of this simplified turbulent-jet theory is consistent with the intent of trying to predict maximum possible pressure and velocity profiles prior to significant jet-air mixing or jet breakup. The theory assumes the jet width is proportional to axial length of the jet, x, and that the centerline velocity is proportional to $1/x$. The linear jet width growth is in agreement with most experimental data of turbulent axisymmetric jets of water into air. Recent measurements of Yanaida [*15*] show a $x^{1/2}$ growth of the jet width. In addition, the kinematic momentum is taken a constant along the jet axis. These assumptions imply a constant virtual kinematic viscosity, ϵ_0, as well as identical differential equations as for laminar jet flow. Schlichting's solution of these equations is

$$u = \frac{3}{8\pi}\frac{K}{\epsilon_0 x}\frac{1}{(1 + 1/4\eta^2)^2}$$

$$v = \frac{1}{4}\sqrt{\frac{3}{\pi}}\sqrt{\frac{K}{x}}\frac{\eta - 1/4\eta^2}{(1 + 1/4\eta^2)^2} \tag{1}$$

$$\eta = \frac{1}{4}\sqrt{\frac{3}{\pi}}\sqrt{\frac{K}{\epsilon_0}}\frac{r}{x}$$

[2]The italic numbers in brackets refer to the list of references appended to this paper.

where

u = axial velocity component,
v = velocity component perpendicular to jet axis,
x = distance in axial direction of jet,
r = distance in direction perpendicular to axis,
K = jet kinematic momentum divided by fluid density, and
ϵ_o = virtual kinematic viscosity.

These solutions were used to generate velocity profiles at various jet locations downstream of the nozzle exit. Input conditions to these profiles were obtained by first using Bernoulli's equation for incompressible flow to predict the maximum velocity point u_{max} at the center of the jet and exit of the nozzle. Along the jet axis, the centerline velocity u_{cl} was determined utilizing a form suggested by Hinze [*16*]

$$\frac{u_{cl}}{u_{max}} = A\left(\frac{d}{x+B}\right) \tag{2}$$

where d is the jet diameter at the nozzle and A and B are constants. The constants A and B were solved for in Eq 2 from experimentally determined centerline velocity measurements at the $x/d = 25$ and $x/d = 50$ stations. For each axial location, u_{cl} is calculated from the foregoing and then used with the u from Eq 1 to solve for the correct value of virtual kinematic viscosity, ϵ_o, at each axial location. With the proper ϵ_o's, profiles of u can then be generated. System design constraints necessitated having a pipe 6.35 mm inside diameter and 762 mm long upstream of the nozzle. With this supply pipe-nozzle configuration the flow into the nozzle would be fully developed pipe flow. Although the acceleration in the nozzle would thin the boundary layer and flatten the velocity profile at the nozzle exit, the exit flow conditions would more nearly be approximated by a modified pipe flow. Therefore a one-seventh power velocity profile was taken at the velocity exit. This compares well with turbulent smooth-pipe data for the Reynolds number in question [*2*]. The mean velocity can then be obtained from the one-seventh power law, $\bar{u} = 0.816\, u_{max}$. The volume flow rate, Q, then becomes

$$Q = \pi R^2 \bar{u} = 0.816\, \pi R^2 u_{max} \tag{3}$$

The kinematic momentum can be calculated at the nozzle exit and is

$$K = 2\pi \int_0^\infty u^2 r dr = 2\pi u^2{}_{max} \int_0^R \left(\frac{r}{R}\right)^{2/7} r dr \tag{4}$$

The kinematic momentum is then available as input into the foregoing velocity profile equations. Utilizing these equations, velocity data have been generated for the dual diverging jets and then transformed to nozzle axis, x, and to the coordinate normal to the nozzle axis, r. With the control-volume form of the momentum equation, the force on transducer orifice can be calculated. This force is then divided by the transducer orifice area to obtain the pressure.

These same velocity profiles are used as input for the converging dual-jet analysis. The converging dual-jet analysis utilizes the control form of the momentum and mass equations. The momentum equation for a non-moving control volume is

$$\Sigma \mathbf{F} = \int_{cs}\int \rho \mathbf{V}(\mathbf{V}\cdot\eta)\, dA + \frac{\partial}{\partial t}\int_{cv}\int\int \rho \mathbf{V} dR \tag{5}$$

where

$\Sigma \mathbf{F}$ = summation of external forces on control volume,
ρ = fluid density,
$\mathbf{V}$ = fluid velocity,
η = outward normal unit vector of dA,
dA = elemental surface element of control surface, cs,
t = time, and
dR = elemental volume element of control volume, cv.

For steady flow the last term on the right-hand side is zero and for a free jet the pressure forces cancel, leaving

$$\int_{cs}\int \rho \mathbf{V}(\mathbf{V}\cdot\eta)\, dA = 0 \tag{6}$$

This term, which is the momentum flux through the control surface, is nonzero only where the jet crosses the control surface. Figure 1 shows a typical merging jet with the control surface. The merging jets, 1 and 2, use the velocity profile due to Schlichting, given previously. The momentum equation can be rewritten for axisymmetric jets as

$$\int_0^\infty \rho \mathrm{V}_3 \mathbf{V}_3 r dr = \int_0^\infty \rho \mathrm{V}_1 \mathbf{V}_1 r dr + \int_0^\infty \rho \mathrm{V}_2 \mathbf{V}_2 r dr \tag{7}$$

Since the form of velocity is known, and the density remains constant for the pressure range considered, Eq 7 can be solved for V_3.

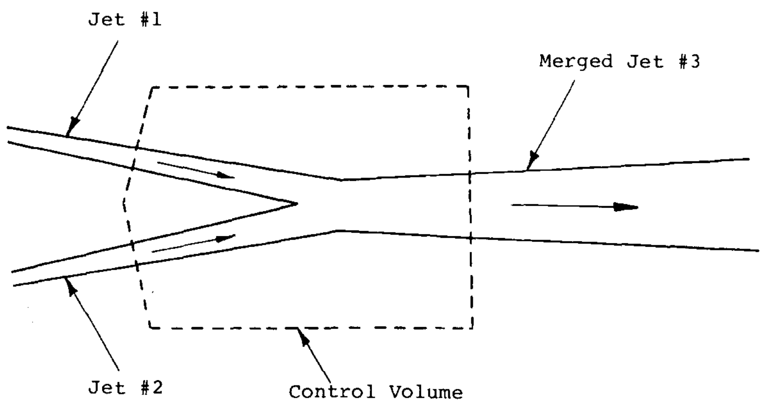

FIG. 1—Merging jets with control volume.

Experimental Apparatus and Procedure

The pressure profiling experiments were conducted on a modified lathe bed. The nozzle supply pipe was mounted onto the lathe chuck with the stagnation chamber located directly upstream of the lathe. Stagnation supply pressures were measured in this chamber. The stagnation chamber was connected to the 5.58×10^4 J/s pump by a flexible high-pressure hose. The strain gage pressure transducer was mounted to a vertical milling attachment which in turn was mounted to the carriage of the lathe for axial and transverse movement. Transverse location was monitored with a linear potentiometer in conjunction with one channel of a chart recorder, with pressure recorded on the second channel of the recorder, yielding a plot of pressure versus transverse distance for each nozzle axial location of the transducer. The experimental setup is shown in Fig. 2.

The pressure transducer itself was mounted inside a steel plug whose front surface was flat and about 38.1 mm in diameter. The surface of the plug was hardened with a small centered hole, 5.00×10^{-1} mm in diameter, leading to the transducer. The transducer system was capable of measuring pressures up to 2.81 MN/m^2. All nozzle tests, in which data close to the nozzle were to be taken, were conducted at a stagnation pressure of 2.81 MN/m^2.

Test procedures involved aligning the pressure transducer in the vertical direction to maximize the signal from the water jet at a stagnation pressure of 4.22×10^3 N/m^2, to ensure that the pressure orifice was at the maximum velocity plane in the vertical direction. The test runs were then conducted at the desired operating stagnation pressure. For each jet and axial location a minimum of two jet traverses were made to ensure data repeatability.

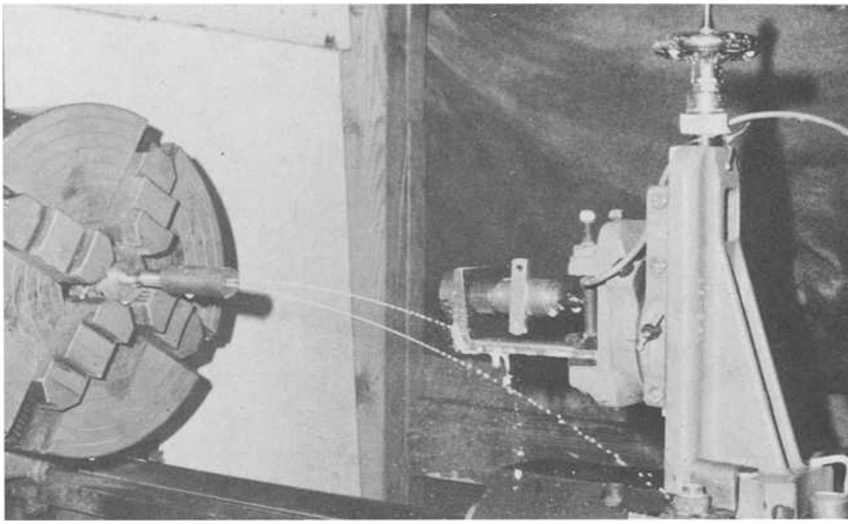

FIG. 2—*Pressure profiling apparatus.*

Results and Discussion

All the dual-orifice nozzles were the same shape, a 13-deg converging cone followed by a 2.5-exit-diameter straight section. Each orifice had an exit diameter of 1.016 mm. Four of the nozzles—the 10 and 20-deg diverging dual-orifice nozzles and the 10 and 2-deg converging nozzles—were machined out of brass and then nickel plated to prevent surface erosion effects. All the brass nozzles were machined by one technician using the same technique and were polished before plating. The 8-deg dual-orifice diverging jet nozzle is an electroformed nickel nozzle in which the nozzle is electroformed around a machined mandrel. The general contour of all the nozzles tested is shown in Fig. 3. Pressure-profiling results are presented in Fig. 4 for the 20-deg diverging nickel-plated dual-orifice nozzle that was machined of brass. The experimental profiles are the solid lines while the theory is shown by the solid circles. There is good agreement between theory and experiment at $x/d = 25$ and $x/d = 50$; however, at axial locations of $x/d = 125$ and larger, there is a rapid deterioration of the experimental data. Both jets are deteriorating at about the same rate, which is caused by an accelerated breakup of the jet core. This premature core breakup is due to some upstream pertubation on the jet which is setting up jet instabilities.

Figure 5 shows theoretical and experimental pressure-profiling results for the 10-deg nickel-plated brass dual-orifice jet. The experimental results, solid line, agree with theory only for the $x/d = 25$ station. The jets are

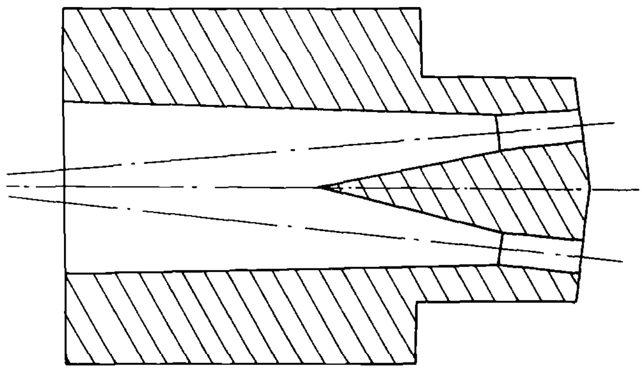

FIG. 3—*Generalized nozzle design.*

decaying rapidly, with the left jet 11 percent of its initial value and 25 percent of the right jet's magnitude at $x/d = 125$. In order to explain this poor agreement, electron microscope photomicrographs were taken of the inside of both nickel-plated brass orifices. Figure 6 is a photomicrograph of the interior surface of the left orifice. The surface finish appears to be uniform and rough. A qualitative estimate indicates roughness heights of 10^{-2} mm, which is approximately 33 times larger than acceptable typical nozzle finishes for nominal-size nozzles. Figure 7 is a photomicrograph of the right orifice. In contrast to the left orifice, the right orifice interior finish is relatively smooth. Maximum roughness heights appear to be on the order of 5×10^{-3} mm but constitute a small percentage of the total surface. However, the right orifice does show faint grooves in the circumferential direction. Figure 8 is a photomicrograph of the entire right orifice. The same circumferential grooves which appear in this figure appear in Fig. 7. The roughness results from these photomicrographs, namely, that the left orifice has larger roughness and that it exists over the entire surface, are consistent with the experimental data, which show the left jet decaying much more rapidly than the right jet. Roughness thus explains the experimental trends observed for the 10-deg diverging dual-orifice brass nozzle.

Converging dual-orifice theoretical and experimental results are shown in Fig. 9 for the 2-deg converging nickel-plated brass nozzle. Again agreement is excellent at $x/d = 50$. At $x/d = 125$ the right jet shows good agreement while the left jet is already breaking up. At $x/d = 175$ the two jets have merged and the agreement is good considering one of the converging jets was breaking up. Likewise at $x/d = 250$ the agreement is good. By $x/d = 375$, however, the merged jet is breaking up rapidly. The narrower experimental results can be attributed to the insufficient momentum input from the left jet to the final merged jet. Although the

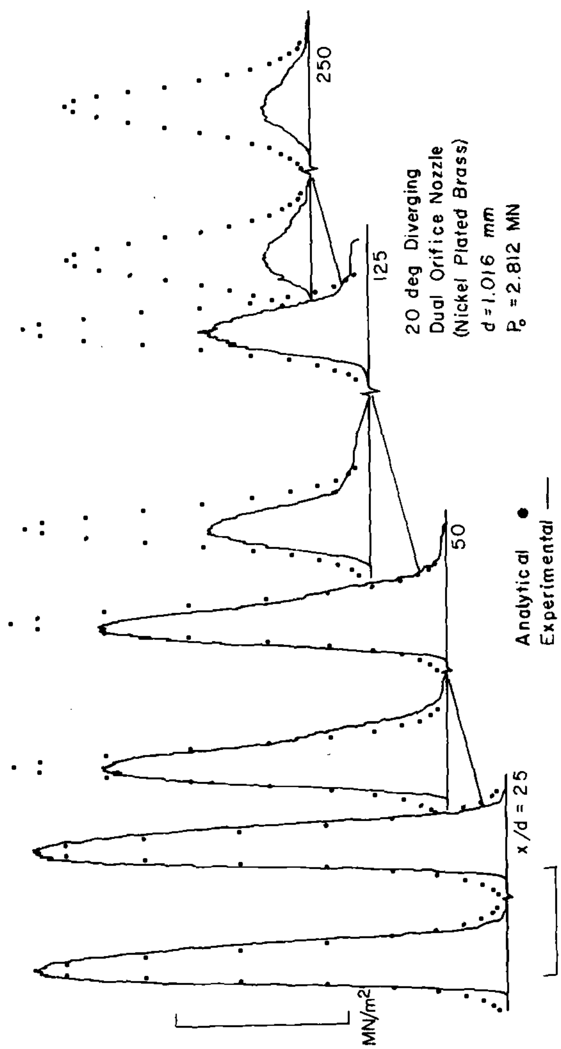

FIG. 4—*Pressure profiles for 20-deg dual-orifice nickel-plated brass nozzle.*

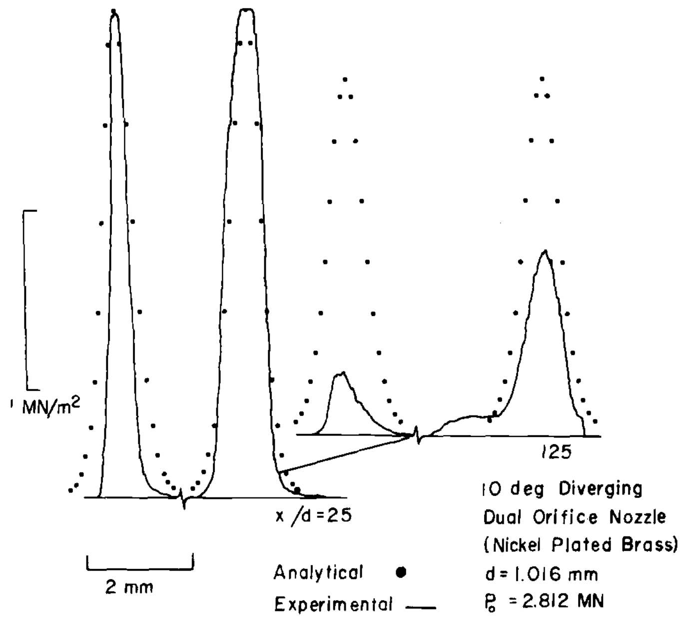

FIG. 5—*Pressure profiles for 10-deg diverging dual-orifice nickel-plated brass nozzle.*

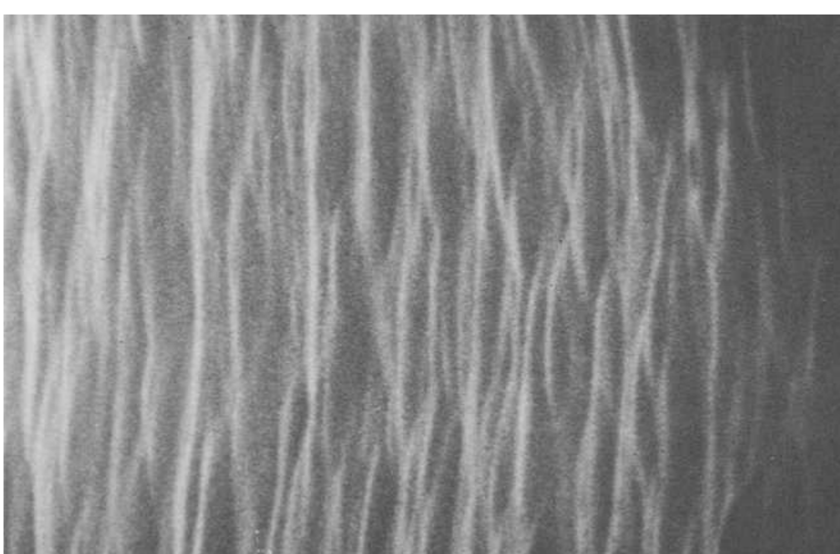

FIG. 6—*Photomicrograph of 10-deg dual-orifice nozzle—left orifice* (×675).

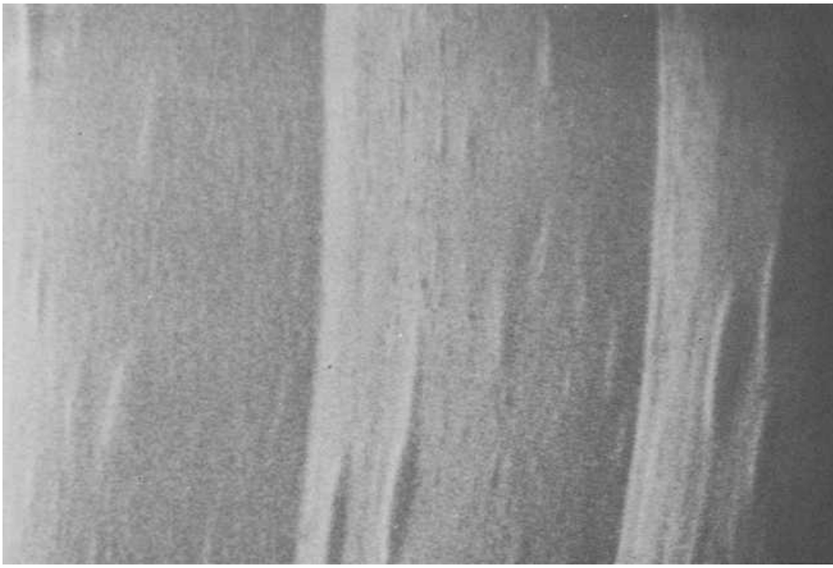

FIG. 7—*Photomicrograph of 10-deg dual-orifice nozzle—right orifice* (×675).

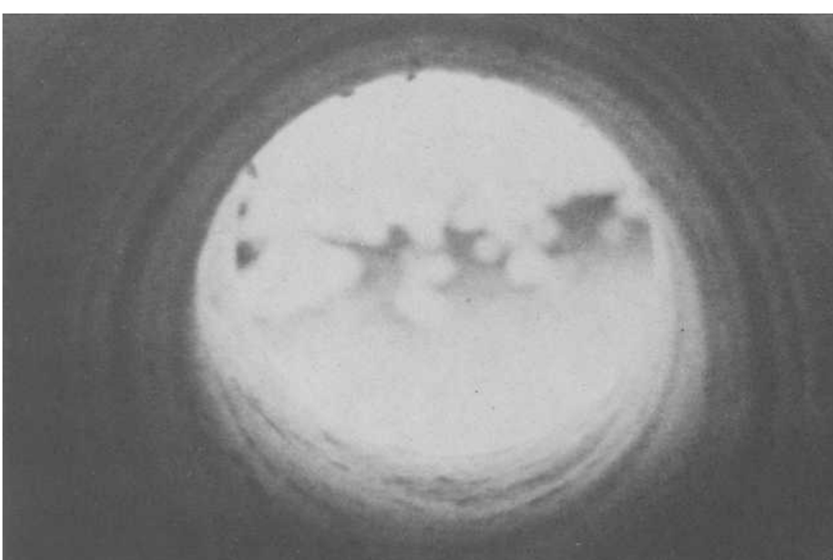

FIG. 8—*Photomicrograph of 10-deg dual-orifice nozzle—right orifice* (×56).

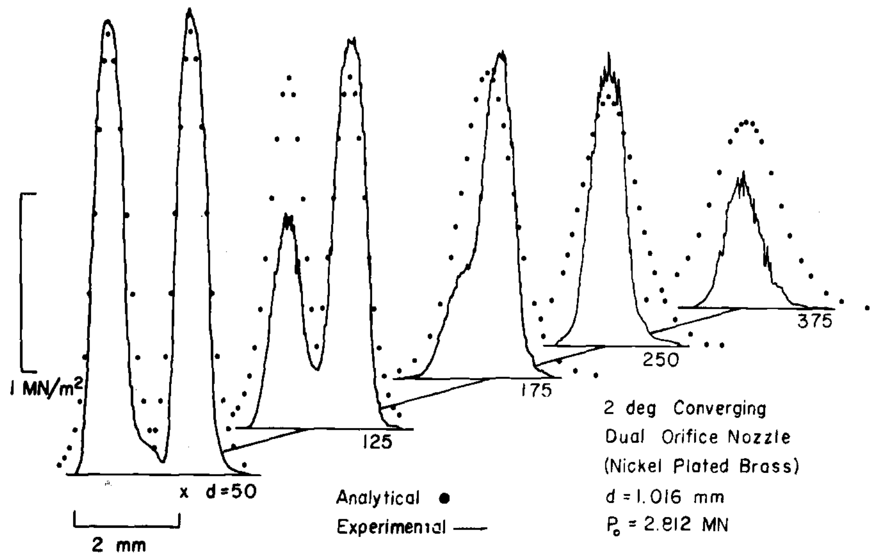

FIG. 9—*Pressure profiles for 2-deg converging dual-orifice nickel-plated brass nozzle.*

merged jet is broader than each of the individual jets, it does not appear to be as broad as a single jet of the same initial mass flow would be. A more significant observation is that the peak velocity of the merged experimental jet exceeds the analytical prediction at both $x/d = 125$ and $x/d = 250$, indicating a slower center velocity decay rate for the merged jet. This may partially explain why merged dual-orifice waterjets are more effective in actual material cutting tests than diverging dual-orifice jets. Figure 10 is a photomicrograph of the right orifice interior surface. The majority of the surface is relatively smooth with a few large protrusions on the order of 10^{-2} mm and a few minor grooves. In contrast, Fig. 11 shows the left orifice surface, which is rough all over, having roughness heights on the order of 10^{-2} mm with a large circumferential groove on the order of 4×10^{-2} mm high by at least an equal width. This circumferential groove along with others are shown clearly in Fig. 12, a photomicrograph of the entire interior surface of the left orifice exit. Each of these grooves, which lie transverse to the flow direction, will perturb the boundary-layer flow and tend to cause temporary boundary-layer separation or flow oscillations, which will result in early jet breakup. Again there is consistency between the rough surface of the left jet and its early decay, and the smoother surface of the right jet and its good agreement with theory.

Results of the 10-deg converging jet are shown in Fig. 13. At $x/d = 25$ the jets are already merged. While good agreement exists initially, there is a rapid decay of the experimental jet. This rapid decay, which may in

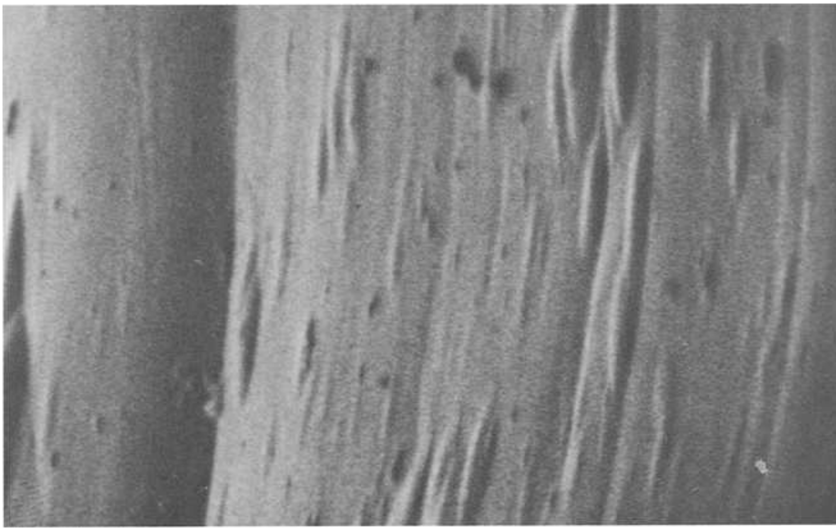

FIG. 10—*Photomicrograph of the 2-deg dual-orifice nozzle—right nozzle* (×675).

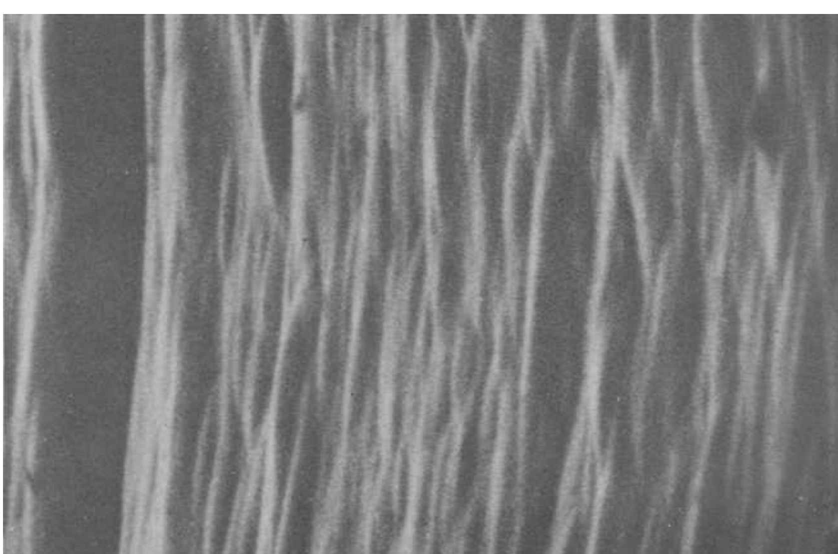

FIG. 11—*Photomicrograph of the 2-deg dual-orifice nozzle—left orifice* (×675).

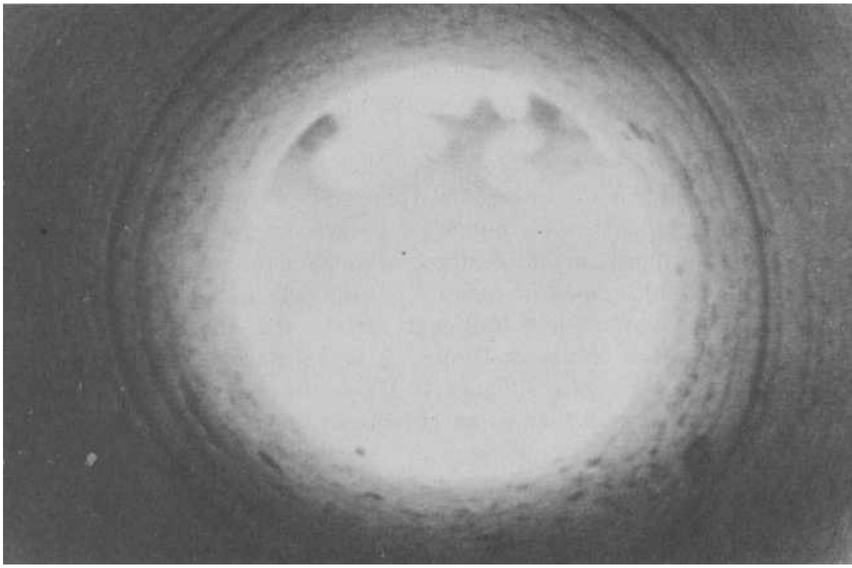

FIG. 12—*Photomicrograph of the 2-deg dual orifice nozzle—left orifice* (×56).

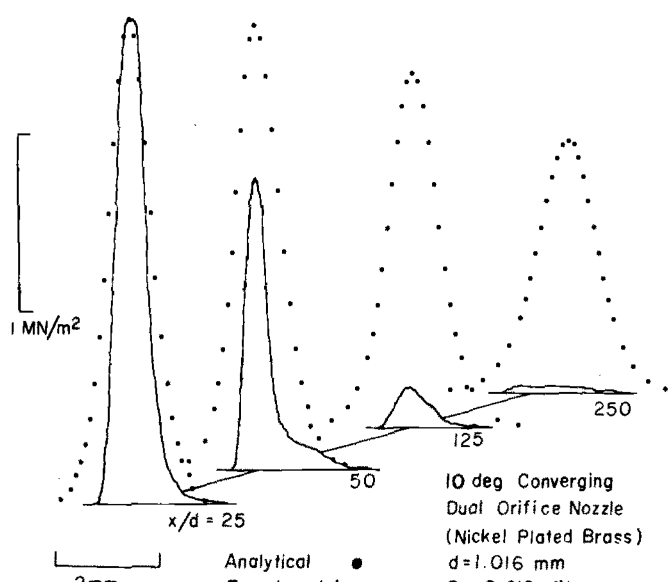

FIG. 13—*Pressure profiles for 10-deg converging dual-orifice nickel-plated brass nozzle.*

part be due to the surface finish of the nickel-plated brass nozzle, is probably also caused by the larger amount of momentum exchange that the two colliding jets are experiencing due to the larger converging angle between them. The theory does not account for this mixing in the sense of the resulting momentum losses.

The results for the electroformed nickel 8-deg diverging dual-orifice nozzle are shown in Figs. 14 and 15. There is excellent agreement between theory and experiment, with minor jet decay occurring in the left jet at $x/d = 375$, substantiating a linear growth law for the wake width. Figures 16 and 17 exhibit photomicrographs of the left and right jet interior surfaces. Both figures show minimal surface roughness, which is not estimatable because of its small size. A few surface imperfections exist but these are not repetitive. Figure 18 shows the left side with a view of the entire orifice. Again there is an absence of surface imperfections. This lack of surface roughness along with the excellent agreement between theory and experiment confirms the postulation that excessive surface roughness in the nickel-plated brass nozzles was causing the boundary layer to locally separate or instabilities to be set up within the jet which led to its early decay, or both.

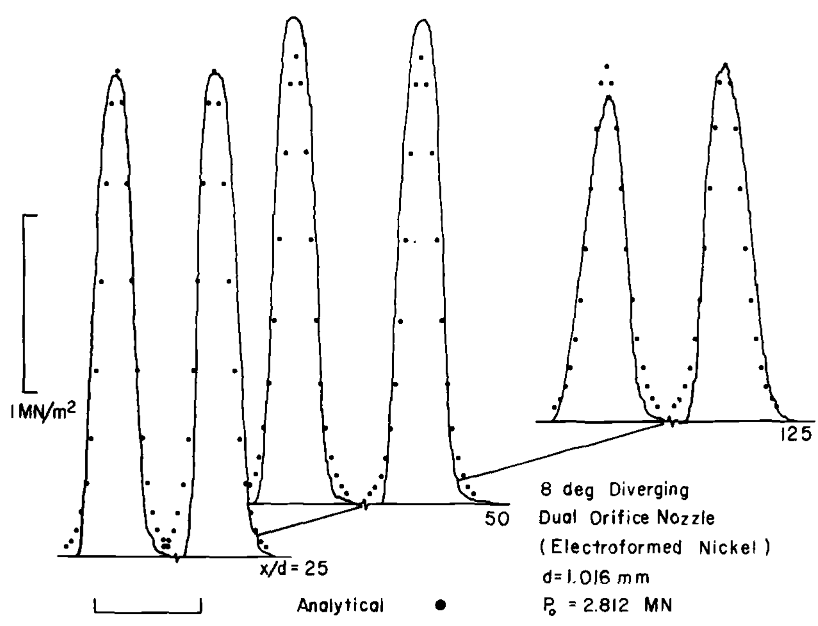

FIG. 14—*Pressure profiles for 8-deg diverging dual-orifice electroformed nozzle.*

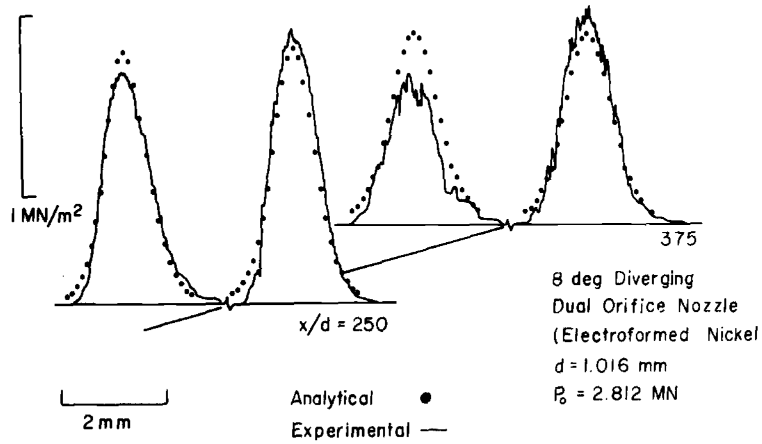

FIG. 15—*Pressure profiles for 8-deg diverging dual-orifice electroformed nozzle.*

FIG. 16—*Photomicrograph of 8-deg electroformed nickel dual-orifice nozzle—left side* ($\times$*675*).

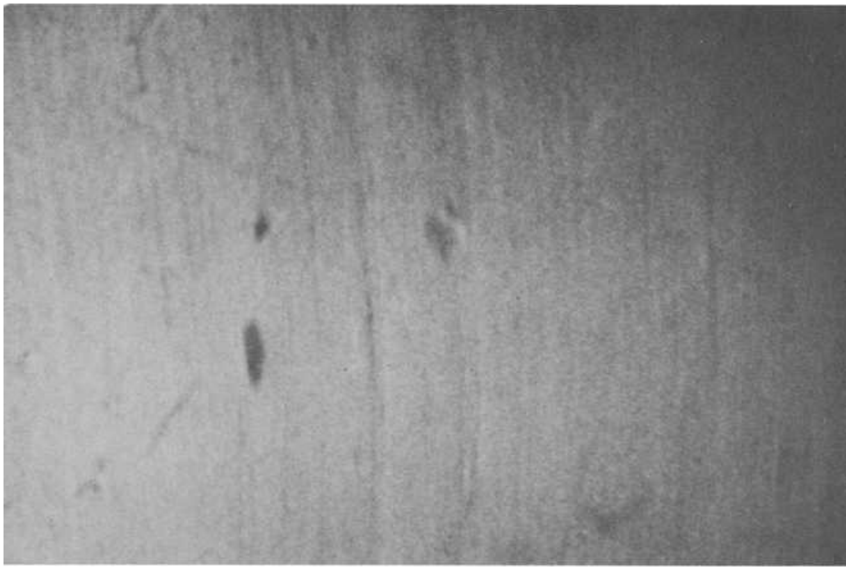

FIG. 17—*Photomicrograph of 8-deg electroformed nickel dual-orifice nozzle—right side* (×*675*).

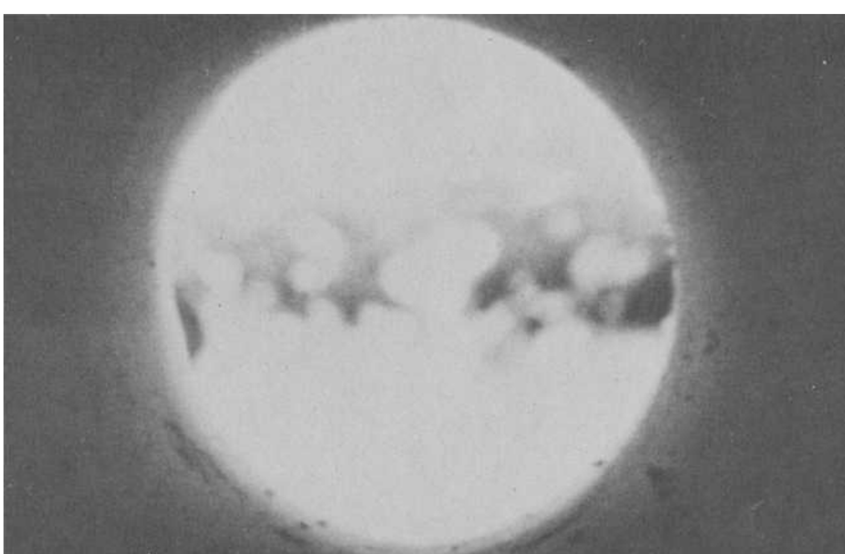

FIG. 18—*Photomicrograph of the 8-deg electroformed nickel dual-orifice diverging nozzle—left side* (×*67*).

Conclusions

The following conclusions are made concerning dual-orifice high-pressure waterjet predictions and experiments.

1. The simplified theoretical analysis is capable of predicting waterjet pressure profiles for dual-orifice diverging nozzles prior to jet breakup.

2. The control-volume analysis shows good promise of being a valid prediction technique for converging waterjets with small convergence angles prior to jet breakup.

3. The experimental results reinforce the importance of manufacturing nozzles to close tolerances such that interior nozzle surface finishes are free of blemishes.

4. Small-angle converging dual-orifice data indicate slower centerline maximum velocity decay rates than diverging jets, which explains the apparent superiority of converging jets to diverging jets in material cutting tests.

5. The electroformed 8-deg dual-orifice nozzle tests substantiate a linear growth rate for the wake width.

References

[*1*] Leach, S. J. and Walker, G. I., *Proceedings of the Royal Society*, London, Vol. 260A, 1966, pp. 295–308.

[*2*] Schlichting, H., *Boundary Layer Theory*, McGraw-Hill, New York, 1968.

[*3*] Lohn, P. D. and Walker, D. A., "Improved Mineral Excavation Nozzle Design Study," Bureau of Mines Report 33-77, 1976.

[*4*] Hokao, J., *Journal of the Japan Mining Association*, Vol. 81, No. 930, Oct. 1965, pp. 907–912.

[*5*] Fowkes, R. S. and Wallace, J. J., "Hydraulic Coal Mining Research-Assessment of Parameters Affecting the Cutting Rate of Bituminous Coal," Bureau of Mines Report 7090, 1968.

[*6*] Summers, D. A., unpublished data, 1974.

[*7*] Voitsekhovsky, V. B. et al, "On the Destruction of Rocks and Metals by High Pressure Jets of Water," Proceedings, 1st International Symposium on Jet Cutting Technology, Coventry, U. K., Paper G8, 1972.

[*8*] Daniel, I. M., Rowlands, R. E., and Labus, T. J., "Photoelastic Study of Water Jet Impact," *Proceedings*, 2nd International Symposium on Jet Cutting Technology, Cambridge, U. K., Paper A1, 1974.

[*9*] Cooley, W. C., "Correlation of Data on Liquid Jet Cutting of Rock and Other Materials," for National Science Foundation, Research Applied to National Needs, Jan. 1975.

[*10*] Franz, N. C., "The Influence of Standoff Distance on Cutting with High Velocity Fluid Jets," *Proceedings*, 2nd International Symposium on Jet Cutting Technology, Cambridge, U.K., Paper B3, 1974.

[*11*] Flow Research, Inc., sales literature, 1975.

[*12*] Nikonov, G. P., "Research into the Cutting of Coal by Small Diameter High Pressure Water Jets, *Proceedings*, 12th Symposium on Rock Mechanics, Rolla, Mo., 1970.

[*13*] Summers, D. A. et al, "Excavation of Coal Using a High Pressure Water Jet System," Final Report, USDI H023064, U.S. Department of the Interior, 1974.

[*14*] Tollmien, W., "Berechnung Turbulenter Ausbreitungsvorgange," NACA TM 1085, National Advisory Committee for Aeronautics, 1945.

[15] Yanaida, K., "Flow Characteristics of Water Jets, *Proceedings*, 2nd International Symposium on Jet Cutting Technology, Cambridge, U.K., Paper A2, 1974.
[16] Hinze, J. O., *Turbulence*, McGraw-Hill, New York, 1959.

DISCUSSION

P. D. Lohn[1] (*written discussion*)—How were A and B chosen? Would normalizing to the merged jet diameter (in the convergent case) be more meaningful? Could the imperfections in the finish trigger a bistable flow favoring the smoother nozzle? (One of the diverging cases appeared not to be due to a bistable effect but to accelerated breakup.)

B. P. Selberg and C. R. Barker (*authors' closure*)—The centerline velocity was determined experimentally at the $x/D = 25$ and the $x/D = 50$ stations and these values were then used to calculate A and B from the centerline velocity decay equation.

While normalizing to the merged jet might be useful in discussing jet properties, it would be difficult to apply since both different convergent angles and different initial converged jet diameters would provide different baseline diameters, which in turn would make the normalizing of jet data difficult to understand and compare. A more interesting approach might be normalizing to a jet equivalent diameter based on the total jet areas of the two converging jets at the nozzle exit. This would allow all converging nozzles to be compared to the equivalent-area single-orifice nozzle.

One would expect that if surface finish imperfections were triggering a bistable flow condition, the smooth nozzles (orifice) would have a coherent jet for a greater distance than without the bistable flow. Subsequent tests with single-orifice nozzles having the same surface finish indicated a longer coherent jet than for the good orifice side of the diverging nozzle; hence the bistable hypothesis is not substantiated.

A. F. Conn[2] (*written discussion*)—Typical jet breakup lengths seen in the literature are in the range of 100 to 200 nozzle-orifice diameters, yet you report jets which have broken up by 375 diameters. Do you attribute these large stable distances to the very smooth surfaces inside the nozzle?

B. P. Selberg and C. R. Barker (*authors' closure*)—Our nozzles, from which we achieved the 375 x/D coherent jet lengths, were the standard Leach-Walker design which have been used and reported on by many

[1] TRW Systems & Energy, Inc., Redondo Beach, Calif.
[2] Hydronautics, Inc., Pindell School Road, Laurel, Md. 20810.

investigators. The only difference is the new nozzle manufacturing process that yields extremely uniform and smooth nozzle surface finishes which are not attainable by standard manufacturing techniques for small nozzles. These coherent jet lengths may have been further increased if more attention had been given to better flow conditioning upstream of our nozzle.

M. M. Vijay[1] *and W. H. Brierley*[1]

A Study of Erosion by High-Pressure Cavitating and Noncavitating Waterjets

REFERENCE: Vijay, M. M. and Brierley, W. H., "**A Study of Erosion by High-Pressure Cavitating and Noncavitating Waterjets,**" *Erosion: Prevention and Useful Applications, ASTM STP 664,* W. F. Adler, Ed., American Society for Testing and Materials, 1979, pp. 512–529.

ABSTRACT: A study was made of erosion by high-pressure noncavitating and cavitating waterjets issuing from five different arrangements of nozzles, consisting of (A) jet in air, (B) submerged jet, (C) jet surrounded by another of lower velocity, (D) jet from long nozzles, and (E) jet from a nozzle containing a cylindrical body insert. The purpose was to evaluate the two methods of erosion for jet cutting applications.

Simple visual examination of the craters on specimens of copper showed distinct type (size, shape, depth, etc.) of erosion. However, microscopic examination did not reveal clearly any characteristics peculiar to cavitating or noncavitating jets.

Quantitative experimental results were obtained by measuring the mass loss of lead specimens as a function of time of exposure for the conditions where either the nozzle pressure or the standoff distance was held constant. By comparing the different arrangements on the basis of material loss, it is concluded that Arrangement B performed best for all periods of exposure and standoff distances followed by Arrangement C for short periods of exposure, smaller standoff distance, and for certain flow conditions.

KEY WORDS: erosion, high pressure, cavitating, noncavitating, water jet, jet cutting applications, nozzle, crater, mass loss, lead and copper specimens, time of exposure, nozzle pressure, nozzle diameter, standoff distance, submerged jet, arrangement, evaluation, comparison, material removal, penetration

The application of waterjets for mining and other problems is well known and is quite well documented [*1*].[2] However, because of the requirement of high pressures, waterjets alone are not adequate to fracture hard rocks which are encountered in tunneling and other operations. To overcome this

[1]Research officer and technical officer, respectively, Gas Dynamics Laboratory, Mechanical Engineering Division, National Research Council of Canada, Ottawa, Ontario, Canada.

[2]The italic numbers in brackets refer to the list of references appended to this paper.

problem of high pressures, methods recently have been proposed whereby the erosive power of a waterjet could be augmented by the generation of cavitation bubbles within the jet [2]. It was argued that since these bubbles create intense transient pressures at the points of collapse (thus fracturing the material), the actual pressure of waterjets could be reduced. While reports claiming their success in certain applications have appeared [3,4], some doubts regarding their usefulness have also been reported [5]. This investigation was undertaken to study the erosion caused by noncavitating and cavitating jets in detail and to compare their performance with regard to jet cutting applications.

Qualitative and quantitative results are given to support the views expressed in the paper.

Experimental Facility and Procedure

The high-pressure experimental facility in our laboratory for jet cutting studies has been described in detail in an earlier publication [6]. The pump used for the tests was the Union Quintuplex pump rated at 69 MPa (10 000 psia) and 50 litre/min (13 gal/min). All the experiments were conducted in a Plexiglas tank and the arrangements used to identify the tests are shown in Fig. 1. The nozzles employed (Fig. 1) were designed to meet the present requirements. The general features of each arrangement are as follows:

(A) The tests done in this arrangement (with Type A nozzle) constitute the conventional noncavitating tests.

(B) Submerged jet, Type A nozzle: the cavitating characteristics of a submerged jet have been clearly shown by Rouse [7] and Lichtarowicz [3].

(C) This arrangement was developed to simulate either (A) or (B) depending upon the velocity (V_a) of the outer stream. As in Type (B), due to the high shear stress between the two jets, cavitation bubbles are expected to be generated at the interface of the two jets.

(D) The long or straight nozzles (Type B) in this case have been investigated by Pearce and Lichtarowicz [8] and their cavitating characteristics are shown to depend on the ratio L/D. In the present study, nozzles of $L/D = 5$ to 50 were used for qualitative tests, whereas nozzles of $L/D =$ 5 to 20 were used for quantitative tests. The discharge coefficients of these nozzles were measured in the laboratory and were found to range from 0.58 to 0.77 (depending on L/D). These were much lower than the value of 0.98 measured for the Type A nozzles, suggesting the possibility of cavitation in the jet.

(E) In this arrangement, nozzles of Type C were tested. That these nozzles cavitate the jet has been shown by Johnson [2] and Beutin [5]. The results reported here are for a nozzle with a cylindrical pin insert across the flow. The cavitating characteristics of such flows were investigated extensively by Shal'nev et al [9].

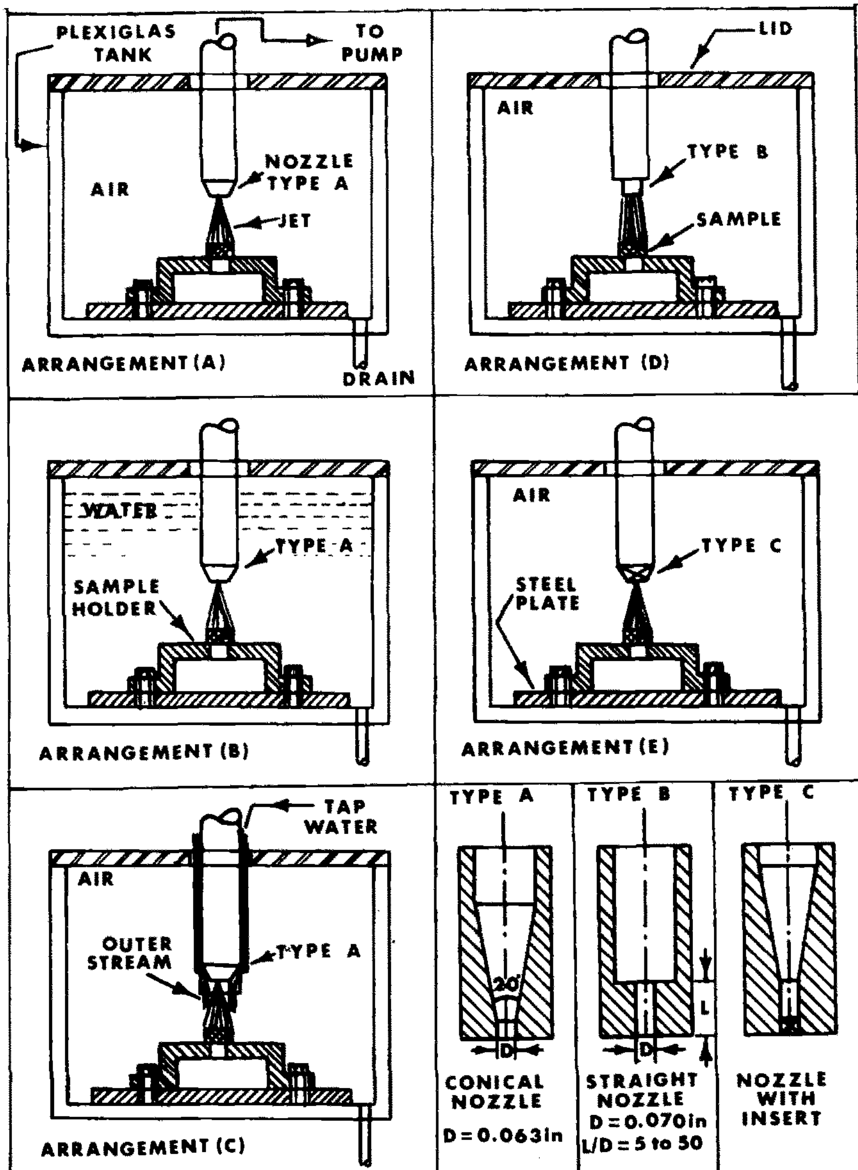

FIG. 1—*Arrangement and type of nozzles.*

Initial trials were devoted to qualitative study of the erosion caused by these jets. Specimens of cold-rolled annealed copper (Rockwell hardness, B scale = 46 ± 2), aluminium, and brass plates of 2.29-mm (0.090 in.) thickness were used for this purpose. Since these materials work-harden and also since the measured values of mass loss were small, for quantitative tests, cylindrical specimens of lead (Brinell hardness number = 4HB) of size 3.8 (diameter) by 3.6 cm (1.5 × 1.4 in) were employed. The homogeneity of these specimens was ascertained by measuring the density (11.36 ± 0.21 g/cm^3). The range of experimental variables is summarized in Table 1.

The temperature of the jet was measured by a copper-constantan thermocouple which was located at about 0.76 m (2.5 ft) upstream of the nozzles. Though the temperature varied from day to day (depending on the season), it was maintained at a constant value during the period of the tests.

The main dependent variable which was used to compare the performance of the nozzles was the mass loss, which was obtained by measuring the mass of the specimen before and after exposure to the jet.

Experimental Results and Discussion

The type (size, shape, depth, etc.) of erosion caused by the jets on copper and lead specimens is shown in Fig. 2*A*-*R* and Fig. 3*A*-*R*. As for the performance, comparison was made on the basis of mass loss with respect to time, taking Arrangement A as reference. This is plotted in Figs. 4 to 7.

Figures 2 and 3 clearly show that each arrangement produces a distinct type of erosion, depending on the material and to a certain extent on the standoff distance (*SD*). For standoff distances less than 2.5 cm (1.0 in.), none of the arrangements produced any perceptible erosion on the copper plates. In such cases the flow was purely radial on the surface of the specimen. The erosion started to become appreciable for values of $SD > 5$ cm (2 in.), as shown in Fig. 2*A*-*D*. The flow in this instance was initially radial, then changing instantaneously to conically upward flow, the pattern depending on the type of crater formed. Figure 2*A*, *D*, *E*, *R* and Fig. 3*A* show that the irregular or the ring type of erosion, well known in the case of brittle materials [*10,11*], also occurs for metals. This type of erosion of metals has also been observed by other investigators [*12,13*]. Although exact reasons are as yet unknown, it appears that it is caused by shear due to high-velocity radial flow on the surface of the deformed (due to jet impact) specimen. A closer examination of the crater in Fig. 2*D*, however, reveals the presence of erosion at the point of impact. It is argued that this is caused by the cavitation bubbles which are generated within the jet due to the vena contracta effect. This is strongly supported by the fact that the same type of craters appeared for tests done in Arrangements B (Figs. 2*B* and 3*C*, 3*D*), C (Figs. 2*C*, *H* and 3*E*, *F*), and E (Fig. 3*Q*, *R*). For standoff distances greater than about 13 cm (5 in.), quite different results were obtained as shown in Figs. 2*G*—2*M* and Fig. 3*B*. What exactly happens in these cases is hard to explain, but it appears that the liquid drops which form due to the breakup of the jet at large standoff distances contribute to the process of

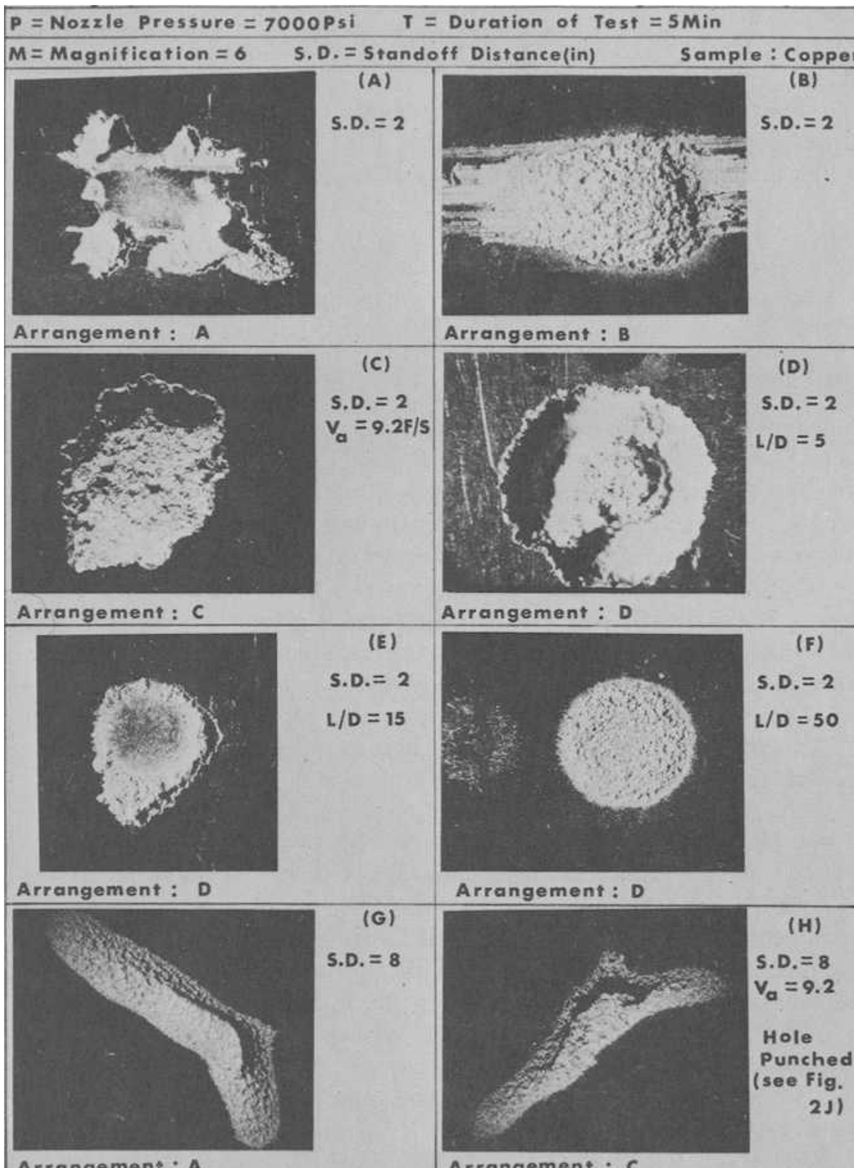

FIG. 2—*Photographs of craters caused by different arrangements.*

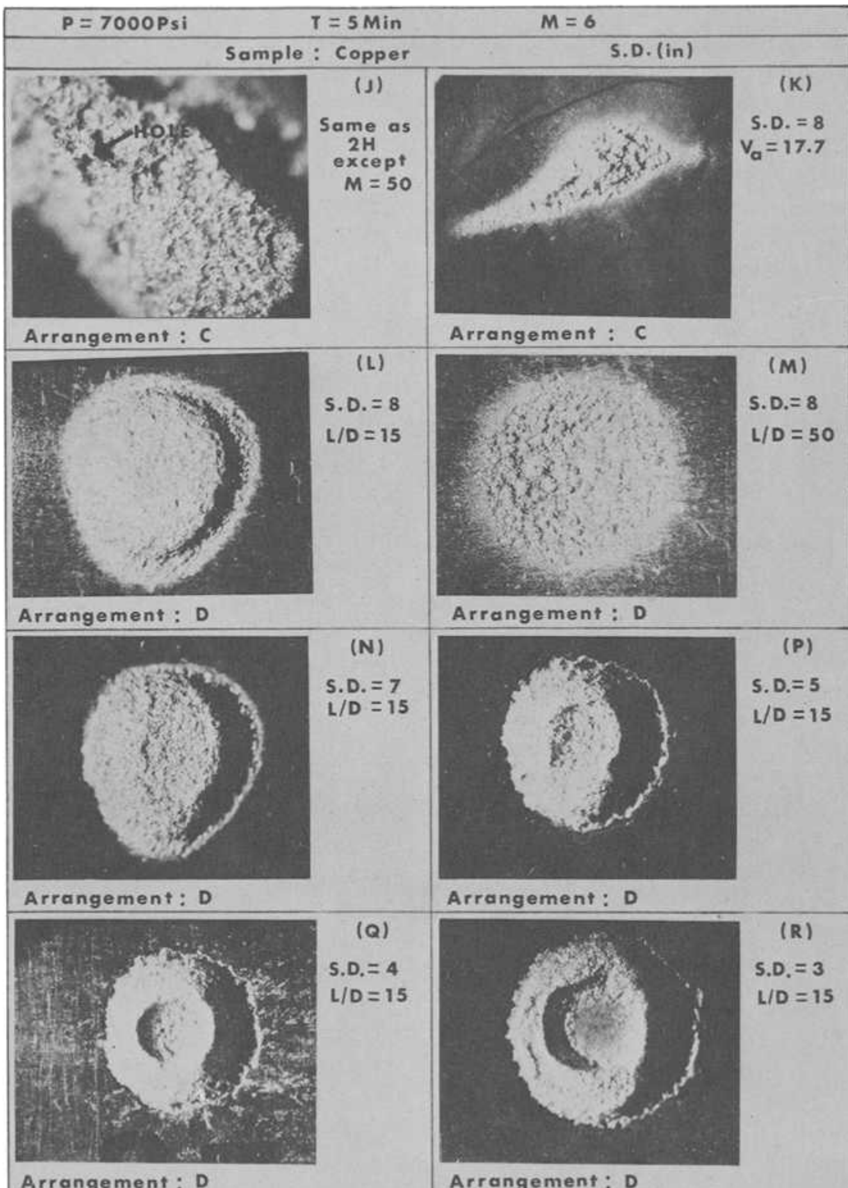

FIG. 2—(*Continued*).

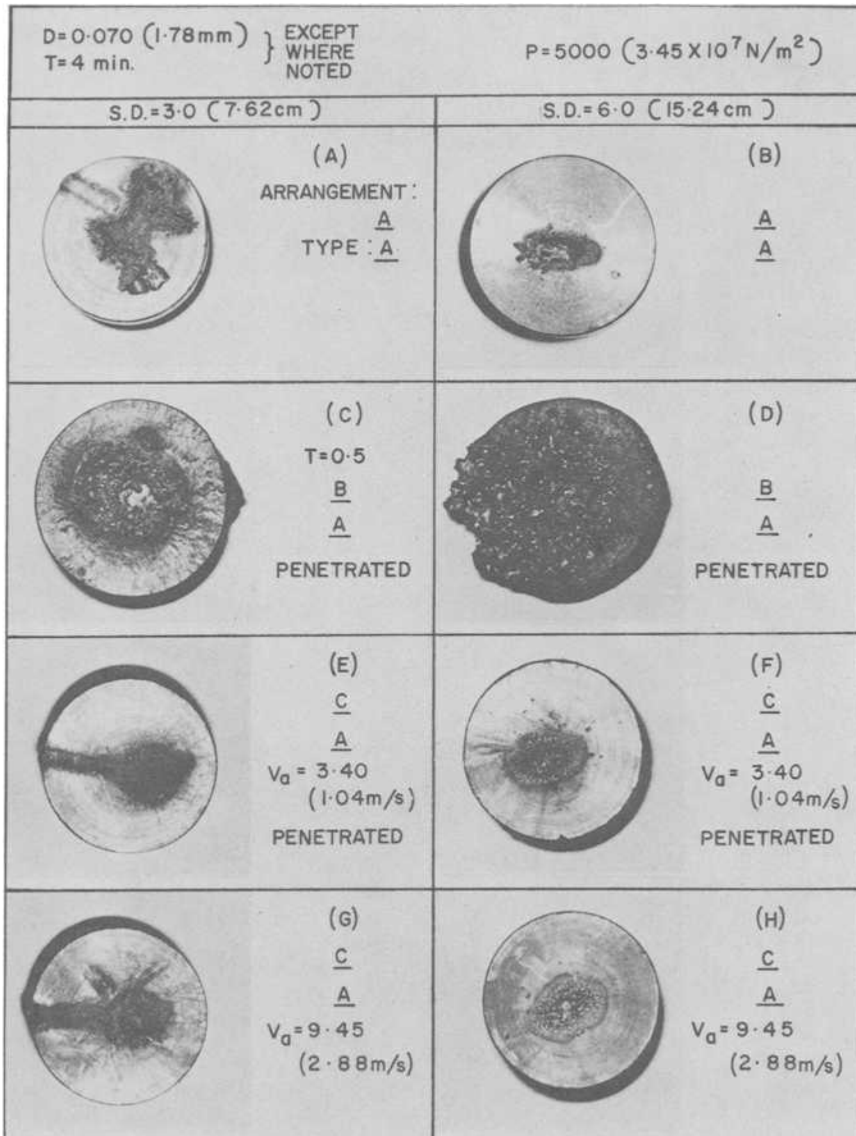

FIG. 3—*Erosion of lead specimens by different arrangements.*

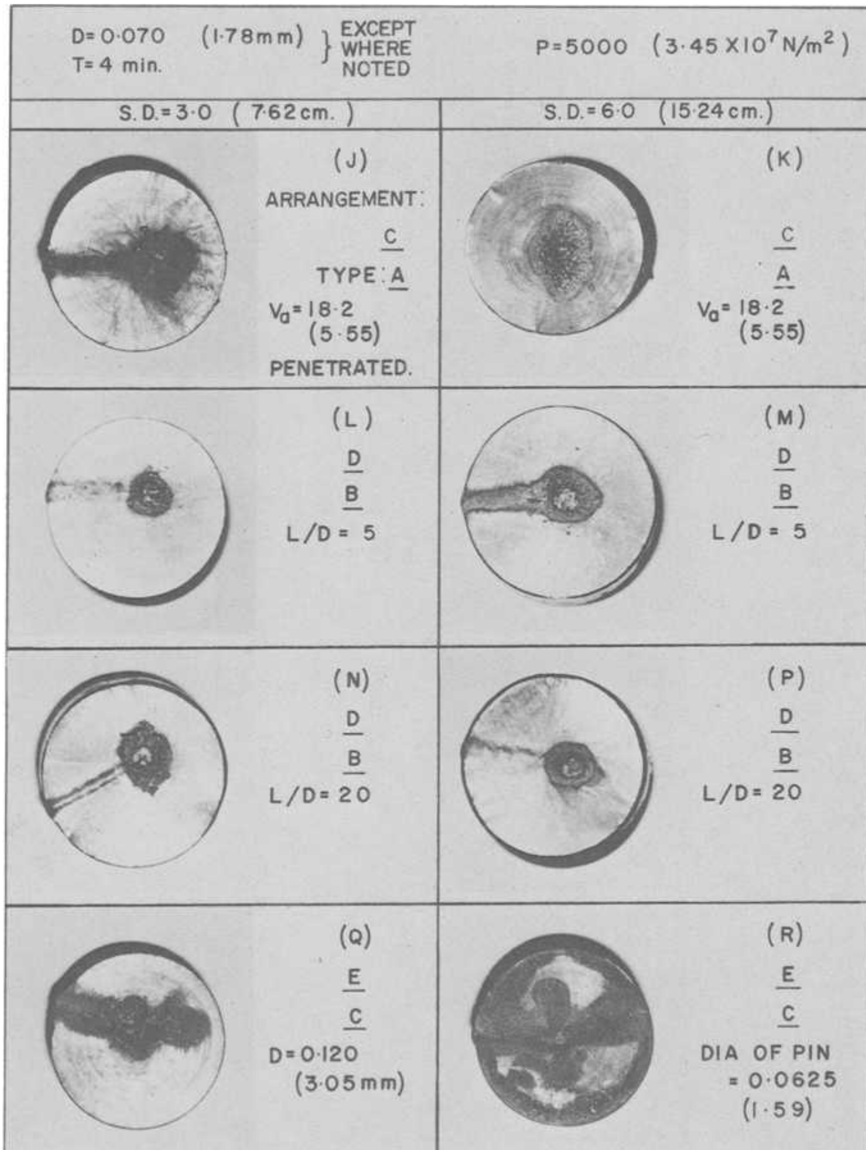

FIG. 3—(*Continued*).

TABLE 1—*Range of experimental variables.*

P, MPa (psi)	V_o m/s (ft/s)	SD, cm (in.)	T, min	V_a, m/s (ft/s)	Jet Temperature, °C	Comments
34.4 (5000)	263 (860)	2.5 to 20.3 (1.0 to 8.0)	5	2.7 to 10.7 (9 to 35)	10	D = 1.60, 1.78 mm (0.063, 0.070 in.) L/D = 2 to 50
48.3 (7000)	311 (1020)	2.5 to 20.3 (1.0 to 8.0)	5	2.7 to 10.7 (9 to 35)	10	qualitative tests
6.0 (1000)	117 (385)	7.6 (3.0)	0.25 to 10	1.0 to 15.4 (3.4 to 50.6)	12.8 to 24.4	quantitative tests. Temperature was constant for tests done on any particular day
13.8 (2000)	166 (545)	7.6 (3.0)	0.25 to 10	1.0 to 15.4 (3.4 to 50.6)	12.8 to 24.4	
34.4 (5000)	262 (860)	7.6 and 15.2 (3 and 6)	0.25 to 10	1.0 to 15.4 (3.4 to 50.6)	12.8 to 24.4	

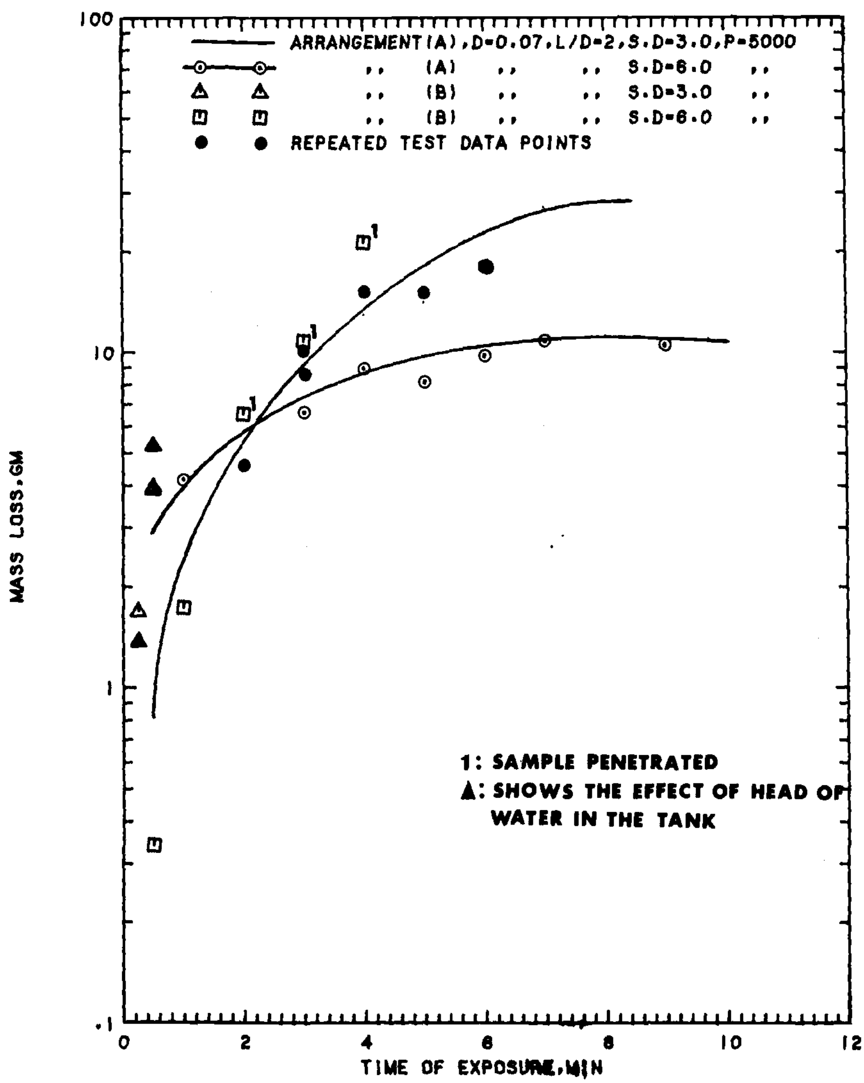

FIG. 4—*Comparison of Arrangements B and A.*

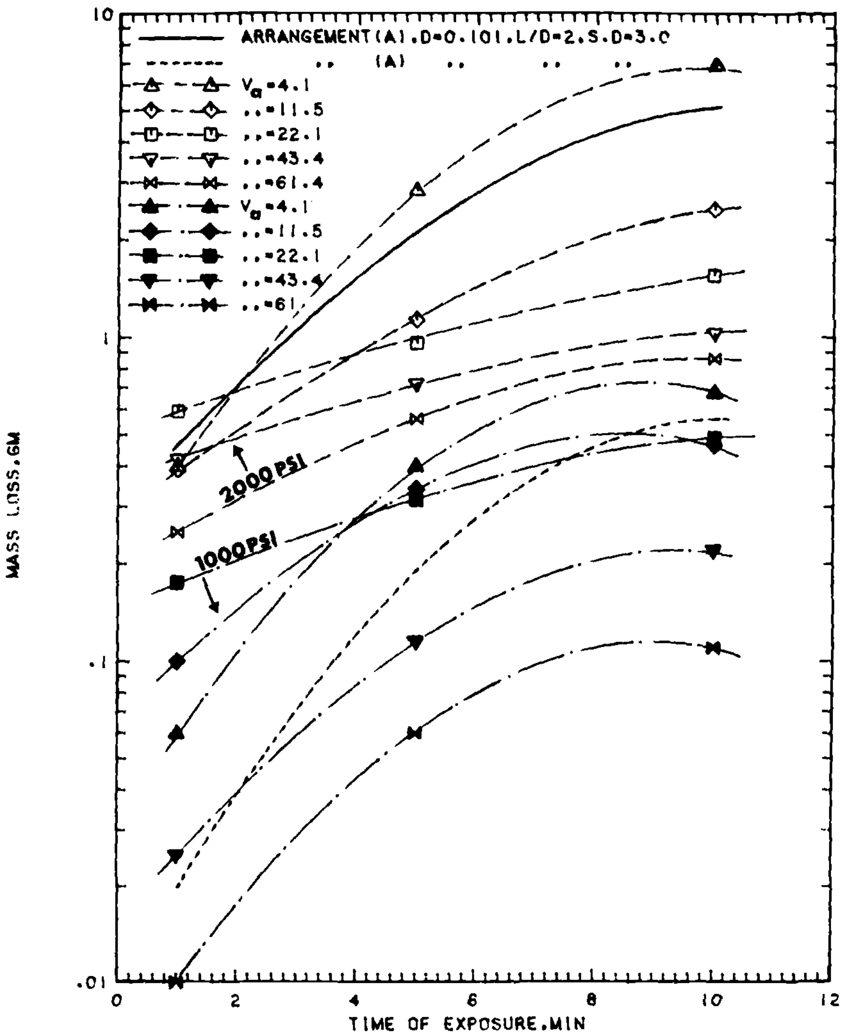

FIG. 5a—*Comparison of Arrangements C and A.*

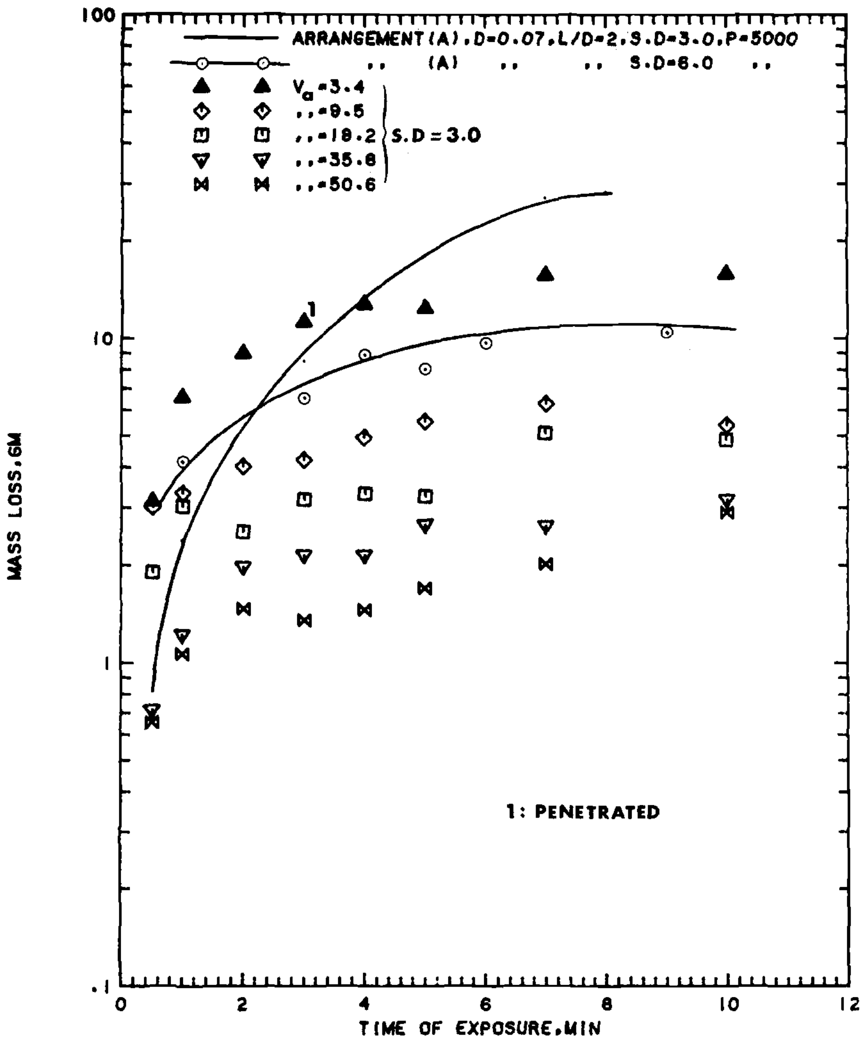

FIG. 5b—*Comparison of Arrangements C and A.*

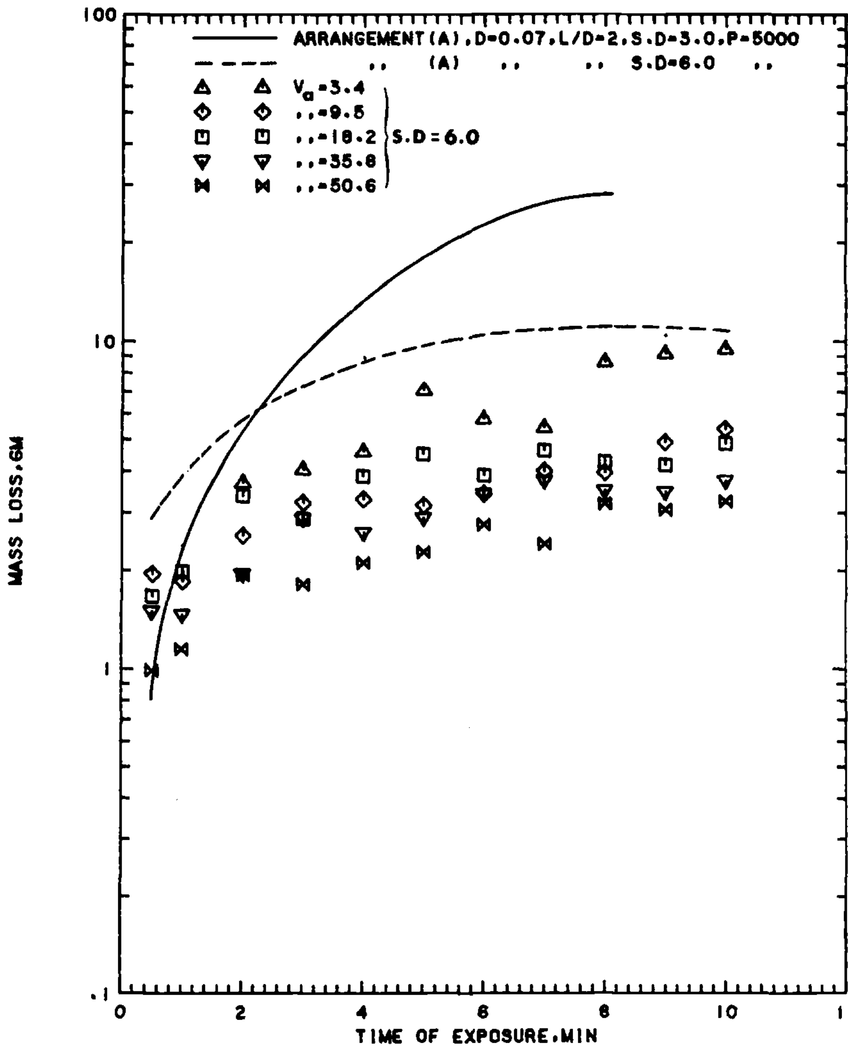

FIG. 5c—*Comparison of Arrangements C and A.*

erosion (see Fig. 2*M* for shape of the dents on the surface). Figure 2*E,R,Q,P, N, L* shows vividly the effect of *SD* on the nature of the craters produced.

Figure 2 *J* shows a magnified (×50) view of the crater shown in Fig. 2*H*. Such microscopic examinations did not reveal clearly any characteristics peculiar to cavitating or noncavitating jets. It should be mentioned, however, that the crater produced by a cavitating jet was much rougher than that caused by a noncavitating jet.

Figure 2*H, K* and Fig. 3*E, G, J* show the effect of V_a on erosion. Since the probability of generation of the cavitation bubbles is a function of the interfacial shear stress, higher V_a implies lower shear stress and hence less bubbles in the jet, resulting in reduced erosion.

The mass loss of the lead specimens in Arrangement B is compared against Arrangement A in Fig. 4. Since the specimens were completely penetrated within a short period of time, the data do not represent the true mass loss; however, the figure, clearly shows the high destructive power of the cavitating jet.

Figure 5*a–c* compares the performance of Arrangement C with Arrangement A. In Fig. 5*a*, the results obtained at 6.9 and 13.8 MPa (1000 and 2000 psi) and SD = 7.6 cm (3.0 in.) are plotted. As discussed earlier, the plots show increased mass loss for short periods of exposure and for low values of V_a. Figure 5*b* shows the same trends at a pressure of 34.5 MPa (5000 psi). In this instance many specimens were penetrated as indicated in the figure and therefore the true mass loss would be much higher. Plotted in Fig. 5*c* are the results of SD = 15.2 cm (6.0 in.). In this case, though the mass losses were much lower, the depths of penetration were higher compared with the conventional noncavitating jet.

Figure 6*a*, 6*b* and Fig. 7 compare the performance of Arrangements D and E against Arrangement A. From the point of view of mass loss, they were inferior to the noncavitating jet. Surprisingly, the standoff distance did not have any significant effect on erosion. The depth of penetration caused by these jets was, as before, much deeper.

The results obtained show strongly that erosive power of the cavitating jets is intense for short times of exposure. This suggests that they would be very effective for applications where it is necessary to employ high traversing speeds of the jet or the specimens.

Conclusions

Tests conducted at moderate standoff distances (≃7.6 cm) show that it is possible to recognize the cavitating or noncavitating nature of jets by a visual examination of the craters formed on metals. Erosion was imperceptible for standoff distances less than about 2.5 cm. At standoffs greater than about 15 cm, erosion by droplets was predominant.

On the basis of material loss, Arrangement B performed best for all

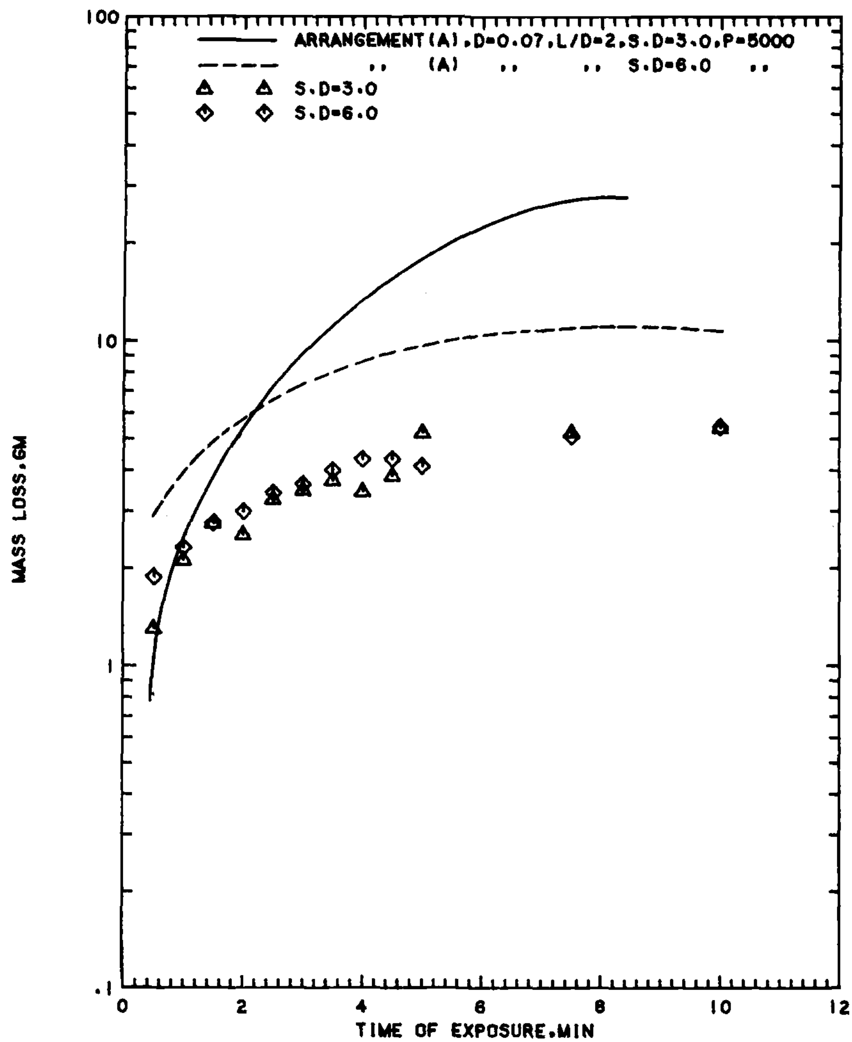

FIG. 6a—*Comparison of Arrangements D and A.* L/D = 5.

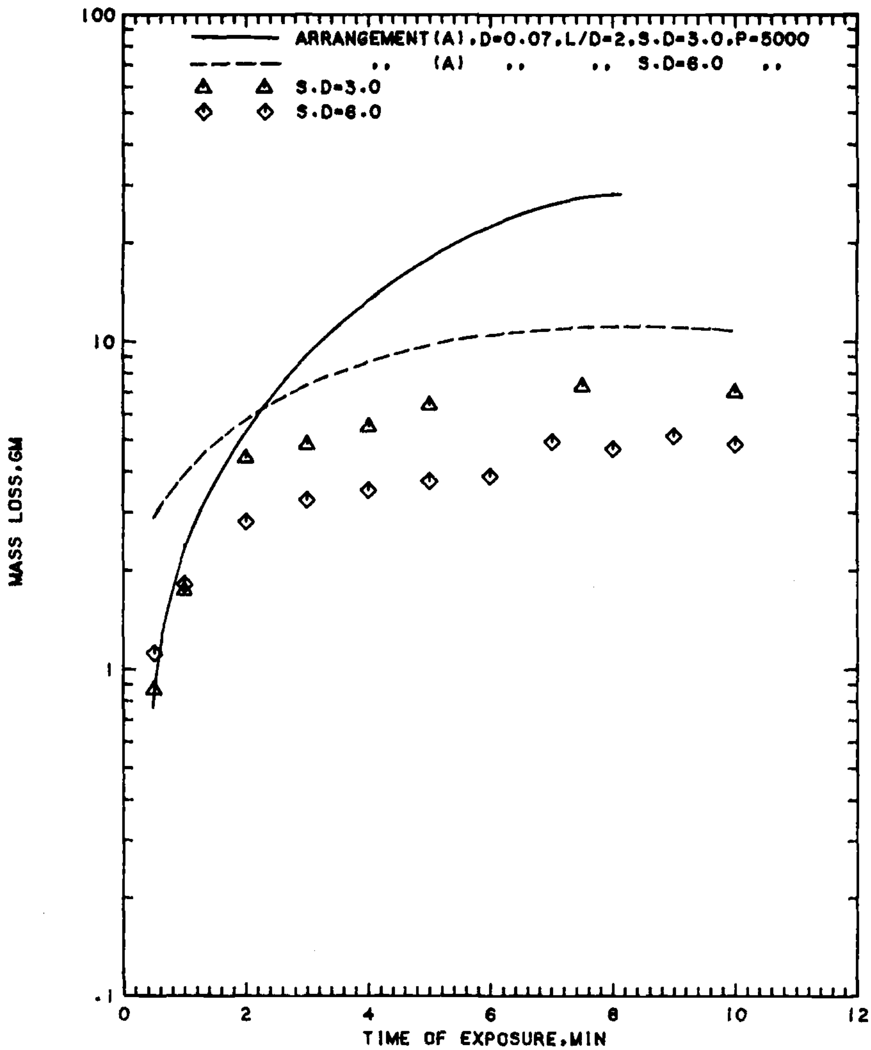

FIG. 6*b*—*Comparison of arrangements D and A,* L/D = *20.*

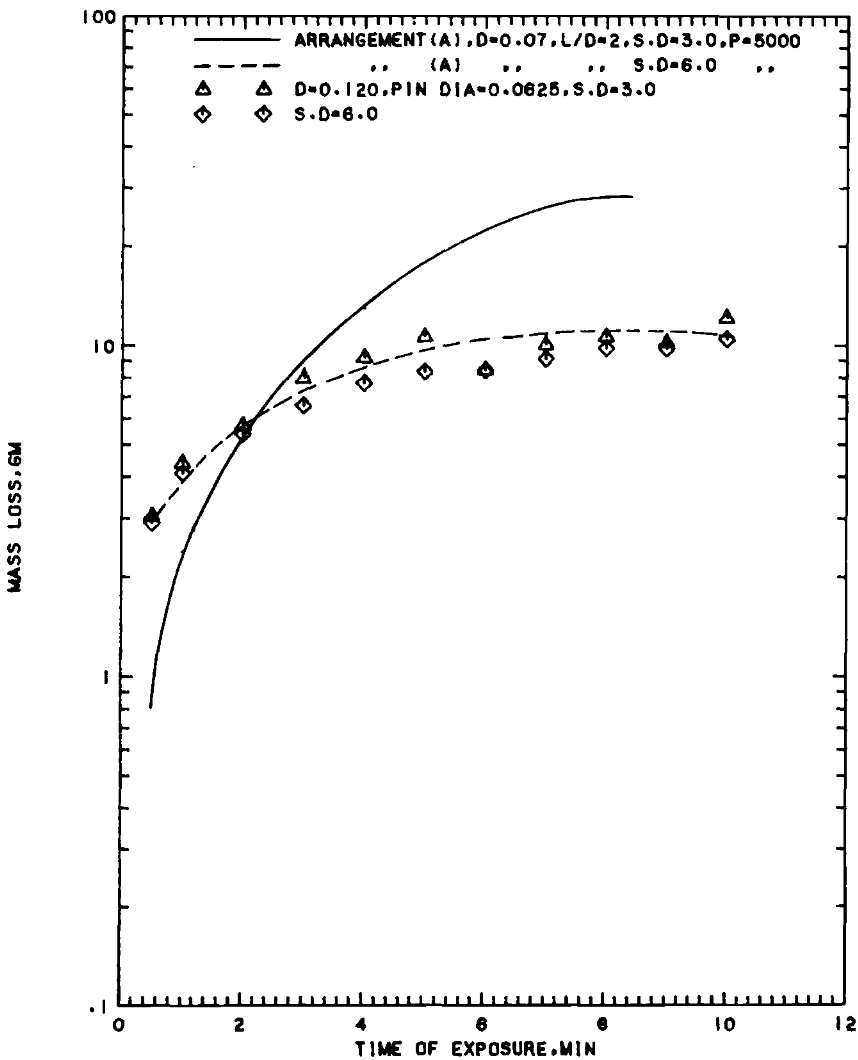

FIG. 7—*Comparison of Arrangements E and A.*

periods of exposure and standoff distances. This was followed by Arrangement C for short periods of exposure, smaller standoffs, and for low values of V_a.

The results suggest that the cavitating jets would be attractive for material removal or for deeper penetration at high traverse speeds. However, to fully assess their capabilities, further study on erosion of brittle materials is required.

References

[*1*] 1st, 2nd and 3rd International Symposia on Jet Cutting Technology, British Hydromechanics Research Association, Fluid Engineering, Cranfield, Bedford, England, 1972, 1974, and 1976.

[*2*] Johnson, V. E., Jr., Thiruvengadam, A., and Kohl, R. E., "Rock Tunneling with High-Speed Water Jets Utilizing Cavitation Damage," ASME Paper No. 68-FE-42, American Society of Mechanical Engineers, 1968.

[*3*] Lichtarowicz, A., "Experiments with Cavitating Jets," 2nd International Symposium on Jet Cutting Technology, British Hydromechanics Research Association, Bedford, England, Paper D1, April 1974.

[*4*] Conn, A. F., Rudy, S. L., and Mehta, G. D., "Development of a Cavijet^{TM} System for Removing Marine Fouling and Rust," 3rd International Symposium on Jet Cutting Technology, British Hydromechanics Research Association, Bedford, England, Paper G4, May 1976.

[*5*] Beutin, E. F., Erdmann-Jesnitzer, F., and Louis, H., "Influence of Cavitation Bubbles in Cutting Jets," 2nd International Symposium on Jet Cutting Technology, British Hydromechanics Research Association, Bedford, England, Paper D3, April 1974.

[*6*] Harris, H. D. and Brierley, W. H., "Application of Water Jet Cutting," 1st International Symposium on Jet Cutting Technology, BHRA Bedford, England, Paper G1, April 1972.

[*7*] Rouse, H., *La Houille Blanche,* Jan.-Feb. 1953, pp. 9-19.

[*8*] Pearce, I. D. and Lichtarowicz, A., "Discharge Performance of Long Orifices with Cavitating Flow," 2nd Fluid Power Symposium British Hydromechanics Research Association, Bedford, England, Paper D2, Jan. 1971.

[*9*] Shal'nev, K. K., Varga, I. I., and Sebestyen, D., *Philosophical Transactions of the Royal Society,* London, Series 1110, Vol. 260, July 1966, pp. 256-266.

[*10*] Bowden, F. P. and Field, J. E. in *Proceedings of the Royal Society,* Series A., Vol. 282, 1964, pp. 331-352.

[*11*] Rehbinder, G., "Some Aspects on the Mechanism of Erosion of Rock with a High Speed Water Jet," 3rd International Symposium on Jet Cutting Technology, British Hydromechanics Research Association, Bedford, England, Paper E1, 1976.

[*12*] Beutin, E. F., Erdmann-Jesnitzer, F., and Louis, H., "Studies of Material Surfaces Subjected to Single Liquid Jet Impact," *Proceedings*, 4th International Conference on Rain Erosion and Associated Phenomena, Neus Schloss, Meersburg, Germany, Vol. 1, May 1974.

[*13*] Smith, D. G. and Kinslow, R., *Experimental Mechanics,* Vol. 16, Jan. 1976, pp. 21-25.

A. Lichtarowicz[1]

Cavitating Jet Apparatus for Cavitation Erosion Testing

REFERENCE: Lichtarowicz, A., "**Cavitating Jet Apparatus for Cavitation Erosion Testing,**" *Erosion: Prevention and Useful Applications, ASTM STP 664,* W. F. Adler, Ed., American Society for Testing and Materials, 1979, pp. 530–549.

ABSTRACT: A submerged cavitating jet is used to erode a specimen placed in its path. The erosion depends primarily on the jet velocity, the downstream pressure, and the standoff distance of the specimen. An apparatus for erosion testing based on this principle is described. Results are presented showing the effect of these parameters on erosion. They indicate that scaling should be carried out on the basis of constant cavitation number. The results show that the method is suitable for cavitation erosion testing and that testing time and jet velocity (and hence the upstream pressure) can be traded one against the other provided that the cavitation number remains constant. In this method, all of the variables can be controlled independently. The method offers the advantages associated with flow-induced cavitation together with the short testing time offered by magnetostriction devices.

KEY WORDS: erosion, cavitation, liquid jet cutting, scaling

Various test techniques are used to investigate the resistance of materials to cavitation erosion. In one of these, a test specimen is vibrated at a high frequency (20 kHz) in an appropriate fluid. Cavitation occurs at the surface of the specimen as a result of the high accelerations produced. In this test the cavitation number (σ) cannot be defined, because the velocity is not involved at all. This method provides a simple and not very expensive way for relative grading of different materials, but the results are difficult to correlate with flow situations usually met in practice. The testing times are relatively short and are measured in hours. In other methods, cavitation is produced in a low-pressure region of a venturi, or behind a bluff object placed in a water tunnel or even on a rotating disk immersed in a chamber which can be pressurized. In these methods both the velocity and the surrounding pressure

[1] Senior lecturer, Department of Mechanical Engineering, University of Nottingham, Nottingham, U.K.

can be changed independently so that the cavitation number can be controlled at will. The test conditions are much more closely related to the conditions occurring in practice. The flow velocities are not very high (up to say 40 to 50 m/s); consequently tests take a long time and the apparatus tends to be bulky. This paper describes a new method of testing recently proposed by the author [*1,2*][2] which uses a high-velocity (greater than 100 m/s) submerged liquid jet. In such a jet, cavitation occurs in shear layers provided that the velocity is sufficiently high, and the back pressure not too large. If a target is placed within this cavitating region, considerable cavitation erosion will occur.

For the past three years, work has been going on at Nottingham University to develop this new method. Some of the results are given by Nolan [*3*], Stawski [*4*] and Munton [*5*]. Recently Kleinbreuer [*6*] published a paper in which a similar testing technique is proposed.

Principle of Operation

In a long orifice (or a short tube) the flow after separation at the sharp inlet corner reattaches itself to the orifice bore and encloses a separation region. As the pressure difference across the orifice is increased, the pressure in the separated region decreases until eventually cavitation occurs when the vapor pressure is reached. As the pressure difference is further increased, the now cavitating separation region will extend in length till eventually it will outgrow the orifice length and will emerge as a cavitation tail outside the orifice. The flow is now choked, because it depends only on the upstream pressure (and on the vapor pressure, which is constant and usually very small) and is independent of the downstream pressure [*7*]. The orifice is said to be "supercavitating." As the upstream pressure is increased or the downstream pressure is reduced, cavitation intensity increases.

It should be noted here that since the cavitation bubbles collapse downstream of the nozzle there is no damage to the orifice. This is confirmed by the fact that the same nozzle has been used throughout all the tests carried out at Nottingham and, as yet, no detectable change in the nozzle characteristics have been found.

The cavitating tail emerging from the orifice appears to the eye to be very steady in both space and time. Its appearance and the noise produced depend very much on the cavitation number and on the air content of the liquid used. A full discussion of these effects is given by Lichtarowicz and Pearce [*8*].

A specimen placed in the region where cavitation bubbles collapse will be quickly eroded and the erosion can be quantified by measuring the mass lost in a given time.

[2]The italic numbers in brackets refer to the list of references appended to this paper.

The cavitation number is usually defined as

$$\sigma = \frac{p_d - p_v}{\frac{1}{2}\rho v^2}$$

and can be modified to

$$\sigma = \frac{p_d - p_v}{p_u - p_d} = \frac{p_d - p_v}{\Delta p}$$

where

p_u, p_d, p_v = upstream, downstream, and vapor pressures, respectively,
v = velocity through the orifice, and
ρ = density of the fluid.

All pressures are absolute. In many cases the vapor pressure is negligibly small when compared with other pressures, so that the cavitation number reduces to

$$\sigma = \frac{p_d}{p_u}$$

The function of the orifice bore, which must be at least one diameter long, is to stabilize the cavitation bubble especially at high cavitation numbers near cavitation inception [7].

Apparatus

Figure 1 shows an arrangement of the test chamber. A cavitating jet supplied from a pressure source p_u discharges into the test chamber held at the required constant pressure p_d. A circular specimen (Fig. 2) is mounted coaxially with the jet in such a way that the separation between the nozzle and the target can be set to any desired value by adjusting the screws locating the holder. The nozzle itself (Fig. 3) consists of a synthetic sapphire orifice jewel clamped in position by the nozzle holder. The sapphire was chosen as it provides cheaply a well-finished nozzle. The conical entry increases its discharge coefficient without affecting its general cavitating performance.

Windows were provided on both sides of the chamber so that cavitation could be observed. The whole assembly was designed to withstand 35-MPa pressure, and it is suitable for use with water or with oil.

Pressures were measured by appropriate test gages while the temperature was measured by a mercury in glass thermometer located in a well just downstream of the chamber exit.

A test chamber assembly which would be required for routine test work

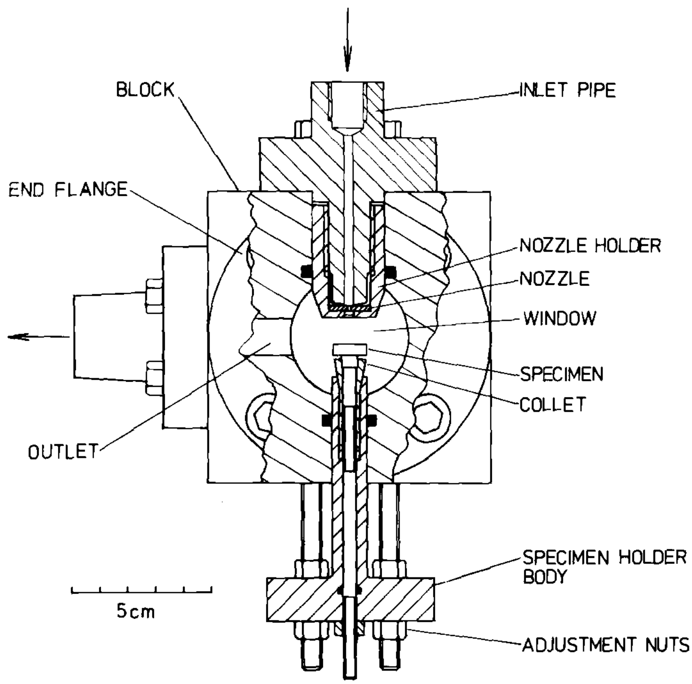

FIG. 1—*Jet cavitation erosion rig.*

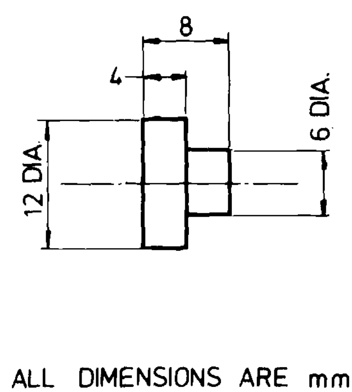

FIG. 2—*Specimen for cavitation erosion.*

can be considerably simplified, as the existing unit incorporated additional features that enabled it to be used for other purposes.

The unit was supplied from an existing laboratory facility; hence only the essential features of the system will be specified. Both upstream and downstream pressures are held constant during the test, but their settings

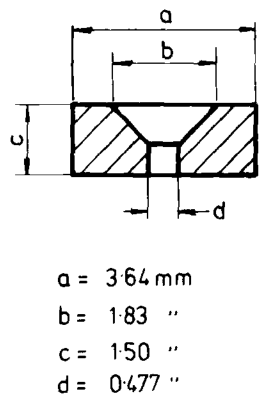

FIG. 3—*Nozzle details.*

may be varied from one test to the other. An oil cooler was fitted in the high-pressure supply line to allow for temperature control. Supply to the nozzle was well filtered (5 μ) so that neither the nozzle nor the specimen would be damaged by particle erosion. Furthermore, an efficient debris-removal system was provided on the downstream side so that the pressure control valve would not be affected by small eroded particles blocking the flow passages. A fine wire mesh was found to be sufficient on the rig used. Facilities for a quick buildup and cutoff of the supply to the test chamber and for automatic test timing were provided to enable short test runs to be made.

As the hydraulic power pack available could use only hydraulic oil, all the tests to date have been carried out using Esso NUTO H32 hydraulic oil. The exact specification of the oil is given in the Appendix.

Testing Procedure

Before each test a dummy specimen was inserted in the test chamber and the machine run so that all the controls could be preset to the desired values and a steady temperature could be reached. A previously weighed specimen was then inserted, the automatic timing was preset, and the rig started up with the flow to the test chamber shut off. As soon as the required pressure built up, the valve was opened and the timer started. Usually, small adjustments had to be made to the settings. Some adjustments were also required to the cooling water flow since there was no thermostatic control. After the machine had stopped the specimen was weighed again to determine mass loss and the cumulative erosion rate (CER). CER is defined as the total mass loss divided by the elapsed time t.

All specimens were weighed down to 0.1 mg, but in a few cases a machine capable of weighing down to 0.01 mg was used to determine the initial erosion. In some tests the eroded surface was photographed. The specimen then was inserted again, taking care to locate it in the same position. This was ensured by alignment of two marks, one on the specimen and one on the holder. Tests were also made where the standoff distance l was altered.

All testing so far has been done to determine the characteristics of the apparatus; consequently aluminium specimens were used throughout to keep the testing times shorter. A few specimens of other materials were tested to illustrate the practicability of the method. All aluminium specimens were heat treated to ensure uniform hardness (see the Appendix).

Experimental Work

Test program

The cavitation intensity, and hence the erosion, depends on a number of parameters which can be conveniently divided into a number of groups. As the number of parameters is large, it was possible to test the effects of only some of them.

The first group of variables consists of geometrical parameters describing the size of the unit. These comprise the nozzle diameter d, standoff distance l, specimen diameter D, and the chamber size. The nozzle size was determined mainly by the capacity of the available pumping equipment and was kept constant throughout all the work. Only the standoff distance l was changed to test for optimum distance. The chamber size (Fig. 1), that is, both the diameter and width, were made sufficiently large so as not to affect the flow pattern as the standoff distance was altered of the flow pattern changed as the erosion of the test specimen progressed. It was hoped that the 10-mm-diameter specimens would be sufficiently large for erosion not to be affected by the specimen diameter, but it was found later that at higher upstream pressures the eroded area covered the whole of the specimen face. Additional tests were made which indicated that the diameter had to be increased to 12 mm.

The second group of variables describes operating conditions and comprises the upstream and downstream pressures as well as the operating temperature and the air content of the liquid. Air content was not investigated here at all. It is known that, for vibratory tests, erosion rate peaks with a relatively flat plateau between 40 and 70°C; thus most of the current tests were carried out within this temperature range.

The main part of this work describes the effects of various pressure changes on erosion. Tests were made at

1. constant cavitation number $= p_d/p_u$,
2. constant downstream pressure, and
3. constant upstream pressure.

The last group comprises "materials" parameters, that is, the variation of the specimen material and its state and the type of liquid used. As mentioned previously, only one aluminium and one liquid were used. A few steel specimens were tested to demonstrate that the method is suitable for other materials.

Experimental Results

As the jet leaves the nozzle, cavitation is confined to its circumference and, as it travels along, cavitation spreads both into and out of the jet. Eventually it will decay. When a jet strikes a plate target placed normal to its axis, the flow is deflected radially outward and a stagnation region is formed at the center. Thus erosion on a target will occur in a ring around the central uneroded area. If the standoff distance l is increased, the central area will diminish. Similar effects can be obtained by increasing σ and holding l constant. Figure 4 shows the test rig in operation. The jet is made visible by the cavitation cloud surrounding it. The erosion pattern can be seen in Fig. 5, which shows various stages of erosion of an aluminium specimen. Machining marks at the center remain visible for a very long time and they disappear only as the center region is slowly eroded away from the rim inwards as the specimen surface geometry changes. The absence of cavitation at the center was confirmed by viewing a similar, but scaled up, cavitating jet through a transparent Perspex specimen mounted in a rig used for other tests.

Figure 6 shows the mass loss (Δm) and the cumulative erosion rate (CER) time graph for Specimen 7. The shape of both curves is very typical of all the results obtained. Figure 5 shows the photographs of the eroded surface of this specimen at various stages of erosion. The feature already mentioned is the ring pattern of erosion which gradually extends inwards and outwards. At longer erosion times, deep pits are visible and the central noneroded core has disappeared, leaving a rather large hole in the center. Under these circumstances the flow pattern around the specimen is affected, because the flow no longer leaves the surface radially but is deflected backwards. This occurs after approximately 1200 s exposure in this particular case. The effective standoff distance has by now increased, but as this occurs at the exposure times considerably longer than the time required to reach the peak erosion rate, it does not further affect correlations. For example, the mean depth of erosion for Specimen 7 shown in Figs. 5 and 6 is only the order of 0.15 mm at the time of peak erosion rate.

Figure 7 shows a set of cumulative erosion rate curves obtained at constant cavitation number $\sigma = 0.025$. As the upstream pressure is increased from 8 MPa upwards, the flat plateau associated with the steady-state zone becomes shorter until eventually it disappears altogether, leaving a peak which becomes more pointed as the pressure is further raised. It should be noted here that the maximum pressure used in all this work was only 20 MPa, while the ultimate tensile strength of aluminium is 67 MPa.

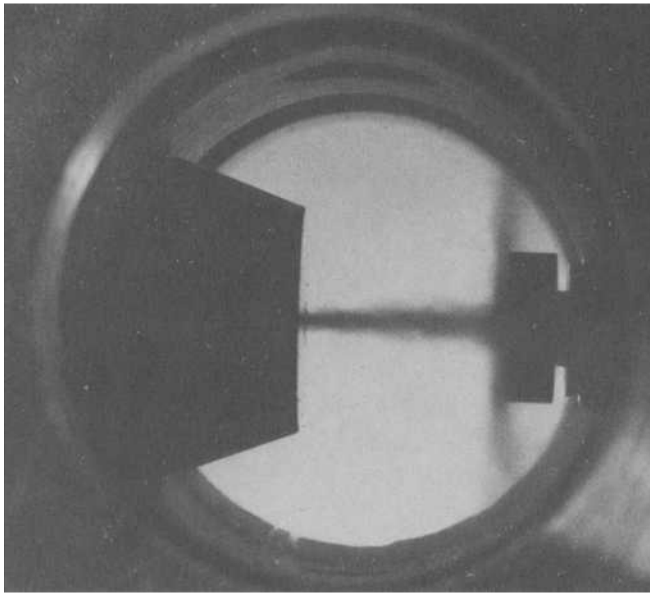

FIG. 4—*Cavitating jet in operation.*

Figure 8 shows initial mass loss for two specimens. In both these cases a more sensitive weighing machine was used to illustrate that, in the incubation zone, material loss occurs at very early stages. A photograph of the specimen (No. 19) in the early stages of erosion is shown in Fig. 5. Here σ is larger and consequently the central uneroded area is much smaller.

As suggested by Thiruvengadam [9], the erosion rate versus time curves were normalized, taking as the reference values the peak erosion rate and the time to reach that peak. All of the relevant erosion rate curves obtained in this study were so correlated. Figure 9 shows most of the results plotted in this way. Other data which are not shown also fall within the two bounding curves drawn around these points. Table 1 gives the peak erosion rates and the actual times to reach that peak. Thus, it is possible from the graph and the erosion rate table to calculate the actual time taken to reach that rate and hence the mass lost. The region around the incubation zone is not sufficiently well covered, since the balance used in most of the tests was not sufficiently sensitive at these small erosion rates.

Tests at Constant Cavitation Number and at Constant Back Pressure

The peak erosion rate for two constant values of the cavitation number is shown plotted against the upstream pressure in Fig. 10, and Fig. 11 shows

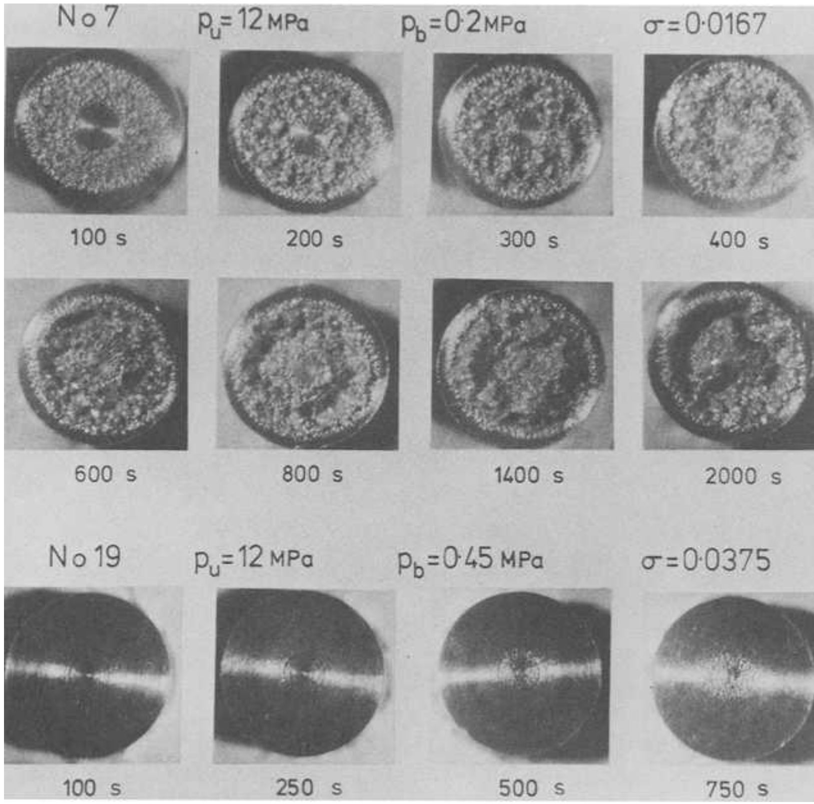

FIG. 5—*Stages of erosion in aluminum specimens.*

the time to reach the peak, plotted also against the upstream pressure. It can be seen that

$$\text{peak erosion rate} \propto \text{upstream pressure}^n \propto \text{jet velocity}^{2n}$$

and that the time to reach the peak T is nearly linearly related to the upstream pressure. The value of n and the slope of the linear graph both depend on the cavitation number. The present tests show that for pure aluminium

$$n = 4.2 \quad \text{for} \quad \sigma = 0.0143$$
$$n = 3.5 \quad \text{for} \quad \sigma = 0.025$$

On the same graphs the corresponding values obtained at constant back pressure are also shown. These do not form simple relationships, because

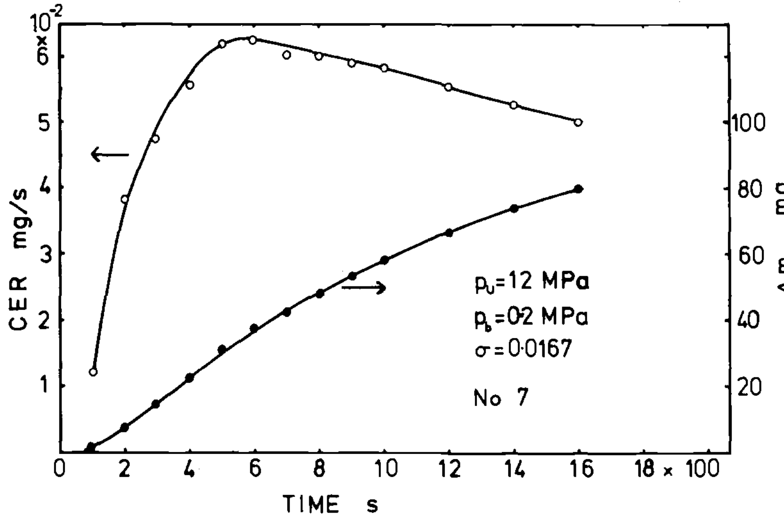

FIG. 6—*Typical mass loss and cumulative erosion rate time graphs.*

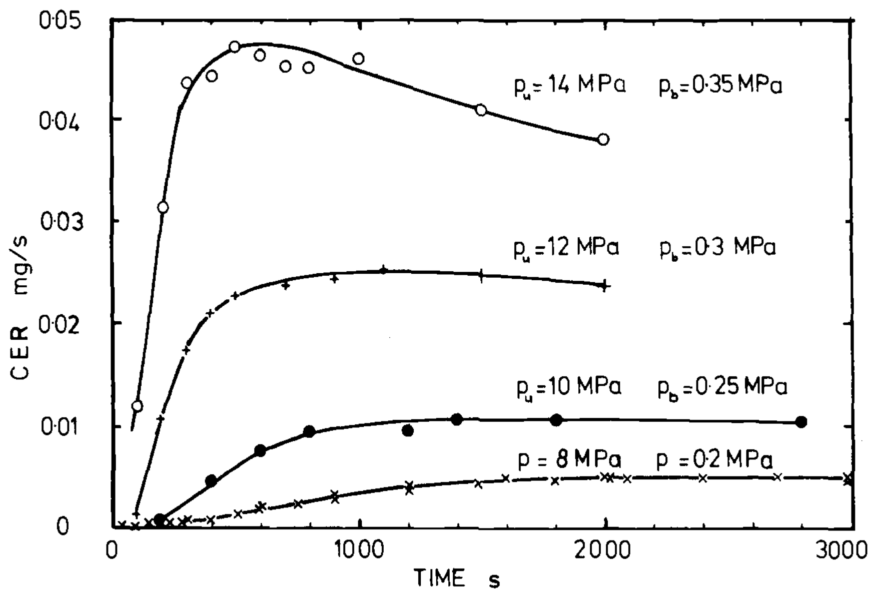

FIG. 7—*Cumulative erosion rate for various pressures at constant σ = 0.025.*

they were not taken under dynamically similar conditions and because some scale effects are present.

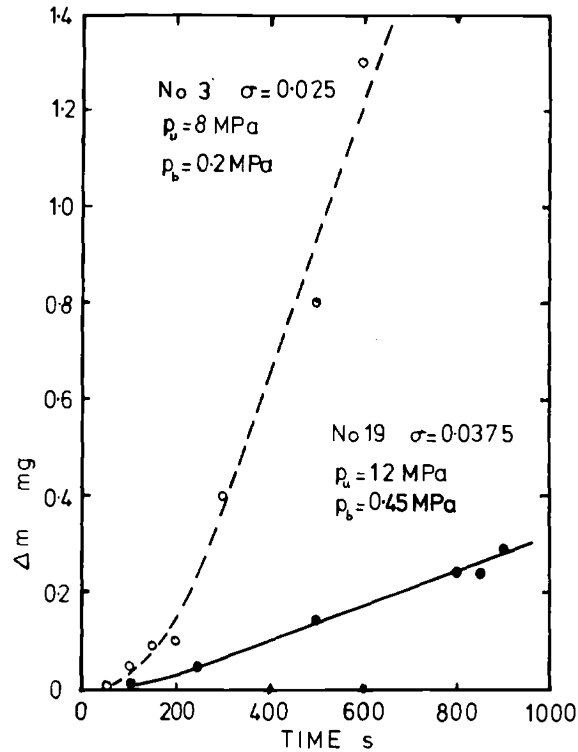

FIG. 8—*Early stages of erosion.*

Effect of Back Pressure

The next two sets of tests were conducted with upstream pressure kept constant (at two different values) while the downstream pressure was changed. For each pressure the peak erosion rate was established; these rates are shown in Fig. 12 as functions of the back pressure. As expected (Knapp et al [*10*]), there is an optimum back pressure to give maximum erosion rate and there is a corresponding minimum time to reach that peak. These results, like all others so far, were obtained at a constant standoff distance.

Effect of the Standoff Distance

A number of tests were also made where pressures were kept constant and the standoff distance was varied from 5 to 18 mm. The peak erosion rate obtained at each standoff distance is shown plotted against the standoff distance in Fig. 13. As expected, there is an optimum separation at which the erosion rate is a maximum, but this distance depends on flow conditions as shown by Kleinbreuer [*5*]. Kleinbreuer kept the upstream pressure constant

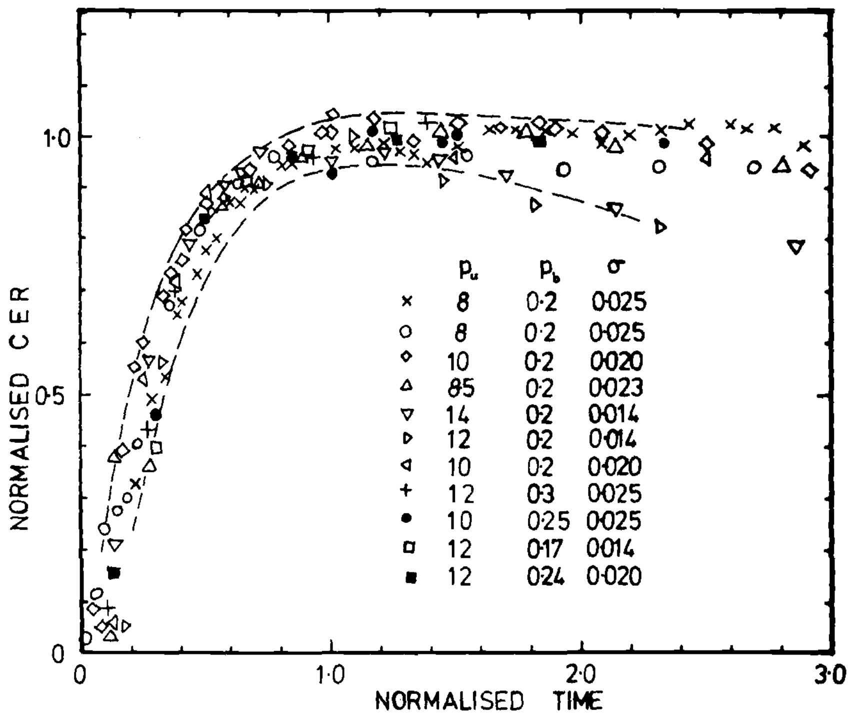

FIG. 9—*Normalized cumulative erosion rates—time graph.*

and altered the downstream pressure, and for each value of the downstream pressure he varied the standoff distance. At each distance he measured the material loss occurring in a fixed time (17 h in his case). His results show that for each value of the standoff there is an optimum downstream pressure to give maximum erosion in a specified time.

Tests on Other Materials

To show that the test rig is suitable for use with other materials, a few specimens of mild steel (EN3) were tested; the results are shown in Fig. 14. In 8 h, about 62 mg of steel were eroded with a jet having a stagnation pressure of 20 MPa. Tests on a similar material carried out elsewhere in a vibratory apparatus working at its maximum power resulted in a mass loss of less than 50 mg in the same time.

Discussion

The tests described show some of the characteristics of the cavitating jet testing apparatus. They indicate that the method is suitable for testing of

TABLE 1—*Summary of test results.*

Specimen No.	p_u, MPa	p_b, MPa	σ	Peak ER, mg/s	Time to Peak, s	Remarks
1	8	0.2	0.025	...	...	specimen: $D = 10$ mm
2	8	0.2	0.025	0.0053	2400	...
3	8	0.2	0.025	...	...	...
4	8	0.4	0.050	...	...	erosion too small
5	8	0.3	0.0375	...	...	erosion too small
6						dummy specimen
7	1.2	0.2	0.167	0.062	600	...
8-14						erosion outgrowing specimen
15	10	0.2	0.02	0.034	1800	...
16	10	0.2	0.02	0.034	1800	...
17-23						erosion outgrowing specimen—abandoned
24	85	0.2	0.0235	0.055	3000	...
25	...	...	...	...	...	dummy specimen
26	...	...	...	...	...	specimen size test, $D = 12$ mm
27	14	0.2	0.0143	0.061	750	...
28	12	0.2	0.0167	0.051	550	...
29	10	0.2	0.020	0.032	2000	...
30	14	0.35	0.025	0.048	600	...
31	14	0.2	0.0143	0.059	750	$D = 18$ mm

32	14	0.35	0.025	...	...	...
33	12	0.3	0.025	0.0254	1200	...
34	10	0.25	0.025	0.0107	1800	...
35-39	...	...	...	...	...	various check specimens
40	12	0.172	0.0143	0.027	1000	D = 12 mm
41	12	0.240	0.020	0.054	800	from this test down: D = 12 mm
42-50						grain size and heat treatment checks
51	14	0.35	0.025	...	...	...
52-55						check runs at different standoff distances
56	14	0.35	0.025	...	...	abandoned
57-61	14	0.35	0.025	...	...	tests at 10, 13, 5, 11.5, 18 mm standoff
62-65	14	0.35	0.025	...	...	heat treatment checks
66	10	0.48	0.05	...	...	no measurable erosion after 1000 s
67	12	0.6	0.05	...	...	no measurable erosion after 1000 s
68	10	0.14	0.0143	0.012	1200	...
69	16	0.23	0.0143	0.108	550	...
70	8	0.35	0.0437	...	...	no measurable erosion after 1000 s
71	10	0.35	0.035	...	...	error in weighing
72	16	0.35	0.022	0.095	350	...
73	16	0.112	0.007	...	...	Δm to small to weigh
74	16	0.4	0.025	0.079	700	...
77	20	2.86	0.0143	0.174	320	...
78	18	2.57	0.0143	0.134	400	...

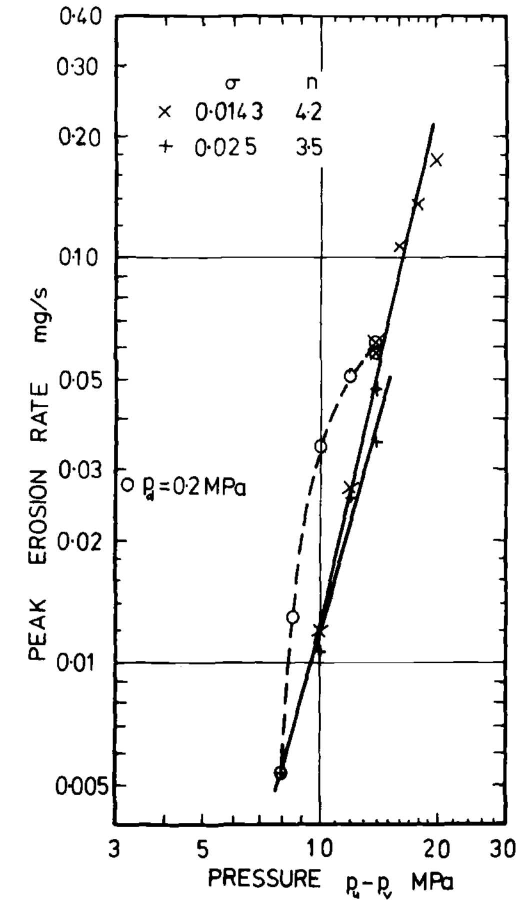

FIG. 10—*Peak erosion rate pressure relationships.*

materials for their resistance to cavitation erosion. The method offers many advantages over existing methods. The apparatus is small and utilizes flow effects to produce cavitation; hence it offers all the advantages of venturi and tunnel-type devices without their main drawbacks of size and long testing times. The testing times can easily be adjusted by choosing a suitable upstream pressure, and the results can then be scaled up or down easily as long as the cavitation number is kept constant.

Care must be taken, however, not to use too high pressures for erosion testing, as the material can be damaged by the jet or even cut by it. If one is in doubt, cavitation can easily be suppressed by raising both the upstream and downstream pressures. It must be remembered, however, that since in jet cutting it is the velocity which is important, the velocities under non-cavitating and cavitating conditions should be the same. This results in

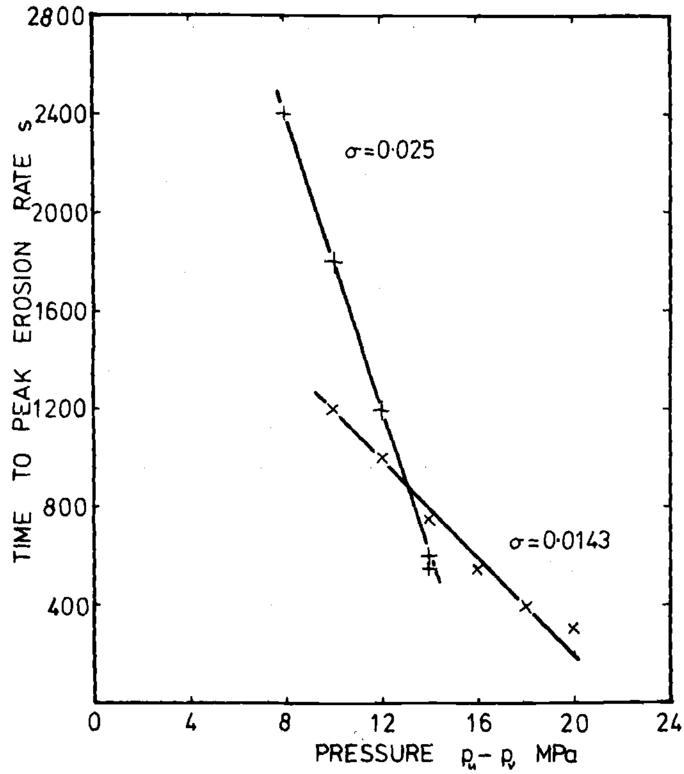

FIG. 11—*Time to reach peak erosion rate.*

$$(p_u - p_d)_{\text{noncavitating}} = (p_u - p_v)_{\text{cavitating}}$$
$$\approx p_{u\,\text{cavitating}}$$

The importance of scaling laws has been emphasized by the constant-cavitation-number and constant-back-pressure tests (Fig. 10).

Further tests should be carried out to extend the range of the test results and to investigate the effect of nozzle size. This is especially important since the power required to drive the rig is proportional to the nozzle cross-sectional area. In the present unit the maximum power dissipated by the jet was only 620 W. Thus a 2-kW power pack would be sufficient to drive the unit.

As a testing device, the unit should be simple to use and preferably the number of variable parameters should be minimized. Therefore, it is suggested that testing be done at a fixed standoff distance as was done in these tests, irrespective of whether it is optimum or not for the particular flow condition. The geometrical similarity essential for scaling is also retained.

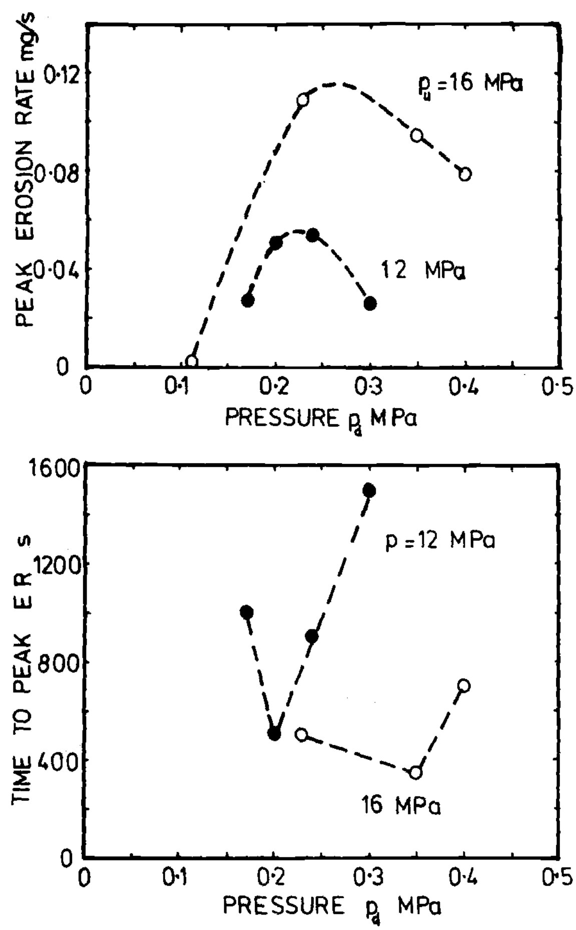

FIG. 12—*Effect of downstream pressure on peak erosion rate and on time to reach the peak.*

Good-quality pressure-regulating valves must be used in the testing because the erosion is very sensitive to changes in both pressures.

Conclusions

The tests described show that the cavitating jet method of testing provides a viable alternative to the existing methods of cavitation erosion testing. The apparatus is simple, pressures required are within current industrial practice (20 MPa) and, above all, the flow parameters can be easily controlled independently.

The importance of testing at a constant cavitation number to avoid scale effects was clearly demonstrated.

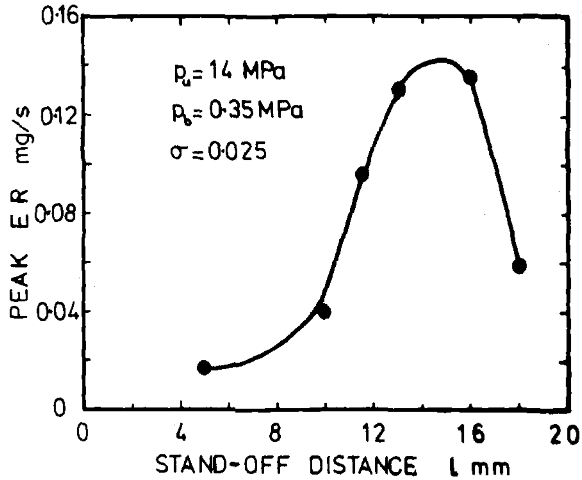

FIG. 13—*Effect of standoff on peak erosion rate.*

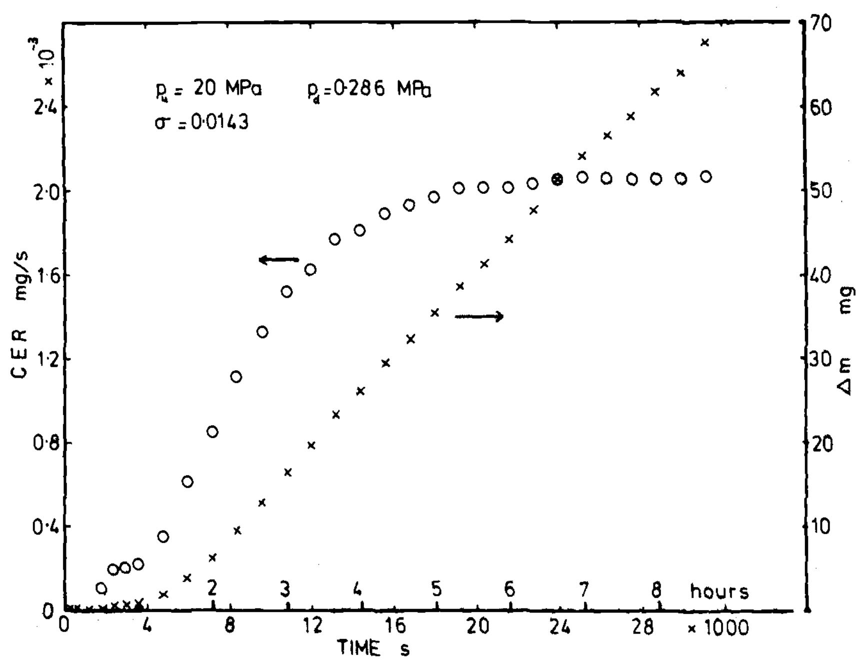

FIG. 14—*Tests on EN 3 mild steel.*

This type of apparatus is also suitable for more basic studies on cavitating flows and on cavitation erosion.

Acknowledgments

The author wishes to thank the authorities of the University of Nottingham for providing the facilities required, his final year undergraduate students M. D. Nolan, T. S. Stawski, and R. J. Munton, who have carried out most of these tests, and finally Lucas Industries Kinnear Moodie (1973) Ltd. and the Hamworthy Engineering Ltd. for some financial support.

APPENDIX

Properties

Aluminium (99.6 percent pure)

Ultimate tensile strength, 67.4 MN/m^2
Vickers Hardness Number range, 21.5 to 23.8
Heat treatment: heat for 2 h @ 400°C. Cool in air.

Steel

Low-carbon mild steel, EN 3
Ultimate tensile strength, 460 MN/m^2

Oil

Esso NUTO H32 hydraulic oil

Temperature	Kinematic viscosity
38°C	4.53 mm^2/s
93°C	1.55 mm^2/s

Temperature	Density, kg/m^3
30°C	843
50°C	831

Vapor pressure @ 38°C 2.26 Pa

References

[1] Lichtarowicz, A., "Use of a Simple Cavitating Nozzle for Cavitation Erosion Testing and Cutting," *Nature: Physical Science*, Vol. 239, No. 91, 25 Sept. 1972, pp. 63-64.
[2] Lichtarowicz, A., "Experiments with Cavitating Jets," *Proceedings*, Second International Symposium on Jet Cutting Technology, Paper D1, British Hydromechanics Research Association, Fluid Engineering, Cambridge, U.K., 1974.

[3] Nolan, M. D., "New Methods of Cavitation Erosion Testing," B.S. thesis, Department of Mechanical Engineering, University of Nottingham, Nottingham, U.K., 1975.
[4] Stawski, T. S., "Cavitation Erosion Testing," B.S. thesis, Department of Mechanical Engineering, University of Nottingham, Nottingham, U.K., 1976.
[5] Munton, R. J., "The Effect of Flow Parameters on Cavitation Erosion," B.S. thesis, Department of Mechanical Engineering, University of Nottingham, Nottingham, U.K., 1977.
[6] Kleinbreuer, W., "Werkstoffzerstörung durch Kavitation in Ölhydralishen Systemen," *Industrie-Anzeiger*, Vol. 98, No. 61, 28 July 1976, pp. 1096–1100.
[7] Pearce, I. D. and Lichtarowicz, A., "Discharge Performance of Long Orifices with Cavitating Flow," *Proceedings*, Second Fluid Power Symposium, Paper D2, British Hydromechanics Research Association, Fluid Engineering, Guildford, U.K., 1971.
[8] Lichtarowicz, A. and Pearce, I. D., "Cavitation and Aeration Effects in Long Orifices," Conference on Cavitation, The Institution of Mechanical Engineers, London, U.K., 1974.
[9] Thiruvengadam, A., "Scaling Laws for Cavitation Erosion," Hydronautics Inc. Technical Report 233-15, Laurel, Md., Dec. 1971.
[10] Knapp, R. T., Daily, J. W., and Hammitt, F. G., *Cavitation*, McGraw-Hill, New York, 1970, p. 369.

DISCUSSION

A. F. Conn[1] (*written discussion*)—Did you examine the interaction between optimum standoff distance and chamber pressure? We have done some limited elevated ambient pressure tests, in the Cavijet, and found that the optimum standoff decreases with increasing ambient pressure.

A. Lichtarowicz (*author's closure*)—I have done a few tests at higher downstream pressure and I have found, as you have, that the optimum standoff distance decreases as the pressure is increased. For constant upstream pressure the erosion decreases at optimum standoff as the ambient pressure is raised. Some more information on the subject can be found in Ref *6* of the paper.

[1]Hydronautics, Inc., Pindell School Road, Laurel, Md. 20810.

Liquid Jet Applications

Michael Hood[1]

Mechanism of Fracture of Hard Rock Using a Drag Bit Assisted by Waterjets

REFERENCE: Hood, Michael, "**Mechanism of Fracture of Hard Rock Using a Drag Bit Assisted by Waterjets,**" *Erosion: Prevention and Useful Applications, ASTM STP 664*, W. F. Adler, Ed., American Society for Testing and Materials, 1979, pp. 553-561.

ABSTRACT: It is shown that the mechanism of rock fracture is similar both when a blunt drag bit is used to cut strong rock and when a flat-bottomed punch is pressed into the rock surface. In order to study this fracture mechanism an experimental technique was developed which involved indenting the rock specimen in a quasi-static manner, using a drag bit as the punch. The effect of directing waterjets adjacent to the bit was investigated and it was found that these jets caused a rock chip to form with lower than normal forces applied to the bit. This finding agrees with results of previous experiments where lower forces were applied to the bit during the cutting operation when waterjets were used. A hypothesis is proposed to explain the action of the waterjets on the rock to produce this reduction in the indentation force.

KEY WORDS: drag bits, waterjets, hard rock, cutting, indentation, rock fracture, erosion

In recent years considerable attention has been paid to the development of techniques for cutting in hard rock, for application both in the mining and tunneling fields.

This work has concentrated largely on improvements to roller cutter technology, but drag bit cutting tools have been employed successfully in certain applications. For example, drag bits are used both on the Atlas-Copco tunneling machine and on the rock-cutting machines developed by the Chamber of Mines of South Africa [*2*]. Research work related to this latter project has shown that when a blunt drag bit was used to cut in hard rock, the forces acting on the bit were reduced dramatically when coherent water-

[1] Assistant professor, Department of Materials Science and Mineral Engineering, University of California, Berkeley, Calif. 94720; previously, project leader, Mining Technology Laboratory, Chamber of Mines of South Africa.

jets at moderate pressures (50 MPa) were directed immediately ahead of the bit [1][2]. These reductions in the bit forces were greater than had been expected in the light of existing knowledge that waterjets by themselves, at these moderate pressures, would not cause damage to the rock [3]. An interesting aspect of the influence of waterjets on these reductions in the bit forces was that the force normal to the direction of cutting, known as the bit penetrating force (Fig. 1), was more sensitive to parameters such as the pressure of the waterjets or the point of impingement of the jets relative to the bit than was the force in the direction of cutting, known as the bit cutting force. An explanation of this behavior was sought. This paper discusses the results of an investigation directed toward establishing details of the action of waterjets on the rock adjacent to a drag bit.

Mechanism of Fracture of Strong Rock, Using a Drag Bit with No Waterjets.

In order to understand how waterjets assist a drag bit when cutting in hard rock, it is necessary first to examine the mechanism of rock fracture caused by drag bits without waterjets.

Previous research work [4], has suggested that a drag bit cutting in strong rock acts in a fashion similar to a flat indentor moving through the rock. The results of this work indicated that the rock spalled ahead of the leading face of the bit and that this leading face, therefore, did not affect the rock breaking process.

In order to investigate this proposal, experiments were designed by the author to determine whether the leading face of the bit was ever in contact with the rock during the cutting operation. A series of high-speed films was made of a bit cutting in a block of Witwatersrand quartzite in order to study, in a slow motion, the method of fracture of the rock adjacent to the bit. These films, which were taken at 3000 frames a second using a revolving-prism type camera showed that initial fracture was caused by indentation of the rock by the bit wearflat. A rock chip was formed ahead of the bit and this was observed to rotate while being ejected at a high velocity in the cutting direction.

It was observed also that the cemented tungsten carbide inserts deformed plastically ahead of the leading face of the bit (Fig. 1). If this leading face had functioned as a cutting surface, it would not have been possible for plastic deformation of the tungsten carbide to occur by flowing ahead of the bit. It was concluded, therefore, that the leading face of the bit was not in contact with the rock at any time during the cutting process.

It was concluded from these tests that the mechanism of rock failure during the cutting operation might be similar to that produced by a flat-bottomed indentor pressing into a rock surface. This proposal was in-

[2]The italic numbers in brackets refer to the list of references appended to this paper.

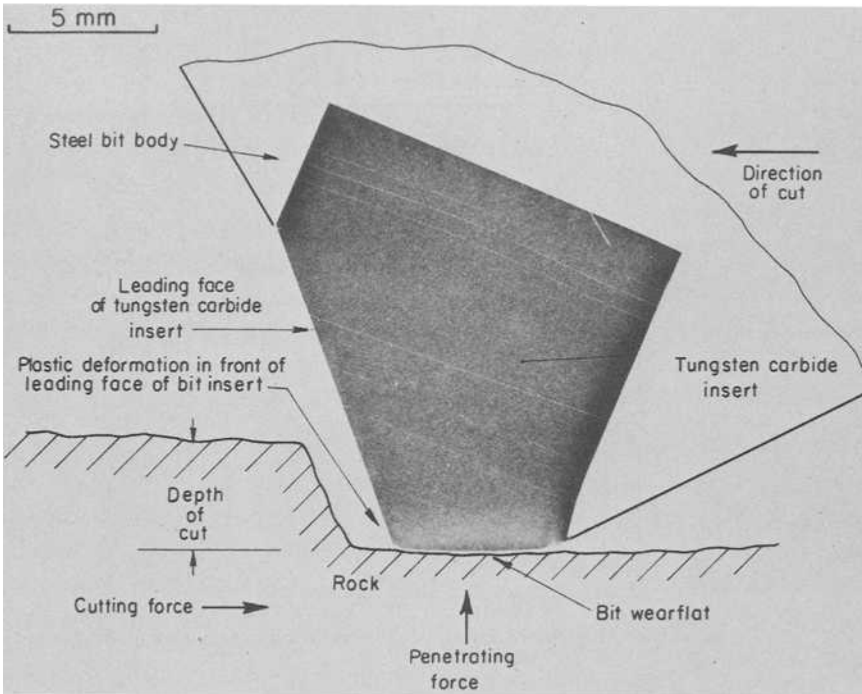

FIG. 1—*Magnified section of a cemented tungsten carbide bit insert, showing plastic deformation of the insert ahead of the leading face.*

vestigated further by conducting experiments to find out whether the rock chip that was formed when a quasi-static indentation force was applied to a rock surface (using a drag bit as the punch) resembled the rock chips that were formed during the cutting operation. It was considered that if rock chips of similar geometry could be produced by these two different methods, then this would be a strong indication that rock fracture during the cutting process could be simulated, in a controlled fashion, by conducting a suite of indentation tests.

A stiff, 2-MN compression testing machine was used for these experiments. A detailed description of this machine has been given in Ref. 5. The bit was placed between the machine loading piston and the cylindrical rock specimen, with the bit wearflat in contact with the rock (Fig. 2). Force was applied to the rock specimen using a fixed rate of displacement of the machine loading piston.

Small rock chips about 2 mm in diameter and 0.5 mm thick were observed to form next to the corners of the bit when the force applied was between 100 and 150 kN. Increasing this load produced a situation where a major rock chip was formed immediately ahead of the leading face of the bit. No damage

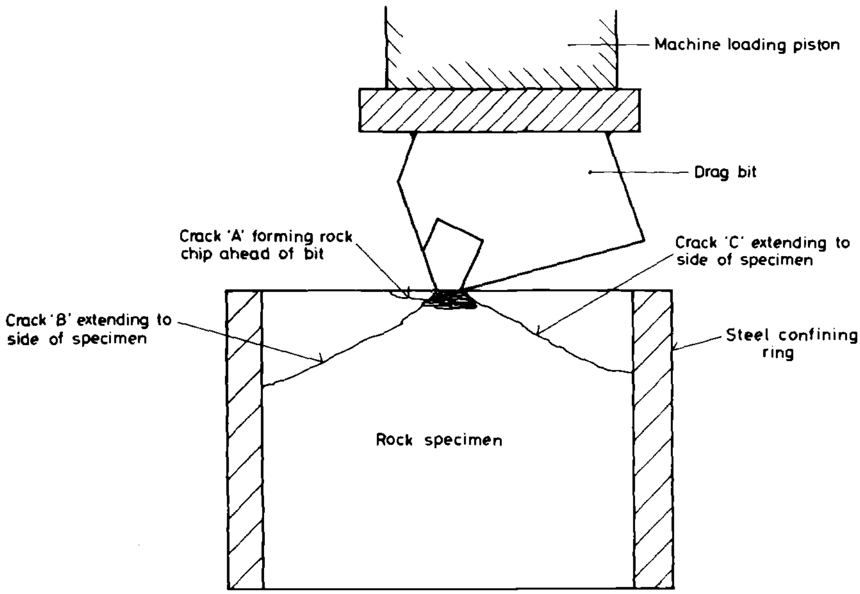

FIG. 2—*Diagram illustrating the method used to mount the bit and the rock in the compression testing machine.*

to the specimen in the form of cracking, other than the minor chipping in the vicinity of the bit corners, was visible until this major chip was formed. This large chip in front of the bit extended across the full 35-mm thickness of the bit and for some 10 to 15 mm ahead of the bit. The force required to form this rock chip, in both the norite and the quartzite specimens, was between 250 and 350 kN. Examples of curves showing the applied load plotted against bit penetration for a norite specimen is given in Fig. 3.

Rock chips would be expected to form symmetrically on either side of a flat-bottomed rectangular punch which was pressed against a flat rock surface. With all of the specimens tested during this experimental program, however, the large rock chips were formed always on one side of the bit and ahead of the leading face. The reason for this preferential cracking ahead of the bit is found in the asymmetrical bit geometry which permits the steel bit body behind the rear face of the tungsten carbide insert to press against the rock, thereby applying a confining force in this region during the indentation process.

Examination of the rock chips which formed ahead of the bit during these quasi-static indentation tests showed that geometrically they resembled very closely the rock chips that were formed during the cutting process (Fig. 4). It was concluded that rock fracture while cutting was duplicated reasonably well by these indentation tests.

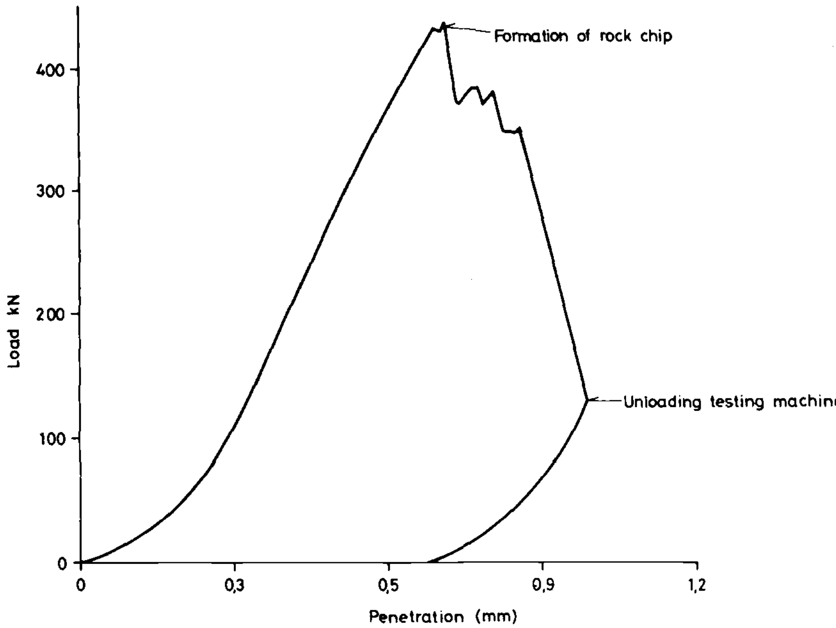

FIG. 3—*A typical curve taken from the indentation test series showing the indentation force plotted against the bit penetration.*

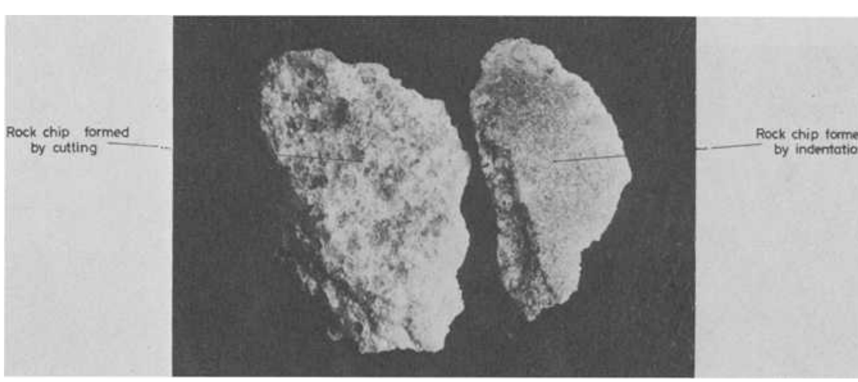

FIG. 4—*Geometric similarity beteen rock chips formed during the cutting operation and those formed during indentation tests.*

Rock Fracture Adjacent to a Blunt Drag Bit

In order to examine the cracks as they were developed in the rock, a further series of tests was carried out where the indentation was stopped at predetermined intervals during the loading operation prior to the formation of a rock chip. The rock specimens then were sectioned with a diamond saw and the fractured zones adjacent to the bit were studied using a scanning electron microscope (SEM).

A section through one of the quartzite specimens from the indentation tests (Fig. 5) shows that the rock immediately underneath the bit wear flat was crushed intensely to a depth of several millimetres. The crack which indicates the formation of a major rock chip ahead of the leading edge of the bit is marked "A" in Fig. 5. Other major cracks, "B" and "C" in Fig. 5, extended from the crushed rock zone to the side of the specimen. A crack once initiated develops toward a free surface to form a rock chip. Therefore the prominence of Cracks B and C was attributed to the limited size of the specimen. In a massive block of rock the only available free surface would be the face in contact with the bit wearflat and, consequently, Crack A would be expected to develop in preference to Cracks B and C.

A more detailed study of the propagation of cracks adjacent to the bit was conducted using four rock specimens, two of norite and two of quartzite. A bit was used to indent the rock surface and the compression was stopped at selected levels of the applied load. The rock specimens were sectioned in a manner similar to that illustrated in Fig. 5 and the region of interest, immediately underneath the bit wearflat and ahead of the leading face of the bit, was mounted on an SEM specimen holder.

Figure 6 is an SEM micrograph of a section through one of the norite

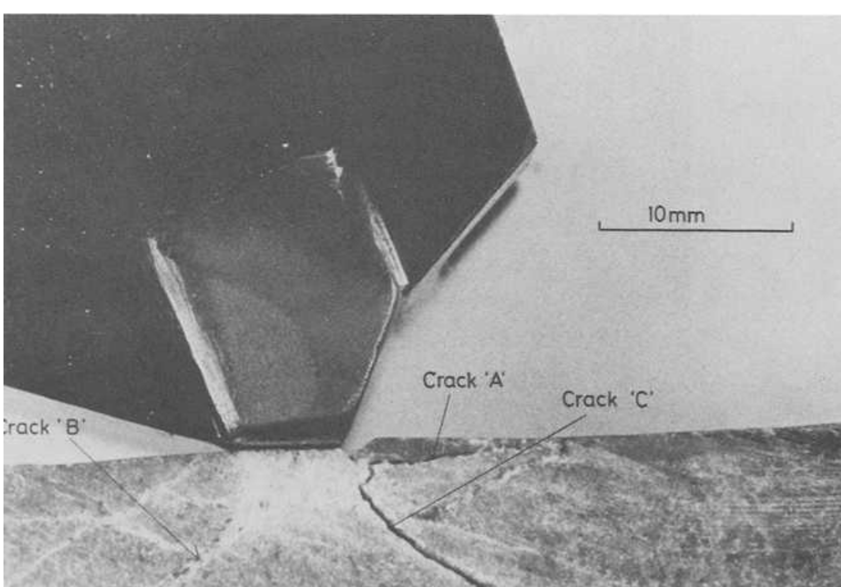

FIG. 5—*Section through a rock specimen illustrating the cracks which formed during the indentation tests.*

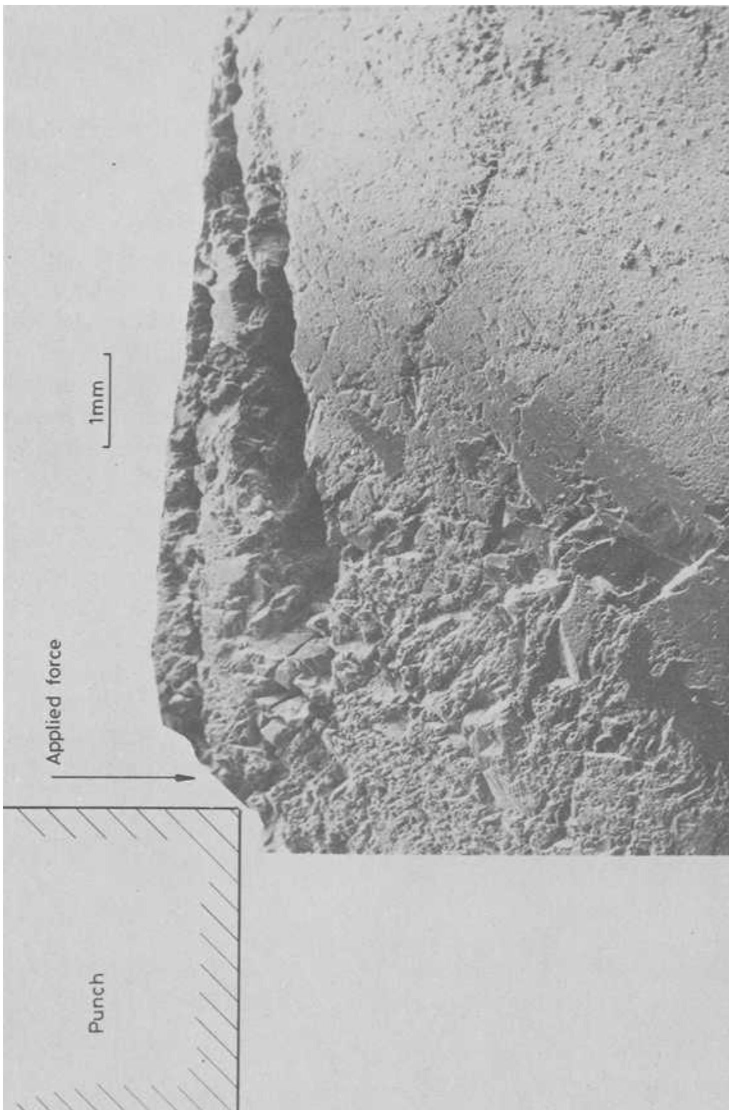

FIG. 6—*Micrograph of a section through a norite specimen, illustrating the cracks which developed adjacent to the punch.*

specimens. The most clearly defined fracture in Fig. 6 is that closest to the rock surface. If the force applied to the bit had not been removed but increased, this crack would have extended to form a large rock chip. The geometric similarity between this chip and those from other indentation and cutting experiments (Fig. 4) is apparent.

Indentation Tests Using High-Pressure Waterjets

A series of indentation tests was then conducted with waterjets at 50-MPa pressure directed 2 mm ahead of the leading face of the bit, toward the corners of the cemented tungsten carbide cutting elements (Fig. 7). The tests were performed with both norite and quartzite rock specimens.

The procedure followed was to apply the load slowly to a level approximately half that required to form a rock chip ahead of the bit, that is, between 150 and 200 kN. The stress in the rock at the corners of the bit with this applied force was sufficient to form small rock chips in this region. At this juncture the waterjets were applied at 50-MPa pressure with a flow rate of 0.5 litres/s. When these jets struck the rock surface the rock chip formed ahead of the bit almost immediately. Since the water spray prevented direct observations of the formation of the rock chip, this was sensed by a fall in pressure of the hydraulic fluid in the press.

This experiment was repeated a number of times and the results were consistent in demonstrating that when waterjets were used, the indentation force necessary to form a rock chip ahead of the bit was reduced by a factor of about two. Additional tests, with waterjets directed 10 mm ahead of the bit, showed that the indentation force was not measurably reduced. Limitations of the test equipment made it impractical to carry out more detailed experiments. Nevertheless it is felt that these tests have demonstrated clearly that when suitable waterjets are used to assist the rock breaking operation,

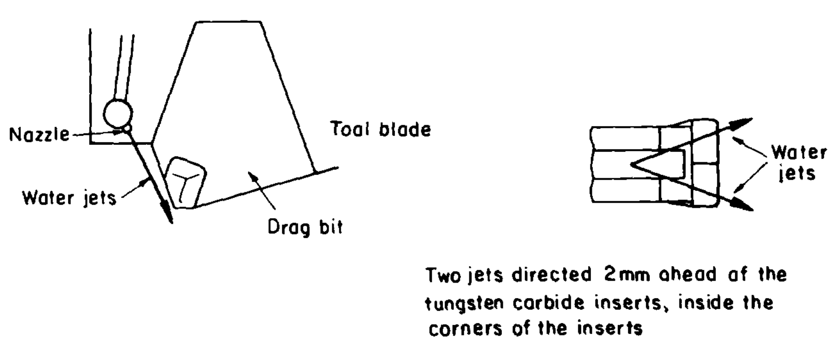

FIG. 7—*Diagram illustrating the position and point of impingement of the waterjets relative to the bit.*

the force normal to the rock surface required to form a rock chip ahead of the bit is reduced substantially.

The mechanism for this force reduction appears to be that cracks, initiated ahead of the bit with a relatively low applied force, are propagated when the water is forced into them to form a rock chip.

Conclusions

The investigation of the mechanism of fracture of strong rock using blunt drag bits showed that the bit penetrating force caused the bit to indent the rock and form rock chips ahead of the leading face of the bit. In addition, it was shown that the leading face of the bit is not in contact with the rock during the cutting operation.

A series of indentation tests showed that when 50-MPa waterjets were directed immediately ahead of the bit, the force required to form a rock chip was reduced by a factor of at least two. Previous experiments cutting the rock [*1*] had shown that the most effective point of impingement of the jets was immediately ahead of the leading face of the bit. It was in this region that cracks were initiated in the rock. Taken together, these experiments indicate that the mechanism by which the waterjets assist the rock breaking process is by the water penetrating and then propagating the cracks which develop ahead of the bit.

Acknowledgments

This work was carried out as part of the research program of South African Chamber of Mines, Mining Technology Laboratory.

References

[*1*] Hood, M., *Journal of the South African Institute of Mining and Metallurgy*, Vol. 77, No. 4, Nov. 1976, pp. 79-90.

[*2*] Joughin, N. C., *Journal of the South African Institute of Mining and Metallurgy*, Vol. 76, No. 6, 1976, pp. 285-300.

[*3*] Labus, T. J., "Energy Requirements of Rock Penetration by Water Jets," Third International Symposium on Jet Cutting Technology, Paper No. E3, Chicago, 1976.

[*4*] Riemann, K. P., "Die Zerspanung von Hartgesteinen Beim Schlitzhobeln.," Dissertation, Technical University of Hanover, West Germany, 1974.

[*5*] Hojem, J. P. M., Cook, N. G. W., and Heins, C., *South African Mechanical Engineer*, Vol. 25, No. 9, 1975, pp. 250-270.

A. F. Conn[1] *and S. L. Rudy*[1]

CAVIJET Coal-Cutting Parameters

REFERENCE: Conn, A. F. and Rudy, S. L., "**CAVIJET Coal-Cutting Parameters,**" *Erosion: Prevention and Useful Applications, ASTM STP 664,* W. F. Adler, Ed., American Society for Testing and Materials, 1979, pp. 562-581.

ABSTRACT: Laboratory coal-cutting experiments with CAVIJET cavitating waterjets have demonstrated the feasibility of this technology for hydraulic coal mining applications. The objective of the first phase of a developmental program, as described in this paper, was to determine the system and operating parameters required to cut coal with CAVIJETS, and to compare the results with those observed for noncavitating jets.

Comparable coal cutting was achieved with the CAVIJET, relative to high-pressure, noncavitating jets, using one-fifth the pressure and one-half the specific energy. These results suggest that CAVIJET-augmented mining devices can be developed with compact, low-pressure pumps. Thus, CAVIJET should be capable of operating with safer, lighter, more suitable support equipment, while providing all of the advantages (reduction of dust and sparks; decreased damage to cutters) of conventional hydraulic mining methods.

KEY WORDS: CAVIJET, cavitation, waterjets, coal, hydraulic mining, erosion

There is growing interest in the use of waterjets for mining, drilling, and cutting applications because of the high levels of deliverable power, the potential for reducing tool damage, the elimination of spark creation which might ignite gas deposits, and considerable reduction in dust levels [*1*].[2] Most of the hydraulic mining has been done either with low-pressure, very-high-flow sluicing jets, high-pressure waterjets [68.9 to 689.0 MPa (10 000 to 100 000 psi)], or with pulsating waterjets in which there is an intermittent ejection of slugs of water [*2*]. In contrast to these jets a unique, cavitating waterjet called the CAVIJET[3] is now being developed. This device is one of the very few successful techniques in which the destructive power of cavitation is harnessed to do useful work. The basic difference between a cavitating waterjet and a high-pressure steady or pulsating waterjet is that the damage

[1]Principal research scientist and head, and associate research scientist, respectively, Material Sciences Division, Hydronautics, Inc., Laurel, Md. 20810.

[2]The italic numbers in brackets refer to the list of references appended to this paper.

[3]CAVIJET is a trademark of Hydronautics, Incorporated, Laurel, Md.

in the former case is amplified by the collapse of cavitation bubbles and is not merely due to the high pressure or velocity of the jet. The CAVIJET method has been successfully demonstrated for various cutting, cleaning, and drilling applications [*3*].

The experiments reported herein were undertaken in order to investigate the feasibility and energy effectiveness of using the CAVIJET method for cutting coal. The ultimate objective of this investigation is the design, fabrication, testing, and evaluation of prototype equipment capable of use in the field to cut coal by the CAVIJET method. Under the first-phase contract a laboratory experimental program was defined to provide controlled test conditions, so that feasibility may be established and values determined of the parameters required for CAVIJET coal-cutting devices.

The CAVIJET method and the Hydronautics CAVIJET test facility are described in the next section. The acquisition and preparation of test specimens are then outlined, followed by a summary of the experimental procedures and parameters. Some typical test results are presented, and the performance of CAVIJET is compared with noncavitating waterjets for coal-cutting applications.

The CAVIJET Cavitating Waterjet Method

CAVIJET is a turbulent waterjet in which vapor and gas cavities are stimulated to grow in order to enhance the destructive power of a relatively low-velocity steady jet. By proper adjustment of the distance between the nozzle and the surface to be fragmented, these cavities are permitted to grow from the point of formation and then to collapse on that surface in the high-pressure stagnation region where the jet impacts the solid material. Because the collapse energy is concentrated over many very small areas at collapse, extremely high, very localized stresses are produced. This local amplification of pressure provides the cavitating waterjet with a great advantage over steady noncavitating jets, which are operated at the same pump pressure and flow rate. Further details about the basic principles for the operation of a cavitating waterjet may be found in Ref *4*.

The CAVIJET Test Facility

The primary components to this facility (see Fig. 1*a*) include a pump, reservoirs to recover and store the water, suitable filters, controls, pressure and temperature gages, flow measuring devices for precisely measuring all system parameters, and a new large test chamber with the means for translation of the CAVIJET nozzle relative to test specimens either in air or in a submerged configuration. During this program, because of the large coal specimens which were to be used, it was decided to design and build a new test chamber. The overall dimensions of this test chamber (Fig. 2) are length

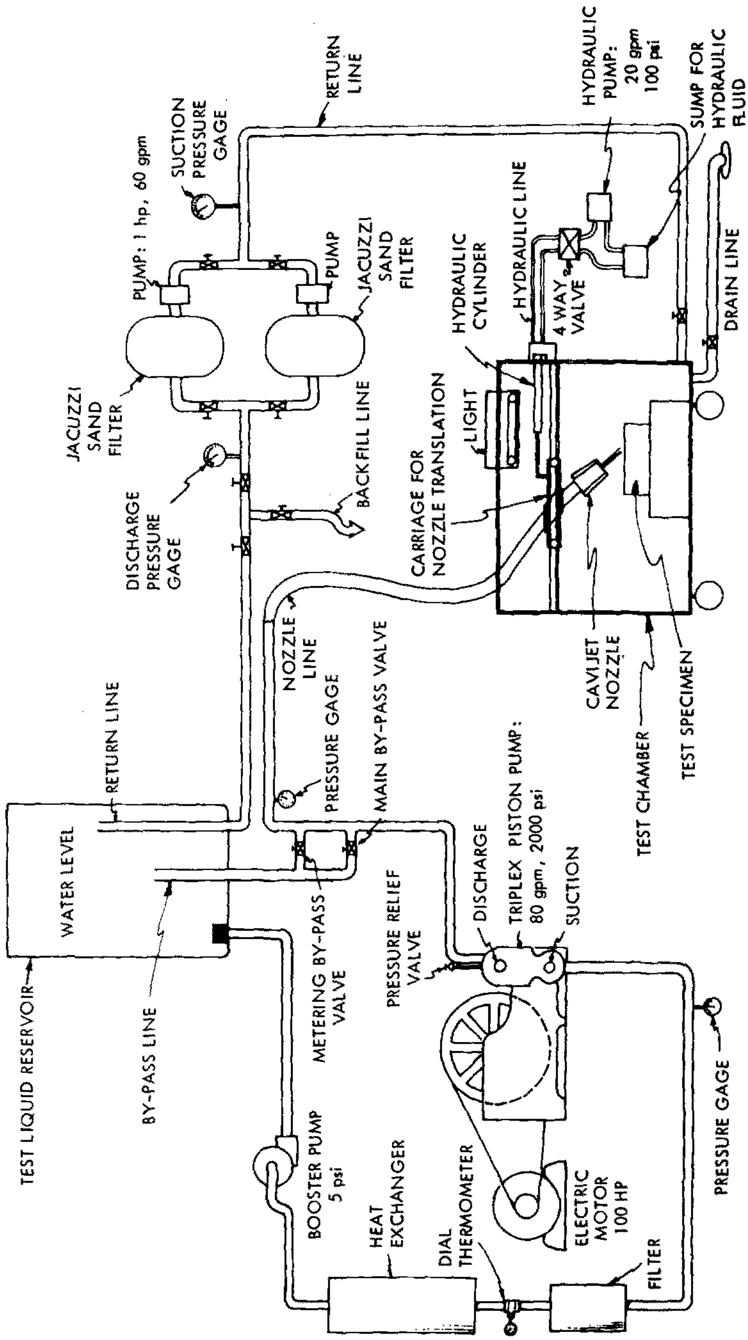

FIG. 1*a*—*Schematic of CAVIJET cavitating waterjet test facility.*

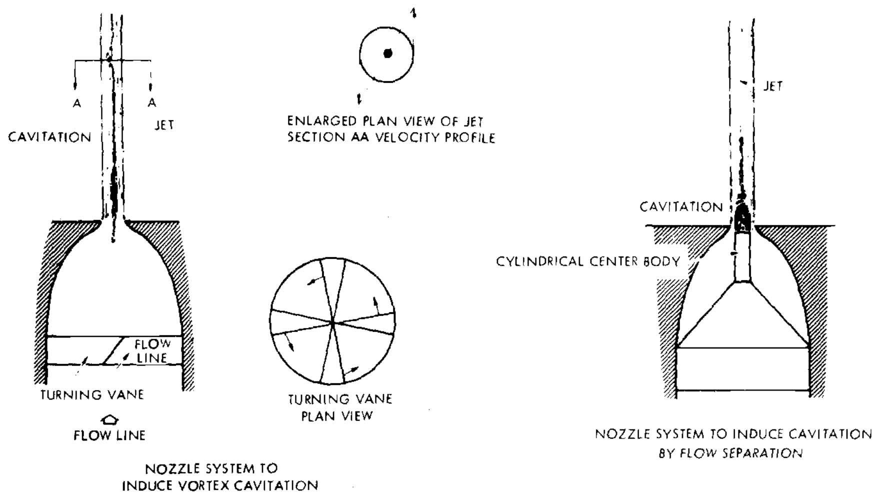

FIG. 1*b*—*Typical cavitating waterjet nozzle configurations.*

1.8 m (6 ft), width 1.5 m (5 ft), and height 1.8 m (6 ft) from the floor of the chamber to the ceiling of the roll-away cover. The height of the lower, water-containing section of the test chamber is 1.2 m (4 ft). Further details about this facility are given in Ref *5*. Some typical CAVIJET nozzle configurations are shown in Fig. 1*b*.

Acquisition and Preparation of Test Specimens

Coal segments were acquired from the Fire Creek Coal Seam near Anjean, W. Va. The medium-hard, low-sulfur bituminous coal seam in this location lies below an overburden of sand stone which is about 9.1 to 10.7 m (29.8 to 35.1 ft) thick. The seam has an average thickness of 1.5 m (4.9 ft).

The test specimen developed for these tests consisted of as many as nine coal segments, each roughly a cube about 0.3 m (0.98 ft) on a side. The coal segments were imbedded in concrete, to provide an overall testing area of about 0.7 m^2 (7.5 ft^2), as seen in Figs. 2 and 3. A steel "girdle" was fabricated to surround the coal-and-concrete specimen to provide compressive loading, and hence some simulation of the actual overburden loading on the coal seam. Thus, any given test run involved cutting across several pieces of coal. The concrete block with imbedded coal specimens was 0.76 by 0.91 m (2.49 by 2.98 ft) by at least 0.25 m (0.82 ft) deep and weighed about 3.5 to 4.0 kN (800 to 900 lb).

Experimental Procedure and Parameters

After the concrete block, containing several coal specimens, was placed in

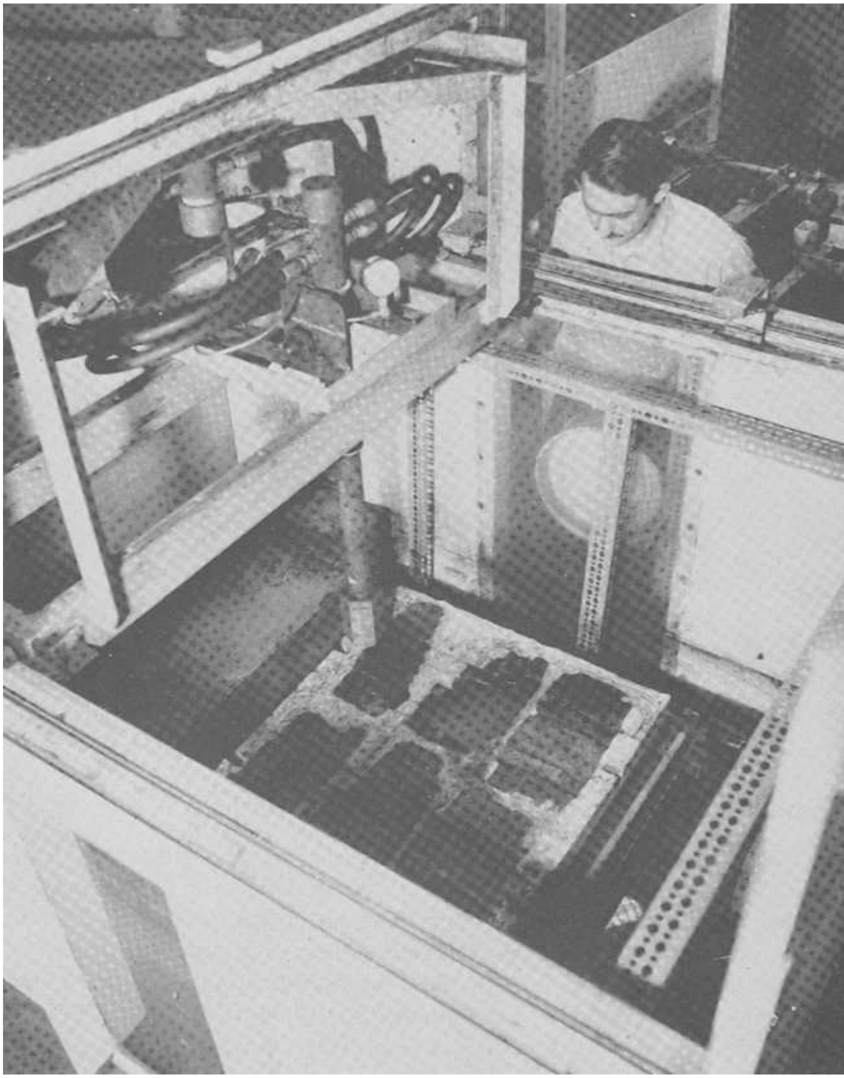

FIG. 2—*Test chamber of CAVIJET cavitating waterjet facility.*

the test chamber, it was properly oriented so that the bedding planes were either parallel or perpendicular to the direction of translation of the CAVIJET. To begin each test, the chamber cover was closed and, with no pressure at the nozzle, trial runs were made to set the desired translation velocity. Once these settings were established for the hydraulic system, the required nozzle pressure was set by adjusting the amount of bypass flow. A single pass

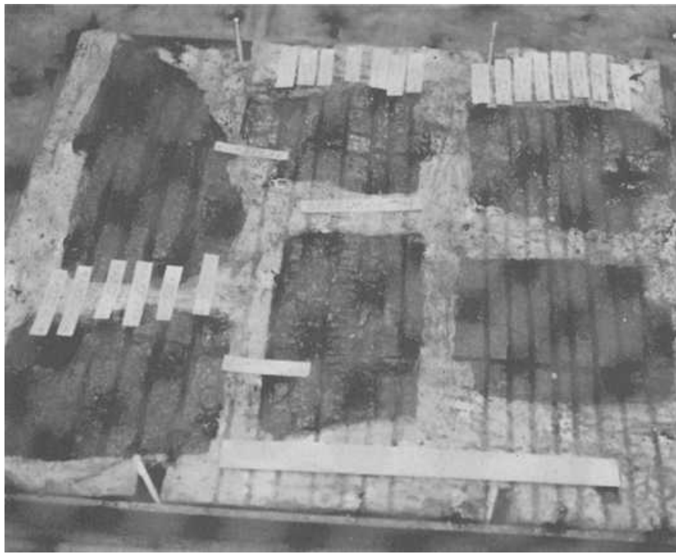

(a) Overall View

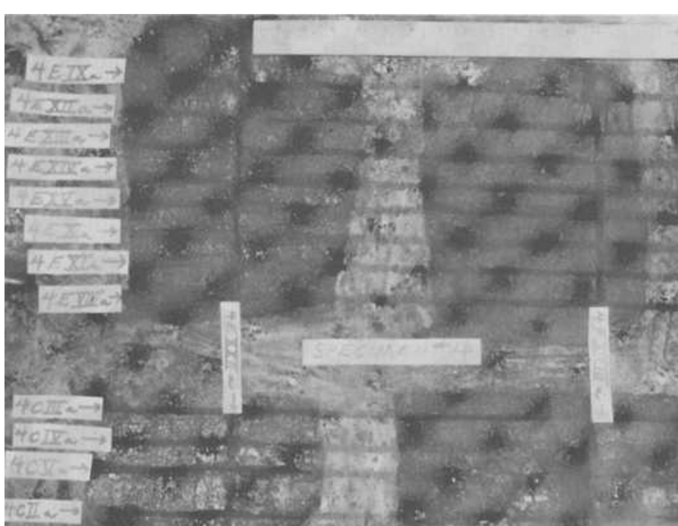

(b) Close-up: Upper right-hand corner

FIG. 3—*Specimen 4; tests with 3.2-mm (1/8 in.) and 6.4-mm (1/4 in.) CAVIJET.*

was then made across the specimen; then the pressure was reduced and the cover opened so that measurements of the slots cut in the coal could be made. Sketches were also made of the shape and position of each coal segment, and the location and configuration of each slot.

For each test run the following system parameters were noted: nozzle size, nozzle type, number of nozzles, and relative placement of multiple nozzles; as well as operating parameters: translation velocity, v; angle of impingement, θ; nozzle pressure, p; flow rate, Q; standoff distance, that is, the distance between the nozzle face and the coal surface, l; and the mode of operation, which was in-air for all of these tests. At the completion of each test run the slot depth, Z, and the slot width, W, were measured.

From these dependent and independent variables, the following performance parameters were determined:

$$\text{Rate of area cutting, } \dot{A} = Z \cdot v$$
$$\text{Rate of volume removal, } \dot{V} = Z \cdot W \cdot v$$

$$\text{Kerfing effectiveness, } e_a = \dot{A}/P$$
$$\text{Volume removal effectiveness, } e_v = \dot{V}/P$$

where P is hydraulic power, and e_a and e_v are the measures of area of slot created per unit energy and volume of coal removal per unit energy, respectively.

As is evident from Fig. 3*a,b*, the slots were very clearly defined in almost all the tests, thereby making it quite easy to measure the widths and depths. Several measurements along the length of the slot were made to establish a "typical" or "modal" value, and this value is used for analyses in the next section. Maximum and minimum were also recorded. The slot depths were measured to within $\pm$6.4 mm (1/4 in.), and the widths to within $\pm$3.2 mm (1/8 in.). The translation velocity was measured over a predetermined distance of 0.616 m (24.25 in.). Microswitches at two positions started and stopped an electric timer, measuring the time of travel to within $\pm$0.02 s.

Although no attempt was made to control the moisture content of most of the coal segments used in this study, a few tests were run to assess the importance of this parameter. A batch of coal blocks was removed from the mine, kept continuously moist by completely covering them in wet newpapers, and encased into the concrete specimen format within 48 h after being mined. Testing was done after the concrete block was cured for two days under several inches of water in the mold. The experimental data showed that the widths and depths for these tests were well within the scatter for comparable tests without any moisture control.

Test Results

In this section a summary of the experimental results for coal cutting with single and dual CAVIJET nozzles is presented. Three nozzle orifice diameters were utilized, namely, 2.2, 3.2, and 6.4 mm (0.086, 1/8, and 1/4 in.), and for each, the centerbody CAVIJET configuration was utilized (see Fig. 1*b*). The centerbody was cylindrical in shape, flat ended, and had a diameter one half of the nozzle orifice diameter in each case. The measurements were made over a translation velocity range of 5 cm/s (12.7 in./s) to about 100 cm/s (254 in./s). Three nozzle pressures were utilized in the tests, namely, 10.3, 13.2, and 14.8 MPa (1500, 1910, and 2150 psi).

The standoff distance was varied from 1.3 to 6.4 cm (0.5 to 2.5 in.) for the 3.2-mm (1/8 in.) CAVIJET, and from 1.3 to 12.7 cm (0.5 to 5 in.) for the 6.4-mm (1/4 in.) CAVIJET. Over these ranges of standoff, the slot dimensions were constant to within measurable accuracy. Thus, all subsequent tests were run at a standoff of 3.8 cm (1.5 in.) for the 3.2-mm (1/8 in.) nozzle, and 10.8 cm (4.25 in.) for the 6.4-mm (1/4 in.) nozzle. The angle of impingement parameter was varied from 0 deg (perpendicular to the surface of the coal) to 30 deg, in increments of 10 deg. These tests were run with the 3.2-mm (1/8 in.) nozzle, and over this range no measurable differences (see tolerances given in the foregoing) were detected. Thus, all subsequent tests were run at normal incidence to the surface of the coal.

Data Reduction

Before deriving the various performance parameters, it was first necessary to define the variation of slot depth, Z, and slot width, W, with respect to nozzle size, d, nozzle pressure, p, and translation velocity, v. In order to reduce the uncertainty due to the inherent variations in the coal properties and the randomness associated with the statistical processes that cause cavitation erosion, kinematic scaling concepts were used to process the raw data for Z. The raw data were plotted for different nozzle sizes, but at the same pressure, by introducing the variables: nondimensional slot depth, $\bar{Z} = Z/d$, and nondimensional translation velocity, $\bar{v} = v\tau/d$, where τ is the "intrinsic erosion time" for coal, which is assumed to be constant. Thus a large set of data points was used to estimate the average slot depth as a function of translation velocity. A typical nondimensional plot of $\bar{Z}$ versus $\bar{v}$ is presented in Fig. 4. Since the intrinsic erosion time τ is taken to be constant for a particular material, it was arbitrarily set at one second for these analyses. The solid curve in Fig. 4 was faired through the average values of all the data points at each nondimensional velocity. Thus, by this method of pooling the data, the uncertainty in determining the mean value of the slot depth at each translation velocity was reduced. The dependence of mean slot depth, Z, on the jet translation velocity, v, for each nozzle size was then obtained from these nondimensional curves by multiplying each $\bar{Z}$ and $\bar{v}$ by the respective nozzle diameter, d. A typical set of curves derived by this procedure is shown in Fig. 5.

It should be noted that over the range of translation velocities covered in

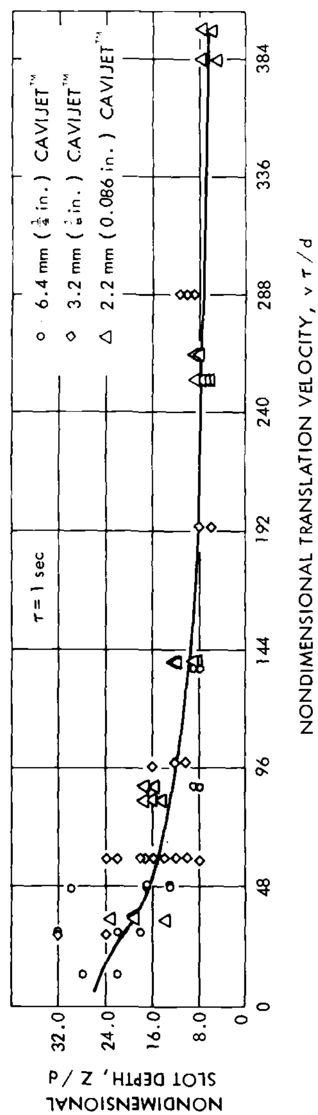

FIG. 4—*Nondimensionalized CAVIJET performance at 13.2 MPa (1910 psi).*

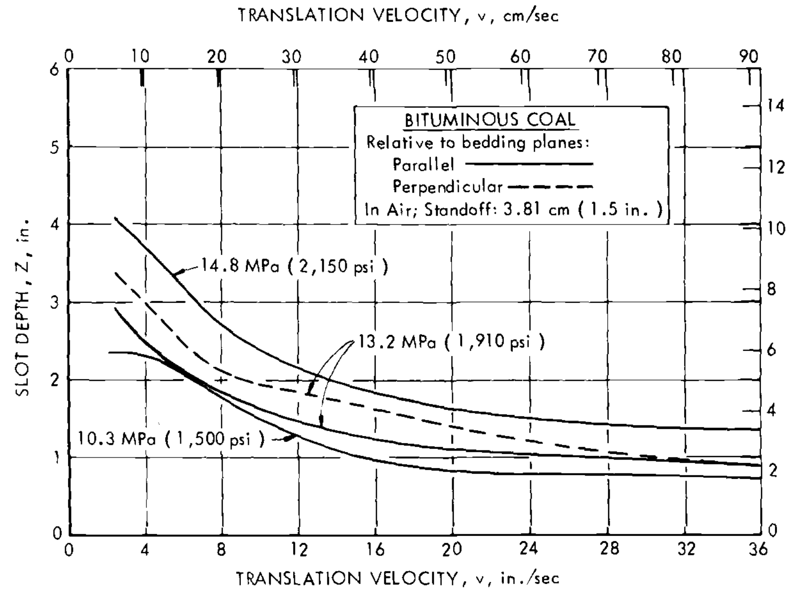

FIG. 5—*Effect of pressure on slot depth; 3.2-mm (1/8 in.) CAVIJET.*

these tests the slot widths were found to be essentially constant. Moreover, the slot width was the same when cutting was done either parallel or perpendicular to the bedding planes. The width of the slot for the 3.2-mm (1/8 in.) jet at 14.8 MPa (2150 psi) was 8.9 mm (0.35 in.), slightly bigger than the 7.9-mm (0.316 in.) width at 13.2 MPa (1910 psi). The width was 16 mm (0.64 in.) for the 6.4-mm (1/4 in.) jet at 13.2 MPa (1910 psi). Hence, in all the derivations of performance parameters, the slot width was a fixed value over the entire velocity range for each test pressure and nozzle size.

Performance Parameters

Typical curves showing the effects of pressure, nozzle size, and translation velocity on volume removal rate are given in Figs. 6 and 7. Results for each nozzle size, showing the effects of the operating parameters on $\dot{V}$ and $\dot{A}$, were obtained [5]. A compilation of some results for volume removal effectiveness, e_v (or specific energy, E_v, which is the inverse of e_v), is shown in Fig. 8. These data indicate that larger nozzles provide larger e_v's, but an inverse dependence on pressure is observed at velocities below 65 cm/s (25 in./s). A similar pressure effect was seen for the kerfing effectiveness, e_a; that is, lower pressures correlate with higher e_a's. However, smaller nozzles were observed to allow higher e_a values (see also Fig. 11).

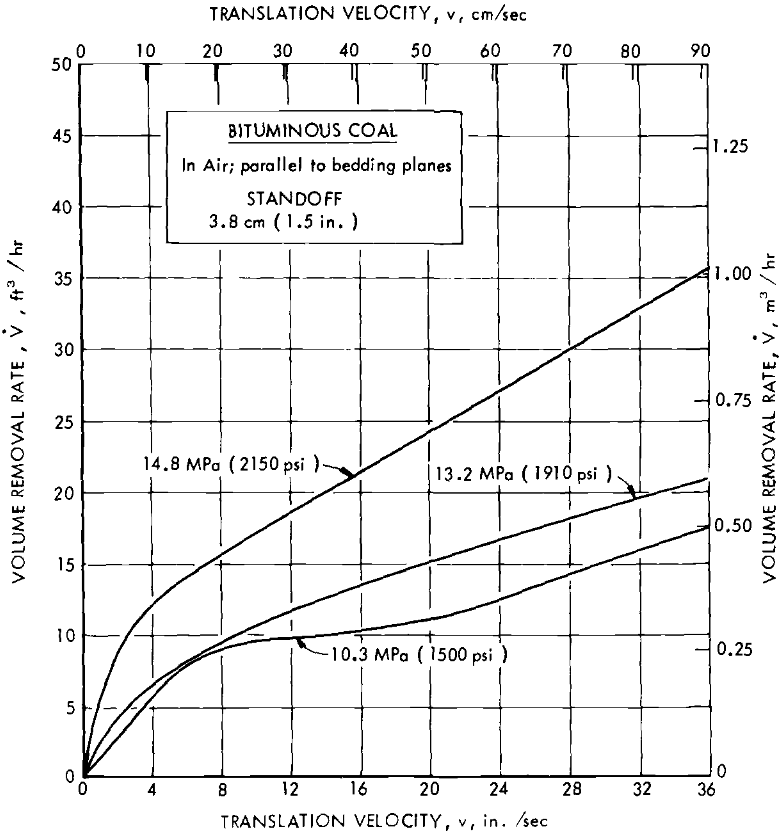

FIG. 6—*Effect of pressure on volume removal rate for 3.2-mm (1/8 in.) CAVIJET.*

Testing with Dual Nozzles

Tests were also conducted with two 3.2-mm (1/8 in.) CAVIJET nozzles "side-by-side," and with one jet following immediately after the other along the same slot. The center-to-center distance between the two jets was varied from 3.18 to 3.81 cm (1.25 to 1.50 in.). Based upon the results of more than 40 tests [*4*] in the side-by-side operation, there exists a strong possibility for consistent removal of the lands between the kerfs, particularly if one or both of the jets are suitably angled inward to provide a cutting action and removal force on the base of the land.

The optimum orientation of two side-by-side 3.2-mm CAVIJETS, at suitable angles and center-to-center spacings, might be expected to produce volume removal rates of 2.8 to 5.7 m^3/h (100 to 200 ft^3/h). Using a density for the Fire Creek coal of 12.9 kN/m^3 (82 lb/ft^3), this extrapolates to a cut-

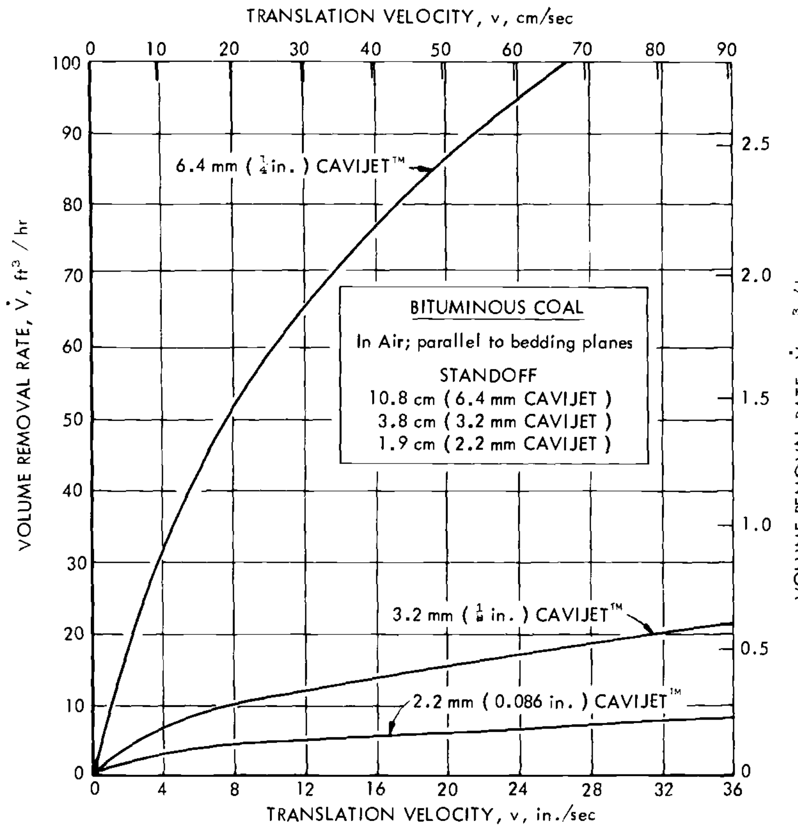

FIG. 7—*Effect of nozzle size on volume removal rate at 13.2 MPa (1910 psi).*

ting rate of 0.6 to 1.2 kN/min (0.07 to 0.13 tons/min), and energy requirements of 0.33 to 0.67 kWh/kN (3 to 6 kWh/ton).

To compare the performance of dual-nozzle cutting with the analogous cutting by a *nonsimultaneous* jet, the results of cutting parallel slots with a single jet, when the land width between the fresh slot and the previous slot was smaller than 3.18 cm, were studied. It was found that the blowout for the land, for side-by-side cutting by a single jet, occurred about 35 percent of the time. This should be compared with the results for simultaneous dual-CAVIJET tests, where blowouts occurred 49 percent of the time over the full velocity range, and even more frequently for lower velocities [6 cm/s (2.36 in./s)]. Thus, these results suggest that there may be an advantage to using dual simultaneous jets for optimizing coal removal rates. These dual-nozzle tests were not extensive, and further tests, preferably on *in situ* coal, should be performed before final conclusions can be drawn.

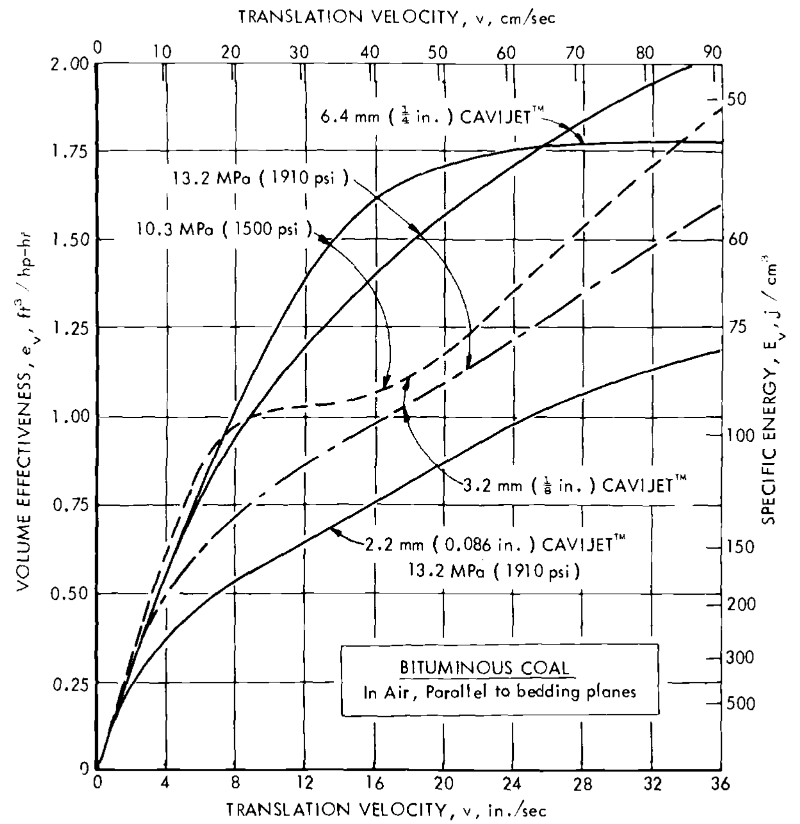

FIG. 8—*Comparisons of volume removal effectiveness: 2.2-mm (0.086 in.), 3.2-mm (1/8 in.), and 6.4-mm (1/4 in.) CAVIJETS.*

In contrast to these simultaneous dual-nozzle, side-by-side tests, the results from simultaneous testing of two 3.2-mm (1/8 in.) CAVIJETS, operated so that one jet followed the other at a distance of 3.18 cm (1.25 in.), do not indicate any advantage over tests with a single jet when the second pass is made at a later time by the same nozzle along the same slot.

Evaluations of Test Results

Coal Cutting Comparisons

In this section the results of the coal-cutting tests with the CAVIJET method, as summarized in the previous section, are compared with similar tests conducted with noncavitating jets. The noncavitating jet data are from two sources: (1) tests run in the HYDRONAUTICS laboratory during the present program, using a nozzle with a 1.78-mm (0.070 in.) orifice diameter at 12.2 MPa (1910 psi), and (2) a recent coal-cutting study by Summers and Mazurkiewicz [*6*], using an 0.80-mm-diameter (0.035 in.) jet at 68.9 MPa (10 000 psi). Although the nozzle geometry was not described in Ref *6*, discussions with the authors indicated it was similar to the so-called Leach and Walker [*7*] configuration we used for the 1.78-mm nozzle, namely, a conical transition with an included angle of 14 deg, followed by a cylindrical exit section with a length equal to 2.6 orifice diameters.

It should be emphasized that the following comparisons between CAVIJET coal cutting and the noncavitating jet studies by Summers and Mazurkiewicz are not on identical coal under identical conditions. These comparisons are made in order to indicate that the CAVIJET method shows the capability, at much lower pressures, of creating similar slot depths, and with lower specific energies. However, any more exact comparisons can only be obtained for tests in the same pieces of coal, and preferably under actual mining conditions.

In Figs. 9 and 10 we have plotted slot depth and rate of area cutting versus translation velocity, respectively, both for the CAVIJETS [6.4 and 3.2 mm

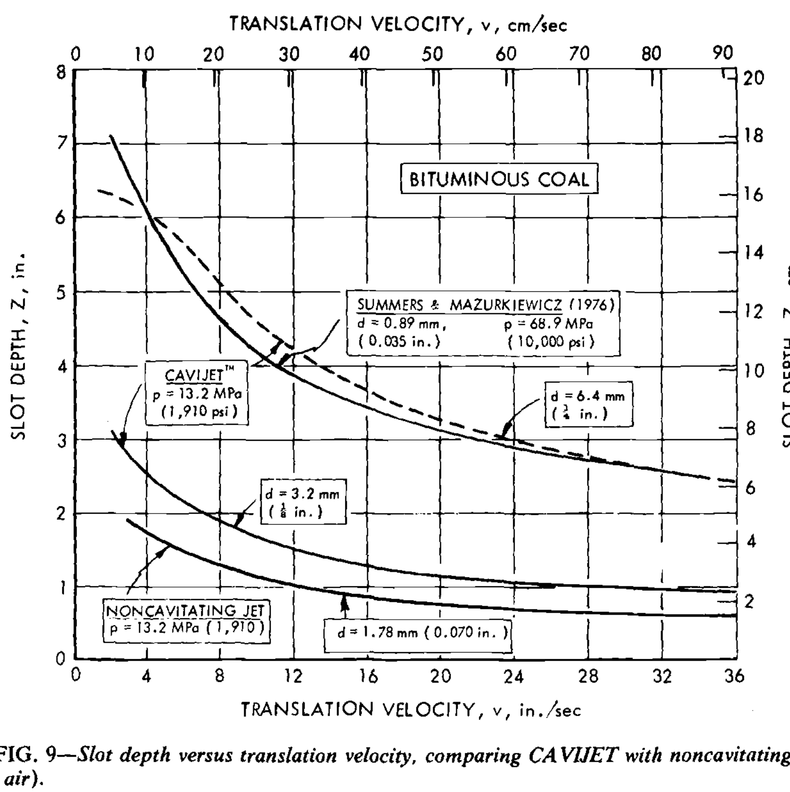

FIG. 9—*Slot depth versus translation velocity, comparing CAVIJET with noncavitating jets (in air).*

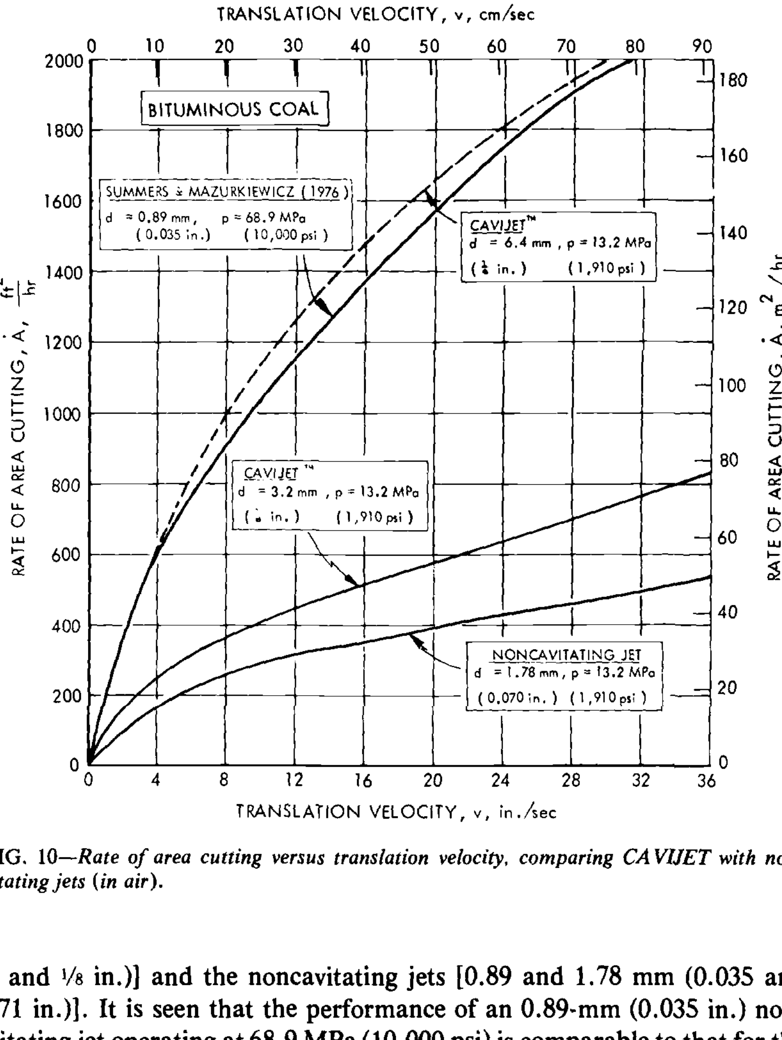

FIG. 10—*Rate of area cutting versus translation velocity, comparing CAVIJET with noncavitating jets (in air).*

(¼ and ⅛ in.)] and the noncavitating jets [0.89 and 1.78 mm (0.035 and 0.071 in.)]. It is seen that the performance of an 0.89-mm (0.035 in.) noncavitating jet operating at 68.9 MPa (10 000 psi) is comparable to that for the 6.4-mm (¼ in.) CAVIJET operating at only 13.2 MPa (1910 psi), which is less than one fifth of the pressure used in the noncavitating jet. The slot depth and area cutting rate by the 1.78-mm (0.071 in.) noncavitating jet are less than those provided by the 3.2-mm (⅛ in.) CAVIJET at the same operating pressure. It should be noted, however, that the flow rate and hydraulic horsepower for the 1.78-mm (0.07 in.) noncavitating jet are only about one half of the corresponding values for the 3.2-mm (⅛ in.) CAVIJET.

The curves for kerfing (or area cutting) effectiveness are plotted in Fig. 11 for the two CAVIJETS and the two noncavitating jets. Here we observe the trend mentioned earlier of smaller-diameter jets providing more area cutting effectiveness. The slot width is not a factor in deriving this particular

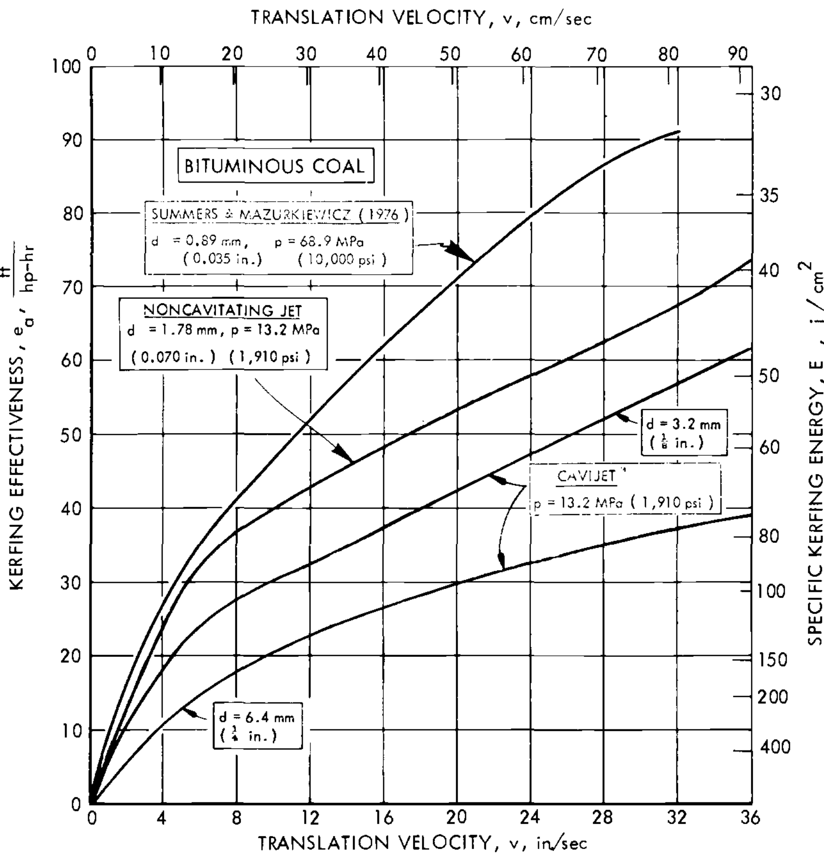

FIG. 11—*Area cutting effectiveness, comparing CAVIJET with noncavitating jets (in air).*

parameter. However, because the slot width was only about 3.5 times the 0.89-mm (0.035 in.) noncavitating nozzle diameter, or about 3.1 mm (0.12 in.) wide, this width was too narrow for subsequent mechanical fracturing. Thus, a dual nozzle was developed [*6*] which, of course, requires twice the power and hence halves the kerfing effectiveness for this noncavitating jet configuration. The slot width for the 1.78-mm (0.071 in.) noncavitating jet was 4.83 mm (0.19 in.), or 2.7 times the nozzle diameter. As cited earlier, this factor is about 2.5 for the CAVIJET nozzles. The curves plotted in Fig. 12 compare the specific energies (or volume removal effectiveness) for the CAVIJETS and the noncavitating jets. It is seen, over this range of velocities, that the CAVIJET is more than twice as effective in volume removal, despite operation at less than one-fifth the pressure used for the 0.89-mm (0.035 in.) noncavitating water jet. The 1.78-mm (0.071 in.) noncavitating jet at 13.2 MPa (1910 psi) produces a more effective volume removal as compared with

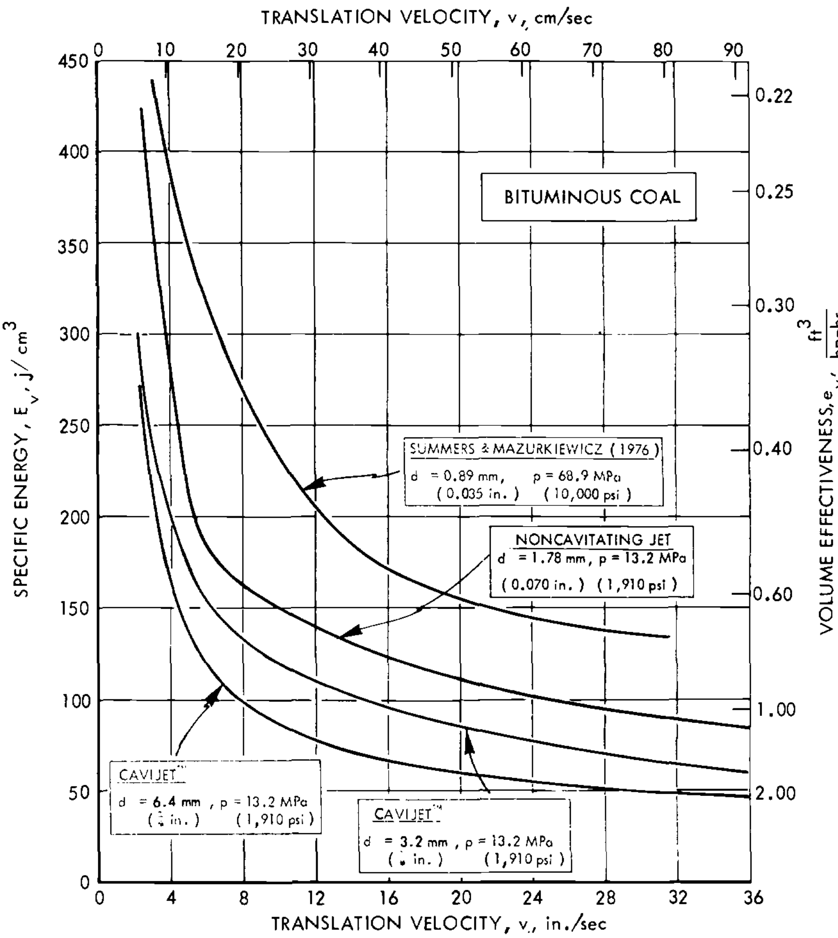

FIG. 12—*Specific energies for coal cutting, comparing CAVIJET with noncavitating jets (in air).*

an 0.89-mm (0.035 in.) jet operating at 68.9 MPa (10 000 psi). These trends seem to be consistent with earlier coal-cutting work by Summers and Peters [*8*].

Coal Removal Comparisons

In a review paper on hydraulic mining, Frank [*9*] summarized a variety of coal mining projects using noncavitating waterjets, at pressures up to 34.5 MPa (5000 psi). The removal rates in these tests ranged from 0.9 to 7.7 kN/min (0.10 to 0.87 tons/min). Although these removal rates are somewhat higher than those mentioned earlier for the slot-plus-land removal by two

3.2-mm (1/8 in.) CAVIJETS, namely, 0.6 to 1.2 kN/min (0.07 to 0.13 ton/min), it should be noted that the overall power, and hence the energy per unit of coal, is considerably lower for these CAVIJET tests. For instance, to achieve the 7.7-kN/min (0.87 tons/min), a pump rated for 34.5 MPa (5000 psi) at 19 litres/s^{-1} (300 gal/min), or 625 kW (875 hp), was used. This removal rate was therefore produced at an energy per unit weight of 1.5 kWh/kN (13.3 kWh/ton) whereas the corresponding values for dual 3.2-mm (1/8 in.) CAVIJETS are 24 kW (32 hp) and 0.33 to 0.67 kWh/kN (3 to 6 kWh/ton).

Conclusions

The following conclusions have been drawn from this investigation:

1. Over the translation velocity range studied:
   Slot depths are scalable by the CAVIJET diameter,
   Effects of standoff are negligible in the range of 4 to 20 nozzle diameters.
   Effects of impingement angle are negligible, from 0 to 30 deg, and
   The performance parameters (rate of area cutting, rate of volume removal, kerfing effectiveness, and volume removal effectiveness) all improve with increasing translation velocity.
2. Kerfing effectiveness varies inversely with CAVIJET diameter.
3. Volume removal effectiveness increases with CAVIJET diameter.
4. In comparison with laboratory tests of small (< 1 mm), high-pressure, noncavitating jets, the CAVIJET:
   Cut slots of comparable depths, with larger widths, using one fifth of the pressure,
   Has smaller kerfing effectiveness, and
   Has larger volume removal effectiveness.
5. In comparison with coal mining tests with large [up to 9.5 mm (0.38 in.)], high-pressure, noncavitating jets, the dual-CAVIJET laboratory tests:
   Produced comparable coal-removal rates with much lower pressure and input power, and
   Required about one-half the energy per unit weight of coal cut.

These conclusions suggest that a CAVIJET-augmented coal-cutting device will be able to operate in a coal mine, with lighter and safer hardware, and still produce effective cutting rates with the same advantages of conventional hydraulic mining machines currently in use. In addition, utilization of lower system pressures should yield an increase in pumping-hardware life and reliability, and allow for a reduction of the energy consumption required to reach any given coal mining objective.

Acknowledgments

The authors are grateful to W. H. Engelmann and Hamilton Reese of the

U. S. Bureau of Mines for their encouragement and cooperation. We also thank Dr. T. R. Sundaram of HYDRONAUTICS, Incorporated for his many valuable suggestions during the course of this work; Dr. G. D. Mehta for assistance in the data reduction; and G. S. Frederick for his careful and dedicated efforts in creating and demolishing those test specimens.

The contents of this paper are based on a research project at HYDRONAUTICS, Incorporated, Laurel, Maryland, sponsored by the U. S. Bureau of Mines, Advanced Coal Mining Technology Program, under USBM Contract No. H0252025, with W. H. Engelmann, Twin Cities Mining Research Center, as the technical project officer.

References

[1] Lohn, P. D. and Frank, J. N., "Airborne Respirable Dust Generated During Cutting of Coal with Water Jets," Twin Cities Mining Research Center, USBM RI 8014, U. S. Bureau of Mines, 1975.

[2] *Proceedings*, Third International Symposium on Jet Cutting Technology, British Hydromechanics Research Association, Fluid Engineering, Chicago, Ill., May 1976.

[3] Conn, A. F., Mehta, G. D., and Sundaram, T. R., "Cavitating Water Jets I. Review and Applications," ASME Cavitation and Polyphase Flow Forum, American Society of Mechanical Engineers, March 1976, pp. 12-15.

[4] Mehta, G. D., Sundaram, T. R. and Conn, A. F., "Cavitating Water Jets II. Basic Principles of Operation," ASME Cavitation and Polyphase Flow Forum, American Society of Mechanical Engineers, March 1976, pp. 16-17.

[5] Conn, A. F. and Rudy, S. Lee, "Parametric Study of Coal Cutting with the CAVIJET™ Cavitating Water Jet Method," Hydronautics, Incorporated Technical Report 7511-1, Laurel, Md., Sept. 1976.

[6] Summers, D. A. and Mazurkiewicz, M., "The Effect of Jet Traverse Velocity on the Cutting of Coal and Jet Structure," *Proceedings*, Third International Symposium on Jet Cutting Technology, Paper D5, British Hydromechanics Research Association, Fluid Engineering, Chicago, Ill., May 1976.

[7] Leach, S. J. and Walker, G. L., *Philosophical Transactions of the Royal Society*, London, Vol. 260, 1966, pp. 295-308.

[8] Summers, D. A. and Peters, J. F., "Preliminary Experimentation on Coal Cutting in the Pressure Range 35 to 200 MN/m^2," *Proceedings*, Second International Symposium on Jet Cutting Technology, Paper H2, British Hydromechanics Research Association, Fluid Engineering, Cambridge, England, April 1974.

[9] Frank, J. N. in *Proceedings*, 34th Annual Mining Symposium, Annual Meeting of the American Institute of Mining Engineers and the University of Minnesota, Duluth, Minn. Jan. 1973, pp. 129-142.

[10] Busch, J. W., "Hydraulic Mining of Anthracite: Engineering Development Studies," BuMines Report of Investigation 6610, U. S. Bureau of Mines, 1964.

DISCUSSION

D. A. Summers[1] (*written discussion*)—One of the controversial problems which crops up with the use of cavitating jets is the comparison of like with like. This is, I am afraid, true again here since in the comparison of Dr. Conn's results with those we got at University of Missouri-Rolla, we are not comparing equivalent items. In a paper we gave in 1974 [*8*] we indicated the benefits of increasing nozzle diameter as opposed to increasing jet pressure for obtaining more effective cutting at higher horsepower. (To put it crudely, if you double the jet energy by increasing pressure, you approximately double the material removed; if you double the energy by increasing the diameter, you quadruple the material removed). However, under the constraints of a system to fit into an existing underground operation with perhaps water-sensitive material in the vicinity, we imposed an upper limit of 3 litres/s^{-1} (50 gal/min) through the system or perhaps 0.31 litres/s^{-1} (5 gal/min) per orifice. Thus, while a comparison with our data can be made, it should be understood that at lower pressures and higher flow rates such as those used by Dr. Conn, the specific energy of jet cutting without cavitation would be at equivalent or possibly lower levels.

A. F. Conn and S. L. Rudy (*authors' closure*)—We appreciate the observations of Dr. Summers, which emphasize the importance of making "apples-to-apples" comparisons. We are well aware of the flow limitations inherent to his specific application, namely, the "Hydrominer," and did not intend in our comparisons to imply that this was the best specific energy which he could produce. As stated in our paper, however, the objectives of this CAVIJET study were much broader; that is, we were not limited to a particular mining device. This program required us to examine the feasibility and effectiveness of using much lower pump pressures plus cavitation phenomena to cut coal. We succeeded in reaching these objectives, and the comparisons made with Dr. Summers' earlier work serve only as an example of the results of our investigation.

[1] University of Missouri-Rolla, Rolla, Mo.

J. A. Hilaris[1] *and T. J. Labus*[2]

Marine Applications of High-Pressure Waterjets

REFERENCE: Hilaris, J. A. and Labus, T. J., "**Marine Applications of High-Pressure Waterjets,**" *Erosion: Prevention and Useful Applications, ASTM STP 664,* W. F. Adler, Ed., American Society for Testing and Materials, 1979, pp. 582-596.

ABSTRACT: High-pressure waterjets were investigated for hull cleaning, metal cutting, and concrete weight coating removal from submarine pipelines. All testing was performed in the submerged condition and a selective material removal capability was observed for the hull cleaning operation. This selective material removal capability was a sensitive function of jet pressure and jet angle at fixed cleaning rates. Results for the metal cutting indicated that positive jet angles and low concentrations of polymers could increase depth of cut significantly. Projected concrete weight coating removal rates were five times that achieved by conventional methods.

KEY WORDS: jet cutting, hull cleaning, metal cutting, underwater cutting operations, high-pressure waterjets, erosion

Offshore construction activities have increased dramatically as the energy industry continues to develop various ocean resources. This activity has defined the need for improved underwater construction tools and techniques to increase the efficiency of the working diver, and where possible introduce automation for cost reduction. Waterjets hold the potential for achieving these goals over a broad range of marine activities. Currently, waterjets are used for ship hull cleaning in drydock operation [*1*],[3] offshore rig structural cleaning, cable trenching operations, and heat-exchanger descaling. This investigation deals with underwater ship hull cleaning, metal cutting, and the removal of concrete weight coatings from submarine pipelines.

The hull cleaning studies were aimed at establishing the proper jet parameter combinations that would allow the removal of marine fouling from metal surfaces having an antifouling coating, without damaging this coating.

[1]Associate research engineer, IIT Research Institute, Chicago, Ill. 60616.
[2]Engineering consultant, SCIRE Corporation, Downers Grove, Ill. 60515.
[3]The italic numbers in brackets refer to the list of references appended to this paper.

A basic investigation of underwater metal cutting by waterjet was undertaken to establish performance levels for this method. The influence of nozzle size, jet pressure, cutting rate, jet angle, abrasive injection, and fluid additives was evaluated with the goal of increasing the cutting rate for a given power input. Abrasives were evaluated both in the submerged and ambient condition to establish the influence of the water environment.

Concrete weight coating removal studies were aimed at establishing the performance of the jet as compared with conventional methods, and to determine if a nonpenetrating nozzle could be used to achieve complete coating penetration. This process and the hull cleaning operation can be automated to greatly enhance the diver's work efficiency for a given bottom time.

Experimental Operations

The underwater testing for the cleaning and metal cutting studies was performed in the test tank shown in Fig. 1. A specimen carriage is mounted in the bottom of the tank and driven through a timing belt arrangement by a hydraulic cylinder. Limit switches were provided at the extreme points in the travel to provide automatic reversing of the carriage. The nozzle was mounted on a rigid bar with standoff distance maintained at 12.69 mm throughout the test programs. For the cleaning studies, two groups of test specimens were utilized: (1) plain steel specimens and (2) steel specimens

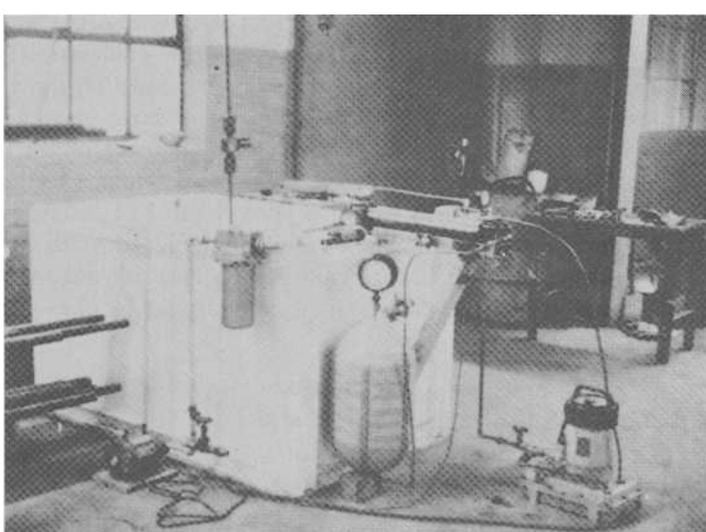

FIG. 1—*Underwater test tank.*

with an antifouling paint coating. An accumulator system was used for the cleaning studies. A 82.7-MPa pump was used to charge a large-volume accumulator to the appropriate test pressure. The accumulator was then discharged through a lance containing the cleaning nozzle, producing a high-pressure jet.

The main high-pressure laboratory intensifier was employed for the metal cutting and concrete weight removal studies. This unit is a gas-backed linear intensifier capable of 1379-MPa bars pressure and power outputs in excess of 447 kW. A detailed description of this unit is given in Ref *2*.

Cleaning Test Results

The initial criteria established for evaluating the results of the cleaning tests were mass loss and damage caused to antifouling coating for specified test conditions. Areal exposure rates which relate to cleaning applications were not determined. Figure 2 shows the effects of jet pressure and jet angle on the mass loss for both coated and uncoated specimens (that is, with and without antifouling paint). Test pressures ranged from 51.7 to 65.5 MPa and jet angles from 0 (normal impact) to a positive 45 deg. Figure 3 shows a similar plot but with cleaning rate as the major independent variable. The uncoated specimens show the highest weight loss because the fouling, in general, was much greater on these specimens. The fouling was generated by exposing the specimens in a marine environment at the Naval Coastal Systems Laboratory in Panama City, Florida. Much of the scatter in the data for the uncoated specimens was due to nonuniform fouling distribution. The coated specimens were prepared using the standard anti-fouling paint and standard application procedures. The marine fouling consisted of barnacles and other marine growth. As shown on these plots, increased mass loss occurred with increasing jet pressure, cleaning rate, and shallow jet angles. This must be qualified in the case of the coated specimens, since jet angles less than 45 deg produced damage to the anti-fouling paint undercoat. Figures 4 and 5 show typical coated specimens cleaned by a waterjet. Figure 4 shows a specimen damaged by the waterjet when the jet angle was less than 45 deg, while Fig. 5 shows a cleaned specimen without damage to the undercoating. The test conditions for the specimens shown in Figs. 4 and 5 were

jet pressure: 65.5 MPa
nozzle diameter: 0.4 mm
cleaning rate: 30.5 cm/s
jet angles: 0 and 45 deg, respectively

The initial testing was performed with circular nozzles, but a rectangular slit nozzle was also tested. The rectangular nozzle had an opening of 1.52 by 0.25 mm with an initial entry angle of 13 deg and exit angle of 0 deg.

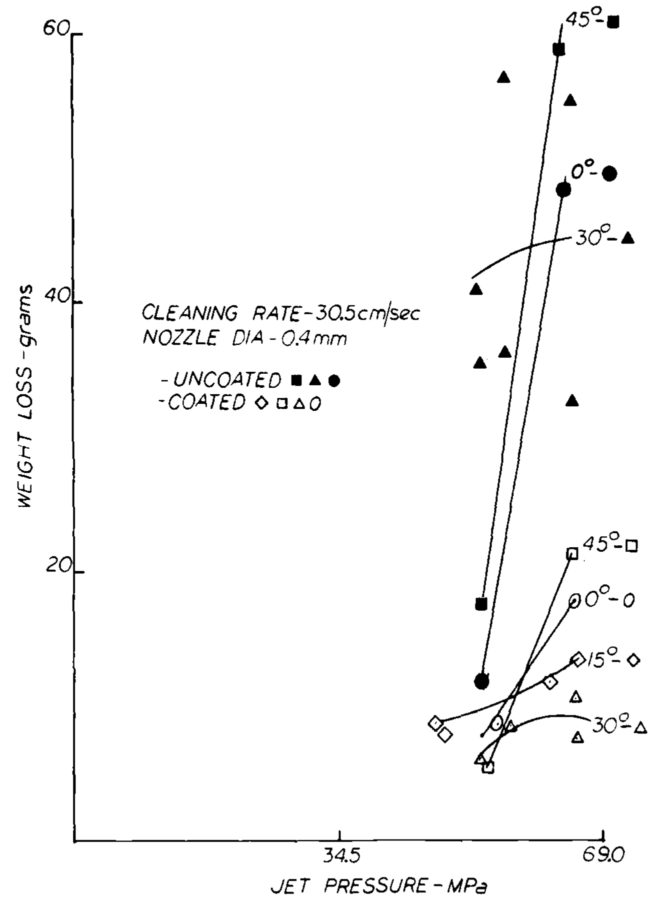

FIG. 2—*Weight loss versus jet pressure for coated and uncoated specimens at various jet angles.*

Testing was performed with the long dimension parallel and perpendicular to the direction of cleaning. This alternative design produced a 275 percent increase in mass loss as compared with the circular nozzles, but both designs had equivalent specific energies. This increase occurred regardless of the nozzle orientation since the jet was oscillated while it was moved across the fouled surface. Thus, both nozzles are approximately equal in mass removal efficiency at equivalent operating conditions, and the judgment on which nozzle to use will be based on other considerations such as cost, wear, thrust, areal exposure rate, and exposure rate/kilowatt-hour of energy input.

From the foregoing results, the operating conditions of a cleaning system should be at a rapid cleaning rate, a low jet angle, and an operating pressure

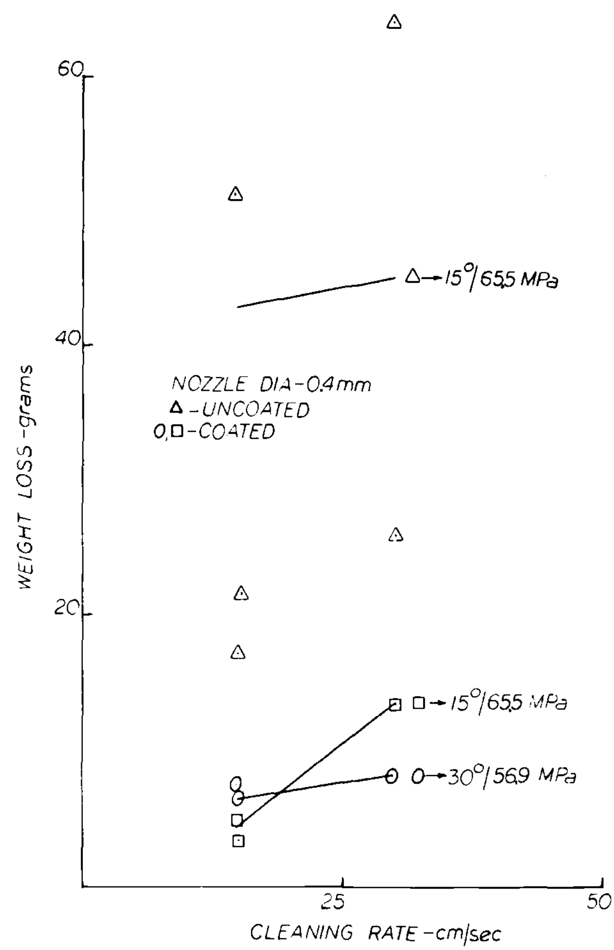

FIG. 3—*Weight loss versus cleaning rate for coated and uncoated specimens for various jet angles and pressures.*

consistent with power availability and the requirements for fouling removal. These conditions must be modified when cleaning hulls with anti-fouling paint, in that the jet angle should not be below 30 to 45 deg to insure consistent removal of the marine growth without causing damage to the antifouling undercoat. By keeping the antifouling undercoat intact, the benefits of low power consumption due to reduced fouling of the ship hull could be realized without the need for a repainting of the hull.

Metal Cutting Studies

In a second experimental study, the influence of the various jet parameters

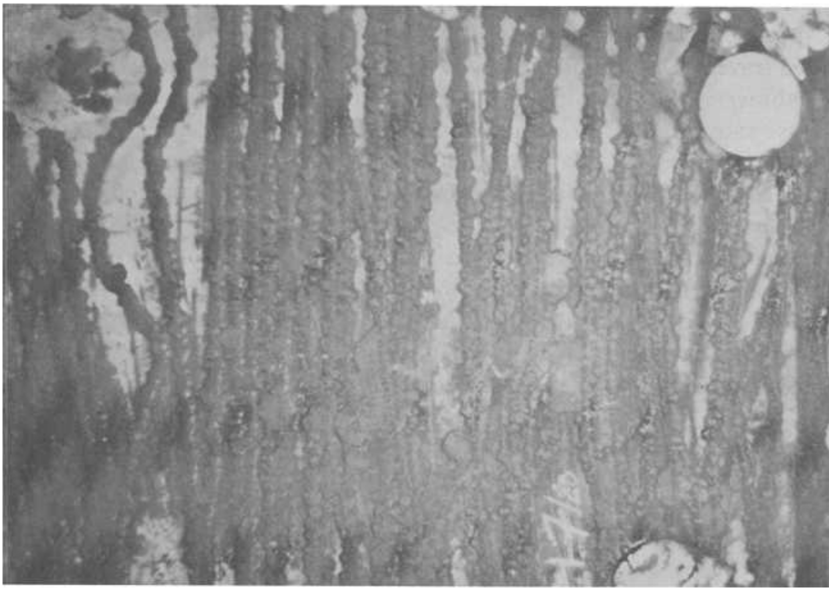

FIG. 4—*Coated specimen damaged by waterjet.*

FIG. 5—*Coated specimen cleaned and undamaged by waterjet.*

on underwater cutting of steel was investigated. Initial testing was performed on specimens of 1020 steel (σy = 552 MPa). The parameters varied included traverse rate, jet pressure, nozzle diameter, jet angle, fluid properties, and abrasive injection. Figure 6 shows the variation in penetration with traverse rate for 1020 steel specimens. The trends of the curves are similar to those observed for other materials. Using these results, the cutting rate was fixed at 0.635 cm/s and the effects of jet angle investigated. Figure 7 shows the variation in h/d (h is the penetration and d the nozzle diameter) with jet angle. All jet angles are positive (that is, the jet velocity component parallel to the cutting surface is in the same direction as the motion of the nozzle). There is a 23 and 27 percent increase in penetration over the normal impact condition for the 0.4- and 0.5-mm curves, respectively. For both nozzles the optimum jet angle was approximately 15 deg, hence

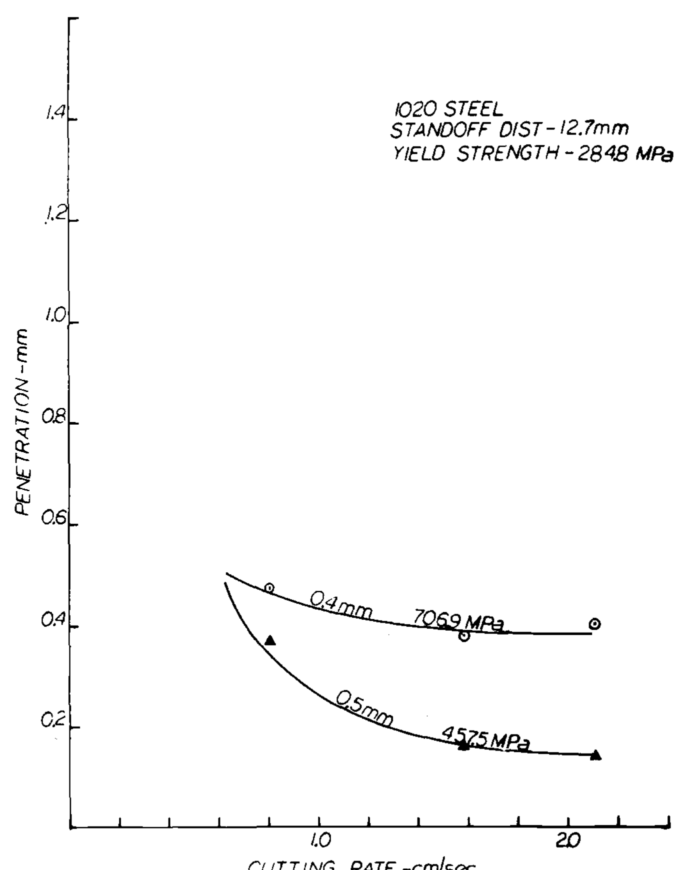

FIG. 6—*Penetration versus cutting rate for 1020 steel at various nozzle diameters and jet pressures.*

for the remainder of the testing on HY80 this jet angle would be used. Prior to beginning testing on the HY80, the effects of fluid additives and abrasive injection were also evaluated.

Figure 8 shows the effect of abrasive particles contained in the jet on the total penetration achieved. From this plot it could be inferred that the abrasives are only potentially beneficial at elevated pressures, but the method of injection plays an important role. For the data in Fig. 8, a layer of the particular abrasive (0.32 cm thick for fiber glass and 1.27 cm thick for transite) was placed directly over the metal surface through which the jet passed before impacting the target. Thus, there was a relatively short distance in which the particles could be accelerated before impact, and, at the slow cutting rates used, the concentration of particles would not be very great. This injection method would be similar to using an abrasive-

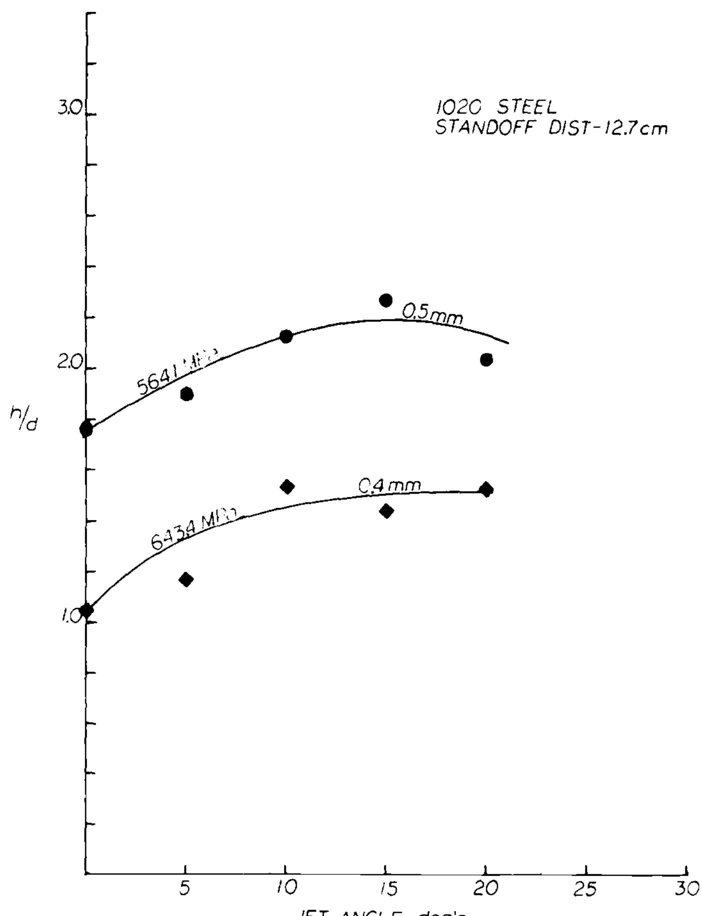

FIG. 7—h/d *versus jet angle for 1020 steel.*

ladened tape on the surface of the metal along the cut path. The effects of standoff distance, which is a significant parameter in metal cutting, and abrasive effectiveness are illustrated in Fig. 9. For the current investigation, d/s (s is the standoff distance) lies in the range of 0.032 to 0.39, which is at the low end of the curve. All of the curves shown are for water only, except the water-sand curve, which illustrates the effect of sand particles (nominally 0.25 in mm size, rounded profile) injected into the jet stream at the exit of the nozzle, as opposed to cutting through a sacrificial material directly at the surface. Using the nozzle method of injection, the abrasive jet outperformed the water-only jet by 25 percent. This change was obtained at an increase of the power requirements by 0.13 percent. The data in Fig. 9 are for testing in air, hence they must be qualified for submerged operation. But past experience has shown that the trends are generally not altered substantially, hence the conclusions drawn should still be valid.

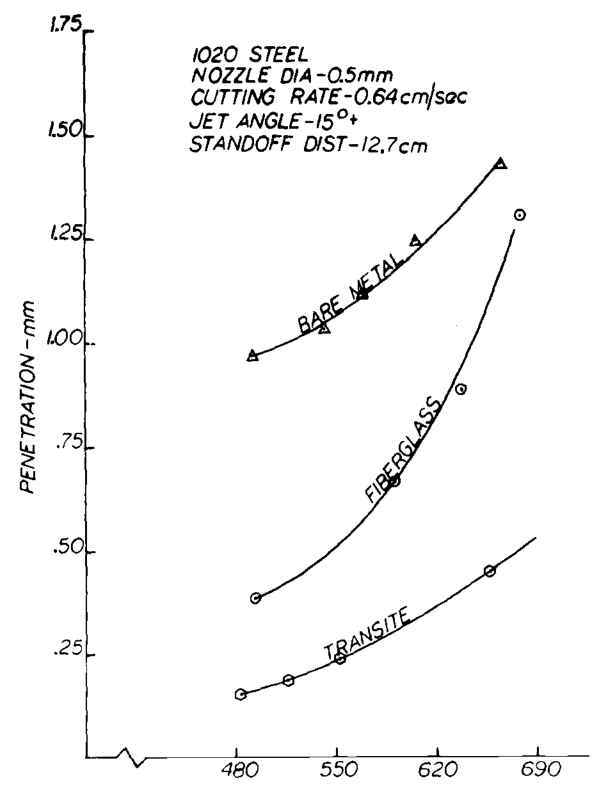

FIG. 8—*Penetration versus jet pressure for 1020 steel and various abrasives.*

Fluid additives have been investigated previously for other materials and have been found to contribute to the cutting capabilities of the jet. Figure 10 shows the effect of various concentrations of additive BX-254 (NALCO Chemical Co.) on the penetration. Similar tests were run on the 0.5-mm nozzle with similar results, but not as large as for the 0.4-mm nozzle. This decrease in additive effect with increasing nozzle size has been observed by other investigators [*3*].

Combining all these results together, a series of tests was performed on HY80 using various combinations of these best parameters. Figure 11 shows the results for the HY80 test specimens. As previously indicated, the additive augmented jet at a jet angle of 15 deg should give the best results, which Fig. 11 verifies. Note also that the abrasive jet does not enhance the cutting for HY80. This may be caused by the change in material properties of the HY80 versus the 1020 steel. (The abrasive was not changed.)

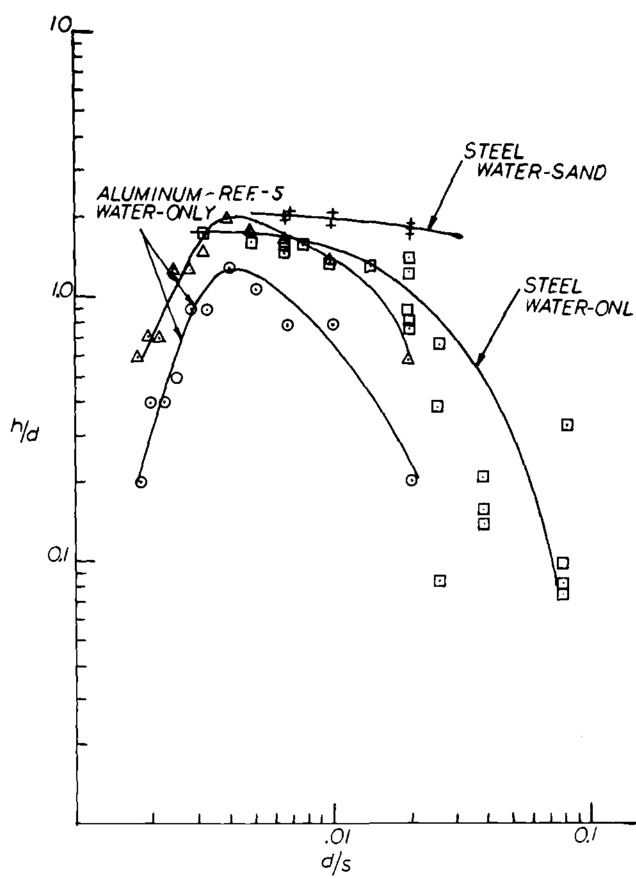

FIG. 9—h/d *versus* d/s *for steel and aluminum.*

The combined additive-abrasive jet was the least successful, indicating that these two augmentation techniques are not mutually beneficial under the stated operating conditions.

Concrete Weight Coating Removal Studies

Maintenance and construction of submarine pipelines present some unique problems due to the hostile work environment. Conventional methods of removal of concrete weight coatings are time-consuming, costly, and can cause physical damage to the pipelines. Jet cutting systems may provide a more cost-effective method of attacking these coatings. Figure 12 shows the required number of passes to achieve a full-depth cut (that is, to the surface of the steel pipe) for two typical concrete weight coatings. Coating No. 1 was a relatively weak concrete with a chicken wire reinforcing used.

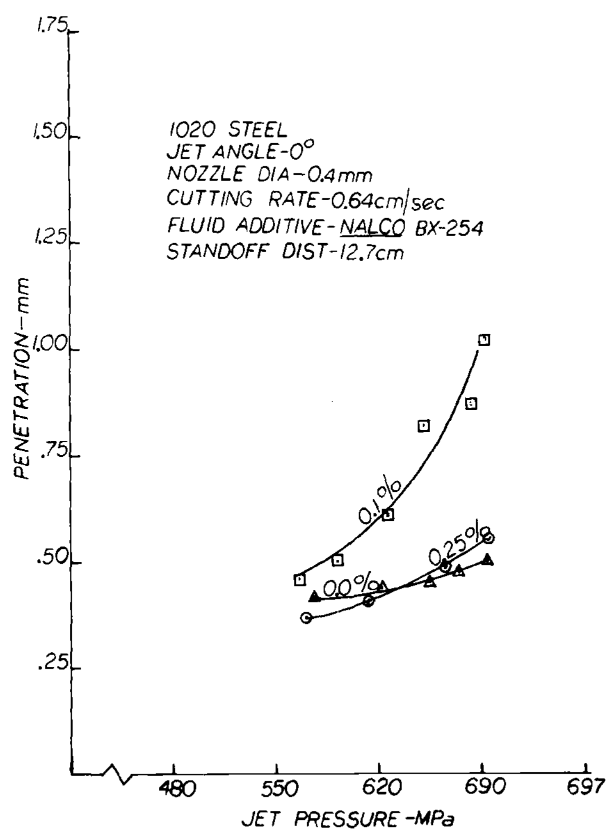

FIG. 10—*Penetration versus jet pressure for 1020 steel and various jet augumentation combinations.*

The almost uniform depth of cut per pass reflects this condition. Coating No. 2 was higher-strength concrete with 0.54-cm steel reinforcing rods. Note that the 0.5-mm nozzle takes one less pass to achieve full penetration, but requires 3.3 times the power of the 0.4-mm curve. Although more power is required by the larger nozzle, it may still be more cost-effective since the economics of this particular application are dictated by labor costs and overall time requirements. If an automated approach is taken, then the smaller nozzle diameter system would be the most cost-effective, since only the cycle-time would influence the operational costs significantly. Capital costs would also be less for the small system if a full 100 percent duty cycle were utilized. The performance curve shown in Fig. 12 is for a nonpenetrating nozzle (that is, a nozzle remaining outside the kerf, as opposed to a penetrating type, which follows into the kerf).

A bottom-operated system would provide the greatest flexibility of operation, but space and weight restrictions would most probably limit it to a duty-cycle type of operation. The intensification would take place on the

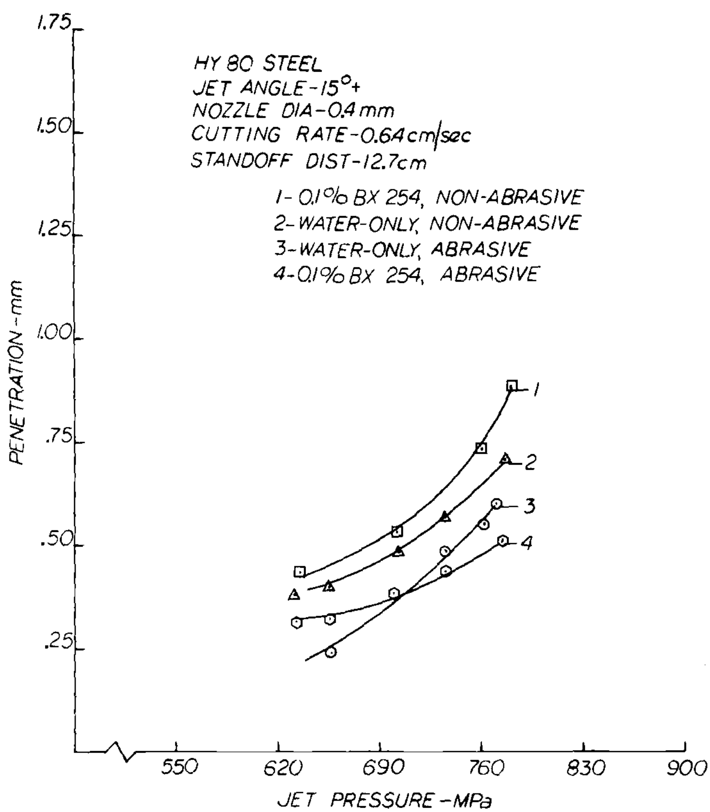

FIG. 11—*Penetration versus jet pressure for HY80.*

bottom with the high pressure transmitted to the work station via rigid tubing and swivel joint connections. The power source could be surface or bottom mounted. For buried or partially buried pipelines a manually operated low-pressure system could be used to remove the backfill from around the pipe prior to attaching the automated system to the pipe.

From the data in Fig. 12 the average exposure rate is 25.4 cm^2/s (Coating No. 1); thus for the particular pipe tested (that is, outside diameter = 0.78 m with a 12.7-cm concrete/asphalt coating) a cutting time of 567 s per linear metre at continuous operating pressure is anticipated. The geometry of the cut is shown in Fig. 13. For a duty-cycle operation, the cutting time is given in Table 1 for various power levels. For a 2.43-m-long section of pipe, and working at an average power level of 22.4 kW, 177 min (2.95 h)

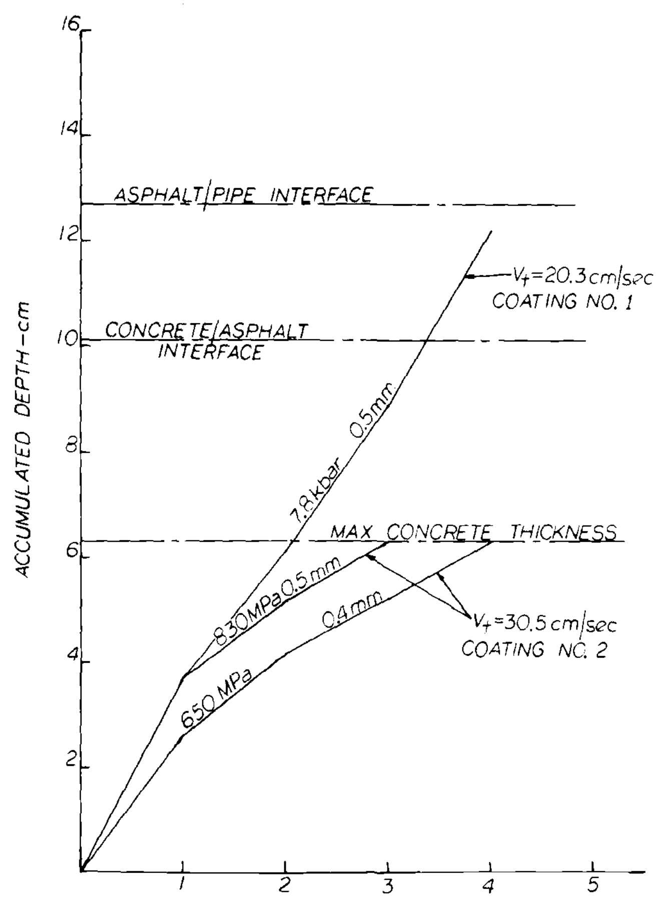

FIG. 12—*Accumulated depth versus number of passes for concrete weight coatings.*

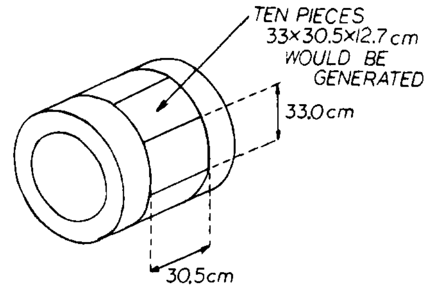

FIG. 13—*Concrete weight coating cut geometry.*

TABLE 1—*Power requirements/cutting time summary for different duty cycles.*

Average Power, kW	Duty Cycle, %	Cutting Time per 30.5 cm Length, s
176	100	173
112	63	274
75	42	412
37	21	823
22	13	1330
15	8	2162

would be required to cut the length into 33 by 30.5 by 12.7-cm blocks. The actual cutting time would be slightly longer since the jet would dwell at the intersection of the reinforcing bars to enlarge this area to create a tool access for cutting the bars. This projected cutting time compares favorably with the reported 16 h [*4*] for the same conditions using mechanical saws and chipping hammers.

One additional point is worthy of note, and that concerns the safety of this approach with respect to potential damage to the pipeline. Referring to Fig. 6, the cutting rate for steel is in the range of 0.64 to 1.29 cm/s and for the weight coatings 20.3 cm/s. This wide difference in cutting rate precludes any damage to the pipeline since the cutting of steel, even at elevated pressures, is restricted to slow cutting rates. At high cutting rates, the dwell time of the jet is insufficient to cause penetration. Thus the jet cutting system is inherently safe and allows complete material removal down to the surface of the pipeline.

Conclusions

The use of waterjets for submerged cleaning of ship hulls and other structures has been clearly demonstrated. Integration of the jet systems with an automated traversing system should produce a viable technique for cost-effective cleaning of submerged structures. A selective removal capability has also been demonstrated, which is not currently available in present mechanical systems. Jet angle and pressure have been shown to be significant parameters in controlling the removal of marine growth without damaging the antifouling undercoating.

Results from the metal cutting studies are inconclusive to determine its commercial application, but the test data indicate that the process would be limited to thin sections. Also, positive jet angles and fluid additives increased penetration, while abrasive injection using a sacrificial material at the surface of the metal did not enhance penetration. In its present state, the continuous jet is not competitive with conventional techniques on an economic basis, but may be justified if an explosive environment exists where conventional techniques cannot be utilized safely.

A significant reduction in process time was established for stripping of weight coatings from submarine pipelines by using waterjets. The safety of the system should be also much greater due to the mutually exclusive cutting regimes for each material. Full penetration of the coating could be achieved using a nonpenetrating nozzle, which can simplify the operation considerably. The economics of the system are yet to be established, but at this point are worthy of serious consideration.

Acknowledgment

This work was partially supported by the Naval Training Equipment Center. Mr. R. E. Elliott of the Naval Coastal Systems Laboratory acted as program monitor and provided valuable input.

References

[*1*] Pardey, P. H., "Notes On Marine Applications of Jet Cutting," *Proceedings*, First International Symposium on Jet Cutting Technology, Paper No. D2, British Hydromechanics Research Association, Fluid Engineering, Coventry, England, 5-7 April 1972.

[*2*] Labus, T. J. and Hilaris, J. A., "An Experimental Investigation of an Underwater High Pressure Water Jet Metal Cutting Tool," for Naval Training Equipment Center, IITRI Report No. D6103, Illinois Institute of Technology, Jan. 1976.

[*3*] Savanick, G. A., Ricketts, T. E., Lohn, P. D., and Frank, J. N., Bureau of Mines Report of Investigations No. 8095, 1975.

[*4*] Guardiano, A., personal communication, Taylor Diving and Salvage Co., 1975.

[*5*] Franz, N. C., "The Influence of Standoff Distance on Cutting with High Velocity Fluid Jets," *Proceedings*, Second International Symposium on Jet Cutting Technology, Paper No. B3, Bristish Hydromechanics Research Association, Fluid Engineering, Cambridge, England, 2-4 April 1974.

F. A. Huszarik,[1] *J. M. Reichman,*[2] *and J. B. Cheung*[2]

Use of High-Pressure Waterjets in Utility Industry Applications

REFERENCE: Huszarik, F. A., Reichman, J. M., and Cheung, J. B., "**Use of High-Pressure Waterjets in Utility Industry Applications,**" *Erosion: Prevention and Useful Applications, ASTM STP 664,* W. F. Adler, Ed., American Society for Testing and Materials, 1979, pp. 597-615.

ABSTRACT: During the past several years, waterjets with pressures up to 408 MPa have become a reliable tool for industry and have been used for a variety of factory applications. In addition, waterjets have been tested for rock cutting in mining and tunnel applications. The utility industries do a considerable amount of work that requires excavation in rock and concrete. The potential of using high-pressure waterjets to meet their field needs has been considered. To date, the telephone, electrical power, and gas industries have conducted studies on the use of high-pressure waterjets. This paper contains descriptions of the various applications of waterjets in the utility industry, descriptions of the appropriate equipment and cutting techniques, discussions of some possible systems and their operating parameters, and an economic analysis of waterjet methods for trenching and pole-hole drilling.

A study was conducted to examine the use of waterjets in utility industry applications. The study was a three-phase program. In the first phase, the possible applications and their significance to utility company operations were examined. In the second phase, a strategy for cutting rock and concrete with waterjets as well as a conceptual system design was developed. Various rock types were tested, and rates were predicted for two specific applications: trenching and pole-hole drilling. In the third phase an economic analysis of the cost of using waterjet methods for trenching and pole-hole drilling was performed and costs were compared with current methods on a per-hole or per-foot of trench basis. In addition, the advantages and disadvantages of waterjet methods on a system basis were compared with those of existing methods.

The study has demonstrated that there is a wide variety of applications for high-pressure waterjets in the utility industry. The study further shows that waterjet devices are both technically and economically feasible. The predicted rates and the costs indicate that, in rock, the waterjet system is better than current methods.

A detailed overview of this study as well as the results are presented in this paper.

KEY WORDS: high-pressure waterjets, utility applications, trenching, pole-hole drilling, deep-kerfing, hard rock, erosion

[1]Manager, Construction Methods, Bell-Northern Research, Ottawa, Canada KIY 4H7.
[2]Senior research scientist, Flow Industries, Inc., Kent, Wash. 98031.

Background

In North America, utilities such as power, telephone, water and sewer, gas, and more recently cable television deal with at least one common element in the construction of their distribution systems: the ground. Depending on the location, the ground can provide the ideal medium for cost-effectively constructing distribution systems, or it can be the major cause of high construction costs and inefficiency.

In order to fully appreciate the impact of ground conditions on utility construction, it is important to become aware of two basic facts. First, in recent years public and political pressure in both the United States and Canada has forced the power and communications utilities to construct more and more of their distribution systems below ground as opposed to aerial. This policy of "out-of-sight" distribution systems has had a major impact on both construction and maintenance costs, especially in areas where the ground is predominantly rock.

Secondly, from a geological point of view, only about one third of the populated areas of Canada and the United States can be considered to be good burying areas. These areas consist generally of the Canadian Prairies and the Midwestern and Southeastern parts of the United States. The rest of the continent is either bare rock or a mixture of rock and soil in various proportions. An example of the impact of these ground conditions on below-ground telephone cable installation costs is found by comparing cable installation costs in the Canadian Prairies with those in Eastern Canada. In the Canadian Prairies, cable can be installed by plowing at a cost of approximately 66 to 164 cents per metre. The cost of installing the same cable in the eastern part of Canada, where the ground is predominantly hard rock, can be as high as 49.2 dollars per metre.

These two prime considerations have forced utilities to reevaluate the construction methods which have traditionally been used to construct below-ground distribution systems. Obviously, cheaper and faster installation methods for poor ground conditions such as bouldery soil, hardpan, soft, and hard rock are essential requirements for reducing utility construction costs. High-pressure waterjetting, as applied to cutting rock for various utility construction applications, is one technology which may result in new space-age construction tools capable of meeting these requirements.

Waterjetting: Utility Construction Applications

Based on the present and predicted future capabilities of waterjets, several aspects of utility construction appear to qualify as potential users of this technology. A number of these, together with a system concept, are described in the following. It should be remembered that none of the tools described herein have yet been developed. Therefore, it is difficult to ascertain the specific operational characteristics of each concept at this time.

Drilling Pole-Holes in Bedrock—A rotating nozzle head or waterjet-mechanical cutter, using one or more nozzles, could be used to cut a circular slot in bedrock to any diameter. The remaining rock cylinder would be mechanically fractured and removed, leaving a hole slightly larger than the pole diameter. The space around the pole could be efficiently backfilled with an expanding semiridged urethane foam.

Drilling Guy Rod Anchor Holes—The drilling device used for this application would probably be similar to the pole-hole cutting equipment just described. Most anchor holes need be only 5.08 cm (2 in.) in diameter and 45.72 cm (18 in.) deep. A hybrid system, combining waterjets with a mechanical cutter, would significantly increase penetration rates compared with standard drilling devices.

Frozen Soil Excavation—In most of Canada and the Northern United States, the extension of construction activities into the winter months is always a primary objective. To meet this objective, a waterjet system combined with a conventional frost saw or blade may be feasible. This type of hybrid system would not only increase the cutting speed, but also reduce both wear and general maintenance costs. Furthermore, this type of cutting operation would result in fewer cleanup problems.

Rock Trenching—A hybrid waterjet-mechanical cutter or rotating nozzle head system could be used for this application. The hybrid cutter would consist of a rolling-disk cutter assisted by waterjets located ahead of the cutting edges. The jets would cut narrow slots into the rock face, allowing the disk cutter to easily break to the unconfined rock kerfs. A mucking system incorporated into the unit would remove the fractured rock particles from the trench. Alternatively, a rotating nozzle head (or heads) could cut 1.27- to 2.54-cm (½ to 1 in.)-wide parallel slots into the rock surface to a depth which would allow a loaded wheel to break the remaining rock ridges between the slots. After removing the broken rock, the process would be repeated until the desired depth is achieved.

Road Crossings—Two alternatives appear feasible. The first method requires the waterjet to "slice" the concrete or asphalt into pieces, which are then removed by hand. A mechanical trencher or backhoe is then used to excavate the base material to the required depth. As with normal road crossings, only one lane at a time need be closed to traffic.

The second method would necessitate the digging of a pit if existing ditches were not deep enough or ditches were not present at all. If the road bed material was well compacted, the waterjet would be able to cut without fear of the hole collapsing. In the case of loose material, a pipe could be pushed behind the waterjets as it advanced.

Ice Cutting to Access and Install Submarine Cable—A low-pressure waterjet unit 69 to 138 MPa (10 000 to 20 000 psi) with a hand-held nozzle head could be used to cut through ice buildups on rivers and lakes. This technique would be faster as well as less tedious than cutting with chain saws.

Concrete Cutting—Present research has shown that waterjets can be used effectively to clean and cut concrete surfaces. The jet erodes away the cement and fine aggregate content of the concrete, without cutting through the larger aggregate. The large aggregate can be cut, but the erosion method allows the use of lower pressures to penetrate any strength concrete.

A waterjet capable of cutting concrete would have useful application for cutting duct entrances in manholes or building walls or even removing entire wall sections to allow for building expansion.

Large-Diameter Tunneling (Utilidor)—This application would have an effect not only on utility construction, but also on subway construction and the mining industry. The large tunnel sizes dictate the use of many jets working simultaneously with mechanical cutters. The main advantages this method would have over drilling and blasting include higher productivity, and a reduction in the safety and health hazards, and weakened tunnel roofs due to blasting.

Duct Cleaning—Waterjetting machinery is available which is capable of cleaning and scouring cable ducts. Obstructions can be dislodged and soil buildup on duct walls removed. The nozzle head advances under its own power by means of low-pressure, high-volume jets directed backwards against the duct wall. At the front of the nozzle head, a high-pressure, low-volume jet cuts through obstructions, while radial high-pressure jets scour the duct walls. Dislodged material is carried out of the duct when the nozzle head is retrieved.

Research Scope and Objectives

In an effort to evaluate the technical feasibility of using high-pressure waterjets for utility construction, a study was conducted aimed specifically at rock trenching and pole-hole cutting. Cutting tests on nine different specimens of rock were performed. These rocks were representative of the types commonly found in Eastern Canada. They include limestone, sandstone, granite pegmatite, biotite granite, quartzite, and granite-quartz. Based on the cutting characteristics of these rocks, conceptual designs of a waterjet rock trencher and pole-hole cutter were developed. Details of the research program are presented in the following section.

In addition to the technical evaluations, the operational requirements and economics of waterjet construction tools were studied. This was achieved through a field survey which identified the field requirements and present construction costs commonly experienced in Eastern Canada. The results of this part of the investigation are also discussed.

System Concepts

Method of Cutting

Continuous waterjets can be used in two ways for the applications of interest to the utility industry. In the first method, waterjets can be used to cut narrow slots which assist mechanical cutters. In the second, a combination of jets, oscillating or rotating, can cut a wide, deep slot which completely defines the shape of material to be removed. The remaining material can then be removed by energy efficient mechanical means. For the study conducted by Bell-Northern Research Ltd. and Flow Industries, Inc., the wide-slot, deep-kerf method was examined. The applications considered were pole-hole drilling and trenching in soft and hard rocks.

To demonstrate the technical and economic feasibility of waterjet trenching and pole-hole drilling, it was necessary to conduct test cutting experiments to determine operational parameters and operating rates. It is only with data such as these that estimates of cost per foot or cost per hole can be made. To determine deep-kerfing rates, linear cutting experiments must be conducted. Typically, jet pressure P_o, nozzle diameter d_o, and traverse velocity v_t are varied so that optimum cutting can be determined and scaling factors established. Figures 1-3 show typical linear cutting curves for some of the rocks tested. The standoff distance, l_o, is also indicated on these figures.

The method chosen to cut the deep kerf utilizes a nozzle with two angled jets. The jets are angled so that they cut a slot that is wider than the nozzle. The wide slot enables the nozzle to enter the slot and to maintain an effective standoff distance for both cutting rate and slot shape. In order to cover the material in the slot, the nozzle is oscillated. The resultant coverage pattern is shown in Fig. 4. The method of motion chosen was oscillation because, by applying a torsional force to a length of tubing, the necessary motion can be obtained without the use of any dynamic seals or swivels. The cut made by this device is shown in Fig. 5.

For an oscillating nozzle, the conditions for the jet can be determined from linear cutting tests. The oscillation frequency is directly related to the traverse velocity v_t; pressure and diameter of the jets are determined by the rock to be cut and available power. The cutting parameter that must then be optimized is the nozzle feed rate v_f. Such optimization curves are shown in Fig. 6 for different conditions.

From tests such as the linear cutting tests and the kerfing tests previously described, the cutting rates for the nine rock types indigenous to Eastern Canada were determined. These rates were incorporated into cutting schemes so that projected operational rates could be determined. The cutting equipment and rates are presented next.

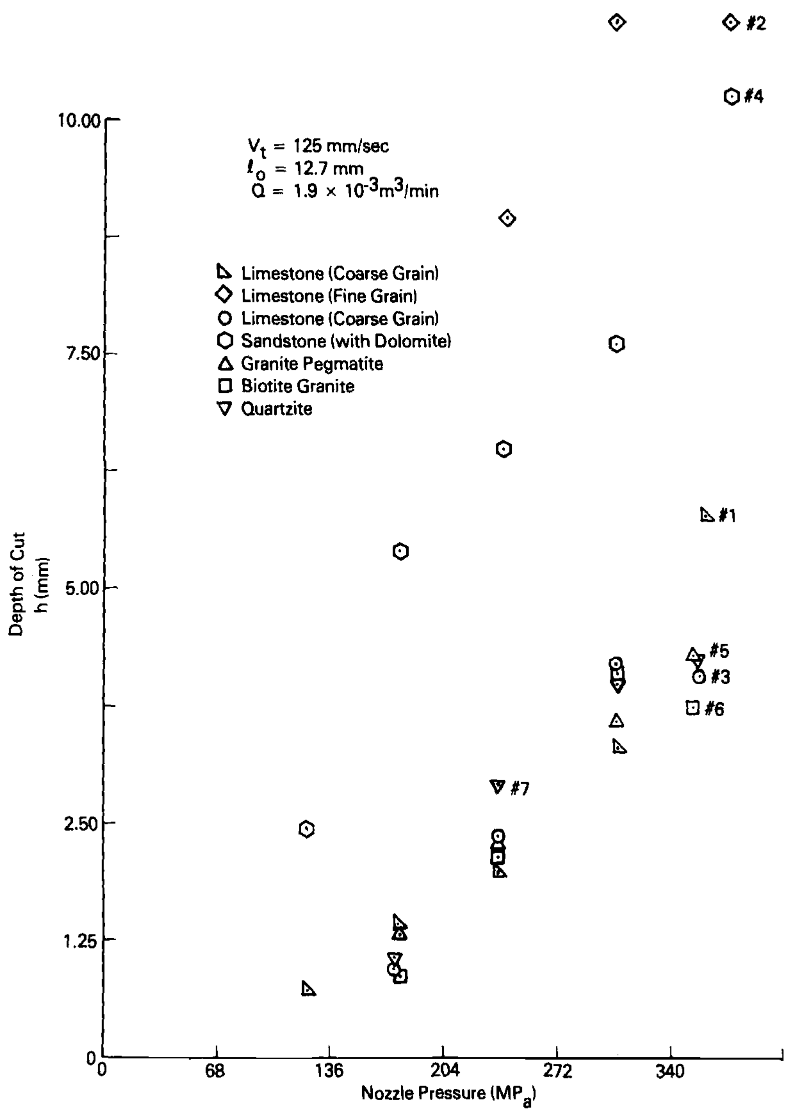

FIG. 1—*Effect of pressure on depth of cut.*

Operating Systems

Figure 7 shows a system concept for trenching and for drilling pole-holes with waterjets in rugged off-road terrain. The basic system components consist of a hydraulic power trailer, a water truck, a tractor, a trencher, and a pole-hole drilling device. Each component is described in the following.

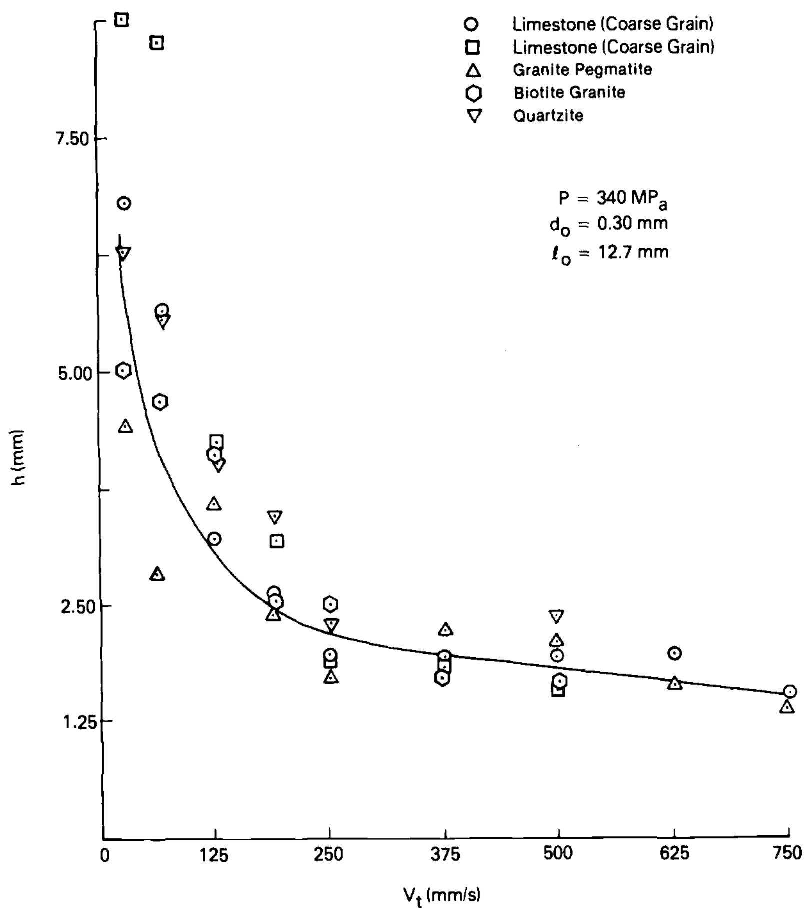

FIG. 2—*Effect of traverse velocity on depth of cut.*

The hydraulic power trailer consists of a diesel engine and hydraulic oil pump to power the intensifier, as well as an oil reservoir and oil cooler. The trailer also has space to place the tractor for transportation between sites. The engine on the trailer that is chosen must be able to power a 188-kW intensifier, which will be mounted on a tractor. These 188-kW intensifiers have been field-tested and have proven to be reliable pieces of equipment.

The tractor is used to carry the high-pressure intensifier and all trenching and drilling equipment, and to move it along the work area. The tractor is attached to the trailer by an umbilical cord, which contains an oil powerline, an oil-return line, and a water line. The umbilical cord is flexible and allows the tractor to move independently of the trailer, thus

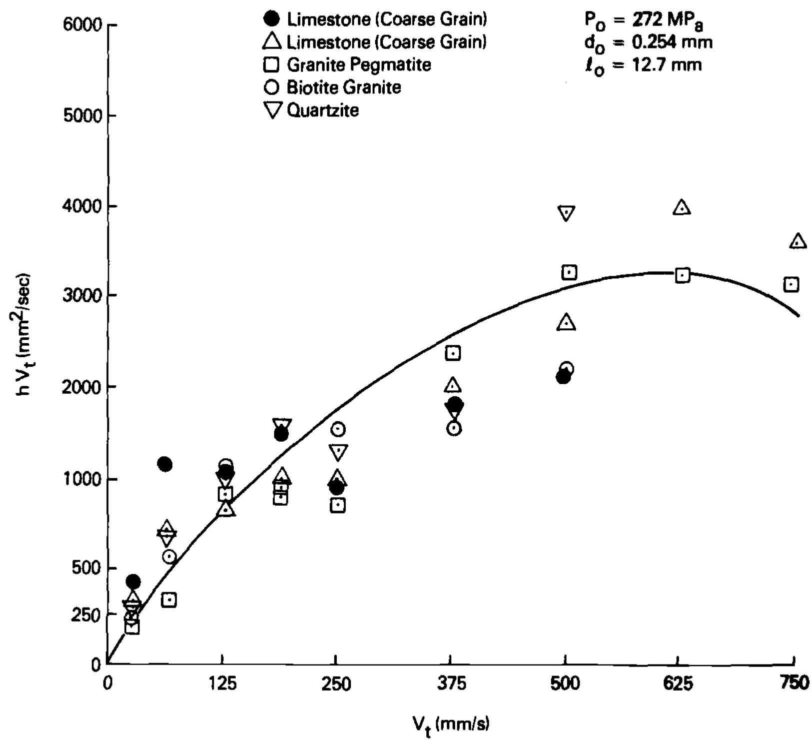

FIG. 3—*Effect of traverse velocity on area removal rate.*

minimizing the number of times the entire system must be moved. The intensifier is separated from the hydraulic power package for two reasons. First, flexible tubing can be used between the trailer and tractor instead of the rigid tubing that would be necessary if the intensifier were mounted on the trailer. Second, if both the hydraulic power package and the intensifier were mounted on the tractor, the tractor would have to be large, and its ability to move over very rugged terrain and to work in confined areas would be hampered.

The tractor and the hydraulic trailer form the heart of the system. With these two components, waterjet cutting systems for various applications can be mounted on the tractor to do the desired job. Devices for trenching and pole-hole drilling have been conceptually designed. Both systems, mounted on a tractor, are shown in Fig. 7. The details of these systems are presented in the following subsections.

The final component of the system is the water truck-trailer. This component supplies the water for the jets and the oil cooling water. It

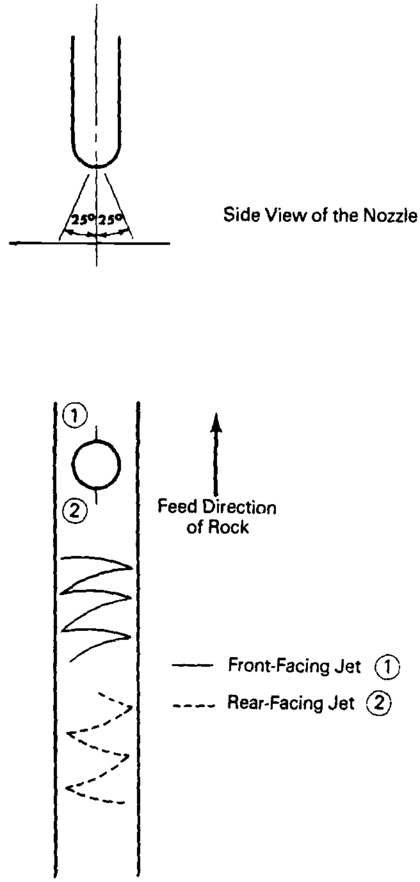

FIG. 4—*Deep-kerf nozzle coverage pattern.*

would require 0.028 m^3 of water per minute to provide 188 kW and a waterjet pressure of 374 MPa. Based on a running time of 6 h/day, 10 m^3 of water per day would be necessary. Since water may not be available at the work site, this amount of water can be supplied best by a water truck.

These three components—the water trailer, the tractor, and the hydraulic power trailer—make up the waterjet cutting system. When used in conjunction with special devices, this system can be used for trenching and hole drilling in addition to other applications.

Waterjet Trenching Device—Both the waterjet trenching device and the pole-hole drilling device operate on the same principle of cutting. Both devices use an oscillating deep-kerf device to cut the slot. In addition, both have a mechanical breakout device which removes large pieces of material,

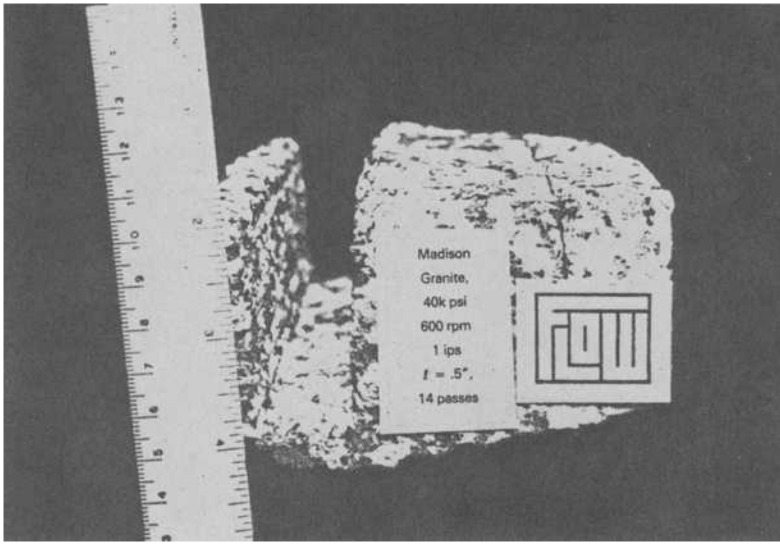

(a) Deep-Kerfing Cut

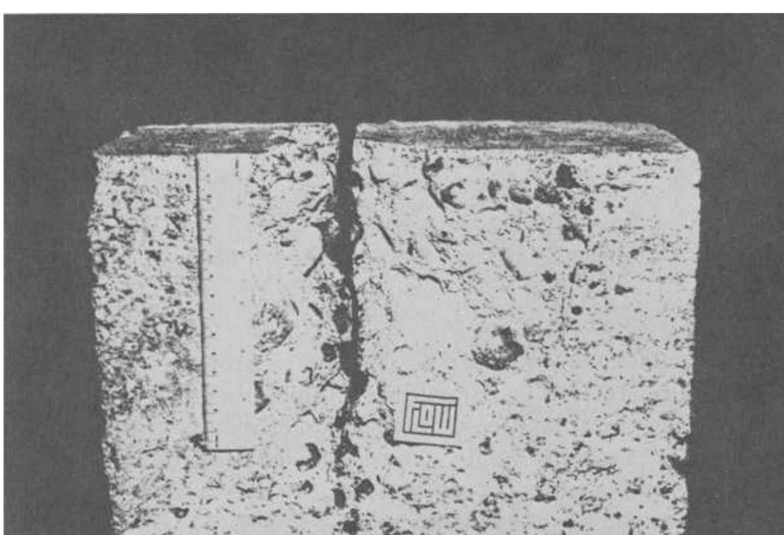

(b) Three Parallel Cuts (Multiple Pass)
(Clear Slot Depth = 51 mm)

FIG. 5—*Oscillating kerfing cuts and parallel linear cuts.*

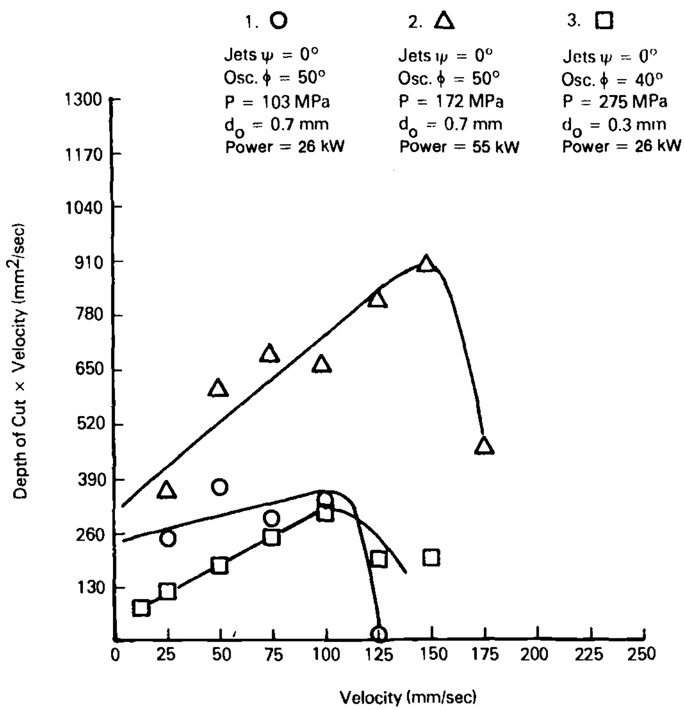

FIG. 6—*Effect of horsepower on cutting performance.*

thus minimizing the amount of material that must be excavated by the oscillating deep-kerf device. From laboratory and field experience, a combination waterjet and mechanical system is the most efficient system from both energy and time considerations.

Figure 8 is a conceptual drawing of the waterjet trenching device, which consists of a pair of oscillating nozzles, each of which is capable of delivering up to 94 kW to the rock. The nozzles are located on a frame, which gives them the necessary motion. Each nozzle has controls that allow *x-y-z* motion in order to cut a trench of a desired depth and width. The *x-y-z* motion is controlled hydraulically from controls located on the tractor. The nozzle oscillation is supplied by a rotating hydraulic motor which converts the rotation to oscillation by a cam-type arrangement.

The frame, as shown in Fig. 7, is attached to the tractor by hydraulic cylinders which can raise and lower the frame. This movement is used for adjusting the position of the frame and for leveling. Once the frame is in place, the trenching operation is controlled from the tractor. The trench is cut to the length allowed by the traverse mechanism. Upon completion of a given length of trench, the tractor raises the frame and moves forward

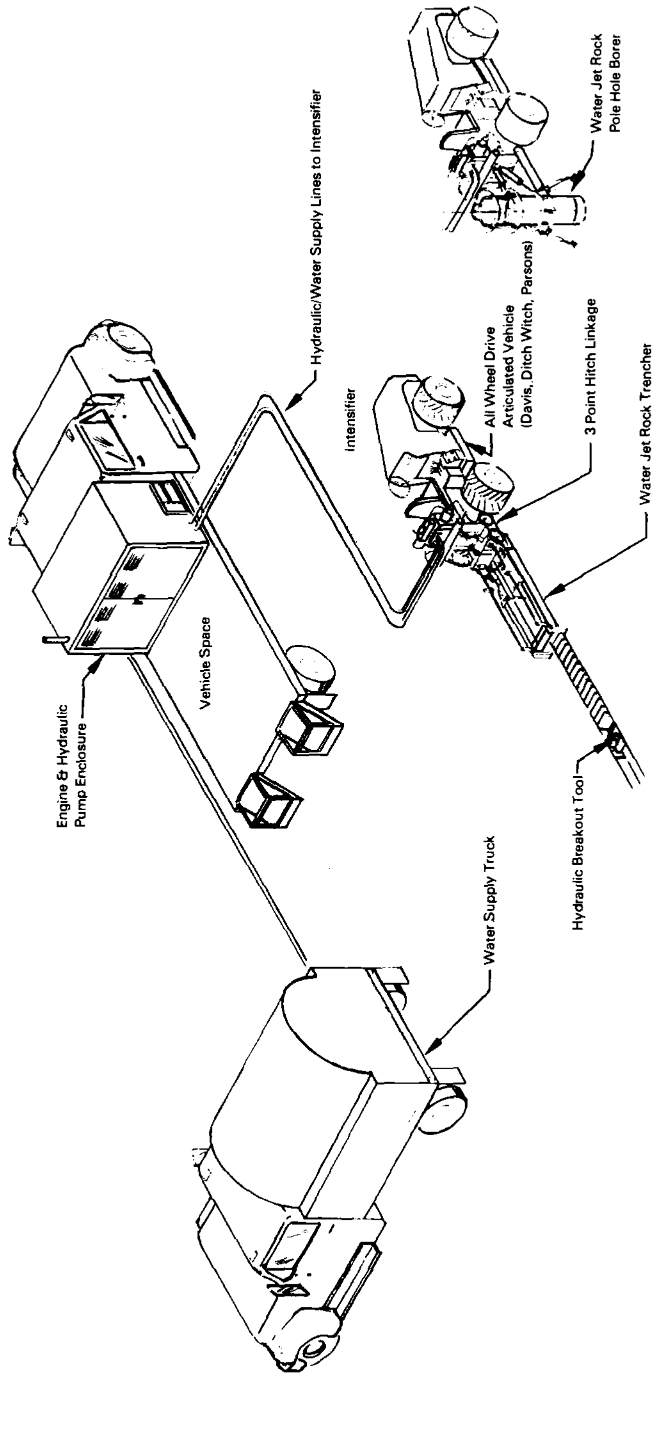

FIG. 7—*Trench and pole-hole drilling system schematic.*

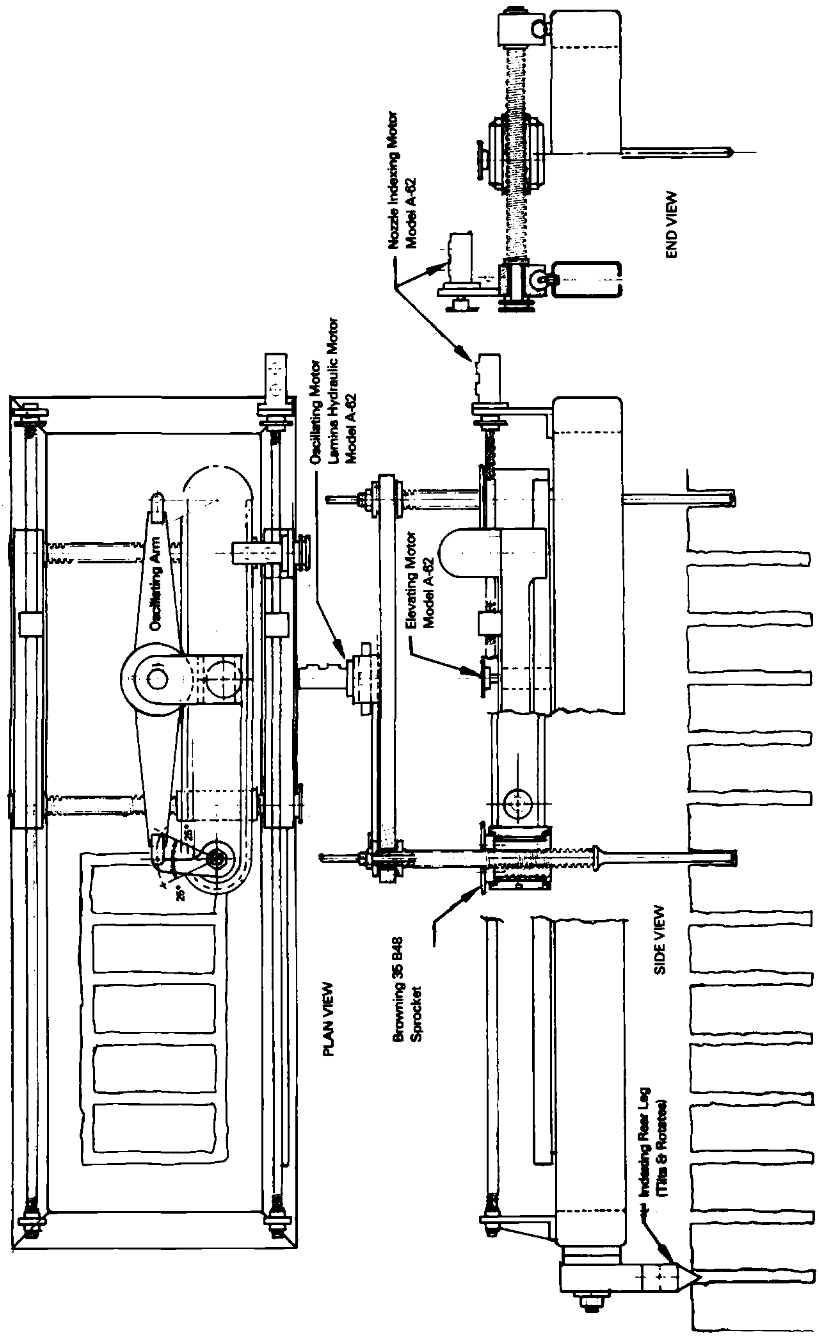

FIG. 8—*Waterjet trenching device schematic.*

to the new position. While the tractor is being moved, a hydraulic breakout tool is used to break out the rock sections left by the waterjet trencher. One such handheld device is shown in Fig. 7. The basic progression just described will be followed until the trench has been cut the desired length. The trench cutting process with the waterjets will probably be slower than the breakout process. If so, the cutting will be the controlling factor in the advance rate. Consequently, optimizing the cutting process will increase the trenching rate.

At the present time, a trenching method that uses two pairs of nozzles is being considered. The two nozzles will cut both sides of the trench in one motion. After the sides have been cut to the desired depth, the nozzles will then move sideways across the trench and form blocks along the length of the trench. The blocks will then be removed by the hydraulic breakout tool.

The conceptual design in Fig. 8 includes some possible drive mechanisms and indicates various components. This design is by no means a detailed one; however, it is meant to be a realistic conceptual design that, with additional detailing, could be built. Changes to the design will have to be based upon considerations of the terrain, environment, and actual operating parameters.

Waterjet Pole-Hole Driller—As in the trencher, the basic cutting mechanism for the pole-hole driller is the oscillating deep-kerf nozzle. The deep-kerf nozzles are used to cut a core, which is then removed by a mechanical breakout tool. The resulting hole is slightly larger than the pole so that minimum work is required to secure the pole in the ground. The conceptual design for a waterjet pole-hole driller is shown in Fig. 9.

The pole-hole driller is mounted in the rear of the tractor and can be raised and lowered during moves from placement site to placement site. When the device is located over the desired spot, it is leveled by the tractor hydraulics, and three legs are put in place to form a secure tripod base for the hole driller. Once the tripod is in place, drilling with the waterjet begins. The waterjet cuts the circumference of the hole, leaving a core, which is then removed by a special breakout tool.

The device shown in Fig. 9 has been proposed to cut the core for the pole-hole. This device has two oscillating deep-kerf nozzles to cut the kerf and has, in addition, a secondary oscillating device which slowly oscillates the deep-kerf nozzles (180 deg) so that they cover the entire circumference. This approach was decided upon instead of a swivel because the oscillating device is more reliable. If a reliable high-pressure swivel is developed, then the swivel would be an alternative to oscillation. A third motion is required to cut the core. This third motion, the downward motion of the core barrel, is achieved by a motor that raises and lowers the device with a screw device. This device can drill only one size hole; if a larger or smaller hole is desired, then a new barrel would be required.

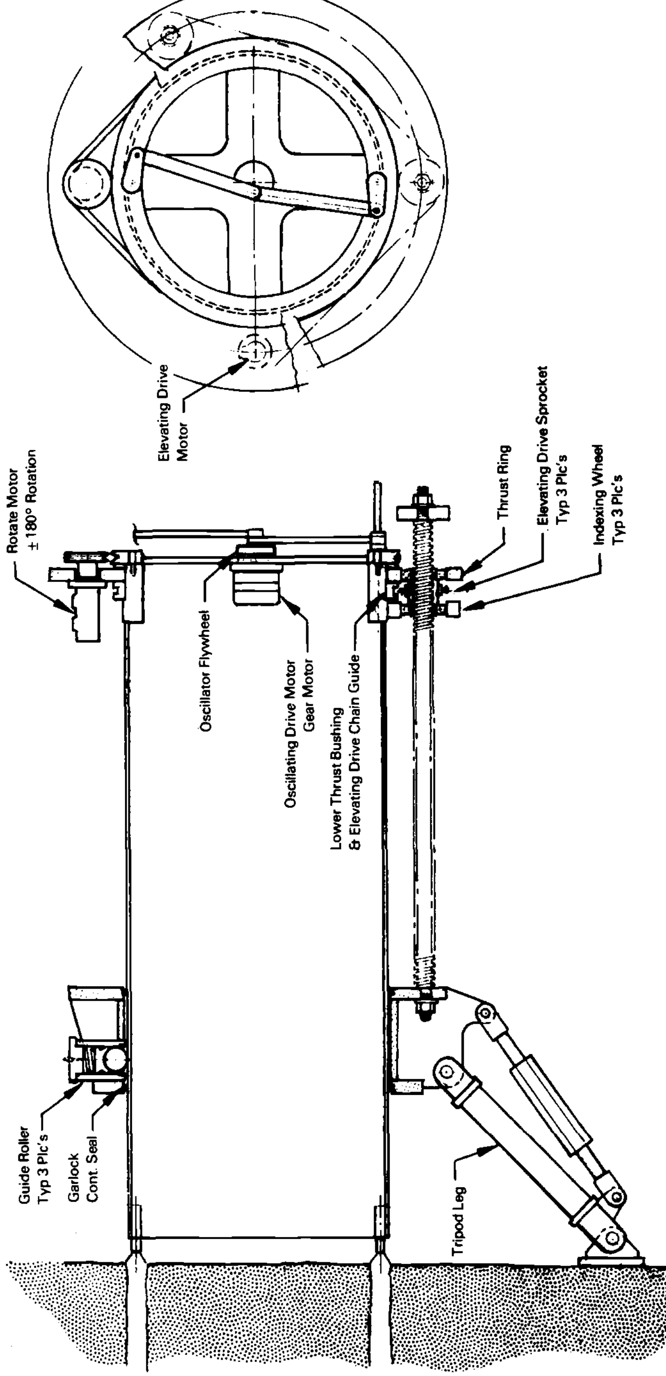

FIG. 9—*Pole-hole driller schematic.*

Projected Cutting Rates

Based on the experimental data, rates can be predicted for cutting pole-holes and trenches. In the laboratory tests, the kerfing nozzle delivered approximately 22.5 kW to the rock. In the proposed trenching machine, 188 kW would be available to power the nozzles. If two pairs of nozzles were used, then each kerfing nozzle would have 94 kW to power it. The depth of cut is determined by direct linear scaling of the cutting data. An estimate of the field cutting rates is presented next.

Trenching—A typical trench would consist of two parallel cuts and a cross cut. Rates for two trench sizes are as follows.

1. Trench dimensions: 100 mm wide by 150 mm deep
   Kerf spacing: 150 mm
   2 nozzle pairs: 94 kW/pair
   Nozzle traverse rate: 100 mm/s
   Nozzle cutting rate: 3.75 mm/pass
   Number of passes to cut: 150 mm = 40
   Side cuts: 40 passes by 3 s/pass = 6.67 min/m
   Cross cuts: 40 passes by 1 s/pass = 2.22 min/m
      Total cutting time: 9 min/m
      Advance rate: 6.67 m/h
2. Trench dimensions: 250 by 300 mm
   Kerf spacing: 150 mm
   Side cuts: 80 passes by 3 s/pass = 12 min/m
   Cross cuts: 6 cuts/m by 80 passes by 2.5 s/pass = 20 min/m
      Total cutting time: 33 min/m
      Advance rate: 1.8 m/h

Pole-Hole Drilling—The pole-hole drilling consists of cutting a core of a given diameter to a specified depth. Rates for two hole diameters are

1. Diameter: 0.355 m; depth: 0.915 m
   2 nozzle pairs: 94 kW/pair
   Nozzle traverse rate: 100 mm/s
   Nozzle cutting rate: 3.8 mm/pass
   Path for each nozzle: 0.56 m (half the circumference)

   $$\text{Time/hole: } \frac{560\text{mm}}{100\text{ mm/s}} \times \frac{240\text{ passes}}{60} = 22\text{ min}$$

   Drill advance rate: 2.5 m/h
2. Diameter: 0.5 m; depth: 0.915 m
   Path for each nozzle: 0.8 m

   $$\text{Time/hole: } \frac{0.8\text{ m}}{0.100\text{ m/s}} \times \frac{240\text{ passes}}{60} = 32\text{ min}$$

   Drill advance rate: 1.75 m/h

Operational Requirements and Economics

Operational Requirements

If high-pressure waterjets are to become practical construction tools for use in the field, they must be capable of meeting certain operational requirements. These requirements will of course vary with the specific application and field conditions. For example, in most of Canada and northern parts of the United States, waterjet tools should be capable of operating under winter conditions. This requirement is obviously not so important in the southern parts of the continent. Similarly, rock cutting tools may have to be capable of cutting a wide variety of rock types and strengths in some geographical locations, whereas in other locations the variation in rock properties over large areas may be relatively insignificant. Some of the more general operational requirements are as follows.

1. As a utility construction tool, the waterjet unit must be easily transportable and maneuverable.
2. Certain applications such as rock trenching, pole-hole cutting, frozen soil trenching, and guy anchor drilling will require the waterjet unit to have an all-terrain capability. This is particularly important in areas where large amounts of rural distribution systems exist.
3. The equipment must be capable of operating in all weather conditions. This implies that north of the 40 deg parallel the equipment should be operable in the temperature range of $-30°C$ to $+35°C$.
4. Additions to the water supply, such as deicers, must be nonpolluting.
5. The equipment must be designed so that a utility company craftsperson can operate and maintain the equipment after a nominal training period.

There are, of course, many other operational requirements specific to each application. From a utility construction viewpoint, however, one of the most important ingredients to the successful implementation of waterjet tools is public acceptance. Since utilities find themselves working virtually in the front lawns and backyards of the general public, the environmental impact of this technology is a major consideration. In fact, this aspect is deemed to be one of the major advantages of waterjet tools. Compared with jackhammers, concrete saws, and blasting, waterjet tools should create considerably less noise and air pollution. Furthermore, when used in a populated environment, waterjets impose considerably less physical danger and discomfort to the general public.

Economics

Since none of the waterjet tools described in this paper have yet been developed on a commercial basis, it is very difficult to establish a factual economic history. The best one can do at this stage is to compare the present-day cost for various types of utility construction to the predicted or estimated cost of achieving the same end result using the appropriate waterjet concept. It is important to recognize that in this type of economic analysis the construction methods used in achieving the same goals, using conventional methods or the waterjet method, may be quite different. For example, trenching small cables in rock will normally require the excavation of a comparatively large trench using conventional blasting techniques. This is due to limitations on the smallest size of trench that can be practicably blasted. Using the waterjet kerfing technique, however, allows one to cut trenches proportionate to the size of cable being placed. Therefore, although the same size of cable is placed, the total amount of rock excavated may be substantially less with the waterjet than by blasting. An economic comparison based strictly on conventional trench sizes is therefore misleading.

An analysis of rock trenching for distribution cable installations reveals that in Eastern Canada the total cost for installing small-diameter (less than 50 mm) cables is approximately \$15 to \$24 per metre. Based on the cutting rates described earlier and on the following assumptions.

1. A three-man operation—that is, one man operating the waterjet, and two men the water truck—preclean the trench, break rock kerfs, and place and backfill cables.

2. The trenching rate per hour is limited by the cutting rate of the waterjet. This means that precleaning and breaking rock kerfs can be performed while the trench is being cut.

3. The trenching rate is approximately 6 m/h; therefore, the labor cost for trenching at \$15 per man-hour is \$45 per 6 m or \$7.50 per metre. The cost of placing cable and backfill is estimated at \$4.00 per metre. Finally, the cost of moving and setting up the machine is estimated at \$0.50 per metre. This results in a total cost of approximately \$12 per metre for waterjet kerfing. For larger cables and pipes requiring larger trenches, that is, for greater than 0.05 m^2 in cross section, conventional blasting techniques are generally less costly than the waterjet kerfing technique. There is, however, some indication that a combination of waterjet kerfing and controlled blasting could result in a cost-effective method of creating larger trenches in rock. This technique has yet to be investigated.

The average cost for installing telephone or hydro utility poles by blasting in hard rock is \$180 per pole in Eastern Canada. In soft rock (for example, limestone, shale, sandstone), the present installation method costs approximately \$100 per pole. These costs do not include the price of the pole. The cost of installing poles in hard rock using the waterjet technique is broken down as follows.

1. Assume it is a three-man operation—that is, one man operating and cleaning the sites and two men placing and backfilling poles:

Preclean and set up	30 min
Drill 1.22 m	30 min
Excavate	15 min
Place pole and backfill	0 min
Move machine	10 min
Total time per installation	85 min

2. The labor cost per installation at $15 per man hour is

$$(3 \times 15) \times \frac{85}{60} = \$63.75$$

Operating expenses:

Gas and oil	$ 3.50
Cost of moving machine/pole	$ 9.50
Cost of backfill material	$12.00

The total cost per installation using the waterjet is $88.75.

These costs will of course vary across the continent. The relative cost difference between present construction methods and the waterjet methods should, however, remain approximately the same. These cost comparisons illustrate that substantial cost reductions can be achieved with high-pressure waterjet tools. What remains to be proven is the technical and practical capability of waterjet tools under field conditions.

Conclusions

The results of this research indicate the following:

1. Waterjetting technology has reached the stage where cutting various types of hard and soft rocks is a technically and economically viable application.

2. More specifically, to the utility industry, waterjetting can impact on the following applications: pole and anchor hole cutting, rock trenching, frozen ground excavation, ice cutting, and concrete cutting.

3. The use of waterjets for rock cutting applications could yield economic payoffs in the order of 20 to 50 percent over present methods.

4. Waterjets are cleaner, safer, and generally less destructive to the environment than existing rock cutting or excavating tools.

5. Waterjet systems have proven to be reliable and easy to operate in factory applications.

6. Using waterjets, the productivity rates for trenching and pole-hole cutting are an improvement over rates achieved with conventional methods.

Summary

Summary

The field of erosion encompasses a diversity of problem areas, and studies are initiated for a variety of reasons. The investigation of erosion phenomena has been motivated mainly by the appearance of a critical problem in a system which adversely affects the operation or minimum performance levels of that system. Excessive operating costs associated with helicopter roter blades in sandy terrains, ingestion of particulates into gas turbines, liquid drop erosion in steam turbines, and cavitation erosion of ships' propellers have stimulated a fair amount of research into ways of reducing or eliminating the resulting erosive damage. Thus erosion of materials has not been investigated in a very organized manner. When the erosion problem becomes severe enough, something is done about it; but, once the need is satisfied or the initial requirements change, the ongoing investigations are terminated. Specialized equipment is constructed and used to get one result, then abandoned; testing programs are initiated for screening purposes, but the types of materials evaluated are far-ranging and so a coherent trend within a class of materials cannot usually be established. This lack of a continuing effort in relation to a particular erosive environment or material category has resulted in a fairly disjointed literature.

This trend is reflected in the contents of the four previous ASTM symposia on erosion [*1-4*].[1] The first *STP* on erosion [*1*] contained six papers with liquid drop, solid particle, and cavitation erosion about equally represented. The contents of the next three *STP*'s [*2—4*] are equally divided between papers on topics in liquid impingment and cavitation erosion. During the period covered by these three volumes (1966 to 1974), only one paper was included on solid particle erosion [*5*]. These observations are interesting in relation to the contents of the present *STP*, in which more than a third of the papers are devoted to solid particle erosion, followed by liquid drop erosion, with a much smaller representation of cavitation erosion investigations. The present volume also contains a significant number of papers covering waterjet technology and waterjet applications. These topics are included as constructive uses of controlled erosion damage.

Thus it would appear on the basis of this limited sampling that a de-

[1] The italic numbers in brackets refer to the list of references appended to this paper.

cisive shift in the problem areas of major concern has taken place over the past few years. This is due in part to recognition and engineering experience in the magnitude of the erosion problems which will be encountered in coal conversion processes [*6*] and the need for improved mining procedures using liquid jets [*7*].

The objective of an erosion investigation is an important consideration in the research adopted and the level of effort required. For example, the erosion rates for specific materials may be needed to implement semi-empirical correlations for design purposes; screening of state-of-the-art or developmental materials or both may be required in order to select the best material for a particular application; or a material development program may be required to improve the erosion resistance of a restricted class of materials as dictated by other engineering considerations.

Material screening with respect to an erosive environment is represented in the papers by Hansen [*8*], Schmitt [*9*], and to a lesser extent in the papers by Gulden [*10*] and Barkalow et al [*11*]. Many of the general material screening programs in the past were based on the use of specialized erosion equipment which was not readily available. Therefore a considerable amount of the data generated are unique to the erosive environment utilized for the application of interest. The ASTM G-2 Committe has been active in trying to standardize the test conditions for widely used erosive devices and, when this is not possible, to at least standardize the data reporting procedure. These efforts should make the data obtained have more general utility than would otherwise be possible.

An important aspect of material screening, if it is to be reasonably independent of the laboratory conducting the tests, is characterization of the erosive environment. The paper by Maji and Sheldon [*12*] indicates that the initial characteristics of the solid particles used in a blast tube apparatus can be significantly modified in the apparatus itself before reaching the specimen's surface. This effect is dependent on the properites of the particles used, but it points out the need for detailed characterization of the erosive environment a specimen actually experiences even for a widely used test configuration. These effects are important with respect to establishing accurate correlations with the material properties of the material being tested.

Along these same lines one notes that there is a much stronger materials orientation represented in this volume compared with the previous volumes [*1-4*]. More work is devoted to examining the eroding material microscopically and to undertaking more basic investigations of the changes which occur in the material as well as identification of the microstructural features which may contribute to the onset and development of the erosion damage. The work of Ives and Ruff [*13*] provides understanding of the changing character of the eroding surface of copper specimens subjected to solid-particle impacts. Using metallographic procedures, they were able to observe the role of particle embedding as a function of attack angle and length of exposure as well as the subsurface damage produced. On the basis of these observations a model is proposed to describe the embedding process. Their results emphasize the fact that the surface layer of highly ductile materials is transformed into a composite material as the erosion process proceeds, with properties which can be quite distinct from those of the initial material. The range of materials for which particle embedding is a significant effect and a quantitative evaluation of how it may influence the erosion rates for the initial target material require further investigation. The latter consideration may have important implications in attempts to correlate the measured erosion rates with the original thermomechanical properties of the target materials.

A number of conceptual models have been used as the basis for the development of analytical descriptions of erosion processes. Generally these models do not incorporate an accurate experimentally based representation of the material removal process into the analytical formulation. The mode of material removal is simply a conjecture or is not specified at all in several of these analyses. Within the past few years, however, experimental studies pertaining to erosion mechanisms have been pursued, so a better indication of what is actually responsible for material removal can be obtained. These approaches are represented in a number of the papers in this volume.

Finnie et al *[14]* and Hutchings *[15]* have provided reviews of much of the work on modeling solid-particle impact damage and the range of erosion mechanisms which have been proposed in the past. Professor Finnie's discourse on his modeling efforts over the past 20 years was a significant contribution to the symposium which was instructive to all in attendance. His perspectives are incorporated in the paper by Finnie et al *[14]*, which explains recent extensions of his notable early contributions to the solid particle erosion literature.

Hutchings *[15]*, on the other hand, idealizes the solid particle erosion process in a series of clever single-particle impact experiments which can be used to model the mechanics of particle impacts on metallic surfaces. This work is quite innovative in the field of solid particle erosion and a much needed new approach to advance understanding of the particle/target interactions, which are extremely difficult to identify for more conventional solid particle erosion test conditons.

Adler and Evans *[16]* have constructed a reasonably complete description of the impact process and the potential sources for the damage associated with hypersonic solid-particle impacts on carbon-carbon composite materials. This is the first time that a number of observations derived from microscopic examinations of the impacted specimens, high-speed photographic records of the impact event, idealized experimental conditions, and relevant analyses of the transient response of the target have been ature erosion rate, and that the corrosive environment can also cause the results obtained are of limited interest, the scope of the investigative procedures used to obtain them is instructive as a productive methodology for wider-ranging problem areas in the field of particulate erosion.

The paper by Preece and co-workers [*17*] is somewhat unique in the field of cavitation erosion in that it examines the process by which material removal develops on metallographically prepared specimens of pure metals exposed to the cavitation field generated by an ultrasonic horn system. The influence of the microstructure of these metals, primarily grain size, on the material removal process is evaluated. An important conclusion from this work is that there is probably no simple correlation between bulk quasi-static mechanical properties and cavitation erosion resistance as was so often thought to be the case in the past [*18*]. This general conclusion—that any correlations between erosion resistance and material properties must also include the microstructural characteristics of the material and in some cases the surface condition—is becoming more widely recognized in the field of liquid drop impingement. These findings from detailed investigations of liquid drop and cavitation erosion mechanisms cast doubt on the universality of the correlations developed by Thiruvengadam [*19,20*] and Springer [*21,22*] based exclusively on mechanical properties of the material. The success of these latter approaches is that they consider a generic representation for a class of materials, emphasizing that a definite trend is established for an extensive range of materials. There are also more basic conceptual errors inherent in these correlations as pointed out by Adler [*23*]. Those investigators concerned with identifying actual erosion mechanisms and trying to improve the erosion resistance of a particular material are looking at a much more restrictive class of materials. The work of Preece et al is an example, among several, which demonstrates the magnitude of the change in the erosion rate which may result from modifications in the basic material. The data base is still too restricted to obtain an accurate quantitative estimate of how much the fabrication process, surface finish, microstructural features, and bulk mechanical properties can affect erosion resistance; however, the effect can be significant for both metals and nonmetals.

Relatively little of the solid particle erosion data pertain to elevated-temperature test conditions. However, the major impetus for the development of elevated temperature and corrosive environmental testing capabilities and procedures is the need for these data in the cost-effective operation of coal conversion plants [*6*]. The work presented by Finnie et al [*14*], Tabakoff and Wakeman [*24*] and Barkalow et al [*11*] is a small sampling of the work which will be appearing in these areas over the next few years. It is seen from these preliminary studies that elevated temperatures can increase the erosion rate for some metals compared with the room temperincorporated into a coherent picture of the crater formation process. While significant changes to occur, with the magnitude of the enhancement effect dependent on the size and properties of the erosive particles.

The addition of elevated temperatures and corrosive environments to the list of test parameters which must be considered in solid particle erosion testing expands to unmanageable proportions the screening test matrix to evaluate the effects of the test conditions on the erosion rate for a single material. Consideration should therefore be given to the information required and an organized and coordinated program should be established as soon as possible to optimize the data collection activities which may be required [*6*]. There are several functions the ASTM G-2 Committee can provide for this purpose: round-robin testing for evaluating the variability in test results due to the test procedures in different laboratories and for developing a broader data base than otherwise would be possible; standardization of the test reporting procedures for enhanced data interchange; and establishment of study groups to resolve general issues concerning a range of erosion/corrosion problem areas and to serve as a focal point for interaction among active workers in various erosion-related fields. Moreover, the magnitude of the erosion/corrosive conditions which may have to be considered warrants support for more detailed materials-oriented investigations for the purpose of identifying the commonality of erosion mechanisms and dominant material properties influencing the erosion rates. These investigations should provide guidance for the development of materials with improved erosion resistance and contribute to limiting the scope of the test evaluation required.

The work of Menguturk and Sverdrup [*25*] illustrates the steps required to use erosion (and ultimately erosion/corrosion) data for practical applications. A number of questionable assumptions are made in their analysis of particulate erosion of the blading in a gas turbine, however, in going through the available flow analyses and incorporating the available erosion data, although not completely relevant, they have demonstrated the weaknesses in the existing erosion data base. This paper represents an example of how much of the work contained in the other papers on solid particle erosion in this *STP* will be utilized and provides some idea of the directions for improving the form these data must have to be useful for design purposes.

The water drop impact damage modeling carried out by Rosenblatt et al [*26*] raises several interesting issues. For example, how well are the material properties controlling liquid impact damage in the subsonic regime represented in these computations? How much can be learned from a computer modeling effort of this type for improving the erosion resistance of a specific material, such as zinc selenide? Is the cost of these computations, which increases as more of the microstructural features of the material are included in the computer model, justified in comparison with a more direct materials-oriented approach?

Numerical analyses of particle impact have been extensively developed for the hypersonic velocity regime where a hydrodynamic response of the material is assumed. A strong interaction between the impacting particle and penetration of the target material takes place; the final crater dimensions are to be determined. At subsonic impact velocities the water drop is much less damaging and subtle changes occur within the target material governed to a large extent by its microstructure and defects in its microstructure. Computational representations for a polycrystalline target material with an average grain size on the order of to two orders of magnitude less than the drop diameter become exceedingly complex if they are to simulate the microstructural features of the target, such as textural variations, solid inclusions, grain orientations, and grain boundary strengths. One therefore questions if the investigation of the contribution of these features to damage initiation can be more productively accomplished by well-conceived experiments and detailed materials characterization. Rosenblatt and co-workers have made a significant contribution to the evaluation of the spatial and temporal distributions of pressure for a water drop impacting rigid or elastically deformable surfaces at subsonic velocities. This pressure distribution, as described in their paper [*26*], can be used to provide some idea of the temporal development of the stresses in a homogenous and isotropic elastic body as a guide in identifying those regions within the target where critical stress conditions are likely to occur; however, caution is advised in going beyond this basic model in that the novelty of the explicit computational results may overshadow the physical aspects of the actual fracture initiation and propagation process. Numerous computations can be made, but these have to be balanced against the real extent to which the numerical results contribute to improvement of the erosion resistance for a particular material.

The foregoing perspective on the role of finite-difference models in subsonic water drop impact damage would not be necessary if Rosenblatt et al [*26*] did not stipulate that one objective of their work is to identify the mechanisms responsible for internal crack formation and propagation in infrared windows subjected to *subsonic rain erosion*. However, there is nothing in the paper which is directed toward this objective. The relevance of a numerical analysis is to describe and provide quantitative data for a physically observed mechanism. A considerably more detailed computational model would be required before a crack formation mechanism could be *identified* in zinc selenide via a numerical simulation. The authors have not identified any mechanisms but have assumed a particular model and a critical crack length for their computer analysis of the damage due to a single water drop impacting a zinc selenide target. Once the model is accepted, then the sensitivity of the fracture response can be computed in terms of the relatively few material parameters and the impact parameters entering the numerical analysis.

It is difficult to rectify on physical grounds the nature of the crack patterns shown in Fig. 19 and 22 of Ref *26*, especially Fig. 22. (A question about this was raised by N. MacMillan (p. 000) and does not appear to have been adequately addressed by the authors.) The cracks produced in a real material would be discrete with a quantity of undamaged material separating these cracks. The numerical results imply that a large quantity of material would be highly fragmented and would in essence be free to fall loose from the specimen. This does not seem to be the case for actual drop impacts at velocities below 342 m/s (1120 ft/s). The manner in which the failure criteria are introduced in the numerical computations and the way in which the stress is redistributed in the computer code once a cell is fractured appear questionable. The cell size may be too large for the fracture response which is to be described. Therefore the stated fracture trends for the grain size and flaw size variations have no significance until the fracture patterns can be properly interpreted.

Furthermore, the final crack formations are on a scale such that comparisons with experimental data are almost meaningless. The authors have been adjusting their results to compare with experimentally observed fracture patterns as they become available [*27*]. In essence, they are simply describing general observations and not providing directions for optimization of material properties for increased erosion resistance. Modeling the dynamic fracture response of a polycrystalline material and the onset of fracture in homogeneous brittle materials due to water drop impingement are complex problems if the computational models are to reflect a realistic picture of the material and its surface condition [*28,29*].

There are many aspects to erosion modeling. The most prominent is the development of a predictive model. A predictive model provides the capability to prescribe the rate of material removal from a particular material exposed to a specified erosive environment. Although several examples of semi-empirical correlations can be found in the literature [*14,15*] and several attempts to derive definitive predictive models can be cited [*30,31*], it seems doubtful that a definitive predictive model will be forthcoming in the near future. A predictive model implies that the erosion rates can be determined entirely from data independent of erosion test data. All the models proposed for this purpose invoke empirical correlations at some point in their implementation. However, computer simulations (models) can be helpful in obtaining quantitative information on various aspects of the material removal process in all fields of erosion. In contrast to the approach of Rosenblatt et al [*26*], the computer analyses should be formulated on the basis of materials-oriented models which characterize the dominant failure modes that can occur in a particular material or class of materials [*30,31*]. With more investigators examining erosion damage on a microscopic scale, there is excellent potential for developing physically realistic computer analyses for small portions of the general erosion process.

The papers herein pertaining to waterjets are concerned with concepts to improve their cutting or fragmentation capability [*32*—*34*] and with some of the applications for waterjets [*35*—*37*]. At the present time there is considerable emphasis on the development of systems for particular areas of application. The general approach is thus the reverse of that described in relation to particulate and cavitation erosion, where the response of the material and ways to improve its erosion resistance are of prime concern, since it is now the creation of a more effective erosive environment which is the major consideration. There is considerable breadth exhibited in the innovative systems for enhancing, concentrating, or pulsating a jet. However, the measure of its effectiveness is typically evaluated in terms of its gross cutting rate. To date, there does not appear to be any concentration of effort on just what is happening to the material as the jet penetrates or cuts it. Detailed investigations of the jet/material interaction should certainly contribute to customizing or selecting the jet configuration which would be most efficient for a particular material. Some initial evaluations along these lines were described by Vijay and Brierly [*38*].

There is a problem, however, in comparing one waterjet system with another in that criteria must be established which are acceptable to most workers in the field for making such a comparison. The ASTM G2 Committee is presently addressing this critical issue. A second area under consideration is the selection of standardized materials for specifying cutting rates.

In summary, there are several areas of erosion receiving attention at the present time which represent a change in emphasis from the recent past based on the contributions to this publication. The areas of current interest are solid particle erosion at ambient and elevated temperatures and in corrosive environments for metals and ceramics, limited applications of liquid drop impingement primarily for nonmetallic materials for high-speed aircraft and coupled erosion/ablation of reentry vehicles, with relatively little activity in cavitation erosion. The background of an increasing number of contributors to the erosion literature is in metallurgy or materials science, so basic materials investigations of erosion are becoming more prevalent. The identification of the damage modes in real materials coupled with accurate representations of the mechanics of the erosion process should be productive in advancing basic understanding of the of the erosion of materials. This general level of activity in several erosion problem areas (different from the past) is once again becoming substantial, so the prospects for many important advances in combating the erosion process in certain material systems and for the development of improved erosion-resistant materials are most encouraging. It is hoped these new investigations will be undertaken in a more organized manner than in the past.

Waterjet technology is increasing at a rapid pace to meet the demands in the growing number of application areas for waterjets, although a sizable portion of the current support is connected with mining operations. Considerable emphasis is being placed on the development of more efficient waterjet systems; however, it is envisioned that once optimization of the general system parameters has been achieved, the material damage mechanisms will be considered in more depth to determine additional directions for improving jet operating efficiencies. The erosion process due to cavitating fields and water drop impingement may be helpful in understanding the damage produced in the material by various waterjet systems.

W. F. Adler

Effects Technology, Inc., Santa Barbara, Calif. 93111; editor.

References

[1] *Symposium on Erosion and Cavitation, ASTM STP 307*, American Society for Testing and Materials, 1962.

[2] *Erosion by Cavitation on Impingement, ASTM STP 408*, American Society for Testing and Materials, 1967.

[3] *Characterization and Determination of Erosion Resistance, ASTM STP 474*, American Society for Testing and Materials, 1970.

[4] *Erosion, Wear, and Interfaces with Corrosion, ASTM STP 567*, American Society for Testing and Materials, 1974.

[5] Adler, W. F. in *Erosion, Wear, and Interfaces with Corrosion, ASTM STP 567*, American Society for Testing and Materials, 1974, pp. 294-315.

[6] *Erosion Control in Energy Systems*, Publication NMAB-334, National Materials Advisory Board, Washington, D.C., 1977.

[7] Frank, J. N., "An Overview of the U.S. Bureau of Mines Hydraulic Mining Program," presented at the ASTM Symposium on Erosion: Prevention and Useful Applications, American Society for Testing and Materials, Vail, Colo., Oct. 1977.

[8] Hansen, J. S., this publication, pp. 148-162.

[9] Schmitt, G. F., Jr., this publication, pp. 376-405.

[10] Gulden, M. E., this publication, pp. 101-122.

[11] Barkalow, R. H., Goebel, J. A., and Pettit, F. S., this publication, pp. 163-191.

[12] Maji, J. and Sheldon, G. L., this publication, pp. 136-147.

[13] Ives, L. K. and Ruff, A. W., this publication, pp. 5-35.

[14] Finnie, I., Levy, A., and McFadden, D. H., this publication, pp. 36-58.

[15] Hutchings, I. M., this publication, pp. 59-76.

[16] Adler, W. F. and Evans, A. G., this publication, pp. 345-375.

[17] Preece, C. M., Vaidya, S., and Dakshinamoorthy, S., this publication, pp. 409-433.

[18] Garcia, R., Hammitt, F. G., and Nystrom, R. E. in *Erosion by Cavitation or Impingement, ASTM STP 408*, American Society of for Testing and Materials, 1967, pp. 239-283.

[19] Thiruvengadam, A., in *Proceedings*, Third International Conference on Rain Erosion and Associated Phenomena, A. A. Fyall and R. B. King, Eds., published by the Royal Aircraft Establishment, England, 1967.

[20] Thiruvengadam, A., Rudy, S. L., and Gunasekaran, M. in *Characterization and*

Determination of Erosion Resistance, ASTM STP 474, American Society for Testing and Materials, 1970, pp. 249-287.

[*21*] Springer, G. S. and Baxi, C. B. in *Erosion, Wear, and Interfaces with Corrosion, ASTM STP 567,* American Society for Testing and Materials, 1974, pp. 106-127.

[*22*] Springer, G. S., *Erosion by Liquid Impact,* Scripta Publishing Co., Washington, D.C., 1976.

[*23*] Adler, W. F., "The Mechanics of Liquid Impact," to be published in the *Treatise on Materials Science and Technology.*

[*24*] Tabakoff, W. and Wakeman, T., this publication, pp. 123-135.

[*25*] Menguturk, M. and Sverdrup, E. F., this publication, pp. 193-212.

[*26*] Rosenblatt, M., Ito, Y. M., Eggum, G. E., this publication, pp. 227-254.

[*27*] Hackworth, J. V., Kocher, L. H., and Snell, I. C., this publication, pp. 255-278.

[*28*] Adler, W. F. and Hooker, S. V., *Wear,* Vol. 48, 1978, pp. 103-119.

[*29*] Adler, W. F. and Hooker, S. V., *Wear,* Vol. 50, 1978, pp. 11-38.

[*30*] Adler, W. F., *Wear,* Vol. 37, 1976, pp. 345-352.

[*31*] Adler, W. F., *Wear,* Vol. 37, 1976, pp. 353-365.

[*32*] Eddingfield, D. L. and Albrecht, M., this publication, pp. 461-472.

[*33*] Mazurkiewicz, M., Barker, C. R., and Summers, D. A., this publication, pp. 473-492.

[*34*] Selberg, B. R. and Barker, C. R., this publication, pp. 493-511.

[*35*] Conn, A. F. and Rudy, S. L., this publication, pp. 562-581.

[*36*] Hilaris, J. A. and Labus, T. J., this publication, pp. 582-596.

[*37*] Huszarik, F. A., Reichman, J. M., Cheung, J. B., this publication, pp. 597-615.

[*38*] Vijay, M. M. and Brierley, W. H., this publication, pp. 512-529.

Index

D

Optical, 79, 105, 282, 525

R

S

T

U